Optical Characterisation of Astronomical Submillimetre Receivers including ALMA Bands 5 and 9

Presented by

Mark Whale, B.Sc. (Hons.)

A thesis submitted for the degree of

Doctor of Philosophy

NUI MAYNOOTH

Ollscoil na hÉireann Má Nuad

Department of Experimental Physics,

NUI Maynooth,

Maynooth, Co. Kildare,

Ireland

January 2010

Head of Department

Prof. J. Anthony Murphy

Research Supervisor

Dr. Neil Trappe

To my parents

Table of Contents

Abstract

The primary concern of this thesis is the analysis of long wavelength quasioptical receiver systems operating within the Terahertz and submillimetre wavebands. Specific attention is paid to the front-end coupling optics of the Band 5 and Band 9 receiver channels of the Atacama Large Millimetre Array (ALMA). The theory of Gaussian Beam Mode Analysis (GBMA) is expanded and developed as the basic analytical tool for the work presented. This technique is utilised to model both classical optics diffraction and interference patterns. An alternate method of describing these diffraction patterns is developed using the Angular Spectrum of Plane Waves (ASPW). The general GBMA technique is supplemented by the commercially available Physical Optics (PO) package GRASP9 developed by TICRA. A comprehensive analysis of the ALMA Band 5 front end optics was conducted in conjunction with the Group for Advanced Receiver Development (GARD). This analysis was developed to investigate the efficiency of various configurations of the optics and was supplemented by a rigorous measurement campaign at GARD. As part of our ongoing collaboration with the Space Research Organisation of the Netherlands (SRON) a series of theoretical and experimental analyses were performed with the aim of improving the cross polar efficiency of the ALMA Band 9 receiver.

In addition to these investigations of long wavelength receiver optics the theory of GBMA was combined with mode-matching theory to describe the behaviour of standing waves in typical submillimetre receiver systems. The reflection and transmission amplitude response patterns of several standing wave cavities were predicted with this technique and compared with experimental measurements. The effect of minor alterations to the feed horn structures on the resonance profiles are studied in depth. The eigenmodes of these resonant cavities are also analysed. A complex stray light baffle structure is introduced within the cavity and its effect upon the system is quantified.

Acknowledgements

I would firstly like to extend my warm and sincere thanks to my supervisor, Dr. Neil Trappe, for his valuable guidance on the work presented in this thesis. I greatly appreciate his advice and patience during my studies and his time spent sharing his knowledge of the area so clearly. I would also like to thank Prof. Anthony Murphy for the use of the facilities here at NUI Maynooth.

I would like to thank all of the staff of the Department of Experimental Physics who made my time here so enjoyable, both during my undergraduate and postgraduate years. Particular thanks go to Mr. Tully Peacocke, whose invaluable insight and sharp mind were positive influences on my research. Warm thanks go to Dr. Creidhe O' Sullivan whose door was always open for guidance. I am also very grateful to Dr. Marcin Gradziel who aided me with my experimental measurements and provided tutorials on MODAL.

To the administrative and technical staff at the Department of Experimental Physic I owe a debt of gratitude: to Ms. Grainne Roche whose friendship, advice and laughter helped so much; to Mr. John Kelly for all the assistance with my computer problems down the years, to Mr. David Watson for his skilled work in making any of the components for my experiments. To my fellow postgraduates over the years, especially those within the THz optics group, whose friendship and company made my time here so enjoyable, I thank you all. I would especially like to thank Dr. Priscilla Mooney; those coffee breaks got me through the long days.

During my travels to SRON and GARD I have worked closely with some fantastic people. I wish to heartily thank Dr. Andrey Baryshev for his valuable support and facilitating my measurement campaigns during my trips to Groningen. I extend my sincere and warm gratitude to Prof. Victor Belitsky who was always eager to discuss

my work and over guidance. Thanks also to Olle Nyström and Hawal Rashid, whose tireless efforts ensured I had plenty of measurement data for my thesis.

To Keith; for your inestimable friendship, advice and encouragement I thank you. To all the guys down at the Self Defence Club, thank you for keeping me in shape throughout my studies.

I wish to acknowledge the financial support provided by Science Foundation Ireland (SFI) to undertake this research.

To my family, I thank you all sincerely for your understanding and support throughout all my studies. A special thank you and dedication also goes to my Granny, Brigid O' Reilly.

Finally, to Ciara; your steadfast companionship, encouragement and love have been my rock throughout this entire process. I could not have done it without you.

1. Introduction to Submillimetre Astronomy

One of the constant endeavors of mankind has been to understand and decipher the meaning of the heavens. From the dawn of civilization records have shown that every major civilization has been concerned with the structure of the sky, interpreting what they saw in many different ways. Though methods of observation and interpretation have evolved significantly, the pursuits of modern astronomers and cosmologists are scarcely different from those early scientists. Knowledge of the movements of the Sun, Moon and stars was important in early times for survival; the timing of crop plantations, land and sea navigation and even the reading of divine meaning.

In recent times the aim of astronomical observation has shifted to the search for the very structure of the Universe around us, and this has given birth to a wide variety of scientific disciplines. Giants of astronomy such as Copernicus, Tycho Brahe and Galileo all relied on what their naked eye could see and/or what rudimentary telescopes could magnify for them. It wasn't until the discovery of radio waves and the eventual discovery of astronomical radio waves by Karl Jansky [1] that techniques for astronomical observations exploited other regions of the electromagnetic spectrum. The past century has been an extremely exciting time in the field of astronomy. As soon it was possible to detect or generate radiation from a certain region of the EM spectrum, developments were made to use this technology to detect signals from the sky. Vastly different methods of observation now exist for nearly every frequency and have been employed in equally disparate detection systems – examples include the Very Large Array (VLA) operating at radio frequencies, the Hubble Space Telescope at optical/Infrared, the XMM Newtown space observatory for X-ray, the Infrared Astronomical Satellite (IRAS) for Infrared and more recently the Herschel Space Telescope and the Planck Surveyor that have been designed to map the Universe in the submillimetre and far-infrared wavebands. Each of these telescopes has added a new layer to our understanding of the structure and mechanics of the greater Universe.

Every development adds a further layer of understanding to our knowledge of the Universe, as well as posing new questions.

Observing at different wavelengths will reveal different information; that which was obscured or blocked in one region of the EM spectrum may be transparent in another. This is illustrated below in Figure 1-1. The Horsehead nebula is a star forming region located within the Orion constellation. In the left most image it can be seen that the nebula is mostly dark, with visible radiation from the region being obscured by dust.

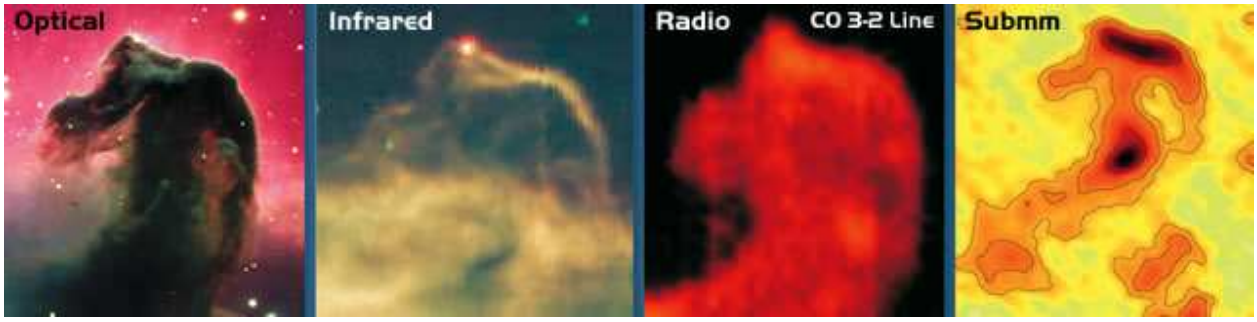

Figure 1-1 - The Horsehead Nebula (a.k.a. Barnard 33) in the Orion constellation viewed at different wavelengths [19]

The hot thin layer of gas around the nebula is observed at the infrared and the radio wavebands. At submillimetre wavelengths (rightmost image) information about the interior structure of this star forming region is revealed. The darker regions show that there is peak emission at submillimetre wavelengths, thus indicating the presence of dusty, star forming clouds.

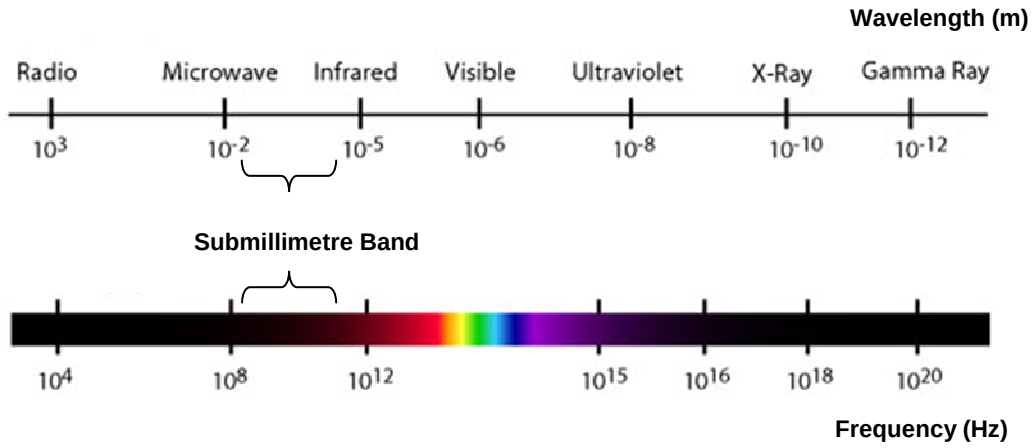

Figure 1-2 - Location of submillimetre band in the scheme of the electromagnetic spectrum

The region of the EM spectrum that is of interest in this thesis is referred to as the submillimetre (or far-Infrared) waveband which is taken to lie at the upper frequency limit of the infrared band and just below the start of the microwave band – c.f. Figure 1-2. This waveband has in recent times been grouped with the terahertz (THz) waveband, which is taken to lie between frequencies of 300 GHz and 3THz, though the limits are sometimes considered to be from 100 GHz to 10THz [2]. This waveband is one of the last explored regions of the EM spectrum in terms of astronomy, owing chiefly to the difficulty in developing sensitive detection and source techniques. Terahertz radiation propagation within receivers has also historically proved difficult to model. The waveband lies between two disparate optical regimes, one of which is well approximated by the technique of geometrical optics; where high frequency visible radiation is propagated using ray-tracing. At the other regime is the very low frequency radio spectrum; diffraction effects heavily dominate the propagation of radiation thus requiring solutions to Maxwell's equations.

Detection of submillimetre radiation requires a blend of both waveguide and optical techniques, yet even at the upper frequency limit of the band (> 3THz) modern sophisticated detectors are still in development. The optical modeling of the submillimetre band is usually referred to as 'Quasioptics' [3] and is based primarily on the propagation of Gaussian beam modes as solutions of the paraxial wave equation. The initial application of these Gaussian beam modes to approximate the propagation

of radiation was for laser optics at near-IR wavelengths [4]. Quasioptics provide an elegant and computationally efficient modeling technique for the submillimetre band; the application of which is one of the main subjects of this thesis.

The importance of astronomical observations at submillimetre wavelengths is immediately apparent; with the equivalent blackbody temperature range for the waveband from *4K* up to *480K (hf ≈kT).* The submillimetre waveband thus permits the observation of continuum and line emission from 'cool' objects and diffuse media such as circumstellar and interstellar gas and dust. There are many important astronomical sources whose emission spectra peak within this frequency range and are considered elements of the 'cool' Universe. Temperatures of the dense interstellar medium gas range from *10K* in cooler regions to approximately *100* or *200K* in the hotter, denser parts. The corresponding frequencies thus range from about *200 GHz* up to *4THz*. There is significant emission from the Cosmic Microwave Background at sub-THz frequencies as well as high redshifted young galaxies obscured by dust. The same process that obscures these star forming extragalactic regions also obscures both protostars and protoplanetary disks. Also contained within this frequency range are many interesting molecular rotation and atomic transition lines which are observed using spectroscopic techniques [5].

Observation of the early, high-redshifted Universe is ideal for the submillimetre waveband. Radiation from distant sources is typically highly redshifted and obscured by interstellar dust, making observations at other wavebands (optical, UV, IR) difficult. It is precisely these processes that enhance the emission of these objects in the submillimetre domain. For a young redshifted galaxy the majority of the optical and UV radiation emitted from forming stars is absorbed by the surrounding interstellar matter and re-radiated at longer wavelengths falling within the terahertz band as continuum thermal emission [6]. An example of how submillimetre observations can provide a more complete picture of the young Universe is illustrated below in Figure 1-3.

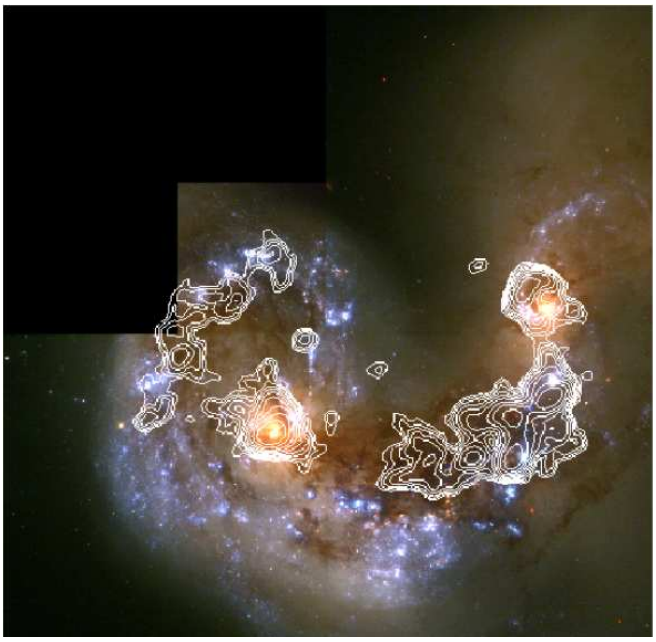

Figure 1-3 - Optical and submillimetre observations of the *AntennaeI (NGC 4038/89)*, a pair of interacting galaxies [110]

The optical picture has been taken with the Hubble Space Telescope (HST) while the contour plot (in white) shows carbon monoxide (CO) line emission taken from the Caltech Millimetre Array (CMA) The figure illustrates well the point that at optical wavelengths the precise details of star forming regions are hidden while they are revealed at longer wavelengths. Identifying the origin of the intense star formation produced in galaxy mergers such as this one is an important step towards understanding the formation of galaxies in the early Universe [7]. CO is one of the most important molecules observable at submillimetre/terahertz wavelengths, showing one of the strongest observed line intensity profiles for any molecule The relevant observable transitions occur at frequencies of 115 GHz, 230 GHz and 345 GHz, which are all within the submillimetre waveband and it is highly abundant within galactic clouds with a long transition lifetime, making it an important tracer for the interstellar medium comparable with the classic radio 21cm emission line [8]. CO line emission can serve as both a measure of the total amount of H_2 gas available for future star formation as well as previous stellar mass assembly by serving as a dynamical mass tracer [9]. An excellent example of the use of CO line emission is given by [10]. The submillimetre

galaxy (SMG) GN10 has remained difficult to detect by either the Hubble Space Telescope (optical) or the IRAS (near IR). Successful and accurate detection of CO emission lines redshifted to z = 4.05 at a frequency of 91.4 GHz has been conducted by the Institut de Radioastronomie Millimetrique (IRAM) Plateau de Bure Interferometer (P dBI). The internal structure of this galaxy has been revealed, showing that it is a very active 'proto-cluster' region with significant star formation activity. These submillimetre galaxies provide critical information about young galactic structure and reveal more detail about the processes behind star formation. Submillimetre galaxies are extremely massive and are the most luminous, heavily star-forming galaxies in the Universe [9]. The SMG GN10 is only one of a host of recently detected young galaxies at high redshifts which have been up until recently obscured but are now observable at submillimetre wavelengths. There are still many unanswered questions about these SMGs and many others just being posed – are they isolated galaxies or the product of galactic mergers? Where do they fit in the galactic evolution sequence? With submillimetre observations of increased resolution and wider bandwidths there is no doubt that many of these questions will be answered in the near future.

It is believed that the chief processes of stellar formation, evolution and demise are known, with most of the unobservable processes described theoretically. However, star formation is also understood to be very complex and observations are required to determine those processes that are dominant and those that are insignificant and can be neglected [11]. Specifically, observational evidence is required to improve understanding of the mechanisms that drive the birth and, to a lesser extent the death of stars. Pre-stellar cloud cores are crucial to understanding the initial conditions behind the gravitational collapse that typifies a newly born star. Before, during and after stellar birth these cloud cores are typically obscured to all but the submillimetre band. Submillimetre observations will also allow a more comprehensive insight into the differences between high and low mass star formations. Protostellar objects, or recently born stars are usually cloaked by a thick envelope of dust and gas left over from after

the star was formed. Current knowledge of these envelopes is limited, especially for the youngest and most obscured protostars, known as 'Class 0' objects. These objects are typically cold objects prior to the formation of the star, and the bulk of the energy emitted is at submillimetre wavelengths. The advent of precise submillimetre observations will reveal the complex behavior inherent in these stellar clouds. The processes of gravitational infall that ignite the star, bipolar outflows that remove excess angular momentum for the infalling cloud and the rotational kinematics will be better understood when imaged at these wavelengths

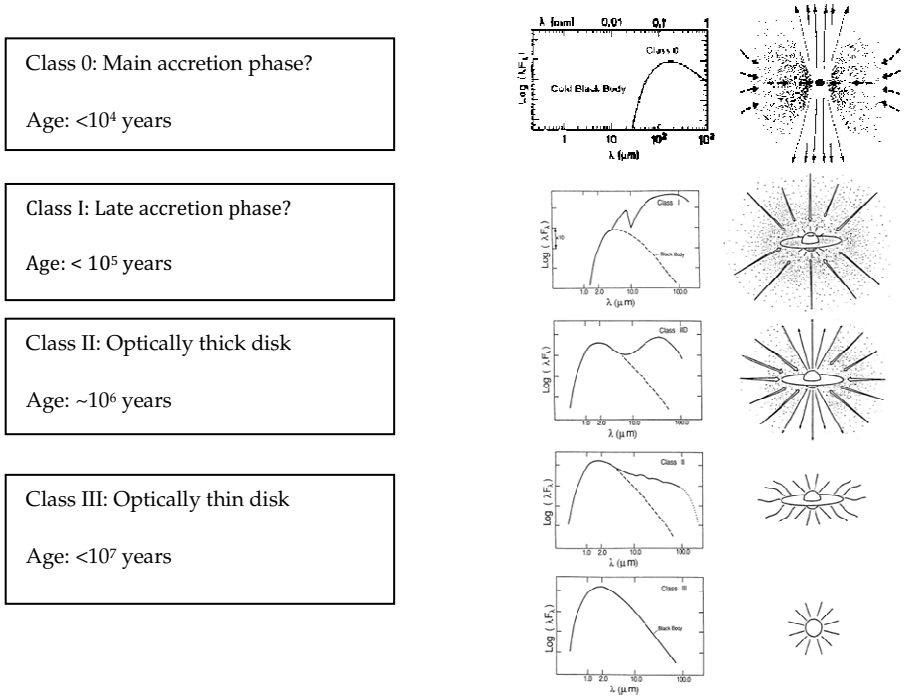

Figure 1-4 – Quasi-continuous evolutionary cycle for low mass stars [112], adapted to include earliest stage Class 0 object [15].

Stars at the end of their main life cycle will also be revealed in greater detail. Stars with a main-sequence mass of 0.8 – 8$M_{\odot}$ become White Dwarfs, evolving via the Red Giant and Post Asymptotic Giant Branch (Post AGB). At the end of the Red Giant phase and during the Post AGB phase these stars eject the bulk of their mass in the form of a cool molecular wind in a relatively short space of time, thus enriching the surrounding ISM

and galactic space. The exact processes of these mass ejections are still not well understood, but will be ideally observable at submillimetre wavelengths.

Dust extinction is a process that also obscures the formation of planets and planetary systems. The evolution of planets about recently formed stars is still largely described theoretically. This can be attributed mainly to the lack of direct observations of planets either in formation or 'completion', outside of our own Solar System. Indeed, the concept of the formation of our own planetary system as a result of the mutual accretion of matter in the 'protoplanetary disk' about our Sun is natural; the orbital angular momentum vectors of each planet are all nearly in line with one another and that of the Sun itself [12]. Up until very recently, direct observation of extrasolar planets was not possible [13]. As such, current theories about planetary formation are borne out of local and indirect observations of protoplanetary disks and T-Tauri stars. T-Tauri stars are Main Sequence (MS) stars of spectral class G, K and M, originally identified by their prominent characteristics; Balmer emission lines, excess UV and IR emission and outflows. These are the defining characteristics of the presence of circumstellar accretion discs [12]. In the nearest star forming region of Orion over 200 protoplanetary disks have been detected using the HST. Yet, as with previously described objects, specific details within these regions are obscured to all but the THz region. Observations of some of these protoplanetary disks has already been conducted with the Submillimetre Array (SMA) exposing new details and allowing further characterisation of the complex planet formation model [14]. The observed spectral energy distribution from such thermal processes reveals information about the emission mechanisms and the temperature distribution. Additionally it gives a measure of the mass of the emitting dust, be it from young galaxies, dying stars, protoplanetary structures or circum stellar disks.

Other examples of high redshifted and/or dust obscured objects that are observable at terahertz wavelengths include absorption lines of Quasi-Stellar Objects (QSO's), which

are used as background continuum sources, the driving forces behind Active Galactic Nuclei (AGN) and the Magellanic Clouds [15]. Since only a small amount of dust is required to absorb a sufficient amount of short wavelength photons, emission processes such as brehmstrahlung, synchrotron radiation and inverse Compton scattering have spectral energy distributions within the submillimetre band Of course one of the most important and topical observations in this band is the CMBR. Peak emission from the CMBR occurs at a temperature of 2.73K which is just below the submillimetre limit. This does not however exclude the use of submillimetre observations to characterise the CMBR at wavelengths near its peak. This has already been achieved with novel measurements by the Balloon Observations Of Millimetric Extragalactic Radiation and Geophysics (BOOMERanG). Future work with more advanced devices (PLANCK) will add even more detail to the results from the first observations of the CMBR by both COBE and WMAP.

1.1 Observing at Submillimetre Wavelengths

Research and development of submillimetre astronomy has exploded in recent years. This is primarily due to the recent development of the required technologies for these wavelengths. There are today many telescopes and devices, both ground-based and space-borne that provide almost complete coverage of the submillimetre range, with more technologies on the way.

Space borne telescopes have the excellent advantage of unobscured observation, but are restricted by mechanical considerations for successful launch into orbit and are consequently much smaller in size than their ground based counterparts. The most recent and most advanced space missions that will operate at submillimetre frequencies are the Herschel Space Observatory and the Planck Surveyor. The Herschel Space Observatory developed by the European Space Agency is the world's largest astronomical telescope developed for space based observations. Herschel will carry out imaging and spectroscopy in the submillimetre band using three instruments. The

Heterodyne Instrument for the Far Infrared (HIFI) on board Herschel is a very high resolution spectrometer with a continuous frequency coverage from 480 to 1250 GHz in five bands, while a sixth band will provide coverage for 1410-1910 GHz. The Spectral and Photometric Imaging Receiver (SPIRE) instrument is a submillimetre camera and spectrometer. SPIRE comprises a three-band imaging photometer operating at 250, 350 and 500 µm and a Fourier Transform Spectrometer (FTS) covering 200-670 µm. The Photodetector Array Camera and Spectrometer (PACS) instrument is an imaging photometer and integral field line spectrometer operating between 60 and 210 µm [16].The Planck Surveyor has been developed to map the anisotropies of CMBR with high angular resolution and temperature sensitivity. The Planck Surveyor will observe over a total of nine frequency channels, using two instruments; the Low Frequency Instrument (LFI) with a frequency range of 27 GHz to 77 GHz and the High Frequency Instrument (HFI) which covers a frequency range of 84 GHz to 1THz [17]. At the time of writing the various instruments on board Herschel have made their first test astronomical observations. A sample of these images taken from [16] are illustrated below in Figure 1-5, Figure 1-6 and Figure 1-7.

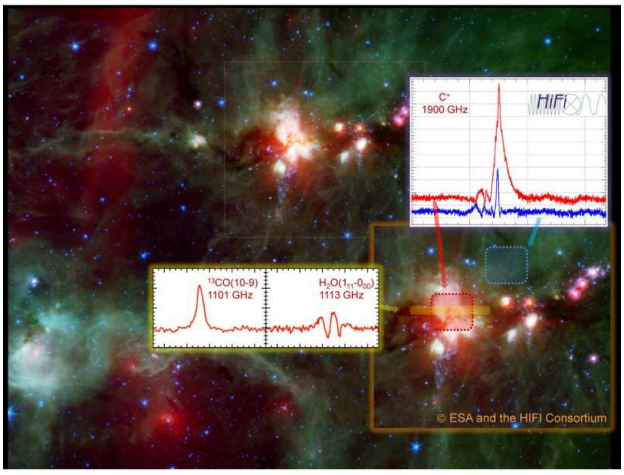

Figure 1-5 – Composite image from Spitzer telescope overlaid with spectra measured from HIFI of DR21 star forming region

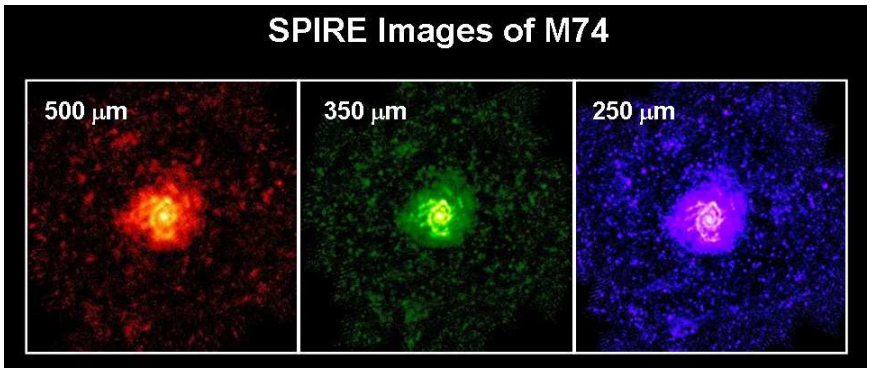

Figure 1-6 – SPIRE images of M74 spiral galaxy at its three operational wavelengths.

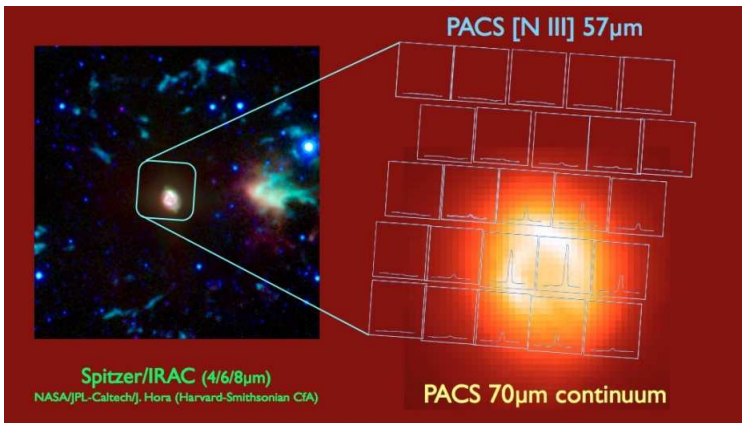

Figure 1-7 – Leftmost image from Spitzer of NGC6543 overlaid with component spectra of far-IR Nitrogen line taken with PACS

Ground-based observatories are typically limited by atmospheric absorption. This is expected with any ground-based telescope, but at the THz waveband absorption is more severe, with only specific frequency windows allowed. An example of these transmission windows at the Chajnantor Plain in the Atacama Desert, Chile is displayed below in Figure 1-8. This site represents one of the ideal ground sites available for Submillimetre astronomy as it is very dry, with almost non-existent interfering weather conditions and is extremely flat with a height above sea level of approximately 5000 m.

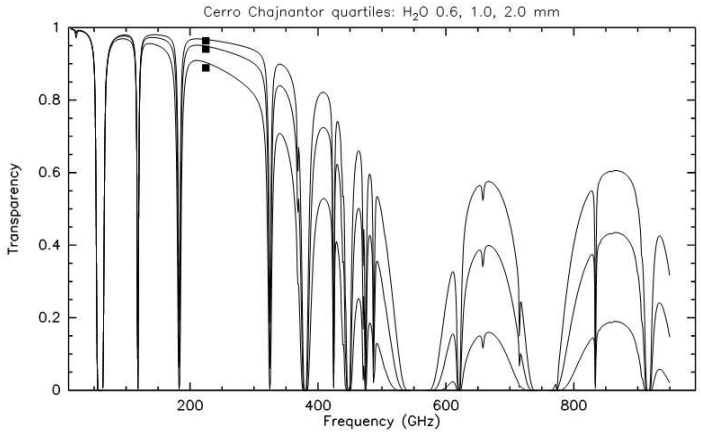

Figure 1-8 - Zenith transmission as a function of frequency under typical conditions at the Chajnantor Plain (ALMA site) 3 curves represent the 25%, 50% and 75% percentiles [15].

However, despite the drawback of atmospheric absorption, ground based submillimetre observatories have the distinct mechanical advantage of size over their space based relatives. The mechanical constraints for ground based observatories are much more generous than those for satellite telescopes. The larger the collecting area of the telescope the greater the accuracy and the sharper the spatial resolution.

The largest single telescope operating in the submillimetre domain is the James Clerk Maxwell Telescope (JCMT), at Mauna Kea in Hawaii. The JCMT has a primary reflector of 15m diameter made up of 276 individual lightweight reflector panels that are individually adjusted with stepper motors to maintain an accurate parabolic shape while the antenna is moved through different elevations. The Caltech Submillimetre Observatory (CSO) is another single dish reflector telescope located on Mauna Kea. These two telescopes were combined to form the first Submillimetre interferometer observatory. There is a new single aperture telescope being developed by the Caltech group, called the Cornell Caltech Atacama Telescope (CCAT) which will take over from the CSO, which will be dismantled in the near future [18].

The Submillimetre Array (SMA) is also located on Mauna Kea. It is the first purpose built interferometer for Submillimetre observing, consisting of eight 6-meter diameter antennas. The interferometric array method of detection allows individual telescopes to

act together to provide very high angular resolution observations. A single dish telescope has an angular resolution limited by its diameter D ($\theta \approx 1.22\lambda / D$). Even the largest radio telescopes, when operating at their shortest operating wavelengths have an angular resolution of only one arc-minute. To achieve the much smaller angular resolution required to accurately distinguish the fine detail of observable objects in the sky, the principles of interferometry are used to synthesize a much larger aperture. A much larger equivalent telescope can be achieved using several such telescopes together over large distances or 'baselines' and combining their signals using methods of aperture synthesis. This is the operating principle of the Very Long Baseline Array (VLBA), the world's largest radio interferometer, combining single dish antennas from all over the globe using extremely accurate signal synchronization.

1.2 The Atacama Large Millimetre Array

The main submillimetre instrument under scrutiny in this thesis is the Atacama Large Millimetre Array (ALMA). When completed, ALMA will be the world's largest interferometric array completely devoted to ground based submillimetre astronomy. The array represents a massive collaboration between the European Southern Observatory (ESO), the National Radio Astronomy Observatory (NRAO), the National Research Council of Canada and the National Astronomical Observatory of Japan (NAOJ). The array will be comprised of up to 66 12 meter on-axis Cassegrain antennas. The development of these antennas has been contracted to three companies: the AEC Consortium working under the ESO, Vertex RSI working under the NRAO and the Mitsubishi Electrical Company working under the NAOJ. Each company has produced a prototype 12 meter antenna that has been rigorously tested to ensure they meet the required ALMA standards. As the name suggests, the array will be located in the Atacama Desert in Chile; specifically on the Chajnantor Plain of the Chilean Andes in the District of San Pedro de Atacama, with a height of 5000m above sea level (23°01'9.42"S 67°45'11.44"W). As previously mentioned in Section 1.1 of this chapter this

location provides the best possible observing for submillimetre frequencies – c.f. Figure 1-8 above.

These antennas will make up two separate array systems. The main 12 metre array is made up of fifty 12 metre antennas that will, through the use of dedicated transporters, be reconfigured into arrays of varying area. The smallest baseline area for this area is 160 x 250 metres, and the largest configuration baseline separation between antennas is approximately 15 kilometres. The other array, known as the Atacama Compact Array (ACA), will be made up of four 12 metre antennas and twelve 7 metre antennas. The specifications of both of these arrays are summarized below in Table 1-1.

Parameter	**12m Array**	**ACA**
Antennas	50(12 m)	12(7m) & 4(12m)
Total Collecting Area	5650 m^2	460m^2 & 450m^2
Angular Resolution	0.02″	5.7″
Baseline Lengths	15 – 16000m	
Surface Accuracy	<25μm	<20 μm & <25 μm

Table 1-1 Parameters of the 12 m array and the ACA: component arrays of the ALMA [19].

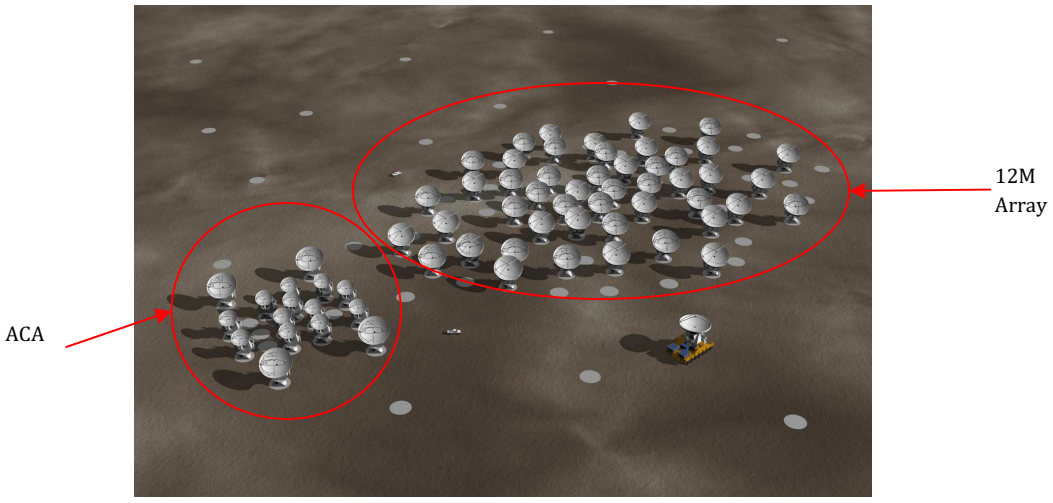

Figure 1-9 - Artist's rendering of the two ALMA antenna arrays

To this end, a r.m.s. surface accuracy requirement of less than 25 µm has been placed on the 12 meter antennas, and less than 20 µm for the 7 meter antennas. The antennas themselves will have 2″ absolute pointing over the entire sky and a 0.6″ offset pointing and will be able to fast switch over a 2 degree range in less than 1.5 s [20], [21].

The array will operate over a frequency range of 30 GHz to 950 GHz, spread over ten separate receivers. These receiver channels or bands are chosen to best match the zenith atmospheric transmission windows at the Chajnantor Plain (c.f. Figure 1-8). The development of the optics, mixers and local oscillators for each of these bands has been contracted out to receiver developers around the globe. All bands are designed to receive dual polarised signals, and all but two of the lowest frequency bands will be cooled down to 4K to reduce noise and to facilitate the operation of the complex superconductor-insulator-superconductor (SIS) mixers and ensure extremely low receiver noise. Cooling of the receivers is achieved through use of a Dewar flask cryostat and receivers will have a modular design that will allow for easy insertion and removal. A more detailed description of the analysed receivers is given in later chapters.

The chief scientific goals specified for the ALMA Observatory are summarized below [20].

- To detect CO line emission to determine the redshift of star-forming galaxies, enabling ALMA to build up a history of the star forming process.
- To image the gas and dust kinematics in protostellar and protoplanetary disks around young Sun-like stars.
- To image the redshifted dust continuum emission from young evolving submillimetre galaxies at epochs as early as z=10.
- To probe the cold dust and molecular gas of nearby galaxies, allowing detailed studies of the ISM within different environments and how such environments influence the physical and chemical processes of the ISM. Such

interesting environments will include dusty objects such as protostellar disks, protostellar outflows, circumstellar envelopes surrounding Red Giant and post-AGB stars, AGN's and Quasars.

- To image the molecular gas dynamics at the centre of our own galaxy, the Milky Way, thus revealing the tidal, magnetic and turbulent processes of star formation at the extreme environment of a galactic core.
- To reveal in detail the exact process of star formation from the gravitational collapse of molecular clouds and determine the chemical composition of the gas and dust within these coulds.
- To image the formation of molecules and dust grains in circumstellar shells about evolved stars as well as novae and supernovae.
- To refine the dynamical and chemical models of the atmospheres of planets within our own Solar System and provide unobscured images of comets, asteroids, Centaurs and Kuiper Belt Objects.

1.3 Content of Thesis

This thesis is devoted primarily to the analysis and measurement of the optical systems within the submillimetre astronomical receiver systems, specifically the Band 5 and Band 9 receiver channels of the ALMA Telescope. Other work presented includes a detailed performance study of the currently available optical modeling software packages that are utilised by telescope developers. A theoretical analysis into the complex beam scattering process within quasioptical waveguide and scalar feed horn structures is also presented. Below is a summary of the thesis layout by chapter, detailing original work by the author.

- Chapter 2 - *Preliminaries*. This chapter contains the mathematical tools required to interpret the work conducted within the thesis. The fundamentals of Gaussian Beam Mode Analysis (GBMA) are derived, and this forms the basis of quasioptical analysis for submillimetre optical

systems. The theory of GBMA is extended to modeling the diffraction patterns from a Michelson interferometer. Fresnel diffraction patterns are also predicted with a verification performed using the theory of Angular Spectrum of Plane Waves. This chapter also contains summaries of the optical software packages (GRASP9, MODAL & ZEMAX) that are used and tested in this thesis. A description of the mathematical principles behind the approximations made by each of these software packages is provided. An application of Gaussian Beam Mode Analysis to the modeling of interferometers is novel and interesting in that both the near field and farfield behaviour of the interfering beams is automatically recovered within the analysis.

- Chapter 3 – *Far-Infrared Optics and Design Software Verification Tools*. This chapter is an extension of work previously conducted for an ESA Study by combined efforts of research groups at the Space Research Organisation of the Netherlands (SRON), the UK Astronomy Technology Centre, the University of Cambridge and the National University of Ireland, Maynooth (NUIM) [22]. The test case scenarios employed in this report have been extended in this chapter to include two software packages, ZEMAX and MODAL and results are compared against those of the GRASP optics package. The Author has taken important optical test cases and reviewed and evaluated the performance of all optical packages and their various advantages and disadvantages in analyzing a specific example.
- Chapter 4 – *Standing Wave Analysis of Waveguide and Feed Horn Structures*. An extension to the theoretical framework behind standing waves in quasioptical system components is presented in this chapter. The effect of small scale mechanical errors within feed horn structures is theoretically simulated using methods established by the NUI Maynooth research group. A corrugated to corrugated horn cavity and a stray light baffle structure are

analysed and a novel technique to plot the spatial form of the reflected power components is outlined.

- Chapter 5 – *Quasioptical Verification and Measurement of the ALMA Band 5 Receiver Optics*. Within this chapter a complete quasioptical and physical optics analysis treatment of the optics for the ALMA Band 5 receiver is presented. Comparative analyses between several versions of the optical surfaces are presented with recommendations made to the Band 5 receiver development group at the Group for Advanced Receiver Development (GARD) at the Chalmers Technical University, Gothenburg, Sweden. Measurements conducted at the GARD facility on the Band 5 optics are also presented. The Author assisted in an experimental measurement campaign in GARD and has made various recommendations that have been implemented in the ALMA Band 5 receiver.
- Chapter 6 – *Post Assembly Analysis of the ALMA Band 9 Optics with Suggested Improvements.* This chapter details several possible improvements to the design of the ALMA Band 9 optics, specifically for reducing the levels of cross polar leakage. This work was performed in collaboration with the ALMA Band 9 receiver development group at SRON. An interesting effect of cross polarisation reduction through manipulating projection angles on a polarising wire grid is theoretically analysed and subsequently measured at the Band 9 test facility at SRON. This grid projection effect is thoroughly quantified and measured using the THz laboratory at NUI Maynooth.
- Chapter 7 – Conclusions and future work are outlined.

2. Preliminaries – Quasioptical Analysis

In this chapter the various analysis techniques that have been applied throughout this thesis are described. These theoretical techniques form the basis of Quasioptical Analysis (QO) for optical systems that operate between the domains of geometrical optics and diffraction dominated optics [4], [23], [24]. When we speak of geometrical optics we are referring to optical systems that generally operate in the visible spectrum, where $\lambda \rightarrow 0$ and the dimensions of optical elements are very large when measured in wavelengths. Propagation of radiations in such systems can be accurately predicted using ray tracing methods. Diffraction dominated systems are typically in the microwave to radio portions of the electromagnetic spectrum, where system element dimensions are typically comparable to λ, and as such, diffraction effects dominate the propagation of radiation.

It is between these two areas of distinct propagation techniques lies quasioptical propagation methods. The traditional name for this portion of the electromagnetic spectrum is the Terahertz Gap. Despite its name, the terahertz gap is considered to span frequencies from 100 GHz to 10THz. Within this domain the size of the optical beam is only moderately large compared to the wavelength. Quasioptical systems are comprised of both waveguide and optical components, illustrating the combination of techniques between geometrical and diffraction dominated optics. Analysis of these systems takes a variety of forms, which are detailed below in Figure 2-1. The techniques that have been applied throughout this thesis are a combination of Gaussian Beam Mode Analysis and Physical Optics, hereafter referred to by their acronyms GBMA and PO respectively. The term quasioptical analysis will refer to the application of the GBMA method and will be described in full throughout this chapter. This method, simply put, approximates a typical antenna source field with a linear combination of Gaussian beam modes, representing this field evolution through its optical train using ABCD matrices with the desired output field being reformed with new beam

parameters after appropriate phase slippage between modes. The method is scalar and approximate, requiring that the beam is reasonably well collimated (paraxial approximation) throughout the optical train into the far field.

The PO method can be summarized as a computationally intensive technique that uses solutions to Maxwell's Equations at the surface of a metallic reflector to generate source currents which are used in turn to create a reflected field, and then propagated to the next reflective element. This method, although very accurate, is computationally intensive and is typically employed for final stage analysis of optical systems after initial GBMA has been performed [22]

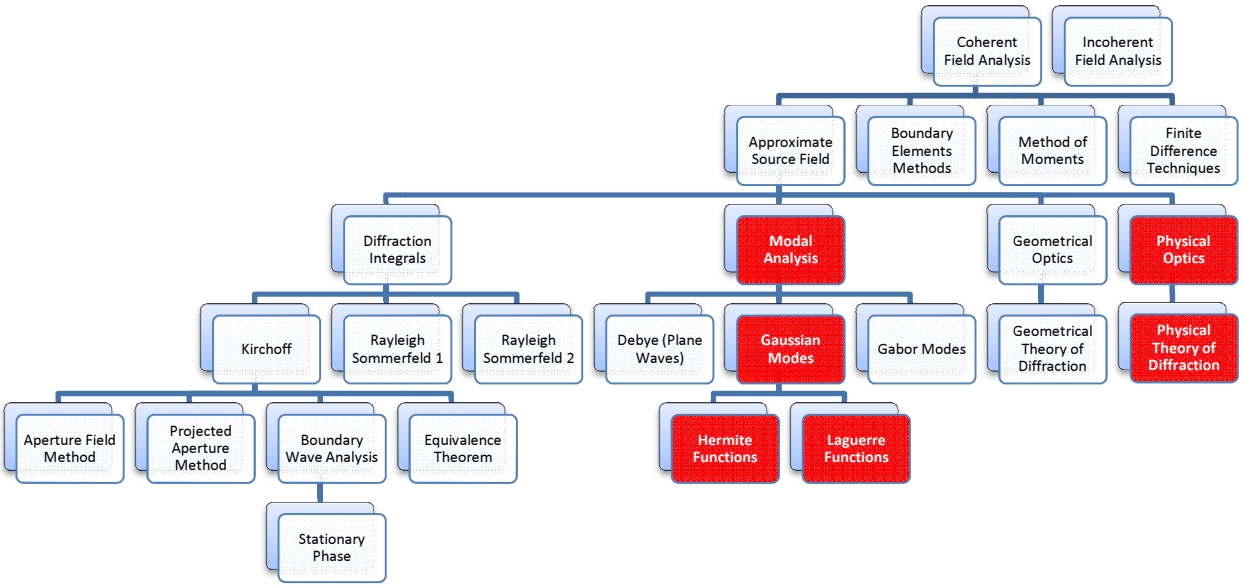

Figure 2-1 - Hierarchy of optical analysis techniques applied to long-wavelength systems

2.1 Gaussian Beam Mode Analysis

The fundamental requirement for computational/theoretical optical analysis is the ability to accurately predict the electromagnetic field distribution at some arbitrary field away from a complex field source object. Modeling the effects of diffraction at the geometrical limit is traditionally achieved using either the methods of Fresnel and

Fraunhofer diffraction theory [25], or the use of the geometrical theory of diffraction. At the long wavelengths that typify the submillimetre domain diffraction effects dominate beam evolution. Prediction of such fields using the classical diffraction methods requires prohibitively intense numerical evaluation, and the accuracy of the resultant fields is difficult to quantify. What is more desirable is an analytical approach to the problem of diffraction limited beam evolution. This analytical solution requires the ability to describe complex electromagnetic field propagation and transformation at any point in its optical train. A very successful approach to this problem is the use of Gaussian beam modes [24], [26], [27].

Gaussian beams have long been used in the description of optical laser beams and other long wavelength systems and have been shown to be excellent approximation to the radiation patterns of sub-millimetre and far-infrared optical systems [28], [29]. Aside from their accuracy at describing diffraction dominated radiation, one of the main advantages to using Gaussian beam modes is that they are computationally non-intensive. These 'modes' are analytical solutions to the paraxial approximation of the wave equation. A field may be represented by a carefully chosen selection of these modes, superimposed upon one another. One of the main advantages to this approach is that once a 'source' field has been described using these modes, the transformed field at another arbitrary plane can be described without any further integration techniques; i.e. the evolution of a few beam characteristics suffices to accurately represent the field [30].

2.1.1 Derivation of Gaussian Beam Modes

In this section the technique of modeling quasioptical beams through the Gaussian Beam Mode solution to the paraxial wave equation is described. As mentioned previously, it is necessary to be able to describe the electromagnetic field under consideration at some 'source plane'. This source field $E(x,y)$ may be represented as a

discrete summation of beam modes ψ_{mn} and their corresponding modal coefficients A_{mn} which determine the contribution to the amplitude description of each mode:

$$E(x,y) = \sum_m \sum_n A_{mn} \Psi_{mn} \tag{2.1}$$

where m and n represents the order of the mode. These modes are usually chosen so that at this source plane they share the same beam characteristics of beam radius $w(z)$, where $w(z)$ is the radius at which the beam field falls to $1/e$ relative to its on-axis value, and phase front radius of curvature $R(z)$. The modes obey the orthogonality condition such that

$$\left\langle \Psi_{mn} \middle| \Psi_{m'n'} \right\rangle = \delta_{mm'} \delta_{nn'} \tag{2.2}$$

where we have utilised the bra-ket Dirac notation $\left\langle \Psi_{mn} \middle| \Psi_{m'n'} \right\rangle$ to signify the inner product of the beam modes ψ_{mn} by its complex conjugate ψ^*_{mn}. Thus, the modal coefficients can be recovered at another plane:

$$\begin{aligned} &\left\langle E(x,y) \middle| \Psi_{mn} \right\rangle = \sum_m \sum_n \left\langle A_{m'n'} \Psi_{m'n'} \middle| \Psi_{mn} \right\rangle \\ &\Rightarrow A_{mn} = \left\langle E(x,y) \middle| \Psi_{mn} \right\rangle \end{aligned} \tag{2.3}$$

If the modes and field are normalized then the square of the modal coefficients $|A_{mn}|^2$ represents the relative power carried by that mode with the index mn.

Each of these modes propagates without losing its characteristic amplitude profile shape, yet they all share the same w and R at the known 'source plane'. The values of w and R do not depend on the mode order; rather they depend on propagation distance away from this source plane, defined in the z-axis with the source plane location denominated by the position z_0. As such, all modes share the same characteristic w and R at any plane of the beam. However, to account for the effects of diffraction along the path of such a beam, the relative phase slippage between modes must be taken into account. For a single mode beam the amplitude profile will remain constant throughout transformation, and is thus a poor representation of the changing form of the beam usually encountered in diffraction. By including multiple modes, the modal phase

slippage in propagating along the optical axis vary as this phase slippage term is dependent on the mode number. The phase relationship between modes will change as the beam evolves, thus altering the resultant total field pattern [24]. This principle is outlined below.

In defining a scalar mode solution certain assumptions must be made regarding the nature of the propagating beam [31]. It is assumed that the beam is relatively well collimated, having a well defined direction of propagation with little angular spreading away from the optical axis. The beam does however undergo some transverse amplitude and phase variation, unlike that for a plane wave propagating along the beam axis [24]. The transverse dimensions of the beam at its waist positions are not too large or small in terms of λ. This approximation, known as the paraxial approximation, is the fundamental driver behind the Gaussian beam mode technique. The Helmholtz wave equation describes the free space propagation of a coherent electromagnetic field such that

$$(\nabla^2 + k^2)E = 0 \tag{2.4}$$

where E is the coherent electromagnetic field, k is the wavenumber equal to angular frequency w divided by the speed of light c. Letting the direction of propagation be in the positive z direction and with amplitude varying in the x and y directions the expression for a paraxial electromagnetic beam is given as a modulated plane wave of the form

$$E(x, y, z) = u(x, y, z)\exp(-jkz) \tag{2.5}$$

where $u(x,y,z)$ is a complex scalar function defining the non plane wave part of the beam. Applying this beam to the Helmholtz equation (Equation 2.4) the following solution, known as the reduced wave equation is obtained

$$\left(\frac{\partial^2 u}{\partial x^2} + \frac{\partial^2 u}{\partial y^2} + \frac{\partial^2 u}{\partial z^2}\right) - 2jk\frac{\partial u}{\partial z} = 0 \tag{2.6}$$

By applying the paraxial assumption to this beam, the complex scalar function *u(x,y,z)* will vary slowly with propagation; that is the axial variation will be small when measured in wavelengths. From this approximation the *z* (third) term of the Laplacian in Equation 2.6 is negligible compared to other terms and is thus dropped. This solution to the Helmholtz equation is now referred to as the paraxial wave equation [3]

$$\left(\frac{\partial^2 u}{\partial x^2}+\frac{\partial^2 u}{\partial y^2}\right)-2jk\frac{\partial u}{\partial z}=0 \tag{2.7}$$

The simplest solution to this paraxial wave equation is written as

$$u(x,y,z)=\frac{1}{\alpha(z)}\exp\left(-\frac{(x^2+y^2)}{\beta(z)}\right) \tag{2.8}$$

Solving for the complex constants $\alpha(z)$ and $\beta(z)$ the solution has the form

$$u(x,y,z)=\frac{const}{q(z)}\exp\left(-jk\frac{(x^2+y^2)}{2q(z)}\right) \tag{2.9}$$

The complex number q is known as the complex beam parameter, or Gaussian beam parameter, that characterizes the beam properties with propagation distance z along the beam path. It is given by the following equation:

$$\frac{1}{q}=\frac{1}{q_0+z}=\frac{1}{R(z)}-j\frac{\lambda}{\pi w(z)^2} \tag{2.10}$$

where *w(z)* is the radius at which the beam field falls to *1/e* relative to its on-axis value, known as the beam radius. From examining the real and imaginary parts of the complex beam parameter q the characteristics of the beam can be found:

$$R(z)=z\left(1+\left(\frac{\pi w_0^2}{\lambda z}\right)^2\right) \tag{2.11}$$

$$w(z)=w_0\sqrt{1+\left(\frac{\lambda z}{\pi w_0^2}\right)^2} \tag{2.12}$$

where *R(z)* is the phase radius of curvature of the beam and *w(z)* is the beam width at z and w_0 denotes the source plane beam radius, called the beam waist. Note from Equation 2.11 the dependence of the phase radius of curvature on λ; as we approach the

geometrical limit (i.e. $\lambda \rightarrow 0$) the value of $R(z)$ approaches the propagation distance z and the beam is now more appropriately defined as a classical ray trace.

This complete form of the complex beam parameter is complex, containing real and imaginary components. Reapplying this to the wave equation solution (Equation 2.7) the field distribution is now

$$u(x,y,z) = \frac{const}{w_0^2} \exp\left(-\frac{(x^2+y^2)}{w(z)^2}\right) \exp\left(-jk\frac{(x^2+y^2)}{2R(z)^2}\right) \tag{2.13}$$

The real part to this solution is the Gaussian amplitude description of the beam shape, while the imaginary part describes a parabolic wavefront that approximates a spherical wavefront at the paraxial limit. This wavefront evolves with z away from the beam waist location, where the phase is flat.

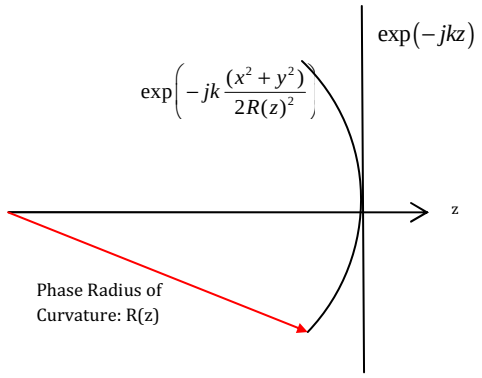

Figure 2-2 Phase shift of beam propagating along z-axis relative to flat phase front of plane wave

The phase slippage between the beam travelling along the z axis with respect to an infinite plane wave is defined as

$$\phi = \arctan\left(\frac{\lambda z}{\pi w_0^2}\right) \tag{2.14}$$

The electric field description can now be fully described. The fundamental Gaussian beam mode solution to the paraxial wave equation in rectangular coordinates is given by [24]:

$$u(x,y,z) = \frac{w(z)}{w_0}\exp\left(-\frac{(x^2+y^2)}{w(z)^2} - jk\left(z + \frac{(x^2+y^2)}{2R}\right) + j\phi\right) \tag{2.15}$$

The normalised form for the expression of the electric field distribution is obtained by integrating the power contained within the area of the beam and equating it to unity.

$$u(x,y,z) = \sqrt{\frac{2}{\pi w(z)^2}}\exp\left(-\frac{(x^2+y^2)}{w(z)^2} - jk\left(z + \frac{(x^2+y^2)}{2R}\right) + j\phi\right) \tag{2.16}$$

The first part of the equation is the normalisation constant. The first term within the exponent gives the solution a Gaussian amplitude envelope; the second term is a combination of the plane wave term and the parabolic phase radius of curvature terms and the final term is the phase slippage between the propagated beam at z and its initial point at $z = 0$. It is easy to re-interpret the above solution in cylindrical coordinates by replacing $(x^2 + y^2)$ with r^2:

$$u(r,z) = \sqrt{\frac{2}{\pi w(z)^2}}\exp\left(-\frac{r^2}{w(z)^2} - jk\left(z + \frac{r^2}{2R}\right) + j\phi\right) \tag{2.17}$$

2.1.2 Propagation of Gaussian Beams

The fundamental Gaussian beam mode (Equation 2.17) can be described at any point along its propagation path. The scale size or radius w and phase radius of curvature R of the beam vary with propagation distance z. The illustrations below (Figure 2-3, Figure 2-4) describes the evolution of the fundamental Gaussian beam as it propagates through a focus position where the beam radius reaches its minimum value known as the beam waist w_0 [32]. After passing through the waist position w increases with propagation distance. Taking left to right to be the positive propagation direction the complex phase radius of curvature R to the left of the beam waist is negative. Approaching the waist position the absolute value of R increases until it reaches infinity

at the beam waist. After the beam waist R is now positive and its absolute value increases with propagation distance.As the beam propagates towards the waist position the beam is said to be converging, and after the waist the beam is diverging.

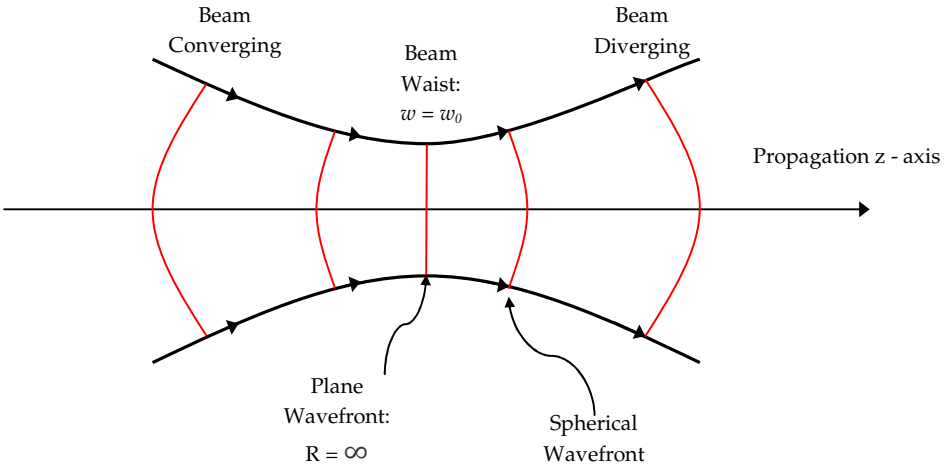

Figure 2-3 - Evolution of complex phase radius of curvature (red curves) for Gaussian beam as it propagates through a waist position [23], [32].

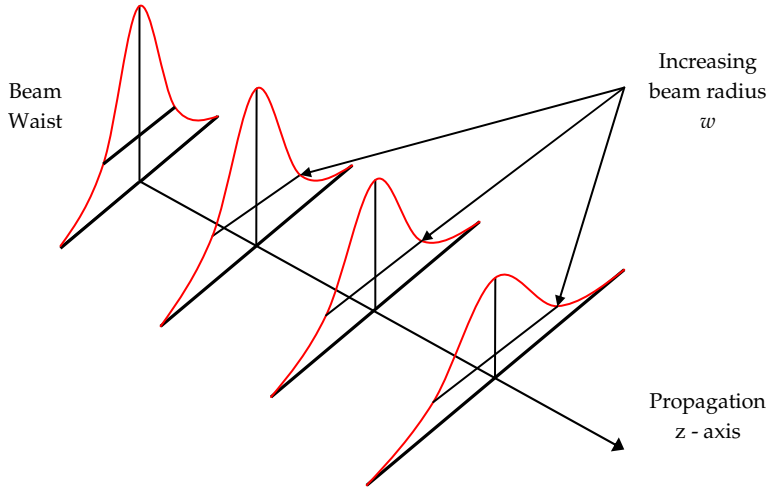

Figure 2-4 - Evolution of the Gaussian amplitude profile as the beam diverges away from a beam waist location [23], [32].

The evolution of this fundamental Gaussian beam with increasing z can be described in terms of a characteristic distance known as the confocal distance z_c [24],

$$z_c = \frac{\pi w_0^2}{\lambda} \tag{2.18}$$

Using the confocal distance the beam parameters of phase radius of curvature, beam radius and phase slippage may be rewritten as

$$R(z) = z + \frac{z_c^2}{z} \tag{2.19}$$

$$w(z) = w_0 \sqrt{1 + \left(\frac{z}{z_c}\right)^2} \tag{2.20}$$

$$\phi_0 = \arctan\left(\frac{z}{z_c}\right) \tag{2.21}$$

This confocal distance is a useful measurement for approximating the beam parameters in two distinct regions along the z axis; the near-field region where $z << z_c$ and the far-field region where $z >> z_c$. In the near-field region it is observed that the phase radius of curvature $R(z)$ is inversely proportional z and in the far field region the phase front radius of curvature can be approximated as $R(z) \approx z$. Note below in Figure 2-5 the asymptotic nature of $R(z)$ and that at the beam waist position ($z = 0$), $R(z)$ approaches infinity, implying a flat phase radius of curvature at the beam waist.

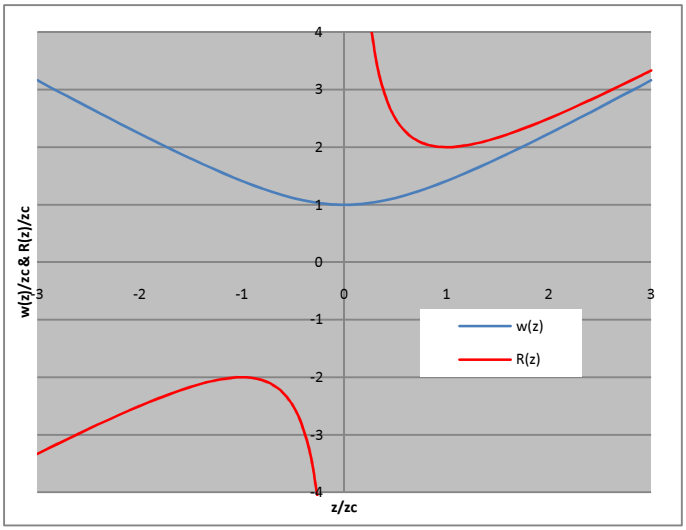

Figure 2-5 - Variation of beam radius *w* (blue) and phase front radius of curvature *R* (red) in terms of confocal distance from the beam waist position *z=0*

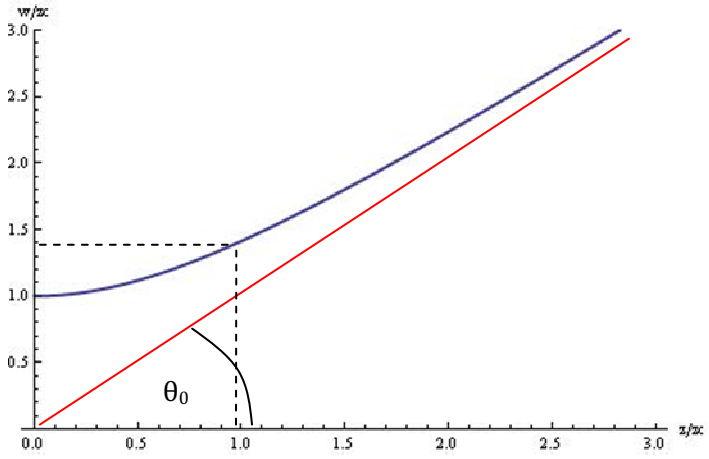

Figure 2-6 - Far field divergence angle θ_0 showing linear growth of beam radius in the far field $z>>z_c$

It should be noticed also from Figure 2-5 that the beam radius w starts increasing linearly with z in the far-field region. With this approximation a useful new characteristic called the far-field beam angle [24] can be applied to the evolution of the Gaussian beam, and it has the form

$$\theta_0 = \arctan\left(\frac{\lambda}{\pi w_0}\right) \tag{2.22}$$

Note that this angular growth of the beam radius applies to the far-field region only. For small angles that typify a beam obeying the paraxial limit the angle θ_0 can be approximated thus:

$$\theta_0 \approx \left(\frac{\lambda}{\pi w_0}\right) \tag{2.23}$$

Another use of the confocal distance, or Rayleigh range, is in defining the region of collimation of the beam. At the confocal distance away from the beam waist the beam radius has only increased slightly to a value of $\sqrt{2}\ w_0$ c.f. dotted lines in Figure 2-6. Beyond this point the beam radius begins to grow at a faster rate defined by the far field divergence angle. It is within this distance z_c therefore that the beam can be said to be approximately collimated, and is called the depth of focus of the beam. This value is of importance when designing quasioptical systems that require strict beam collimation.

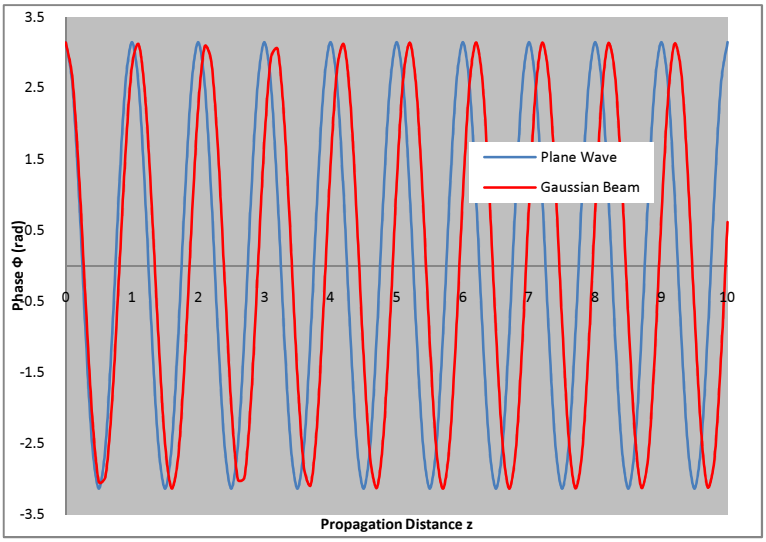

Figure 2-7 - Phase evolution for propagating Plane Wave (blue) and Gaussian Beam (red)

As the Gaussian beam propagates from a waist position at $z = 0$, its phase is seen to evolve faster than that for a simple plane wave. This phase slippage is best visualised by comparing the evolution of the phase of a propagating plane wave, given as

$$g(z) = \mathrm{Re}(\exp(-jkz)) \tag{2.24}$$

and the phase for the propagating Gaussian beam (given by Equation 2.14) is seen below in Figure 2-7. This phase slippage becomes more significant when dealing with higher order mode descriptions of the complex field, with phase slippage occurring between adjacent modes over increasing propagation distance z.

The power contained within the fundamental Gaussian beam mode at any plane is given by the edge taper ratio T_e. This edge taper gives the relative transverse power density of the beam at some radius r_e to the on axis value. The power distribution at any plane for the fundamental Gaussian beam is proportional to the square of the transverse electric field and thus has a Gaussian profile itself - [24]:

$$T_e = \frac{P(r)}{P(0)} = \exp\left(-2\frac{r^2}{w^2}\right) \tag{2.25}$$

The edge taper is a useful tool for determining the power conservation of a source beam within a particular optical system. Measured in decibels (dB), the edge taper provides

an insight into the level of truncation of relative power density for a particular radius measured from the centre. The truncated radius of the fundamental Gaussian can be retrieved from the edge taper using the following

$$\alpha = \left(\frac{r_a}{w_a} \right)^2 = 0.115 T_e(dB) \tag{2.26}$$

Where α is called the taper ratio and it gives the degree of central concentration of the illumination of the antenna aperture. Table 2-1 below lists some sample beam radii and their corresponding power conservation levels measured in both percentages and decibels. As an example of optimum beam truncation at the aperture of an optical element, ample power conservation can be achieved for truncation radii of at least $2w$, ensuring $>99.9\%$ power conservation within a single element.

r/w	Conserved Power F_e	Relative T_e	Te (dB)
0.0	0.00000	1.00000	0.0
0.5	0.39347	0.60653	-2.17
1.0	0.86467	0.13534	-8.69
1.5	0.98889	0.01111	-19.54
2.0	0.99967	0.00034	-34.74
2.5	0.99999	$3.73 * 10^{-6}$	-54.29

Table 2-1 - Edge Taper (T_e) and Power Conservation (F_e) for a fundamental Gaussian beam for increasing radial distance r measured against beam radius w

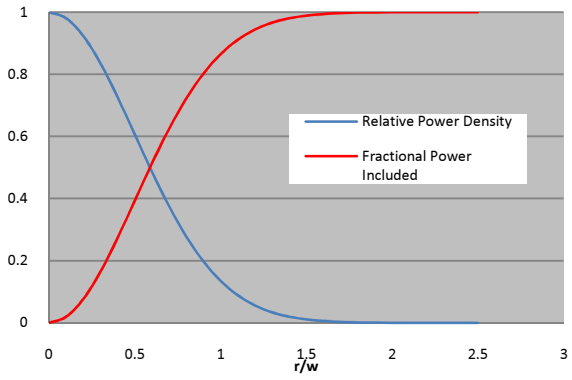

Figure 2-8 - Plot comparing the conserved power (F_e) and edge taper (T_e) of fundamental Gaussian beam as a function of aperture radius r over beam radius w [3].

A summary of the defining characteristics or parameters for the fundamental Gaussian beam is given below in Table 2-2

Beam Radius	$w(z) = w_0\sqrt{1+\left(\frac{\lambda z}{\pi w_0^2}\right)^2}$
Phase Radius of Curvature	$R(z) = z\left(1+\left(\frac{\pi w_0^2}{\lambda z}\right)^2\right)$
Phase Shift	$\phi = \arctan\left(\frac{\lambda z}{\pi w_0^2}\right)$
Edge Taper	$T_e = \frac{P(r)}{P(0)} = \exp\left(-2\frac{r^2}{w^2}\right)$
Far Field Divergence Angle	$\theta_0 = \arctan\left(\frac{\lambda}{\pi w_0}\right)$

Table 2-2 - Defining equations for characteristics of fundamental Gaussian beam

2.1.3 Higher Order Modes: Rectangular Coordinates

The Gaussian beam expression of the electromagnetic field distribution given by Equation 2.17 is the fundamental or lowest order solution to an infinite number of higher order solutions to the same paraxial wave equation. To provide a more accurate description of the diffracted radiation patterns found in quasioptical systems it is necessary to go beyond the base fundamental Gaussian beam mode description. To achieve this, higher order Gaussian beam modes are included in the description of these transverse electromagnetic fields. By using these higher order modes, a more physical description of the beam as it propagates through an optical system can be found. As mentioned previously, it is the relative phase slippage between modes that allows for a successful description of diffracted fields. These higher order modes are described by a particular polynomial which depends on which coordinate system is used, and are multiplied by the Gaussian envelope amplitude pattern which effectively removes the beam in the transverse direction. The higher order solutions can take the form of Hermite-Gaussian polynomials when dealing with rectangular coordinates or of Laguerre-Gaussian polynomials for cylindrical coordinates.

To derive the higher order Hermite-Gaussian solutions to the paraxial wave equation in two dimensional rectangular coordinates, the general two-dimensional Gaussian beam mode solution is simply the product of two one-dimensional solutions. In rectangular coordinates these one-dimensional solutions can be separated into products of identical solutions in the *x* and *y* directions;

$$u_{n,m}(x, y, z) = u_n(x, z) \times u_m(y, z) \tag{2.27}$$

The mathematical form of both of these one-dimensional solutions is equivalent, and as such only one coordinate system is solved, and the other will be equivalent by analogy. Applying a trial solution of the form given below,

$$u(x, z) = A(z) H\left(\frac{\sqrt{2}x}{w(z)}\right) \exp\left(-j\frac{kx^2}{2q(z)}\right) \tag{2.28}$$

where the beam waist *w(z)* and the complex beam parameter *q* are the same as described for the derivation of the fundamental beam mode. The function *H* is the Hermite polynomial, which satisfies the following standard differential equation

$$H(u)'' - 2uH' + 2mH(u) = 0 \tag{2.29}$$

where *m* is a positive integer denoting the order of the polynomial. By applying the same normalization parameter as was done to Equation 2.17 the higher order mode expression of the Gaussian beam of order *m* is given as

$$u_m(x, z) = \sqrt{\frac{2}{\pi}} \sqrt{\frac{1}{w_x 2^{m-1/2} m!}} H_m\left(\frac{\sqrt{2}x}{w_x}\right) \exp\left(-\frac{x^2}{w_x^2} - j\left(kz - \frac{\pi x^2}{\lambda R_x}\right) + j\frac{(2m+1)\phi_{0x}}{2}\right) \tag{2.30}$$

This solution ensures that the beam will have the same normalised transverse shape at any plane *z*; i.e. the beam radius *w* and phase radius of curvature *R* will evolve with propagation distance, but the amplitude of u_m will retain the same shape. From the last exponent term, the phase evolution term, the phase shift for the higher order modes will be greater than for those of lower order. As the beam propagates there is a relative phase slippage from one mode to the next. By analogy, the solution for the *(x,z)* coordinate system may be applied to the *(y,z)* coordinate system. The complete,

normalised two-dimensional expression of the higher order mode solution in rectangular coordinates is thus given by

$$u_m(x,y,z) = \sqrt{\frac{1}{\pi w_x w_y 2^{m+n-1} m!n!}} H_m\left(\frac{\sqrt{2}x}{w_x}\right) H_n\left(\frac{\sqrt{2}y}{w_n}\right)$$
$$\exp\left(-\frac{x^2}{w_x^2} - \frac{y^2}{w_y^2} - jkz - j\left(\frac{\pi x^2}{\lambda R_x} + \frac{\pi y^2}{\lambda R_y}\right) + j\frac{(2m+1)\phi_{0x}}{2} + j\frac{(2n+1)\phi_{0y}}{2}\right) \quad (2.31)$$

Considering the case where the beam has equivalent beam parameter values in x and y leads to the following reduced version of Equation 1.31

$$u_m(x,y,z) = \sqrt{\frac{1}{\pi w^2 2^{m+n-1} m!n!}} H_m\left(\frac{\sqrt{2}x}{w}\right) H_n\left(\frac{\sqrt{2}y}{w}\right)$$
$$\exp\left(-\frac{(x^2+y^2)}{w^2} - jkz - \frac{j\pi(x^2+y^2)}{\lambda R} + j(m+n+1)\phi_0\right) \quad (2.32)$$

Some examples of the different shapes achievable from Hermite-Gaussian mode functions of various orders of the Hermite polynomial function are given below in Figure 2-9. These figures illustrate the increasing complexity of the field profiles for the higher order modes.

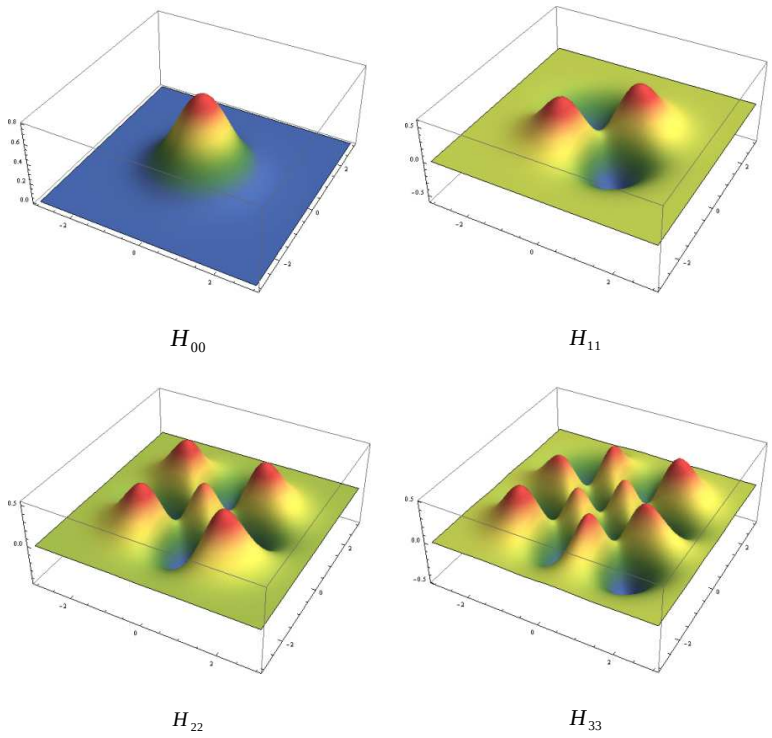

Figure 2-9 - Hermite Gaussian field distributions of increasing order - $H_{m\,n}$

2.1.4 Higher Order Modes: Cylindrical Coordinates

An alternative and equally valid solution to the paraxial wave equation exists for cylindrical rather than rectangular coordinates. To define a Gaussian beam mode solution to the paraxial wave equation in cylindrical coordinates, the general solution must allow for variation of the electric field distribution as a function of the azimuthal angle θ . As before, a trial solution is implemented:

$$u(r,\theta,z) = A(z)\exp\left(-j\frac{kr^2}{2q(z)}\right)S(r)\exp(jm\theta) \tag{2.33}$$

where *S(r)* is an undetermined function of *r* and m is a positive integer. With this trial solution applied to the paraxial wave equation the following result for *S(r)* is obtained:

$$S(r) = \left(\frac{\sqrt{2}r}{w}\right)^m L_{pm}\left(\frac{2r^2}{w^2}\right) \tag{2.34}$$

where L_{pm} is the generalized Laguerre polynomial. The full higher order mode solution, known as the Associated Laguerre Gaussian mode set, is written in terms of associated sine and cosine Laguerre-Gaussian modes [32]

$$\begin{pmatrix} u^{c}_{n,\alpha}(r,\theta,z) \\ u^{s}_{n,\alpha}(r,\theta,z) \end{pmatrix} = \sqrt{\frac{2(2-\delta_{0N})n!}{w(z)^2\pi(n+\alpha)!}}\left(\frac{2r^2}{w(z)^2}\right)^{\frac{\alpha}{2}} L_n^{\alpha}\left(\frac{2r^2}{w(z)^2}\right) \\ \exp\left(-\frac{r^2}{w(z)^2} - j\left(kz + \frac{\pi r^2}{\lambda R(z)}\right) + j(2n+\alpha+1)\phi_0(z)\right)\begin{pmatrix}\cos(\alpha\theta)\\ \sin(\alpha\theta)\end{pmatrix} \tag{2.35}$$

where $L_n^{\alpha}(x)$ are the associated Laguerre polynomials of order n and degree α and all other quantities w, R, and ϕ_0 are exactly equivalent to those as in the Hermite Gaussian and fundamental mode Gaussian solutions. These higher order modes have been normalized so that each mode is integrated to unity power, and that they obey the orthogonality rule

$$\int_{-\infty}^{\infty}\int_{0}^{2\pi} u^{C}_{m,\alpha}(r,\theta,z)u^{S}_{p,\beta}{}^{*}(r,\theta,z)r\,dr\,d\theta = 0 \qquad \forall\,\alpha,\beta,m,n \tag{2.36}$$

and the individual associated modes form a complete infinite basis set of ortho-normal modes such that

$$\int_{-\infty}^{\infty}\int_{0}^{2\pi} u^{S}_{m,n}(r,\theta,z)u^{S}_{p,q}{}^{*}(r,\theta,z)r\,dr\,d\theta = \delta_{mp}\delta_{nq} \tag{2.37}$$

$$\int_{-\infty}^{\infty}\int_{0}^{2\pi} u^{c}_{m,n}(r,\theta,z)u^{c}_{p,q}{}^{*}(r,\theta,z)r\,dr\,d\theta = \delta_{mq}\delta_{np} \tag{2.38}$$

It is useful to consider those higher order modal representations that are axially symmetric; they have no dependence on the azimuthal angle θ. This is achieved by setting the azimuthal mode index m to zero. Such modal descriptions can be used to describe the complex aperture field from a cylindrical corrugated horn or conical smooth walled horn:

$$u(r,\theta,z) = \sqrt{\frac{2}{\pi w(z)^2}}L_{pm}\left(\frac{2r^2}{w(z)^2}\right)\exp\left(-\frac{r^2}{w(z)^2} - j\left(kz + \frac{\pi r^2}{\lambda R(z)}\right) + j(2p+1)\phi_0(z)\right) \tag{2.39}$$

This cylindrically symmetric field description is mathematically equivalent to the $u_{n,\alpha}^{C}(r,\theta,z)$ mode set of the overall associated Laguerre Gaussian mode set from Equation 2.35. The figure below shows contour plots of the real components for the associated Laguerre-Gaussian fields of increasing order n with degree $\alpha = 0$. The field distribution of lowest order L_0^0 is equivalent to the fundamental Gaussian beam distribution. With higher orders brings increasing complexity, though the distributions remain azimuthally symmetric.

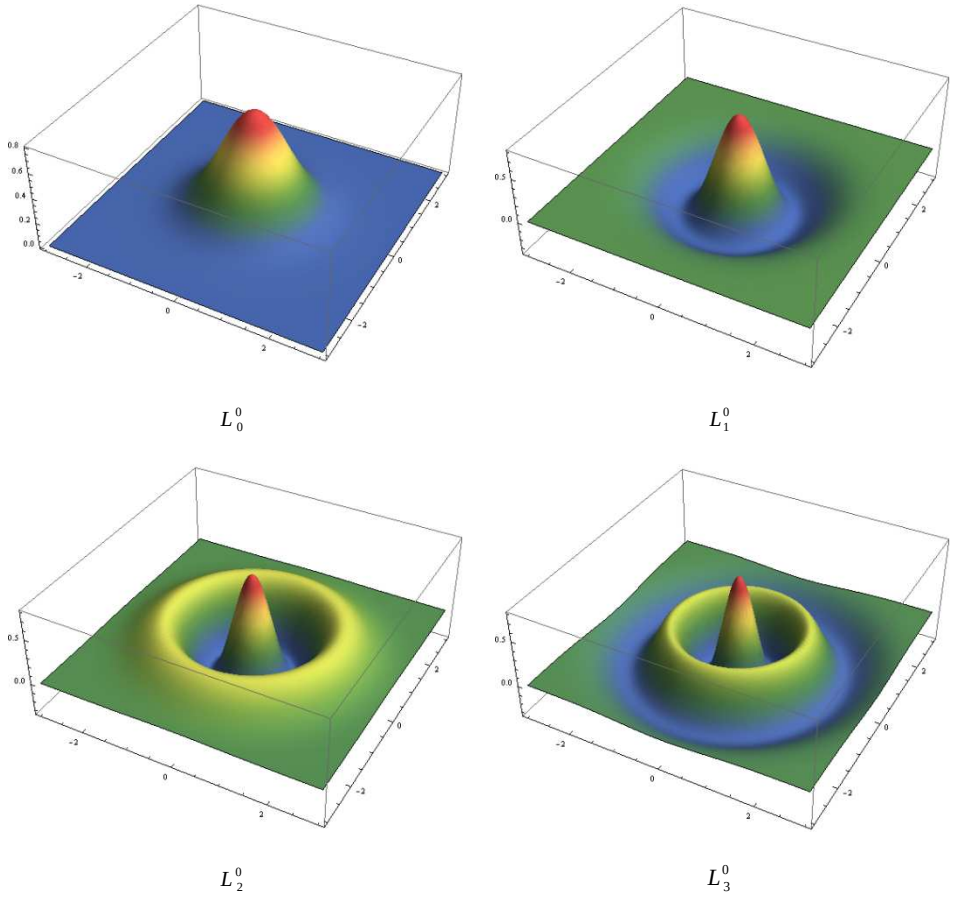

Figure 2-10 – Associated Laguerre Gaussian field distributions of increasing order *n*

If the degree α of the mode set is increased from zero the cosine term in Equation 2.35 comes into effect; by modulating the field and increasing its complexity. Some examples of these higher order mode field descriptions are shown below in Figure 2-11.

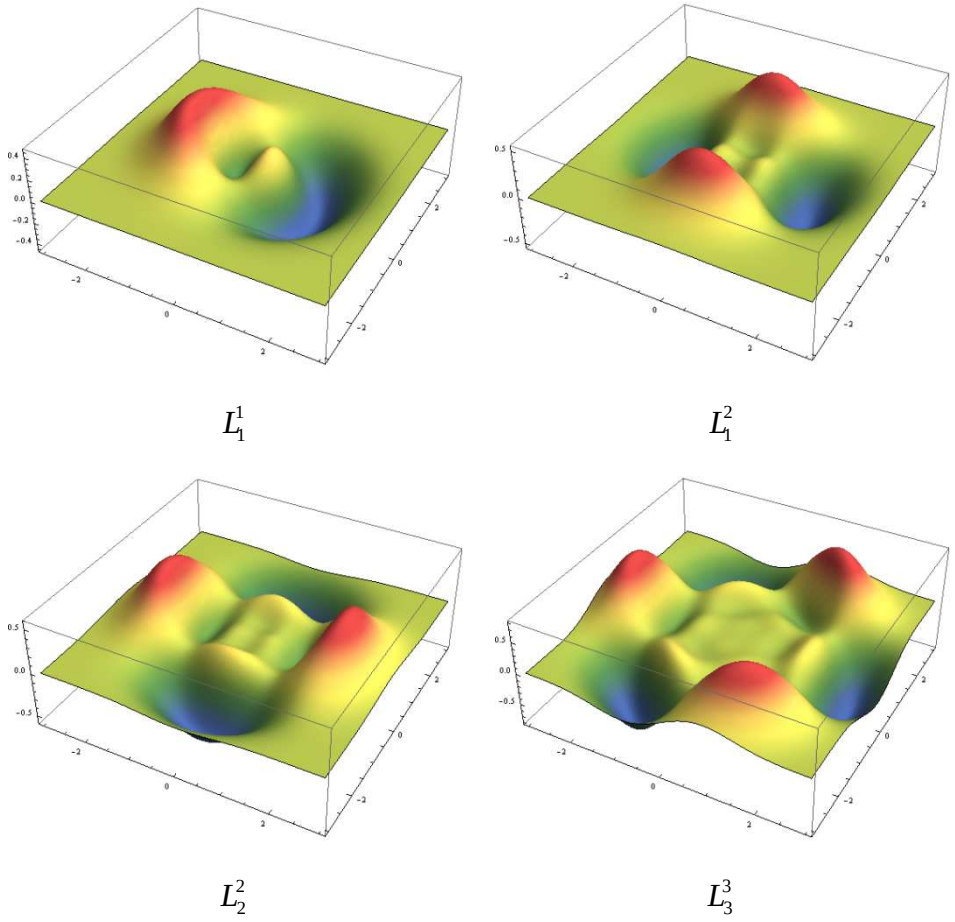

Figure 2-11 - Associated Laguerre Gaussian field distributions of increasing order *n* and degree *α*

2.1.5 Gaussian Beam Transformation

The ability to describe a beam such as those from a laser cavity or a corrugated horn in terms of Gaussian beam modes is only a small part of the process of GBMA. Through the use of ray transfer matrices and scattering matrices, it is possible to build a complete picture of an entire quasioptical system. In the following subsection, derivation and application of these ray or ABCD matrices as they apply to GBMA is described [3], [4] while the technique of scattering matrices is covered in detail in Chapter 4. In the previous section the defining characteristics of a Gaussian beam, that is the beam waist size $w(z)$ and the radius of curvature of the phase $R(z)$, or indeed the complex beam parameter $q(z)$, were defined in terms of their propagation distance z from some known

location. However, simple freespace propagation of a Gaussian beam will not build a complete picture of a quasioptical system that contains reflective or refractive elements such as mirrors and lenses. The purposes of such systems are many, though they all serve to manipulate a source beam to some output plane or planes. The effects of these quasioptical elements on a Gaussian beam are easily determined through the use of ABCD matrices, and thus a prediction of the output field can be calculated.

2.1.5.1 ABCD Matrices

A ray can be described by its height from the optical axis y and the slope angle α relative to the optical axis [33]. A ray can thus be defined as a vector, and if this ray is incident upon an optical system described using an ABCD matrix then the ray emerging from the system can be calculated using matrix multiplication. The diagram below illustrates this principle.

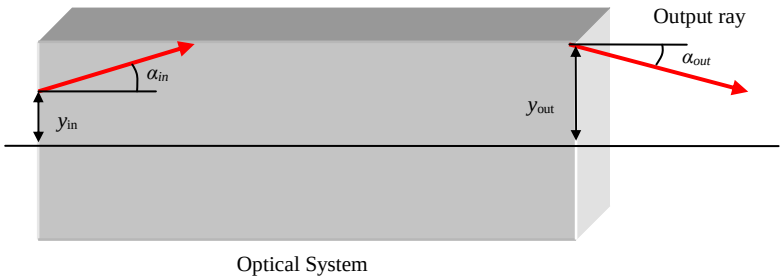

Figure 2-12 – An incident ray is transformed by an arbitrary optical system into an output ray. The transformation performed by the optical system is described by the ABCD matrix

The parameter y is the perpendicular distance between the optical axis and the origin of the ray vector and the angle α is the angle the ray vector makes with the horizontal. The ray incident upon the optical system has parameters y_{in} and α_{in} and after emerging from the optical system the ray now has new parameters y_{out} and α_{out}. This is shown mathematically below, where the ABCD matrix representation of the optical system acts upon the incident ray vector to produce the output ray vector

$$\begin{bmatrix} y_{out} \\ \alpha_{out} \end{bmatrix} = \begin{bmatrix} A & B \\ C & D \end{bmatrix} \begin{bmatrix} y_{in} \\ \alpha_{in} \end{bmatrix} \tag{2.40}$$

It then follows that:

$$\begin{aligned} y_{out} &= Ay_{in} + B\alpha_{in} \\ \alpha_{out} &= Cy_{in} + D\alpha_{in} \end{aligned} \tag{2.41}$$

The radius of curvature R of an ordinary spherical wave can be related to the vector ray parameters [4]:

$$R = \frac{y}{\alpha} \tag{2.42}$$

Dividing Equation 2.41 by Equation 2.42 the following is obtained:

$$R_{out} = \frac{AR_{in} + B}{CR_{in} + D} \tag{2.43}$$

This is the standard result for a ray transformation approach to an arbitrary optical system. This method can be extended to apply to Gaussian beams through a simple replacement of the radius of curvature element R with the complex beam parameter q, yielding the following ABCD matrix for quasioptical systems

$$q_{out} = \frac{Aq_{in} + B}{Cq_{in} + D} \tag{2.44}$$

The complex beam parameter of a Gaussian beam q evolves in a very similar way to the real radius of curvature from a geometrical point source. By using the ABCD matrix approach in combination with the complex beam parameter q, the Gaussian beam parameters at the output plane can be recovered providing that the parameters at the input plane are known. The beam waist w and phase radius of curvature R are determined from the complex beam parameters from the following equations:

$$w = \sqrt{\frac{\lambda}{\pi \operatorname{Im}\left(-\frac{1}{q}\right)}} \tag{2.45}$$

$$R = \frac{1}{\operatorname{Re}\left(\frac{1}{q}\right)} \tag{2.46}$$

The phase slippage $\Delta\phi_0$, defined as the difference between the phases of the output and incident beams is given by a combination of the ABCD matrix elements A and B and the complex beam parameter of the incident beam q_{in}:

$$\Delta\phi_0 = -\arg\left[A + B\left(\frac{1}{q_{in}}\right)\right] \tag{2.47}$$

The table below lists the ABCD matrices for the most commonly used components in quasioptical systems [3].

Element	Matrix	Comment
Reflection from flat mirror	$\begin{bmatrix} -1 & 0 \\ 0 & 1 \end{bmatrix}$	Modified identity matrix (negative A (or D) element ensures reversal of R and π phase change)
Free space propagation	$\begin{bmatrix} 1 & d \\ 0 & 1 \end{bmatrix}$	d = propagation distance
Refraction at flat interface	$\begin{bmatrix} 1 & 0 \\ 0 & \frac{n_1}{n_2} \end{bmatrix}$	n_1 = initial refractive index n_2 = final refractive index
Refraction at curved interface	$\begin{bmatrix} 1 & 0 \\ \frac{n_1 - n_2}{R.n_2} & \frac{n_1}{n_2} \end{bmatrix}$	R = radius of curvature, $R>0$ for convex surface n_1 = initial refractive index n_2 = final refractive index
Reflection from curved mirror	$\begin{bmatrix} 1 & 0 \\ -\frac{2}{R} & 1 \end{bmatrix}$	R = radius of curvature, R>0 for convex surface
Propagation through dielectric	$\begin{bmatrix} 1 & d\frac{n_1}{n_2} \\ 0 & 1 \end{bmatrix}$	d = propagation distance within dielectric n_1 = initial refractive index n_2 = final refractive index
Thin lens	$\begin{bmatrix} 1 & 0 \\ -\frac{1}{f} & 1 \end{bmatrix}$	f = focal lengh, $f > 0$ for converging lens. Thin lens valid if f >> thickness of lens

Table 2-3 - List of ABCD matrices for typical optical components

To illustrate the ABCD matrix method as applied to quasioptical systems, a simple Gaussian Beam Telescope (GBT) example is outlined below. The transformation of a

Gaussian beam by an arbitrary optical system of N elements is described by the following matrix:

$$M = \begin{bmatrix} A_N & B_N \\ C_N & D_N \end{bmatrix} \cdot \begin{bmatrix} A_{N-1} & B_{N-1} \\ C_{N-1} & D_{N-1} \end{bmatrix} \cdots \begin{bmatrix} A_1 & B_1 \\ C_1 & D_1 \end{bmatrix} \tag{2.48}$$

where the order of multiplication of the ABCD matrices is reverse to their 'physical' order; that is the leftmost matrix describes the last element at the output and the rightmost matrix describes the first element on the input side, as is conventionally illustrated in figures.

The GBT is comprised of a pair of focusing elements separated by the sum of their focal lengths; that is their respective focal lengths are coincident. The determination of the GBT ABCD matrix is relatively straightforward. The GBT is considered to consist of two thin lenses of focal lengths f_1 and f_2 with the propagation distance between them set to $d = f_1 + f_2$. This is illustrated below in Figure 2-13.

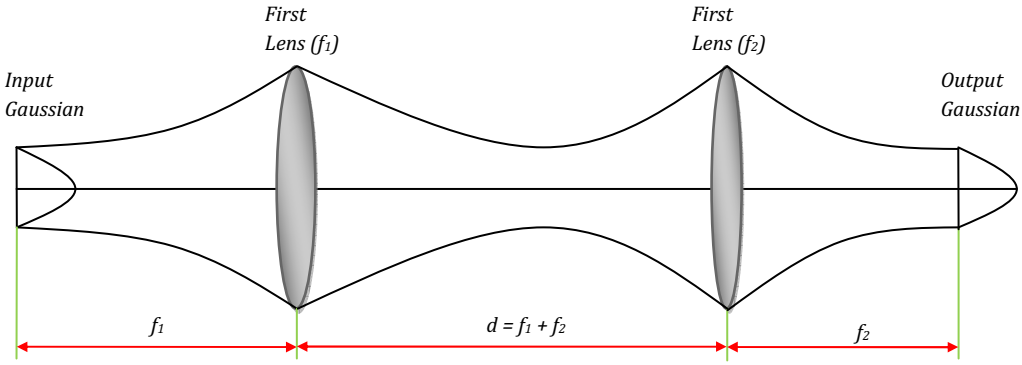

Figure 2-13 - Illustration of Gaussian Beam Telescope optical arrangement

The combined ABCD matrix for this optical system is written in order as:

$$M = \begin{bmatrix} 1 & f_2 \\ 0 & 1 \end{bmatrix} \cdot \begin{bmatrix} 1 & 0 \\ -\frac{1}{f_2} & 1 \end{bmatrix} \cdot \begin{bmatrix} 1 & f_1 + f_2 \\ 0 & 1 \end{bmatrix} \cdot \begin{bmatrix} 1 & 0 \\ -\frac{1}{f_1} & 1 \end{bmatrix} \cdot \begin{bmatrix} 1 & f_1 \\ 0 & 1 \end{bmatrix}. \tag{2.49}$$

which simplifies to

$$M = \begin{bmatrix} -\frac{f_2}{f_1} & 0 \\ 0 & -\frac{f_1}{f_2} \end{bmatrix} \tag{2.50}$$

Using this result combined with Equation 2.44 the following is obtained:

$$\begin{aligned} q_{out} &= \frac{A}{D} q_{in} \\ \Rightarrow q_{out} &= \left(\frac{f_2}{f_1} \right)^2 q_{in} \end{aligned} \tag{2.51}$$

The output beam parameters may now be determined:

$$\begin{aligned} R_{out} &= \left(\frac{f_2}{f_1} \right)^2 R_{in} \\ w_{out} &= \left(\frac{f_2}{f_1} \right) W_{in} \end{aligned} \tag{2.52}$$

The output phase radius of curvature R_{out} and beam waist w_{out} are independent of wavelength and are only dependent on the input and output distances and hence the focal lengths of the lenses. It should be noted here that there is a relative phase shift between the input and output beams of π. As the matrix element B is zero the complex number within the argument in Equation 2.47 becomes real, which results in a π phase shift. It is not specifically implied that a beam waist must exist at the input plane. The calculation will still result in a frequency independent image at the output plane.

2.1.5.2 Fresnel Diffraction by Circular Aperture

As an example of how the theory of Gaussian Beam modes models long wavelength electromagnetic fields we consider the classical Fresnel diffraction of a plane wave by a truncating circular aperture. The classical treatment for solving the Fresnel diffraction pattern by a circular aperture is achieved by applying the Fresnel – Kirchoff diffraction integral.

By utilizing the theory of Fresnel zones [33] an approximation to this diffraction pattern can also be derived using a Fourier-Bessel transform, or a Hankel transform of zero order [34], [35] .

The scheme is illustrated below in Figure 2-14 where a plane wave illuminates a circular aperture. The Gaussian beam mode analogue of this system is to model a truncated plane wave, or top-hat field. The top-hat field is described using Laguerre-Gaussian modes of a similar form as Equation 2.17:

$$u(r,\varphi,z)=\sqrt{\frac{2}{\pi w(z)^2}}L_{pm}\left(\frac{2r^2}{w(z)^2}\right)\exp\left(-\frac{r^2}{w(z)^2}\right) \tag{2.53}$$

where it is assumed that the field at the aperture is a waist with infinite phase radius of curvature, hence the removal of the initial phase term from Equation 2.17.

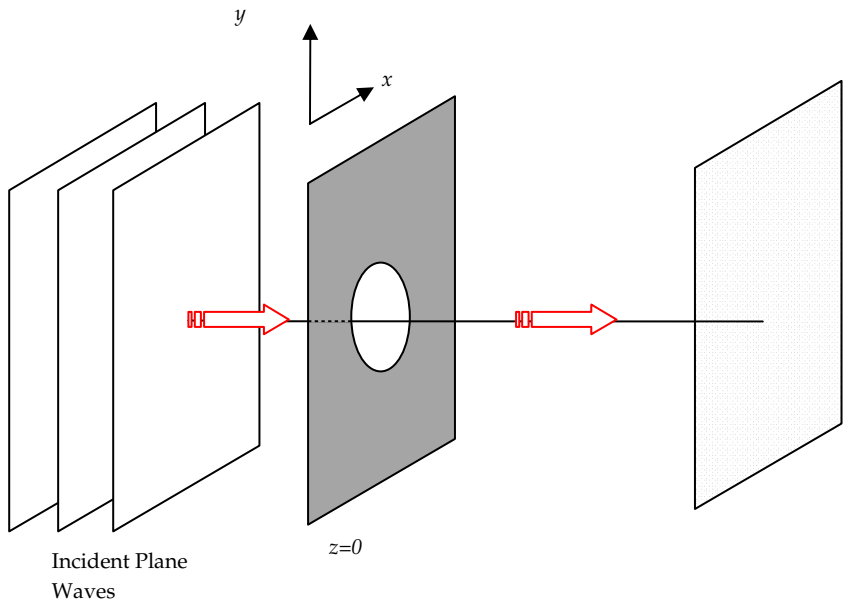

Figure 2-14 - Optical layout for Fresnel diffraction - plane wave incident upon circular truncating aperture

The choice of the beam waist size w determines the distribution of power among the mode coefficients A, which in turn are required to describe the complex field in the

typical manner (Equation 2.1). A waist to aperture ratio of *0.18* generates the following top-hat field approximation:

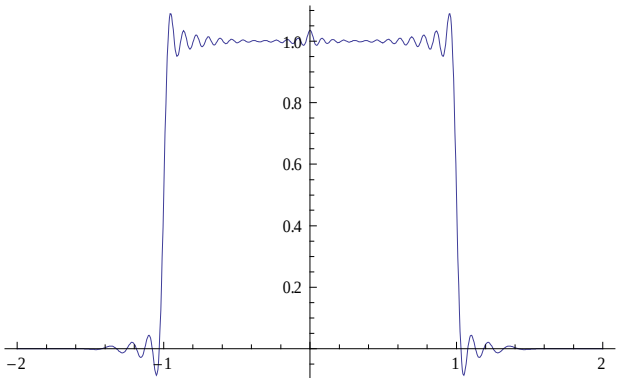

Figure 2-15 - Laguerre Gaussian beam mode description of Top-Hat field of unit radius *1 mm*

Once these mode coefficients have been determined the field may now be described at any plane beyond $z = 0$. The evolution of the source beam parameters is determined using the ABCD matrix technique. Given that the beam undergoes a simple propagation the mode coefficients remain unaltered, with the phase slippage between adjacent modes of the beam being carried by the evolving phase term. The new modes are thus given by the complete Laguerre-Gaussian mode set (Equation 2.17). Following [29] the beam is sampled at three distinct planes along the propagation axis representing different points of evolution in the diffraction pattern; $z = a^2/6\lambda$, $z = a^2/3\lambda$ and $z = 2a^2/\lambda$, where a refers to the radius of the truncating aperture. The Gaussian beam diffraction patterns are also compared against the classical analytical expressions for Fresnel diffraction from [34], [35] below.

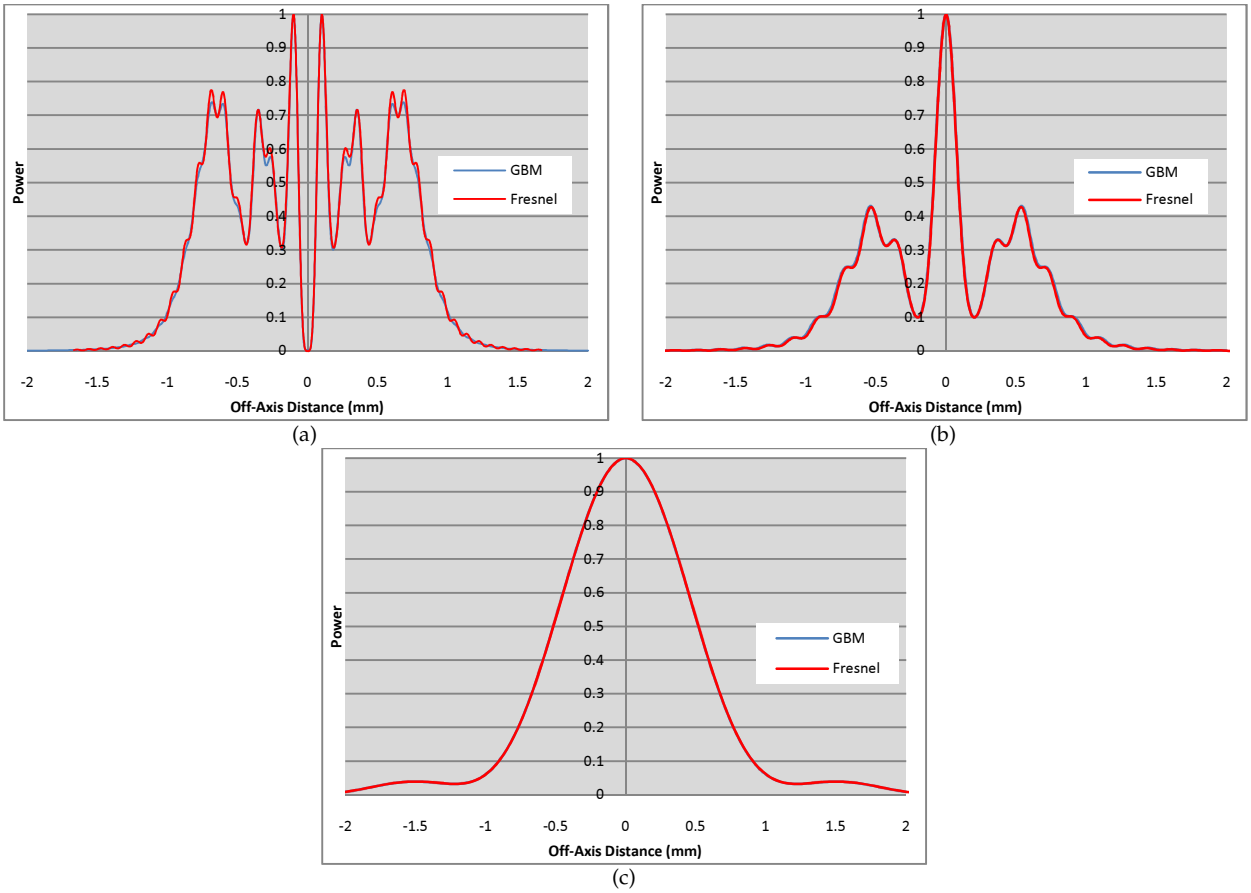

Figure 2-16 - Gaussian beam mode descriptions (blue) for Fresnel diffraction of a plane wave at a circular aperture for increasing propagation distance *z*: (a) $z = a^2/6\lambda$, (b) $z = a^2/3\lambda$, (c) $z = 2a^2/\lambda$. Classical diffraction patterns are plotted in red.

The comparisons between the GBM predictions and those of the classical Hankel transform show excellent agreement for the two theories. This is in line with the results by Murphy from [29].

2.1.6 Angular Spectrum of Plane Waves

An alternative approach to describing the transformation of a complex field distribution is achieved using the Angular Spectrum method (ASPW) [34]. If a complex field distribution across any plane is Fourier analysed, the various spatial Fourier components are identified as plane waves, each travelling in a different direction. The field amplitude at any other plane can then be calculated by adding the contributions of

these plane waves, taking into account the phase shifts of the individual plane waves as they propagate.

If a complex electromagnetic disturbance is given by *U(x,y,0)* then the 2D Fourier transform is given by

$$A_0(f_X, f_Y) = \int_{-\infty}^{+\infty}\int U(x, y, 0)\exp[-j2\pi(f_X x + f_Y y)]dxdy \tag{2.54}$$

where f_X and f_Y are the spatial frequencies of the spectrum of plane waves. This transform of the original field U can be interpreted as its angular spectrum of component plane waves, each travelling in their own unique direction. A unit-amplitude plane wave can be described as follows:

$$B(x, y, z) = \exp\left[j\frac{2\pi}{\lambda}(\alpha x + \beta y + \gamma z)\right] \tag{2.55}$$

where α, β and γ are direction cosines and are related by

$$\gamma = \sqrt{1-\alpha^2-\beta^2} \tag{2.56}$$

These direction cosines are related to the spatial frequencies by

$$\alpha = \lambda f_X, \qquad \beta = \lambda f_Y, \qquad \gamma = \sqrt{1-(\lambda f_X)^2-(\lambda f_Y)^2} \tag{2.57}$$

The Fourier transform (ref above) is thus re-written as

$$A_0\left(\frac{\alpha}{\lambda}, \frac{\beta}{\lambda}\right) = \int_{-\infty}^{+\infty}\int U(x, y, 0)\exp\left[-j2\pi\left(\frac{\alpha}{\lambda}x + \frac{\beta}{\lambda}y\right)\right]dxdy \tag{2.58}$$

The original complex field U can be written as the inverse Fourier transform of its angular spectrum:

$$U(x, y, 0) = \int_{-\infty}^{+\infty}\int A_0\left(\frac{\alpha}{\lambda}, \frac{\beta}{\lambda}\right)\exp\left[j2\pi\left(\frac{\alpha}{\lambda}x + \frac{\beta}{\lambda}y\right)\right]d\frac{\alpha}{\lambda}d\frac{\beta}{\lambda} \tag{2.59}$$

If the field is propagated a distance z, the new complex field $U(x,y,z)$ is calculated as follows:

$$U(x,y,z)=\int_{-\infty}^{+\infty}\int A_0\left(\frac{\alpha}{\lambda},\frac{\beta}{\lambda}\right)\exp\left[j\frac{2\pi}{\lambda}\sqrt{1-\alpha^2-\beta^2}\,z\right]\exp\left[j2\pi\left(\frac{\alpha}{\lambda}x+\frac{\beta}{\lambda}y\right)\right]d\frac{\alpha}{\lambda}\,d\frac{\beta}{\lambda} \qquad (2.60)$$

where the second exponential term determines the effects of wave propagation upon the angular spectrum A_0.

The diffracting effects of a truncating aperture of radius r within an opaque screen of infinite extent can be accounted for through calculation of the angular spectrum of the original disturbance $U(x,y,0)$. A transmittance function t for the aperture is defined as

$$t(x,y)=\begin{cases}1 & \left(x^2+y^2\right)<r\\ 0 & \textit{otherwise}\end{cases} \qquad (2.61)$$

The field immediately behind the aperture U_t is taken to be the geometrical shadow of this transmittance function upon U

$$U_t(x,y,0)=U(x,y,0)t(x,y) \qquad (2.62)$$

The convolution theorem of Fourier analysis is now used to write the angular spectrum of the transmitted field as

$$A_t\left(\frac{\alpha}{\lambda},\frac{\beta}{\lambda}\right)=A_0\left(\frac{\alpha}{\lambda},\frac{\beta}{\lambda}\right)*T\left(\frac{\alpha}{\lambda},\frac{\beta}{\lambda}\right) \qquad (2.63)$$

where T is the Fourier transform of the transmittance function and * represents the convolution operation. For a unit amplitude plane wave illuminating the aperture at normal incident, the above result simply becomes

$$A_t\left(\frac{\alpha}{\lambda},\frac{\beta}{\lambda}\right)=T\left(\frac{\alpha}{\lambda},\frac{\beta}{\lambda}\right) \qquad (2.64)$$

Thus the transmitted angular spectrum is found by a direct Fourier transform of the transmission function of the aperture. The transmitted field can then be propagated in

the same manner as Equation 2.60 by replacing the original unaffected angular spectrum A_0 with the new A_t.

The ASPW technique was used as a further demonstration of the Fresnel diffraction patterns described previously in Section 2.1.5.2. A source field disturbance *U(x,y,0)* was generated numerically as a circularly symmetric top-hat field of radius *1 mm*. This field represents the transmission function of a circular aperture. From Equation 2.64 the Fourier transform of this field gives the angular spectrum of the transmission function. This angular spectrum representation is then propagated and transformed back into the spatial domain to give the propagated field *U(x,y,z)*. As before (Section 2.1.5.2) the diffraction patterns are predicted using this ASPW technique at three distinct planes and are compared with the predictions from classical diffraction theory and GBMA below in Figure 2-17.

The resulting diffraction pattern generated by the ASPW technique shows a much smoother profile when compared to the same patterns predicted classical theory. These smoother patterns predicted by ASPW are technically more physically correct than those from classical theory, which contain sharper ringing effects. The reason for this is that the angular spectrum components that are below the *evanescent wave cutoff* are removed. Note that the propagated angular spectrum components may be written as [34]

$$A_t\left(\frac{\alpha}{\lambda},\frac{\beta}{\lambda}\right)=A_0\left(\frac{\alpha}{\lambda},\frac{\beta}{\lambda}\right)*\exp(-\mu z) \tag{2.65}$$

where

$$\mu=\frac{2\pi}{\lambda}\sqrt{\alpha^2+\beta^2-1} \tag{2.66}$$

Note that μ is a positive real number, such that these wave components are rapidly attenuated by propagation [34]. These *evanescent waves* are thus cut off and do not contribute to the overall diffracted field. These components do however contribute to

the classical Fresnel diffraction pattern, and thus result in the observed sharp fringes. No conventional imaging system is able to resolve any periodic structure with a period that is finer than the operating wavelength, and these evanescent components are thus not recoverable.

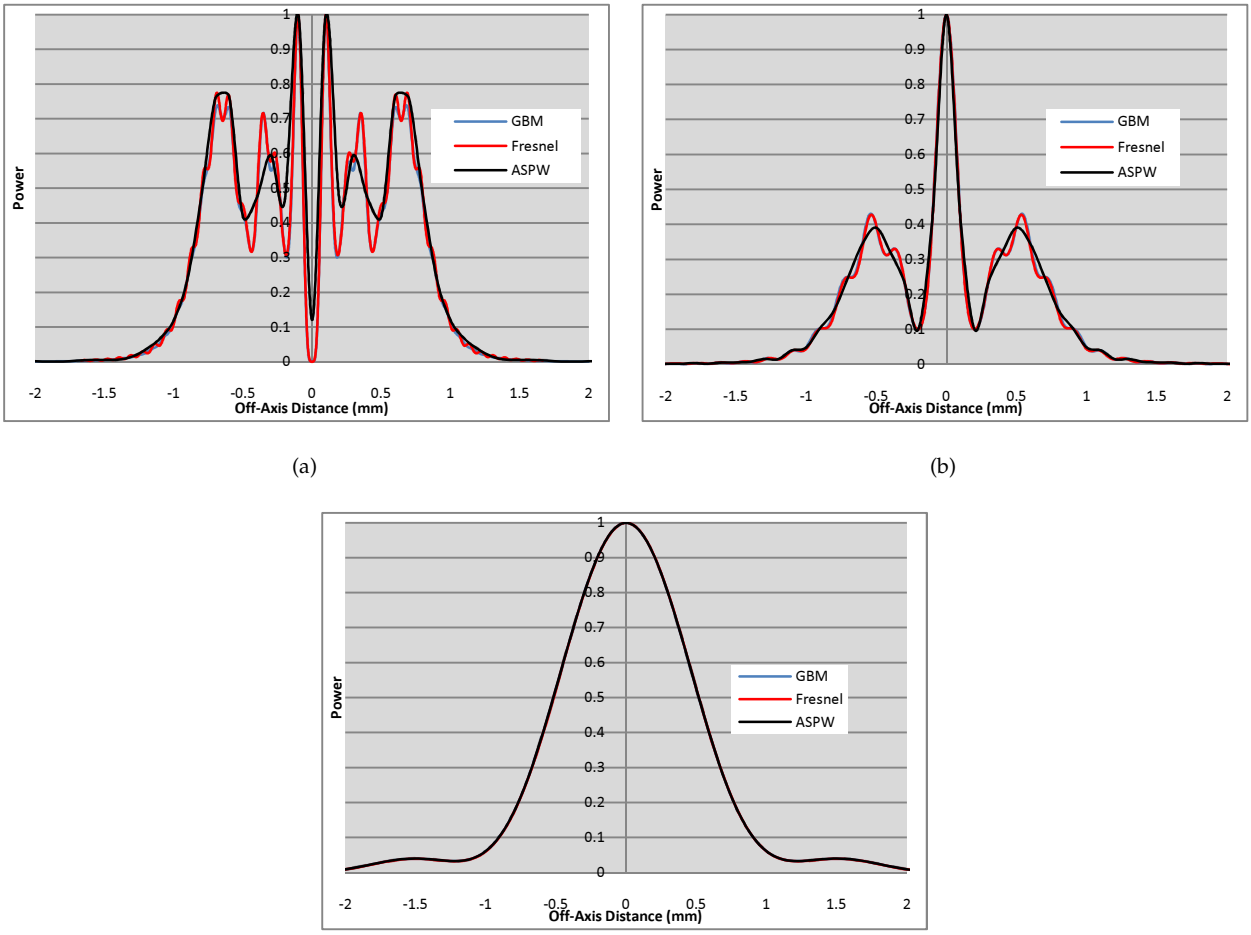

(a)

(b)

(c)

Figure 2-17 - Fresnel diffraction patterns predicted using ASPW (in black) for three distinct planes: (a) $z = a^2/6\lambda$, (b) $z = a^2/3\lambda$, (c) $z = 2a^2/\lambda$. Predictions from classical diffraction theory and GBMA are included for comparison.

2.2 The Michelson Interferometer

The theory of GBMA can be extended to describe the interference patterns of classical interferometers. This has already been applied to the examples of a Fabry Perot interferometer and Young's Slit Experiment [36].These optical devices are commonly comprised of mirrors or partially transmitting mirrors, referred to as beam splitters. A beam splitter is formed by coating a dielectric slab with a metallic or dielectric coating that transmits a portion of the incident beam, while reflecting the remainder. One common interferometer configuration is the Michelson interferometer. The simplest form of this type of interferometer is shown below [37].

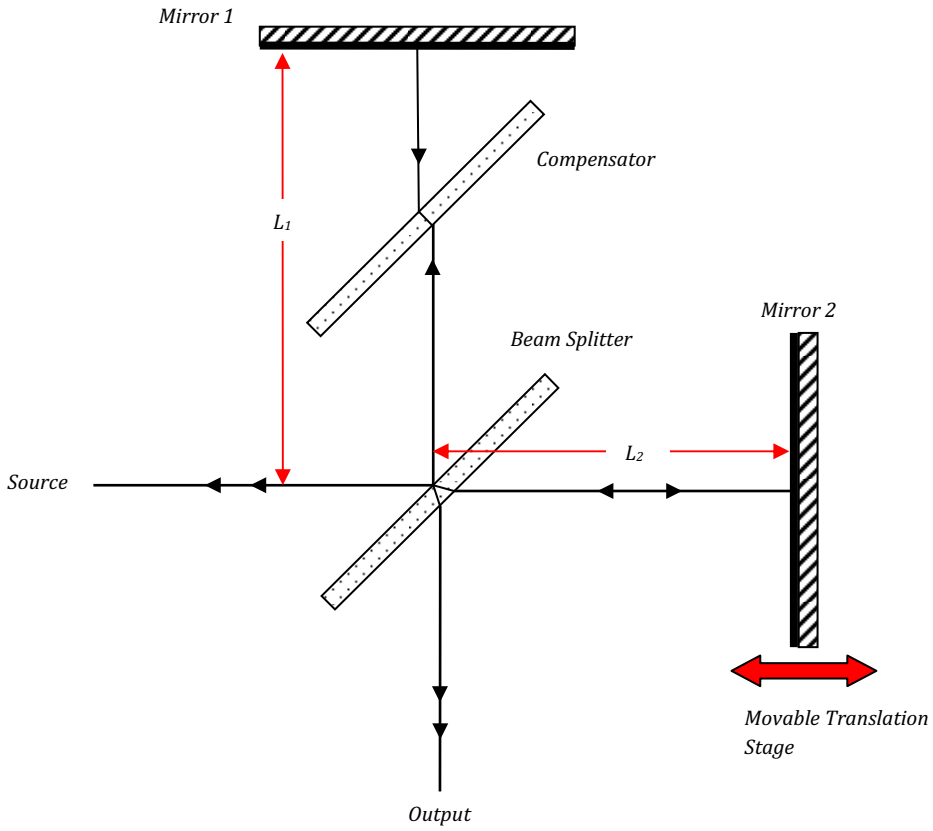

Figure 2-18 - The Michelson Interferometer

In the interferometer layout in Figure 2-18 above the source beam is incident upon a *50:50* beam splitter oriented at *45°* relative to the optical axis. The reflected and transmitted beams are then reflected by *Mirrors 1* and *2* respectively, after which they recombine back at the beam-splitter. The beam reflected by *Mirror 2* traverses the beamsplitter a total of three times compared with the single passage for the beam reflected by *Mirror 1*. This asymmetry is removed through use of the compensator plate of material and thickness identical to the beamsplitter [25]. The two beams propagate through different optical distances L_1 and L_2. In the above design the distance L_2 is varied through the use of a movable translation stage. The optical path difference δ between the two mirrors is given as

$$\delta = 2L_2 - 2L_1 = 2\Delta L \tag{2.67}$$

After re-combining at the beam splitter, two newly reflected and transmitted beams are formed. The re-combined reflected beam will illuminate the output plane where an interference pattern is observed. The nature of this pattern is determined by the how the two beams interfere with each other. The beams will constructively interfere when δ is an integer number of wavelengths:

$$\delta = m\lambda \tag{2.68}$$

while constructive interference is obtained for

$$\delta = \left(m + 1/2\right)\lambda \tag{2.69}$$

In its most simple format, the Michelson interferometer combines two monochromatic beams with differing phases leading to varying levels of interference. The complex fields of the individual beams can be described using the Laguerre Gaussian or Hermite Gaussian beam mode sets. The two beams can then be propagated in the typical manner using the ABCD matrix technique [Section 2.1.2]. The optical path difference between the two beams is determined by the propagation distances for the two beams.

As an example, a source beam is described using the Hermite-Gaussian beam mode set with a wavelength of 500nm and an initial waist of radius 5λ. As the main factor leading to interference fringes is the optical path length we ignore the reflections and partial transmissions and assume they are ideal. The incident beam was described as a Gaussian distribution using the Hermite Gaussian mode set using 10 modes. The interference patterns shown below in Figure 2-19 are found by combining the two fields as the optical path length varies. In this instance the optical path difference is varied from 2000λ to 2000.5λ. As δ varies from an integer value to a half integer value of λ the central spot will go from bright to dark, which corresponds to the constructive and destructive interference conditions of Equations 2.72 and 2.70 above.

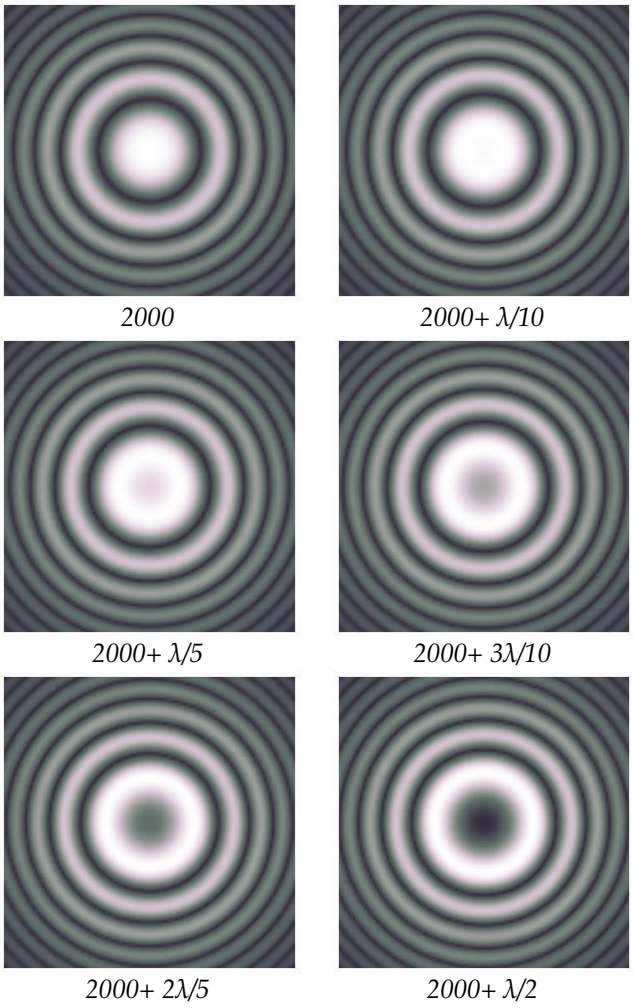

Figure 2-19 - Haidinger fringe patterns for combined fundamental Hermite Gaussian beams with varying optical path difference

The interference technique is compared against an experimental result taken from [38]. These circular interference fringe patterns, known commonly as Haidinger fringe patterns [39] here obtained from a Michelson interferometer with a source beam of monochromatic sodium light of λ = 589 mm. The stated optical path differences from [38] are 5.1 mm for the first set of fringes *(a)* and 2.1 mm for the second set *(b)*. The fringe pattern in *(a)* exhibits destructive interference with a central dark spot, while the central spot in *(b)* is bright, signifying constructive interference. These measured fringe patterns are easily predicted using GB modes. It is first noted that the exact values of δ for *(a)* and *(b)* are recalculated as 5.10026 mm and 2.1004 mm respectively. By setting these values for δ the correct interference patterns will be observed. Given the high

frequency of the source radiation the value of δ is extremely sensitive, and will thus impact upon the output interference fringe pattern.

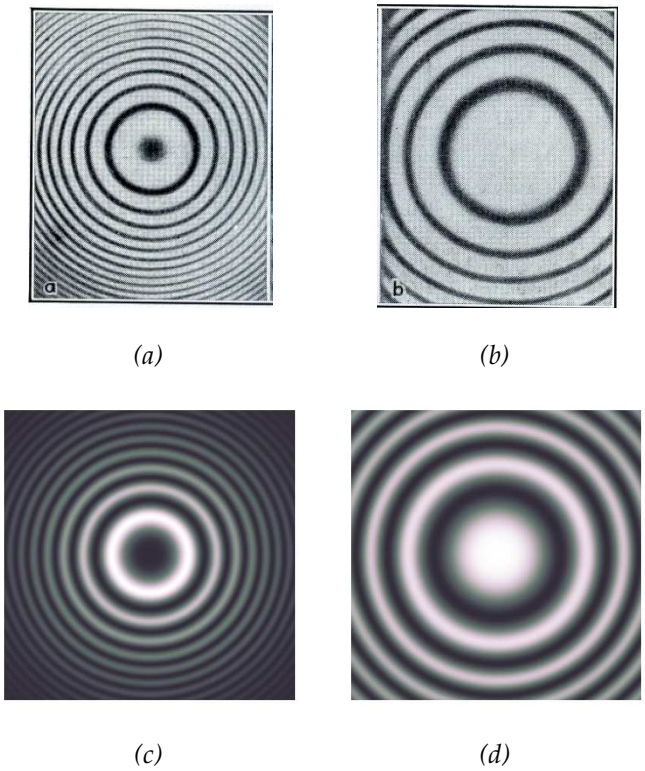

Figure 2-20 - Circular interference fringe patterns for Michelson interferometer taken with monochromatic sodium light. Experimental results from [38]. - *(a)* δ = 5.1 mm, *(b)* δ = 2.1 mm. Gaussian Beam mode predictions – *(c)* δ = 5.10026 mm and *(d)* δ = 2.1004 mm

The predicted fringe patterns *(c)* and *(d)* exhibit the same central spot features as their experimental counterparts as well as the general trends of the outer fringe radii. In going from *(a)* to *(b)* and *(c)* to *(d)* the rings shrink in radius as δ decreases. It is difficult to draw any further comparisons between the experimental and predicted plots given the lack of any extra information from [38] regarding the interferometer setup.

If the two mirrors are not exactly parallel, fringe patterns will still occur at the output plane but will be distorted or asymmetric. This orientation of the two mirrors effectively means that the two mirrors now form a wedge. For a zero δ and a non-orthogonal angle between the two mirrors the fringe pattern observed will consist of straight lines that are parallel to the edge of the wedge. If δ increases then the variation in the angle

between the mirrors comes into effect and the fringes become curved. These fringes are usually referred to as localised fringes or Fizeau fringes [40].

To achieve this tilt using Gaussian beam modes, a phase tilt term [4] is added to the mode description. For the Hermite Gaussian modes two phase tilt terms are included, representing a tilts in either the x or y directions, or both. The amended Hermite Gaussian modes have the following form:

$$u_m(x,y,z) = \sqrt{\frac{1}{\pi w^2 2^{m+n-1} m!n!}} H_m\left(\frac{\sqrt{2}x}{w}\right) H_n\left(\frac{\sqrt{2}y}{w}\right) \\ \exp\left(-\frac{(x^2+y^2)}{w^2} - jkz - \frac{j\pi(x^2+y^2)}{\lambda R} + j(m+n+1)\phi_0\right) \exp[-jkx\sin\theta_x]\exp[-jky\sin\theta_y] \tag{2.70}$$

where θ_x and θ_y are the tilts to the beam in the x and y directions.

The following localised interference patterns displayed below in Figure 2-21 are formed by setting the angle θ_x to *0.1°*. As the separation distance between the mirrors varies the fringe patterns will change accordingly across the observation field, with a new fringe crossing the centre each time δ changes by $\lambda/2$. At zero path difference *(b)* the fringes become straight. Beyond this point the fringe lines start to curve in the opposite direction as shown in *(c)*.

These fringe patterns show very good agreement with a similar experimental configuration taken from [40]. This illustrates that modal analysis of classical interference arrangements such as the Michelson, Young's double slit or the Fabry-Perot is quiet an efficient way to examine the result interference patterns. Indeed the big advantage of this GBMA approach is that there is no differentiation between the near and far field and the evolution of the fringe pattern with distance can be easily treated unlike in the classical approach.

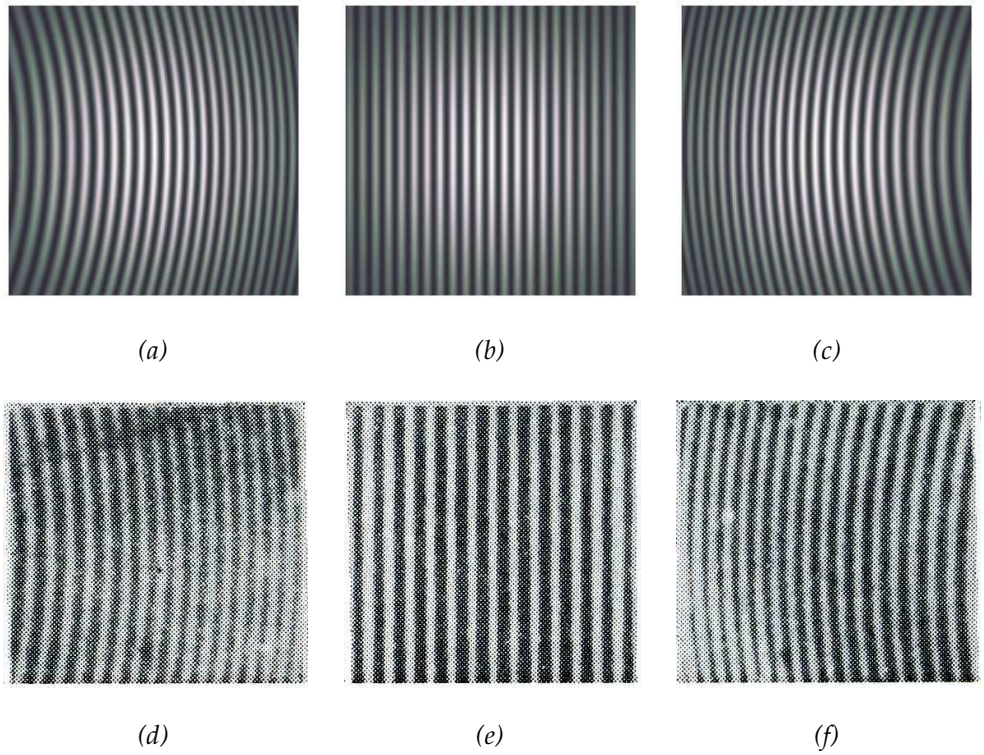

Figure 2-21 - Fringe patterns formed by Michelson interferometer with the angle between mirrors θ_x equal to *0.1* and path difference increasing from a negative value at *(a)* to zero at *(b)* and to a positive value at *(c)*. Experimental results taken from [40] *(d)*, *(e)* and *(f)* shown similar Fizeau fringe patterns for interferometer with tilted mirror.

2.3 Analysis of Antenna Feed Systems

The typical antenna feed system dealt with in this thesis is of the large reflecting antenna type. Such an antenna is designed to couple radiation from an observed source through a series of reflective and refractive elements and couple the beam to a quasioptical feed structure, typically a horn. The GBMA approach is a very useful and computationally efficient tool for analyzing such systems, especially those operating in the long wavelength region where diffractive propagation dominates. The principle of reciprocity [41] allows such antennas to operate equivalently in receive/backward or transmit/forward mode. Thus the coupling of a beam from an antenna to a quasioptical feed horn is equivalent to propagating a source beam from the feed horn to illuminate the sky with the typical antenna reception pattern.

2.3.1 Feed Horns – Conical Corrugated Horn

To analyze an antenna system in transmission mode, an accurate description of the source field is required. Through expansion in terms of Gaussian beam modes the transverse electromagnetic field distribution of a quasioptical beam can be described. This source field can then be propagated through the entire antenna optical system and reproducing the field at any point throughout the optical train is relatively simple. The field distribution from a feed horn can be described with a small number of modes, making the Gaussian beam mode approach to analyzing antenna systems very computationally efficient [42]. This is where the true advantage of GBMA lies.

There are many varieties of antenna feed horns that have their own unique field distribution and thus their own unique beam mode expansion. These expansions can be in either Laguerre-Gaussian modes or Hermite-Gaussian modes, depending on the axial symmetry of the horn. These feed horns are designed to couple radiation from the antenna to a waveguide. A waveguide is a metallic transmission 'pipe' that conveys electromagnetic radiation from one end to another. In antenna systems the waveguide is typically coupled to the back end of a feed horn to convey radiation to the mixer and local oscillator and thus interpret a sky signal using heterodyning techniques [43]. For this section of the thesis the Gaussian beam coupling to feed horns is the prime concern, while a detailed mode-matching treatment of the electromagnetic radiation within the horn structure is described in Chapter 4.

Corrugated horns are a common type of feed horn; they are circularly symmetric and thus their field distributions are expanded in terms of Laguerre-Gaussian modes. The corrugated horn is excited by a waveguide mode known as the hybrid HE_{11} mode [3] [44]. The polarisation state/angle for the horn is determined by the polarisation state of the HE_{11} mode. The corrugations within this horn are designed in such a way as to generate an infinite reactance on the metallic surface within the horn, thus preventing currents from being established. This reactance condition for the corrugations is

frequency dependent and thus the operational bandwidth is limited. This bandwidth limitation is also dependent upon the method of transition in propagating the waveguide mode through the horn and a variety of approaches to this transition have been developed [3]

Decomposition of the field distribution from a feed horn is defined from the field distribution from the waveguide. From waveguide theory [24] the field distribution for a circularly symmetric waveguide is given as

$$E(r) = J_0\left(\frac{2.405r}{a}\right) \tag{2.71}$$

where r is radial distance from the central axis, a is the radius of the waveguide and J_0 is the zero order Bessel function. At the feed horn aperture the field distribution has an additional spherical phase curvature term defined by radial length of the horn R_h, represented using a quadratic approximation shown below:

$$E(r) = J_0\left(\frac{2.405r}{a}\right)\exp\left(-j\frac{\pi r^2}{\lambda R_h}\right) \tag{2.72}$$

The maximum coupling for this aperture field distribution to the fundamental Gaussian is achieved for a beam radius $w = 0.6435a$. This choice of beam radius gives a power coupling coefficient of *0.99*. The field distribution can now be expanded using Laguerre-Gauss beam modes:

$$E(r,\varphi) \approx \sum_{p=0} A_p \Psi_p(r,\varphi) \tag{2.73}$$

where ψ_p and A_p represent beam modes of and corresponding coefficients of increasing order p. With the beam radius at the aperture defined to optimize power coupling to the fundamental mode, i.e. for $p=0$, the modal coefficients for the higher order modes carry a remaining fraction of the power of the beam. The relative power distribution for the first ten modes for a corrugated horn is given below in Table 2-4.

Mode Order p	Modal Coefficient A_p
0	0.99032
1	-0.00003
2	-0.12049
3	-0.04306
4	0.01959
5	0.03413
6	0.02000
7	0.00019
8	-0.12515
9	-0.01518
10	-0.01051

Table 2-4 - Modal coefficients for coupling of first ten Laguerre Gaussian modes to aperture distribution for conical corrugated horn

Note that the mode coefficient for the fundamental mode is maximized, with fractional power distributed among the other modes. Using modes of higher order than the fundamental *(p=0)* will successfully describe the essentially non-Gaussian behavior of the aperture field distribution. These diffractive effects are specifically the appearance and evolution of sidelobe structures (secondary maxima) as the beam propagates. As the beam is transformed by optical elements with finite aperture sizes, such as mirrors or lenses, truncation will cause additional diffraction and thus may alter the beam shape. Power will be scattered into these sidelobes from the main beam. Away from the aperture the typical field distribution will vary, and hence the ordering of power to the various modes will be altered.

The phase centre of the corrugated horn is defined as the location of the beam waist position where the radius of curvature of the phase front is flat. These are given by the formulae below and are illustrated in Figure 2-22.

$$\Delta z = \frac{R_h}{\sqrt{1+\left(\frac{\lambda R_h}{\pi w_h^2}\right)^2}} \tag{2.74}$$

$$w_0 = \frac{w_h}{\sqrt{1+\left(\frac{\pi w_h^2}{\lambda R_h}\right)^2}} \tag{2.75}$$

We now compare the abilities of both the fundamental Gaussian beam mode field distribution (Equation 2.39) in Section 2.1.4 and the truncated Bessel amendment of the same Gaussian beam mode field (Equation 2.72) in describing the field distribution from a corrugated feed horn. The horn in question is a typical conical corrugated feed horn with a cylindrically symmetrical field distribution with low sidelobes for the farfield of the output beam. The central operating frequency of this horn is *94 GHz*, or a wavelength of 3.19 mm. The far field amplitude patterns of the horn for the fundamental Gaussian field and the truncated Bessel field are shown in the plot below (Figure 2-23).

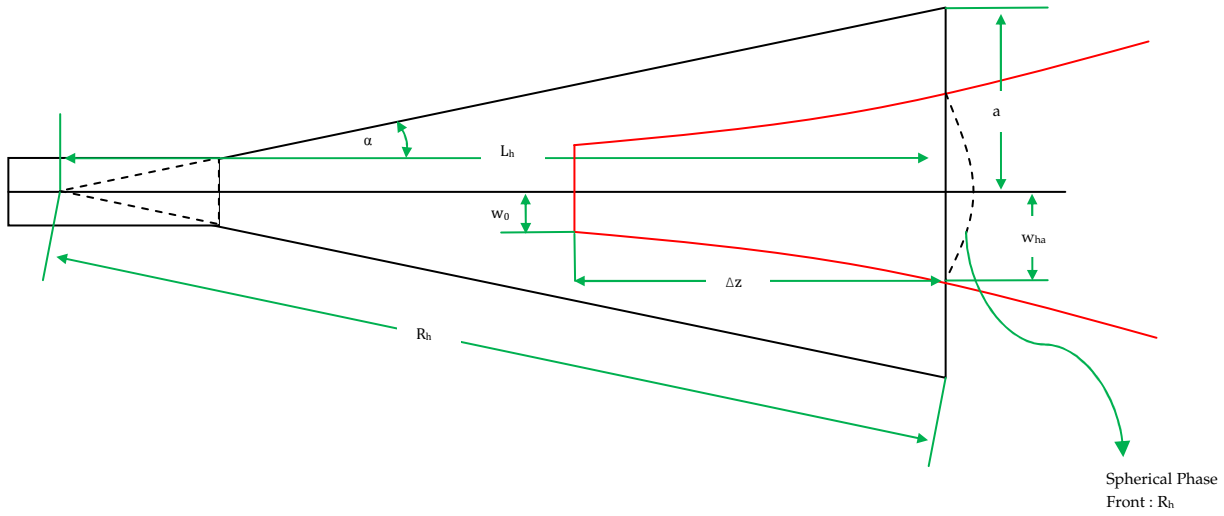

Figure 2-22 - Conical corrugated horn geometry including defining Gaussian beam parameters.

For comparison a modematch description of the horn field generated using the software SCATTER [45] is included, which is propagated to the farfield using Fourier transforms.

The SCATTER software generates very accurate complex field distributions based on propagating a TE and TM mode set through the horn and conserving power scattered at each section that makes up a conical corrugated horn, and, as stated previously this application will be discussed in further detail in Chapter 4.

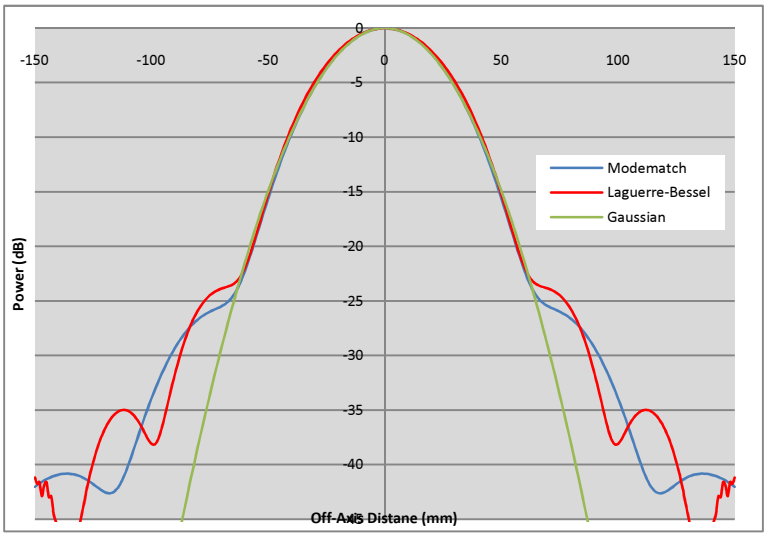

Figure 2-23 - Comparison of farfield distribution of a corrugated feed horn - modematching field (blue), Truncated Bessel (red), fundamental Gaussian (green)

At this distance there are distinct sidelobe structures present. The fundamental Gaussian beam is incapable of describing such complex beam structures, being able to describe the main lobe pattern of the beam down to approximately -25 *dB*. The truncated Bessel modification of the Gaussian field distribution describes the evolution of the diffracted side lobe structures. The truncated Bessel field gives a much better match to the SCATTER field pattern.

2.3.2 Cassegrain Antenna System

There are many types of reflector antennas employed today for millimetre/submillimetre astronomy. All follow the same principle of operation in that they focus incident plane wave radiation from a source through reflective optics to a receiver. The type of reflector described here is the Cassegrain reflector antenna which is one of the most widely used antenna configurations for either single dish or

interferometric arrays in submillimetre astronomy (e.g. ALMA) [43]. Incident radiation from the sky is focused by a primary dish of paraboloidal shape onto a secondary reflector, or subreflector of hyperboloidal shape that reflects the beam towards a feed horn usually via secondary matching optics.

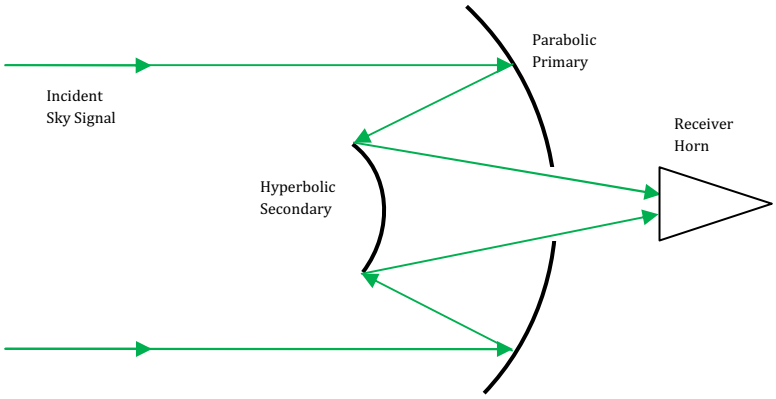

Figure 2-24 - Simple Cassegrain reflector antenna layout

Operating in forward mode, the antenna works as a transmitter and the reflectors serve to couple the feed horn field distribution to free space. The amplitude pattern at the telescope aperture plane can be approximated as the farfield pattern from the feed horn or the feed horn combined with the appropriate coupling optics, providing that the farfield divergence angle is not too large. Such an antenna can be reasonably well described in terms of a fundamental Gaussian beam, with some truncation effects expected at the aperture of the primary reflector and the edge of the secondary.

2.3.3 Antenna Aperture Efficiency

Antenna aperture efficiency is a basic parameter for defining the sensitivity of the antenna. The effective area or absorption area of the antenna is a determination of how well an antenna will couple incident power from the aperture through to the receiver and is given by

$$A_e = \frac{P_0}{S_{inc}} \tag{2.76}$$

where P_0 is the amount of power coupled from the antenna to the feed and S_{inc} is the total incident flux on the antenna. By comparing this effective area of the antenna to its physical area A_g the aperture efficiency η_a can be determined:

$$\eta_a = \frac{A_e}{A_g} \tag{2.77}$$

Total aperture efficiency is determined by a number of components that are related to physical aspects of the antenna in question. These components are given below by Equation 2.78 as taken from [46]

$$\eta_a = \eta_i \eta_s \eta_e \eta_b \tag{2.78}$$

These individual components are described as follows [3]

→ η_i : Illumination or Taper efficiency. This is a measure of the degree of central concentration of the illumination field distribution caused by the tapered radiation pattern. Outer radial areas of the antenna are weakly illuminated compared to at the centre and hence will reduce the contribution of other efficiency components to the overall aperture efficiency dependent on their location on the aperture. For example, if it is established that the greater degree of ohmic or surface error losses occur towards the outer edge of the antenna their contribution to the overall aperture efficiency calculation is diminished by the reduced illumination at the outer edge. The taper efficiency is defined by the following equation:

$$\eta_i = \frac{\left| \iint_{AP} E_a dS \right|^2}{\iint_{AP} |E_a|^2 dS . \iint_{AP} dS} \tag{2.79}$$

where E_a is the antenna aperture field and the integral is extended over the antenna aperture plane only (hence subscript AP). Evaluating the integral for a Gaussian illumination with edge taper a will yield the following relation:

$$\eta_i = \frac{2}{\alpha} \frac{(1-\exp(-\alpha))^2}{1-\exp(-2\alpha)} \tag{2.80}$$

where the taper ratio α is the ratio of the radius of the antenna aperture r_a to the Gaussian beam radius at the aperture w_a .

→ η_s : Spillover efficiency. The spillover efficiency is directly related to the taper efficiency. Only a certain proportion of the feed power will be intercepted by the antenna, the remainder is 'spilled' over the aperture edge. Spillover is given by

$$\eta_s = \frac{\left| \iint_{AP} E_a dS \right|^2}{\iint \left| E_a \right|^2 dS} \tag{2.81}$$

where the denominator is integrated over the entire aperture plane and the numerator is integrated over the antenna aperture plane. It should be noted that any spillover will intercept radiation from the ground, thus increasing the noise temperature of the antenna [43]. Integration of Equation 2.81 gives the spillover efficiency to be

$$\eta_s = 1 - \exp(-2\alpha) \tag{2.82}$$

The aperture efficiency is defined as a compromise between the taper and the spillover, with the product of the spillover and taper efficiencies approximately equal to the entire aperture efficiency. Evaluating the entire efficiency integral yields the following relation for efficiency for a Gaussian feed with edge taper α

$$\eta_i = \frac{2}{\alpha}(1 - \exp(-\alpha))^2 \tag{2.83}$$

→ η_b : Blockage efficiency. The central subreflector and its support structure cause a partial blockage of the aperture, decreasing overall efficiency. The fractional blockage f_b caused by a circularly symmetric subreflector of radius r_b is taken to be $f_b = r_b/r_a$. The net effect on the aperture efficiency is then given as

$$\eta_b = \frac{2}{\alpha}(\exp(-f_b\alpha) - \exp(-\alpha))^2 \tag{2.85}$$

→ η_e : Surface error. Any small scale surface deformations on the surface of the constituent reflector surfaces of the antenna will lead to phase errors over the

aperture. The effect has been quantified by Ruze [47] and is given by the following equation

$$\eta_e = \exp\left(-\frac{16\pi^2(\sigma_p^2 + \sigma_s^2)}{\lambda}\right) \tag{2.86}$$

where σ_p and σ_s are the RMS tolerances of the primary and secondary reflector surfaces. This 'Ruze' factor is evidently frequency dependent, with efficiency decreasing for increasing wavelength λ.

The plot below in Figure 2-25 shows the illumination efficiency, spillover efficiency and aperture efficiency values with blockage effects included with respect to the taper ratio.

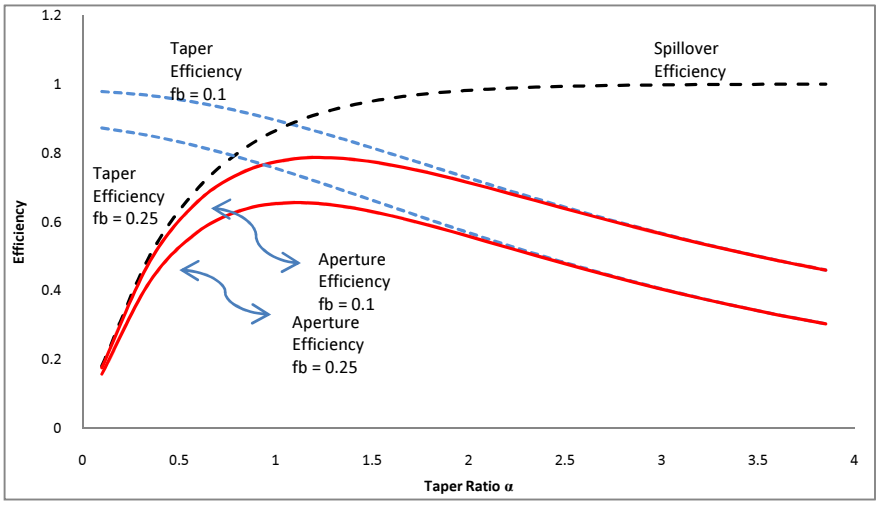

Figure 2-25 - Contributions of taper efficiency and spillover efficiency to the aperture efficiency. The effect of blockage size can be seen on the taper efficiency

It is evident from Figure 2-25 that the aperture efficiency is a tradeoff combination of the illumination and spillover taper. The maximum aperture efficiency is achieved for a taper ratio α = 1.2564, or from the edge taper equation in dB (Equation 2.26) T_E = -10.9 dB. For an unobstructed Gaussian illumination the maximum aperture efficiency is 0.8145. For increasing blockage fraction f_b the maximum aperture efficiency value decreases. The contour plot shown below in Figure 2-26 illustrates the evolution of the

blockage efficiency n_b (Equation 2.85) as a function of taper ratio α and fractional blockage f_b

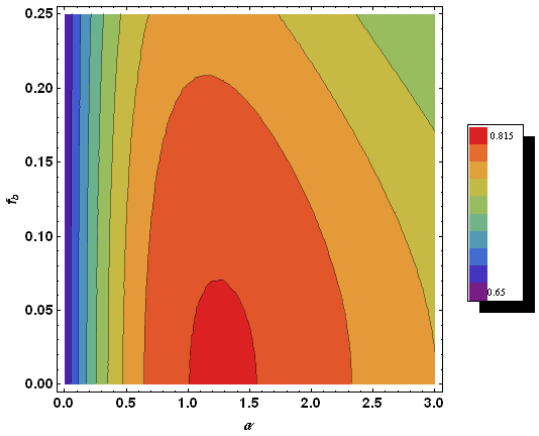

Figure 2-26 - Contour plot of the blockage efficiency as a function of taper ratio α and blockage fraction f_b

The maximum aperture efficiency value will also be degraded further by the Ruze factor. The larger the RMS values of the surface of the reflectors the greater the degradation of the aperture efficiency.

2.3.4 Antenna Main Beam

An important consideration for any long-wavelength antenna is to understand where the observed power is coming from in the sky. A typical antenna power pattern is given below [48] and it describes how the antenna intercepts incident radiation over an angular extent. The power pattern consists of various parts known as lobes. The central main lobe is defined as the lobe containing the direction of maximum radiation. Any lobe other than the main lobe is called a minor lobe, which are themselves composed of sidelobes and backlobes. For a typical antenna the sidelobes are taken to be those lobes closest to the main lobe. If these sidelobes are strong relative to the main lobe then they could contribute undesired radiation from directions other than that of the main beam.

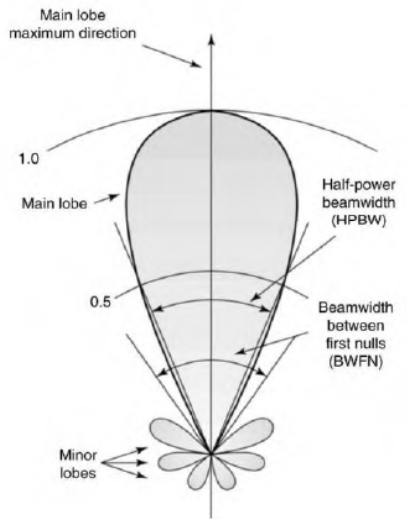

Figure 2-27 - Typical antenna power patter [48]

The half power beam width (HPBW) is defined in a plane as the angular width within which the radiation intensity is one half the maximum value of the beam. For an unblocked circular antenna this is given by [49] as

$$HPBW = 1.02\frac{\lambda}{D}\text{rad} \tag{2.87}$$

where D is the diameter of the primary aperture. A more accurate description of the HPBW for a circularly symmetric antenna illuminated by a Gaussian beam is given by [3] as

$$HPBW = \left[1.02 + 0.0135T_e(dB)\right]\frac{\lambda}{D}\text{rad} \tag{2.88}$$

where T_e is the edge taper of the illuminating Gaussian field at the antenna aperture. The values obtained in these equations (2.87 and 2.88) are obtained numerically [3]. It should be noted here that as the edge taper increases the sidelobe levels will decrease, yet the main lobe will subsequently broaden as it is under illuminated.

2.4 GRASP9 Software Description

The principle optical software package that is utilised throughout this thesis for optical characterization is GRASP9 (General Reflector and Antenna Farm Analysis Software), developed by TICRA. This software is considered the benchmark physical optics software package for use within the long wavelength optics regime for reflective optics systems, typically reflecting antenna systems for the ground based and space based astronomy industry and has been developed and refined based on industry requirements and backed by the European Space Agency (ESA) [50]. Within the Far Infrared and Submillimetre Optics group at NUI Maynooth GRASP9 has been used to model the optical performance of the Planck Surveyor, the Herschel Space Telescope, and more recently the optics for various receivers of ALMA by the Author [51], [52].

The GRASP9 package predicts the electromagnetic field from long wavelength reflector systems by first determining the fields from a source object and then predicting the resultant radiation after interaction with the reflective optics. This is achieved by solving the time variant Maxwell's equations using approximations known as the Physical Optics (PO) approximation and the Physical Theory of Diffraction (PTD). The software is also capable of calculating output fields for high frequency systems where the geometrical limit holds true. At this limit the approximations become the Geometrical Optics (GO) approximation and the Geometrical Theory of Diffraction (GTD). Throughout this thesis only reflector systems operating in the mm/sub-mm range are considered, and hence only the PO and PTD approximations are discussed in detail here. In the following section a detailed treatment of these approximations is given [53], [54]. This is then followed by a description of how systems comprised of source feeds and reflector surfaces are generated in the GRASP9 software environment.

2.4.1 PO & PTD Methods

The PO technique is an approximation to the classical analytical solution of Maxwell's equations, which concisely describe the behaviour of electric and magnetic fields. A

brief treatment of the analytical solutions of Maxwell's equations is firstly reported here, which leads on to the description of the PO and PTD approximations.

Direct solutions to Maxwell's equations are very difficult for all but the simplest configurations. The aim here is to solve the expressions for the electric and magnetic fields due to an electric current source **J** and an equivalent magnetic current source **M**. To calculate these solutions, new functions of the electric and magnetic fields known as vector potential functions must first be determined. The electric and magnetic vector potential functions **F** and **A** are determined by **J** and **M**. The radiated electric and magnetic fields can be calculated in a straightforward manner from these potential functions. The magnetic vector potential is related to the magnetic field by [43]:

$$\mathbf{H}_A = \frac{1}{\mu}\nabla \times \mathbf{A} \tag{2.89}$$

where μ is the magnetic permeability of the conductor and the subscript A refers to the magnetic field due to the magnetic vector potential. From Maxwell's curl equation for the magnetic field:

$$\nabla \times \mathbf{E} = -j\omega\mu\mathbf{H} \tag{2.90}$$

where w is the angular frequency of the radiation the following relation for the electric field is thus determined:

$$\mathbf{E}_A = -\nabla\phi - j\omega\mathbf{A} \tag{2.91}$$

where ϕ is a scalar electric potential which is a function of position. By employing the Lorenz condition, which is a partial gauge fixing of the magnetic vector potential **A** given in this situation is given as [43]

$$\phi = -\frac{1}{j\mu\omega\varepsilon}\nabla \cdot \mathbf{A} \tag{2.92}$$

the magnetic vector potential will satisfy the Helmholtz equation such that:

$$\nabla^2\mathbf{A} + k^2\mathbf{A} = -\mu\mathbf{J} \tag{2.93}$$

where k is the wavenumber. With this result the electric field **E** (i.e. Equation (2.91)) is then given as

$$\mathbf{E}_A = -j\omega\mathbf{A} - j\frac{1}{\omega\mu\varepsilon}\nabla(\nabla\cdot\mathbf{A}) \tag{2.94}$$

Similar expressions for the electric and magnetic fields due to the harmonic magnetic current **M** are given as

$$\mathbf{E}_F = -\frac{1}{\varepsilon}\nabla\times\mathbf{F} \tag{2.95}$$

$$\mathbf{H}_F = -j\omega\mathbf{F} - j\frac{1}{\omega\mu\varepsilon}\nabla(\nabla\cdot\mathbf{F}) \tag{2.96}$$

where **F** is the electric vector potential. The total fields are obtained as a superposition of the individual fields due to **A** and **F**. The magnetic vector potential **A** due to the electric current distribution **J** is given as

$$\mathbf{A} = \frac{\mu}{4\pi}\iint_S \mathbf{J}\frac{e^{-jkR}}{R}ds \tag{2.97}$$

and the electric vector potential F due to the magnetic current distribution **M** is given as

$$\mathbf{F} = \frac{\varepsilon}{4\pi}\iint_S \mathbf{M}\frac{e^{-jkR}}{R}ds \tag{2.98}$$

where R is the distance from any point in the source distribution to the observation point and the integration takes place over the surface of the source distribution S. The total fields are thus calculated by combining Equations 2.94, 2.95, 2.89 and 2.98.

$$\mathbf{E} = \mathbf{E}_A + \mathbf{E}_F = -j\omega\mathbf{A} - j\frac{1}{\omega\mu\varepsilon}\nabla(\nabla\cdot\mathbf{A}) - \frac{1}{\varepsilon}\nabla\times\mathbf{F} \tag{2.99}$$

$$\mathbf{H} = \mathbf{H}_A + \mathbf{H}_F = \frac{1}{\mu}\nabla\times\mathbf{A} - j\omega\mathbf{F} - j\frac{1}{\omega\mu\varepsilon}\nabla(\nabla\cdot\mathbf{F}) \tag{2.100}$$

The electric and magnetic fields from a set of induced or equivalent currents can thus be calculated, assuming that the current distribution in known. The near and far fields of this radiated field are calculated by applying the appropriate approximations to these integrals with regard to the distance of the observation point from the source distribution.

The PO approximation to the solution of the radiated fields from a known current distribution can now be formulated. A radiated field from a scatterer surface is treated as a solution to a scattering problem, where the following relation applies:

$$\mathbf{E}_{tot} = \mathbf{E}_{inc} + \mathbf{E}_{scat} \tag{2.101}$$

Where $\mathbf{E}_{tot}$ is the total electrical field, $\mathbf{E}_{inc}$ is the incident field and $\mathbf{E}_{scat}$ is the scattered field. The process of determining the scattered field is threefold:

- The first step is to calculate the induced (or equivalent) currents on the surface of the scatterer. In the PO framework these induced currents are generated by an incident electromagnetic field.
- The second step is to calculate the scattered (radiated) field from these current distributions
- The final step is to combine the incident and scattered fields to give the total field distribution.

The PO approximation allows for a simple calculation of the induced currents upon the surface of the scatterer, which is assumed to be large in terms of wavelengths. The PO approximation method can calculate the radiated fields for both perfect and imperfect conductors, providing the reflection and transmission coefficients are known. Without this approximation the first step of the scattering problem is very time consuming, requiring the calculation of intensive integrals. The PO approximation is expressed as the calculation of the currents induced upon a perfectly conducting infinite plane surface that is illuminated by an arbitrary incident field [50], [53]

$$\mathbf{J} = 2n \times \mathbf{H}_i \tag{2.102}$$

where n is the unit normal vector of the scatterer surface and H_{inc} is the incident magnetic field. This equation will work for curved surfaces where the local radius of curvature is large in terms of wavelengths.

Depending on whether the fields are sought for the near or far field the integrals will take different approximate forms [50]. The electric and magnetic fields are calculated as

two-dimensional numerical integrations of these equations. The integration area of the scatterer is determined by its rim, which in GRASP9 is commonly a smooth curve, a parallelogram or a triangle. The accuracy of the PO integration is determined by the degree of sampling over the scatterer surface, which as will be explained can be either chosen manually or calculated in GRASP9 through the PO convergence tool.

2.4.1.1 Spillover Calculation

As the induced PO currents on a scatterer are calculated it is possible to calculate the power contained within the incident field. This incident power is calculated using the Poynting vector $\bar{\mathbf{S}}$ over the scatterer surface:

$$\bar{\mathbf{S}} = \tfrac{1}{2}\,\mathrm{Re}\left(\mathbf{E}\times\mathbf{H}^{*}\right) \tag{2.103}$$

where *Re* denotes the real part and * the complex conjugate. The power ΔW hitting a finite surface element of area Δs is calculated using $\bar{\mathbf{S}}$:

$$\Delta W = -\bar{\mathbf{S}}\times\hat{\mathbf{n}}\Delta s \tag{2.104}$$

where $\hat{n}$ is the unit surface normal pointing towards the illuminate face of the scatterer. The total power over the entire surface is calculated through a two-dimensional surface integral of the form

$$W = -\iint_{S}\mathbf{P}(r)\cdot\hat{\mathbf{n}}(r)\,ds \tag{2.105}$$

which can be evaluated numerically. The spillover, defined as the amount of power that misses the scatterer surface, is calculated in dB [50]

$$SO = 10\log_{10}\left(\frac{4\pi}{W}\right) \tag{2.106}$$

where the factor of 4π signifies the normalization of the incident field to 4π watts. This spillover calculation can thus be interpreted as a logarithmic subtraction of power incident upon the scatterer from unity power. By keeping track of the spillover values, the total power lost from a normalised source field such as a feed horn over a series of scatterers can be calculated using Equation 2.106. For a series of n reflectors, the spillover calculation is given as

$$SO = 10\log_{10}\left(\frac{W_n}{W_{n-1}}\right) \tag{2.107}$$

This is illustrated in the following diagram:

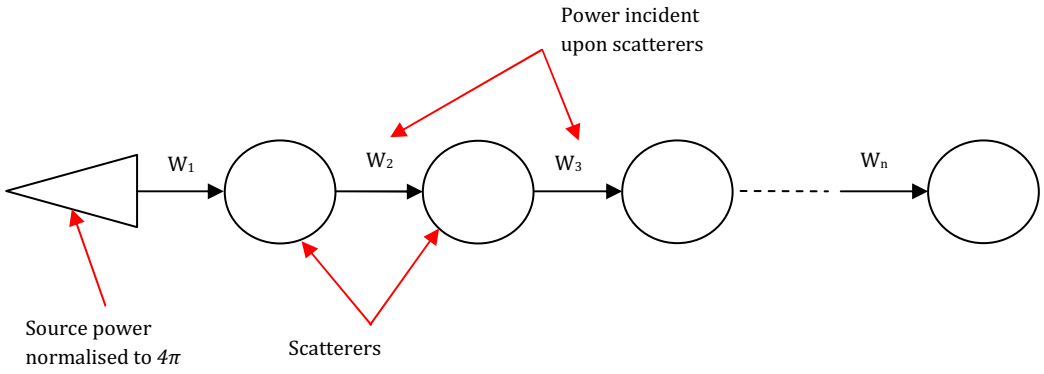

Figure 2-28 - Spillover calculation for multiple reflectors

It is noted also here that the spillover efficiency of a system is defined as the ratio of power transmitted to the desired output plane over the incident power, which is essentially the ratio of the logarithm in Equation 2.107.

2.4.1.2 Physical Optics Convergence

One of the strengths of the PO calculations in GRASP9 is the convergence tool [50]. This tool calculates the minimum required sampling for a PO integration grid to produce the required radiated field. If the sampling of the grid is too low then the results will be inaccurate, and if they are too large the calculation of the numerical integrations will be unnecessarily long. The density of the PO integration grid is specified by the variables *po1* and *po2*. These values can be automatically determined, and are dependent on both the current distribution on the scatterer and the location of the output points, which can be either the integration grid of the next reflector in the optical path or the field points of an output plane. The values for *po1* and *po2* are determined using an iterative accuracy technique. Output fields are determined for increasing values of *po1* and *po2* until the difference in the fields is less than $10^{\xi/20}$ relative to the maximum field values at

all output points, at which point the convergence is deemed acceptable. The value ξ, known as the field accuracy, is given in dB and is specified by the user. This procedure is performed for an increasing value of *po1* while *po2* is fixed. When the desired value of *po1* is determined, the process is repeated with the numbers swapped. The product of the two *po* values gives an indication of the time required for calculation of the output field pattern. The geometry of the reflector surface and its rim will determine the number of required *po* points and the overall calculation time. For complex surfaces and rims a high degree of accuracy *(*-80 dB ≤*)* is typically recommended.

2.4.2 Physical Theory of Diffraction (PTD)

The PO approximation gives an approximate solution to the scattered field by calculating the induced currents providing the surface can be locally defined as planar. This does not hold at the truncated edges of the scatterer, and thus the edge effects of the field here are not truly approximated by the PO technique. To calculate the currents at these non-uniform edge sections the Physical Theory of Diffraction (PTD) is employed. According to [55] these non-uniform surface fields are determined using the results of scattering problems, referred to as canonical problems. The PTD technique employed by GRASP9 involves calculating the equivalent edge currents along the illuminated edge of the scatterer for incremental surface area strips. Along these incremental strips the PTD contributions are separated into *TE* and *TM* components, which are then combined to give the local radiated field. This PTD approximation is only valid if the local incident field at the edge of the scatterer behaves as a plane wave [50]

The PTD technique is recommended when the reflectors being modeled have a moderate degree of truncation. Another application of the PTD technique is for the contribution to the overall field due to a gap or hole in a reflector surface, such as the central hole in the primary reflector for a Cassegrain antenna. In this situation the PTD calculation will account for the induced currents on one edge due to the currents on another edge. The canonical problem according to [55], [50] is the diffraction of an

appropriately oriented plane wave on a slit or gap. The problem reduces to two scalar solutions for the incident electric and magnetic fields. The desired non-uniform surface field associated with the edge is found from the total field minus the PO field. In GRASP9 this technique is based upon the Babinet principle, where the gap or hole is treated as a perfect electrical conductor of the same spatial dimensions of the gap. If the gap is narrower than 0.32λ then a narrow-gap approximation is used, otherwise a wide-gap approximation is used. These approximations will set the accuracy of the integration grids, where the integration variables *ptd1* and *ptd2* similar to the *PO* integration values are employed. For the narrow-gap approximation only the *ptd1* variable is used. For the wide-gap approximation, a 2D integration grid is defined using both *ptd1* and *ptd2*.

The combined PO and PTD field calculations provide very accurate results for the fields scattered by uniform and non-uniform reflectors illuminated by radiation from typical long-wavelength sources such as feed horns. In Chapter 3 of this thesis the differences in the PO calculation compared to the full PO and PTD calculations are highlighted with respect to a Fresnel-type diffraction setup. The predicted electromagnetic output fields from that of the ALMA front end optics channels covered in Chapters 4 and 5 of this thesis were generated using the PO and PTD tool.

2.4.3 System Generation in GRASP9

Implementing and analysing systems is achieved primarily through the use of two graphical user interfaces (GUIs); the pre-processor and post-processor, though it is also possible to create systems and perform analysis using the TICRA Object Repository (*.tor) and TICRA Command Input (*.tci) files. These files form the structure of any GRASP project file and describe the input of objects describing the system to be calculated and the list of analysis calculation commands to be implemented respectively. The pre-processor GUI allows the user to create these *.tor and *.tci files

without direct coding. The pre-processor also provides an OpenGL 3D description of the system, allowing the user to keep a visual track of the system. The post-processor tool is primarily used for plotting the resultant fields from the pre-processor calculations.

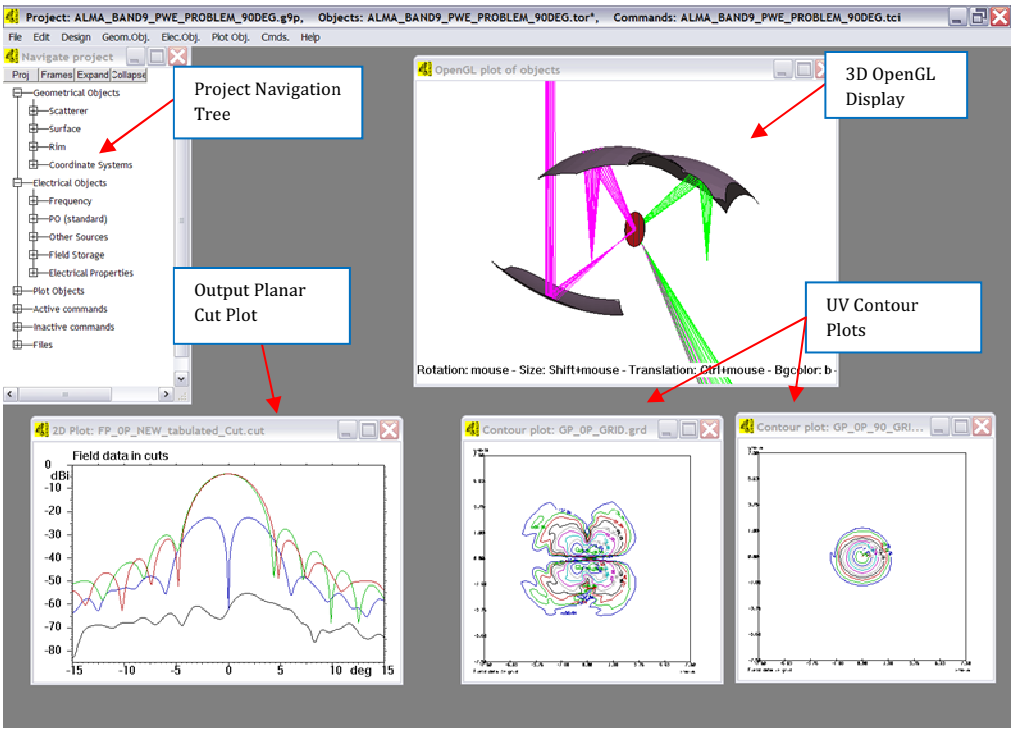

Figure 2-29 - GRASP9 pre-processor GUI with main components highlighted

There are many diverse types of optical systems that can be analysed using GRASP9, and several methods to implement them. Each element within an optical system is defined using a set of properties specific to that particular element. All elements are located within the optical system using a local coordinate frame of reference. The descriptions contained below will be limited to those that have been chiefly utilised by the Author throughout the course of this thesis. These systems can be considered typical mm/submm optical systems containing off-axis quadratic surfaces such as ellipsoids or paraboloids illuminated by a feed horn such as a conical corrugated horn.

2.4.4 Sources

For the analysis presented in this thesis, three methods were employed to create electromagnetic source fields. The first two source objects are generated by GRASP9 itself and the third is a user generated source field.

2.4.4.1 – Gaussian Beam – Near Field

This is the most basic field description used in the analysis of the reflector optics in this thesis. This feed radiates a fundamental Gaussian beam, defined using the near-field parameters of the Gaussian beam. This provides the source field with a Gaussian taper and satisfies Maxwell's equations in both the near and far field. A fundamental Gaussian beam is used as first order model for the radiation from a conical corrugated horn. Parameters required are illustrated in Figure 2-30 and are defined below:

- Beam Radius – perpendicular distance from axis at which the field is decreased to *1/e* of the on-axis field.
- Phase Front Radius – radius of curvature of the beam phase-front surface at the desired plane. This can be positive or negative, and for an infinite phase-front radius of curvature at a beam waist the value is set to zero.

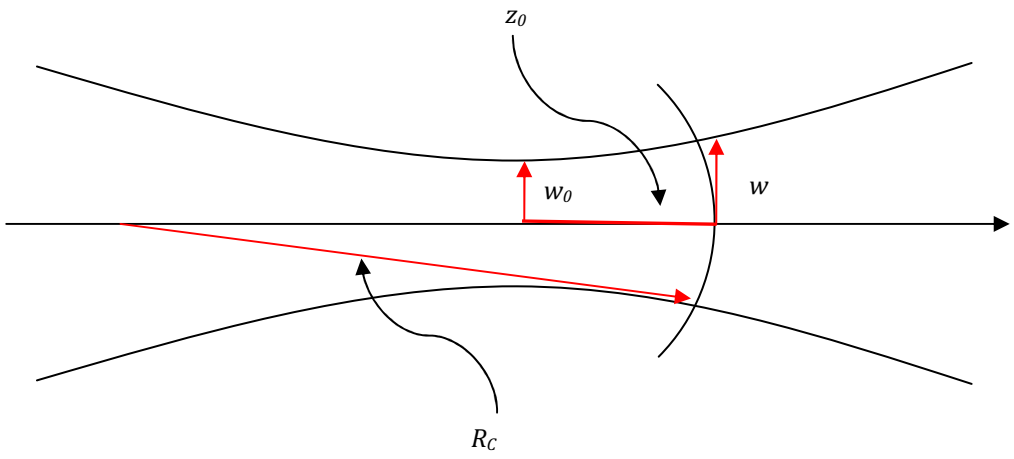

Figure 2-30 - Gaussian Beam - Near field definition; R_c = phase front radius of curvature, w_0 = beam waist, w = beam radius at desired plane, z_0 = distance from beam waist

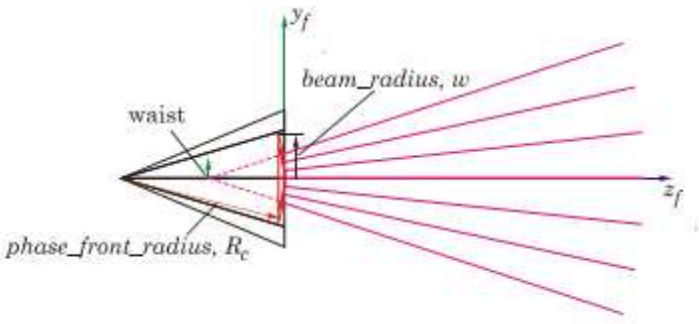

Figure 2-31 - Gaussian Beam as illustrated in GRASP9 environment

2.4.4.2 Hybrid Mode Conical Horn

This feed pattern is a more rigorous description of the beam produced from a conical corrugated horn, the details of which have already been covered previously in this chapter (Section 2.3.1). This pattern makes the assumption that the horn is operating under the balanced-hybrid condition [44] and has a narrow flare angle of <20°. The required inputs for this source object are the aperture radius, the semi flare angle and the distance to the phase centre of the horn [Section 2.3.1]. The hybrid modes HE_{mn}, EH_{mn} and cylindrical modes TE_{0n} and TM_{0n} are supported by this feed type.

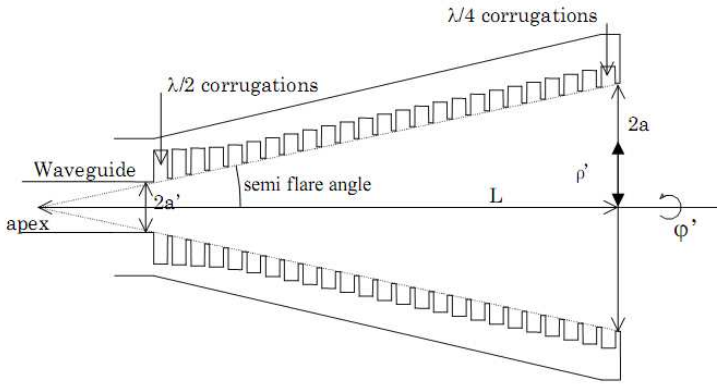

Figure 2-32 – The typical geometrical description for a conical corrugated horn, as modelled in GRASP9 using the Hybrid Mode Conical Horn source object.

2.4.4.3 Tabulated Planar Source

This source object is created externally by the user, either from some theoretical prediction method or a physical measurement from a real source and can then be propagated within the system. This is the principal source object used for analysis throughout this thesis. The electromagnetic field at the aperture of the desired feed horn is generated by the mode matching software SCATTER, the details of which are covered in Chapter 4. This aperture field is then implemented as a complex 3D vector field source. This field is defined in a specific GRASP9 grid format.

The SCATTER approach has been justified as an excellent prediction of the aperture field distribution from a conical corrugated horn [45], [56] and as such is more desirable as a source field within GRASP9 over either the Gaussian Beam or Hybrid Mode Conical Horn source fields. The advantage of accuracy of the SCATTER field description is balanced by increased calculation time compared to those of the GRASP9 specific sources. Physical optics calculations for these objects may be streamlined for efficiency using the PO convergence method, whereas for the tabulated source object the sampling must be assigned manually. The lack of a convergence calculation to determine the optimum degree of sampling requires the user to typically over-estimate the sampling to ensure accuracy.

2.4.5 GRASP Reflectors

A reflector object is generated in GRASP using three main objects; a surface object, a rim object and a material or electromagnetic properties object. The GRASP9 library itself already contains the most popular surface types, including simple plane surfaces and quadratic surfaces such as ellipsoids and paraboloids. These surface objects are typically created using their fundamental parameters such as vertex or focal length. The majority of surfaces that have been analysed throughout this thesis have been off-axis ellipsoids, which have been implemented in GRASP9 using the 2nd order polynomial description.

The subsection below contains a brief description of how the polynomial description of such an off-axis ellipsoidal surface is calculated.

2.4.5.1 Off-Axis Ellipsoidal Surface

An ellipsoid is a three dimensional surface generated as an ellipse rotated about one of its axes. The defining parameters of an ellipse are given below in Figure 2-33. The ellipse below includes the standard defining parameters: the major axis *2a*, the minor axis *2b*, the focal points *F1* and *F2* and the interfocal distance *2c*.

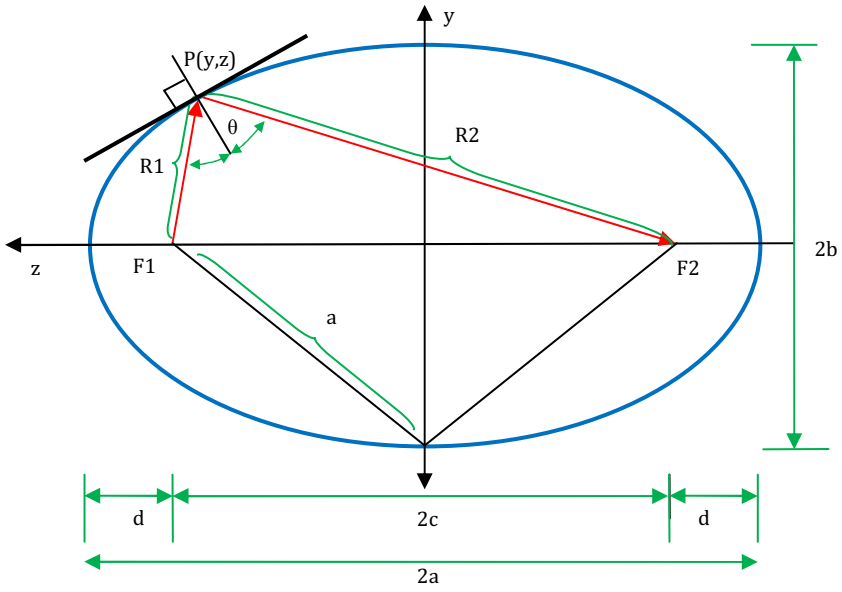

Figure 2-33 - Ellipse parameters including input and output radii of curvature for typical incident and reflected beam between foci

To create the desired ellipsoid to correctly reflect an optical beam the source of incident radiation is located at one focal point, ensuring that upon reflection the beam will be focused to the other focal point. This is best illustrated below in Figure 2-33 by the input and output radii of curvature, *R1* and *R2* in red, representing a typical optical train for an incident and reflected beam between the two foci. The sum of these two radii is equal to the length of the major axis *a*:

$$a = \frac{R1 + R2}{2} \tag{2.108}$$

The focal length of the ellipse is defined using the geometrical relation

$$\frac{1}{f} = \frac{1}{R1} + \frac{1}{R2} \tag{2.109}$$

The angle of throw, θ is used in combination with the focal length to then find the minor axis length b:

$$b = \sqrt{R1R2}\cos(\theta) \tag{2.110}$$

The interfocal distance and eccentricity of the ellipse are then determined:

$$c = \sqrt{a^2 - b^2} \tag{2.111}$$

$$e = \sqrt{1 - \frac{b^2}{a^2}} \tag{2.112}$$

The defining polynomial equation for an ellipsoid is given as:

$$\frac{x^2 + y^2}{2Rad} + \frac{(1+k)z^2}{2Rad} + z = 0 \tag{2.113}$$

h

where k is the conic constant of the ellipse, given as $k = -e^2$ and Rad is the radius of curvature of the ellipsoid, given as $Rad = a\ (1 - e^2)$. The ellipsoidal surface can then be generated in GRASP9 as a 2nd order polynomial quadric surface. The surface may then be tilted and decentred as required within the definition of the surface object.

2.4.5.2 Ideal Grid

Reflector surfaces are typically defined in GRASP9 as perfect electrical conductors, whereupon they have perfect unity reflectivity and zero transmission. In GRASP9 an electrical properties element can be assigned to the description of the scatterer. This element describes the reflection and transmission properties of the material of which the scatterer is comprised. The ideal grid electrical properties element is an idealization of strip or wire grids. It can be thought of as an infinitely thin sheet of closely spaced perfectly conducting parallel wires. This grid is projected upon the surface of the scatterer from a chosen inclination direction. For a linearly polarised beam incident upon this grid, all parallel field components will be reflected while those orthogonal

components will be transmitted. This ideal grid element is used to approximate the reflection and transmission properties of two wire grid polarisers, detailed in Chapter 6.

2.5 MODAL Software Description

MODAL (Maynooth Optical Design & Analysis Laboratory) is an optics software package developed by the Terahertz Space Optics Group at the Experimental Physics Department at NUI Maynooth. The software was designed specifically for operation in the Far-Infrared to Terahertz regime, and uses a variety of optics propagation methods, including scalar Fresnel propagation, full vector PO and Singular Value Decomposition (SVD) of Gaussian Beam Modes [57]. The software also integrates the SCATTER mode-matching software, allowing direct contribution from waveguide and feed horns. The MODAL working environment is shown below in Figure 2-34.

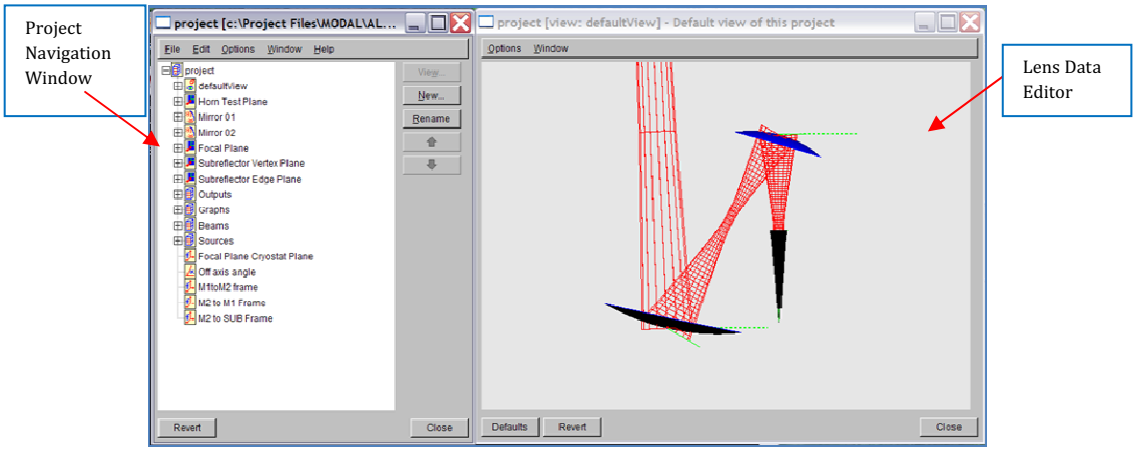

Figure 2-34 - MODAL design environment displaying project window and 3D OpenGL display of project components

In a similar process to GRASP9, all optical elements in MODAL are placed within the overall system by local coordinate frame. These coordinate frames can be defined in many different ways; by Cartesian or polar coordinates relative to any other defined frame, by vectors from a surface normal or by a transformation of some other frame. Each system element is defined by its own set of specific properties. For example, a mirror element will have a geometrical surface property that defines the mathematical surface and a bounding volume property that determines the calculable area of the

mirror. Once the components of the system have been defined the source field as it is propagated throughout the system is described using the MODAL field propagators, the details of which are given below in Section 2.5.1. Once the required field propagation calculations have been performed the field at the desired output plane is calculated. The output field is represented in an output dataset which can then be plotted within the MODAL environment or exported as a formatted data file.

2.5.1 MODAL Propagation Techniques

The radiated fields from either source objects or optical elements such as mirrors and lenses are determined by a propagator object. A scalar treatment of the radiated fields can be calculated through calculation of the classical Fresnel diffraction integrals. Another method of propagating a scalar field description of a source beam throughout the optical system is the Singular Value Decomposition (SVD) of the GBM description of the field. As discussed earlier in Section 2.1 GBM's represent a scalar solution to the paraxial wave equation. If a field is known at a particular point within the optical train of the beam it is straightforward to model the propagation of the field by keeping track of the evolution of the Gaussian beam parameters using ABCD matrices (c.f. Section 2.1.5.1) If the beam interacts with an optical element such as a mirror or a lens then power will become scattered between adjacent modes. Indeed, if an off-axis mirror is treated as an inclined phase transformer then it is necessary to calculate the mode coefficients of the scattered field over a plane that is not orthogonal to the direction of propagation and therefore over which the mode set itself is not orthogonal [58]. Such considerations limit the ability of GBMs to accurately describe the scattered field. An alternative calculation of these mode coefficients is found through use of SVD. A complete treatment of the SVD technique as it applies to MODAL can be found in [59] and [60]. The SVD of GBMs in MODAL represents an improvement in computational efficiency for scalar representations of the electromagnetic beams within an optical system.

The vector treatment of a propagated field in MODAL is realised through the PO approximation. The PO integrals utilised in MODAL are equivalent to those described for GRASP in Section 2.4.1. At the time of writing there was no PO convergence tool included in MODAL. The number of integration points for the PO propagator, and hence the accuracy of the calculations is currently determined manually by the user. The sampling of PO points upon a scatterer surface must be sufficiently dense to accurately describe the scattered fields. The software package also currently lacks a PTD tool for calculating the contributions to the scattered field by edge currents.

2.5.2 MODAL Sources

There are several available source beam descriptions available in MODAL. Those source objects that were most commonly used throughout this thesis are briefly described below. All source objects in MODAL are defined by the following elements:

- Geometry - this defines the coordinate frame of the object and its physical properties
- Fields – this defines the characteristics of the electromagnetic fields emanating from the source itself
- Propagators – this defines the propagators for the source object and whether they are of a scalar or vector nature.

2.5.2.1 Hermite Gaussian Mode

This source element defines a standard Hermite-Gaussian beam of arbitrary order. The field is defined using the Gaussian beam parameters of beam radius w, phase radius of curvature R and the Hermite x and y orders n and m. This type of source represents a basic, scalar field description of a typical submillimetre source beam such as a scalar feed horn.

2.5.2.2 Conical Corrugated Horn

This source element generates a scalar field representation of the beam from a conical corrugated horn operating under the balanced hybrid condition. This is a similar field

representation as the Hybrid Mode Conical Horn source object from GRASP (Section 2.4.4.2). The field is defined by the aperture radius and slant length of the horn.

2.5.2.3 SCATTER Horn

This source element generates the aperture field distribution for a feed horn through use of the mode-matching SCATTER code. This is similar to the Tabulated Planar Source from GRASP except that the SCATTER code has been directly integrated into the MODAL package. The user requires only an input text file that contains a geometrical description of the horn. The figure below shows a SCATTER horn object displayed within the MODAL OpenGL window.

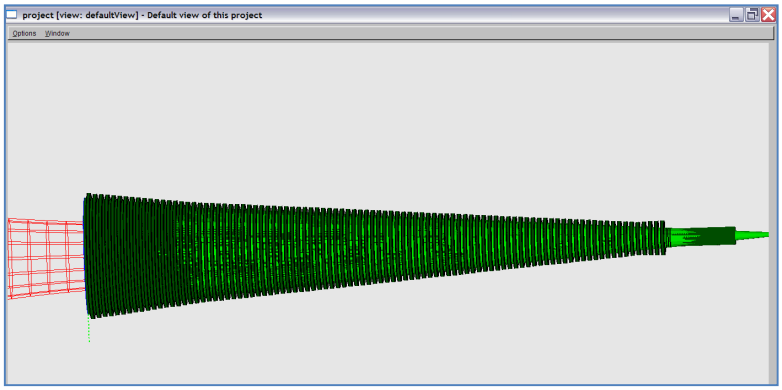

Figure 2-35 -3D display of a SCATTER horn object in MODAL

2.5.3 MODAL Reflectors

Reflectors can be defined within the MODAL environment in a number of ways. The most commonly used reflector shapes are pre-defined as ellipsoidal, paraboloidal and hyperboloidal. The user is also free to define a mirror object from a selection of surface types such as even or odd aspheric surfaces, intersecting planes or spheroid shapes. Each of these mirror objects is defined by its position within the system and its physical parameters such as its focal length and dimensions. Each mirror will also have its own propagator element, which is defined as either scalar or vector in nature and must also have a source element that defines the field incident upon its surface. Such propagator

sources can be from either a source object such as those described in Section 2.5.2 or from another coupled mirror object.

Unlike GRASP9, MODAL is capable of calculating the propagation of electromagnetic vector fields through dielectric elements such as lenses or windows. A brief description of how MODAL calculates the reflected and transmitted fields through a dielectric by PO is given below.

2.5.3.1 Dielectric Lenses

An advantage of the MODAL software is that it can model the effects of dielectric lenses. Lens objects are simulated in MODAL by treating their two faces as dielectric interfaces. The PO approach to calculating the effect of a dielectric lens from [60] is illustrated below in Figure 2-36.

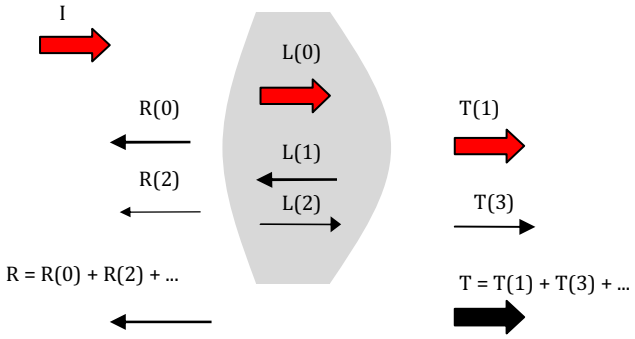

Figure 2-36 - PO propagation through a dielectric lens

The incident field *I* at the front surface is first decomposed into the transmitted and reflected components *L(0)* and *R(0)* respectively, by treating it as a locally spherical wave. The local direction of the Poynting vector and the normal to the surface are used to determine the angle of incidence. The orientation and complex amplitude of the transmitted and reflected fields are determined using the standard Fresnel relationships [25]. The transmitted component is then propagated to the back surface, where new transmitted and reflected components *L(1)* and *R(1)* are determined. This process is repeated for a number of iterations *n* and the total transmitted and reflected fields are calculated by summing the contributions from all completed iterations.

2.6 ZEMAX Software Description

The ZEMAX software package from the ZEMAX Development Corporation is an extensively used commercial optical design and analysis tool, most traditionally used within the optical components industry. The ZEMAX package is primarily used within the geometrical optics waveband and has the capability to model many complex optical systems. Examples of such systems include commercial applications such as LCD backlighting, light engines for digital projectors and camera lenses as well as research and science based applications such as optical telescopes, microscopes, lasers and other coherent optical systems such as interferometers. The software is chiefly used for paraxial systems with optics that generally lie in line with one another, whether sequentially or otherwise though it has also been used for off-axis systems such as Cassegrain telescopes. The software is very powerful in determining those image distortions that inhabit lens based systems such as coma, astigmatism and irregular field curvature effects such as the Petzval Wavefront aberrations [61].

Alongside the ability to design and model such systems, ZEMAX also contains two very useful tools known as solves and optimization. Solves are functions which actively adjust specific values such as curvature, thickness, radius, conics etc., which best suit the specified output for the system. The optimization feature is a powerful tool capable of improving lens designs, providing the user defines a reasonable starting point and a set of variable parameters. The optimization algorithms, of which there are many types, use a merit function as a numerical representation of how closely a system matches the desired outcomes such as image quality, focal length, magnification etc. This merit function is calculated using the sum of squares differences between the actual system values and the target values, and then the optimization feature seeks to minimize these differences to achieve the best possible system configuration.

2.6.1 Propagation Techniques

The geometrical optics method in ZEMAX uses ray tracing to analyse the optical system. This method is not well suited to successfully model diffraction effects that are dominant in THz systems. The software also features a Physical Optics Propagation (POP) tool that was developed to model these diffraction effects. The POP tool uses an array of discretely sampled points to represent the electromagnetic source field and propagates this field through the systems using mutually interfering wavefronts. A transfer function is then used to transfer the beam from one side of the optical surface to another. The POP tool uses two propagator methods which are essentially approximations, depending on the system parameters. It should be noted that neither of these techniques uses the PO integrals utilised by either GRASP or MODAL.

For a system defined with an aperture of radius a, a propagation distance from said aperture of D the Fresnel number F is

$$F = \frac{a^2}{D\lambda} \tag{2.114}$$

where as usual λ is the wavelength of radiation. For systems with small Fresnel numbers i.e. less than 1, the output plane is in the farfield or Fraunhofer region. When the Fresnel number is large i.e. greater than 1, then the output plane is in the near field. In ZEMAX the angular spectrum propagator is used for systems where the Fresnel number is large. This includes when a beam is both propagated over a short distance or when propagating over a large distance when the beam divergence is kept to a minimum. The method of angular spectrum propagation decomposes the field into plane waves using a Fourier transform, then propagates the field using a plane to plane propagator and then the resultant field is formed by inverse Fourier transforming the plane wave distribution. For systems with a small Fresnel number a different propagator is used, referred to as the Fresnel diffraction propagator. This propagator uses the assumptions of Fresnel diffraction theory. However, both the angular spectrum and Fresnel diffraction propagator are developed assuming that the beam does not

diverge too quickly; that is to say that the beam cannot be too fast. Neither theory will accurately predict the correct diffraction results in this case.

2.6.2 Source Beams

The initial source beams in ZEMAX can be defined as either a Gaussian beam, a Top Hat, a Multimode source or a user created source file. The Gaussian beam can be defined in a number of ways. The Gaussian Waist source object defines an optionally truncated and decentred Hermite-Gaussian beam of arbitrary order. The Gaussian Angle beam is an optionally decentred TEM00 mode whose waist size is determined by the farfield divergence angle θ defined earlier by Equations 2.2 and 2.3. A Gaussian source can also be defined using the Gaussian Size+Angle beam which is an optionally decentred TEM00 mode defined by local beam radius at the starting surface and the far field divergence angle. The Top-Hat beam is an optionally decentred circularly symmetric uniform amplitude beam. A beam may also be defined by the user as a binary or ASCII format file containing a beam of size n_x*n_y with x and y field amplitude values. The multimode beam object consists of a sum of any number of other beams which is also defined by the user in an ASCII file that contains information regarding the separate beams and determines whether the beams are added coherently or incoherently [61]

2.6.3 Surfaces

Creating optical systems in ZEMAX is achieved through the use of the Lens Data Editor (LDE). The LDE is the primary spreadsheet where the majority of the system data is entered and altered. The main entries of the LDE include the surface type, the radius, the thickness, the glass type and the semi-diameter. Different surface types will include different parameter entries that will define the surface. Other system parameters are defined in various tabs.

Inserting a surface in ZEMAX is performed in the LDE. Each row of the LDE represents a single surface; therefore two surfaces separated by glass can comprise a single element. Defining a single lens will therefore require four surfaces: the object surface (OBJ) from where the rays are launched, the front and back surfaces of the lens and the image surface where the ray trace stops.

Defining on-axis elements such as sequential lenses or even on-axis reflector systems such as Cassegrain telescopes is relatively straightforward in ZEMAX given the nature of the LDE. The defining of off-axis reflectors is more involved, requiring the use of special surfaces called Coordinate Breaks (CBs). These CBs are used to redefine the coordinate system in terms of the current system. A CB can decentre the local coordinate system in either x or y and tilt it about x, y or z.

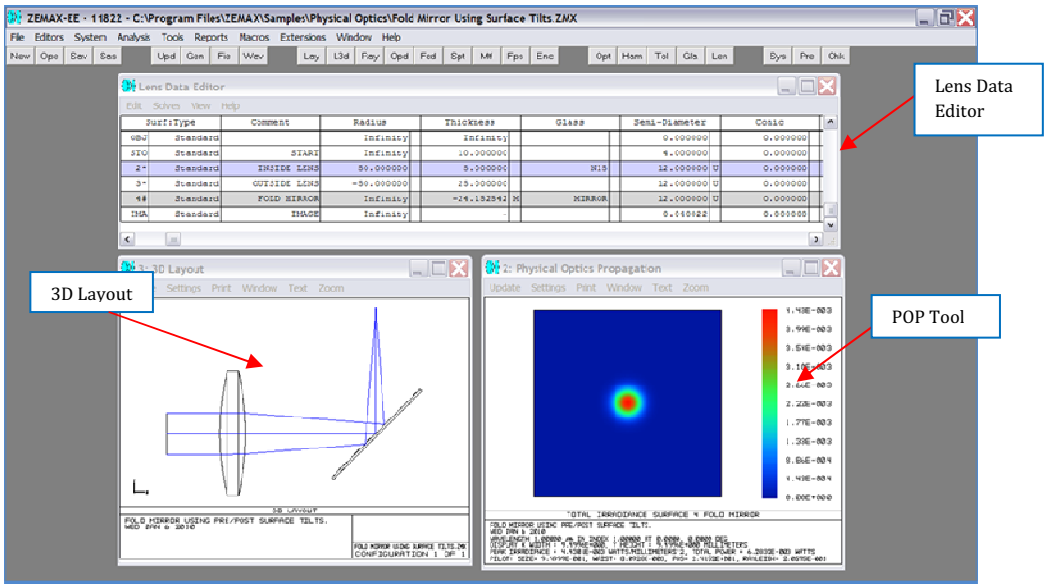

Figure 2-37 - Illustration of ZEMAX software package user window, displaying the LDE, a 3D layout of the optical system and a sample contout output plot from the POP tool.

2.7 CST Microwave Studio

The Computer Simulation Technology Microwave Studio® (CST-MWS) is a commercial electromagnetic design and simulation tool that uses the Finite Difference Time Domain (FDTD) method to solve Maxwell's equations for complex microwave structures. The FDTD method is achieved by replacing the partial space and time derivatives in Maxwell's curl equations by finite differences [62]. This allows for a numerical evaluation of the time dependent Maxwell's equations for a particular structure by dividing it into finite 3D cells or grids. The flow chart below shows the general structure of the FDTD algorithm [63].

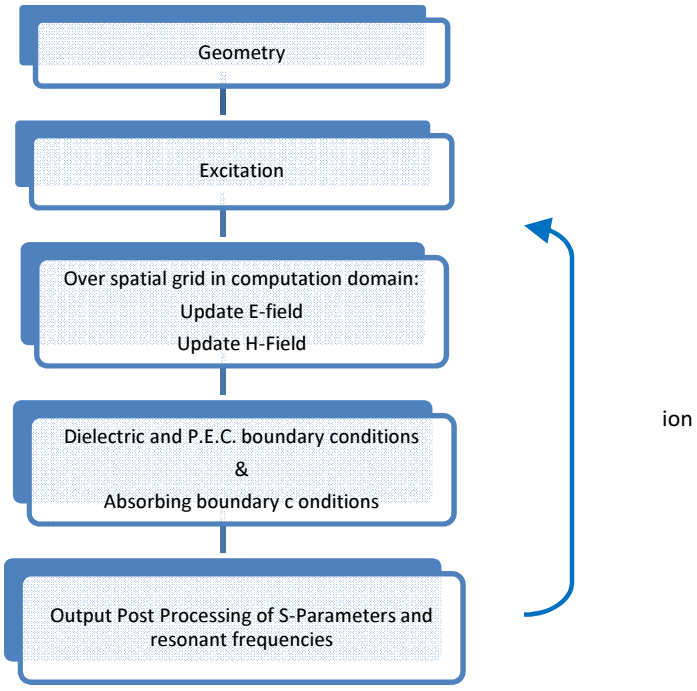

Figure 2-38 - Block diagram of the major building blocks for the FDTD algorithm

The CST-MWS package uses this FDTD technique in its Transient Solver [64]. The FDTD process in CST can be considered a 'leapfrog' method. The electric field vector in a space is solved for a given instant. Then the magnetic field vector is solved in the same space for the next instant in time. This process is repeated until a transient or steady

state EM field is achieved. This Transient Solver allows for the calculation of scattering parameters, electromagnetic field distributions, antenna radiation patterns and other relevant antenna and signal parameters. The CST-MWS package is utilised in Chapter 4 as a verification technique to the mode-matching code SCATTER.

2.8 Conclusion

In this chapter the background theory of the two analysis techniques employed in this thesis are detailed, namely Gaussian Beam Mode analysis and the various electromagnetic propagation methods employed by the software packages GRASP, MODAL and ZEMAX. The various techniques employed by these three software packages are discussed and tested in detail in Chapter 3. In the two following chapters, the analysis of the two ALMA front end optics channels (Bands 5 and 9) is performed as a combination of GBMA and PO and PTD predictions from GRASP. The theory of GBMs is introduced and a complete description of the propagation and transformation of Gaussian beams is detailed. The GBM technique was used to model the Fresnel diffraction patterns from a truncating circular aperture and the Haidinger and Fizeau fringe patterns from a Michelson interferometer. These Fresnel diffraction patterns are also modelled using the Fourier Optics technique of the Angular Spectrum of Plane Waves. The operational procedures for the three optical software packages was described, with specific attention to the design of off-axis reflectors commonly encountered throughout the millimetre/submillimetre regime and more specifically throughout this thesis. A detailed description of the PO and PTD approximations to describing the scattering of electromagnetic beams is also presented.

3. Far Infrared Optics Design and Verification Tools

3.1 Introduction

The work presented in this chapter represents an expansion and development on research from a paper entitled *"Far Infrared Optics Design and Verification"* [22] where various analysis software packages were tested for a variety of different quasioptical examples. The original report [65] summarized in the above paper [22] was a collaborative effort from optics research groups at NUI Maynooth, Cavendish Laboratory at the University of Cambridge, the UK Astronomy Technology Centre (UK-ATC) in Edinburgh and the Space Research Organisation of the Netherlands (SRON) in Groningen. The purpose of this group research project was to compare various commercially available optics software packages (GRASPh, GLAD, ASAP, CODEV) and their ability to correctly model diffraction dominated systems at long wavelengths/submillimetre wavelengths. These optics packages have not been specifically designed for use at these longer wavelengths, being primarily used for the visible spectrum (apart from GRASP9), but do have some diffraction capabilities. The initial research project involved testing these optical packages using various test cases representing extreme cases of diffraction and using different classes of sources.

Since the publication of this report in 2002, there have been two new optical software packages that are considered important in the field: ZEMAX and MODAL. At the time of the original report (1999), diffraction propagation in ZEMAX was relatively new and was considered to mainly serve the commercial geometrical optics market. Indeed, the research report included some simple ZEMAX results and an initial assessment of ZEMAX's capabilities. It was declared at the time that ZEMAX could only handle point sources and plane waves, which were essentially points sources at infinity and there was no ability to model Gaussian beams or scalar horns. Since that time ZEMAX has developed a Physical Optics capability known as the POP tool, as described previously in Section 2.6.1 and has been routinely utilised within the Far Infrared and

Submillimetre Optics Group at NUI Maynooth for analyzing long wavelength systems such as QUaD [66], [67]. It is therefore essential that an independent, in depth investigation into the performance of the ZEMAX POP tool within the long-wavelength regime be carried out and compared with known examples for validation. The Far Infrared Optics Design & Verification report represents an ideal test base for such an investigation.

The other software package that has been tested alongside ZEMAX is the quasioptical software package MODAL (detailed in Section 2.5) which has been developed within the Far Infrared and Submillimetre Optics Group at NUI Maynooth [59]. Though there have been several confirmations of this software's performance within the long wavelength optics regime [57], [60] it is prudent to include MODAL within this set of test cases as they are designed to test the limits of performance for extreme cases of diffraction.

As with the report upon which this chapter expands the GRASP9 Physical Optics (PO) package was used as the benchmark. Since the reports publication there have been improvements made to GRASP9, including more accurate descriptions of sources, more electrical surface characteristics and a Physical Theory of Diffraction (PTD) tool that ensures more accurate prediction of diffracted fields from the edge currents from reflectors. In the original paper the only method of determining the effects of these edge currents was achieved using the Geometrical Theory of Diffraction (GTD). Though this tool is still included in the current GRASP9, it is considered inferior for the test cases presented and is thus not included in the investigation. The processes of implementing optical elements such as sources and reflecting and refracting surfaces within each of the three software packages has been covered in detail in Chapter 2.

3.2 Test Cases

In this section the complete description of the various diffraction dominated optical test cases and the subsequent analysis and results of the analyses performed using GRASP9, MODAL and ZEMAX are reported.

3.2.1 Test Case 1

The first set of test cases involves modelling diffraction effects of a truncating aperture stop in a screen for different types of sources. These sources include an ideal plane wave, an ideal point source and a fundamental Gaussian beam. The near and far field results are analysed for the plane wave sources, while only the far field results are regarded for the ideal point source and the Gaussian beam. The apertures are circular, and their sizes vary for the plane wave source, and are constant for the point source and Gaussian beam. Each of the test cases is described in detail below in Figure 3-1 and Table 3-1. The wavelength of each source, and all sources in each test case presented, is 1.0 mm.

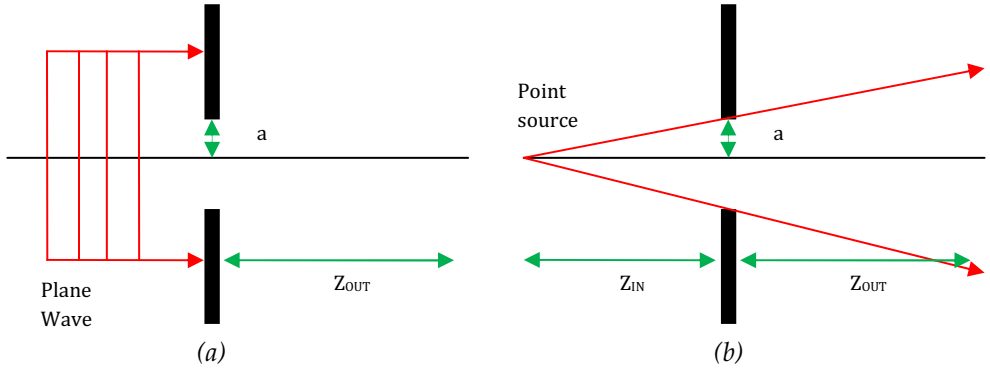

Figure 3-1 – Layouts of Test Cases 1A, 1B & 1C. Plane wave source illuminating truncating aperture for 1A & 1B (c.f. *(a)*) and point source illumination for 1C (c.f. *(b)*)

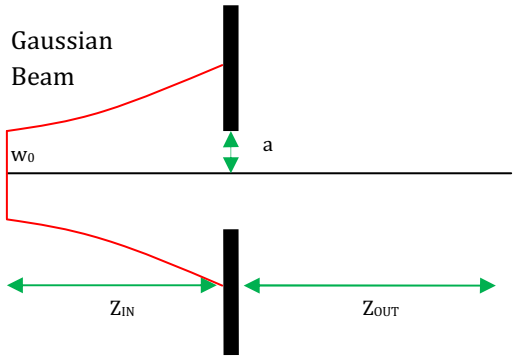

Figure 3-2 - Layout of Test Case 1D. Illumination of truncating aperture by fundamental Gaussian beam of waist w_0

PLANE WAVE (near field, a varies)			
Radius : a	3	10	30
ZOUT (near field)	2.25	25	225
Case No.	**1a1**	**1a2**	**1a3**
PLANE WAVE (far field, a varies)			
Radius : a	3	10	30
ZOUT (far field)	180	2000	18000
Case No.	**1b1**	**1b2**	**1b3**
POINT SOURCE (far field, *F* number varies)			
Radius : a	10		
ZIN	2	60	200
ZOUT (far field)	2000	2000	2000
Case No.	**1c1**	**1c2**	**1c3**
GAUSSIAN BEAM (far field , incident *F* number varies)			
Radius : a	10		
W0	0.637	1.947	5.93
ZIN	20	60	150
ZOUT (far field)	2000	2000	2000
Case No.	**1d1**	**1d2**	**1d3**

Table 3-1 – Test Case 1 details – all dimensions are in millimetres

For the two test cases where the aperture is illuminated by a finite spatial source, i.e. a point source for 1C and a Gaussian beam for 1D, the *F-number* of the incident beam refers to the ratio of the aperture diameter to the input distance.

3.2.2 Test Case 1 Results

Planar cuts of beam intensity at the output planes for each test case are used to compare the results from each software package. In each case the results were normalised for a unity power peak, which allowed plots to be superimposed for easier comparison.

Test Cases 1A – (Near Field of Plane Wave Illuminated Aperture)

These test cases model basic diffraction of a plane wave beam by a truncating circular aperture in the near field. This can be considered classic Fresnel Diffraction **[25]**. The system arrangement was modelled in ZEMAX using a circular aperture stop object and a co-axial measurement plane using the dimensions listed in **Table 3-1**. To predict the diffracted field the POP tool was used. The plane wave source is emulated using the 'Top Hat' source field.

The truncating aperture arrangement was generated in GRASP9 by creating a *reflector object* of a *plane surface* within which a *central hole* object was defined. There is a plane wave source object in GRASP9, the size of which is defined with the aperture radius. To model the diffracted field, both the PO and PTD tools were used in conjunction to give the most accurate result. Firstly the currents on the reflector surface are generated using the *get_currents* command line, and the field is calculated using the *get_field* tool. This is standard practice for the PO & PTD tools in GRASP9 while modelling reflecting surfaces. The field being modelled is behind the reflector, the contribution to the output field from the source object must also be considered. This is done using the *add_field* tool, which adds the field due to the source to the field due to the surface currents on the reflector.

The setup of the system in MODAL can be achieved using two methods: one is an approximately physical system and a more ideal, theoretical setup. Both are equivalent. The first setup is envisioned as a plane wave source object propagating an arbitrary distance to a large (ideally infinite) plane sheet with an axial truncating aperture with the desired diffracted output field behind the aperture. A *plane wave source* is used as the source object and the truncating aperture is created using the *aperture* element. The second setup uses the *uniformly illuminated aperture* source object in place of the combination of plane wave and truncating aperture. Both systems have been shown to give exactly equivalent results, and as such the first system setup is used here as the standard. To use the PO calculations in MODAL, the source and element propagators were chosen as vector propagators. The results for these first set of test cases (1A1, 1A2 & 1A3) are displayed below in Figure 3-3 as planar amplitude cuts. GRASP9 results are plotted in red, MODAL in blue and ZEMAX in green.

Given that the optics packages describe the source as vector fields the state of polarisation must be defined. For these test cases, and all subsequent test cases, the polarisation of the incident source fields is linear and is aligned along the local x axis. Two orthogonal cuts are plotted for both GRASP9 and MODAL as a solid and a broken line. The results from ZEMAX were all found to be symmetrical and are represented as a single planar cut. In the instances where there are two ZEMAX results plotted this indicates different sampling levels and the implications of said sampling are discussed throughout the conclusions.

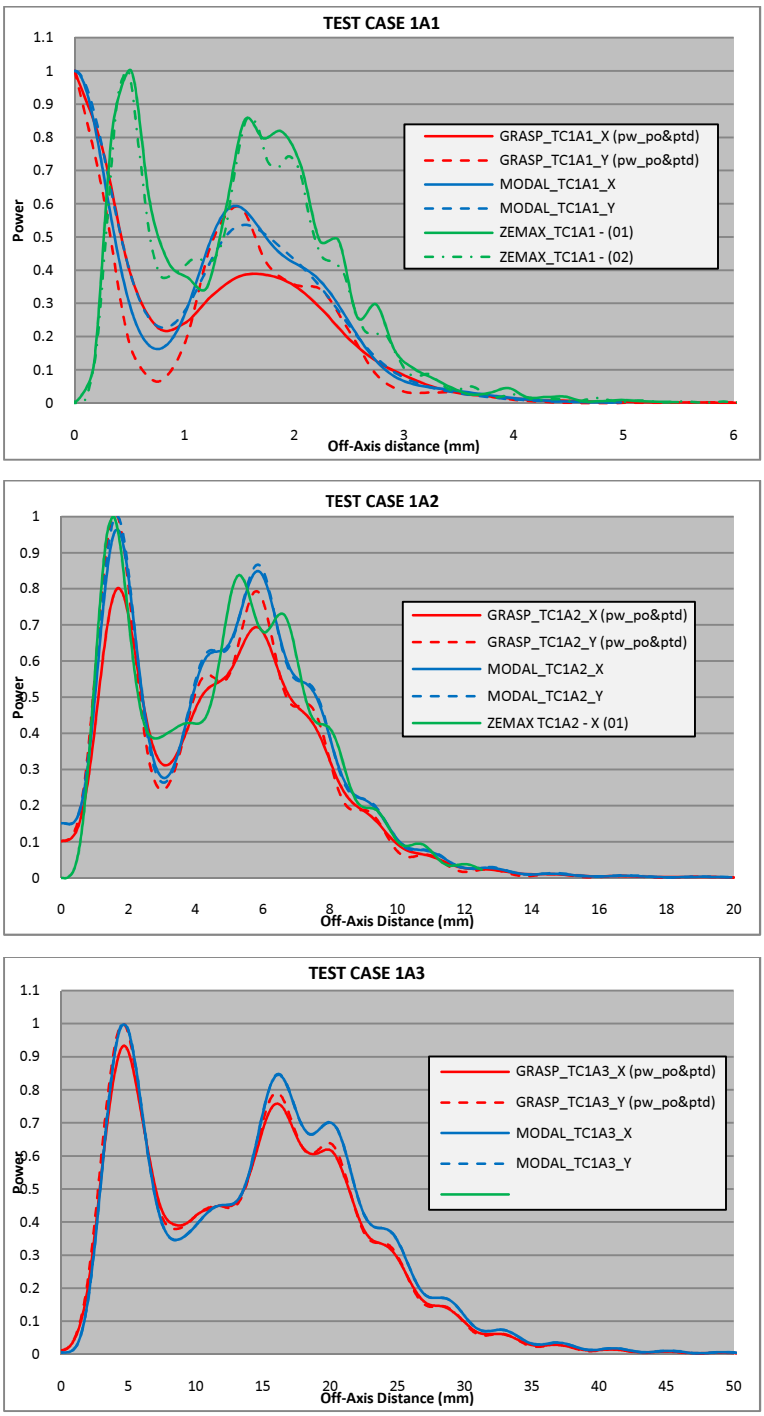

Figure 3-3 - Planar output amplitude patterns for test cases 1A. Note differing results for different sampling levels in ZEMAX (green lines). These disparities highlight the difficulty of accurate predictions for near field diffraction at long wavelengths. For 1A1 $z_{out} \approx a \sim 3\lambda$; for 1A2 $z_{out} > a \sim 10\lambda$; for 1A3 $z_{out} >> a \sim 30\lambda$. For all test cases $a^2 / z_{in}\lambda = 4$

These test cases are designed to generate an on axis minimum in the output power plot in the near field, as calculated using standard Fresnel diffraction [22]. However, there is a significant discrepancy between the different software models, especially for the very near field cases (1A1). Both GRASP9 and MODAL show an on-axis maximum while ZEMAX shows an on-axis minimum. These discrepancies are attributed to the approximations made by the various PO propagator tools in each software package. Comparing the MODAL and ZEMAX plots to those from GRASP9, we see varying degrees of agreement. It is obvious that the ZEMAX predictions show the largest divergence from the GRASP9 plots, with those from MODAL somewhere in between. We shall analyse each test case in turn.

In Test Case 1A1, the diffracted field is being modelled in the very near field. Though this setup is designed to emulate classic Fresnel diffraction, some modifications must be made to the Fresnel-Kirchhoff diffraction approximations for this case to yield the correct result. The Fresnel-Kirchhoff integral for a plane wave incident on circular aperture is given by [25] as

$$E_P = \frac{-ikE_S}{2\pi}\iint F(\theta)\frac{e^{ik(r)}}{r}da \tag{3.1}$$

where E_P is the field at the observation point P, E_S is the source field incident on the aperture, $F(\theta)$ is the variable obliquity factor and r is the radial distance from the area element da to the observation point P.

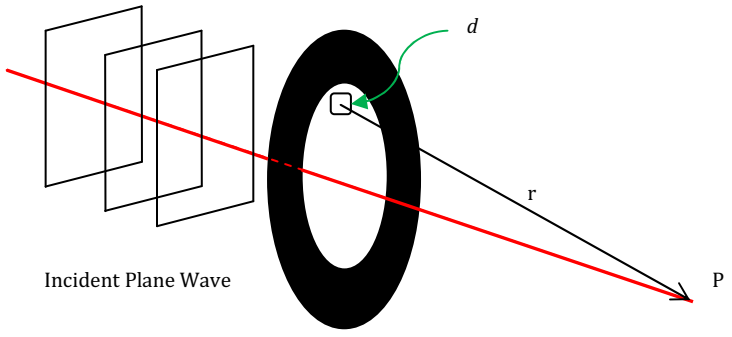

Figure 3-4 - Illustration of circular Fresnel diffraction setup for circular aperture

For specifically modeling the diffracted field from a circular aperture, Fresnel devised a method for dealing with the contribution from various parts of the wavefront at the aperture by dividing the aperture into zones, called Fresnel zones. These zones are created such that if A_N is a point on the outer boundary of the n^{th} zone, then

$$A_N P - A_0 P = \frac{n\lambda}{2} \tag{3.2}$$

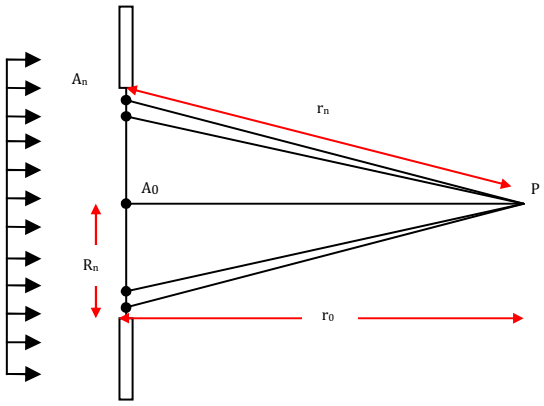

Figure 3-5 - Plane wave incident on a truncating circular stop with Fresnel zones indicated as A_n away from central axis, A_0

This means that each successive zone is $\lambda/2$ farther from the field point P than the preceding zone. Each successive zone's contribution to the diffracted field is exactly out of phase with that of the preceding one. These zones can be divided into smaller subzones. It can be shown that the resultant contribution from these subzones has an effective phase intermediate between the phases at the beginning and end of the Fresnel zone. This is best represented using phasor diagrams to represent the phase differential from each subzone, and hence each Fresnel zone. An illustration of this phasor diagram is given below in Figure 3-6.

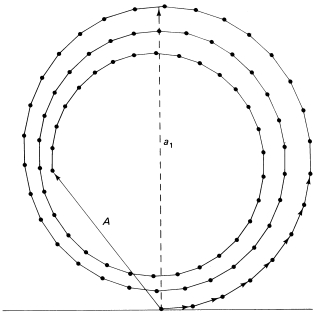

Figure 3-6 - Phasor diagram representing individual phase contributions from Fresnel subzones

In Figure 3-6 above the amplitude a_1 represents the resultant of the subzones within the first Fresnel zone. The effect of the obliquity factor is evident, making each succeeding phasor slightly shorter than the preceding one ensuring that the circles do not close but spiral inward. The summation of the field at P from each Fresnel zone is be expressed as

$$E_P = a_1 + a_2 e^{i\pi} + a_3 e^{i2\pi} + a_4 e^{i3\pi} + \ldots \tag{3.3}$$

or

$$E_P = a_1 - a_2 + a_3 - a_4 + \ldots \tag{3.4}$$

Through extension of the above theory the resultant amplitude oscillates between central maxima or minima depending on whether there are an odd or even number of Fresnel zones. The number of Fresnel zones is generally calculated using the basic geometry of the aperture given above Figure 3-5 using the following equations:

$$\begin{aligned} R_N^2 &= r_n^2 - r_0^2 \\ R_N^2 &= \left(r_0 + \frac{n\lambda}{2} \right)^2 - r_0^2 \\ R_N^2 &= r_0 n\lambda + \frac{n^2\lambda^2}{4} \\ R_N^2 &\cong r_0 n\lambda \\ \therefore n &= \frac{R_N^2}{r_0\lambda} \end{aligned} \tag{3.5}$$

When this is applied to Test Case 1A1, where we let R_N = 3.0 mm, λ=1.0 mm and r_0 = 2.25 mm the number of Fresnel zones is given as four. An even number of Fresnel zones leads to observed power distribution with an on-axis minimum. This is the classic

Fresnel approximation and works well when applied to geometrical optics systems where $r_0 >> l$ and $r_0 >> R_N$. The on-axis minimum predicted by ZEMAX in Figure 3-3 is therefore typical of the Fresnel Propagator tool it uses for near field beam predictions. The on-axis maximum predicted by the PO in GRASP9 and MODAL is explained by the fact that the very near field test cases are not exactly predicted using the Fresnel approximation in its current form. Note that from Equation 3.5 that the higher order term is neglected; this term can no longer be neglected as it has become significant in Test Case 1A1. The number of Fresnel zones is thus corrected:

$$n = \frac{2\left(-r_0\lambda \pm \sqrt{r_0^{\,2}\lambda^2 + R_N^{\,2}\lambda^2}\right)}{\lambda^2} \tag{3.6}$$

Applying the above calculation to Test Case 1A1 and discarding the negative value as non-physical the number of Fresnel zones is given as three. This matches with the geometry of the system – c.f. Figure 3-7.

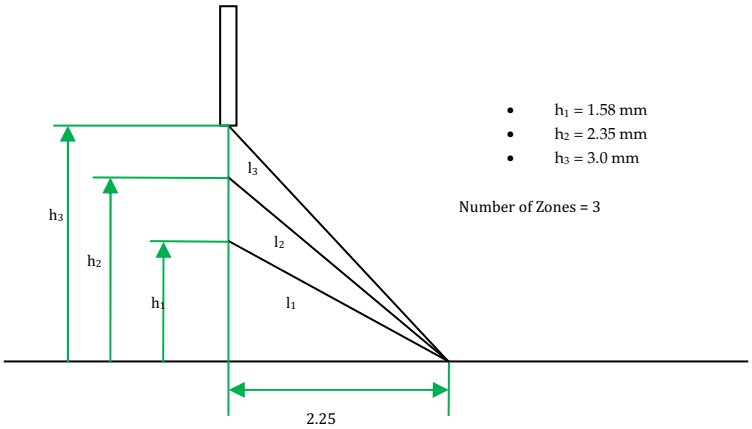

Figure 3-7 - Calculation of Fresnel zones for Test Case 1A1

The classical Fresnel diffraction plots above were generated using the same technique as applied in Section 2.1.5.2 by treating Equation 3.1 as a Fourier Bessel transform or a Hankel transform of zero order [34]. These plots below in Figure 3-8 clearly illustrate the difference in the diffraction patterns for three and four Fresnel zones. With this alteration to the Fresnel approximation, the on-axis maximum in the GRASP9 and MODAL plots is explained.

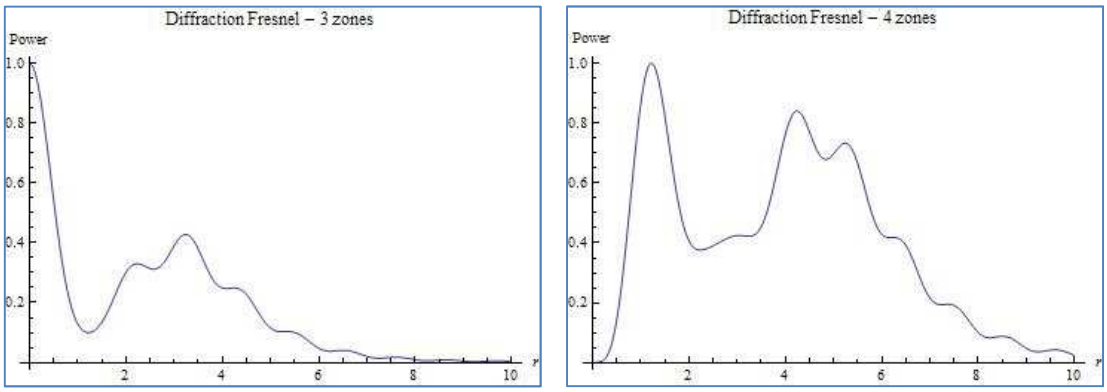

(a) *(b)*

Figure 3-8 - Classical Fresnel diffraction patterns from a circular aperture for 3 Fresnel zones (left) and 4 Fresnel zones (right)

Despite the agreement between GRASP9 and MODAL in predicting the on-axis maximum, they disagree with increasing off-axis distance. The reason for this is due to the PO methods employed by each package. The GRASP9 predictions in Figure 3-3 were obtained using a combination of PO and PTD to ensure maximum accuracy. This is combined with the PO convergence tool that ensures the correct amount of sampling of PO and PTD points at the aperture. As stated previously in Section 2.5, MODAL currently lacks a PTD tool and a method to accurately determine the adequate sampling for a system. Sampling of PO or Vector Propagator points is either defined using a default selection, or can be set by the user. To ensure that MODAL calculated the scattered field with the maximum achievable accuracy the PO sampling points for the aperture were oversampled. Another distinct difference between the PO predictions of GRASP and MODAL and the ZEMAX results is the asymmetry between the x and y planar cuts. Predictions by both PO packages reveal a circularly asymmetrical diffraction pattern – c.f. Figure 3-3. This asymmetry between the x and y planes decreases with increasing propagation distance. The predicted ZEMAX diffraction patterns are equivalent in both x and y. This asymmetry is attributed to the polarisation of the source beams, being polarised linearly in the local x axis of the system. The approximations made by ZEMAX in calculating the diffracted field ensure that the diffracted pattern is independent of polarisation. As we shall see in a later section, this

beam asymmetry is physically real, thus drawing the accuracy of the POP tool from ZEMAX into question. These asymmetrical diffraction patterns are also observed in later test cases.

To highlight the effect of the PTD calculation from GRASP9, the Test Case 1A1 system was re-evaluated using only PO for GRASP9 and the standard vector propagator technique in MODAL. The first plot below (Figure 3-9) is a comparison of the two GRASP9 predictions, where the red lines indicate the combined PO & PTD calculations and the black lines indicate PO calculations only. It is evident here that, at least for heavily diffracted systems in the very near field, the PTD tool plays a significant role in accurate beam predictions. The recommendations made by TICRA [54] indicate that the use of PTD in systems such as this one is prudent. The subsequent plot (Figure 3-10) compares the MODAL predictions with the PO predictions from GRASP9.

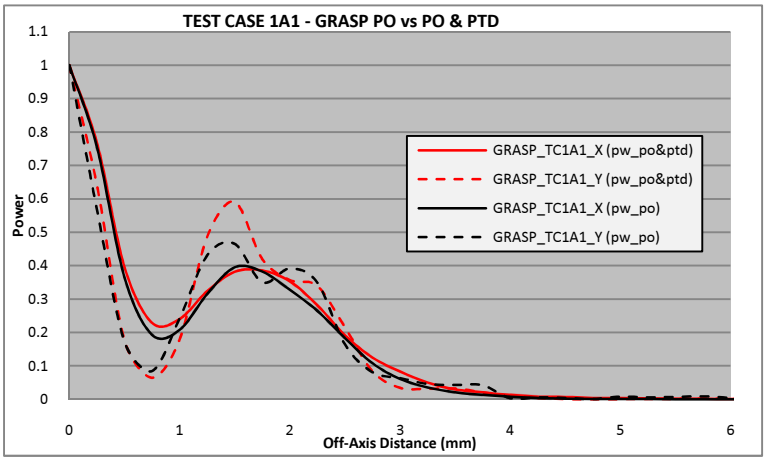

Figure 3-9 - Test Case 1A1 results comparing predictions from GRASP9 using PO (black line) and PO & PTD (red line)

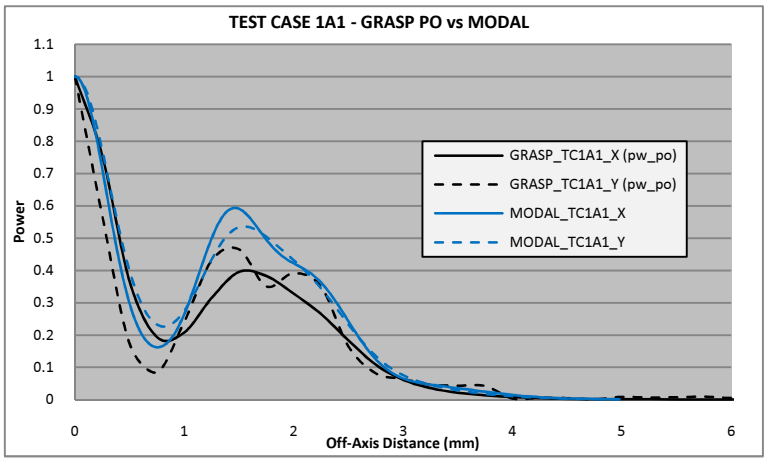

Figure 3-10 - Test Case 1A1 comparing MODAL predictions (blue) with GRASP9 (black), using PO method

The disparity between PO and PO & PTD calculations in GRASP9 is evident in the off-axis pattern structure in Figure 3-9. However, when the GRASP9 PO pattern is compared against the equivalent, oversampled PO pattern from MODAL (Figure 3-10) the agreement between the two has degenerated. Even the disparity for the structure of the on-axis amplitude peak has increased. This leads to an interesting conclusion regarding the PO prediction capabilities of MODAL. Taking the assumption that the GRASP9 PO & PTD calculations are the accuracy standard, the highly sampled MODAL PO prediction displays greater agreement with this standard than the equivalent GRASP9 PO prediction with sampling achieved using convergence.

The results for the next test cases (1A2: $z_{out} > a$, 1A3: $z_{out} >> a$) also show various degrees of agreement between all three of the software packages. For test case 1A2 both MODAL and ZEMAX package predict the location of the primary "off-axis" or non-central peak and the secondary peak, though with less accuracy as with the primary when compared against GRASP9 .However it is here the similarities between the GRASP9 results and those of ZEMAX and MODAL begin to break down. While there is no longer an on-axis peak, GRASP9 predicts a degree of on-axis illumination. MODAL also predicts a similar degree of on-axis illumination, though of less power, while the results from ZEMAX show a clear null at the centre. As with test case 1A1 the GRASP9

predictions here show unmatched patterns in the X and Y planes, revealing a circularly asymmetric beam. As before the ZEMAX results show no circular asymmetry, and the degree of asymmetry shown by MODAL from the first test case is all but removed here.

The on-axis minimum of zero predicted by ZEMAX in Test Case 1A2 is interesting as this would imply that ZEMAX predicts an even number of Fresnel zones for this test case. This is evident by comparing the ZEMAX predictions with the classical Fresnel diffraction pattern for four zones in Figure 3-8. This is a similar conclusion from the results of Test Case 1A1 where ZEMAX evidently predicts an odd number of Fresnel zones, thus generating an on-axis maximum in accordance with the Fresnel-Kirchhoff approximation. From Equation 3.6 the number of Fresnel zones for this test case is given as approximately *3.85.* The diffraction pattern for this number of zones in Figure 3-11 below reveals that, as expected, a non-integer number of zones will yield an on-axis power level somewhere in between the maximum and minimum values. This is revealed below in Figure 3-12 where the on-axis irradiance for Fresnel diffraction is plotted against the number of Fresnel zones. Comparing the classical Fresnel diffraction pattern for test case 1a2 shows good pattern agreement with the two PO packages.

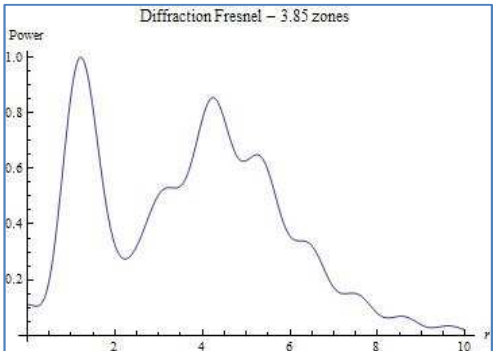

Figure 3-11 - Classical Fresnel diffraction pattern for Test Case 1A2 ($z_{out} > a$) where the number of Fresnel zones is *3.85*.

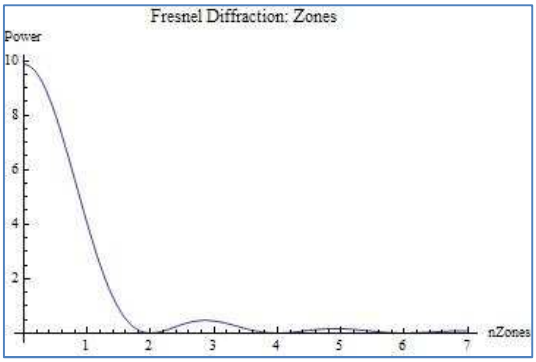

Figure 3-12 - On-axis irradiance for Fresnel diffraction pattern as a function of the number of Fresnel zones

The best overall pattern agreement between the packages is found in test case 1A3 ($z_{out} >> a$). The erratic pattern structure found in the ZEMAX plots is attributed to the beam sampling. This is a common feature for the ZEMAX predictions presented in this chapter. The accuracy of the ZEMAX POP results is directly linked to the sampling of the beam.

The ZEMAX POP tool utilizes Fourier transforms and as such the degree of sampling can be counterintuitive. In defining the source the total number of array points may be set to a constant, such as a 512×512 or 1024×1024 grid. However, though the sampling number will remain constant, the array size and the point spacings Δx and Δy will change as the beam evolves throughout the system. The POP tool samples a beam at the source beam waist using constant spacing, and a linearly scaled spacing far from the waist. This linear scaling is such that if the array width is very large at a beam waist relative to the waist size then there are relatively few points across the beam waist. This will result in a small array size from the waist, with a relatively large number of points across the beam. Conversely, if the array size is small at the waist, the array size will grow large compared to the beam far from the waist, leaving few sample points to represent the beam. This inverse relationship is a necessary but frequently inconvenient product of the Fourier transform theory used to model diffraction. This requires a tradeoff between adequate beam sampling near the waist and far from the waist. The

POP tool attempts to calculate the optimum beam sampling by using the following equations for determining the array size at the beam waist; i.e. where the source beam is defined:

$$X_0 = \omega_{0x}\sqrt{\pi n_x}, \qquad Y_0 = \omega_{0y}\sqrt{\pi n_y} \tag{3.7}$$

where X_0 and Y_0 are the dimensions of the array at the waist, w_{0x} and w_{0y} are the beam waist radii in the x and y directions and n_x and n_y are the number of points chosen to sample the beam. The spacing between points for the beam waist is simply:

$$\Delta x_0 = X_0 \big/ n_x, \qquad \Delta y_0 = Y_0 \big/ n_y \tag{3.8}$$

where Δx_0 and Δy_0 are the spacing values at the waist. As the beam propagates a distance z the beam spacings are defined by:

$$\Delta x_1 = \frac{\lambda |z|}{n_x \Delta x_0}, \qquad \Delta y_1 = \frac{\lambda |z|}{n_y \Delta y_0} \tag{3.9}$$

where Δx_1 and Δy_1 are the beam spacings at the new beam location. This evolution of the beam spacings is linearly dependent upon z. The automatic calculation for array size from Equation 3.6 will provide adequate sampling values for a beam both near and far from the waist for an uninterrupted propagation. The array dimensions at the propagated plane X_1 and Y_1 are thus inversely proportional to the beam waist array size:

$$X_1 = \frac{\lambda |z| n_x}{X_0}, \qquad Y_1 = \frac{\lambda |z| n_y}{Y_0} \tag{3.10}$$

However, for these test cases the beams are truncated by an aperture at various propagation distances and thus the area of interest over the diffracted beam after truncation is much smaller than the uninterrupted beam size. The linear evolution of the beam spacing is unavoidable, and a compromise must be made. As such, to ensure that there is adequate beam sampling over the diffracted beam it is recommended here that the beam waist sampling is appropriately dense, by choosing both a small array size and high sampling numbers.

Recalling Test Case 1A1 (c.f. Figure 3-3) there are two predictions from ZEMAX. These results reflect different levels of sampling to highlight the sensitivity of the output field. For ZEMAX-TC1A1-(01) in Figure 3-3 the sampling of the source field is defined using the automatic sampling algorithms from Equation 3.6. A source top hat field of symmetric waist sizes $w_{0x} = w_{0y} = 3.1\ mm$ and sampling sizes of $n_x = n_y = 1024$ provided an array size of $X_0 = Y_0 = 175.8$ mm. The output point spacing is then calculated by Equation 3.8 as $\Delta x_1 = \Delta y_1 = 12.7$ µm over an array size of approximately 13 mm. The second ZEMAX predicted field (ZEMAX-TC1A1-(02)) was calculated using a source top hat with a manually generated array size of $X_0 = Y_0 = 50.0$ mm which provides an output point spacing of $\Delta x_1 = \Delta y_1 = 48.0$ µm over an array size of approximately 46 mm. The automatic beam sampling provides finer sampling of the output beam over a smaller array area compared to the manual spacing selection. This finer output beam sampling by the automatic process comes at the cost of larger source field sampling compared to the manual sampling size.

The issue of the disparity between the predictions from GRASP9 and MODAL for Test Cases 1A1 and 1A2 required further attention. Through discussion of this issue with Dr. Marcin Gradziel (chief current developer of MODAL) and TICRA (the developers of GRASP9) an alternative argument was formulated to resolve this disparity. Technically the definition of the truncating aperture element is different for the two packages. The calculation process in GRASP9 firstly requires calculating the currents on the surface of a plane reflecting sheet containing a central hole due to the plane wave source. The diffracted field beyond this aperture is then generated due to these surface currents and the plane wave source. The technique employed in MODAL is slightly different, with the diffracted field calculated due to the currents formed on a perfectly absorbing sheet of infinite extent containing a central hole. A more accurate comparison of this MODAL calculation in GRASP9 is to employ Babinet's principle [25] which states that the diffracted field due to a truncating aperture or hole is equivalent to that from the

complementary opaque body of same dimensions as the hole. To test this hypothesis a 'Babinet' version of Test Cases 1A1 and 1A2 were generated in GRASP9 where the planar reflector with central hole was replaced with a planar reflector disc of the same radius as the central hole. The resulting predicted fields were determined using a plane wave source and surface currents on the disc were calculated using PO and PTD. The results of this analysis from GRASP9 are plotted in Figure 3-13 below and compared with the standard MODAL predictions for Test Case 1A1.

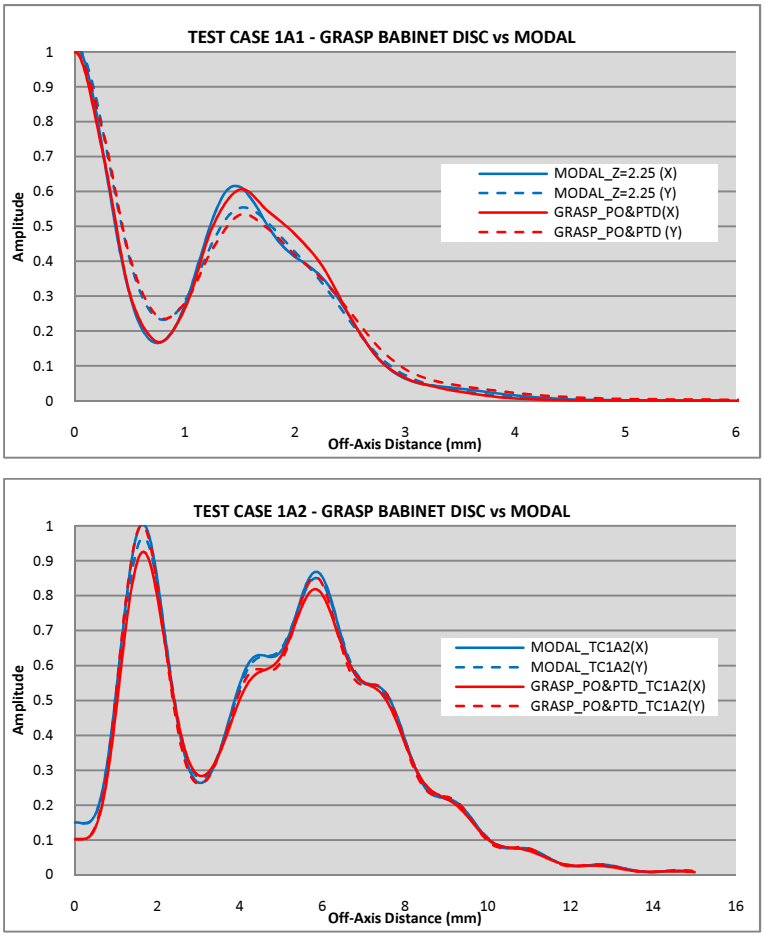

Figure 3-13 – Predictions for Test Cases 1A1 (top: $z_{out} \approx a$) and 1A2 (bottom: $z_{out} > a$) with Babinet disc replacing the truncating aperture element in GRASP9 (in red) compared against standard predictions from MODAL (in blue)

There is evidently greatly improved agreement in the diffracted fields from GRASP9 and MODAL for both test cases, thereby indicating the equivalence of the two techniques. There remain only minor differences that may be accounted for by the

choice of sampling points using the convergence tool in GRASP9 and the sampling levels in MODAL. For all MODAL calculations the optical elements have been oversampled.

It should be noted here that there exists one other method of calculating the diffracted pattern from a truncating aperture in GRASP9. A scatterer object known as the "aperture in screen" allows for the computation of the diffracted field from a truncating aperture in a screen with a plane wave source. This scatterer object exists as an optional extra in the GRASP9 software package and was unavailable to the Author for testing at the time of writing. There therefore remains potential for further exploration of this issue. In a later section the results of a long-wavelength diffraction experiment are outlined. This was performed in an attempt to experimentally resolve the divergence of the results from this first set of test cases between the two PO software packages GRASP9 and MODAL.

Test Cases 1B – (Far Field of Plane Wave Illuminated Aperture)

For the next set of test cases, the aperture radii remain the same as for the previous set (a = 3 mm, 10 mm and 30 mm) with the observation distance increased to the far field region (z_{out} = 180 mm, 2000 mm and 18000 mm respectively). At these distances the higher order term as included in the adapted Fresnel approximation from the previous section is no longer considered significant and an improved agreement between all the software packages is expected. Design of the systems in each package required a simple increase in the distance of the observation planes. It should be noted here that the Plane Wave source object in GRASP9 can only be used for near field calculations. Therefore, an oversized flat phase Gaussian beam replaces the plane wave source in GRASP9 and MODAL and the top hat source field in ZEMAX. (For Test Case 1B1, the Gaussian waist is 20 mm, for Test Case 1B2 the waist is *30 mm* and for test case 1B3 the waist is 60 mm.) These beam waist sizes, coupled with a flat phase front can be considered a close approximation to a plane wave within the limits of the aperture radius. The argument is

academic however since all of the software packages are being compared against one another for the same parameters. The results from all packages are displayed below in Figure 3-14 with logarithmic power.

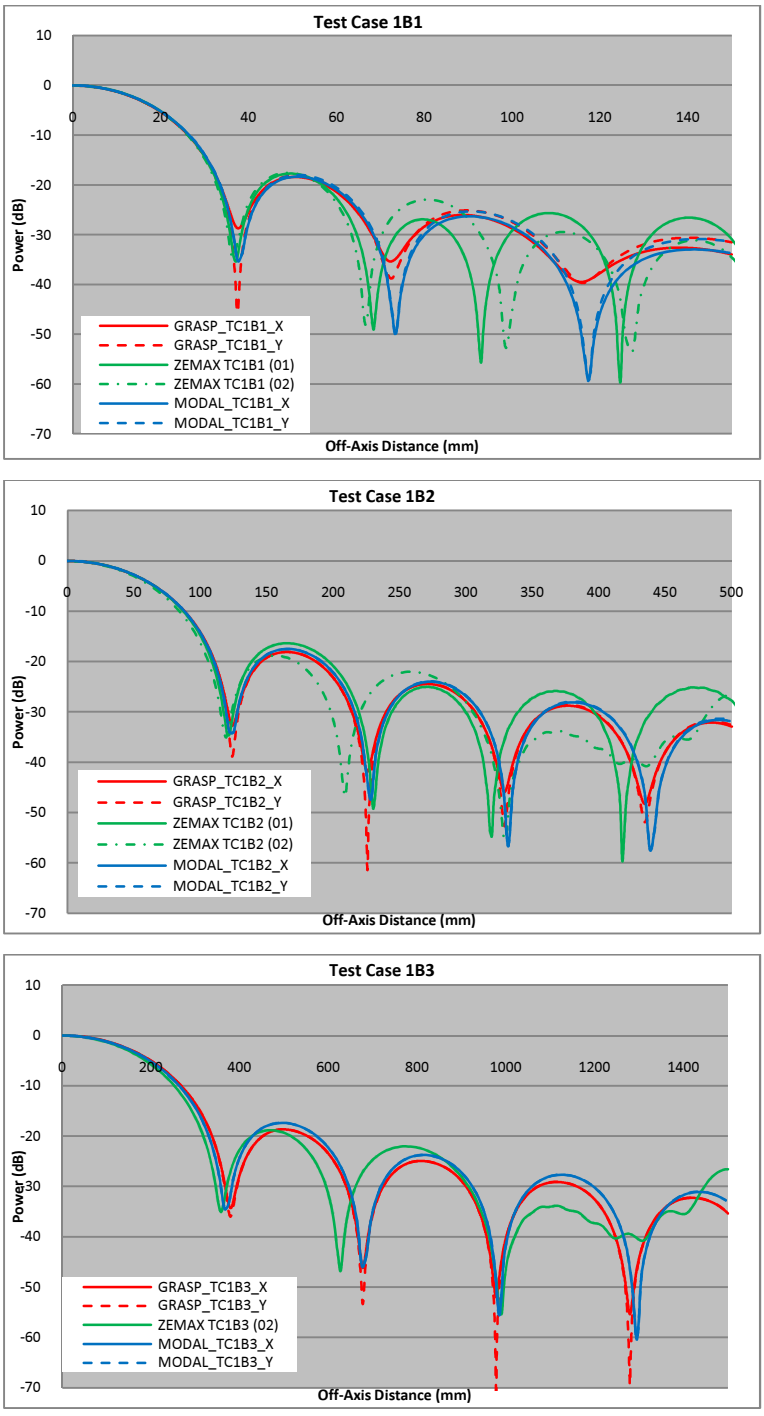

Figure 3-14 – Output farfield diffraction patterns for a plane wave illuminating a circular aperture where Test Case 1B1 has $a / \lambda \sim 1$, Test Case 1B2 has $a / \lambda > 1$ and Test Case 1B3 has $a / \lambda >> 1$.

At the far field the agreement between all the packages has increased significantly, especially between MODAL and GRASP9. The GRASP9 results above are again attained using PO & PTD calculations. The largest degree of discrepancy between GRASP9 and MODAL occurs for Test Case 1B1, which has largest angle of off-axis beam spreading. If the GRASP9 results are calculated using PO only the degree of agreement is greatly improved, as seen below in Figure 3-15 with the new GRASP9 PO predictions plotted in black . As the output plane moves further away from the aperture stop the agreement between MODAL and GRASP9 is significantly improved. Given the high level of agreement between GRASP9 and MODAL at these farfield distances there was no need to re-calculate the GRASP9 predictions using the Babinet disc technique, as was done previously for Test Cases 1A1 and 1A2.

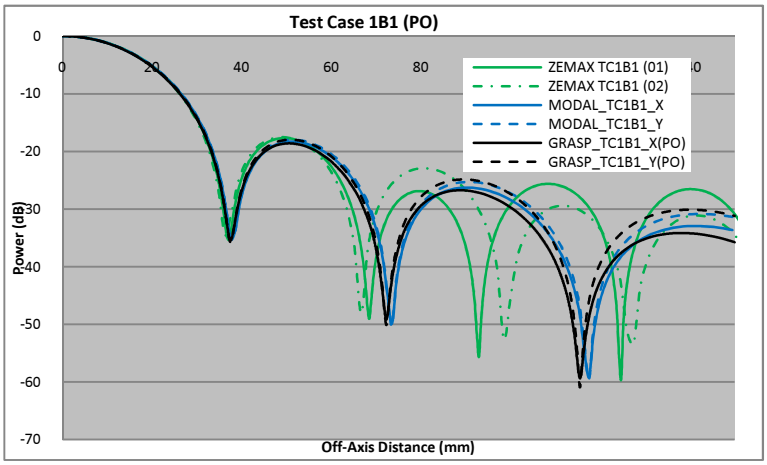

Figure 3-15 - Test Case 1B3: farfield of aperture where $a / \lambda >> 1$ - GRASP9 calculations performed using PO only - comparison with MODAL PO calculations shows significant increase in agreement when compared to Test Case 1B1 (where $a / \lambda \sim 1$)

The ZEMAX predictions reflect different choices of source sampling in an attempt to attain improved agreement with the PO packages. The fit between ZEMAX and GRASP9 is reduced beyond the main lobe structure in each of these test cases. This is accounted for by the large degree of beam spreading. The observation plane is very large relative to the narrow aperture. ZEMAX is primarily a paraxial optics propagator

and has difficulty in accurately predicting such widely dispersed beam at large off-axis angles. This is evident in all plots where agreement starts to decrease with increased off-axis distance. The ZEMAX beam predictions fall away from the GRASP9 and MODAL predictions approximately after the secondary beam lobe – c.f. Figure 3-14. The disparate results between the different beam samplings illustrate the difficulty in determining the correct sampling for source fields in the ZEMAX POP tool. It can be concluded from these results that for this limiting test case for far-field diffraction ZEMAX may only be trusted to give reasonably accurate results for a paraxial beam i.e. for the main lobe and first side-lobe.

Test Cases 1C – (Far Field of Point Source Illuminated Aperture)

For Test Cases 1C, plane wave illumination of a truncating aperture is replaced by a point source. The aperture radius and output observation distance remains constant (a = *10.0 mm*, z_{out} = *2000.0 mm)* and the input distance z_{in} is varied. These diffraction examples are important as they represent propagation of radiation from spatially incoherent sources. With the large aperture radius and farfield output distances, it can be expected that the higher order Fresnel zone modification factor from Test Cases 1A will not be important here. To achieve a point source in ZEMAX, a combination of a truncated plane wave source incident on an ideal lens was used. The *paraxial surface* object is described as a perfectly focusing ideal lens. The truncated plane wave with flat phase front is focused to a point source at the focal point of the lens, and it is from this position on the optical axis that the point source is launched.

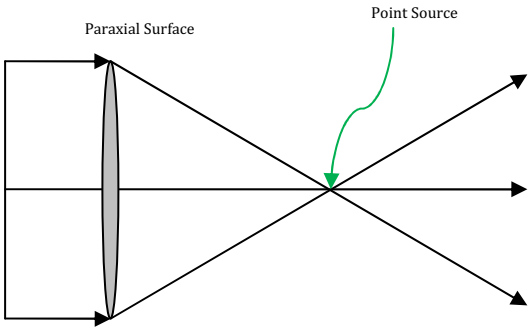

Figure 3-16 – Illustration of technique employed to create an approximate point source in ZEMAX

A point source is achieved in GRASP9 by using a special case of a Gaussian beam source, whereby the beam waist is set to zero. Given the farfield output distances the truncating aperture was again treated in GRASP9 as a finite planar reflector with a central hole.

The definition of a point source object in MODAL was achieved using an extremely small *uniformly illuminated aperture* source object. In these test cases a source radius of 1μm was used. It was possible to go smaller than this but the beam patterns were found to be equivalent and for sources with radii smaller than this there were problems with normalizing the beam patterns in the plotting software owing to peak power output levels being too low. As before, all calculations were performed using full vector PO analysis. As with the preceding test cases, the source polarisation is linear and aligned along the local x axis of the system.

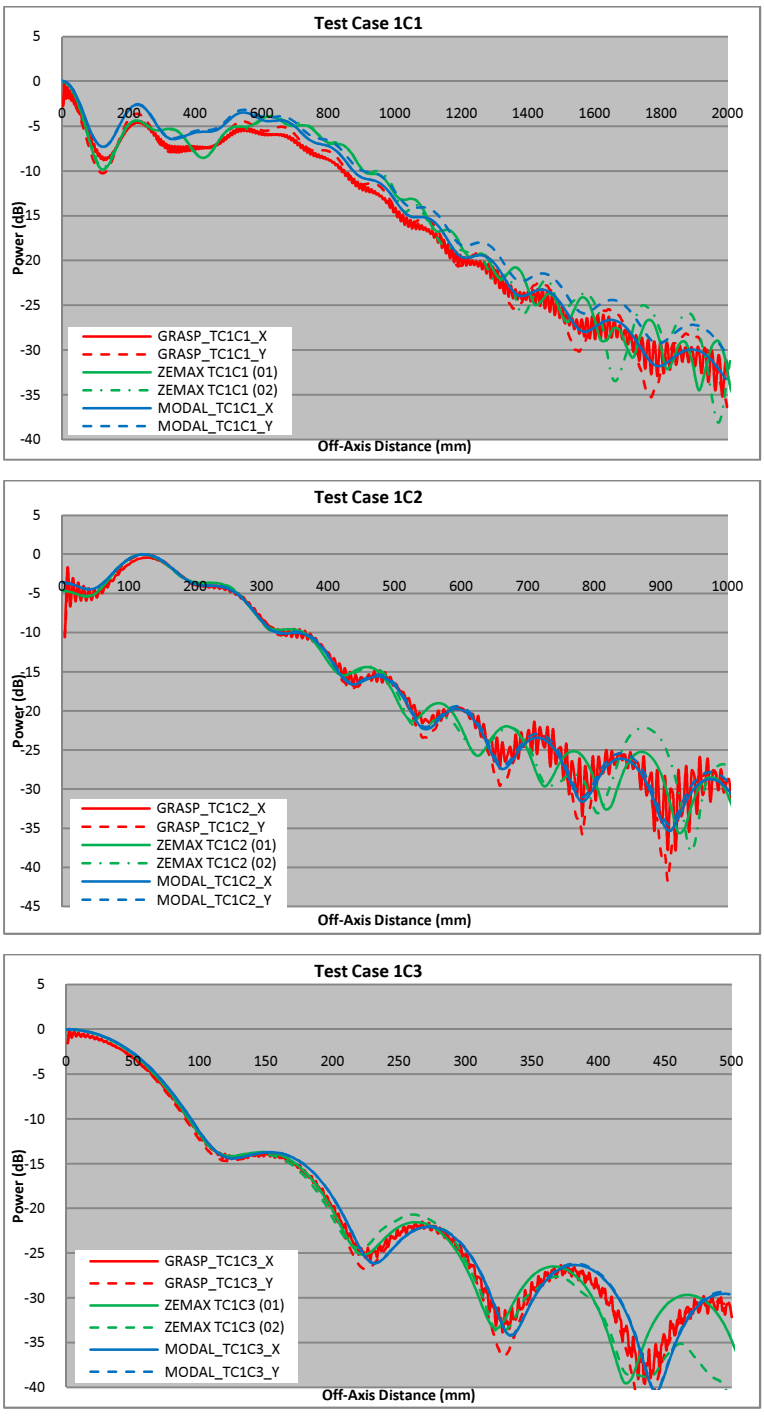

Figure 3-17 - Output beam predictions for test cases 1C1 ($z_{in} \sim 3\lambda$) , 1C2 ($z_{in} \sim 60\lambda$) and 1C3 ($z_{in} \sim 200\lambda$).

Generally there is good agreement between all of the software packages for this set of test cases, and as with previous test cases the agreement improves with increasing observation distance. The degree of asymmetry between the x and y planar cuts is very slight in these test cases. This is in keeping with the results of test case 1A for the diffraction patterns from a truncated plane wave; for the near field test case (1A1: $z_{out} \approx a$) there was a high degree of asymmetry. With increasing propagation distance away from the aperture (1A2: $z_{out} \sim 3a$, 1A3: $z_{out} \sim 10a$) the asymmetry is removed. For the test cases presented here (i.e. 1C1, 1C2, 1C3) the beam is sampled in the farfield of the aperture and thus there is negligible asymmetry. The presence of the 'fringing' or 'ringing' in the GRASP9 calculations is accounted for by aperture object. The aperture object in ZEMAX defines an annular region outside of which all incident rays are vignetted. The aperture object in MODAL works in a similar way. In GRASP9 the aperture object is created as a central hole within a finitely sized plane reflector object. The fringing structure seen in the GRASP9 plots are due to diffraction effects at the edge of the outer rim of this plane reflector. To remove these fringing effects the truncating aperture is re-defined as a Babinet disc, as was done for Test Cases 1A1 and 1A2. These new GRASP9 Babinet predictions are plotted below in Figure 3-18. With the inclusion of the 'Babinet' variation to the results the agreement between each of the packages has improved with the removal of the fringing structure to the GRASP9 diffracted pattern.

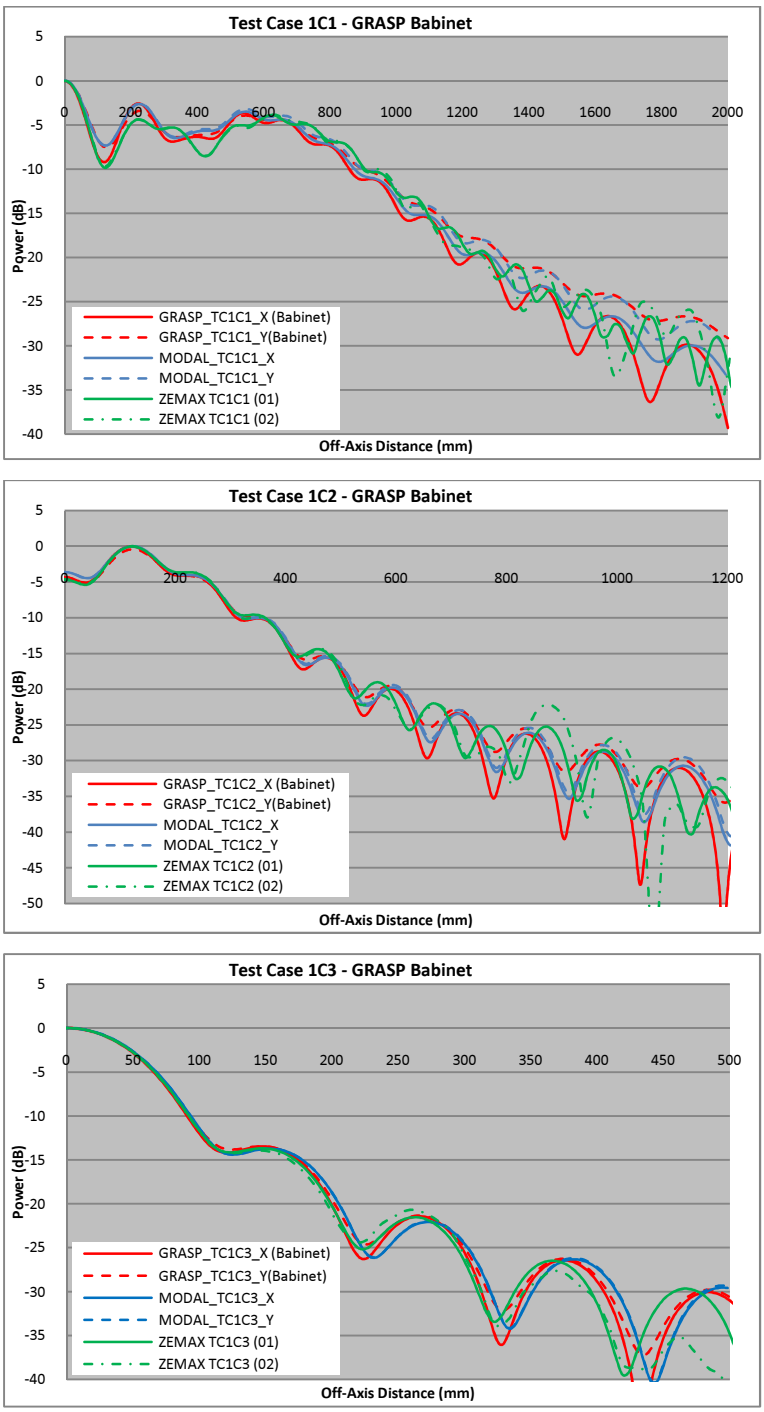

Figure 3-18 - Output beam predictions for test cases 1C1 (z_{in} ~ 3λ), 1C2 (z_{in} ~ 60λ) and 1C3 (z_{in} ~ 200λ) for GRASP9 calculations using the Babinet disc technique. Note the absence of fringing in the new GRASP9 predictions when compared to those from Figure 3-16.

Test Cases 1D – (Gaussian Beam Illumination of Aperture)

This next set of test cases is an advancement of 1C, where a point source object has been replaced with a fundamental Gaussian beam. This test case can be considered more physically relevant to long wavelength setups since quasioptical systems are routinely modeled with Gaussian beams, which are considered good first order approximations of real feed horn patterns [3]. These test cases model a moderate amount of truncation, with the truncating aperture having a radius of the beam width w at the diffracting aperture. This amount of truncation is unusual for most physical systems. Realistically feed horn beams are propagated through systems of mirrors, lenses or truncating apertures with a truncating radius of over $2w$, giving a beam spillover of $-35\ dB$. With this level of truncation there will be significant diffraction effects visible in the Fresnel region for the purpose of comparing packages. Again, as with all previous test cases the source field is linearly polarised in the x direction. The definition of the Gaussian sources for all packages is straightforward, with defining parameters previously outlined in Chapter 2.

GAUSSIAN BEAM (far field , incident *F* number varies)			
Radius : a	10		
W0	0.637	1.947	5.93
ZIN	20	60	150
ZOUT (far field)	2000	2000	2000
Case No.	**1d1**	**1d2**	**1d3**

Table 3-2 - System parameters for test cases 1D - all dimensions are in millimetres

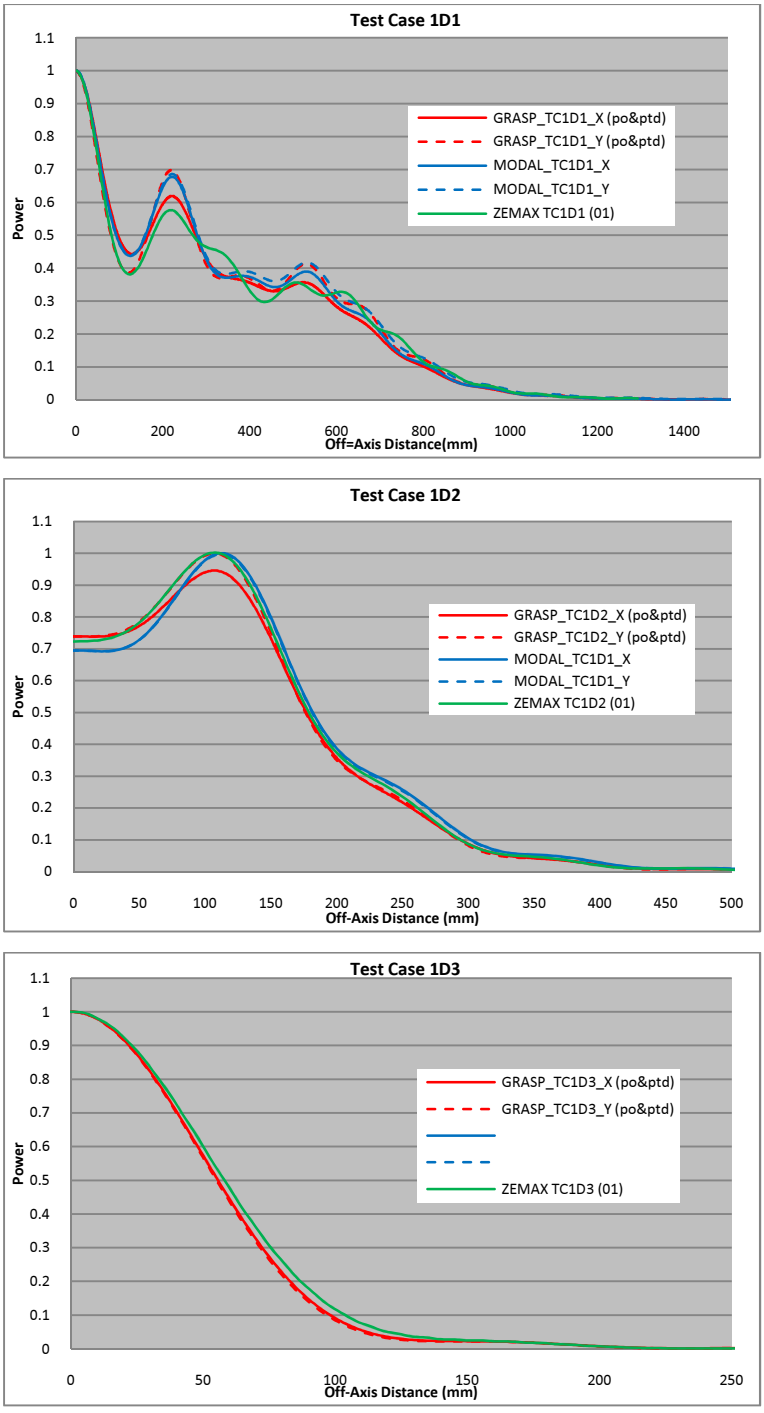

Figure 3-19 - Output planar cuts for test cases 1D1 (near field), 1D2 (Fresnel/Fraunhofer transition) and 1D3 (far field)

The results for the first test case (1D1) exhibit similar structure to the near field Fresnel diffraction patterns seen in Test Cases 1A. Agreement between GRASP9 and MODAL is very good; however there is a small degree of asymmetric disparity for off-axis structure. The ZEMAX result shows reasonable on-axis agreement with the two PO packages that moderately worsens with increasing off-axis distance The general agreement for all packages improves with increasing Gaussian waist size for Test Cases 1D2 and 1D3. There also exists slight asymmetry in the GRASP9 PO & PTD predictions for Test Case 1D2 that is not predicted by MODAL or ZEMAX. There is also slight disagreement between MODAL and GRASP9 in the predicted amplitude of the central beam for this test case. The agreement for all packages in Test Case 1D3 is almost perfect.

The disparity between MODAL and GRASP9 for Test Cases 1D1 and 1D2 is resolved by re-calculating the GRASP9 predictions using PO only. These results are shown below in Figure 3-20 and Figure 3-21 where the GRASP9 PO predictions are plotted in black against MODAL calculations in blue.

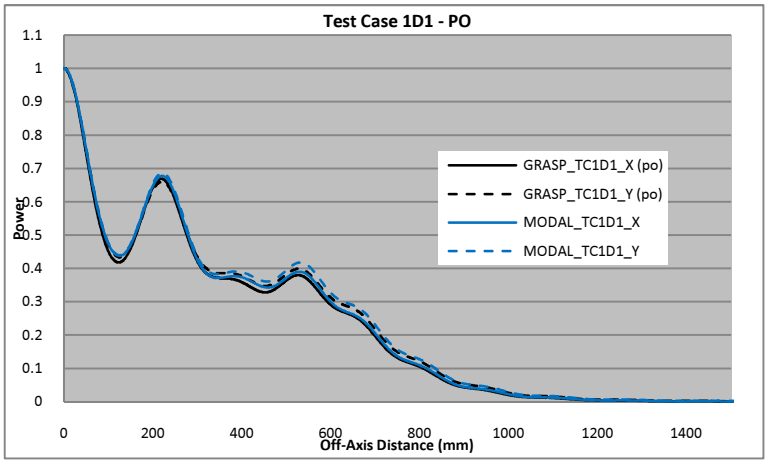

Figure 3-20 - Diffracted beam patterns for test case 1d1 with GRASP9 PO calculations compared with MODAL

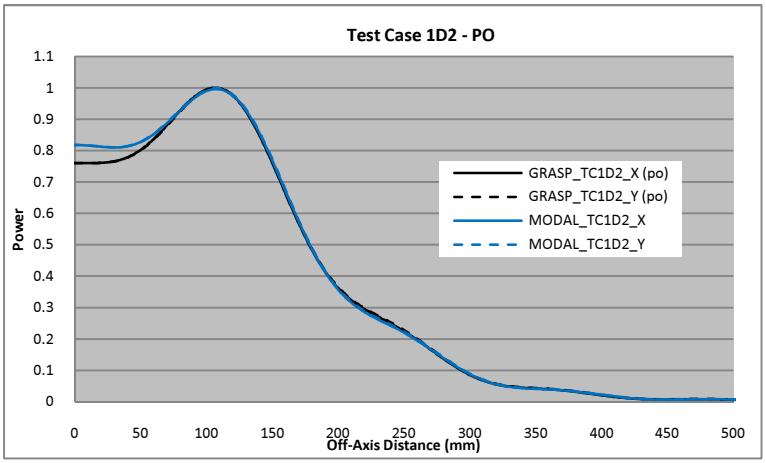

Figure 3-21 - Diffracted beam patterns for Test Case 1D2 with GRASP9 PO calculations in black compared against MODAL predictions in blue

The MODAL predictions show greatly improved agreement with these GRASP9 PO predictions. However there is still minor disagreement between the two packages regarding the on-axis amplitude for Test Case 1D2.

Conclusion

This first batch of test cases was designed as examples of highly diffracting long-wavelength systems. The plane wave and point sources in Test Cases 1A, 1B and 1C can be considered as only mathematical abstractions with little physical bearing to any realistic system. It can reasonably be stated that the Gaussian beam source in Test Case 1D makes this the only physically relevant test case, given the prevalence of Gaussian beam-type field distributions in many typical quasioptical systems.

Overall the PO predictions by MODAL show very good agreement with those from GRASP9 for nearly all test cases. This is to be expected given the similarity in their calculation techniques. In those test cases where there is some disagreement, this can be chiefly attributed to the lack of a PTD and PO convergence tool in MODAL. However, the truncating aperture elements in each software package are defined differently and as such slight disagreements are to be expected.

ZEMAX predictions compare poorly to GRASP9. This is obviously due to the approximations of the POP tool. As stated in Chapter 2, the POP tool uses either Fresnel diffraction integrals or angular spectrum decomposition through Fourier transforms to calculate the output beam. These tools do not technically constitute Physical Optics in the true definition of the term; rather they are classical diffraction techniques. This leads to poor agreement with the other two PO packages for strongly diffracted systems with large angular beam spreading. This is most obvious in test cases 1A1 and 1A2 for the diffraction pattern of a plane wave by a truncating aperture in the very near field.

For the near field test cases 1A1 and 1A2 the polarisation of the source field affected the symmetry of the resultant field diffracted by the aperture. Results from the PO packages revealed unmatched amplitude patterns in the x and y planes. This is counter to the predictions of classical Fresnel diffraction theory, which predicts no dependence on the polarisation of the incident radiation for the output field. This is seen in the results from ZEMAX, which exhibited perfectly matched amplitude profiles in x and y. As shall be shown in a later section, experimental measurements of a similar system to that of test case 1A1 reveal that this asymmetry is real. This is further evidence of the superior capability of the PO method for calculating diffracted beam patterns over the scalar Fresnel diffraction integrals.

3.2.3 Test Case 2

These test cases involved modelling the diffraction effects associated with the focusing and collimating of a coherent beam using a lens of finite size. The lens is defined as a combination of a truncating aperture and phase transformer, where any radiation not intercepted by the lens is absorbed. Using a lens in the long-wavelength limit either focuses a beam of flat phase radius of curvature to a beam waist of finite phase radius of curvature or performs the converse by collimating a narrow waist to wide waist. This is not equivalent to the formation of geometrical images as in classical lens theory. A 'focused' beam waist will not be coincident with the equivalent geometrical focal plane

of the lens. For the long wavelength limit, a focused beam waist position is not coincident at the geometrical focus.

In Test Cases 2A and 2B the focal plane and the Fresnel region of the lens are examined. The source beam is a plane wave with a flat phase radius of curvature. For Test Case 2C the source field is a fundamental Gaussian whose waist coincides with the focal plane of the lens. This is a typical quasioptical setup for long-wavelength optics. In many telescope imaging systems a lens is used in combination with a feed horn. The layout of Test Cases 2A and 2B are illustrated below in Figure 3-22, with the layout of Test Case 2C given by Figure 3-23. The physical parameters for each individual test case are listed below in Table 3-3.It was not possible to model these test cases in GRASP9. The GRASP9 software package is primarily concerned with PO calculations for reflecting metallic surfaces. Therefore only MODAL and ZEMAX have been compared here.

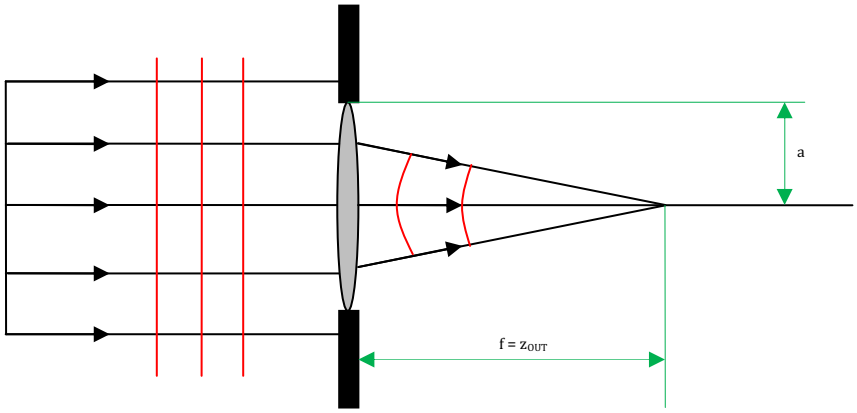

Figure 3-22 - Test Cases 2a & 2b - imaging a plane wave to a focus using a truncating aperture and lens combination

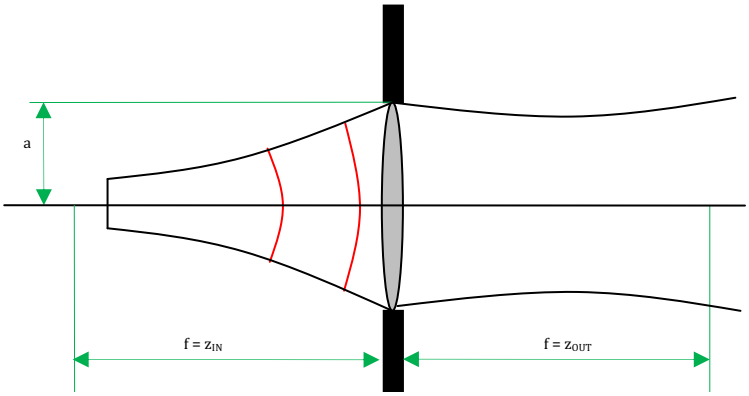

Figure 3-23 – Test Case 2c – collimating a source waist with a truncating aperture and lens combination

PLANE WAVE (field at focus)			
Radius : a	5		50
Focal length : f	100 (F10)		300 (F3)
Z_{OUT} = f	100		300
Case No.	**2a1**		**2a2**
PLANE WAVE (field at near waist)			
Radius : a	5		50
Focal length : f	100 (F10)		300 (F3)
Z_{OUT} = f	9.5		297.5
Case No.	**2b1**		**2b2**
GAUSSIAN BEAM (input waist at focal plane – moderate truncation at lens aperture – input focal ratio F3.14			
$w_{0\text{-}IN}$	2.0	2.0	2.0
Radius: a = 1.5 w_{LENS}	4.2	9.5	30
$Z_{IN} = Z_{OUT}$ = f	12.5	37.5	125
Case No.	**2c1**	**2c2**	**2c3**

Table 3-3 - Parameters for Test Cases 2 – all dimensions are in millimetres.

From the lensmaker equation [33] the focal length *f* of a thin lens is given as:

$$\frac{1}{f} = \frac{n_2 - n_1}{n_1}\left(\frac{1}{R_1} - \frac{1}{R_2}\right) \tag{3.11}$$

where n_1 and n_2 are the refractive indices of exterior and interior of the lens respectively, and R_1 and R_2 are the radii of curvature of the first and second refracting surfaces with the assumption that the surfaces are spherical. This formula is a simplification whereby the thickness of the lens is neglected. For example, the lens in test cases 2a1 and 2b1 has a focal length of 100 mm. Using Equation 3.11 above and assuming reasonable values for the indices of refraction: for air $n_1 = 1$ and for glass $n_2 = 1.5$ both radii of curvature are given to be 100 mm. Implementing such a lens in ZEMAX is straightforward, whereby the lens is a creation of two surfaces representing the two surfaces of refraction. The first surface is given a radius of curvature of 100 mm and a thickness of 0.5 mm. This thickness is deemed appropriate for the thin lens approximation. The next surface, representing the output surface of the lens, is a convex version of the incident surface with a radius of curvature of -100 mm. Generating a lens object in MODAL is similarly straightforward. The *lens object* simply requires the user to enter the input and output radii of curvature as well as the central thickness and the conic constant of the surface. It can be noted here that the strict choice or design of the lens is arbitrary since the two software packages are simply being compared against one another, rather than against the results of a known experiment. As such, as long as the systems are equivalent in each package, that is each element has the same dimensions and distances, the specifics of the lens are not of great concern.

The results from Test Cases 2A and 2B are plotted below in Figure 3-24 and from Test Cases 2C in Figure 3-25. Predictions from MODAL are plotted in blue and ZEMAX predictions in green.

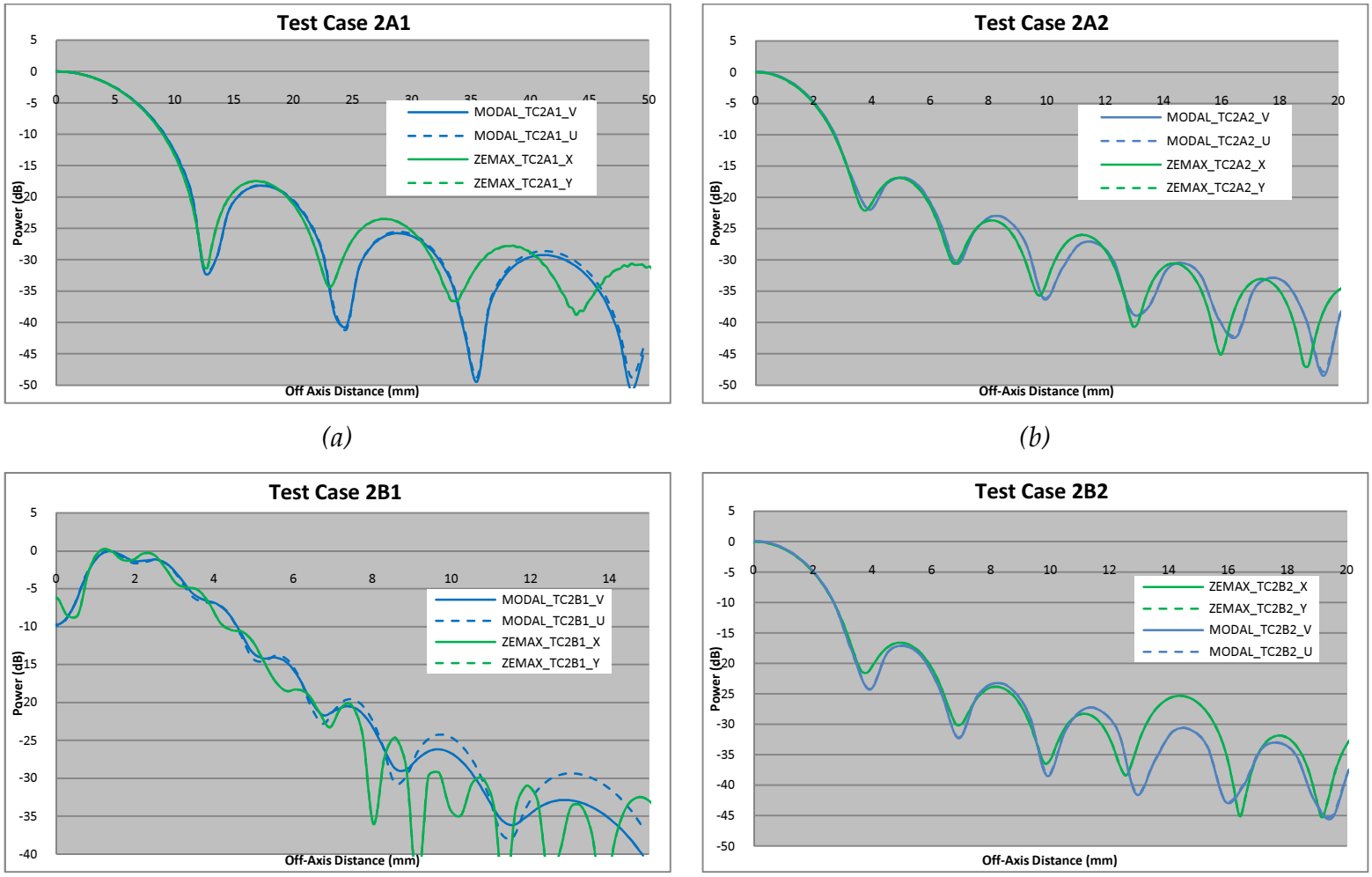

Figure 3-24 - Output planar diffracted amplitude patterns for Test Cases 2A1*(a)* - (F10 beam at the focus), 2A2(*b*) – (F3 beam at the focus), 2B1*(c)* - (F10 beam at the waist) and 2B2*(d)* – (F3 beam at the waist).

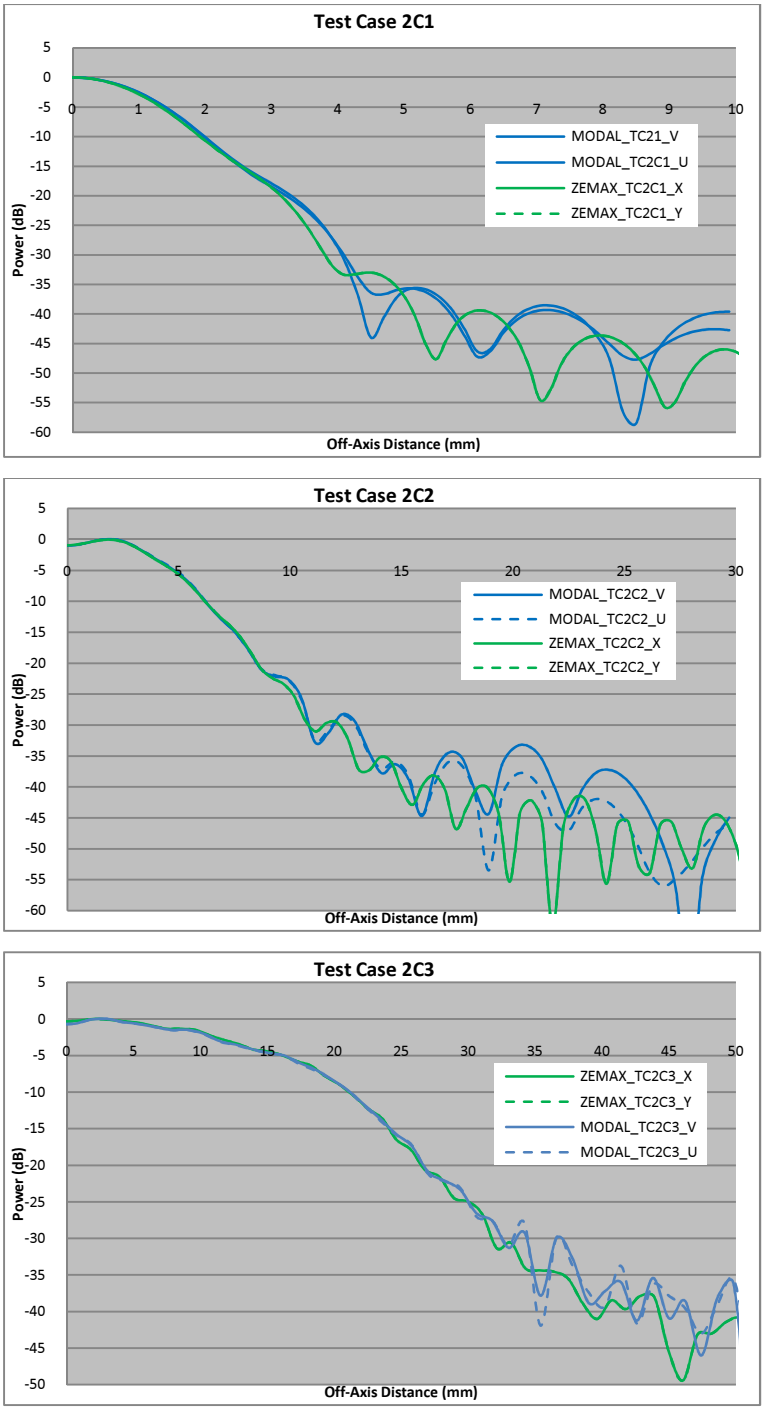

Figure 3-25 - Diffracted patterns for test cases 2c1: $\left(\frac{\lambda f}{\pi w_0^2} \approx 1\right)$, 2c2 $\left(\frac{\lambda f}{\pi w_0^2} \approx 3\right)$ and 2c3: $\left(\frac{\lambda f}{\pi w_0^2} \approx 10\right)$

There is relatively good agreement between ZEMAX and MODAL over most test cases, especially in the main beam. In the absence of a decided benchmark result and no formal experimental results for comparison, the accuracy of two packages can only be speculated upon. Though ZEMAX is considered a front-runner in terms of field calculations from lenses and other refractive elements, the approximations made by the POP tool and the long-wavelength nature of the systems under examination test the accuracy of the results. With a more robust physical optics propagator and being designed specifically to work in the long-wavelength regime, it could be assumed that MODAL can give the more accurate result. The discussion is unfortunately academic; given that there is as yet no industry approved optical propagation software with refractive elements capability to provide comparable results for the long-wavelength regime. This was the same dilemma faced in the original report. It would have been possible to create an experiment to provide comparable results, though such an expenditure of time and resources was considered unnecessary. Working with large scale lenses for the long-wavelength regime is costly and unpredictable imperfections within materials used in lens design such as PTFE would give rise to unaccountable errors, leaving a detailed comparison with EM prediction tools redundant. It was determined that, provided there were no great discrepancies between the results from both packages, a benchmark result would not be required.

For the first set of test cases (i.e. test cases 2A1 and 2A2), the refracted beam is being reproduced at the focal point of the lens. The results from the two packages both show the expected Airy pattern for a beam at the focus of a lens. For the first test case (2A1) the agreement is limited to the main lobe and first side lobe, beyond which the location of the lobe varies – c.f. Figure 3-24 (a). The agreement is greatly improved for the second test case (i.e. 2A2), which has a much larger aperture in terms of λ (50λ) and thus has a smaller degree of diffraction - c.f. Figure 3-24 (b). Both MODAL and ZEMAX illustrate excellent agreement with discrepancies generally occurring near and below *-30 dB* which would be very difficult to measure equivalently with experiments.

The second set of test cases (i.e. test cases 2B1 and 2B2) have the same lens parameters as the first, but the output measurement plane is now located at the Fresnel region or near field of the lens. In the first of these test cases (2B1) there is reasonable beam pattern agreement, yet there are distinct disparities for the fine detail structures - c.f. Figure 3-24 (c). This disparity is similar to that found for the near field Fresnel diffraction patterns seen in test cases 1A. For the next test case (2B2) the agreement has been greatly improved. This is unsurprising given the relatively close distance of the Fresnel region to the actual focal position in terms of λ, where the agreement was also very favourable - c.f. Figure 3-24 (d).

For the last set of test cases (i.e. test cases 2C1, 2C2 and 2C3) the agreement is good for the main lobes, with small scale deviations occurring for increasing off-axis distances. The degree of truncation here is quite low (-19.5 dB) and as such the beam patterns at the output plane should be almost pure Gaussian in shape with some low level sidelobe structure. The discrepancies between the two packages for each of these test cases occur at levels well below -20 dB. Above these levels the agreement is excellent - c.f. Figure 3-245. This is most encouraging for both software packages as this test setup is more common for long-wavelength optics facilities.

One of the more pragmatic results of these tests was the difference in computation time between ZEMAX and MODAL. Performing a POP calculation in ZEMAX for even the largest scale lens, such as in test cases 2B, was relatively quick. By comparison, the same calculation in MODAL was many orders of magnitude slower. This is due partly to the requirement of assigning an overly large number of PO points to the lens object to ensure sufficient accuracy. It was revealed that the default setting of a 40×40 PO grid produced severely inaccurate results and the above results were achieved for a grid sampling of approximately 3 points per *mm*. The lack of a PO convergence tool in MODAL is also a disadvantage, and hence such oversampling is necessary. The process

by which MODAL propagates a field within a lens or other dielectric element is also time consuming, and has been discussed previously in Section 2.5.3.1.

3.2.4 Test Cases 3 (Off-axis Parabolic Mirrors)

This set of test cases involved modelling diffraction effects associated with re-imaging a coherent source beam incident on an off-axis paraboloidal mirror – c.f. Figure 3-26 and Figure 3-27 below. The mirror acts as a phase transformer for the source beam. In the long-wavelength limit the off-axis nature of the reflecting surface introduces distortion of the beam due to projection effects [68], [69]. Truncation associated with the finite size of the mirror will also limit the resolution of the image.

A paraboloidal mirror is routinely required to image a large waist at the mirror to a narrower waist near the geometrical focus. A beam with a flat phase radius of curvature at the mirror will be transformed to a wavefront with a finite radius of curvature centred on the geometrical focus. The converse is also true, wherein a beam of finite phase radius of curvature at the focus will be re-imaged as a beam with a flat phase radius of curvature.

To illustrate the imaging of a typical off-axis paraboloidal mirror, several different test cases were considered. The off-axis paraboloidal mirrors for Test Cases 3A and 3B have the same focal length and aperture diameter as the focusing lenses from Test Cases 2a and 2b with a uniformly illuminated aperture source. In Test Cases 3A the polarisation of the incident beam is set to be in the plane of incidence, whereas in Test Cases 3B the polarisation is set to be perpendicular to the plane of incidence. The source field for Test Case 3C is a scalar feed horn. The source waist is placed near the geometrical focus so that the phase radius of curvature of the beam propagated to the mirror surface will match the radius of curvature of the mirror. This then produces a reflected beam with a flat phase radius of curvature. This setup can be interpreted as the reciprocal of Test

Cases 3A and 3B. In Test Case 3C1 the polarisation of the incident beam is parallel to the plane of incidence (i.e. in the local *y* axis) and perpendicular to the plane of incidence for Test Case 3C2 (i.e. in the local *x* axis). The output beam for this test case is sampled in the far-field of the mirror. The layout for Test Cases 3A and 3B is illustrated in Figure 3-26 and in Figure 3-27 for Test Case 3C.

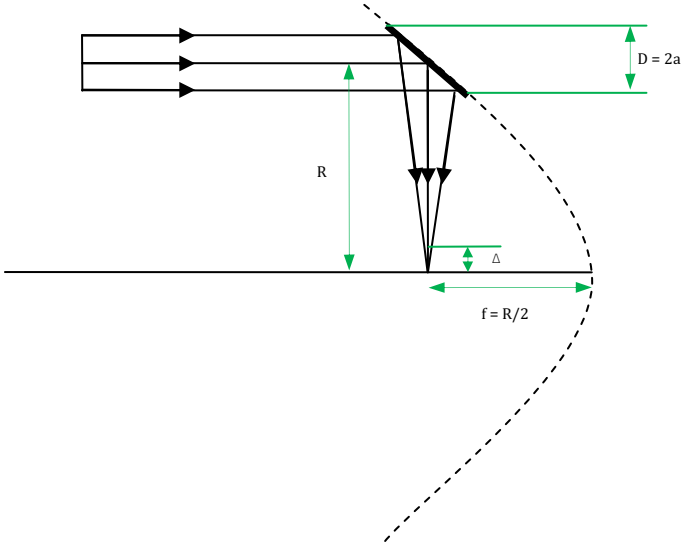

Figure 3-26 - Test Case 3a & 3b - imaging with an off-axis paraboloidal mirror

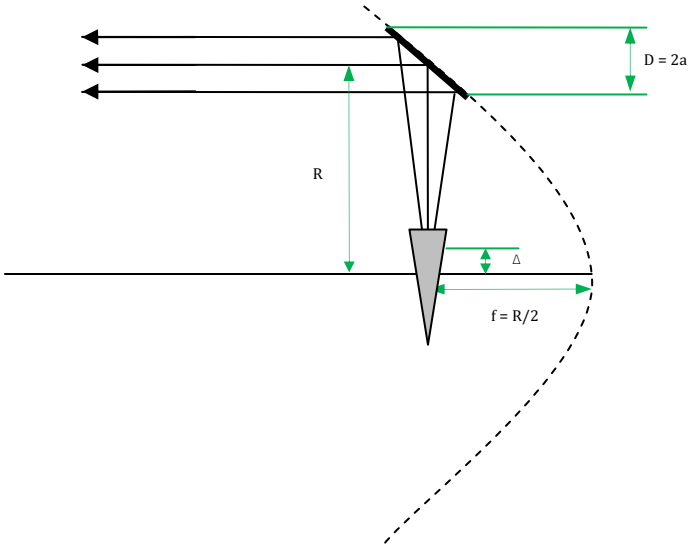

Figure 3-27 - Test Case 3c - collimation with an off-axis paraboloidal mirror

PLANE WAVE (polarization in the plane of incidence – output field at waist position)		
Radius : a	5	50
Radius of curvature : R	100	300
Focal length : f = R/2	50	150
Z_{OUT}	27.9	300
Case No.	**3a1**	**3a2**
PLANE WAVE (polarization in the plane of incidence – output field at waist position)		
Radius : a	5	50
Radius of curvature : R	100	300
Focal length : f = R/2	50	150
Z_{OUT}	27.9	300
Case No.	**3b1**	**3b2**
SCALAR HORN (input waist near focal plane – slight truncation at mirror surface		
Polarisation	Parallel to plane of incidence	Perpendicular to plane of incidence
Mirror Radius : a_{mirror}	30	30
Radius of curvature : R	101.3	101.3
Z_{IN}	100	100
Horn Radius : a_{horn}	3.0 (F3)	3.0 (F3)
Z_{OUT}	8000	8000
Case No.	**3c1**	**3c2**

Table 3-4 - Parameters for Test Cases 3 - all dimensions are in millimetres

Generating these systems in GRASP9 was relatively trivial. An off-axis paraboloidal reflector is achieved simply by defining the paraboloidal surface on axis then shifting the axis of incidence accordingly. The scalar horn source object is represented by the Hybrid Mode Conical Horn object (c.f. Section 2.4.4.2). Defining the system in MODAL was equally trivial, with the off-axis paraboloidal reflector already existing as a pre-defined geometrical object. The scalar horn source was modelled using the equivalent Conical Corrugate Horn (c.f. Section 2.5.2.2).

Designing off-axis reflective optics in ZEMAX is more challenging and less intuitive. The off-axis paraboloidal mirror was achieved using a series of Coordinate Break surfaces to tilt and decentre a curved paraboloidal mirror accordingly. There exists no scalar horn source object in the POP tool in ZEMAX. To accurately model this source object the aperture field distribution of the Hybrid Mode Conical Horn from GRASP9 was re-written as a ZEMAX Beam File source described in Section 2.6.2

Output beams for Test Cases 3A and 3B are presented below in Figure 3-28 and in Figure 3-29 for Test Case 3C.

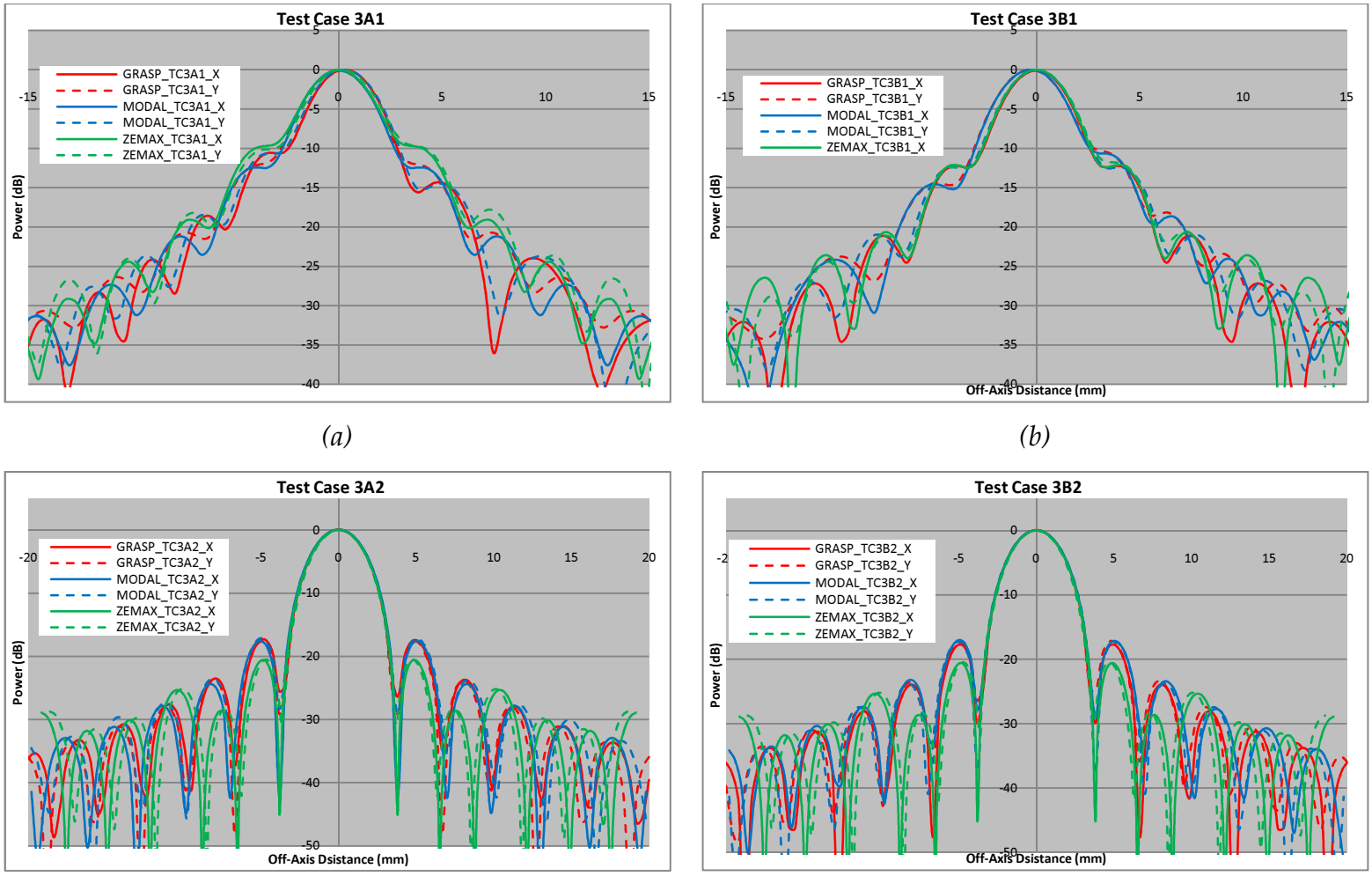

Figure 3-28 - Output planar amplitude plots for Test Cases 3A1(*a*), 3A2 (*b*), 3B1 (*c*) and 3B2 (*d*) where incident flat plane wave is focused by off-axis parabolic mirror. For 3A1 and 3B1 $z_{out} = 27.9\lambda$; for 3A2 and 3B2 $z_{out} = 300\lambda$

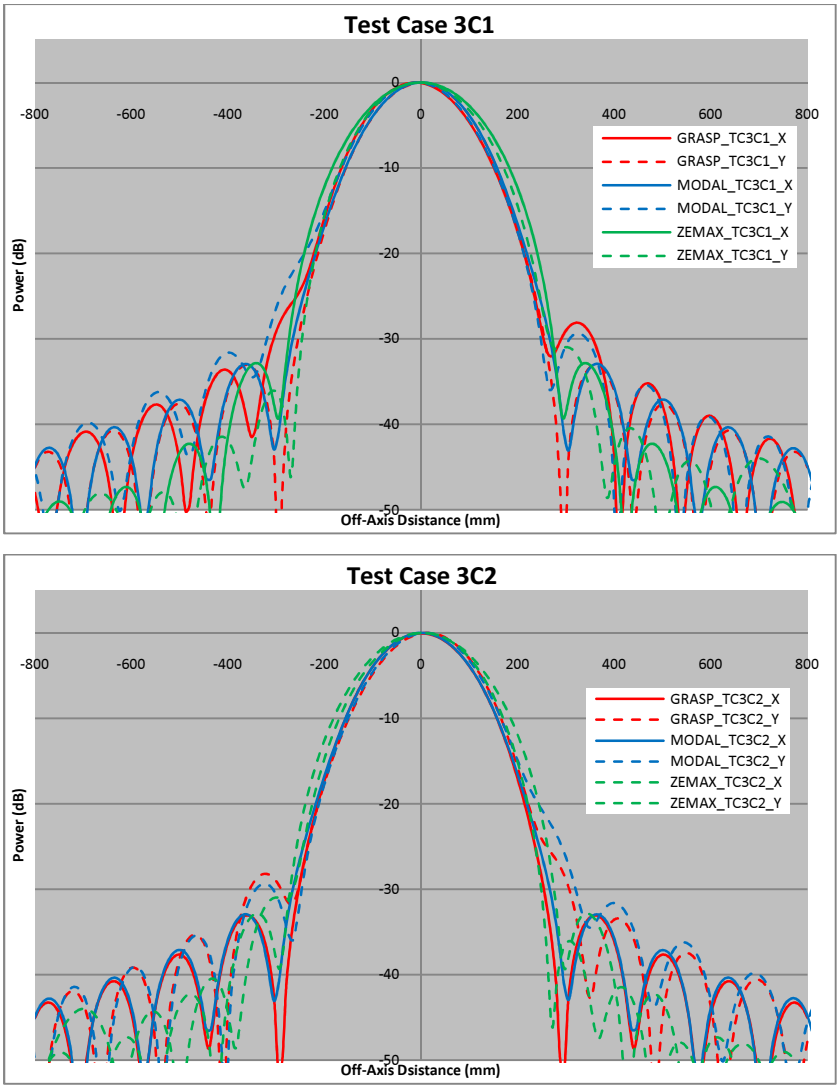

Figure 3-29 - Output amplitude plots for Test Cases 3C – where scalar horn at the focus is reimaged by an off-axis parabolic.

Conclusions

In general there is very good agreement between GRASP9 and MODAL for all test cases with both exhibiting the typical beam distortions due to off-axis reflection for both planes of polarisation. The ZEMAX predictions exhibit reasonable agreement with these two PO packages by accurately predicting the gross features of the main lobes, but routinely misrepresenting the levels and locations of the secondary lobes and the distortions in the main lobe due to the off-axis projection by the paraboloid. The best

agreement for ZEMAX predictions with MODAL and GRASP9 is seen for Test Cases 3A1 and 3A2 which are much less demanding in terms of beam asymmetries, yet the amplitude levels and positions of the secondary lobes are still poorly predicted.

3.2.5 Test Cases 4 (Off-axis Ellipsoidal Mirrors)

This is the final set of test cases where the ability of the software packages to model the reflection from an off-axis ellipsoidal mirror is tested. An ellipsoidal mirror is typically used to re-image a beam from one waist to another [31]. This can serve to magnify, reduce or maintain the same size waist as the incident beam. The off-axis ellipsoidal reflector setup is common in off-axis telescope systems; examples of which include many of the ALMA receiver optics. In these systems the source beam from the main antenna, typically a large radio antenna type reflector such as a Cassegrain, is reimaged from the antenna focal plane into the feed horn. Two such examples of this type of system are explored in further detail in this thesis in Chapter 5 and 6.

There are three ellipsoidal reflectors studied in the following test cases, each of which have differing parameters. The one common thread between each of these mirrors is that they have a large angle of throw; each mirror has an approximate angle of throw of $90°$. Such a large angle of throw would commonly lead to undesired cross polarisation leakage in an off-axis However, for the purposes of this test these ellipsoidal reflectors will serve to probe the limits of the accuracy of the two software packages under scrutiny. This is especially true for ZEMAX, which as previously mentioned is better suited to paraxially coherent/on-axis systems rather than those with large divergence angles.

The two sources used here are a fundamental Gaussian beam and a scalar horn. These two sources represent the typical beam patterns that are usually incident upon an off-axis ellipsoidal reflector. The sources are located at the focal plane of the ellipsoid and phase radius of curvature of the source is defined as an input focal ratio of $F\,3.14$. The

beams are predicted at two planes after reflection, one at one focal length and the other at twice the focal length from the reflector. Beam truncation is relatively high with the radius of aperture of the reflector set to *1.5* times the beam waist at the reflector surface. This level of truncation would be considered impractical for a real optical system, but as with the previous test cases the high truncation level will test the ability of the software packages to model limiting diffraction.

The design of the ellipses is straightforward. The derivation of the defining parameters for an ellipsoidal mirror has already been covered in Section 2.4.5.1, and an example of the ellipse design used in these test cases is given below in Figure 3-30. The parameters for the sources and ellipsoids are listed in Table 3-5

Implementing an off-axis ellipsoidal reflector in GRASP9 and MODAL is relatively straightforward. The scheme for generating an off-axis ellipsoid in GRASP9 was presented in detail in Section 2.4.5.1. In MODAL the off-axis ellipsoid exists as a pre-defined surface object, similar to that for the off-axis paraboloid in Test Case 3. The off-axis ellipsoidal reflector was achieved in ZEMAX through use of the Conjugate Surface [70], which allows the modelling of an elliptical surface when the location of the two foci is known in Cartesian coordinates.

GAUSSIAN BEAM			
$w_{0\text{-}IN}$	2.0	2.0	2.0
Radius : a = 1.5 Wlens	4.2	9.5	30
SCALAR HORN			
Horn aperture : a_H	3.108		
$w_{0\text{-}IN}$ (= 0.6435 a_H)	2.0		
SYSTEM DETAILS			
$Z_{IN} = Z_{OUT} = f$	12.5	37.5	125
R_{IN}	25.13	41.71	126.26
R_{OUT}	25.15	371.4	12493
Ellipse major axis: a	25.14	206.6	6309.79
Ellipse major axis: b	17.78	88.01	888.01
GAUSSIAN OUTPUT			
Z_{OUT} = f (polarisation in plane)	12.5	37.5	125
Case no.	**4a1**	**4a2**	**4a3**
Z_{OUT} =2f (polarisation perp. to plane)	25.14	75.0	250.0
Case no.	**4b1**	**4b2**	**4b3**
SCALAR HORN OUTPUT			
Z_{OUT} = f (polarisation in plane)	12.5	37.5	125
Case no.	**4c1**	**4c2**	**4c3**
Z_{OUT} =2f (polarisation perp. to plane)	25.14	75.0	250.0
Case no.	**4d1**	**4d2**	**4d3**

Table 3-5 - Parameters for Test Cases 4 - all dimensions are in millimetres

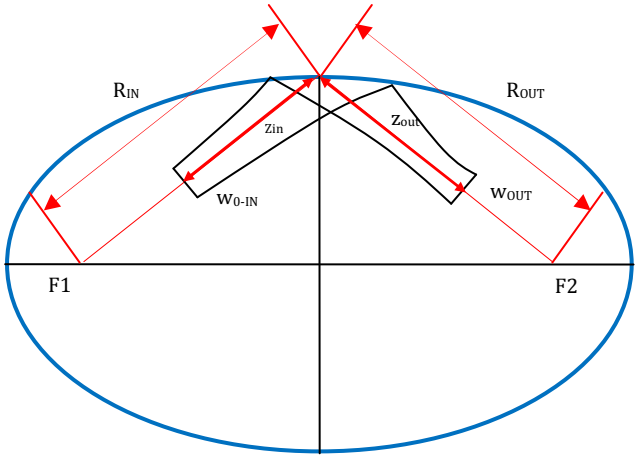

Figure 3-30 – Off-axis ellipsoidal mirror arrangement for test cases 4A1, 4B1, 4C1 and 4D1. Note that $R_{IN} = R_{OUT}$

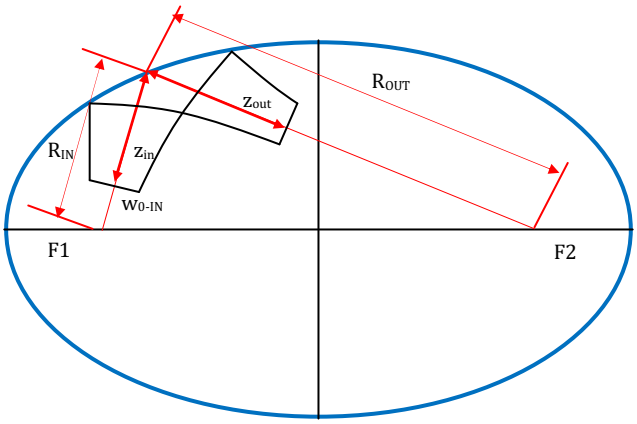

Figure 3-31 - Off-Axis ellipsoidal mirror arrangement for test cases 4A2, 4B2, 4C2 & 4D2. $R_{IN} < R_{OUT}$

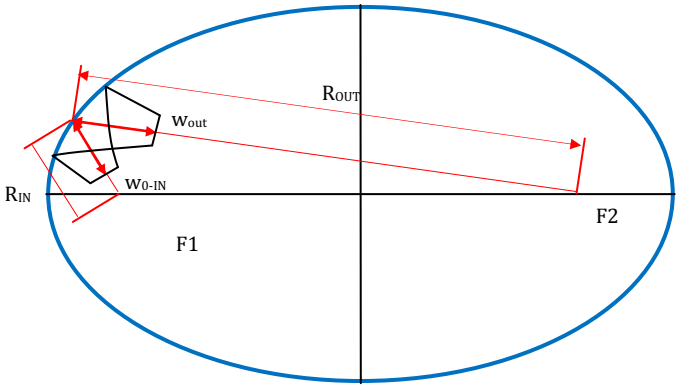

Figure 3-32 - Off-axis ellipsoidal mirror arrangement for test cases 4A3, 4B3, 4C3 and 4D3. $R_{IN} <<< R_{OUT}$

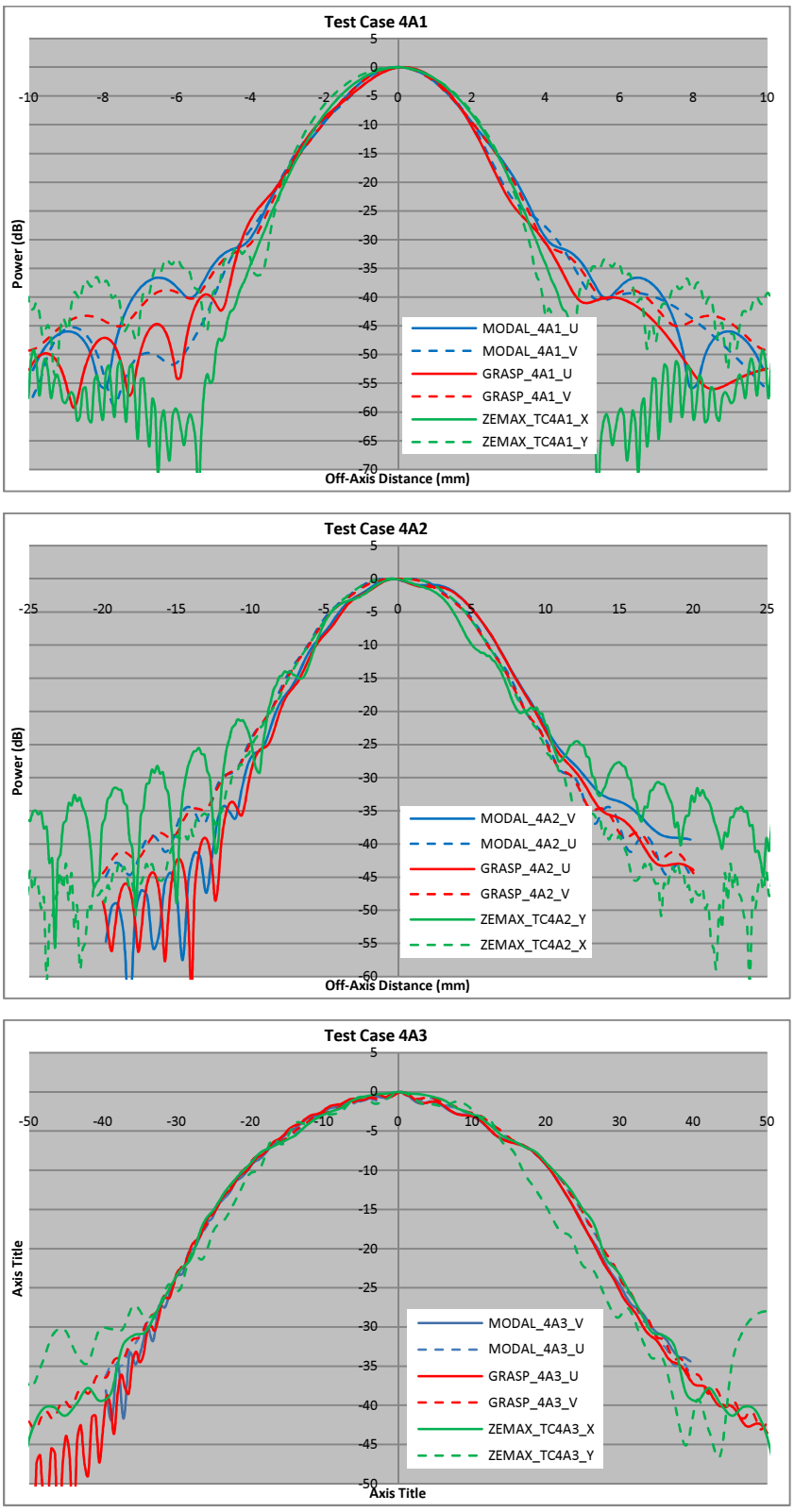

Figure 3-33 – Output amplitude plots for Test Cases 4A with Gaussian beam source, where for 4A1: $R_{IN} = R_{OUT}$, 4A2: $R_{IN} < R_{OUT}$ and 4A3: $R_{IN} <<< R_{OUT}$ and for all cases $z_{in} = z_{out} = f$

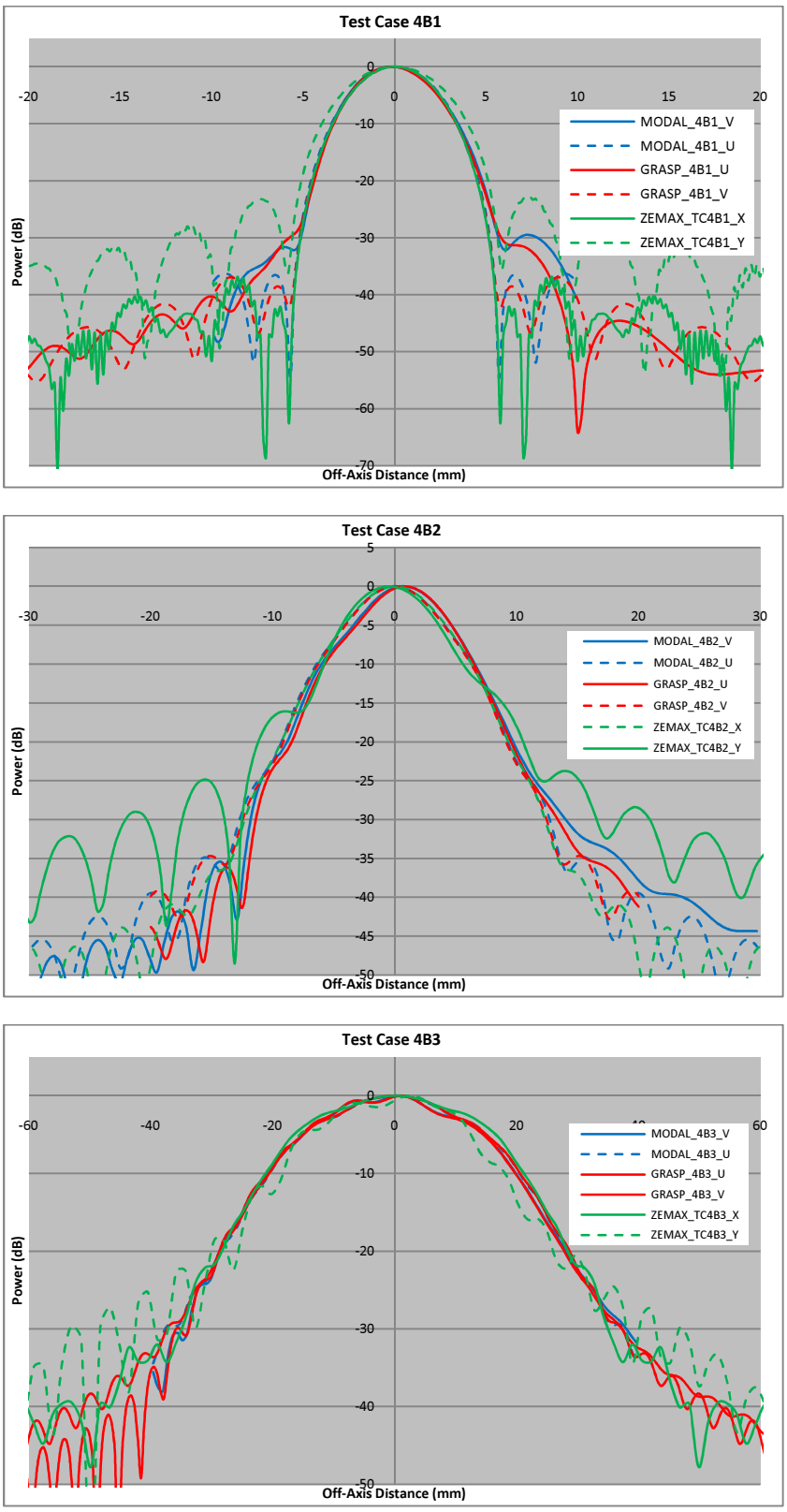

Figure 3-34 - Output amplitude plots for Test Cases 4B with Gaussian beam source, where for 4B1: $R_{IN} = R_{OUT}$, 4B2: $R_{IN} < R_{OUT}$ and 4B3: $R_{IN} <<< R_{OUT}$ and for all cases $z_{in} = 2 \times z_{out} = 2 \times f$

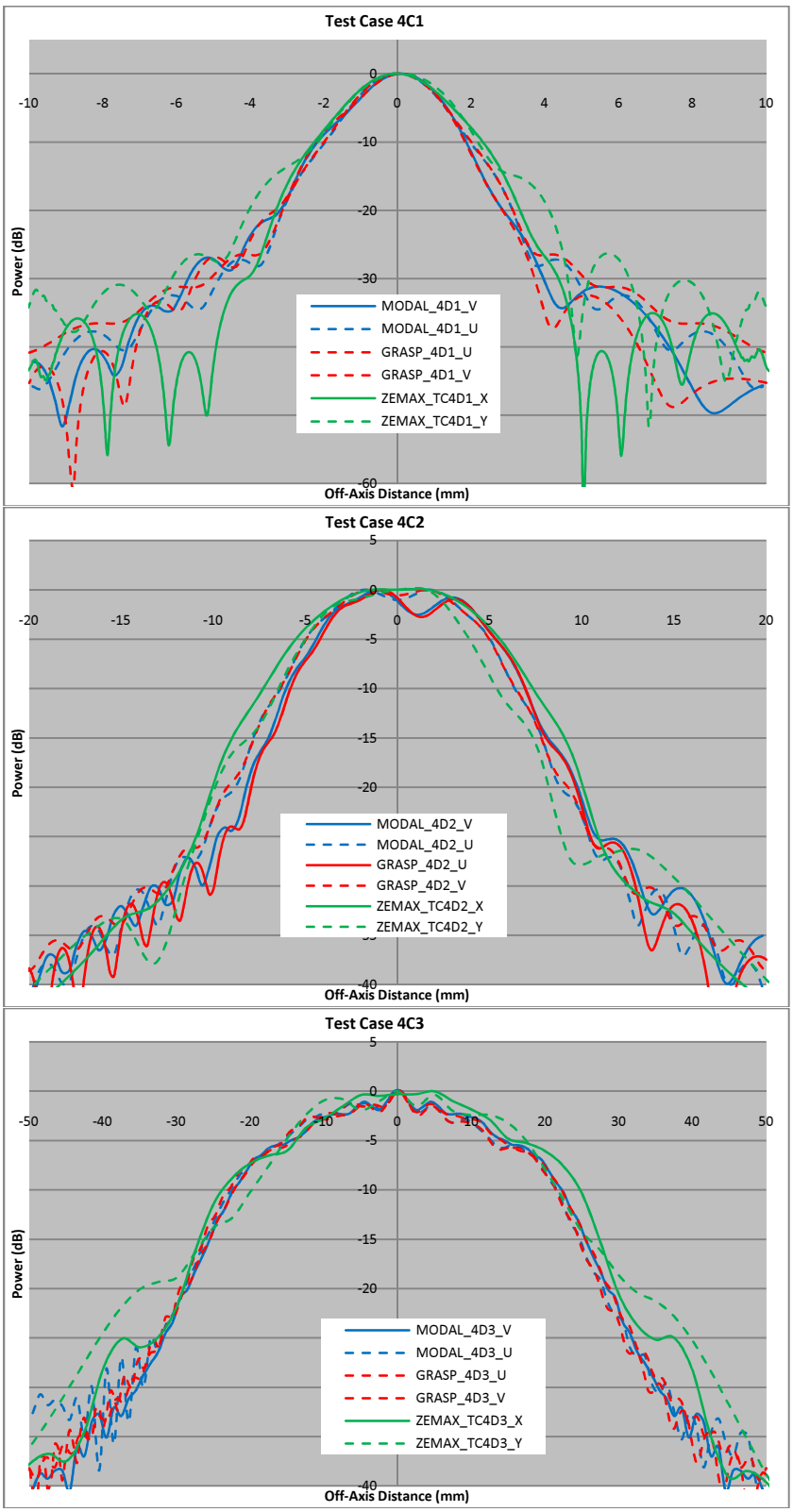

Figure 3-35 - Output amplitude plots for Test Cases 4C with Scalar horn source,, where for 4C1 : R_{IN} = R_{OUT}, 4C2: R_{IN} < R_{OUT} and 4C3: R_{IN} <<< R_{OUT} and for all cases z_{in} = z_{out} = f

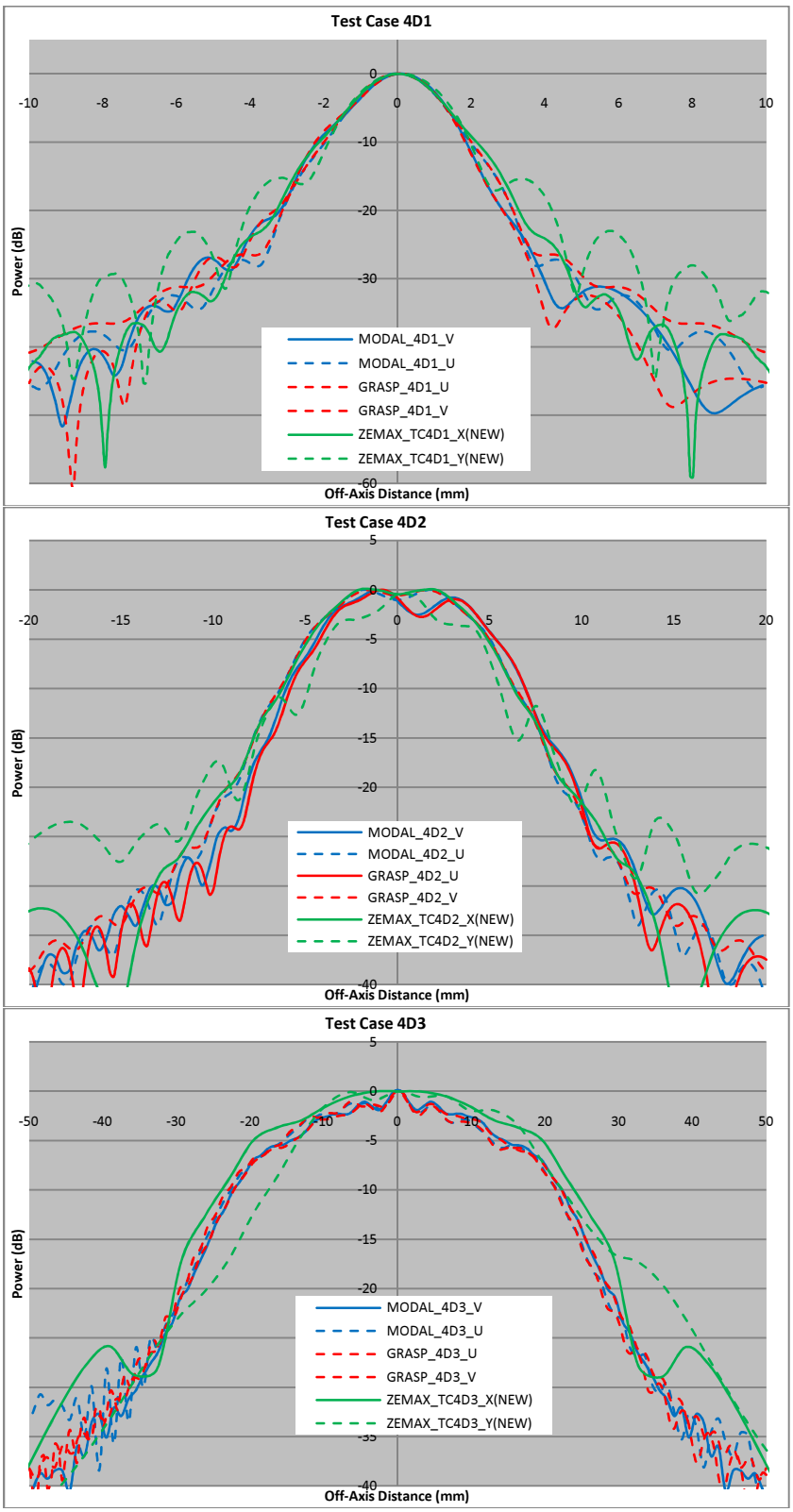

Figure 3-36 - Output amplitude plots for Test Cases 4D with Scalar horn source,, where for 4D1 : R_{IN} = R_{OUT}, 4D2: R_{IN} < R_{OUT} and 4D3: R_{IN} <<< R_{OUT} and for all cases z_{in} =2 × z_{out} = 2 × f

Conclusions

Of all test cases investigated in this chapter, these represent the most physically relevant in terms of realistic quasioptical imaging systems. Pairs of off-axis ellipsoidal reflectors are regularly employed in submillimetre optical systems to re-image the field from a feed horn to an antenna focal plane. Two examples of such systems are ALMA Band 5 and 9 which will be covered in detail in this thesis in Chapters 5 and 6. As with Test Case 3 the predictions by MODAL show very close agreement to those from GRASP9, with accurate representation of the diffracted features and asymmetries in the output beams well below -30 dB. The slight discrepancies exhibited between these two packages are likely accounted for by the PTD tool in GRASP9 and differences in reflector surface sampling.

The results from ZEMAX show relatively poor agreement with the two PO packages, where they routinely fail to accurately predict the major features in the main lobe. There are significant asymmetric sidelobe structures introduced at amplitudes of up to *-10 dB* in some cases.

3.2.6 Overall Conclusions

The conclusions associated with the individual test cases are summarized within their corresponding sections. A summary of these conclusions and observations regarding the performance of MODAL and ZEMAX with respect to GRASP9 is outlined below.

MODAL

For nearly all test cases the MODAL predictions compared very well against GRASP9. This is expected given the similarity in their calculation techniques. Those differences in predicted results have been attributed to a combination of differences in sampling, the lack of PTD calculations and differences in the definition of certain optical elements. For the truncating aperture test cases (1A), there still remains an open topic regarding the calculation of field diffracted by an aperture, with the approximations made by MODAL and GRASP9 differing slightly. In order to truly resolve the matter it is

recommended by the Author that a further analysis of these test cases be performed with the '*aperture in screen*' object add-on for GRASP9 compared to the corresponding results from MODAL. The inclusion of a PTD approximation in MODAL would undoubtedly improve agreement with GRASP9 for those systems defined by strong diffraction effects.

One advantage of MODAL over GRASP9 was the ability to model lenses. At the time of writing GRASP had only recently developed a lens modelling capability and it was not possible given time constraints to include this new capability within this analysis. In comparison with ZEMAX, the PO predictions by MODAL for a variety of lens based optical systems performed extremely well. The only drawback to the PO calculation method for lenses is that to achieve sufficient accuracy the field must be scattered back and forth within the cavity of the lens until a steady state solution is achieved, which is a lengthy process when compared to the same systems predicted in ZEMAX.

ZEMAX

The performance of ZEMAX throughout all test cases was similar to that of the other ray-tracing packages tested in [65] i.e. GLAD and CODE-V. For the truncating aperture test cases ZEMAX failed to predict the diffracted pattern of a plane wave in the very near field. Similar results were seen for the system with a Gaussian source. In the far-field the agreement improved, though beyond the main lobe and secondary lobes the agreement with GRASP9 (and MODAL) breaks down.

The two off-axis reflector systems are the more important test cases. However, these test cases proved very challenging for ZEMAX to be expected to predict with any degree of accuracy, with the incident beams being reflected through a 90° angle of throw for both the off-axis paraboloid and the off-axis ellipsoid reflectors. Its physical optics tools (POP) are ill equipped to handle these large angles of throw for reflecting systems presented both here and for Test Case 3, and are better suited to systems where the

paraxial approximation applies such as on-axis beam guide type systems or very low angle off-axis reflection.

3.3 Experimental Validation – Truncating Aperture

The disparities between the three tested packages are varied. The largest observed disparity occurs for the near field power patterns for the truncating aperture from test cases 1A1 and 1A2, specifically the presence of an on-axis power spot (Poisson Spot) as predicted by both GRASP9 and MODAL that is not predicted by ZEMAX. Though this on-axis power spot was accounted for via a reworking of the Fresnel approximation to the Fresnel-Kirchoff Diffraction theory (c.f. Equations 3.3 to 3.6) it was deemed necessary to duplicate a similar result in the laboratory environment. The aim of this was not only to show the presence of the on axis amplitude peak but also to determine which software package performs the best: GRASP9 or MODAL, while the results from ZEMAX are discounted here.

3.3.1 Experimental Measurement Arrangement

We present an outline of the arrangement of this diffraction experiment, while also detailing the near field measurement arrangement as it has been routinely utilised throughout this thesis for experimental validation. The premise of this simple diffraction experiment was to emulate the layout of test case 1A1, where the greatest disagreement between the PO packages and ZEMAX was discovered. The basic layout for Test Case 1A1 consists of a truncating aperture of radius a = 3 mm in a plane reflecting sheet of infinite (or sufficiently large) extent illuminated by a plane wave and the diffracted field sampled at a distance of z_{out} = 2.25 mm from the aperture – c.f. Figure 3-1 (a). Rather than attempt to replicate a plane wave source, either through the use of an off-axis paraboloidal reflector or a lens it was deemed sufficient to utilize a much less contrived arrangement. A conical corrugated feed horn was used to approximate the plane wave field, with the truncating aperture object located at the farfield of the horn, where the waist of the beam is several times the radius of the

truncating aperture and the phase radius of curvature is relatively large. The conical corrugated horn used in this experimental arrangement (and throughout this thesis) is designed to work in the W-band with an operating frequency range of 75 GHz to 110 GHz. A full treatment of this horn is given in Chapter 4, with only the basic parameters of the horn being stated here to fully describe the overall experimental measurement setup. The system dimensions for the test cases described in the previous section are driven by the operating wavelength λ, which for all test cases was 1 mm. The radius of the truncating aperture a_{aper} and output distance z_{out} can be defined in terms of this wavelength, such that $a_{aper} = 3 \times \lambda = 3$ mm and $z_{out} = 2.25 \times \lambda = 2.25$ mm. The operational waveband for the conical corrugated feed horn is 3 mm. It was thus necessary to re-scale the test case dimensions up to suit a higher operational wavelength of 3 mm. The system dimensions therefore are redefined in terms of this new wavelength: $a_{aper} = 3 \times \lambda = 9$ mm and $z_{out} = 2.25 \times \lambda = 6.75$ mm. To best match the diffracting aperture object a hole of radius 9.0 mm was drilled into a square aluminium sheet of half-side length 400 mm, which is approximately three times the beam radius at the aperture; this was deemed sufficient to prevent any excess spillover.

The general layout of the experimental arrangement is illustrated below in Figure 3-37. The spatial dimensions of the optical elements as well as the fundamental Gaussian beam parameters are listed below in Table 3-5.

Parameter	Units	Value
Frequency	GHz	100.0
Horn Aperture: a_H	mm	7.1345
Waist at Horn Aperture: w_{ha}	mm	4.4254
Horn Slant Length: R_h	mm	80.0
Distance to Truncating Aperture: z_{in}	mm	638.0
Truncating Aperture Radius: a_{aper}	mm	9.0
Beam Radius at Truncating Aperture: w_{aper}	mm	137.6
Phase Radius of Curvature at Truncating Aperture: R_{aper}	mm	638.7
Output Distance: z_{out}	mm	6.75

Table 3-6 - Fundamental Gaussian beam parameters for experimental diffraction arrangement

The measurement of the amplitude and phase of this system was achieved through the use of the submillimetre test facility at NUI Maynooth. This test facility is capable of complex 2D beam pattern measurements with high spatial resolution for the frequency

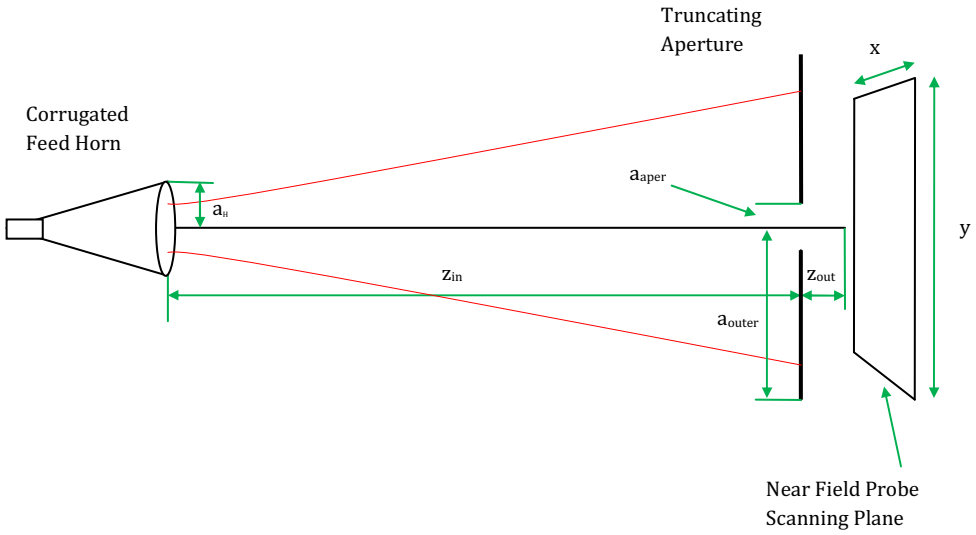

Figure 3-37 - General layout of near field scanning arrangement for diffraction experiment. The horn is linearly polarised along the local *x* axis (c.f. output plane)

range 75 GHz to 110 GHz. Measurements for this system were achieved using a Vector Network Analyser (VNA). A network analyser is a device that is used to characterise the performance of complex electrical systems. A VNA characterises these components by measuring their effect on the amplitude and phase over a defined frequency range for a range of input power signal excitations. The model of VNA used for the Maynooth test facility is the Rohde & Schwarz (R&S) ZVA-24 which has a frequency range of 10MHz to 24 GHz. The frequency range of the VNA is increased to the W-band (75 GHz to 110 GHz) through the use of R&S ZVA-ZV110 Converter units which are designed for WR-10 waveguides and have a wide dynamic range greater than 90 dB. The VNA powers the waveguides that feed the corrugated feed horn and the measurement probe, which is essentially a truncated WR-10 waveguide, through the converter units. It should be also noted that no deconvolution of the waveguide probe was attempted to remove its influence on the output beam.

The waveguide probe is mounted upon a 2-D *XY* precision scanning frame that allows complex beam measurements as either 1-D planar cuts, 2-D raster scans or in a radial pattern. The 2-D XY scanning frame is driven by two precision stepper motors. The maximum achievable stepping precision of these motors is 6.35μm in X and 12.7μm in Y. These precision figures are dependent on the velocity of the scanning frame during measurements. However, these measurements were conducted with ample time delay between steps to ensure best possible precision and to avoid mechanical ringing effects. The corrugated horn is mounted upon a single direction scanning table, which for the purposes of all measurements presented in this thesis is aligned along the global z coordinate. Alignment of the input and output elements as well as any optical elements is currently achieved manually, with distances between elements set by hand.

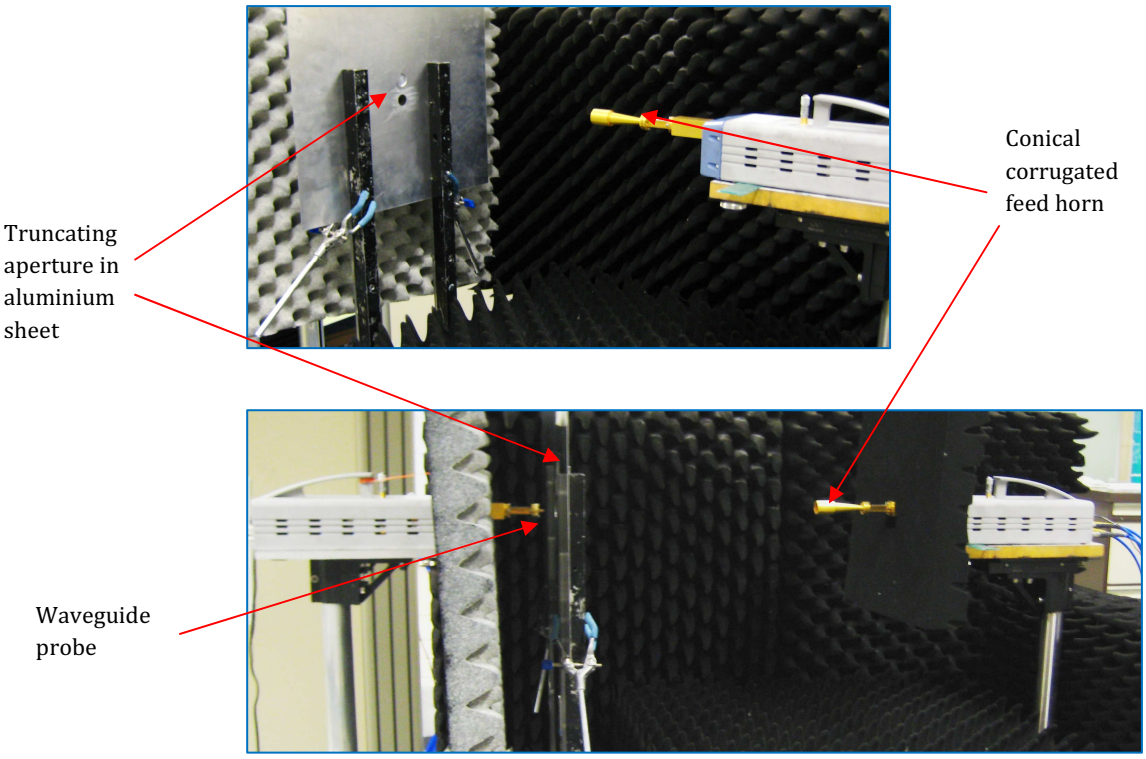

Figure 3-38 - Arrangement of submillimetre near field test facility for diffraction experiment. Corrugated feed horn and waveguide probe are coupled to the VNA through convertor units and entire system is surrounded with ECCOSORB absorber material to reduce stray reflections.

3.3.2 EM Beam Pattern Predictions

This system was modelled in both GRASP9 and MODAL in the typical manner. The source object used in both software packages was the complex aperture field distribution of the corrugated horn, which itself was generated using the mode-matching code called *SCATTER*. The full details of this code are given in Chapter 4 of this thesis. The truncating aperture object was generated in each package in the same manner as in Test Cases 1 described previously in Section 3.2.1.

There are several methods for predicting the diffracted beam behind an aperture in GRASP9. Firstly the user may choose whether to use both PO and PTD calculations or

just PO or PTD. Though it is recommended by TICRA that such a heavily diffracted system would require both PO and PTD calculations, the results using just PO are also included here. The Babinet version of the system (c.f. Section 3.2.1), where the aperture is replaced by an opaque disc with the same dimensions as said aperture, is also implemented in GRASP9 and beam predictions were calculating using both PO and PO & PTD. The results for each of these beam predictions are given below as x and y planar cuts with the central amplitude spot normalized to unity.

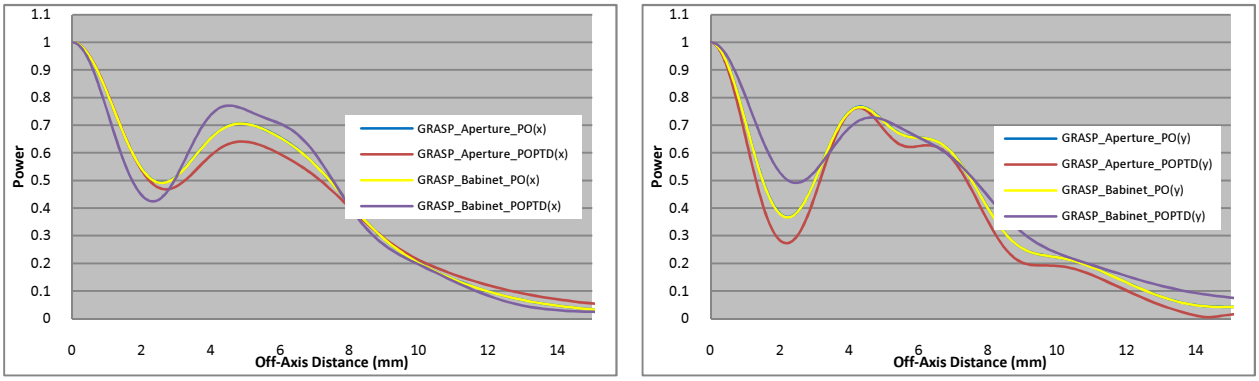

(a) *(b)*

Figure 3-39 – Normalised GRASP9 beam pattern predictions for diffracted beam in x (a) and y (b) - Truncating Aperture w/ PO (Blue), Truncating Aperture w/ PO & PTD (Red), Babinet Disc w/ PO (Yellow) and Babinet Disc w/ PO & PTD (Purple). Note that the horn is polarised linearly in the x axis. Note the usual asymmetry between the x and y planes as exhibited previously by test case 1A1 – c.f. Figure 3-9 and Figure 3-99

Unsurprisingly the different prediction methods yield different beam patterns. Though all agree that there is a central amplitude spot, the predictions for the structure of the secondary maxima differ. What is interesting here is that the PO calculations for both the truncating aperture and the Babinet disc are equivalent, yet the PO & PTD calculations are not. The largest structure deviation is seen for the structure of the secondary maxima in the y-cut where the PO & PTD calculation for the truncating aperture in red shows a degree of Fresnel-type diffraction structure. The PO calculation for the truncating aperture and the Babinet disc show similar diffraction patterns,

though to a lesser extent. The PO & PTD predictions for the Babinet disc display a much smoother pattern.

As mentioned previously in Section 3.2.1 there is a single method for predicting the diffracted beam from a truncating aperture object in MODAL. The MODAL predictions agree closest with the GRASP9 PO calculations for truncating aperture and Babinet disc for both the x and y cuts. The MODAL beam pattern predictions are compared against those from GRASP9 below in Figure 3-40.

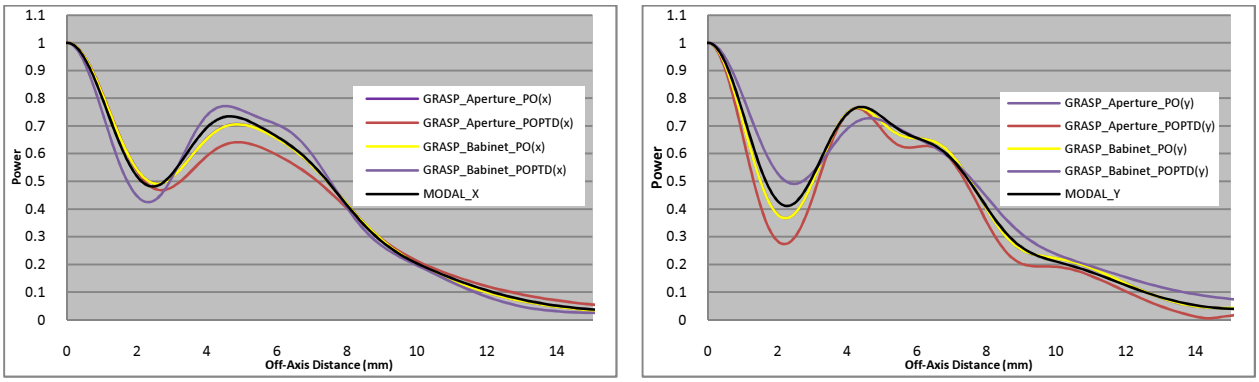

Figure 3-40 - Diffracted patterns with MODAL beam pattern predictions included for comparison (in black)

3.3.3 Experimental Results

The output diffracted beam patterns from the truncating aperture were recorded as 2D complex fields. The contour plots presented below in Figure 3-41 show the amplitude response of the diffracted beam over a 40 mm × 40 mm grid with sampling steps of 0.1 mm. The distance between the output plane and the truncating aperture is a critical factor for this arrangement, with the diffracted beam evolving quickly over short distances. Therefore several measurements were conducted with a complete systematic realignment of the system performed after each measurement run for experimental prudence and to ensure best possible accuracy of system dimensions. Four sample measurements are illustrated below in Figure 3-42. Orthogonal cuts of these beam

measurements were achieved by slicing through the peak on-axis power spot in both x and y directions.

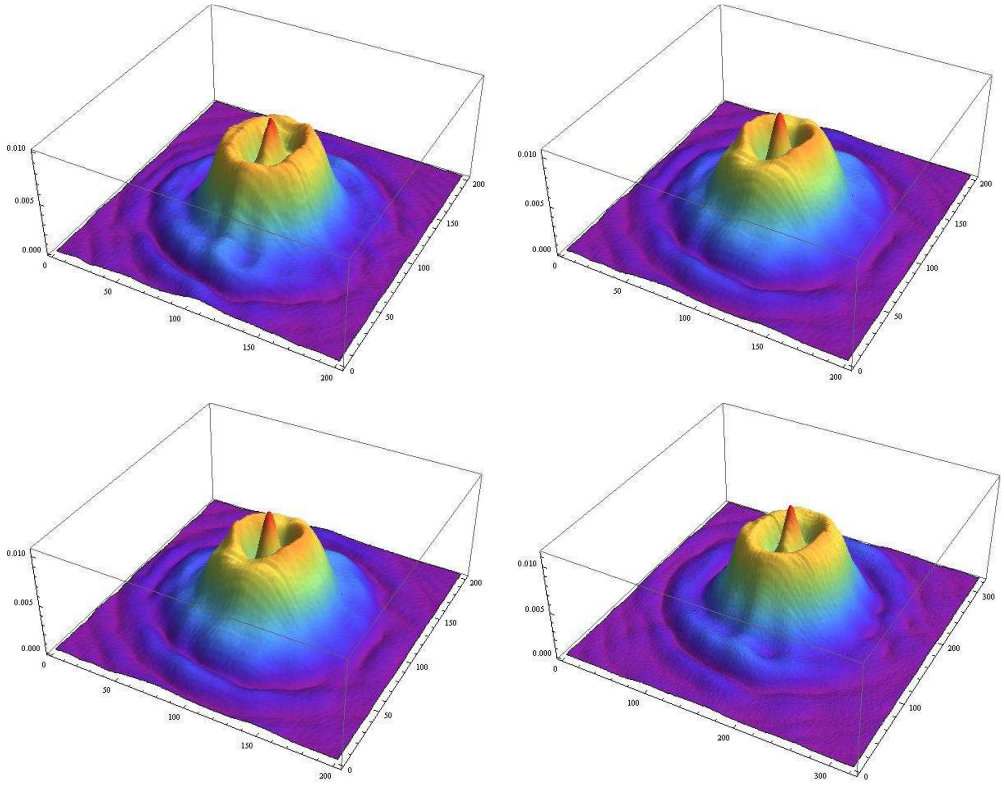

Figure 3-41 – Sample 2D amplitude contour plots of diffracted beam from truncating aperture test

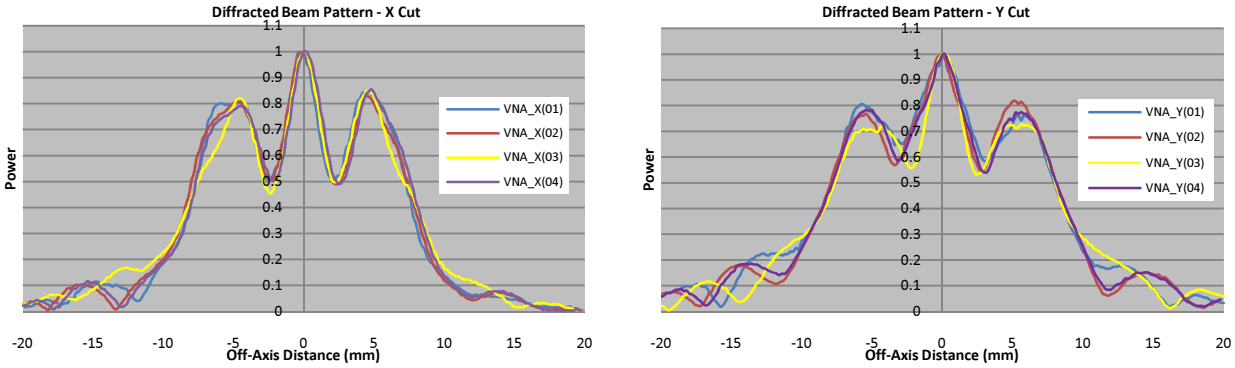

Figure 3-42 - Planar cuts (x on left, y on right) through central spot feature of diffracted beam pattern. Note the structural disparity between the x and y cuts.

The planar cuts above provide a clearer picture of the nature of the diffracted beam pattern. The central Poisson spot feature is well defined in each pattern plot. There is very good agreement between each beam pattern away from the central spot feature in

the x-plane, however agreement in the y-plane is not as strong. This indicates that there is possibly some degree of angular misalignment between the feed horn and waveguide probe in the y-plane. Indeed this is highly likely as a minor angular offset between the horn and probe will lead to a large beam offset at the output plane beyond the confocal distance of the source beam/in the farfield. There is further evidence for misalignment within the individual planar cuts in both the x and y planes. The secondary maxima for each plot have slightly different amplitude power levels. In the x-planar cuts the amplitudes of the secondary maxima on the positive right side of the central spot are higher than those for the right, and exhibit marginally different structure. This slight misalignment is systemic, being consistently true for each cut. There are similar dissimilarities in the secondary maxima amplitude levels evident in the y plane cuts though they are not consistent. This adds further weight to the conclusion that there was some small extent of angular misalignment, primarily in the y-plane. Each of these four VNA measurement plots in Figure 3-42 are overlaid against the various EM predictions from MODAL and GRASP9 (from Figure 3-40) in Figure 3-43 and Figure 3-44 below.

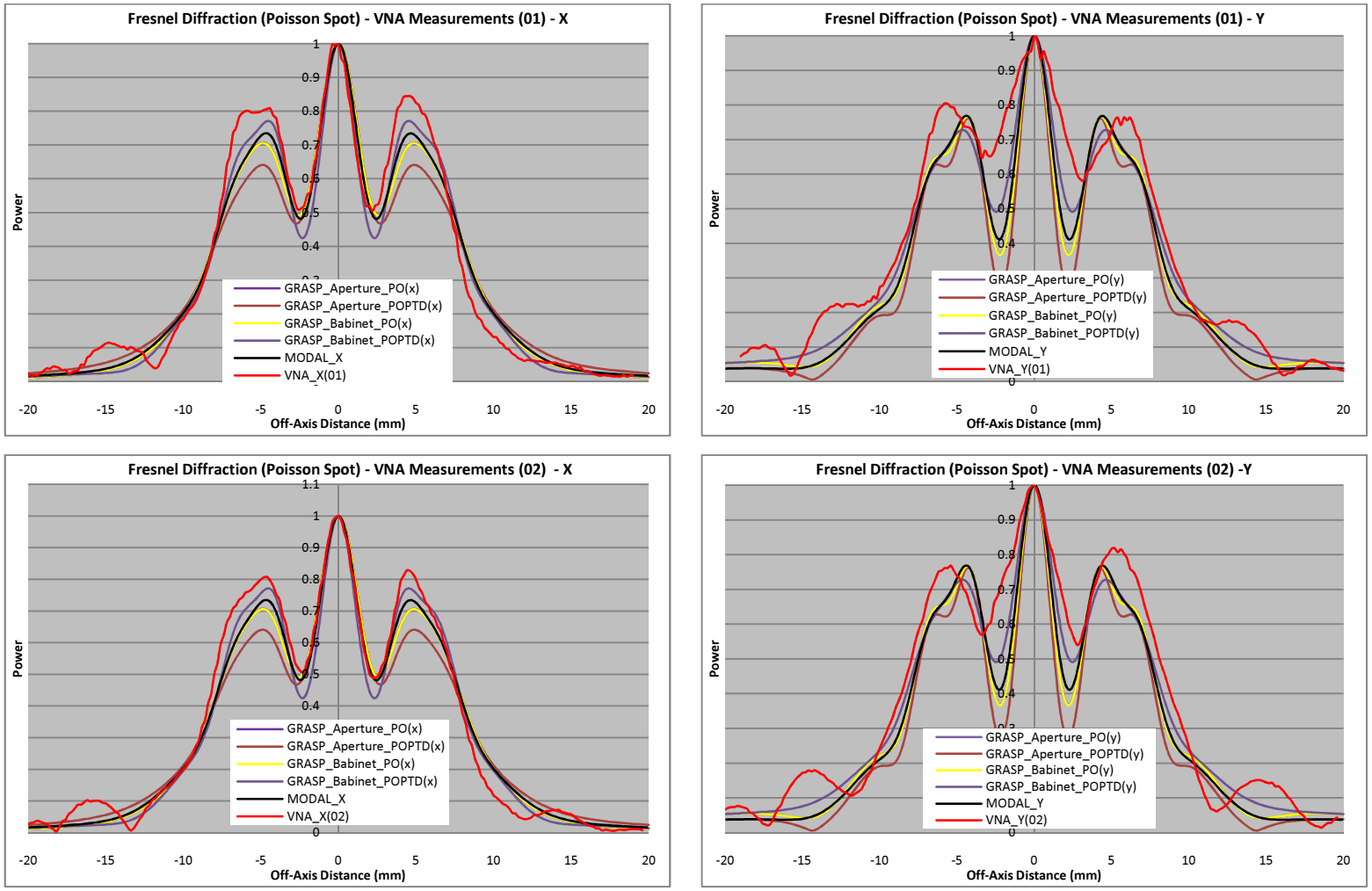

Figure 3-43 - Diffracted beam patterns with from first two measurement scans – VNA 01 and VNA 02 from Figure 3-42 – displayed in red. Experimental measurements are compared against EM predictions from GRASP9 and MODAL from Figure 3-40; x cuts on the left and y cuts on the right.

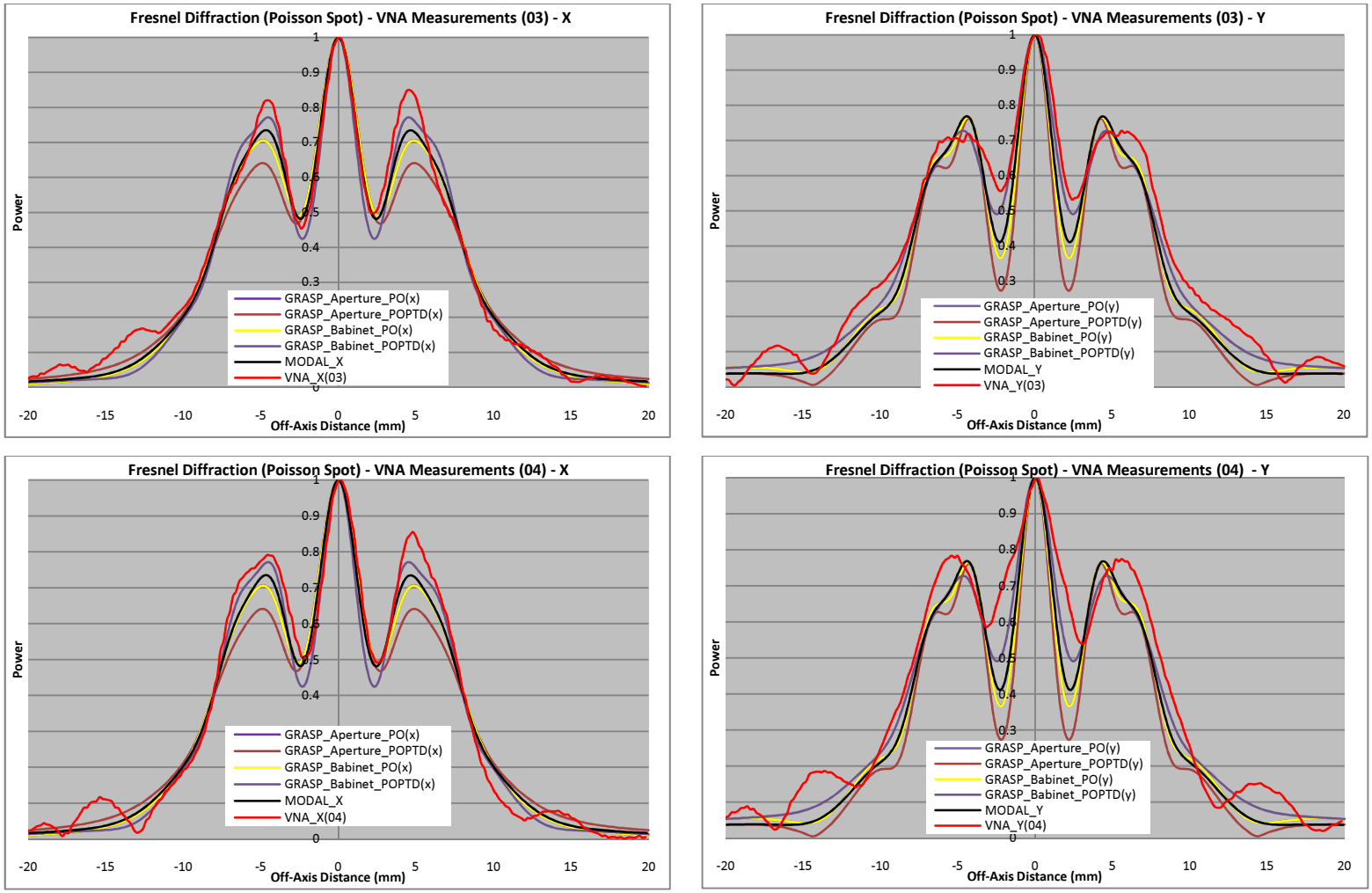

Figure 3-44 - Diffracted beam patterns with from final two measurement scans VNA 01 and VNA 02 from Figure 3-42– displayed in red Experimental measurements are compared against EM predictions from GRASP9 and MODAL from Figure 3-40; x cuts on the left and y cuts on the right.

Comparisons between experimental measurements and beam pattern predictions unfortunately do not provide a clear answer as to which software package provides the more accurate results for this very extreme example. In terms of the structure of the diffracted patterns, the x-plane cuts display the best agreement with the GRASP9 PO & PTD Babinet disc predictions and to a lesser extent the MODAL predictions. The level of agreement between experiment and theory in the y-plane is much more difficult to ascertain. None of the beam pattern predictions show good agreement with the shape of the central amplitude peak. There also exists widely varying structure for the secondary lobe patterns in the y cuts for each of the measured results, thus making any determinations as to which software package provides the more accurate prediction very difficult to infer. The accuracy of the experimental measurements and the high degree of alignment required is also perhaps difficult to realise Given the highly sensitive nature of the output diffraction pattern with respect to the alignment of both the source beam and the truncating aperture measurements of the desired accuracy would require an experimental measurement system with tighter alignment tolerances and fewer sources of error. Also when trying to resolve the subtle structure of the beam patterns predicted by the different approaches a deconvolution of the probe beam should also be included.

3.3.4 Error Analysis

In an attempt to keep track of the effects of optical misalignment of the system components a tolerance test was conducted using MODAL. The degrees of freedom for this tolerancing analysis were chosen on the basis that they represented the major sources of possible misalignment within the physical system configuration. The degrees of freedom chosen for the system alignment are listed below in Table 3-6.

Tolerance Parameter	Unit	Value
Feed Horn $\Delta\theta_{h\text{-}x}$	°	±5
Feed Horn $\Delta\theta_{h\text{-}y}$	°	±5
Probe $\Delta\theta_{p\text{-}x}$	°	±5
Probe $\Delta\theta_{p\text{-}y}$	°	±5
Aperture Plane Δz	mm	±1 mm

Table 3-7 - Selected degrees of freedom for optical mis-alignment of experimental measurement system.

These values represent reasonably assumed errors inherent in the system. The mounting frames for both the feed horn and waveguide probe retained an order of freedom in their tilting angles in the x and y planes. It was therefore deemed prudent in this instance to assign a generous error of ±5° for each frame axis. The variables $\Delta\theta_{h\text{-}x}$ and $\Delta\theta_{h\text{-}y}$ represent angular alignment tolerances of the feed horn mounting frame about the horizontal and vertical axes, and $\Delta\theta_{p\text{-}x}$ and $\Delta\theta_{p\text{-}y}$ represent the equivalent tolerances for the waveguide probe mounting frame. The typical measurement error of ±1 mm was prescribed to the positioning of the aperture plane relative to the plane of measurement. The worst-case scenarios for these alignment errors were modelled in MODAL. Due to the computational intensity of alignment combinations similar calculations in GRASP9 were considered unfeasible for the purposes of this tolerance analysis. The results of this tolerancing analysis are shown below in Figure 3-45 in the typical x and y planar amplitude cuts.

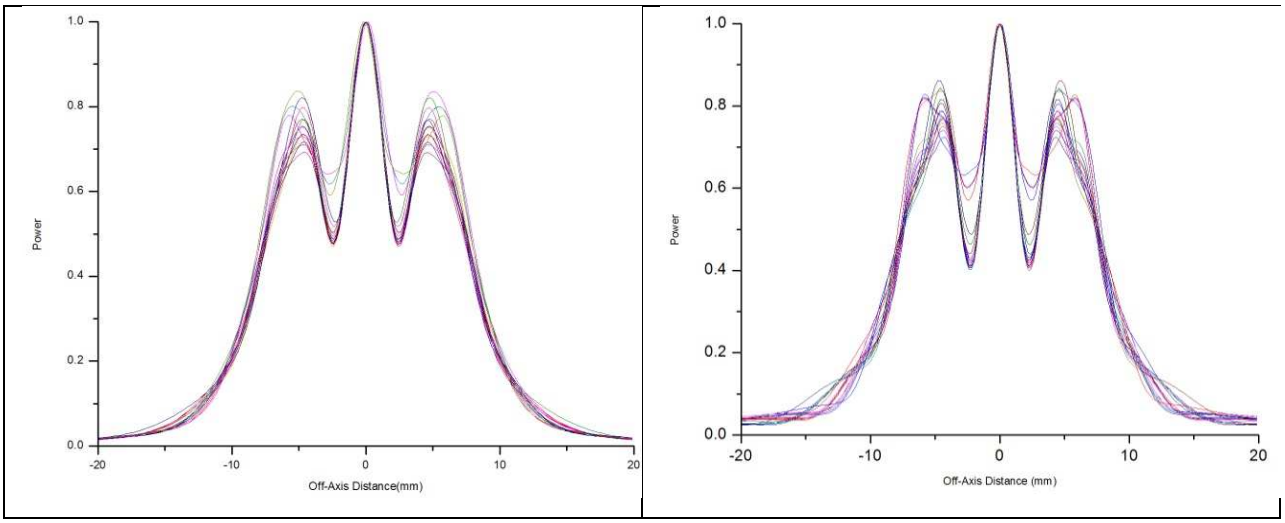

Figure 3-45 - Amplitude cuts (x on the left, y on the right) for MODAL tolerancing analysis of diffraction experiment. The large number of alignment error combinations made the provision of a legend too cumbersome.

The number of alignment error combinations made the provision of a legend for the above tolerancing plots too cumbersome. By overlaying these error combinations above in Figure 3-45 the effects of the modest optical alignment can be seen. The errors are primarily confined to the structure and amplitude levels for the secondary maxima. The greatest structural deformation occurs in the y-plane. The output beams exhibit degrees of symmetry dependent on the angular misalignment of either or both the source and probe structures. To highlight this asymmetry two sample plots taken from Figure 3-45 representing varying degrees of component angular misalignment are illustrated below in Figure 3-46. The planar cuts in Figure 3-46 (a) are in the *x* plane for combinations of angular misalignment of components in the *y* plane and the cuts in Figure 3-46 (b) are in the *y* plane for misalignment in the *x* plane.

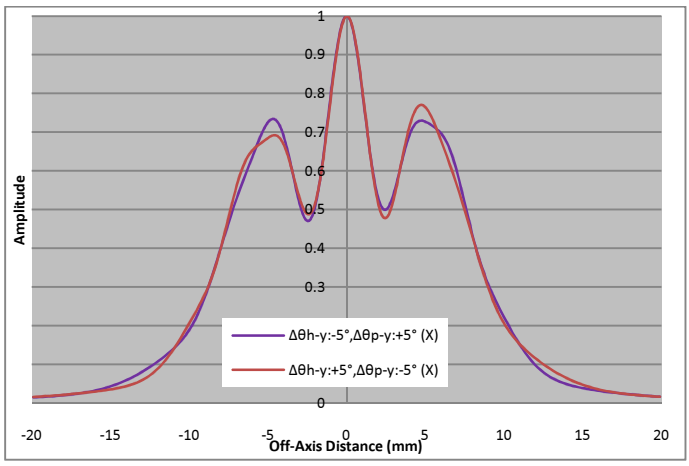

(a)

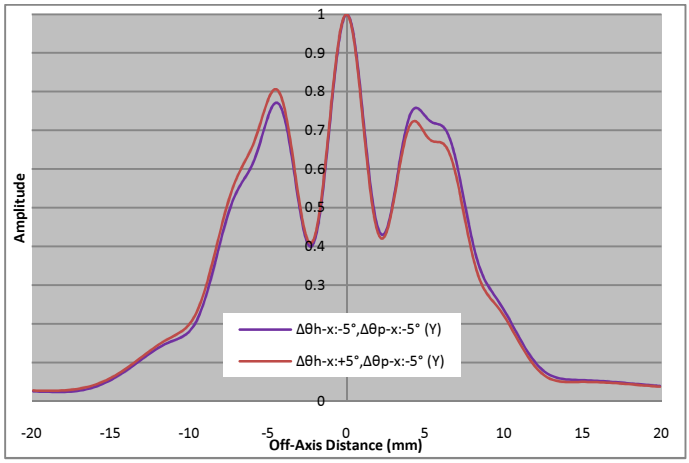

(b)

Figure 3-46 - Sample output plots from tolerancing analysis highlighting beam asymmetry due to combinations of angular misalignment of source and probe structures.

The errors introduced from optical axis misalignment (i.e. ± Δz) only serve to evolve or devolve the diffracted pattern to a minor extent and exhibit no asymmetry in the output beam. The entire extent of these deviations from the ideal system predictions is best accounted for by standard deviation about the mean. The standard deviations are overlaid as error bars with the measurement data below in Figure 3-47.

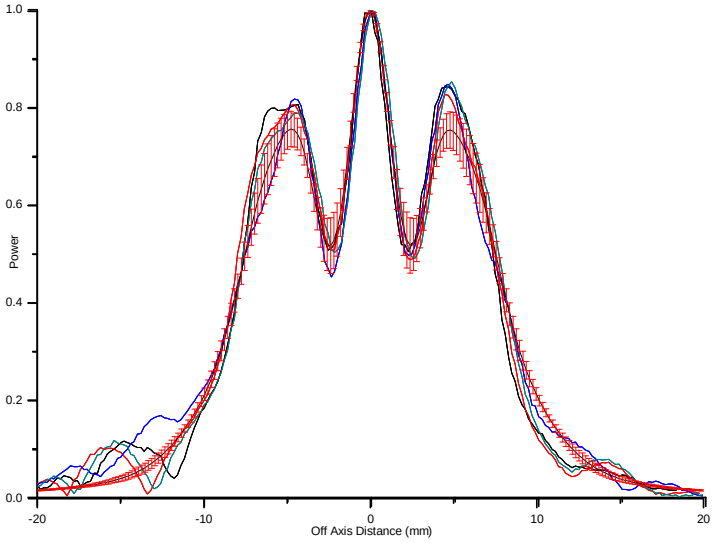

(a)

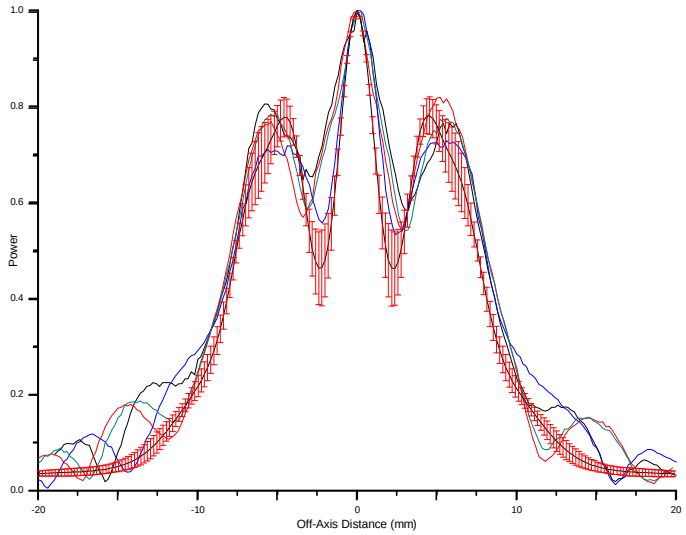

(b)

Figure 3-47 - VNA output amplitude cuts overlaid with standard deviation error bars (in red) determined from tolerancing analysis for *x* on top and *y* on the bottom.

The results above in Figure 3-47 illustrate that the tolerancing analysis accounts for a moderate degree of the disparity between the standard predictions and measurements in Figure 3-43 and Figure 3-44. The measurements still exhibit a large degree of asymmetry, specifically in the *x* plane cuts (c.f. Figure 3-47 (a)), indicating a larger degree of angular mismatch between the probe and feed horn in the *y* plane than was

assumed for tolerancing. The tolerancing predictions also fail to account for the minor lobe structures beginning at approximately $\pm 10\ mm$ off axis distance in both x and y cuts.

3.3.5 Conclusion

Based on the results of this experiment combined with the tolerancing analysis it is difficult to conclude which software package (GRASP9 or MODAL) accurately models the desired diffraction pattern with any reasonable certainty. Given the high spatial sensitivity of the diffraction pattern with respect to minor alterations in the alignment of the system this conclusion is reasonable. The differences between the various predictions from MODAL and GRASP are too minute to be accurately accounted for within a modest measurement system. Further investigation of this matter would require improved spatial alignment tolerance levels for the various optical components. It was not possible to include the effects of the measurement probe in the EM predictions. The field distribution recorded using the probe is a convolution of the amplitude response patterns of the source beam as diffracted by the aperture and the amplitude response pattern of the waveguide probe. Though this effect is generally ignored for standard beam pattern measurements in typical quasioptical systems, the effect for such a highly diffracted system can be considered significant.

4. Standing Waves in Millimetre Wave Optical Systems

This chapter details a series of investigations into the effect of small scale manufacturing errors on the electromagnetic propagation characteristics of a conical corrugated horn. These investigations were borne out of the mismatch between theoretical predictions and experimental measurements of the return loss profile of such a horn, namely the *94 GHz* corrugated feed horn previously described in Chapter3. The return loss profile for a feed horn is a characterisation of the reflected power over the operating frequency range of the horn as it couples to empty space. This analysis was performed using a combination of mode-matching theory developed from [45], [71] and experimental measurements using the near field submillimetre test facility outlined previously in Chapter3. The theoretical predictions of the return loss profile from mode-matching theory are complemented by predictions from FDTD analysis of the feed horn structure by CST-MWS. The horn is first characterised independently with no specific coupling to optical elements. A series of cavity arrangements of two such horns with no intermediate elements are then described, and the standing wave patterns set up between these two horns are studied, with attention paid to the alteration of these patterns with the inclusion of the aforementioned small scale manufacturing errors. Finally, the chapter concludes with a similar characterisation of a baffle-type structure placed in between the two uncoupled horns.

4.1 Standing Waves

Standing waves are formed as the result of a superposition of two or more harmonic waves propagating in the forward and reverse direction along the same axis of propagation. This most commonly occurs when one or the other of the oppositely directed waves experiences a reflection or partial reflection at some point throughout its beam path. In quasioptical systems the issue of standing waves and multiple reflections is a difficult issue to address with models. First order approximations are often used to determine the spatial frequency of standing waves that can occur at a particular

frequency due to a certain reflective elements separated by a distance z ($f = c/z$). Very often when a feed horn is used as an antenna the plane of reflection is taken to be the aperture of the horn. This is not always necessarily true and a more sophisticated model is required to model the propagation within the horn structure. Here a method is presented that can account for the propagation and multiple reflections between the horn waveguide and any optical component placed in front of the feed horn as a Gaussian Beam Mode extension to the modal waveguide description of a horn. For many millimeter/submillimetre systems this then becomes a very powerful technique to understand standing waves or multiple reflections more precisely than standard optical assumptions. In the ALMA optical layouts for Bands 5 & 9 modeled in this thesis a low level standing wave will occur between the feed horn and the secondary mirror as the horn is mapped onto this mirror. The theory expanded on in this chapter can easily be applied to this example and a value for the multiple reflections oscillating about the return loss of the horn itself can be easily predicted [36].

A simple representation of this phenomenon can be described as a system in which a wave E_1 is incident upon an ideal reflecting surface, where it is assumed that no energy is lost on reflection or absorbed at the reflecting surface. The reflected wave E_2 will thus have the same amplitude as the incident wave, but has undergone a π phase shift [33] – c.f. Figure 4-1:

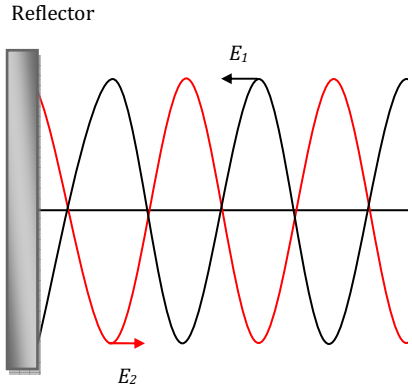

Figure 4-1 – The creation of standing waves by superposition of incident wave E_1 and its reflection E_2

Thus the two waves can be written as

$$E_1 = E_0 \sin\left(wt + kx\right) \tag{4.1}$$

$$E_2 = E_0 \sin\left(wt - kx - \pi\right) \tag{4.2}$$

where E_0 is the amplitude, w is the angular frequency, k is the wavenumber and t and x are the temporal and spatial variables of the waves. Note the π phase change for the reflected wave. The superposition of these two waves gives the resultant wave for the system,

$$E_R = E_1 + E_2 = E_0\left[\sin\left(wt + kx\right) + \sin\left(wt - kx - \pi\right)\right] \tag{4.3}$$

which reduces through standard trigonometric identities to

$$E_R = \left(2E_0 \sin\left(kx\right)\right)\cos\left(wt\right) \tag{4.4}$$

This resultant wave represents a standing wave with amplitude $A(x) = 2E_0 sin(kx)$ and is illustrated below in Figure 4-2. At certain points, namely $x = 0, \lambda/2, \lambda, 3\lambda/2, \ldots$ the disturbance will have zero amplitude for all t. These are known as nodes of the standing wave and are separated by a half-wavelength. These nodes represent a destructive interference of the two superimposed waves. Halfway between each node the amplitude has a maximum value of $\pm E_0$ and these are known as antinodes. These antinodes are formed as a consequence of constructive interference

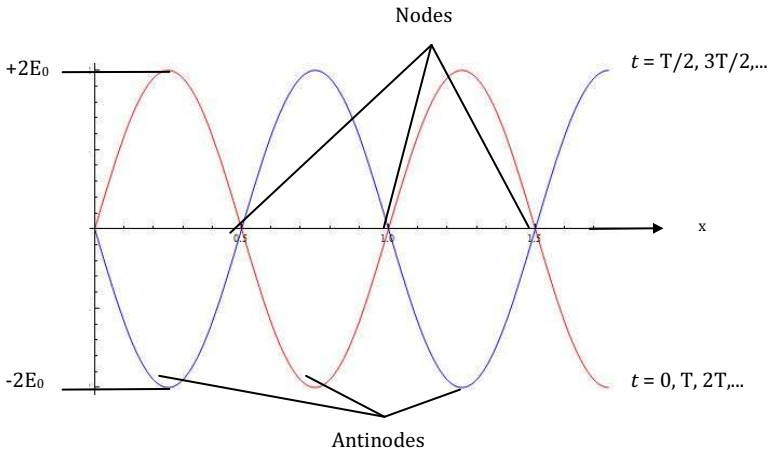

Figure 4-2 – Standing wave pattern for wave of amplitude E_0 showing positions of nodes and antinodes

The resultant wave will have zero amplitude for all values of x whenever $Cos(wt) = 0$. This occurs when

$$wt = 2\pi ft = \left(\frac{2\pi}{T}\right)t = m\pi \qquad (4.5)$$

where f is the frequency and T is the period of the wave. Thus the wave will be zero when $t = T/4, 3T/4,\ldots$. Conversely the wave will have a maximum amplitude for all values of x when $t = 0, T/2, T, 3T/2,\ldots$.

Considering the more general case for the reflection of the incident wave from a reflecting surface the phase shift can be considered arbitrary, thus affecting the location of nodes and antinodes as well as the maximum displacement. However the overall standing wave profile will remain unaffected [33].In Figure 4-3 below the standing wave patterns for various phase shifts representing various degrees of interference are plotted. With decreasing phase shift Φ the positions of nodes and antinodes follows a sinusoidal path, and the amplitude of the antinodes decreases accordingly.

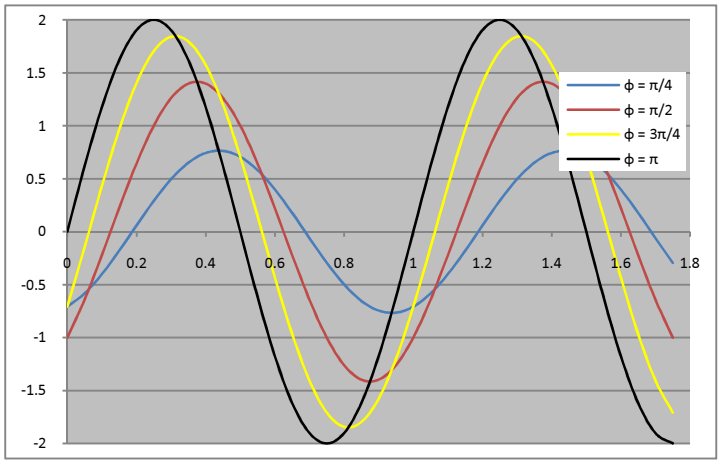

Figure 4-3 – Standing wave patterns for various phase differences between superposed waves

In practical quasioptical systems the simple profile of a standing wave from a single reflecting plane is sometimes obscured due to multiple reflection planes or a standing wave occurring over a finite bandwidth.

The amplitude variation of a standing wave may be characterised from transmission line theory by its *Voltage Standing Wave Ratio* (VSWR), which gives the ratio of the maximum and minimum voltages [72]. We define the VSWR as

$$VSWR = \frac{E_{\max}}{E_{\min}} = \frac{E_i + E_r}{E_i - E_r} \tag{4.6}$$

Where E_i and E_r are the amplitudes of the incident and reflected waves. Defining the reflection coefficient ρ as the ratio E_i/E_r Equation 4.6 is re-written as:

$$VSWR = \frac{1+\rho}{1-\rho} \tag{4.7}$$

The return loss of this standing wave is given by [73] as:

$$Rs\left(dB\right) = 20\log_{10}\left(\frac{VSWR-1}{VSWR+1}\right) \tag{4.8}$$

If the reflection coefficient of a dielectric is given as $\rho = 0.6$ the $VSWR = 4$ from Equation 4.7 giving a return loss of *-4.43 dB* from Equation 4.8.

4.2 Theory of Scattering Matrices for Gaussian Beam Modes

The theory of scattering matrices was originally developed from transmission line theory as a method of characterising a multi port electrical network in terms of the relations between the complex amplitudes for the inward and outward waves at each port. This theory was extended to quasioptical systems in [45] and [71] by representing a wave guide or beam guide structure as a sequence of individual components. Each of these components has its own characteristic scattering matrix which determines the redistribution of power among the modes (modeling the field) that can be used to describe the input field. The field propagating within a freespace beam guide structure can be described by either the higher order Associated Laguerre modes or Hermite-Gaussian modes, depending on the symmetry of the system in free space. The fields propagating within a waveguide structure are typically represented by combinations of *TE* and *TM* modes, whose order depends on the dimensions of the waveguide structure [56]. In this section the theory of scattering matrices is outlined for an arbitrary

(freespace or waveguide) system. This is followed with examples illustrating the application of the theory to the generation of standing waves within a Fabry Perot interferometer arrangement. The technique is also extended to the theory of interference in thin films and multilayer coatings. These classical optical examples of interference or applications of multiple reflections serve as nice examples to demonstrate the scattering modal application and also serve as verification tools to ensure the code is working correctly and can be applied to examples where the answer is known or can be calculated with an independent technique..

The diagram below (Figure 4-4) shows such a scattering matrix represented as a box with the various transmitted and reflected modal coefficients represented as coloured arrows. The column vectors *[A]* and *[B]* are the modal coefficients of the transmitted and reflected fields on the input side of the scattering structure, with the structure working in transmission from left to right.

Figure 4-4 - Scattering matrix representation of a 2 port system

Similarly the *[C]* and *[D]* column vectors are the modal coefficients for the transmitted and reflected fields on the output or right hand side of the structure. The overall reflected and transmitted modal coefficients output from the structure, *[B]* and *[D]* (represented by the red arrows) are determined by scattering the input modal coefficients, *[A]* and *[C]* (represented by the green arrows) using the scattering matrix *[S]*.

$$\begin{bmatrix}[B]\\[D]\end{bmatrix}=[S]\begin{bmatrix}[A]\\[C]\end{bmatrix} \tag{4.9}$$

where the scattering matrix S is comprised of four sub-matrices:

$$\begin{bmatrix}[B]\\[D]\end{bmatrix}=\begin{bmatrix}[S_{11}] & [S_{12}]\\[S_{21}] & [S_{22}]\end{bmatrix}\begin{bmatrix}[A]\\[C]\end{bmatrix} \tag{4.10}$$

$$\begin{bmatrix}[B]\\[D]\end{bmatrix}=\begin{bmatrix}[S_{11}][A] & [S_{12}][C]\\[S_{21}][A] & [S_{22}][C]\end{bmatrix} \tag{4.11}$$

The sub-matrices of *[S]* with the input coefficients *[A]* and *[C]* combine to give the output reflected and transmitted coefficients, thus coupling all incident power with all output power. The scattering matrix representation from Figure 4-4 can be amended to illustrate how the individual sub-matrices couple the modal coefficients [74] – c.f. Figure 4-5.

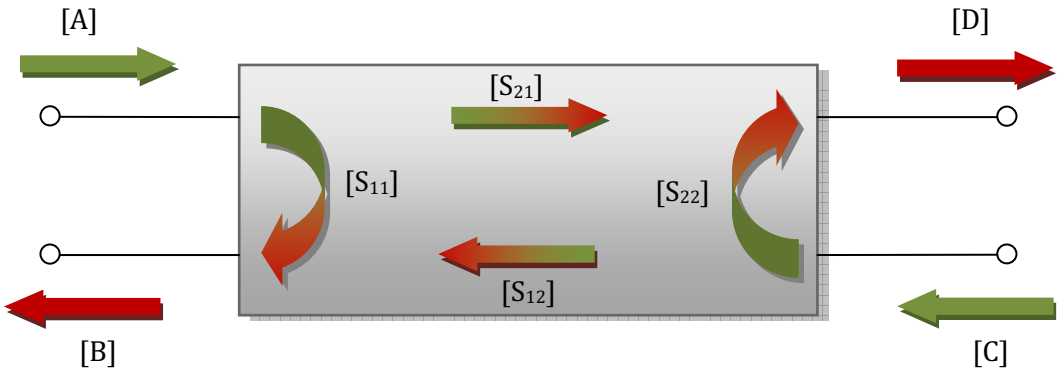

Figure 4-5 - Scattering matrix of a 2-port system showing the pattern of coefficient coupling by the constituent sub-matrices

From this diagram it is easy to relate each of the sub matrices to their respective power couplings: the *[S11]* sub matrix matches the incident modal coefficients from the input (left) side that are reflected back out of the system and the *[S12]* couples incident modal coefficients from the output (right) right side that are transmitted through the system to the input (left) side, hence generating the output modal coefficients *[B]* on the left hand side. The output modal coefficients on the right hand side *[D]* are generated by the *[S21]*

sub matrix that matches the incident modal coefficients from the input (left) side to the output (right) side.

Traditionally such systems operate in forward (or reverse) mode, thus negating the incident power from the right (or left) side. One typical example of such a system is the feed horn fed by a waveguide where there are no other active power sources from the aperture side of the horn. Taking this system to be operating in forward mode, the *[C]* modal coefficients are set to zero, and the reflected and transmitted mode coefficients are given by:

$$\begin{bmatrix}[B]\\[D]\end{bmatrix}=\begin{bmatrix}[S_{11}][A]\\[S_{21}][A]\end{bmatrix} \tag{4.12}$$

Extending the example of a horn fed by a single moded waveguide, total input power is contained within the first mode. A multi moded description of this single moded field consists of a single unity entry and all other mode coefficients set to zero:

$$A=\begin{bmatrix}1\\0\\0\\\vdots\end{bmatrix} \tag{4.13}$$

Another multi-moded description for the aperture distribution of a scalar horn is that of a truncated Bessel function, as calculated by [75] and demonstrated previously in Section 2.3.1. The modal coefficients for such a field description are given approximately as:

$$A=\begin{bmatrix}0.990329\\-0.0003\\-1.2049\\\vdots\end{bmatrix} \tag{4.14}$$

where the modal coefficients are calculated in the usual manner from Equation 2.1 where the source field *E* is taken as the first order Bessel function and the mode-set is of the usual Laguerre-Gaussian form – c.f. Equation 2.17. Alternatively a simple Gaussian

with a beam waist equal to *0.*6435 times the aperture radius will provide a *98%* coupling to the aperture field from a corrugated horn, as seen in Section 2.3.1. The appropriate modal coefficient calculation gives *A* to be:

$$A = \begin{bmatrix} 0.995998 \\ 0.038735 \\ -0.05481 \\ \vdots \end{bmatrix} \tag{4.15}$$

These are freespace modal approximations to the aperture field distribution from a feed horn and can thus be used as the input freespace mode description for a freespace quasioptical system fed by a horn. However this method will not provide the true S-parameter description of the system (internal reflections within the horn) as it evidently does not incorporate the waveguide scattering processes within the physical waveguide structure of the feed horn. We will return to this concept later with analysis of a typical light baffle structure using a horn aperture truncated Bessel field approximation and a complete modal description of an equivalent corrugated horn field fed into a light baffle structure

A complete scattering structure is comprised of individual scattering elements, each with their own scattering matrix. A complete scattering matrix description of the final structure is obtained by 'cascading' the individual scattering matrices together in sequence. The cascade matrix approach combines two individual scattering matrices, $[S_s]$ and $[S_b]$ into an overall scattering matrix $[S_c]$

$$\left[S^a\right] = \begin{bmatrix} \left[S_{11}^a\right] & \left[S_{12}^a\right] \\ \left[S_{21}^a\right] & \left[S_{22}^a\right] \end{bmatrix} \tag{4.16}$$

$$\left[S^b\right] = \begin{bmatrix} \left[S_{11}^b\right] & \left[S_{12}^b\right] \\ \left[S_{21}^b\right] & \left[S_{22}^b\right] \end{bmatrix} \tag{4.17}$$

The overall cascade matrix is calculated using the following relations:

$$
\begin{aligned}
\left[S_{11}^{c}\right] &= \left[S_{12}^{a}\right]\left[[I]-\left[S_{11}^{b}\right]\left[S_{22}^{a}\right]\right]^{-1}\left[S_{11}^{b}\right]\left[S_{21}^{a}\right]+\left[S_{11}^{a}\right] \\
\left[S_{12}^{c}\right] &= \left[S_{12}^{a}\right]\left[[I]-\left[S_{11}^{b}\right]\left[S_{22}^{a}\right]\right]^{-1}\left[S_{12}^{b}\right] \\
\left[S_{21}^{c}\right] &= \left[S_{21}^{b}\right]\left[[I]-\left[S_{22}^{a}\right]\left[S_{11}^{b}\right]\right]^{-1}\left[S_{21}^{a}\right] \\
\left[S_{22}^{c}\right] &= \left[S_{21}^{b}\right]\left[[I]-\left[S_{22}^{a}\right]\left[S_{11}^{b}\right]\right]^{-1}\left[S_{22}^{a}\right]\left[S_{12}^{b}\right]+\left[S_{22}^{b}\right]
\end{aligned}
\tag{4.18}
$$

Where *[I]* is the identity matrix and $[\ ]^{-1}$ signifies the inverse of a matrix. The cascading matrix method as applied to two component scattering matrix is a repetitive process: the cascaded matrix of two individual scattering matrices is then itself cascaded to the next component scattering matrix until the entire system is described by a single scattering matrix – c.f. Figure 4-6

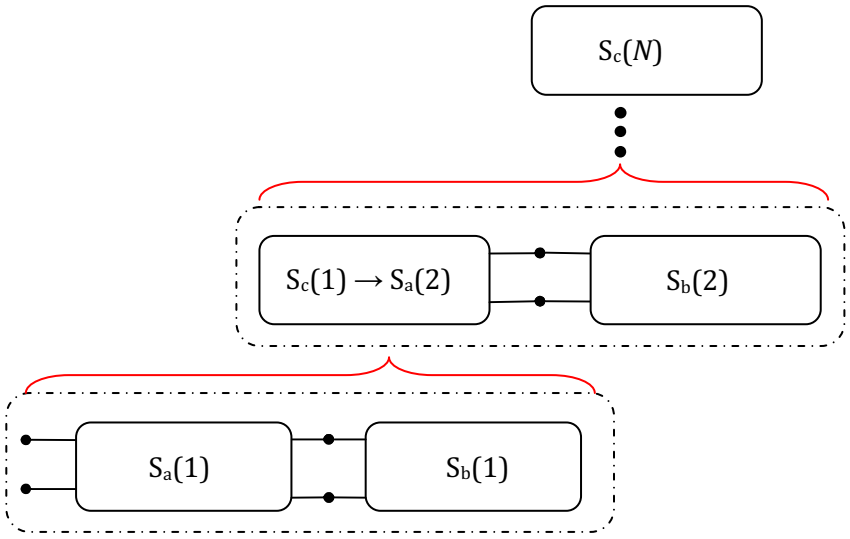

Figure 4-6 - Functional representation of the iterative cascading process for *N* scattering matrices where S_c for *(1)* becomes the S_a for *(2)* and so on.

This complete scattering matrix allows for monitoring of all power flow within the cavity, be it transmitted to the output or reflected to the input or if any particular modes are sustained within the cavity. Such sustained modes are called 'eigenmodes' and are a common feature within the theory of guided electromagnetic waves. Indeed, the operation of lasers requires such stable eigenmodes to propagate within a resonant cavity so as to generate sufficient power output [4]. The scattering matrix technique is

applied to the study of such eigenmodes as they exist within THz systems in a later section. The following subsections describe the scattering matrices for a number of typical quasi-optical components such as partially reflecting sheets, freespace propagation and a truncating aperture/annular ring structure and finally a composition light baffle structure sometimes used to reduce the influence of stray light in an optical system.

4.2.1 Scattering Matrix for reflecting or partially transmitting sheet

This subsection deals with scattering matrix description for an infinitesimally thin partially reflecting/transmitting sheet. This can be viewed as an approximation to a typical thin dielectric window element in a quasioptical system. It is assumed here that the beam is incident from left to right with a positive phase radius of curvature. Upon incidence with the sheet the reflected beam will propagate in the opposite direction to the incident beam. This beam will be seen to be emanating from a virtual waist position behind the sheet; a mirror image of the waist position of the original incident beam. The beam radius will not change upon reflection and the phase radius of curvature will continue to evolve as before, but with a negative value, indicating its direction of propagation. The transmitted beam will appear to continue propagating past the sheet, though with reduced amplitude that is determined by the transmittance of the sheet; the same can be said for the amplitude of the reflected beam which is dependent on the sheet's reflectance.

Taking the incident beam to be described in the typical manner from Equation 2.1 as a sum of forward propagating modes: $E_i = \Sigma A_n \psi^+_n$, where A_m are the mode coefficients and ψ^+_n is the forward propagating mode set, as signified by the + term. The reflected field can be written in similar terms with a reverse propagating mode set ψ^-_n and the corresponding set of mode coefficients B_n : $E_r = \Sigma B_n \psi^-_n$.

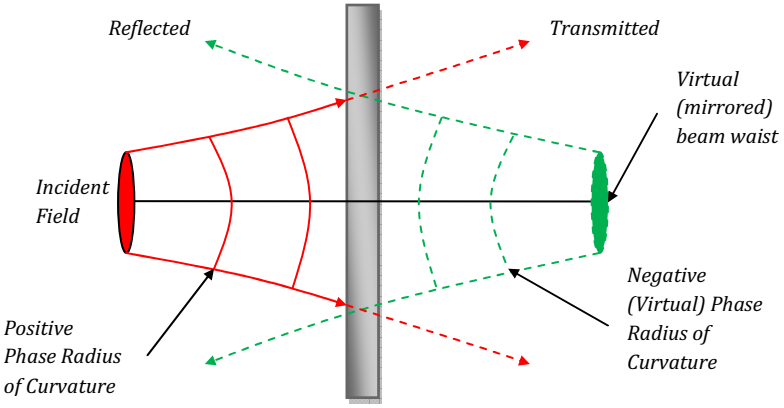

Figure 4-7 - Scattering process of a thin partially reflecting/transmitting sheet showing how the source waist of the reflected beam is a virtual mirrored equivalent to that of the incident beam

The new reflected field mode coefficients B_n are determined from the incident field mode coefficients A_n through the scattering process at the sheet:

$$B_n = \sum_m S_{mn} A_m \tag{4.19}$$

where S_{mn} is the scattering matrix that distributes power between the adjacent modes and appropriately alters the phase radius of curvature.

The phase terms of the forward propagating modes have the form $\exp\left(-j(kz + r^2/2R) + j\Delta\phi_{mn}(z)\right)$, while for the reverse propagating modes the form is $\exp\left(+j(kz + r^2/2R) - j\Delta\phi_{mn}(z)\right)$ where $\Delta\phi_{mn}$is the associated phase slippage. However, the evolution of the $\pm j(kz - \Delta\phi_{mn})$ phase terms are actually carried by the modal coefficients [76]. Therefore, the scattering matrix only accounts for the transformation of the phase radius of curvature and takes the form

$$S_{mn} = \int \left(\psi_n^-\right)^* \psi_m^+ \exp\left(+j\frac{kr^2}{R}\right) dA \tag{4.20}$$

where the complex exponential term accounts for the reversal and continued divergence of the phase radius of curvature R upon reflection by the sheet. The integral takes place over the area of the reflector, which if larger than the beam can usually be assumed to be infinite with no beam truncation

The reflectance R and the transmittance T determine the reflected and transmitted irradiance of the partially reflecting sheet and are determined using the reflection and transmission coefficients r and t respectively.

$$R = |r|^2$$
$$T = |t|^2 \tag{4.21}$$

where the reflection and transmission coefficients are themselves dependent on the refractive index of the dielectric material of the sheet. For the time being the sheet is being treated as a mathematically convenient infinitesimally thin sheet and the relation between the reflectance/transmittance and dielectric refractive index will be discussed in a later section. The system is taken to be lossless, meaning that any power that is not reflected will be transmitted, with no power absorption by the sheet, such that

$$R + T = 1 \tag{4.22}$$

These reflection and transmission coefficients are incorporated into the scattering matrix description of the partially reflecting sheet:

$$\begin{vmatrix} S_{11} & S_{12} \\ S_{21} & S_{22} \end{vmatrix} = \begin{vmatrix} S_{mn}r & S_{mn}t \\ S_{mn}t & S_{mn}r \end{vmatrix} \tag{4.23}$$

In the situation where a beam waist with infinite phase radius of curvature exists at the plane of the sheet then the scattering matrix term S_{mn} is replaced by the identity matrix I. This is because in the scattering integral above (Equation 4.20) the infinite phase curvature R will null the exponential phase term and the Hermitian inner product of the mode sets will reduce to the identity matrix.

4.2.2 Scattering Matrix for Propagation

The propagation scattering matrix describes the simple axial phase evolution of the modes as they propagate through a distance z. If an incident field is described in the typical manner i.e. $E_i = \Sigma A_n \psi_n$, then the field after propagation can be defined as $E_i = \Sigma V_n A_n \psi_n$, where the evolution term V_n is given by

$$V_n = \exp\left[-jkz + j(2n+1)\Delta\phi_n\right] \tag{4.24}$$

where the kz term represents the usual plane wave phase delay and the $\Delta\phi_n$ term represents the relative axial phase slippage of the n^{th} mode as determined using the ABCD matrix method. The propagation term is recognisable from the Gaussian beam mode solution to the paraxial wave equation from Equation 2.15. This scattering matrix is applied to fields as described using the both Laguerre-Gaussian mode set and the Associated Laguerre-Gaussian mode set (Equation 2.35). The scattering matrix has the form of an $N*N$ diagonal matrix, where the diagonal entries are given by Equation 4.24 above and is of the form

$$S_{prop} = \begin{vmatrix} 0 & V \\ V & 0 \end{vmatrix} \tag{4.25}$$

The diagonal matrix form of this scattering matrix ensures that there is no scattering between modes along the propagation path and there is no reflection of the beam.

4.2.3 Scattering matrix for dielectric

This section details the complete scattering matrix formulation for a beam impinging upon a dielectric slab of finite thickness. This process is twofold, where the scattering matrices for reflection and transmission at the dielectric boundary and the scattering matrix for propagation within the dielectric slab itself are required. These scattering matrices are developed from the similar matrices described previously in Sections 4.2.1 and 4.2.2.

When dealing with the propagation of beams within media of different refractive indices it is convenient to introduce the concept of the *reduced complex beam parameter*, which is similar to the reduced radius of curvature $\hat{R}$ used in geometrical optics, and is defined according to [4] as

$$\hat{R} = \frac{R}{n} \tag{4.26}$$

where n is the local refractive index of the material and R is the radius of curvature in freespace. A more formal description of this reduced radius of curvature is given in

terms of the refractive indices for the incident and transmitted regions n_i and n_t – c.f. Figure 4-8:

$$\hat{R}_t = R_i \frac{n_i}{n_t} \tag{4.27}$$

The complex beam parameter, given by Equation 2.10 is now re-written to incorporate the reduced radius of curvature using the following relation:

$$\frac{1}{\hat{q}} = \frac{1}{\hat{R}} - j\frac{\lambda_i}{\pi W(z)^2} \tag{4.28}$$

where $R(z)$ is the freespace radius of curvature, $W(z)$ is the beam radius and λ_i and λ_t are the wavelengths in the incident and transmitted regions respectively. From Equation 4.28 above it is evident that only the radius of curvature $R(z)$ or the complex part of the beam parameter q is affected by the dielectric interface, whereas the beam radius $w(z)$ remains unaffected. The evolution of the Gaussian beam parameters within the dielectric can then be tracked using this reduced complex beam parameter $\hat{q}$ through use of the ABCD matrix technique from Section 2.1.5.1. The evolution of the Gaussian beam parameters is illustrated below in Figure 4-8, where a beam propagates across two dielectric boundaries, as it would in passing through a dielectric slab.

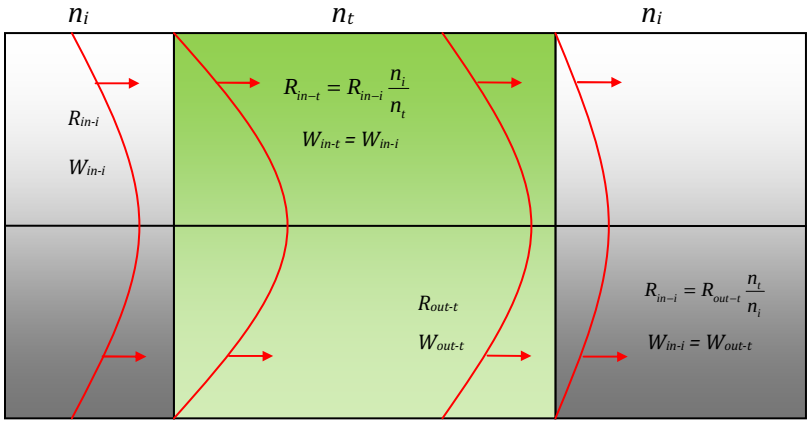

Figure 4-8 - The evolution of the phase radius of curvature and waist as a beam propagates through media of different refractive indices

The scattering matrix for a beam incident upon the dielectric interface has a similar definition to that for the partially reflecting/transmitting sheet i.e. Equation 4.20. For a beam travelling in a medium of refractive index n_i incident upon a plane of dielectric material of refractive index n_t the reflection and transmission coefficients $\rho_{i\to t}$ and $\tau_{i\to t}$ respectively are given by the Fresnel equations from [77]:

$$\rho_{i\to t} = \frac{n_i - n_t}{n_i + n_t} \tag{4.29}$$

$$\tau_{i\to t} = \frac{2n_i}{n_i + n_t} \tag{4.30}$$

Considering the beam travelling in the reverse direction across this same boundary, or indeed the equivalent situation of the beam crossing the second dielectric boundary in Figure 4-8 above, the reflection and transmission coefficients are re-written as

$$\rho_{t\to i} = \frac{n_t - n_i}{n_t + n_i} \tag{4.31}$$

$$\tau_{t\to i} = \frac{2n_t}{n_t + n_i} \tag{4.32}$$

The reflected and transmitted fields at the first dielectric interface E_{refl} and E_{tran} are then related to the incident field E_{inc} by the Fresnel equations by

$$E_{refl} = \rho_{i\to t} E_{inc} \tag{4.33}$$

$$E_{tran} = \tau_{i\to t} E_{inc} \tag{4.34}$$

In a similar manner to the reflected field from the partially reflecting/transmitting sheet the reflected field from this dielectric interface is written in terms of the reverse propagating modes where the phase radius of curvature is reversed : $E_{refl} = \Sigma_n B_n \psi_n^-$. The scattering matrix to describe the reflected field has a similar format to that of Equation 4.23. To accurately account for the complete scattering across a dielectric boundary the reflection and transmission and coefficients for both the forward and reverse directions must be taken into account. The complete scattering matrix for the first dielectric boundary in Figure 4-8 above is given as

$$\begin{vmatrix} S_{11} & S_{12} \\ S_{21} & S_{22} \end{vmatrix} = \begin{vmatrix} S_{i\to t}\rho_{i\to t} & S_{t\to i}\tau_{t\to i} \\ S_{i\to t}\tau_{i\to t} & S_{t\to i}\rho_{t\to i} \end{vmatrix} \tag{4.35}$$

where the matrix elements $S_{i\to t}$ and $S_{t\to i}$ represent the scattering going from n_i to n_t and n_t to n_i respectively:

$$S_{i\to t} = \int \left(\psi_{i-n}^{-}\right)^{*} \psi_{i-n}^{+} \exp\left(+j\frac{k_i r^2}{R_{in-i}}\right) dA \tag{4.36}$$

$$S_{t\to i} = \int \left(\psi_{t-n}^{-}\right)^{*} \psi_{t-n}^{+} \exp\left(-j\frac{k_t r^2}{R_{in-t}}\right) dA \tag{4.37}$$

where k_i and k_t are the wavenumbers for the incident and transmitted regions and $\psi_{i\text{-}n}^{\pm}$ and $\psi_{t\text{-}n}^{\pm}$ are the mode sets describing the beam in the incident and transmitted regions. As the beam radius is unaffected by transmission across the dielectric interface the mode sets $\psi_{i\text{-}n}^{\pm}$ and $\psi_{t\text{-}n}^{\pm}$ are mathematically equivalent. The only difference between these two scattering matrices is accounting for the reduced phase radius of curvature inside the dielectric, hence requiring the two scattering matrices above rather than a single matrix for the case of the partially transmitting/reflection sheet from Section 4.2.1.

Propagation within the dielectric slab is determined in the same manner as for the freespace propagation from Section 4.2.2. The output complex beam parameter $\hat{q}_{out}$ after propagation within the dielectric slab is determined from the evolution of the input reduced complex beam parameter $\hat{q}_{in}$ in the same manner as Equation 2.44:

$$\hat{q}_{out} = \frac{A\hat{q}_{in} + B}{C\hat{q}_{in} + D} \tag{4.38}$$

The evolved beam parameters are thus determined from this new complex beam parameter using ABCD matrices.

4.2.4 Scattering Matrix for Truncating Aperture

From [78] the scattering matrix for a truncating aperture is defined by the overlap integral between the input field at the aperture plane and the output field after truncation. If we consider a circularly symmetric truncating aperture we first describe the incident and output fields in terms of the circularly symmetric Laguerre-Gaussian mode set :

$$\begin{aligned} E_{inc} &= \sum_n A_n \psi_n(r), \\ E_{out} &= \sum_m B_m \psi_m(r), \end{aligned} \tag{4.39}$$

where A_n and B_m are the incident and transmitted field mode coefficients and $\psi_{n,m}$ are the Laguerre-Gaussian basis mode set (Equation 2.39). If the aperture has a radius a the following boundary condition applies to the relation between the incident and output fields:

$$\begin{aligned} E_{out}(r) &= E_{inc}(r) \qquad r \le a, \\ E_{out} &= 0 \qquad\qquad\quad r > a \end{aligned} \tag{4.40}$$

where r represents the off-axis distance measured from the centre of the aperture. This equation essentially states that only the incident field confined within the aperture will be transmitted while the remainder is lost. The transmitted mode coefficients are given by the overlap integral

$$B_m = \int_0^a \psi_m(r) E_{out}(r) 2\pi r dr \tag{4.41}$$

where the output field over the integral limits of the aperture is equivalent to the incident field over the same limits so we now write

$$\begin{aligned} B_m &= \int_0^a \psi_m(r) E_{inc}(r) 2\pi r dr \\ &= \sum_n A_n \int_0^a \psi_m^*(r) \psi_n(r) 2\pi r dr \end{aligned} \tag{4.42}$$

where the scattering matrix S_{mn} is now defined as

$$S = \int_0^a \psi_m^*(r)\psi_n(r)2\pi r dr \tag{4.43}$$

thereby giving

$$B_m = \sum_n S_{mn} A_n \tag{4.44}$$

This scattering matrix will redistribute the power from the incident modes to the transmitted modes. The form of the scattering matrices is consistent with the format required by Equation 4.23

$$\begin{vmatrix} S_{11} & S_{12} \\ S_{21} & S_{22} \end{vmatrix} = \begin{vmatrix} I - S_{mn} & S_{mn} \\ S_{mn} & I - S_{mn} \end{vmatrix} \tag{4.45}$$

where I is the identity matrix. The form of this scattering matrix ensures that the transmitted components (S_{12} and S_{21}) are described by the scatting matrix equation 4.43 and the reflected components (S_{11} and S_{22}) are defined as that field which is not transmitted. This scattering matrix for truncation will be utilised further on this chapter to model a stray light baffle structure composed of several annular rings that approximate truncating apertures.

4.2.5 Multilayer Dielectric Films

The theory of cascaded scattering matrices can be used to model the interference properties of multilayer dielectric films. By combining thin films of alternating dielectric constants it is possible to produce destructive interference conditions between the beams reflected from the front and back faces of each film. Depending on the order of the films in a stack according to their dielectric constant the reflectance of the stack can be reduced or enhanced. These layered films have many practical uses; a high reflectance film may be used as a beam splitter, or a multilayer may also be employed as an optical filter which transmits or reflects a selected region of the spectrum. Two illustrations of such multilayer dielectric films are given below in Figure 4-9.

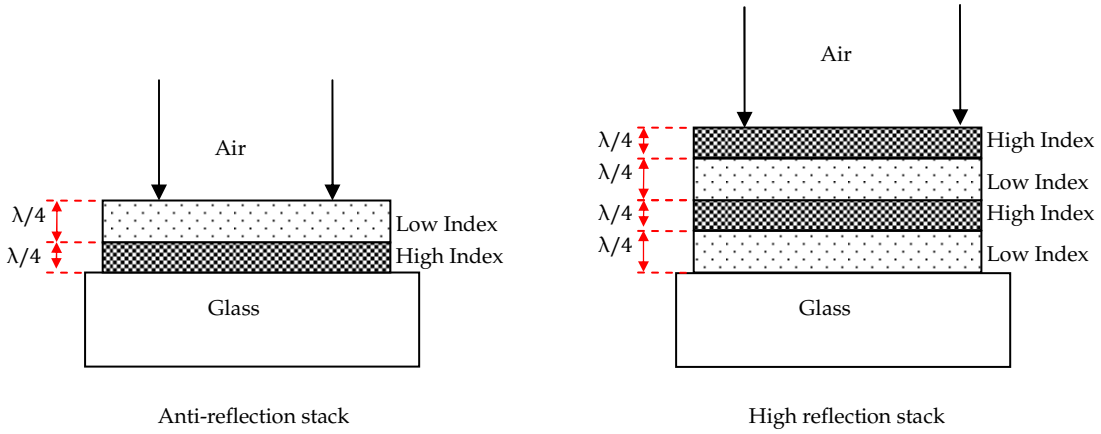

Figure 4-9 - Examples of an anti-reflection stack and high reflection stack

The traditional approach to characterising the reflectance and transmittance profiles for multilayer dielectric is achieved using the *transfer matrix* method as described in [33], which assumes plane wave propagation and not GBMs. This analytical method is discussed in the following subsection. A variety of multilayer films with unique optical properties are discussed and the characteristic reflectance/transmittance profiles for each are calculated using the aforementioned transfer matrix method. The technique of cascaded matrices is applied to each of these films and the results are compared against those of the transfer matrix technique.

4.2.5.1 The Transfer Matrix Technique

A complete discussion and derivation of the transfer matrix technique may be found in [33] with the basic principles being outlined here. The transfer matrix is derived through the process of solving the boundary value problem for a thin dielectric film placed in between an incident region (freespace) and a substrate (glass).

The diagram below (Figure 4-10) shows a thin dielectric film of thickness l of refractive index n_1. It is surrounded on the left by an incident region with refractive index n_0 and on the right by a transmitted substrate region of refractive index n_s. Incident light that transmits into the film will multiply reflect between the two dielectric interfaces. The

reflectance and transmittance is solved using the boundary value approach. Maxwell's equations are solved in each of the three regions in the figure below and these solutions are matched at the boundaries using boundary conditions.

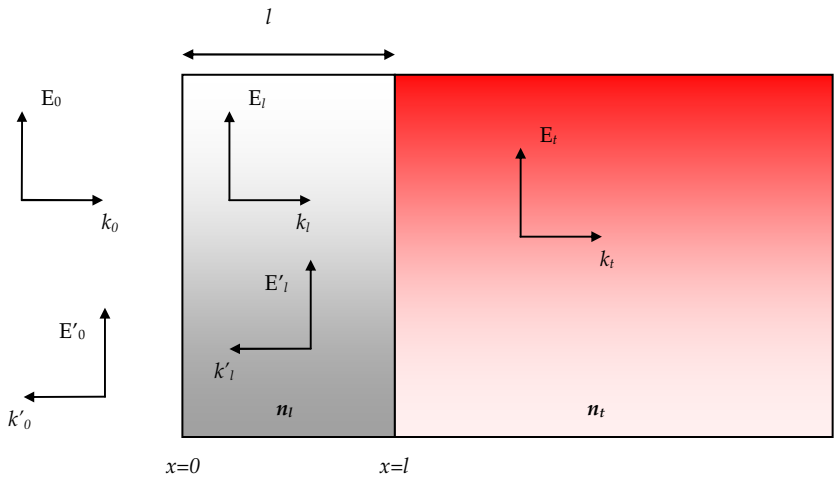

Figure 4-10 - A dielectric film of thickness l and refractive index n_l deposited on a substrate of refractive index n_t [37].

The above figure illustrates the transverse electromagnetic wave solutions in each of the three regions. The incident region contains a forward-travelling wave with field amplitude E_0 and a wave vector k_0 that represents the incident illumination. This region also contains a backward propagating solution with E'_0 and k'_0 that represents the net reflected radiation. Both solutions must be used as they are linearly independent; a forward travelling wave cannot be represented as a linear combination of backward travelling waves and vice-versa. The film region also contains a forward-travelling solution with E_l and k_l and a backward travelling solution with E'_l and k'_l that account for all multiple reflections within this region. Finally the transmitted region only contains a forward travelling wave with E_0 and k_0, since it assumed that a semi-infinite transmitted region that cannot physically produce a backward component.

Assuming normal incidence, the first boundary condition states that the tangential components of the electric field must be continuous at $x = 0$:

$$E_0 + E'_0 = E_l + E'_l \tag{4.46}$$

The tangential components of the magnetic field B must also be continuous at $x = 0$. Note that for the backward travelling wave that if E'_0 points up (as above) then $\boldsymbol{B}$ must point out of the page. Taking 'out of the page' to be positive gives

$$B_0 - B'_0 = B_l - B'_l \tag{4.47}$$

The transverse electromagnetic components E and B are related by (ref)

$$B = \frac{n}{c} E \tag{4.48}$$

which by Equation 4.46 gives

$$n_0 \left(E_0 - E'_0 \right) = n_l \left(E_l + E'_l \right) \tag{4.49}$$

At the second interface where $x = l$ the effects of propagation must be included. It is important to note here that this will be a *steady-state solution*, in that the transmitted and reflected beams are recorded as an average over many cycles, and hence the temporal component of the electromagnetic wave solution is ignored. Accordingly the forward travelling wave is represented as e^{+ikx} and the backward travelling wave is represented as e^{-ikx}. Applying this to the above stated boundary condition at $x = l$ gives

$$E_l e^{ikl} + E'_l e^{-ikl} = E_t \tag{4.50}$$

where the e^{ikl} term is included in the E_t term by allowing it to become complex, since in the transmitted region there is no need to distinguish between forward and backward travelling solutions. Similarly the boundary condition at $x = l$ for magnetic fields gives

$$n_l \left(E_l e^{ikl} - E'_l e^{-ikl} \right) = n_t E_t \tag{4.51}$$

The goal here is to solve Equations 4.46 – 4.51 for the reflected and transmitted beams E'_0 and E_t when the incident illumination E_0 is known. Firstly the fields internal to the layer are eliminated: E_l and E'_l. From Equations 4.50 and 4.51 we get

$$E_l = \frac{1}{2}\left(1+\frac{n_t}{n_l}\right)E_t e^{-ikl} \tag{4.52}$$

$$E'_l = \frac{1}{2}\left(1-\frac{n_t}{n_l}\right)E_t e^{ikl} \tag{4.53}$$

from which we get

$$E_l + E'_l = \left(\cos(kl) - i\frac{n_t}{n_l}\sin(kl)\right)E_t \tag{4.54}$$

$$E_l - E'_l = \left(-i\sin(kl) + \frac{n_t}{n_l}\cos(kl)\right)E_t \tag{4.55}$$

Applying Equations 1.1 and 1.2 we get

$$1+\frac{E_0}{E'_0} = \left(\cos(kl) - i\frac{n_t}{n_l}\sin(kl)\right)\frac{E_t}{E_0} \tag{4.56}$$

$$n_0 - n_0\frac{E'_0}{E_0} = \left(-in_l\sin(kl) + n_t\cos(kl)\right)\frac{E_t}{E_0} \tag{4.57}$$

The notation is simplified by letting $r = {E'_0}/{E_0}$ and $t = {E_t}/{E_0}$ and writing Equations 4.56 and 4.57 in matrix form as

$$\begin{pmatrix}1\\ n_0\end{pmatrix} + \begin{pmatrix}1\\ -n_0\end{pmatrix} r = \begin{pmatrix}\cos(kl) & -\frac{i}{n_l}\sin(kl)\\ -in_l\sin(kl) & \cos(kl)\end{pmatrix}\begin{pmatrix}1\\ n_t\end{pmatrix} t = M\begin{pmatrix}1\\ n_t\end{pmatrix} t \tag{4.58}$$

where M is called the transfer matrix:

$$M = \begin{pmatrix}\cos(kl) & -\frac{i}{n_l}\sin(kl)\\ -in_l\sin(kl) & \cos(kl)\end{pmatrix} \tag{4.59}$$

If another dielectric film layer is introduced into the stack between the first dielectric and the substrate Equation 4.58 is still valid. Generalising for a multilayer of an arbitrary number N layers,

$$\begin{pmatrix}1\\ n_0\end{pmatrix}+\begin{pmatrix}1\\ -n_0\end{pmatrix}r = M_1M_2...M_N\begin{pmatrix}1\\ n_t\end{pmatrix}t \tag{4.60}$$

The overall transfer matrix M_T represents the entire multilayer stack and is the product of the individual transfer matrices in the order in which the incident radiation encounters them: $M_T = M_1M_2M_3\ldots M_N$. Letting the result of N layers result in a final transfer matrix:

$$\begin{pmatrix}1\\ n_0\end{pmatrix}+\begin{pmatrix}1\\ -n_0\end{pmatrix}r = \begin{pmatrix}m_{11} & m_{12}\\ m_{21} & m_{22}\end{pmatrix}\begin{pmatrix}1\\ n_t\end{pmatrix}t \tag{4.61}$$

gives the following set of equations:

$$1+r = \left(m_{11}+n_tm_{12}\right)t \tag{4.62}$$

$$n_0-n_0r = \left(m_{21}+n_tm_{22}\right)t \tag{4.63}$$

These can be solved for r and t to give

$$r = \frac{n_0m_{11}+n_0n_tm_{12}-m_{12}-n_tm_{22}}{n_0m_{11}+n_0n_tm_{12}+m_{12}+n_tm_{22}} \tag{4.64}$$

$$t = \frac{2n_0}{n_0m_{11}+n_0n_tm_{12}+m_{12}+n_tm_{22}} \tag{4.65}$$

The reflectance and transmittance over a boundary are given by $R = |r|^2$ and $T = {n_1}/{n_0}\,|t|^2$ [33].

4.2.5.2 The Cascade Matrix Technique

The transmission and reflection profiles for multilayer films can also be calculated using the cascade matrix technique described above in Section 4.2. These examples illustrate the flexibility of the approach not only to quasioptical systems but also to classical optics examples. The scattering matrix description for radiation incident upon a single dielectric film is a cascade of a dielectric interface scattering matrix, a propagation scattering matrix and another dielectric interface scattering matrix. The dielectric scattering matrix, as described above in Section 4.2.3 determines the degree of reflection

and transmission at the dielectric interface while the propagation matrix will track the evolution of the beam properties through the substrate. Cascaded together, these matrices will keep track of the phase changes upon reflection and transmission between layers. The cascade matrix for more than one layer simply requires the inclusion of the extra required scattering matrices. The incident beam for all examples described below was defined as a Laguerre-Gaussian beam with a waist of size $w_0 = 2.0\ mm$ and flat phase radius of curvature. This ensured a minimum degree of power scattering between modes across the various dielectric boundaries.

4.2.5.3 Example - Antireflection Coating

The concept behind antireflection coatings is to produce the necessary destructive interference condition between the beams reflected from the front and back faces of the film. This is achieved by having the reflections at interfaces characterised by an incident medium that is optically less dense and manipulating the thickness of the proceeding film(s) to produce a $180°$ phase shift in the reflected beams after propagation. This is achieved by setting the thickness of the film to be a quarter wavelength thick for the local medium, such that

$$l = \frac{\lambda}{4} = \frac{\lambda_0}{4n} \tag{4.66}$$

where λ is the wavelength within the film, λ_0 is the free space wavelength and n is the refractive index of the dielectric film. The phase difference over a single propagation distance l is then

$$kl = \left(\frac{2\pi}{\lambda}\right)\frac{\lambda}{4} = \frac{\pi}{2} \tag{4.67}$$

which for a round trip propagation becomes a phase difference of π or $180°$. Such a dielectric film is usually referred to as a *'quarter-wave film'*. The diagram below (Figure 4-11) illustrates the phase changes on reflection and transmission for a typical quarter-wave film.

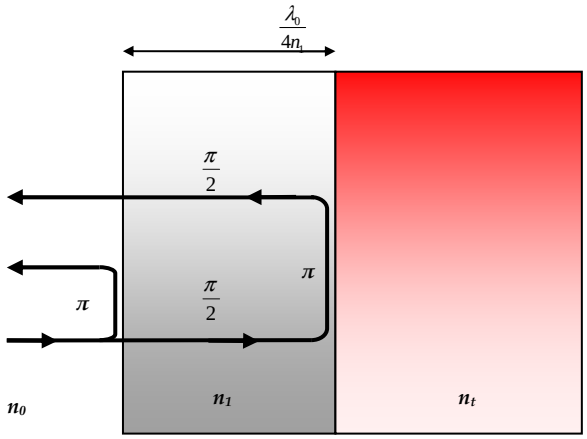

Figure 4-11 - Phase changes upon reflection and transmission in the quarter wave film used at normal incidence

The reflection coefficient for a single dielectric layer of quarter wavelength optical thickness becomes

$$r = \frac{\left(n_t - n_l^2\right)}{\left(n_t + n_l^2\right)} \tag{4.68}$$

At the design wavelength, reflectance $R = 0$ when $n_l = \sqrt{n_t}$. For glass with index n_t = 1.52 the ideal index would be 1.23. Magnesium fluoride (MgF_2) with index n_l = 1.38 is commonly used due to its durability. Note that the index increases across each interface, giving a π phase shift for each reflected component; thus the half-wavelength round-trip travel for the wave that reflects from the substrate combines with the front-surface reflection in destructive interference, giving complete cancellation if $n_l = \sqrt{n_t}$. The film reflectance increases for wavelengths other than the design wavelength [37]. A further reduction in reflectance can be achieved by using more than one layer. A *quarter- quarter* coating consists of two quarter-wave layers of alternating low and high index, where the low index coating is the outer layer. The reflection coefficient for such a quarter-quarter layer is given by [37] as

$$r = \frac{\left(n_l^2 - n_t n_h^2\right)}{\left(n_l^2 + n_t n_h^2\right)} \tag{4.69}$$

where n_l and n_h are the low and high refractive indices respectively.

The transfer matrix and the cascade matrix techniques are applied to several examples of antireflection films. In the scattering matrix formulation for all examples described here, the Laguerre-Gaussian mode set was used. The first example is of an antireflection coating consisting of a single quarter wavelength layer deposited on glass, the layout of which is illustrated in Figure 4-11. The coating reflectance profile is determined for the ideal refractive index of $n_l = 1.23$ and for MgF_2 with $n_l = 1.38$. The thickness of the layers is determined from the design wavelength (c.f. Equation 4.66), which in this case is $550nm$. The thicknesses are $11.27nm$ for the ideal coating and 0.996 mm for the MgF_2 coating.

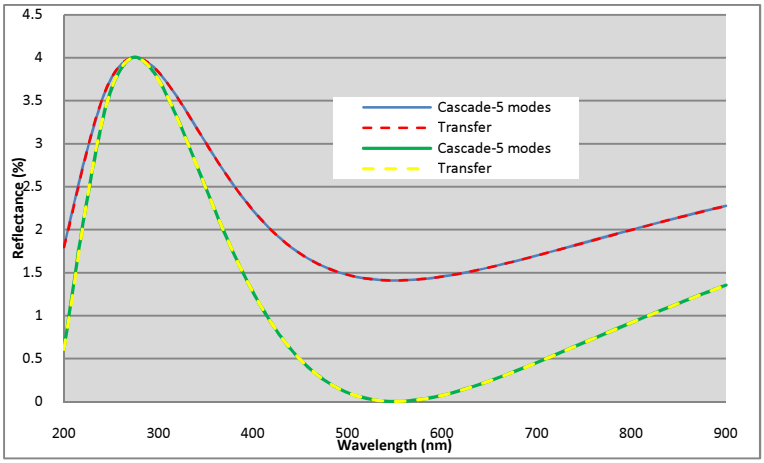

Figure 4-12 - Reflectance profile for single 'quarter layer' anti-reflection coating upon glass substrate. Cascade matrix results shown in blue for ($n_l = 1.38$) and green for ($n_l = 1.22$). Classical transfer matrix results are in dashed red ($n_l = 1.38$) and dashed yellow for ($n_l = 1.22$).

The comparison of the reflectance profiles calculated using the cascade and transfer matrix techniques (Figure 4-12) show perfect overlap, with a null of reflectance predicted at the design wavelength of 550nm. Since the incident Gaussian beam is at a waist at the first dielectric interface the scattering between adjacent modes is practically negligible. The cascaded scattering matrices thus required only 5 modes to fully account for the power scattered between modes.

4.2.5.4 Example - Two Layer Antireflection Coating

The anti-reflection properties of the dielectric coating described above in Section 4.2.5.3 can be further enhanced with the inclusion of another dielectric coating. An example of such a two layer antireflection coating, taken from [33] is described here.

For a glass substrate with radiation incident from air, a two layer coating consisting of a low refractive index dielectric n_1 followed by a high refractive index dielectric n_2 forms an anti-reflection coating. In this instance, the low refractive index dielectric is cerium triflouride, CeF_3 (n_1 = 1.65) and the high refractive index dielectric is zirconium dioxide, ZrO_2 (n_2 = 2.1). The thicknesses of the two coatings are again determined from the design wavelength, as was the case for the single layer coating, from Equation 4.66. For a design wavelength of 550nm the thickness of the CeF_3 layer is l_1 = 0.833nm and of the ZrO_2 layer is l_2 = 0.6547nm. The arrangement of this anti-reflection coating is illustrated in Figure 4-13 below.

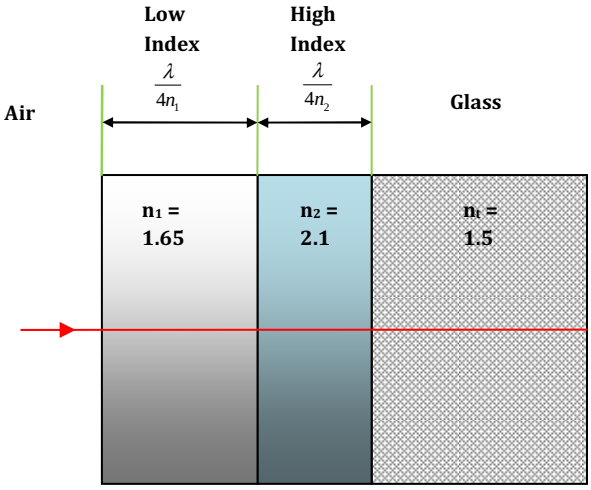

Figure 4-13 – Two layer anti-reflection coating consisting of two quarter wavelength thick dielectrics upon a glass substrate.

The reflectance profile for this coating arrangement is determined using the transfer and cascade matrix techniques as before, with the results plotted below in Figure 4-14 below, where the transfer matrix results are plotted in red and the cascade results in blue.

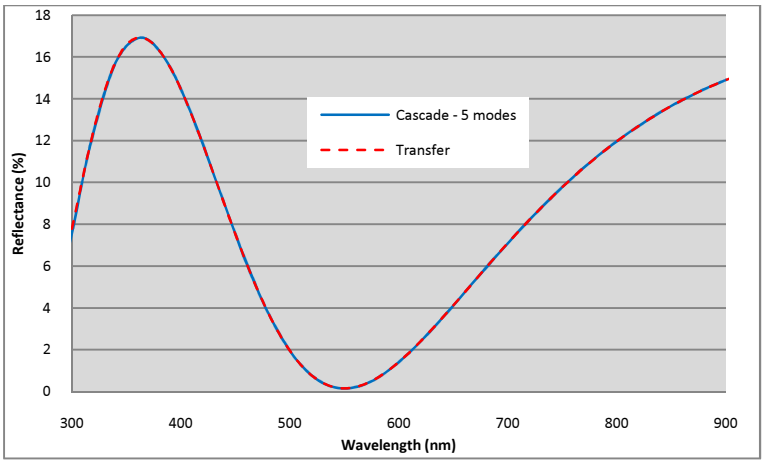

Figure 4-14 – Reflectance profile for two-layer anti-reflection coating.

Once again, the results show excellent agreement between the transfer and cascade matrix techniques.

4.2.5.5 Example - High Reflectance Coating

If the order of the low and high index two layer film from Section 4.2.5.4 that was optimised for antireflection is reversed, so that the order becomes air -> high index -> low index -> substrate, then all reflected beams are in phase upon emerging from the structure and the reflectance is enhanced rather than reduced. A series of such double layers will increase the reflectance further, and the structure is known as a high reflectance stack or dielectric mirror. The analytical expression for the maximum reflectance from such a high reflectance stack is given as [33]:

$$R_{\max} = \left[\frac{(n_0/n_s)(n_L/n_H)^{2N} - 1}{(n_0/n_s)(n_L/n_H)^{2N} + 1} \right]^2 \tag{4.70}$$

where n_H and n_L are the refractive indices of the high and low index dielectrics respectively, and N is the number of double layers. Equation 4.70 predicts *100%* reflectance whether N approaches infinity or when n_H/n_L approaches zero. From [33] a high reflectance stack is fabricated from alternating layers of MgF_2 ($n_L = 1.38$) and ZnS ($n_H = 2.35$). The reflectance profiles for high-low index stacks of increasing order N are

calculated using the analytical and scattering matrix approaches and the results are plotted below in Figure 4-15 below.

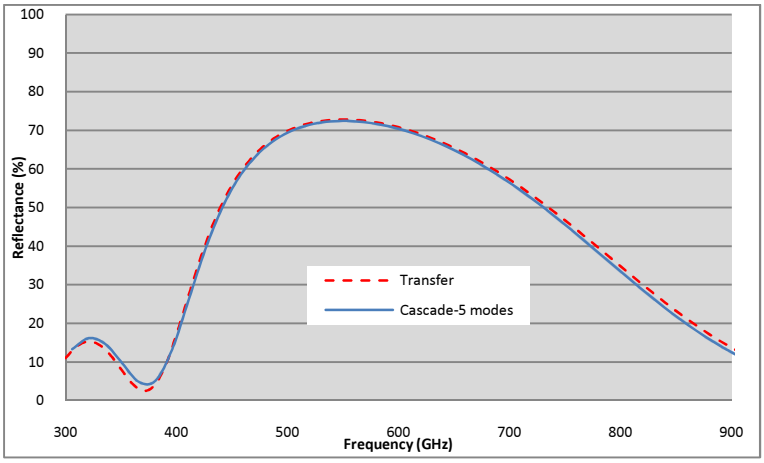

(a)

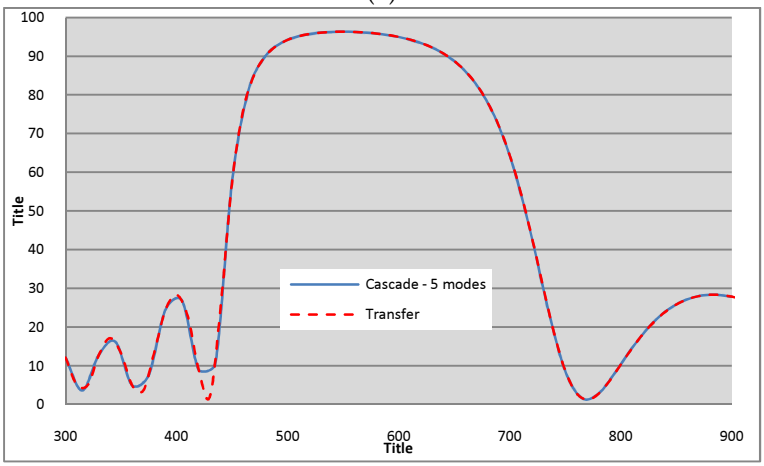

(b)

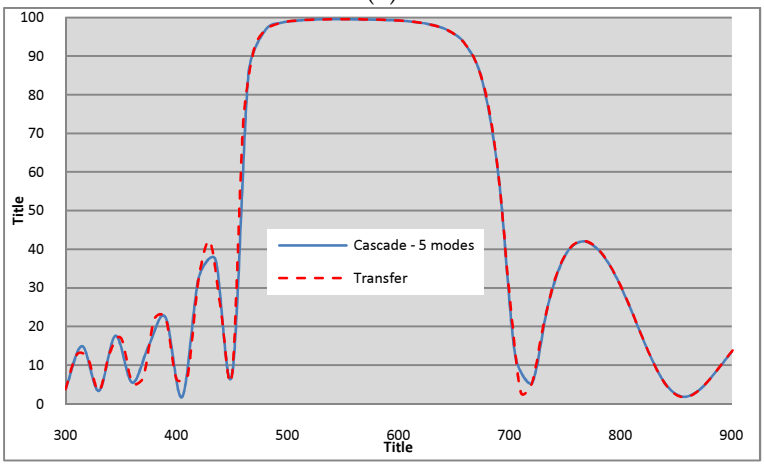

(c)

Figure 4-15 - Reflectance profiles for high-low index stacks of increasing order for (a) $N = 2$, (b) $N = 4$ and (c) $N = 6$

The cascade matrix technique evidently predicts the same reflectance profiles as determined using the traditional analytical transfer matrix technique describing plane waves incident upon various combinations of dielectric layers that exhibit either high or low reflectance.

With increasing stack sizes the propagation distances increase thereby evolving the beam away from a flat phase radius of curvature. This implies that increased numbers of modes will be required for larger dielectric stacks to accurately account for the increasing phase slippage. However, for these test cases a modal field description using five modes has provided excellent agreement with the analytical approach. In all cases presented here for the cascade approach the source field was chosen as a Gaussian beam waist with flat (infinite) phase radius of curvature. A more interesting scenario here would involve a source field with a diverged phase radius of curvature. This would be well modeled using GBMA over the traditional plane wave transfer matrix approach and could be verified by experiment. Herein lies the advantage of the GBMA technique over the transfer matrix technique: the ability to model more physically realistic electromagnetic field distributions as they interact with dielectric structures such as these multilayer films.

4.3 Mode Matching Theory for Feed Horns

This section describes the propagation of radiation within waveguide structures, specifically conical feed horn antennas, according to the mode-matching technique. The mode-matching technique refers to the expansion of the tangential electromagnetic field at a plane of a waveguide discontinuity in terms of the corresponding waveguide modes. This technique was originally applied to waveguide discontinuities by [79] and [80] using the matrix notation and including the higher order mode effects between discontinuities. The mode matching process detailed here is taken from [71] and [45]. The technique involves matching the total modal field description at a junction or plane where the field is altered so that conservation of power is maintained. A waveguide

based structure such as a horn is divided into separate components or sections. For example, a corrugated horn is visualized as a series of hollow cylindrical waveguide sections with alternating radii to account for the corrugations slot depths and edges – c.f. Figure 4-16. A smooth walled horn is visualized in much the same way, with the radii of sequential waveguide sections increasing smoothly along the length of the horn. The greater the number of waveguide sections chosen to represent the smooth walled horn the greater the accuracy, since there are technically no waveguide junctions along the walls of these horns. The number of waveguide sections required to describe the corrugated horn generally much lower, equaling the number of corrugations.

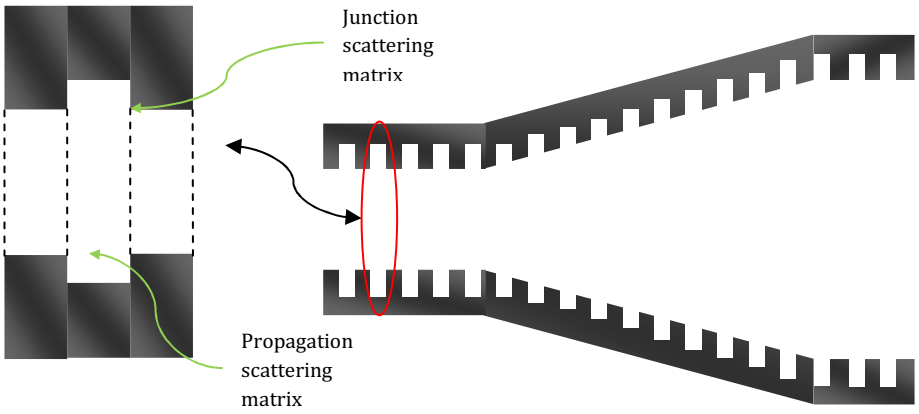

Figure 4-16 - Waveguide component visualisation of conical corrugated feed horn - individual corrugation sections can be described using scattering matrices which are then cascaded together to give complete scattering matrix for the horn

Each of these waveguide sections will scatter the transverse electromagnetic field in different ways, and thus altering the layout of the modal coefficients that describe the field. An input, forward travelling field at a junction will be scattered into both transmitted and reflected components. Each of these sections or junctions is described by a scattering matrix which can be combined to create a complete scattering matrix description of the total structure allowing the calculation of all four S parameters. The individual scattering matrices describe the redistribution of power between the respective modes

4.3.1 Modeling of Feed Horns

In this section the method of mode-matching method of describing propagation and scattering of electromagnetic radiation throughout a waveguide structured feed horn and freespace beam guide is described. A feed horn can be regarded as a series of sequential waveguides with diameters varying with propagation distance along the horn axis. The feed horn acts as an impedance transformer between an input waveguide through to freespace. The primary type of feed horn discussed within this chapter is the conical corrugated feed horn, the design principles of which will be discussed in a later section. All waveguide structures discussed in this chapter possess circular symmetry and thus we will concentrate on the cylindrically symmetric waveguide modes, which are described by a combination of TE and TM modes.

The TE and TM waveguide modes are transformed into freespace Gaussian beam modes at the aperture of the horn by performing an overlap integral at the aperture plane and extending the method to model free space propagation. The propagation and transformation of the source beam can now be described using the standard GBMA method. If a second horn is coupled to the optical system, the freespace Gaussian beam modes can be retransformed back into the appropriate waveguide modes by reversing the initial freespace transformation.

4.3.2 Conical Corrugated Feed Horns

A comprehensive treatment of the mode-matching technique as it applies to conical corrugated and smooth-walled horns was carried out by [45] in the development of the software package SCATTER. This software tool has been repeatedly utilised throughout this thesis to calculate the complex aperture field distributions for corrugated feed horns (c.f. Chapters 3, 5 and 6). An outline of the mode-matching theory based on [45] is presented here.

Conical corrugated feed horns are a popular horn of choice for quasioptical systems such as communication systems, radar, remote sensing and for prime feed and multi-reflector antennas used in astronomical observation. For example, the conical corrugated horn is the preferred feed horn used in each of the ALMA front end optics channels [81]. The boundary conditions of the corrugated horn for the *E* and *H* planes are equivalent, thus ideally ensuring a symmetric co-polar radiation pattern with low side lobes and low cross-polarisation. They belong to the class of feed horns known as hybrid mode horns, since they are designed to propagate the dominant hybrid HE_{11} mode. The overall geometry of a typical corrugated horn is given below Figure 4-17

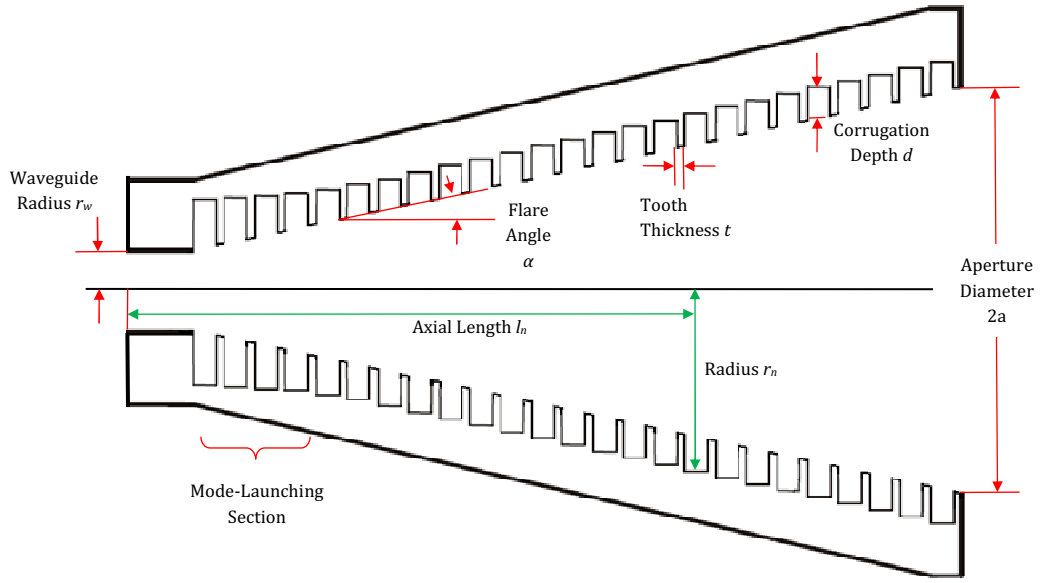

Figure 4-17 - Conical Corrugated Horn Geometry - the input from the left is assume to be in a smooth-walled circularly symmetric waveguide propagating the TE_{11} mode

The most common method of exciting the dominant HE_{11} mode of a circular cross section corrugated waveguide is from a circular waveguide with a uniform wall supporting the TE_{11} mode [82]. Corrugated feed horns are typically connected to a section of smooth-wall circular waveguide as a means of transferring power between the radiating horn and the receiver transmission line where the signal processing is undertaken. The cylindrical waveguide typically carries the dominant TE_{11} mode which is incident at the junction. The HE_{11} mode is excited within the horn, which itself

inevitably generates other higher order modes. Of these the EH_{12} mode most seriously affects the polarisation purity of the radiated fields. Generation of the EH_{12} mode can occur either at the mode-launching or 'throat' section of the horn or indeed along the horn due to conversion from the HE_{11} mode. The reduction of higher order mode generation, especially the EH_{12} mode, is of significant importance and is achieved through careful design of the horn corrugations [82].

Results from field matching calculations support the well established approach to designing an efficient mode-launching section; the first corrugation depth is set to be a half wavelength deep so that a 'short circuit' occurs at the edge of the corrugations. The depths of the proceeding corrugations shorten to the final value of a quarter-wavelength [82]. The depths of the remaining corrugations through the length of the horn remain at this value. This condition, known as the *balanced hybrid condition*, ensures an infinite surface reactance, given by [3] which opposes any axial currents that may be set up on the horn walls.

$$\frac{X_s}{Z_0} = \tan\left(\frac{2\pi d}{\lambda}\right) \tag{4.71}$$

where X_s is the reactance and Z_0 is the free-space impedance. With corrugation depths of $\lambda/4$ the reactance is infinite and is the guide is sufficiently large i.e. $2\pi a/\lambda > 1$, the field distribution of the horn is independent of angle for the central frequency and in theory the cross-polar field will be zero (although in reality there will always exist a very low level cross polar field). There as yet exists no one optimum solution of how the corrugation depths decrease throughout the mode-launching section of the horn. A typical transition from depths of $\lambda/2$ to $\lambda/4$ occurs over approximately 8 to 12 corrugations [71]. A current travelling down a corrugation depth will be 180° out of phase at the opposite side of the groove. The effect of the field produced by this opposite current is to counter the field that set up the original current in the manner of a short circuit. This short-circuit at the bottom of the corrugation groove is transformed

into an open circuit at the top of the corrugation and the fields thus taper to zero at the horn boundary. As the frequency is varied, the surface reactance will change and the hybrid condition will become unbalanced, thus limiting the operable bandwidth of the horn. The farfield co and cross polarizations plotted below in Figure 4-18 are from SCATTER predictions of the 94 GHz corrugated horn from Section 3.3.1. The plots show the E and H plane cuts (blue and red) of the co-polar field as well as a 45° cut of the cross polar field (green) for the central frequency (94 GHz) and for the upper end (110 GHz) and lower end (85 GHz) of the band edge of approximately 30%. The central frequency exhibits the lowest cross polar power and the co-polar field is symmetric out to approximately 37°. The upper and lower band edge patterns show significantly increased cross polar power as well as increased asymmetry in the co-polar beam. This illustrates that the corrugation depth is non ideal for frequencies away from the band centre.

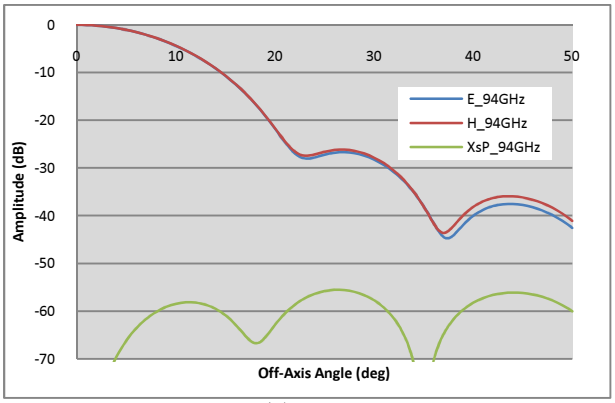

(a) - 94 GHz

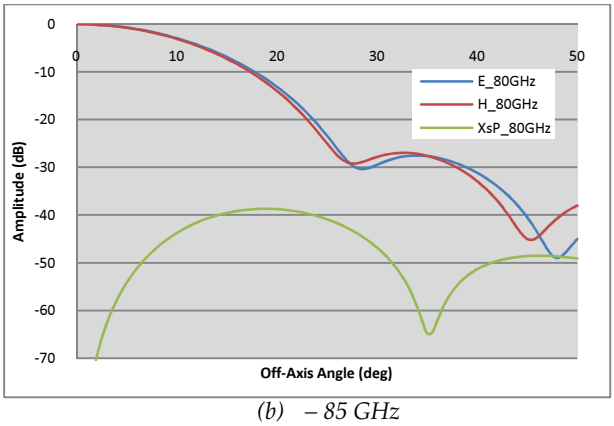

(b) – 85 GHz

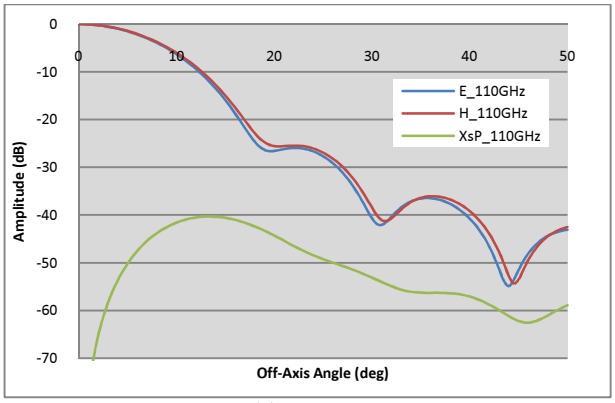

(c) *– 110 GHz*

Figure 4-18 - Co and cross polar farfield patterns for corrugated feed horn for the central frequency *(a)* : *94 GHz, (b)*: *85 GHz, (c): 110 GHz*

If the balanced hybrid mode condition is met and the horn is fed by a *HE11* mode at the waveguide to horn boundary then the field at the horn aperture is given as [75]

$$\begin{aligned} E_x(r) &= 0, \quad E_y(r) = J_0\left(2.405\frac{r}{a}\right)e^{\left(-\frac{kr}{2R_h}\right)}, && r \le a \\ E_x(r) &= E_y(r) = 0, && r \ge a \end{aligned} \tag{4.72}$$

where $r^2 = x^2 + y^2$, k is the freespace wavenumber, J_0 is the Bessel function of zeroth order, 2.405 is the first zero of J_0 and R_h is the slant length of the horn which is approximately equivalent to the phase radius of curvature of the aperture field.

Corrugated horns usually require many corrugations per wavelength so as to ensure that no axial currents are established in the horn walls and that the balanced hybrid conditions are met. With decreasing wavelengths fabrication of these horns becomes difficult and an upper limit of approximately 1.5THz (0.2 mm) is usually enforced [71]. The most common modern method for fabricating corrugated horns with low flare angles such as the ALMA Band 5 and Band 9 horns is through electroforming, whereby the internal geometry of the horn is machined as an aluminium mandrel, upon which the desired metal is electrochemically deposited and then the mandrel is removed by chemical etching [83].

4.3.3 Mode Matching for Cylindrical Waveguides

The modal matching technique is a very powerful method for calculating the transverse aperture field distribution for feed horns [79], [80]. The mode-matching software *SCATTER*, which has been utilised successively/repeatedly throughout this thesis (Chapters 3, 5 & 6) for calculating aperture field distributions, was developed first by Colgan in [45] and extended by Gleeson in [56]. A complete description of the exact analysis and verification of the method is given in their theses. This section contains only a general outline of the theory so as to understand the principles involved.

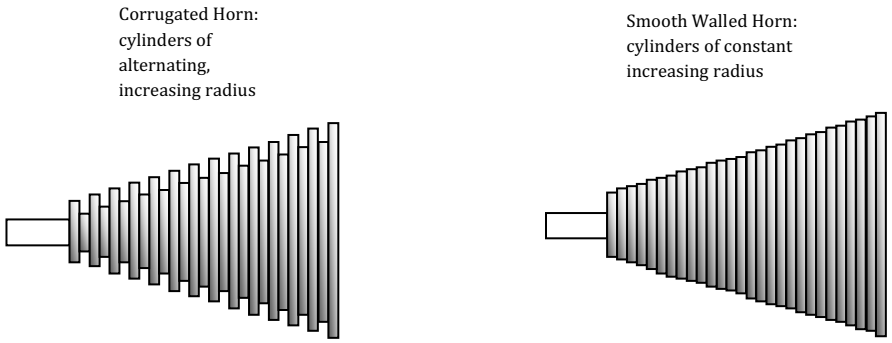

Figure 4-19 - Corrugated and Smooth Walled Feed Horns viewed as a series of waveguide sections

The technique involves treating a feed horn structure as a sequence of short waveguide sections, the diameters of which are dependent on the specific horn profile. This is easily visualized for a typical corrugated feed horn where each corrugation represents an individual waveguide section. The technique can become more involved for smooth walled or profiled horns. In this case the horn profile is divided up into an arbitrary number of waveguide sections, the diameters of which increase linearly for the case of a smooth walled conical horn, or according to the geometry of the profile horn (c.f. Figure 4-19). In these cases the accuracy of the mode-matching results can be seen to be dependent upon the number of waveguide sections chosen; the larger the number of waveguide sections the smoother the transition between junctions and hence a more accurate modal portrayal of the true horn profile. This will however increase the computation time.

This technique may also be applied to corrugated horns; specifically those in which the orientation of the corrugation depths and/or edges is non-orthogonal to the optical axis. Such corrugation geometries are shown below in Figure 4-20; the corrugation orientation in *(a)* is considered the ideal geometry for the modal matching technique, with the corrugations maintaining constant diameter over propagation distance. The other two horn geometries in *(b)* and *(c)* have waveguide sections with increasing radii over their propagation distances. Accurate modelling of these corrugations would

require the slanted waveguide sections to be themselves divided up into an arbitrary number of smaller waveguide sections, in the same manner as for the smooth walled horn.

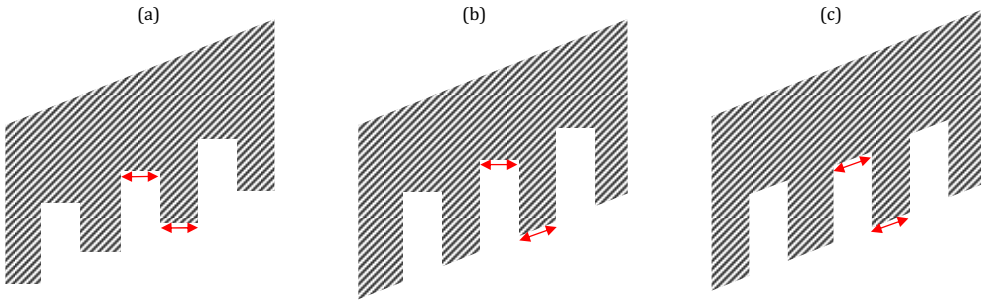

Figure 4-20 - Three sample variations on the geometry of corrugations in a corrugated feed horn [82]

To apply the scattering matrix approach to the horn both the reflection and transmission coefficients for the junctions between individual waveguide sections and the phase slippage between adjacent modes due to propagation within each waveguide section must be accounted for. The phase slippage within a waveguide section is described in a similar manner to the propagation scattering matrix, as described in Section 4.2.2. The diagonal elements of the scattering matrix are given by $V_{mn} = \delta_{mn} e^{-\gamma_n l}$ where l is the length of the waveguide section and γ_n is the propagation constant for the n^{th} mode.

The scattering matrix for the junction between two waveguide sections is calculated by matching the transverse modal field descriptions on either side of the junction. Each waveguide section contains propagating transverse electromagnetic fields represented as a spectrum of N modes. It is assumed that the modes are propagating from left to right. The electric and magnetic fields on the left side of the waveguide junction are given as

$$E_L = \sum_{n=1}^{N} \left\{ A_n e^{(-\gamma_n z)} + B_n e^{(\gamma_n z)} \right\} \mathbf{e}_{nL}$$
$$H_L = \sum_{n=1}^{N} \left\{ A_n e^{(-\gamma_n z)} - B_n e^{(\gamma_n z)} \right\} \mathbf{h}_{nL} \tag{4.73}$$

where A_n and B_n are the forward and reflected amplitude coefficients on the left side of the junction. Similarly the electric and magnetic fields on the right side of the junction are

$$E_R = \sum_{n=1}^{N} \left\{ C_n e^{(-\gamma_n z)} + D_n e^{(\gamma_n z)} \right\} \mathbf{e}_{nR}$$
$$H_R = \sum_{n=1}^{N} \left\{ C_n e^{(-\gamma_n z)} - D_n e^{(\gamma_n z)} \right\} \mathbf{h}_{nR} \tag{4.74}$$

where C_n and D_n are the forward and reflected amplitude coefficients on the left side of the junction.

By matching these transverse fields across the continuous junction the following matrix equations are derived as:

$$[P]\left[[A]+[B]\right] = [Q]\left[[D]+[C]\right],$$
$$[P]^T\left[[D]-[C]\right] = [R]\left[[A]-[B]\right] \tag{4.75}$$

where *[A], [B], [C]* and *[D]* are *N*-element column matrices containing the modal coefficients A_n, B_n, C_n and D_n respectively. The column matrices have the form $\begin{bmatrix} a_{TE} \\ a_{TM} \end{bmatrix}$, where a_{TE} and a_{TM} are subvectors of the mode coefficients for the *TE* and *TM* modes respectively. The matrices *[P], [Q]* and *[R]* represent the coupling between modes at the junction. The *[P]* matrix represents mutual coupled power between modes on the left side of the junction to modes on the right side, while the *[Q]* and *[R]* matrices represent self coupling between modes on the right and left hand sides respectively. Each of these matrices represent scattering between all mode types i.e. *TE* to *TE*, *TE* to *TM*, *TM* to *TE* and *TM* to *TM*. The derivation of the expressions for scattering is detailed in [45] but the overall form of the scattering matrix between modes is given as

$$P = \begin{bmatrix} P_{TE-TE} & P_{TE-TM} \\ P_{TM-TE} & P_{TM-TM} \end{bmatrix} \tag{4.76}$$

By rearranging Equation 4.76 the elements for the scattering matrix of a junction are derived as

$$\begin{aligned}
[S_{11}] &= \left[\left[R^*\right]+[P][Q]^{-1}[P]\right]^{-1}\left[\left[R^*\right]-[P][Q]^{-1}[P]\right], \\
[S_{12}] &= 2\left[\left[R^*\right]+[P][Q]^{-1}[P]\right]^{-1}[P], \\
[S_{21}] &= 2\left[[Q]+[P]\left[R^*\right]^{-1}[P]\right]^{-1}[P], \\
[S_{22}] &= -\left[[Q]+[P]\left[R^*\right]^{-1}[P]\right]^{-1}\left[[Q]-[P]\left[R^*\right]^{-1}[P]\right]
\end{aligned} \tag{4.77}$$

where $[]^*$ is the transpose of the matrix and $[]^{-1}$ is the inverse of the matrix. By cascading the junction scattering matrices together using Equations 4.18 the overall aperture field for the horn is calculated. This is the principle of operation for the *SCATTER* program to predict the aperture field distributions for conical smooth walled and corrugated horns.

4.3.4 Freespace Transformation

Though the modal matching method described above gives an accurate aperture field distribution for a feed horn, the field itself is described in terms of *TE* and waveguide modes. In order to propagate this aperture field throughout a quasioptical beam guide it must first be transformed into freespace Gaussian beam modes. This will allow for a scattering matrix description of the entire quasioptical system and thus the overall standing wave profile of the system can be determined. The required transformation matrix requires the computation of the appropriate overlap integrals at the horn aperture [76], [84]. The transverse electric field E_{total} at the horn aperture is written as a linear sum of *TE* and *TM* modal fields. For conical horns fed by a single TE_{11} mode polarised in the *x* direction the *TE* and *TM* modes $\mathbf{e}^{\mathbf{TE}}$ and $\mathbf{e}^{\mathbf{TM}}$ are written in the following form

$$\mathbf{e}_{1l}^{TE}=\frac{J_0\left(\frac{p_{1l}'r}{a}\right)\mathbf{i}+J_2\left(\frac{p_{1l}'r}{a}\right)\left[\cos(2\varphi)\mathbf{i}+\cos(2\varphi)\mathbf{j}\right]}{\sqrt{2\pi a^2\left(J_1\left(\frac{p_{1l}'r}{a}\right)^2-J_2\left(\frac{p_{1l}'r}{a}\right)^2\right)}},$$
$$\mathbf{e}_{1l}^{TM}=\frac{J_0\left(\frac{p_{1l}'r}{a}\right)\mathbf{i}-J_2\left(\frac{p_{1l}'r}{a}\right)\left[\cos(2\varphi)\mathbf{i}+\cos(2\varphi)\mathbf{j}\right]}{\sqrt{2\pi a^2\left(J_2\left(\frac{p_{1l}'r}{a}\right)^2\right)}} \tag{4.78}$$

where p_{1l} represents the l^{th} zero of $J_1(z)$ and p'_{1l} represents the l^{th} zero of $J'_1(z)$. These modes are normalised in such a way as to make the integral $\int_A\left|\mathbf{e}_l^{TE/TM}\right|^2 2\pi r dr$ equal to unity. In *SCATTER* the waveguide modes are ordered such that when the number of employed modes is $2N$, the first half $(1,\ldots,N)$ are *TE* and the second half $(N+1,\ldots,2N)$ are *TM*. The modes are thus written in linear sum form:

$$\mathbf{e}_{total}=\sum_l \alpha_l\mathbf{e}_l^{TE}+\beta_l\mathbf{e}_l^{TM}=\sum_n A_n\mathbf{e}_n^G \tag{4.79}$$

where $\mathbf{e}_n^G=\mathbf{e}_n^{TE}$, $\mathbf{e}_{N+n}^G=\mathbf{e}_n^{TM}$ $(n\le N)$ and α_l and β_l are subvectors containing the appropriate mode coefficients. For freespace coupling to a conical horn the most it is most appropriate to employ the Associated Laguerre-Gaussian mode set because of the cylindrical symmetry of the system. Recall from Equation 2.35 that for a wave travelling in the positive z direction these modes have the general form

$$\begin{aligned}\begin{pmatrix}\Psi_n^{\alpha,\cos}(r,\phi)\\ \Psi_n^{\alpha,\sin}(r,\phi)\end{pmatrix}&=\Psi(r,\phi)_n^{\alpha}\exp\left(-jkz+j(2n+\alpha+1)\times\arctan\left(\frac{\pi W^2}{\lambda R}\right)\right)\begin{pmatrix}\cos(\alpha\theta)\\ \sin(\alpha\theta)\end{pmatrix}\\ &=\sqrt{\frac{2(2-\delta_{0n})n!}{\pi W^2(n+\alpha)!}}\left(2\frac{r^2}{W^2}\right)^{\frac{\alpha}{2}}L_n^{\alpha}\left(2\frac{r^2}{W^2}\right)\exp\left(-\frac{r^2}{W^2}\right)\exp\left(-jk\frac{r^2}{2R}\right)\\ &\times\exp\left(-jkz+j(2n+\alpha+1)\times\arctan\left(\frac{\pi W^2}{\lambda R}\right)\right)\begin{pmatrix}\cos(\alpha\theta)\\ \sin(\alpha\theta)\end{pmatrix}\end{aligned} \tag{4.80}$$

where α is an integer representing the degree of the Laguerre polynomial, W is the beam waist, R is the phase radius of curvature and $\arctan\left(\pi W^2/\lambda R\right)$ is the phase slippage for the fundamental mode between the waist and the plane of interest. The waveguide

modes will only couple to the free space Associated Laguerre-Gaussian modes of degree 0 and 2 [76] since the horn field is written as a sum of symmetric *TE* and *TM* modes and modes with a $\cos 2\theta\mathbf{i}+\sin 2\theta\mathbf{j}$ dependence. Each waveguide mode is transformed to the corresponding free space mode using the following relation:

$$\mathbf{e}_m^G = \sum_n T_{nm}^0 \Psi_n^0 \mathbf{i} + T_{nm}^2 \Psi_n^2 \left[\cos 2\theta\mathbf{i} + \sin 2\theta\mathbf{j}\right] \tag{4.81}$$

The Associated Laguerre-Gaussian modes of degree 0 and 2 can be treated separately and so an expression for the 0th and 2nd degree freespace modes will have the forms

$$T_{nm}^0 = \int_A \left(\psi_n^0 \hat{\mathbf{i}}\right)^* . \left(\mathbf{e}_m^G\right) r dr d\theta \tag{4.82}$$

$$T_{nm}^2 = \int_A \left(\psi_n^2 \hat{\mathbf{n}}\right)^* . \left(\mathbf{e}_m^G\right) r dr d\theta \tag{4.83}$$

where $\hat{\mathbf{n}}$ is the unit vector equal to $\cos 2\theta\mathbf{i}+\sin 2\theta\mathbf{j}$. The overall horn aperture field $\mathbf{e}_{total}$ is expressed as the following linear modal sum

$$\mathbf{e}_{total} = \sum_n B_n^0 \Psi_n^0 \mathbf{i} + B_n^2 \Psi_n^2 \Psi_n^2 \left[\cos 2\theta\mathbf{i} + \sin 2\theta\mathbf{j}\right] \tag{4.84}$$

By comparing Equations 4.81 and 2.84 it is clear that the *0th* and *2nd* order mode coefficients can be written as

$$\begin{aligned} B_n^0 &= \sum_n T_{nm}^0 A_m, \\ B_n^2 &= \sum_n T_{nm}^2 A_m, \end{aligned} \tag{4.85}$$

where *B* are the freespace mode coefficients and *A* are the waveguide mode coefficients. In a similar way any freespace field incident upon the horn aperture (i.e. travelling in the negative *z* direction) may be written as

$$\bar{\mathbf{e}}_{inc} = \sum_n C_n^0 \Psi_n^0 \hat{\mathbf{i}} + C_n^2 \Psi_n^2 \hat{\mathbf{n}} = \sum D_n \bar{\mathbf{e}}_n^{fs} \tag{4.86}$$

In this instance the free space modes are transformed to waveguide modes at the aperture and in a manner similar to that from above (Equation 4.86) such that

$$
\begin{aligned}
F_m &= \int \left(\mathbf{e}_m^G\right)^* \bar{\mathbf{e}}_{inc} r dr d\theta, \\
&= \sum_n C_n^0 \left(\mathbf{e}_m^G\right)^* \Psi_n^0 \hat{\mathbf{i}} + C_n^2 \left(\mathbf{e}_m^G\right)^* \Psi_n^2 \hat{\mathbf{n}}, \\
&= \sum_n C_n^0 \left(T_{mn}^0\right)^* + C_n^2 \left(T_{mn}^2\right)^*
\end{aligned}
\tag{4.87}
$$

and thus the free space mode coefficients B_n are transformed back to waveguide modes, where T_{mn}^* is the conjugate transpose of T_{mn}.

In order to properly transform the modes at the horn aperture from waveguide to free space (or vice versa) the transformation matrices T and T^* must be implemented as a scattering matrix of the same form as (ref equation):

$$
[S] = \begin{bmatrix} S_{11} & S_{12} \\ S_{21} & S_{22} \end{bmatrix} = \begin{bmatrix} 0 & T^* \\ T & 0 \end{bmatrix} \tag{4.88}
$$

In this formulation the transformation matrix *[T]* represents the $[S_{21}]$ scattering sub-matrix that transforms the waveguide modes to freespace modes at the aperture. In going from freespace back into the horn the direction is reversed the $[S_{12}] = [S_{21}]^*$. As such, the conjugate transpose transformation matrix *[T]** in Equation 4.88 above represents the reversal transformation of freespace modes to waveguide modes. For a horn with an aperture radius that is wide in terms of λ it is reasonably assumed that there is negligible reflection of the waveguide modes at the aperture back into the horn. At the aperture any possible reflections back into the horn will be carried by the higher order modes, which themselves will contribute little to the overall beam and will have a guide impedance appreciably different from that of free space [85]. This implies that the scattering sub-matrix from [ref equation] $[S_{11}] = [0]$. This argument also applies to the freespace radiation that propagates in the reverse direction and does not couple to the horn and is not reflected back along the positive direction, implying that $[S_{22}] = [0]$. The cross section of the reflected beam that overlaps with the horn will be coupled to the waveguide modes by the $[S_{12}]$ matrix [76].

The exact forms of the transformation matrices required for the scattering matrix S (Equation 4.88) are determined by representing the waveguide modes as Bessel functions and the freespace modes as Associated Laguerre-Gaussian modes. The *TE* and *TM* waveguide modes are coupled individually to the Associated Laguerre-Gaussian freespace modes of order *0* and *2* using separate overlap integrals at the aperture. These overlap integrals are given for the *TE* modes as:

$$T_{mn}^{0,TE} = \frac{\int_0^a J_0\left(p'_{1m}\frac{r}{a}\right) L_n^0\left(2\frac{r^2}{w^2}\right)\exp\left(-\frac{r^2}{w^2}\right)\exp\left(-\frac{jkr^2}{2R}\right)2\pi r dr}{\sqrt{2\pi a^2\left(J_1\left(p'_{1l}\right)^2 - J_2\left(p'_{1l}\right)^2\right)}\sqrt{\int_0^\infty L_n^0 \exp\left(2\frac{r^2}{w^2}\right)^2 \exp\left(-\frac{r^2}{w^2}\right)^2 2\pi r dr}} \tag{4.89}$$

$$T_{mn}^{2,TE} = \frac{\int_0^a J_2\left(p'_{1m}\frac{r}{a}\right) L_n^2\left(2\frac{r^2}{w^2}\right)\left(2\frac{r^2}{w^2}\right)\exp\left(-\frac{r^2}{w^2}\right)\exp\left(-\frac{jkr^2}{2R}\right)2\pi r dr}{\sqrt{2\pi a^2\left(J_1\left(p'_{1l}\right)^2 - J_2\left(p'_{1l}\right)^2\right)}\sqrt{\int_0^\infty \left(2\frac{r^2}{w^2}\right)^2 L_n^2 \exp\left(2\frac{r^2}{w^2}\right)^2 \exp\left(-\frac{r^2}{w^2}\right)^2 2\pi r dr}} \tag{4.90}$$

where $T_{mn}^{0,TE}$ and $T_{mn}^{2,TE}$ are the transformation matrices for the *TE* waveguide modes to the Associated Laguerre modes of order *0* and *2* respectively, *a* is the aperture radius and p'_{1l} is the l^{th} zero of J_1. The matrices are rectangular with *m* rows and *n* columns representing the number of waveguide and freespace modes respectively. The overlap integrals for the *TM* modes are given as:

$$T_{mn}^{0,TM} = \frac{\int_0^a J_0\left(p'_{1m}\frac{r}{a}\right) L_n^0\left(2\frac{r^2}{w^2}\right)\exp\left(-\frac{r^2}{w^2}\right)\exp\left(-\frac{jkr^2}{2R}\right)2\pi r dr}{\sqrt{2\pi a^2\left(J_2\left(p'_{1l}\right)^2\right)}\sqrt{\int_0^\infty L_n^0 \exp\left(2\frac{r^2}{w^2}\right)^2 \exp\left(-\frac{r^2}{w^2}\right)^2 2\pi r dr}} \tag{4.91}$$

$$T_{mn}^{2,TM} = \frac{\int_0^a J_2\left(p'_{1m}\frac{r}{a}\right) L_n^2\left(2\frac{r^2}{w^2}\right)\left(2\frac{r^2}{w^2}\right)\exp\left(-\frac{r^2}{w^2}\right)\exp\left(-\frac{jkr^2}{2R}\right)2\pi r dr}{\sqrt{2\pi a^2\left(J_2\left(p'_{1l}\right)^2\right)}\sqrt{\int_0^\infty \left(2\frac{r^2}{w^2}\right)^2 L_n^2 \exp\left(2\frac{r^2}{w^2}\right)^2 \exp\left(-\frac{r^2}{w^2}\right)^2 2\pi r dr}} \tag{4.92}$$

These rectangular transformation sub-matrices comprise the elements of the transformation sub-matrices:

$$[T]=\begin{bmatrix} T_{TE}^{0} & T_{TM}^{0} \\ T_{TE}^{2} & T_{TM}^{2} \end{bmatrix} \tag{4.93}$$

This sub-matrix is then implemented into the overall transformation scattering matrix from Equation 4.88. The transformation of the waveguide modes to freespace at the horn aperture is then achieved by cascading the transformation scattering matrix with the overall waveguide propagation scattering matrix.

The freespace transformation technique is validated by comparing the farfield patterns of the waveguide and freespace mode descriptions of the horn aperture field. The farfield pattern for the waveguide modal field is achieved by the Fourier transform [34]. The farfield pattern of the freespace modal field is obtained by propagation of the freespace Associated Laguerre-Gaussian modes. The farfield distribution is obtained by applying a Gaussian beam evolution term to the modal sum description of the aperture field distribution from Equation 4.84 [85]

$$\begin{aligned} E(r,\phi,z)=&\left[\exp\left(-\frac{r^2}{w(z)^2}-j\left(\frac{r^2}{2R(z)}+kz\right)\right)\right]\sum_n A_{n0x}L_n^0\left(-2\frac{r^2}{w(z)^2}\right)\exp\left((2n+1)\,j\phi(z)\right)\mathbf{i}+ \\ &\sum_n\left(L_n^2\left(-2\frac{r^2}{w(z)^2}\right)\exp\left((2n+3)\,j\phi(z)\right)\right)\left(A_{n2x}\cos(2\theta)\mathbf{i}+A_{n2y}\sin(2\theta)\mathbf{j}\right) \end{aligned} \tag{4.94}$$

where $w(z)$, $R(z)$ and $\varphi(z)$ and represent the usual Gaussian beam parameters of beam radius, phase radius of curvature and phase slippage (c.f. Section 2.1.2). The evolution of these parameters to the farfield is governed by the usual ABCD matrix technique in Section 2.1.5. This technique of verification is employed here for the 94 GHz corrugated horn from Chapter 3. The aperture distribution of this horn was generated by SCATTER, and the farfield patterns were plotted using both the Fourier transform of

the waveguide modal and the farfield propagation of the freespace Associated Laguerre-Gaussian modal field – c.f. Figure 4-21 below. For this calculation *10* Laguerre modes of degree *0* and 10 modes of degree *2* were used for the freespace modal distribution, which corresponded to the *10 TE* and *10 TM* modes used for the waveguide modal distribution.

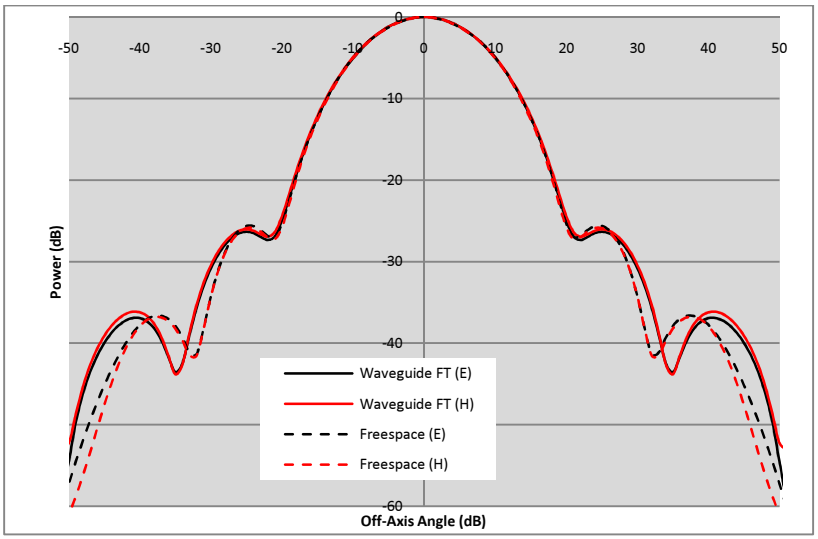

Figure 4-21 – Farfield *E* (in black) and *H* (in red) plane pattern cuts for the *94 GHz* conical corrugated horn. Fourier transform of waveguide modal fields plotted as solid lines; farfield propagation of free space modal fields plotted as broken lines

These two farfield pattern prediction methods show good mutual agreement down to approximately -30 dB, which is good agreement for the finite number of Associated Laguerre-Gaussian modes used.

4.4 Corrugated Horns – Characterisation of Return Loss Profile

In this section comparisons are drawn between the return loss profile of a typical corrugated feed horn as predicted by SCATTER and as measured in the laboratory. The specific horn in question is the same used previously in Section 3.3 for measurement of the Fresnel diffraction pattern for a circular aperture. Four of these horns were

purchased by the Far-Infrared Optics Group at Maynooth from Thomas Keating Ltd. These horns were developed using a copper electroforming process from the same mandrel piece, the geometry of which is illustrated below in Figure 4-22.

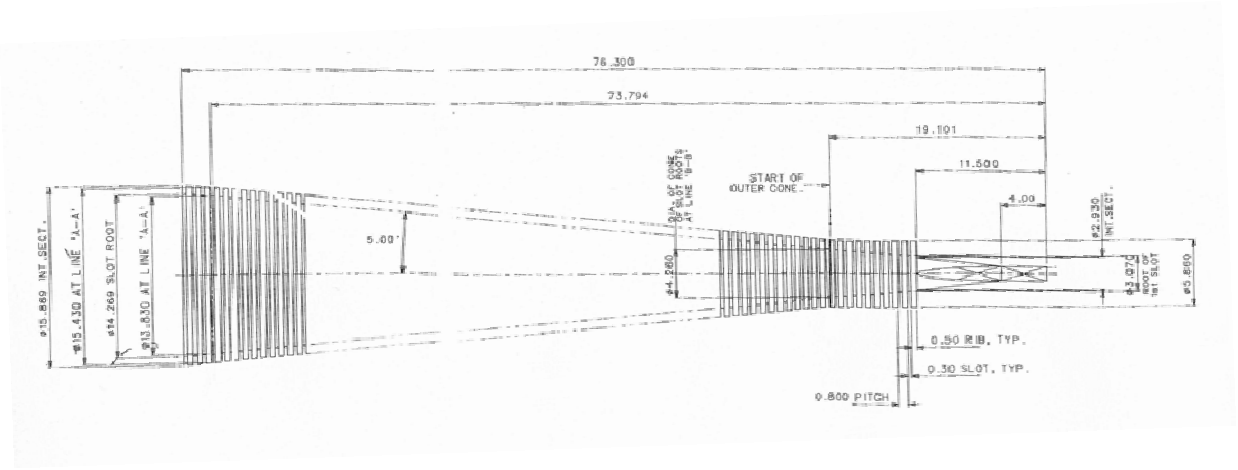

Figure 4-22 - Geometrical profile of *94 GHz* conical corrugated horn mandrel

The return loss profile for a feed horn refers to the degree of reflected power over the operating frequency range of the horn as it couples to empty space. This reflected power is typically due to impedance mismatches at the waveguide to horn transition and at the horn aperture. For a corrugated horn these reflections can also occur along the entire length of the horn where corrugations are located. Corrugated horns are typically designed to produce a minimum returned power within the optimal frequency range of the horn, outside of which the horn no longer achieves the balanced hybrid mode condition. For frequencies outside the balanced hybrid condition, excitation of other higher order hybrid modes will occur, thereby worsening the symmetry of the output beam and worsening the polarisation purity [71].

Firstly the return loss profiles of the four corrugated horns were recorded using the VNA with the horns directed at empty freespace where there would be a minimum of reflection of radiation back into the horn. To ensure this, the outer edges of the beam path were covered with the absorber ECCOSORB from Emerson & Cumming ® which is designed for a minimum of reflection for a broad range of frequencies across the

mm/submm range. These horns are hereafter referred to as MH01, MH02, MH03 and MH04, where MH is an abbreviation of 'Maynooth Horn'. These return loss profiles were measured over the cited operating frequency range of the horn (75 GHz to 110 GHz) and are displayed below in Figure 4-23.

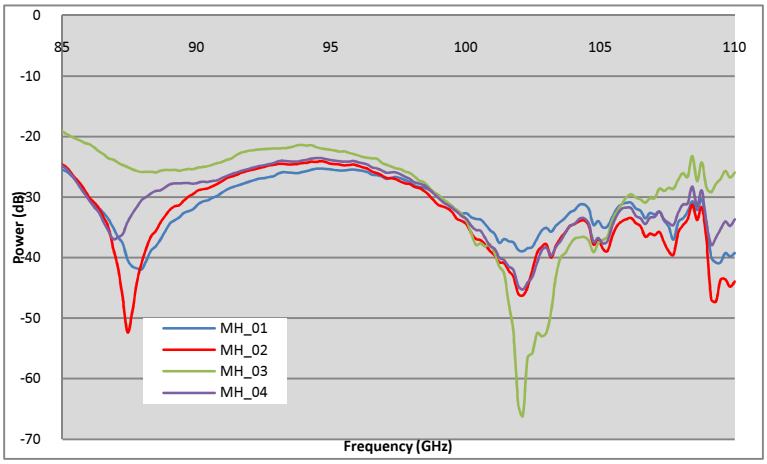

Figure 4-23 - Return loss profiles of four corrugated horns across frequency range (75 GHz - 110 GHz)

As can be seen from Figure 4-23 above the four horns each share a similar return loss profile across the frequency band. Each horn displays a minimum power dips at approximately 87 GHz and again at approximately 102 GHz. The degree of returned power at these points varies for each horn, with no two horns being exactly alike. The greatest agreement between horns in Figure 4-23 is between *MH02* (red line) and *MH04* (purple line). The strongest returned power dip is exhibited by *MH03* (green line) at approximately 102 GHz of -64 dB.

The next step in the characterisation process was to compare the predicted return loss profile from SCATTER with the experimental measurements. Firstly the return loss profile for the horn was predicted using 20 modes (10 *TE* and 10 *TM* modes) with no alterations to the geometry file. This was overlaid with the measured results from Figure 4-23 above:

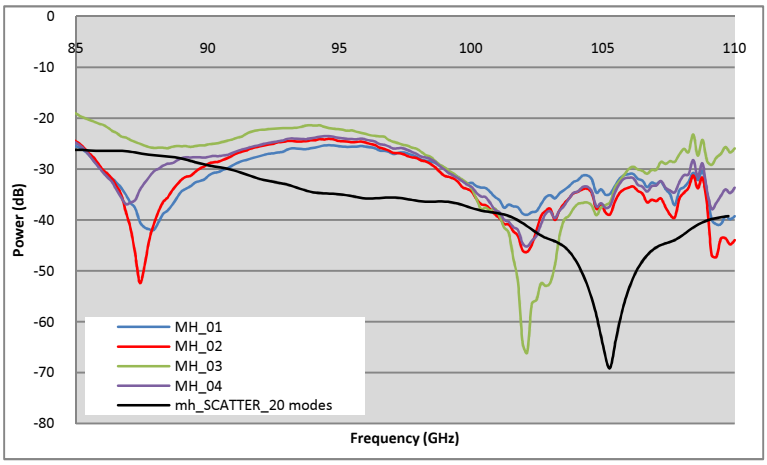

Figure 4-24 - Horn return loss profile predicted by SCATTER for 20 modes i.e 10 TE and 10 TM modes (black line)

The accuracy of a 20 mode SCATTER calculation was further verified with a higher mode number calculation of 64 modes. This was achieved using a modification of the SCATTER code currently under development by Mr. Tully Peacocke, a member of the Far Infrared Optics Group at Maynooth which allows mode-matching predictions with mode numbers of up to 200. Comparison between predictions for *20* modes and *64* modes (Figure 4-25 below) reveals excellent convergence for 20 modes. This result thus justifies the decision to use calculations at 20 modes for the remainder of the analysis presented in this chapter.

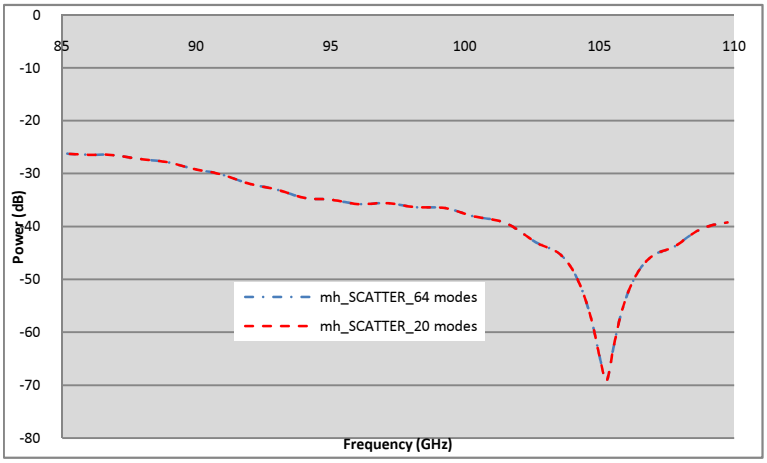

Figure 4-25 - SCATTER predictions of horn return loss profile for 20 modes (red dotted line) and 64 modes (blue dotted line)

Comparing experimental results and theoretical predictions of the horn return loss profile in Figure 4-24 above reveal a distinct disagreement. The SCATTER predictions do exhibit a return loss minimum in a similar fashion to the measured patterns, though this occurs at a higher frequency of approximately 104 GHz. The lower frequency power dip at 87 GHz is not predicted by SCATTER. Though some degree of experimental disagreement between the return loss profiles for each of these horns is expected, as seen between the horn return loss profiles in Figure 4-23 , it is difficult to ascertain what constitutes reasonable agreement.

The chief difference between the SCATTER model of the horn and the actual horn geometry is the rectangular to circular waveguide transition zone at the back of the horn. At this transition zone the rectangular WR-10 waveguide that propagates the TE_{10} waveguide mode is converted into the dominant HE_{11} that propagates through the feed horn. The current configuration of SCATTER allows for the computation of the scattering matrices of circularly symmetric feed horns (i.e. conical corrugated, conical smooth walled and profiled horns). As such, it is not currently possible to include the effects of this transition zone in the mode-matching calculation. Later on in Section 4.4.2 an attempt is made to predict the effect of the transition zone on the overall return loss profile of the horn using an FDTD calculation process from the CST-MWS described earlier in Section 2.7.

The following section details an investigation into the effect of small scale alterations in the horn geometry profile on the transmission and reflection properties for the feed horn. The purposes of this analysis were to ascertain whether minute surface errors in the horn corrugations could contribute to the disparity between prediction and measurement. This study was performed using SCATTER predictions of the horn return loss profiles and farfield patterns using several versions of the horn geometry profile.

4.4.1 Effect of Tolerancing & Manufacturing Errors on the Horn Geometry Profile

As the following investigation will refer to alterations to specific elements of the horns geometric profile, we will first introduce specific nomenclature for these geometric elements. This is presented below in Figure 4-26 as a cross section for a corrugated horn. This illustration is adapted from Figure 4-17, with the nomenclature now more formally defined.

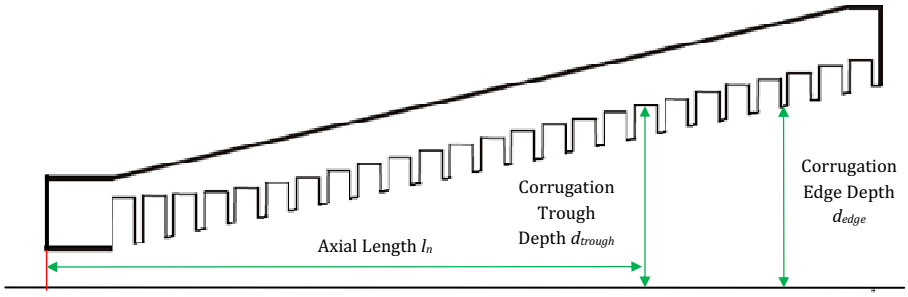

Figure 4-26 - Cross section of corrugated horn with specific titles for elements

The waveguide sections that comprise the corrugate horn profile are now specified as either a corrugation depth with radial depth d_{trough}, or a corrugation edge with radial depth d_{edge}. The position of each waveguide section along the length of the horn is still defined using the axial length l_n, with n referring to the specific waveguide section. Several variations of the geometry characterisation of the corrugated horn profile were generated which were based upon the manufacturing tolerances of the horn mandrel. The manufacturing tolerances for the mandrel were cited as ± 0.013 mm for all dimensions [86]. This represents a tolerancing accuracy range of 0.33% to 0.48% over the frequency range of the horn (75 GHz to 110 GHz). The first batch of variations to the standard horn geometry profile was generated as *random* deviations from the original horn geometry.

This was achieved by adding or subtracting an error value of 0.01 mm, representing a relative deviation range of 0.25% to 0.37% across the frequency range, to a random selection of 50% of the corrugation troughs, corrugation edges or axial lengths. The choice of either adding or subtracting the error value was also decided randomly. This

technique generated an altered geometry profile of the corrugated horn that was still within the manufacturing tolerances as defined in [86]. This process was repeated 10 times to generate 10 different horn geometry profiles, each with randomly assigned tolerancing errors. The return loss profiles for each of these horn profiles were predicted using SCATTER for 20 modes in the same manner as for the original horn geometry profile.

The results reveal a relatively large degree of variation in the return loss profile for the 10 horn profiles when compared against the original (black line in Figure 4-27 below). This was a surprising result, given that the randomly assigned variations to the horn profile were within the cited tolerance levels for the horn. It is thus reasonably concluded that the return loss profile for the corrugated horn is sensitive to small scale manufacturing errors. Extending this reasoning, it can be argued that the disparities in the measured return loss profiles shown in Figure 4-23 above may be due to similar small scale deviations from the optimal horn geometry.

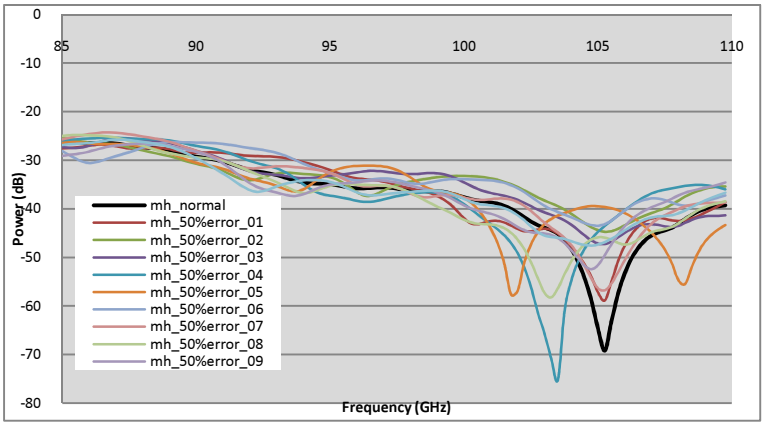

Figure 4-27 - Return loss profiles of 10 randomly generated horn profiles across (75 GHz to 110 GHz) - Original horn profile: (broken black line)

To ascertain whether any of the return loss profiles from the randomly generated horns possess a greater degree of agreement with experimental measurements, the SCATTER predictions from Figure 4-27 above were overlaid with the return loss profiles of the four corrugated horns from Figure 4-23. These comparison plots are shown below in

Figure 4-28, with SCATTER predictions plotted as solid lines and the measured results plotted as broken lines.

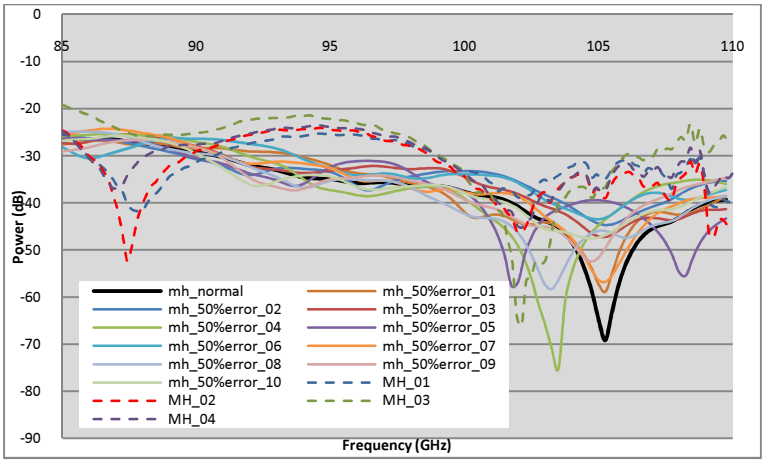

Figure 4-28 - Return loss profiles of randomly generated horn geometry profiles (solid lines) plotted against measured return loss profiles (broken lines)

From the plots above it is evident that the variations in the return loss profiles of the randomly generated horns do not resolve the disparity between prediction and measurement. Some of the predicted return loss profiles exhibit the power dip at a lower frequency than that of the original (at 105 GHz). Specifically, *mh_error_04* and *mh_error_08* in Figure 4-28 above show the power dip at approximately 103 GHz, which is closer to the experimental pattern with a power dip at approximately 102 GHz. However, as stated previously, none of these altered horn profiles exhibit the lower power dip from measurements, or the curved power profile between these two nulls. This furthers the argument that the rectangular to circular waveguide transition zone may be the source of the disparity.

The effect of these randomly assigned alterations to the horn profile upon the aperture distribution of the horn must also be accounted for. The co and cross polar farfield patterns for each of these randomly altered horn profiles are plotted below in Figure 4-29 and Figure 4-30. The farfield patterns are predicted here for 90 GHz, 100 GHz and 110 GHz. The cross polar patterns are taken at a 45° cut of the farfield distribution.

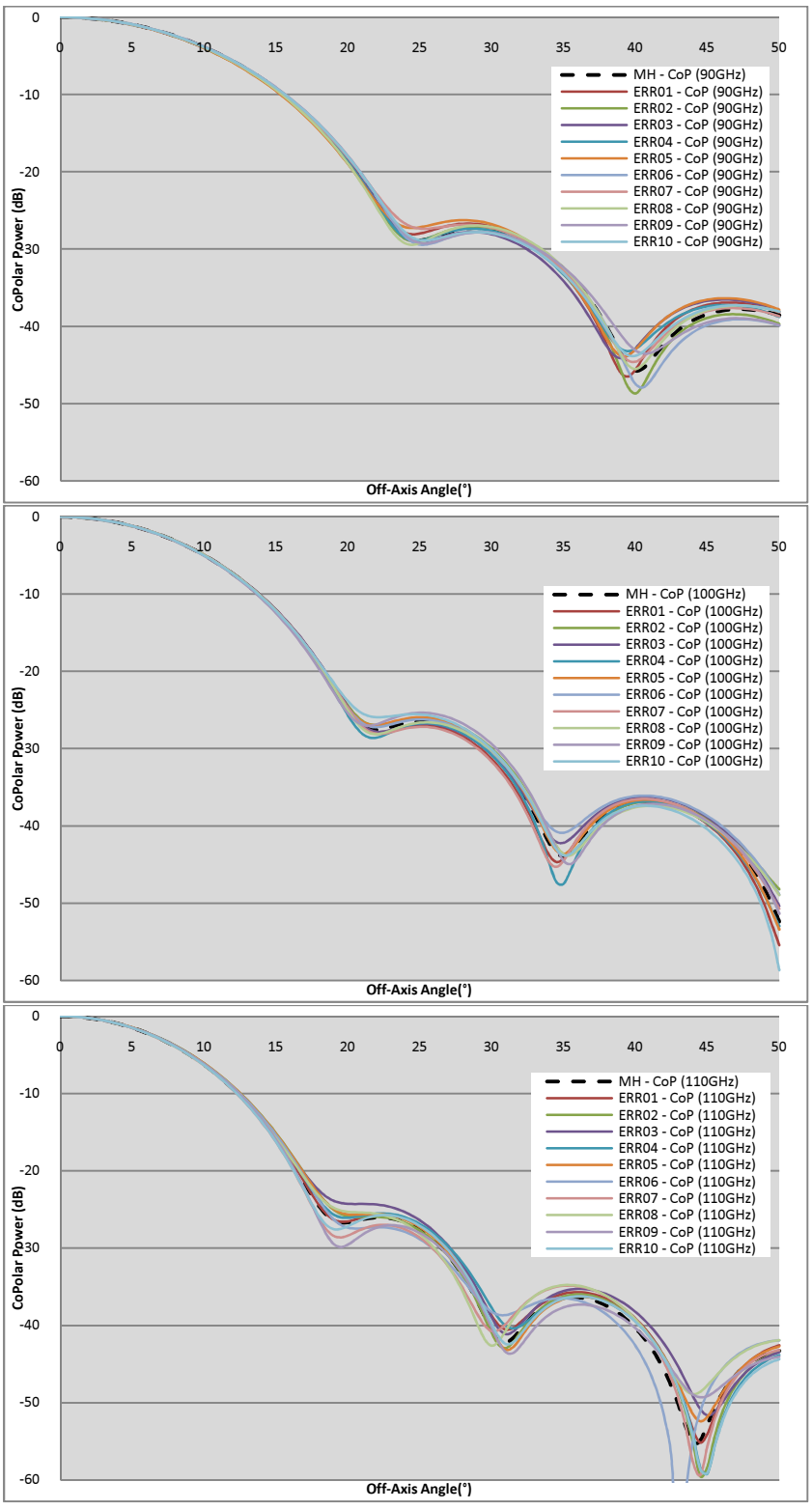

Figure 4-29 - Predicted (SCATTER) co polar farfield patterns for 10 randomly deviated horn geometry profiles (Top - 90 GHz , Middle – 100 GHz, Bottom – 110 GHz) – original horn broken black line

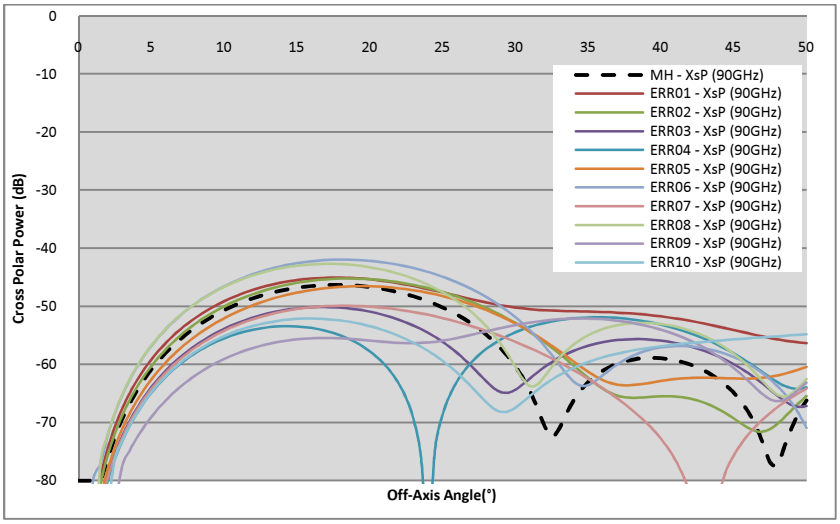

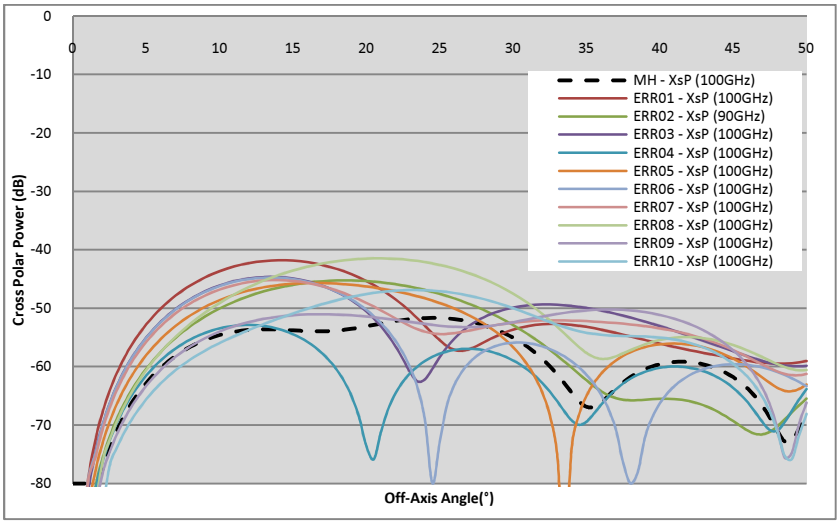

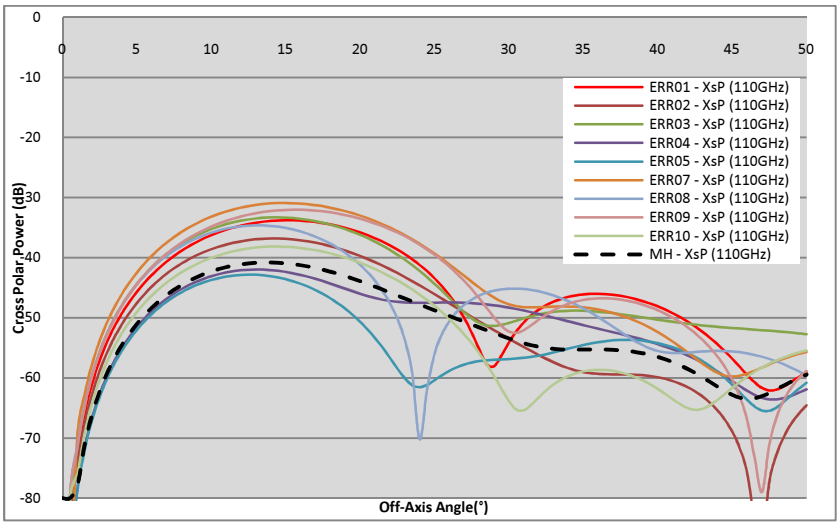

Figure 4-30 - Predicted (SCATTER) cross polar farfield patterns for 10 randomly deviated horn geometry profiles (Top - 90 GHz , Middle – 100 GHz, Bottom – 110 GHz) line

There is negligible alteration of the co-polar farfield patterns (Figure 4-29). However, several of the horn profiles exhibit significantly altered cross polar power patterns. According to [82], the level of cross polar power radiated is determined by the size of the aperture and the geometry of the corrugations, specifically the slot depths. Since the aperture size is the governing factor for the co-polar characteristics of the horn, the cross polar designer will normally have no control over aperture size: thus the corrugation geometry determines the cross polar power of the horn. Assuming that the corrugations for the original horn geometry were designed for minimal cross polar power, any alteration to their design will also alter the cross polar power level. The unbalancing of the corrugation geometry has also significantly altered the physical shape of the cross polar power patterns, suggesting the excitation of extra higher order modes. This is evident from the results in Figure 4-30 above.

For the next stage in this investigation another set of altered non-perfect horn geometry profiles was analysed. Instead of introducing random manufacturing errors into the horn geometry, it was determined that a more *constant* error might be more physically correct. In the process of turning the mandrel for the horn on a machining lathe, it is likely that any errors introduced would be of a constant nature due to machining offsets and tolerances. In terms of the horn geometry profile, this would mean that constant error would be introduced to the corrugation troughs or edges. A series of six horn geometry files was generated to emulate this constant error effect and are described briefly here:

1. All corrugation depths (troughs and edges) increased by 0.01 mm
2. All corrugation depths (troughs and edges) reduced by 0.01 mm
3. All corrugation edges increased by 0.01 mm
4. All corrugation edges reduced by 0.01 mm
5. All corrugation troughs increased by 0.01 mm
6. All corrugation troughs reduced by 0.01 mm

The same error value from the randomly altered horns of 0.01 mm was used for these constantly altered horns. The return loss profiles for each of these horns are compared against that of the original horn (plotted in black) below in Figure 4-31.

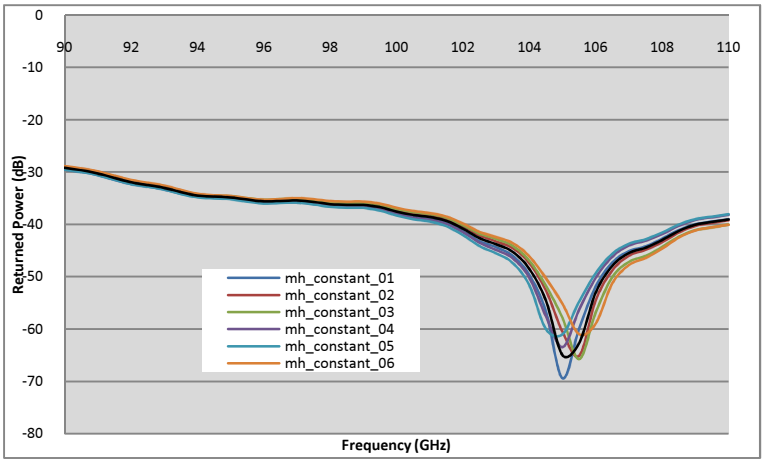

Figure 4-31 - Return loss profiles for horn profiles with constant errors introduced to geometry profiles

The conclusion from these predictions is that the effect of the constant errors introduced to the horn geometry profile is negligible. The only significant effect is found in the slight deviation of the single return loss dip which typifies this horn. The frequency of the dip varies over approximately 104.5-105.5 GHz, with no other significant alteration in the profile. This is a reasonable result given the nature of the alterations introduced. By applying a constant error to the corrugation edges and or depths we have essentially created horns with slightly different profiles but who retain the balanced hybrid condition, albeit at slightly different frequencies.

By comparing the co and cross polar farfield patterns from these horns the relatively negligible effect of the constant error alterations becomes clear. The co polar farfield distributions in Figure 4-32 below show near perfect mutual agreement down to approximately -45 dB. The agreement between cross polar pattern distributions in Figure 4-33 is also very close, with all patterns exhibiting very similar cross polar pattern distributions. This further reinforces the conclusion that these horns represent deviations from the original while still maintaining a balanced hybrid mode condition.

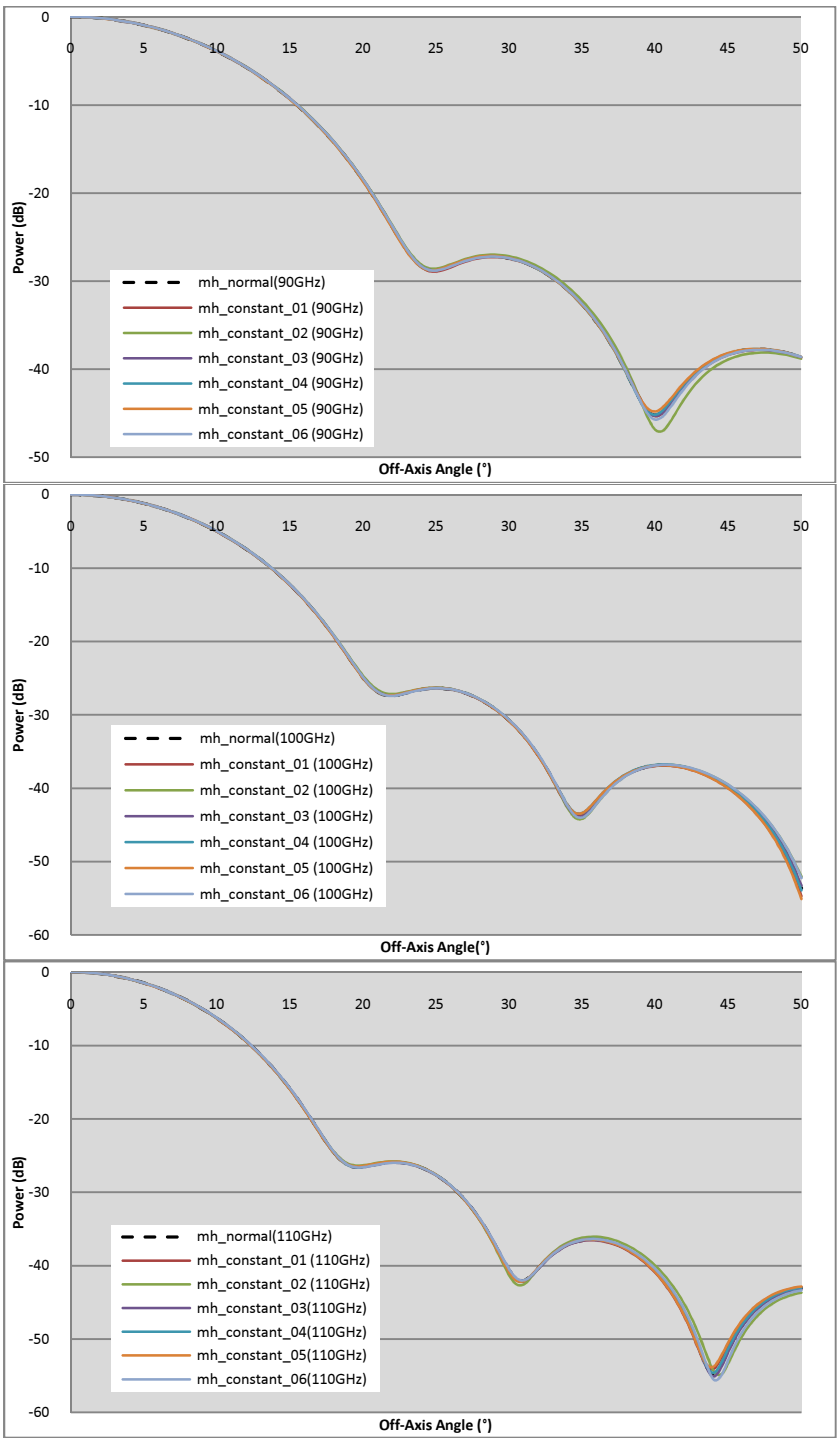

Figure 4-32 - Predicted (SCATTER) co polar farfield patterns for 6 geometry profiles with altered constant errors (Top - 90 GHz , Middle – 100 GHz, Bottom – 110 GHz) – original horn broken black line

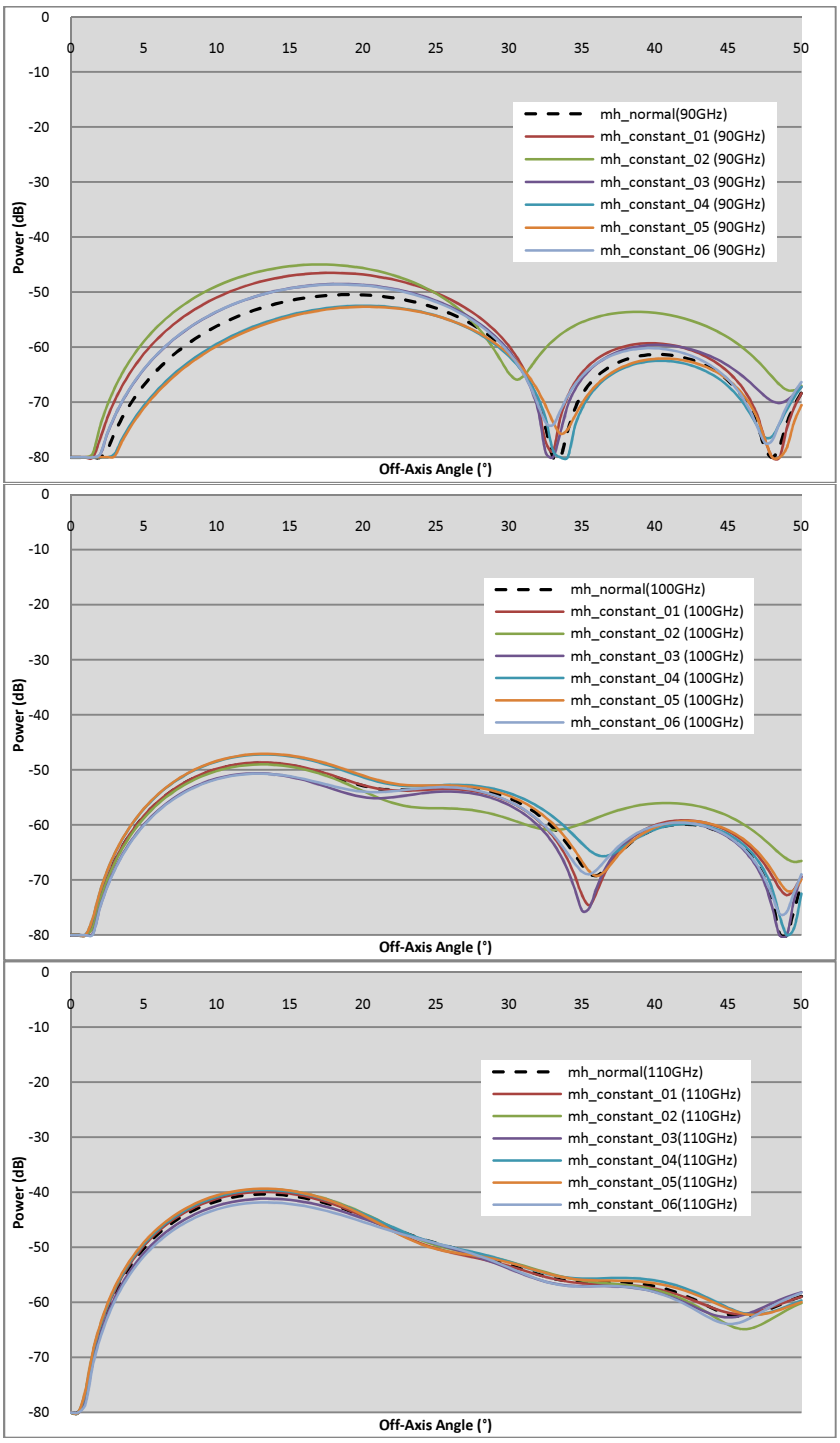

Figure 4-33 - Predicted (SCATTER) cross polar farfield patterns for 6 geometry profiles with altered constant errors (Top - 90 GHz , Middle – 100 GHz, Bottom – 110 GHz) – original horn broken black line

Several conclusions can be drawn from these investigations. Firstly, given the evident sensitivity of the return loss profile to slight randomly generated deviations in the geometrical description of the horn it can be inferred that there may exist an altered horn geometry profile that will possess a greater degree of agreement with measurements. However, the determination of such an optimally modified horn geometry profile would require large scale modeling of an innumerable amount of altered geometry profiles. It can be equally concluded that a resolution to the disparity between predictions and measurement may not be possible. This conclusion is still overshadowed by the inability to account for the transition zone. Another possible source of error may be due to there existing some degree of asymmetrical error within the actual corrugated horn geometry. This can take the form of an axial mismatch between one or several corrugations, or the circular profile of the corrugations may have become asymmetrically altered/shifted/warped. Equally with the transition zone problem it is not currently possible to account for propagation within asymmetrical waveguide sections in SCATTER.

4.4.2 CST Modeling of the Corrugated Horn

As an alternate verification of the validity of the predictions from the SCATTER mode-matching technique for the reflection/transmission characteristics of a feed horn was undertaken using the FDTD technique in the CST-MWS software package. This is a commercially available package that uses a full vector numerical simulation to model propagation of electromagnetic waves through various media. CST is an equivalent package to HFSS which is more commonly used in the field. The FDTD calculation process was previously outlined in Section 2.7. This technique is used to solve for the S-parameters of the horn as well as the output farfield pattern. The major difficulty of applying this turnkey solution is the computational intensity of a calculation of a structure of this size (circa 30 wavelengths long). CST is designed to deal with much smaller structures accurately and we are pushing the limits of the feasibility of applying such a technique to a structure of this large geometrical design. The physical structure

of the feed horn was generated in CST-MWS using the same geometrical profile used by SCATTER. The structure of the horn in CST-MWS is displayed below in Figure 4-34.

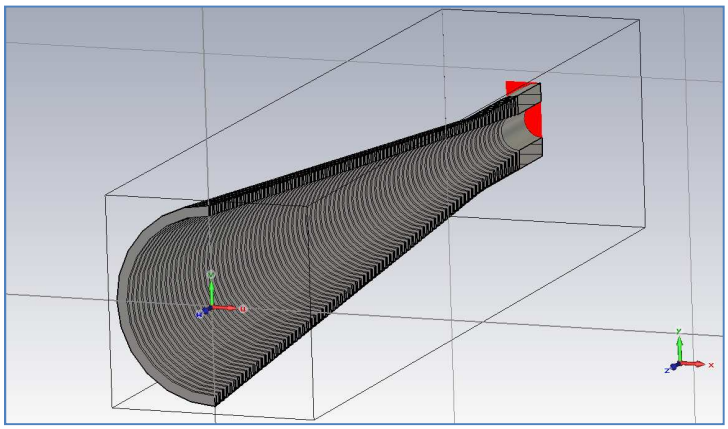

Figure 4-34 - Physical structure of *94 GHz* conical corrugated horn in CST-MWS with a cut-away in *yz* plane revealing structure of internal corrugations.

The FDTD technique is implemented in CST-MWS through the Transient Solver. This time-domain simulation tool stimulates the feed horn structure at the input circular waveguide with a 'waveguide port'. The waveguide port is a special type of boundary condition within the calculation domain and is considered as a simulation of an infinitely long waveguide that is connected to the structure in question. The waveguide port object automatically determines of the dominant propagating mode (TE_{11} in this case) while the user is free to select the number of permitted modes to stimulate the structure, although this is not necessary here as the horn is single moded. As this feed horn is single moded, the number of modes for the waveguide port is set to one. Given the circular symmetry of the horn it was possible to reduce the solver calculation time by defining planes of symmetry within the boundary conditions of the structure. In this instance the electric field is set to zero in the *yz* plane and the magnetic field is set to zero for the *xz* plane. These symmetry conditions essentially reduce the total calculation time by one quarter. The definition of these boundary conditions within the CST-MWS environment is illustrated below in Figure 4-35.

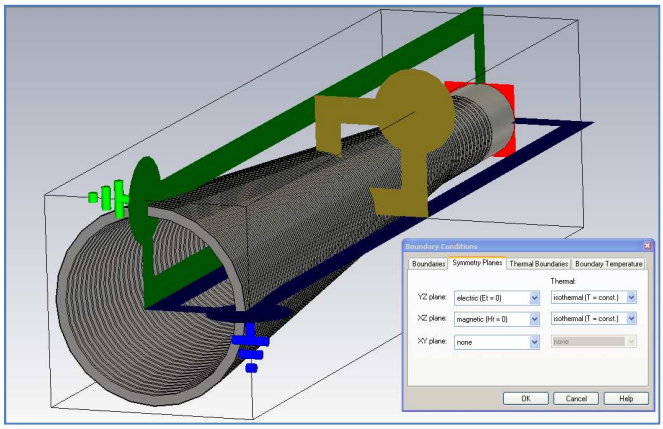

Figure 4-35 - Planes of symmetry within the boundary conditions of the horn structure

The FDTD calculation process require the volume of the structure under consideration to be discretised into finite 3D cells similar to as Yee cells within which the time dependent Maxwell's equations are solved [63]. The number and size of these cells is defined in CST-MWS using the Mesh Generator. The global definitions for this tool are the number of lines per wavelength, the lower mesh limit and the ratio limit or smallest mesh step. The number of lines per wavelength defines the number of mesh lines in each coordinate direction based on the highest frequency of evaluation. The lower mesh limit defines the maximum mesh step to be used for the mesh creation, regardless of the number of lines per wavelength. The ratio limit defines the ratio between the biggest and smallest mesh lines, and the smallest mesh step defines an absolute value for the distance between mesh lines [64]. The mesh for the calculations presented here was defined with 29 *lines per wavelength*, a *lower mesh limit* of 3 and a *smallest mesh step* of 0.03, generating 18,378,871 cells. The formation of these mesh cells is shown below in Figure 4-36 in a cut away view of the throat section of the horn.

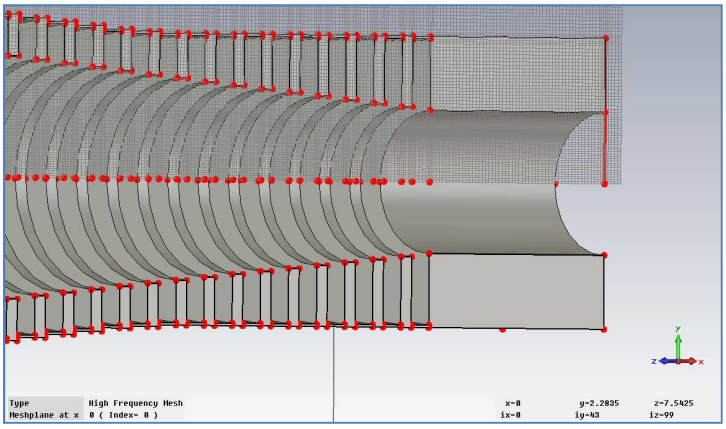

Figure 4-36 - Cut-away view of throat section of horn showing formation of mesh cells.

The return loss profiles of the horn over the frequency range (85 GHz – 110 GHz) as calculated by SCATTER and CST-MWS are plotted below in Figure 4-37.

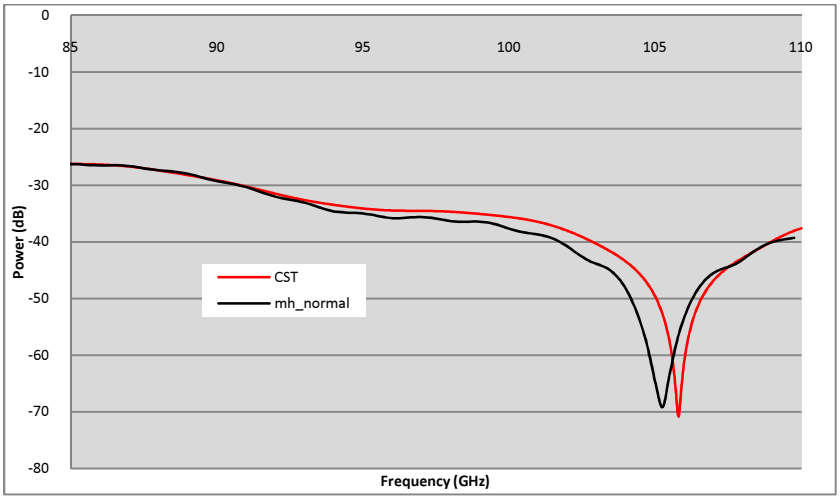

Figure 4-37 - Return loss profile of *94 GHz* corrugated horn as calculated by SCATTER (black) and CST-MWS (red)

The farfield amplitude patterns of the horn as calculated by SCATTER and CST-MWS are plotted below in Figure 4-38. The SCATTER predictions are the same as those in Figure 4-21, using both the Fourier transform of the waveguide modal field and the farfield propagated freespace modal field descriptions of the horn aperture field.

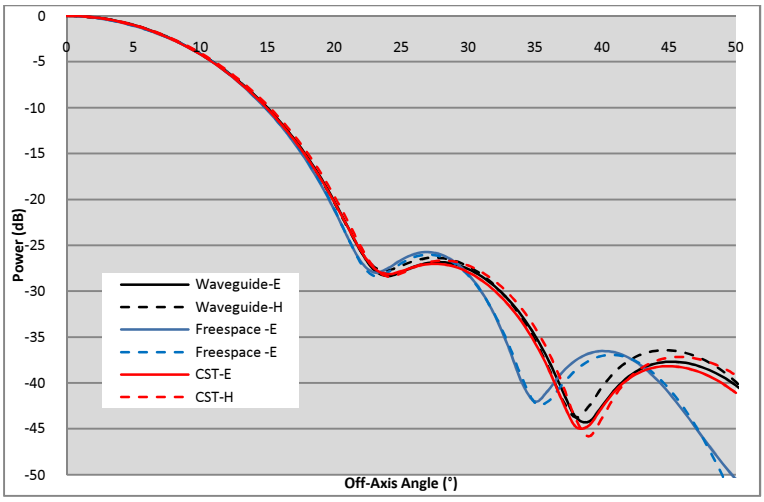

Figure 4-38 - Farfield amplitude patterns (E and H cuts) for the *94 GHz* corrugated horn as predicted by SCATTER (waveguide modes: black, freespace modes: blue) and CST-MWS (red)

The return loss profile and farfield power pattern for the 94 GHz corrugated horn were calculated by the Transient Solver at an accuracy of -30 dB. This was the best achievable accuracy for the computing power/memory available to the Author at the time of writing. The CST-MWS package has been designed for analysing structures at lower frequencies than those investigated here. The Transient Solver tool was unable to reach a steady state solution for higher accuracy levels (i.e. lower dB levels). There thus exists a degree of uncertainty with the CST-MWS predictions. Despite this relatively low accuracy level the agreement between SCATTER and CST-MWS for both the horn return loss profile and farfield amplitude patterns is very good. The return loss profile as calculated by CST-MWS exhibits a very similar pattern to that from SCATTER (Figure 4-37) with the only disagreement occurring at the specific location of the return power null. Agreement between SCATTER and CST-MWS predictions of the farfield amplitude patterns is excellent, especially for the waveguide modal description (black lines in Figure 4-38). These results thus serve as an independent verification of the accuracy of the SCATTER mode-matching technique.

At the time of writing, incorporation of the rectangular-to-circular waveguide transition into the overall structure of the Thomas Keating corrugated horn was also attempted.

This should then form a complete model of the physical horn used in measurements. However the exact geometry of the transition zone was unknown and difficult to determine from the schematics of the horn, illustrated previously in Figure 4-22. One such attempt to describe this transition zone is shown below in Figure 4-39, where the rectangular and circular waveguides were joined using a 'lofting' technique specific to the CST-MWS package.

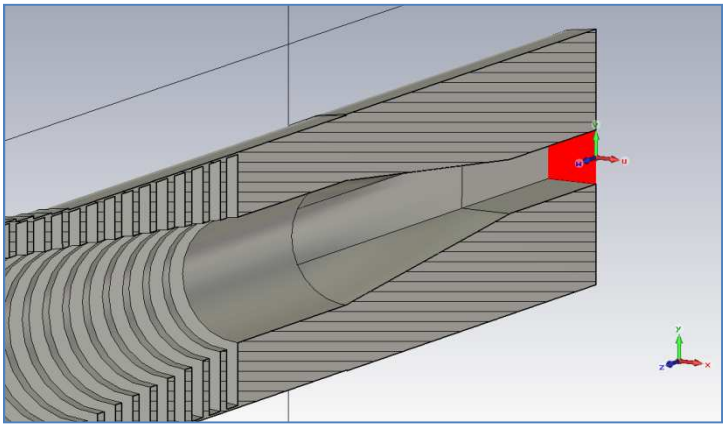

Figure 4-39 - Attempted rectangular to circular waveguide transition zone as a lofted surface

The Transient Solver predictions for return loss profile (Figure 4-40) and farfield amplitude pattern (Figure 4-41) revealed obvious errors when compared to those for the purely circularly symmetric horn and have been reasonably concluded as un-physical results. At the time of writing this issue has remained unresolved and is still under investigation by the Far-Infrared Optics Group at Maynooth. Previously when comparing the return loss profiles from SCATTER (where a purely circular geometry was modeled) we saw close agreement between measurement and simulation indicating that there does not seem to be a large influence from this square to circular transition. A potential difficulty of using CST for this particular example is the assumed use of the symmetry and boundary conditions of only using one quarter of the horn and assuming circular symmetry (the electric field is set to zero in the *yz* plane and the magnetic field is set to zero for the *xz* plane). In many ways the user needs to apply this condition to allow the structure to be analysed due to the sheer computational

efficiency gained through use of assumed symmetry. Perhaps in this transition region the assumed boundary conditions become invalid through scattering along the length of the extrusion and a true representation of the actual field cannot be realized. Therefore the CST simulation seems to become unsteady or unstable. So where naively, the user expects to see little or no influence in the CST model on farfields or return loss profile when compared with the purely circularly symmetric case already seen the internal calculations of CST breakdown.

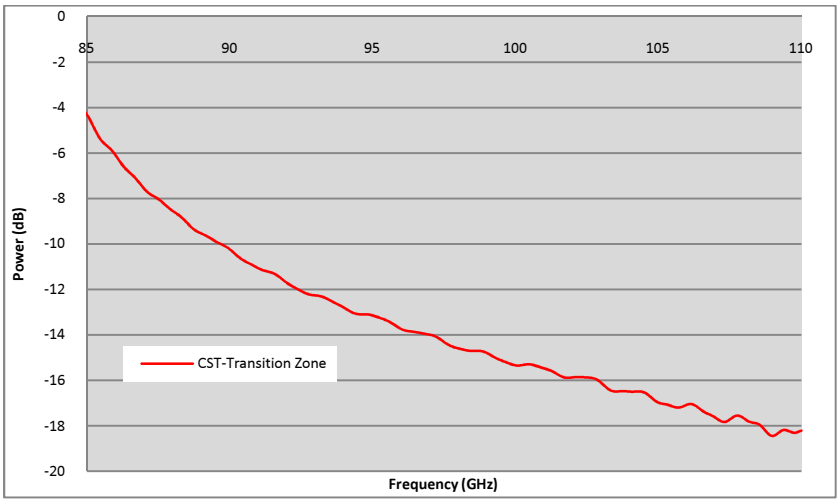

Figure 4-40 - Return loss profile predicted by CST-MWS for 94 GHz corrugated horn with rectangular to circular waveguide transition zone included

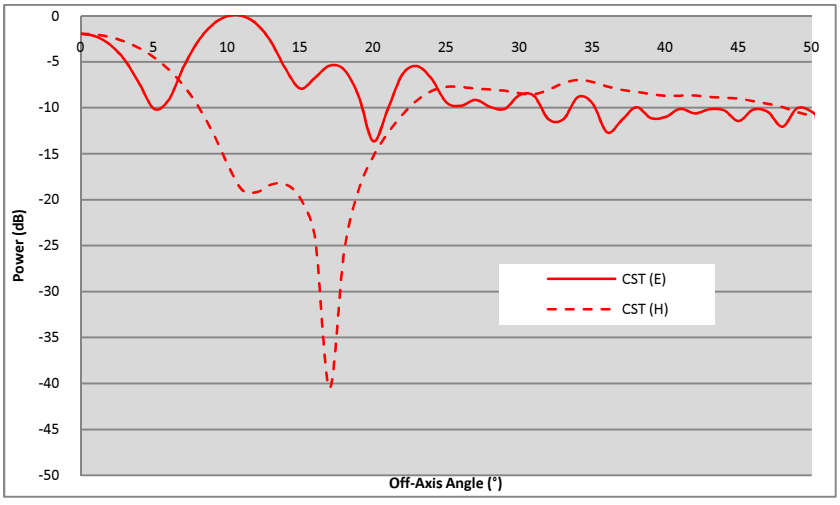

Figure 4-41 - Farfield amplitude patterns (E and H cuts) for 94 GHz corrugated horn with rectangular to circular waveguide transition zone included

The difficulties in applying CST to accurately and confidently model such horn structures or this large size are clearly evident with this example. The computational efficiency of the modal scattering technique is also highlighted in comparison to the lengthy calculations required within the CST environment. The farfield plot of the field obtained from CST with the rectangular section included is very different from the traditional corrugated farfield leading to the conclusion not to trust the computation without further investigation

4.5 Freespace Coupling of Horn-Horn Cavity/Standing Waves

In this section we consider two horns coupled to one another through freespace, as illustrated in Figure 4-42, forming what is referred to as a horn-horn cavity. The horns are unmatched, i.e. there are no optics to couple the aperture distributions of the horns and as such there are inherent mismatches of beam radius and phase curvature for the horns. This is perhaps the simplest coupled system that can exist between horns where the scattering technique can be applied to model multiple reflections

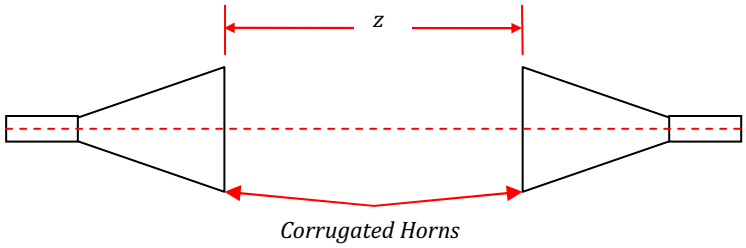

Figure 4-42 - Horn-Horn cavity arrangement - freespace quasioptical coupling of two corrugated horns separated by arbitrary distance *z*.

Arrangements similar to this one are typical for submillimetre quasioptical systems, albeit with some degree of optical coupling; one example is the heterodyne system for the ALMA Band 9 front end optics where a local oscillator (LO) signal from a feed horn is coupled to the mixer/detector feed horn quasioptically in freespace [87]. Similar horn-horn cavity arrangements to this one have been previously investigated in [36], [76] and [88]. These investigations were concerned with the measurement and modeling of the characteristic standing waves established within a horn-horn cavity both with

and without coupling optics for varied separation distances. The investigation of the horn-horn cavity or simply cavity from here on, in this section will focus primarily on the standing wave patterns of the reflected and transmitted amplitude response patterns over the operational bandwidth of the horns for a fixed separation distance between the horn apertures. Specific attention has been paid to the effect of differing geometries of the feed horn upon these standing wave patterns. In the preceding section the return loss profiles for a number of non-perfect horn geometry profiles were modeled with the aim of reconciling the disparities between mode-matching predictions and experimental measurement. This will form the basis for the following investigation.

Once again comparisons are drawn between experimental measurements and theoretical SCATTER predictions. The measurement system is an extension of that described in Section 3.3 and consists of two feed horns facing one another, with one horn operating as receiver and the other as transmitter and being separated by an arbitrary distance z. The inter horn distance is controlled through both a manually controlled micrometer stage and a single axis scanner table aligned along the beam axis which is controlled remotely by computer. This arrangement is illustrated below in Figure 4-43.

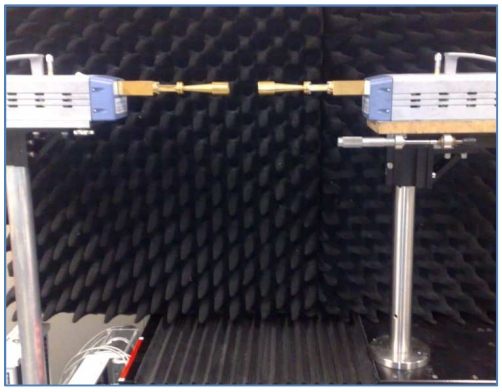

Figure 4-43 - Horn-horn cavity experimental arrangement using two 94 GHz corrugated horns fed by VNA and propagation distance managed by manual micrometre stage and computer controlled translation table

To describe this system analytically using the mode-matching technique firstly the complete scattering matrix for the feed horn is obtained using SCATTER. The waveguide modal field description is then transformed into the freespace Associated Laguerre-Gaussian mode set (c.f. Section 4.3.4). This freespace modal description of the complex horn field distribution is propagated a distance z using the propagation scattering matrix (Equation 4.25) with the evolution of the beam parameters calculated using the ABCD matrix technique. After the field is propagated the required distance to the second/receiver horn, the freespace modes must be transformed back into waveguide modes. This is achieved by retransforming the freespace mode set taking into account the evolved beam parameters at the second horn aperture. Finally, the scattering matrix of the receiver horn working in reverse is described as the reverse/inverse of the initial horn scattering matrix. This modal-matching description of the horn-horn cavity is illustrated below in Figure 4-44. The transmitted and reflected amplitude response profiles for the cavity are defined by the S_{21} and S_{11} sub-matrices of the complete scattering matrix of the cavity. Unlike the examples published previously where the inter horn distance was varied, the complete scattering matrix must be calculated for each horn as the scattering profile is wavelength dependent. This means that the computation is more intensive.

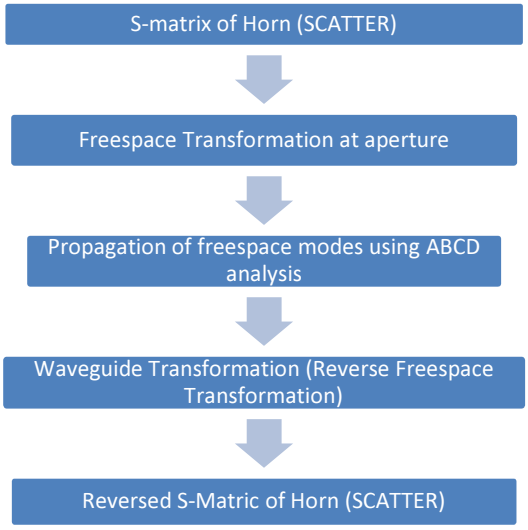

Figure 4-44 - Mode-matching scattering matrix process for modelling horn-horn cavity. SCATTER models scattering matrix of feed horn and freespace propagation described using ABCD matrices

The reflected and transmitted standing wave patterns/power profiles for horn-horn cavities of increasing separation distance were predicted using the above mode-matching technique and measured using the VNA measurement system. The cavity separation distances were z_1 = 10 mm, z_2 = 30 mm and z_3 = 50 mm. The separation distances were kept short so as to ensure a high degree of interaction between the horns.

For the purposes of simplicity only a small selection of the altered horn profiles described in Section 2174.4.1 will be utilised from here on. The six horns with constant machining errors introduced to their geometric profiles are dispensed with due to their very close agreement with the original horn in terms of return loss profile and farfield antenna patterns. Of the ten horns with random machining errors, three were chosen that exhibited the greatest deviance from the original horn; specifically in their predicted return loss profiles.; horns *mh_50%error_04*, *mh_50%error_05* and *mh_50%error_08* from chosen with this criteria in mind. The return loss profiles of these three horns are re-plotted below in Figure 4-45 along with that of the ideal horn (plotted as black broken line) to illustrate their disagreement with the ideal.

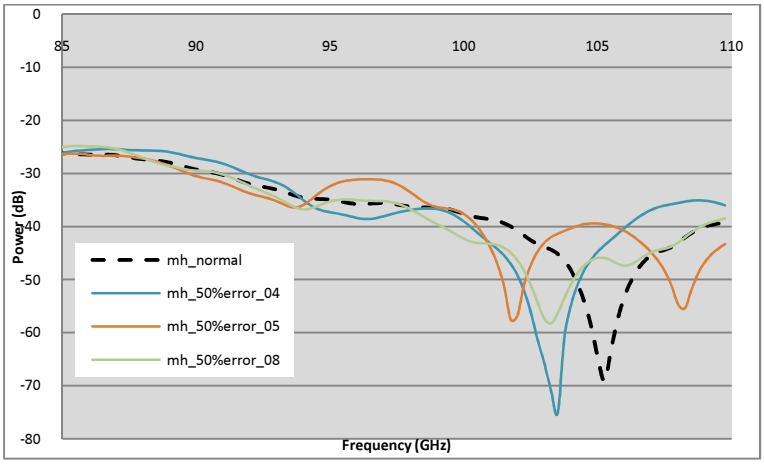

Figure 4-45 - Return loss profiles for the three horns with random deviations that show worst pattern agreement with the original ideal horn

These three horns are used for the same horn-horn cavity calculation as for the original horn, and as such all predictions for cavities in the following sections will be four-fold.

Experimental measurements of the transmitted and reflected amplitude response patterns for the various horn-horn cavities are plotted below with various combinations of the four 94 GHz feed horns used as transmitter and receiver, i.e. *MH01_MH02* indicates that *MH01* is the transmitter while *MH02* is the receiver in Figure 4-42.

z	Transmitted	Reflected
10 mm	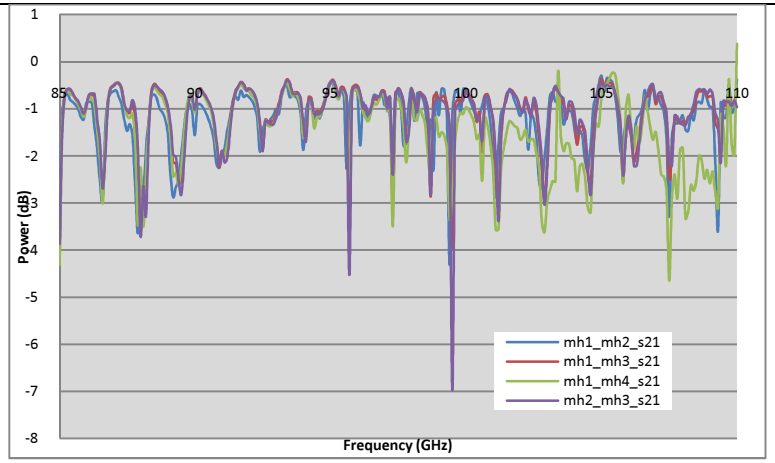	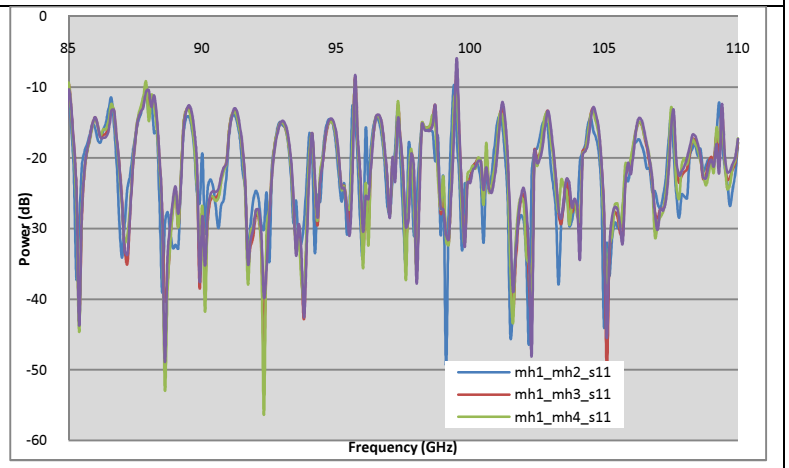
30 mm	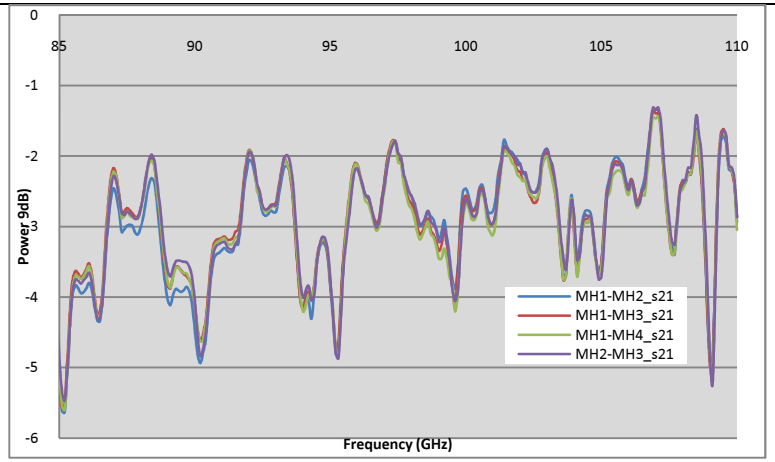	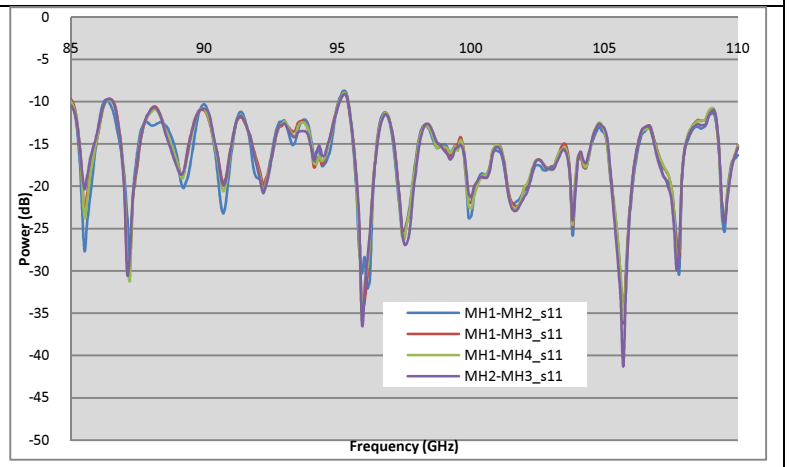

Table 4-1 – Measured transmitted (left side) and reflected (right side) standing wave patterns for horn-horn cavities of separation distance z_1 = 10 mm (top) and z_2 = 30 mm (bottom).

z	Transmitted	Reflected
50 mm	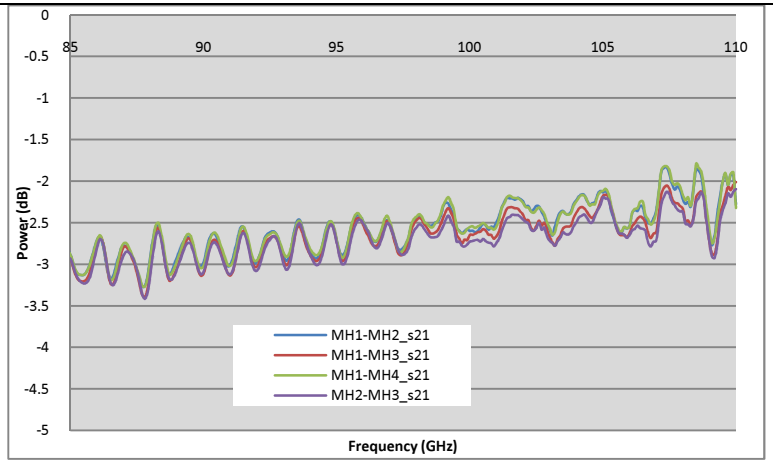	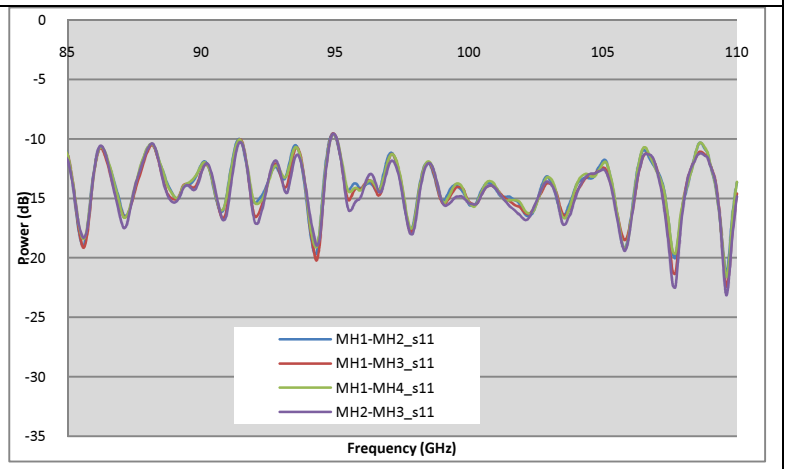

Table 4-2 - Measured transmitted (left side) and reflected (right side) standing wave patterns for horn-horn cavities of separation distance z_3 = 50 mm.

It is firstly noted that the level of pattern agreement of each of the measured horn-horn cavities for all combinations of transmitter and receiver horns is high. This is in line with the agreement between the return loss profiles for the four horns seen in Figure 4-23. The largest pattern disagreement, which is itself still quite low, occurs for the shortest horn-horn cavity separation distance of z_1 = 10 mm, and agreement improves with increasing separation distance.

There are evidently resonant multiple reflections occurring within these cavities It is observed that at the shortest separation distance of z_1 = 10 mm the standing wave patterns exhibit significant high Q cavity features, which are displayed as sharp quasi-random resonances in both the reflected and transmitted power profiles. This was an expected consequence of the short propagation distance for the cavity and was previously recorded by Trappe [88]. These sharp features are accounted for by the reflection of higher order modes within the feed horn structure that reduce with increasing separation distance. With increasing separation distances the occurrence of these high Q features decreases and the standing wave patterns exhibit smoother profiles. Another expected consequence is the decrease in the average transmitted amplitude level with increasing separation distance.

The following Table 4-3 and Table 4-4 display the reflected and transmitted standing wave patterns for the horn-horn cavities as predicted using the mode-matching technique in the same manner as the measured amplitude response patterns presented in Table 4-1 and Table 4-2.

z	Transmitted	Reflected
10 mm	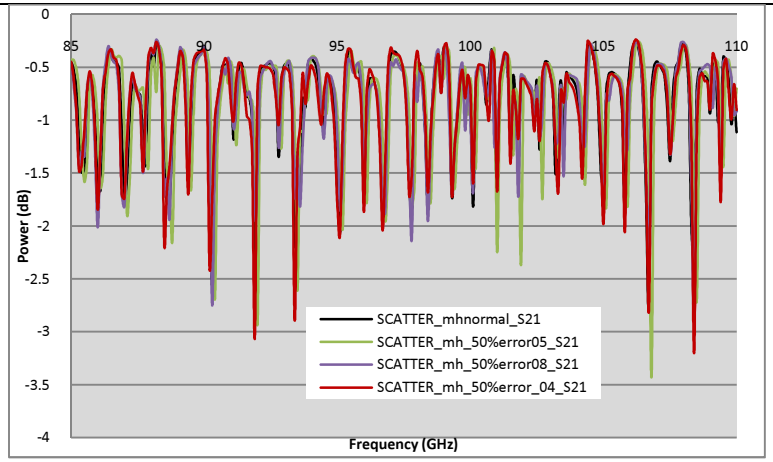	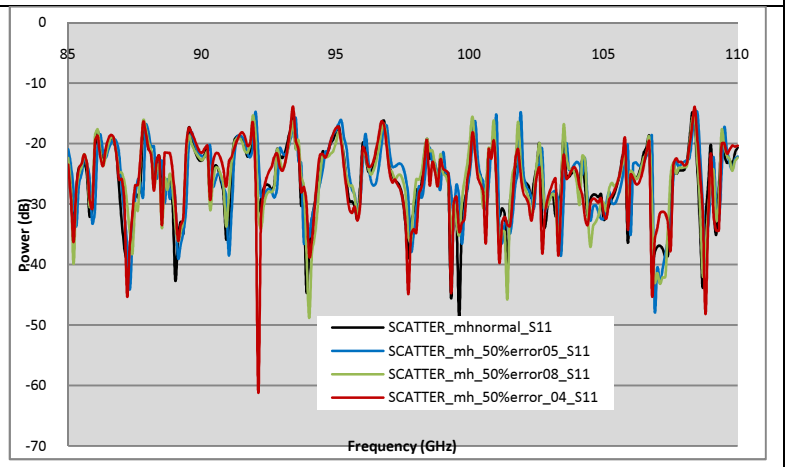
30 mm	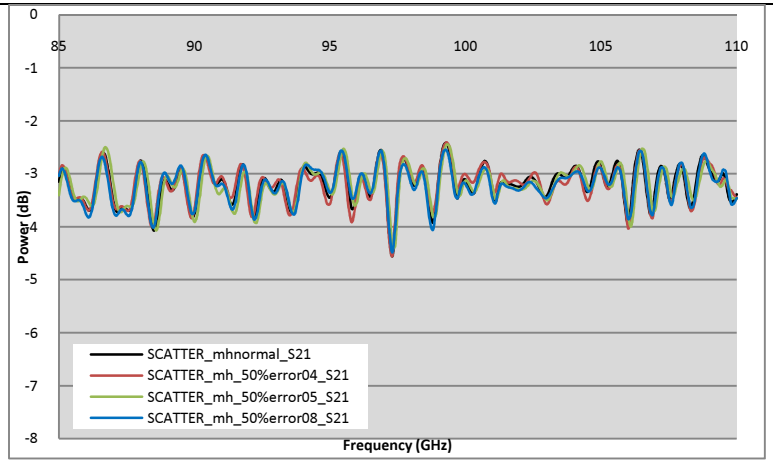	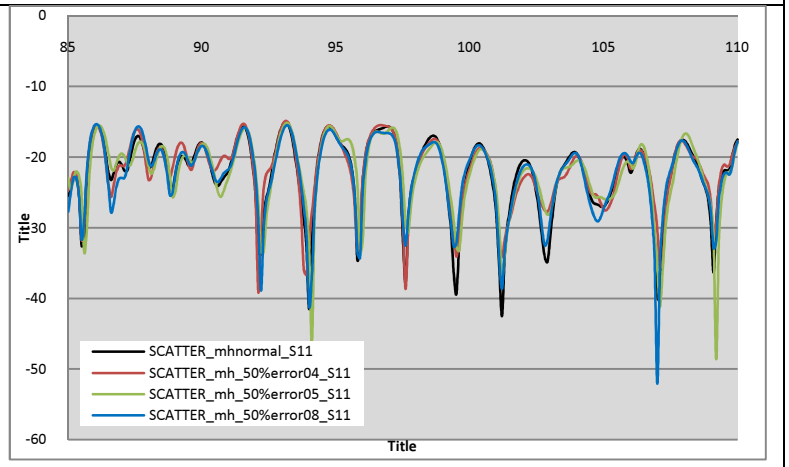

Table 4-3 - Predicted transmitted (left side) and reflected (right side) standing wave patterns for horn-horn cavities of separation distance z_1 = 10 mm (top) and z_2 = 30 mm (bottom). Results from ideal horn are plotted in black, with three random error horns plotted in red, green and blue.

z	Transmitted	Reflected
50 mm	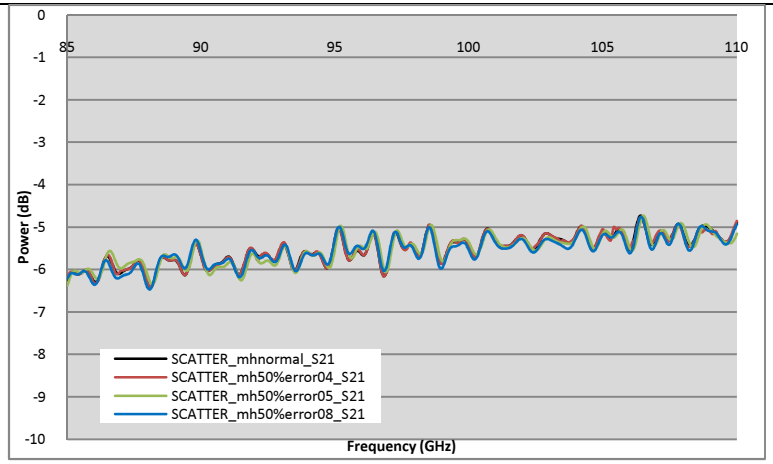	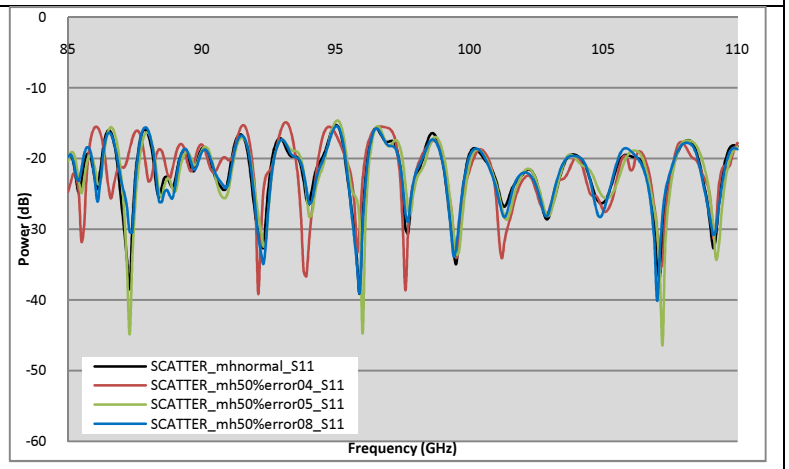

Table 4-4 - Predicted transmitted (left side) and reflected (right side) standing wave patterns for horn-horn cavities of separation distance z_1 = 10 mm (top) and z_2 = 30 mm (bottom). Results from ideal horn are plotted in black, with three random error horns plotted in red, green and blue.

The predicted standing wave patterns display similar characteristics to those from measurements. It is difficult however to establish exact agreement between the measurements and simulations due to a number of approximations made in the model. Firstly a rectangular to circular transition exists in the Thomas Keating horns measured in the lab. Obviously from Table 4-5 and Table 4-6 below the levels of predicted reflected power close to measurement and actual detail of resonances at various frequencies agree roughly for locations of maxima and minima in the pattern. This might indicate that the model sets the path lengths at which the reflections occur internally in the horn as this would set the relative location of nodes or antinodes. This would seem to indicate that the flared transition section from WR10 waveguide to circular corrugations does not have a large influence on the standing wave pattern.

It is also assumed that an exact calibration has been carried out on the network analyzer used in the experiments as the model assumes all power arriving at the waveguide is absorbed in the model and not reflected. The freespace description of the beam is also modeled using scalar Gaussian Beam Modes which will not facilitate an accurate description of near field horn interaction. At close distances the model still does a reasonable job of representing erratic or anharmonic structures in the reflected power component reproducing many features or resonances especially at a horn separation of 10 mm (circa 3 wavelengths). At increasing interhorn distances many of the higher order modes not coupling back to the horn are lost due to diffraction and the reflected power patterns smooth out and amplitude levels decrease as expected. Here the classical repeatable pattern is more evident.

The mutual pattern agreement for the four different horn geometry profiles is very close (i.e. the ideal perfect horn profile and the three randomly altered horn profiles *mh_50%error_04*, *mh_50%error_05* and *mh_50%error_08*). These results therefore indicate that despite the relative disagreement between the return loss profiles of these four horns (as shown in Figure 4-45), there is negligible effect upon the transmitted and

reflected amplitude response patterns for the various cavities using these slightly different horns geometries. Any disagreements between the various predicted patterns occur over relatively small frequencies with the overall structure over the band showing similar agreement. The exact level of disagreement for the various horns is investigated further in the next section. This conclusion indicates that despite the relatively disparate return loss profiles for the individual horns, the standing wave patterns generated with their corresponding cavities (using an identical horn in transmission and reception) are quite similar. This might suggest that the gross structure of the horn dominates the characteristics of the standing wave patterns generated.

It is difficult to clearly compare predictions with measurement for all of the various configurations. For clarity the predicted standing wave profiles for the ideal perfect horn geometry will be used to represent the entire set of predictions. This is considered a reasonable approximation given the relatively high level of agreement between the various measured standing wave patterns. The tables below illustrate comparison plots for the various predicted and measured standing wave patterns. The predicted results for the original horn profile are plotted in black.

z	Transmitted	Reflected
10 mm	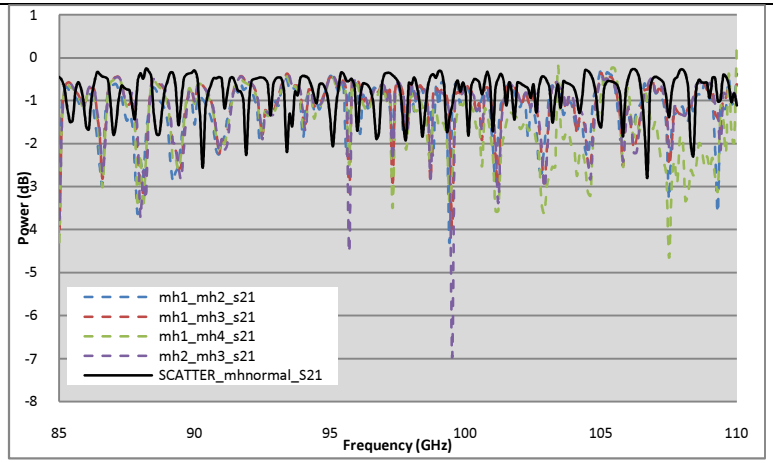	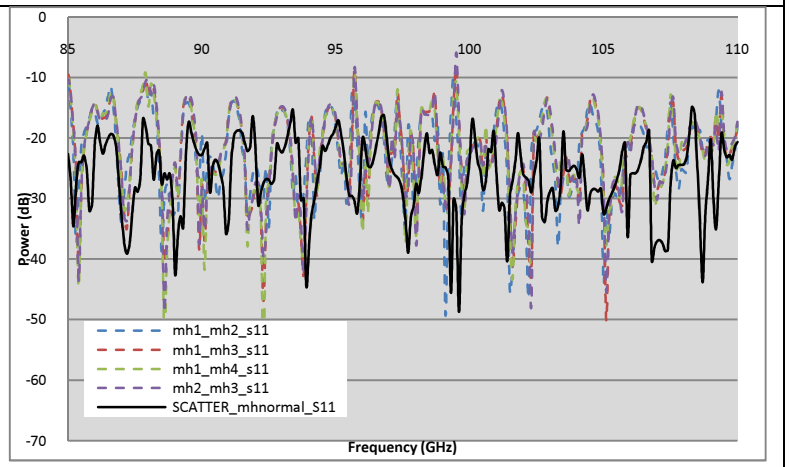
30 mm	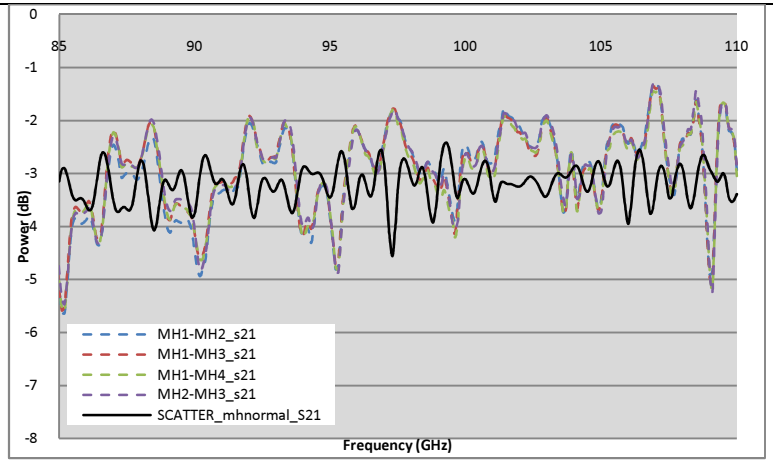	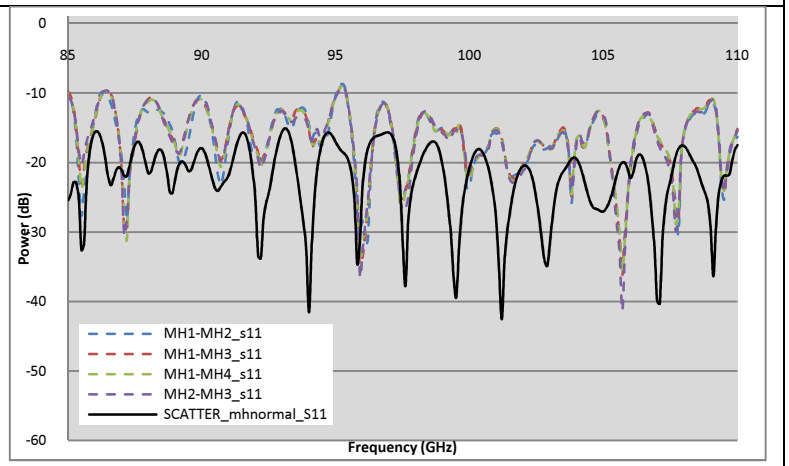

Table 4-5 – Comparisons of measured and predicted transmitted (left side) and reflected (right side) standing wave patterns for horn-horn cavities of separation distance z_1 = 10 mm (top) and z_2 = 30 mm (bottom). Predictions are for original horn only (in black)

z	Transmitted	Reflected
50 mm	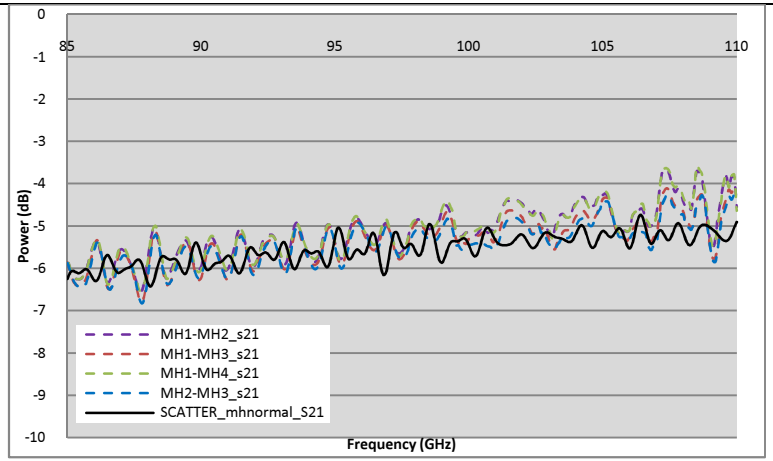	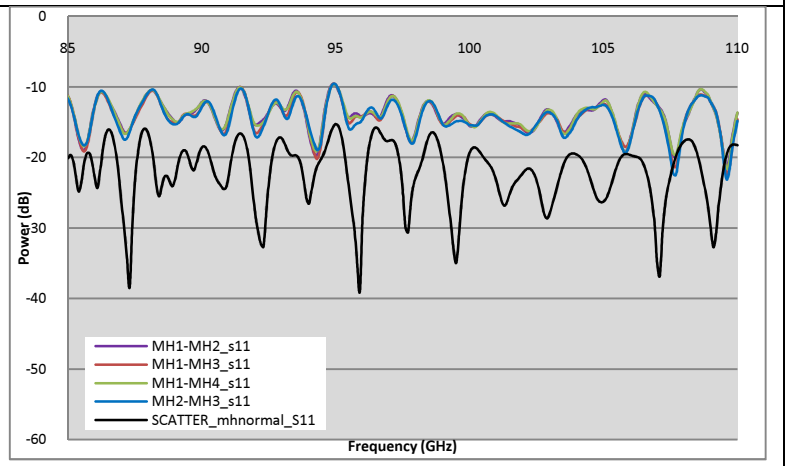

Table 4-6 – Comparisons of measured and predicted transmitted (left side) and reflected (right side) standing wave patterns for horn-horn cavity of separation distance z_3 = 50 mm Predictions are for original horn only (in black)

The mode match predictions for the cavity exhibit varying degrees of agreement with experimental measurements. Overall similar levels of reflected power are predicted and measured and similar agreement between maxima and minima across the band is observed. For the first cavity (z_1 = 10 mm) the predicted model compares poorly with experiment. This is most pronounced for the transmitted standing wave pattern. The agreement is improved for the reflected profile where the predicted model reproduces the locations and amplitudes of many of standing wave resonance dips. This is most apparent in the lower frequency range for the cavity i.e. from 85 GHz to approximately 100 GHz. However, this agreement does not extend to the shape of the resonance amplitude peaks. The predicted model closely estimates the average amplitude levels of the experimental standing wave patterns. As this inter-horn is distance is quite near field and the free space scalar capability will not be capable of getting the all interaction correctly. Nonetheless the frequency maxima and minima are well reproduced.

For the 30 mm separation again the transmitted power levels predicted with SCATTER do not match the structure of the measured profile but the correct levels are reproduced. As for the previous results at 10 mm separation the predicted reflected power profile reproduces the frequency maxima and minima within the same frequency range (85 GHz to 100 GHz).

When the horn separation is widened to 50 mm and therefore there is much less coupled radiation the model underestimates the level of reflected amplitude across the band but does however exhibit similar locations/frequencies of a large proportion of the amplitude resonances – in keeping with the level of agreement between model and measurement for shorter separation distances. The model accurately predicts the average level of transmitted power; however, it does a very poor job of predicting shape and locations of resonance patterns.

4.5.1 Eigenmodes of Horn-Horn Cavity

In this section we extend a framework developed by [89], [90] and extended [91] to these simple cavities containing corrugated horns, where the concept/notion of eigenmodes and eigenfields within the context of systems in which standing waves are present is discussed. In [91] this technique was employed to investigate the form and shape of these cavity or eigenmodes. An eigenmode is hereby defined as a natural mode of the system that is sustained after multiple reflections. In the horn-horn cavity setup there clearly exist standing waves between the two horns. The power distributions that do not couple to either the transmitting or receiving horn are considered the eigenmodes of the system. These eigenmodes essentially propagate unaltered on a round trip after a single reflection from each horn with a phase delay of $2n\pi$, where n represents the number of round trips, thus meeting the condition for constructive interference.

Through analysis of the cascade matrix calculations (c.f. Section 4.2) the form and shape of such an eigenmode can be identified [91]. Looking at the cascade matrices (Equations 4.18) it is clear that part of these matrices must include the round trip component of the system i.e. that component that is sustained upon a roundtrip within the cavity. In the case of the transmitted amplitude response for the horn-horn cavity we are concerned with the S_{21} component of the cavity scattering matrix. In the cascade matrix calculation of the cavity scattering matrix, the S_{21} component is given as

$$\left[S_{21}^{c}\right]=\left[S_{21}^{b}\right]\left[[I]-\left[S_{22}^{a}\right]\left[S_{11}^{b}\right]\right]^{-1}\left[S_{21}^{a}\right] \tag{4.95}$$

From [91] the term $\left[S_{22}^{a}\right]\left[S_{11}^{b}\right]$ in Equation 4.95 represents the multiple reflections of radiation within the cavity. If this component is zero (i.e. $\left[S_{22}^{a}\right]\left[S_{11}^{b}\right]=[0]$) then this equation reduces to the product of the transmitted power of the two subsections $\left[S_{21}^{b}\right]\left[S_{21}^{a}\right]$, thereby giving the transmitted power for the overall system S^{c}.

The eigenmode is seen as a solution to the matrix equation:

$$S.a = \lambda.a \tag{4.96}$$

where S is the round trip component of the complete scattering matrix, a are the eigenvectors and λ are the corresponding eigenvalues. In [91] the eigenvalues and eigenvectors of the roundtrip component were analysed as the transmitted amplitude pattern passed through a resonance or transmission minimum. When compared to the non-resonant case, (away from resonant dip) it was noted that the complex arguments of certain eigenmodes were zero at individual resonances, which indicated that this eigenmode was responsible for the resonance dip. Technically, the argument is rarely found to be exactly zero, and an upper numerical bound is employed to signify zero. In [91] this upper bound was taken as 0.02. The spatial form of these resonant eigenmodes E_{res} can be constructed from:

$$E_{res} = \sum_n \psi_n P_n \tag{4.97}$$

where ψ_n is the modal basis set and P is the column of eigenvectors that correspond to the resonant eigenvalue. For a circularly symmetric cavity the basis mode set are the Associated Laguerre-Gaussian modes described earlier in Section 2.14. When this eigenmode is analytically removed the resonance in question was significantly reduced. The eigenmode is removed by setting it to zero and the roundtrip component is then re-composed and re-inserted back into the cascade matrix. This novel technique therefore presents a theoretical method of removing the roundtrip component analytically and allows one to plot the spatial profile of the standing wave itself, which is interesting if not very practical in actually damping or removing reflected power. If this technique is applied to a laser cavity, for example, the spatial form of the reflected or cavity modes is that of the classical solution of Hermite Gaussian or Laguerre Gaussian depending on the symmetry conditions of the reflecting walls.

This technique could also be tentatively employed here to further investigate the effect of altered horn geometries upon the amplitude response patterns for a cavity

arrangement. The cavity with the shortest separation distance of 10 mm is analysed here for the four different horn geometry profiles and used to see if the spatial form of the reflected power in each of the slightly different geometries is similar in form.

So to look into this application we take a prominent resonant dip in transmission and investigate the phase of the decomposed eigenmodes and try to isolate the eigenmode responsible for that particular resonance. The transmitted amplitude null investigated occurs approximately between 90 and 91 GHz for all horn geometries, although as will be shown later the exact frequency at which the null occurs varies from cavity to cavity. A sequential search for an eigenvalue with zero argument was conducted for the horn-horn cavity of the original horn profile. At 90.25 GHz the third eigenvalue had an approximate zero argument (less than 0.02). It was suspected that this was the eigenmode responsible for the transmitted amplitude dip. The eigenvalues for the other cavities were also predicted at this specific frequency assuming that they would also exhibit a similar eigenvalue decomposition with equivalent zero argument. In Table 4-7 below the absolute values and arguments for the first nine eigenvalues of the four horn-horn cavities are listed. The absolute power of the eigenvalue can be used as an indication of the relative level of power carried by that mode and the eigenmodes are usually ordered with decreasing levels of power

From these results it is clear that the argument of the third eigenvalue of the other three cavities is no longer zero. This thus leads to two possible conclusions. Firstly, the third eigenmode is no longer responsible for the amplitude null in the other cavities. However, from Table 4-7 there are evidently no other eigenvalues with zero arguments at this frequency. The next conclusion is that the zero argument condition, whether it is the third or some other eigenvalue, has been met at another frequency. This second conclusion is more likely given the minor differences in the exact frequency at which the amplitude null for the four different cavities occurs. This is illustrated below in Figure 4-46, where the transmitted amplitude response patterns for the four horn-horn cavities are plotted from 90-91 GHz.

igenvalue	1	2	3	4	5	6	7	8	9
Cavity	**mh_original**								
Absolute Value	0.678	0.667	0.611	0.2521	0.159	0.136	0.021	0.014	0.001
Argument	-0.56	0.992	0.0	0.356	-0.800	-0.031	-0.885	0.421	-0.472
Cavity	**mh_50%error_04**								
Absolute Value	0.69	0.648	0.647	0.239	0.164	0.136	0.021	0.013	0.002
Argument	-0.522	-0.959	-0.069	0.365	-0.805	-0.0247	-0.853	0.464	-0.293
Cavity	**mh_50%error_05**								
Absolute Value	0.697	0.637	0.576	0.288	0.165	0.139	0.020	0.012	0.001
Argument	-0.399	-0.894	0.229	0.415	-0.72	0.033	-0.892	0.523	-0.252
Cavity	**mh_50%error_08**								
Absolute Value	0.691	0.689	0.572	0.265	0.163	0.142	0.018	0.014	0.001
Argument	0.958	-0.53	0.038	0.313	-0.816	-0.05	-0.948	0.413	-0.341

Table 4-7 - Absolute value and argument of the first nine eigenvalues for roundtrip component at the frequency for a resonant dip at 90.25 GHz for the horn-horn cavity of separation distance z_1 = 10 mm.

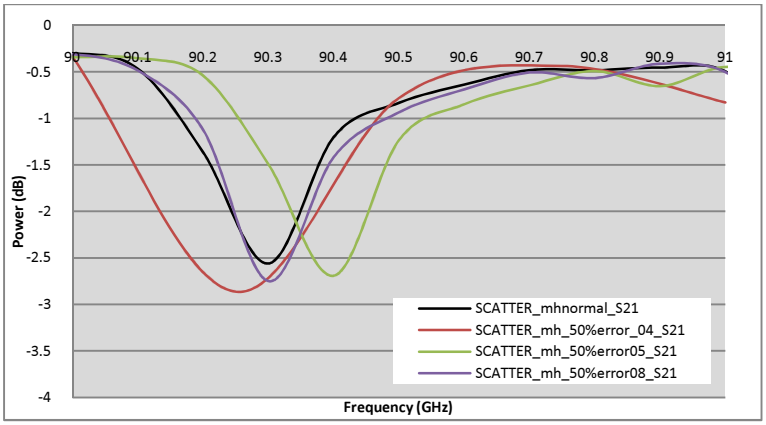

Figure 4-46 - Resonance dip for the four horn-horn cavity arrangements

A simple test to determine if the third eigenvalue is the one responsible for the amplitude null for all cavities was to analytically set it to zero for all cavities and re-calculate the response patterns with this mode removed. The newly altered response patterns are plotted below in Figure 4-47 as solid lines with the original response patterns plotted in broken lines for comparison.

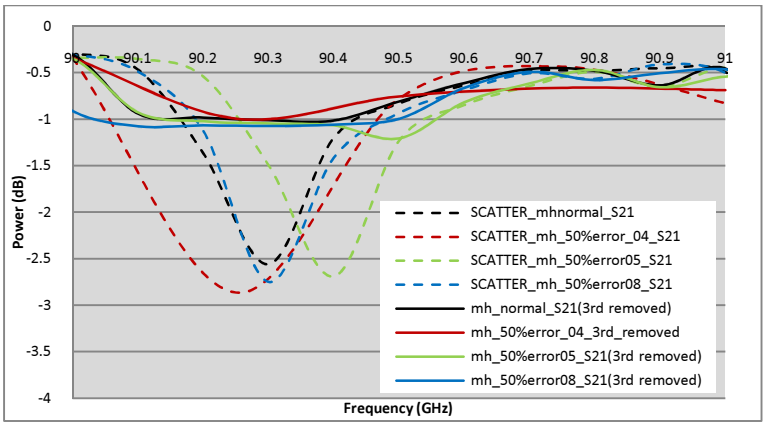

Figure 4-47 - Original resonance dips for various horn-horn cavity arrangements (broken lines) compared against removed resonance dip with 3rd eigenmode removed (solid lines)

The amplitude response dip is effectively removed for all cavities, thus indicating that the third eigenmode is responsible for the resonance dip in all instances. Similar calculations for other eigenvalues revealed no significant alteration to the amplitude response pattern, thereby further confirming the responsibility of the third eigenvalue for this amplitude dip. As one moves across the band it is noticed that different resonant dips are linked with different eigenmodes and continuous decomposition of the reflected power is required to identify the responsible eigenmode.

This technique allows the spatial form of the reflected power component to be visualised theoretically and the shape of the eigenmodes for the three cavities that exhibited the zero argument condition for the third eigenvalue (i.e. *mh_original*, *mh_50%error_05* and *mh_50%error_08*) may be determined using Equation 4.97 where P is the column of eigenvectors for the roundtrip component of each cavity which corresponds to the specific eigenvalue. The Associated Laguerre-Gaussian mode set was chosen as the basis set for the field description, with the beam parameters being defined at halfway between the horns at 5 mm propagation distance. The plots displayed below in Figure 4-48 are the distributions of the first four eigenmodes (i.e. the fields formed from the first four columns of eigenvectors) for the three horn-horn cavities.

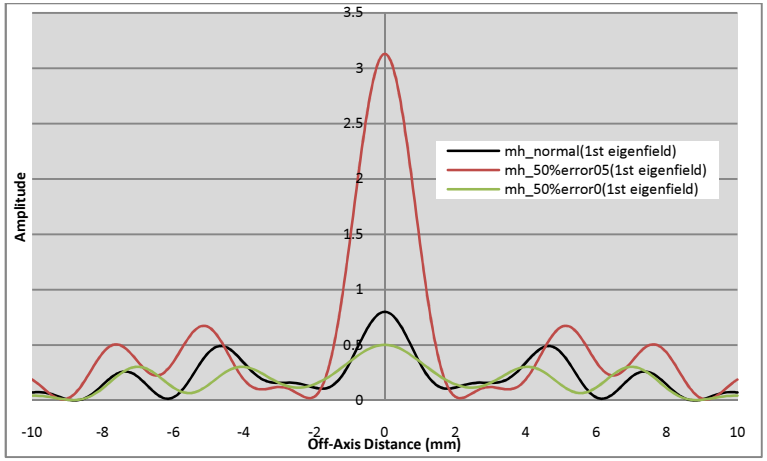

(a)

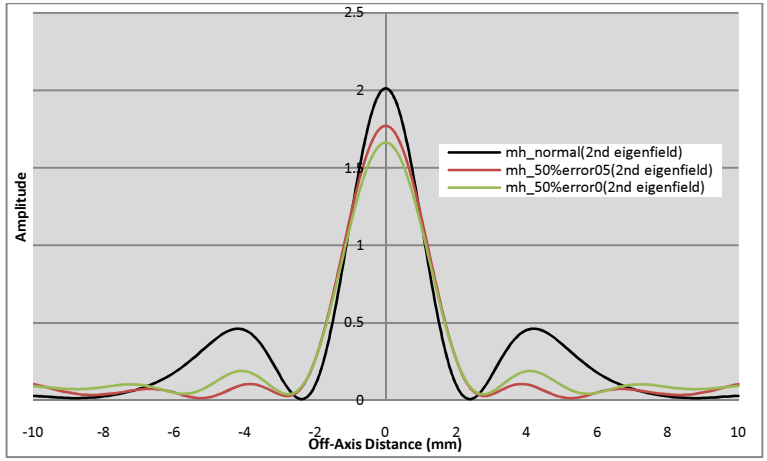

(b)

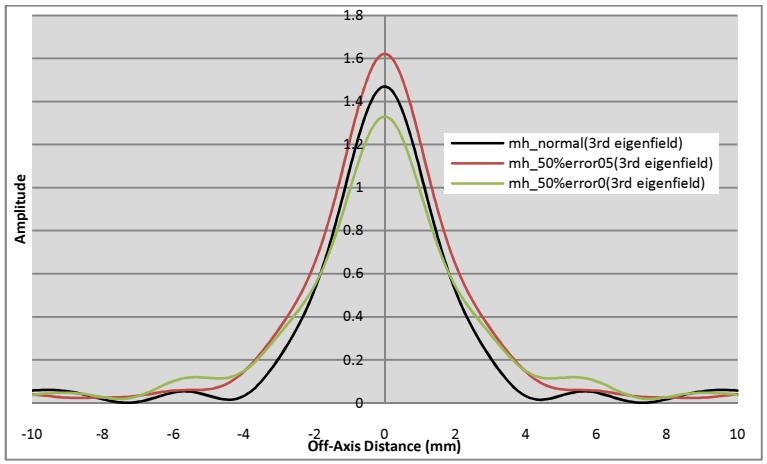

(c)

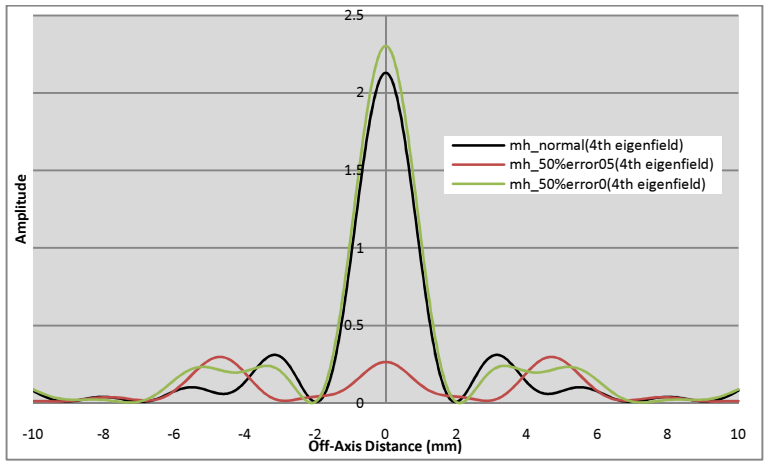

(d)

Figure 4-48 - Comparison plots of first four eigenmodes for three horn-horn cavities that exhibited the zero argument condition of the third eigenvalue. *(a):* 1st eigenmode, *(b)*: 2nd eigenmode, *(c):* 3rd eigenmode, *(d):* 4th eigenmode.

It is difficult to draw any firm conclusions about the differing shapes of the eigenmodes for the different horn geometries. It can be noted that the shapes of the first, second and fourth eigenmodes widely varied for each cavity arrangement and that for third eigenmode which shows very similar Bessel type beam shapes for all cavities, perhaps collocating with responsibility for the transmitted amplitude dip at this particular frequency. Any definite conclusions need more investigation and testing to try to understand the meaning of the eigenmode shapes. It is important to note that the cavity under investigation here is made up of a horn with a radius (including aperture lip) of 8 mm and all the power is contained within this range.

4.6 Modelling a Stray Light Baffle

In this section we predict the reflected and transmitted amplitude response profiles for a stray light baffle structure using the mode-matching technique and compare these predictions with measurements from an equivalent laboratory arrangement. A stray light baffle is an element commonly employed in submillimetre systems to prevent any radiation that is unpredictably scattered within the system from coupling to the receiver elements. For example, in the HIFI instrument on the Herschel Space Observatory a baffle is used along the LO chain to minimise scattered light in the system.

The baffle structure modelled and measured here is comprised of four annular ring structures with inner radius r_{inner} = 30 mm and outer radius r_{outer} = 100 mm. The annular rings are evenly spaced by a distance of Δz = 15.0 mm. The annular ring structures are made from aluminium sheets with an approximate thickness of 1.0 mm. The baffle is formed by affixing these annular rings along two threaded rods with nuts holding them in place. Balsa wood spacers are used to reinforce the spacings between the rings, being effectively transparent at around 100 GHz. The baffle is placed midway between two unmatched horns that form a horn-horn cavity similar to those modelled in {ref previous section} albeit with greater separation distances between the horns. As with the previous horn-horn cavities, the horns used are the 94 GHz conical corrugated horns and the amplitude response patterns are recorded using the VNA measurement system. The cavity system with baffle included is shown below in Figure 4-49

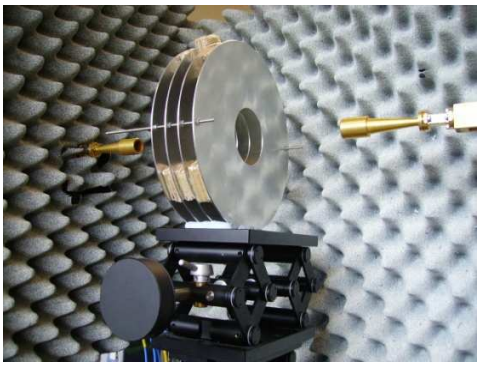

Figure 4-49 - Stray light baffle structure located between two unmatched corrugated horns within VNA measurement facility

Although the distances between the annular rings is fixed at 15.0 mm the model for this system requires the planes of the truncating apertures to be infinitesimally thin. Therefore the actual propagation distance between the truncating apertures is given as Δz = 49.0/3 = 16.33 mm. The scheme for the layout of the baffle cavity is illustrated below in Figure 4-50

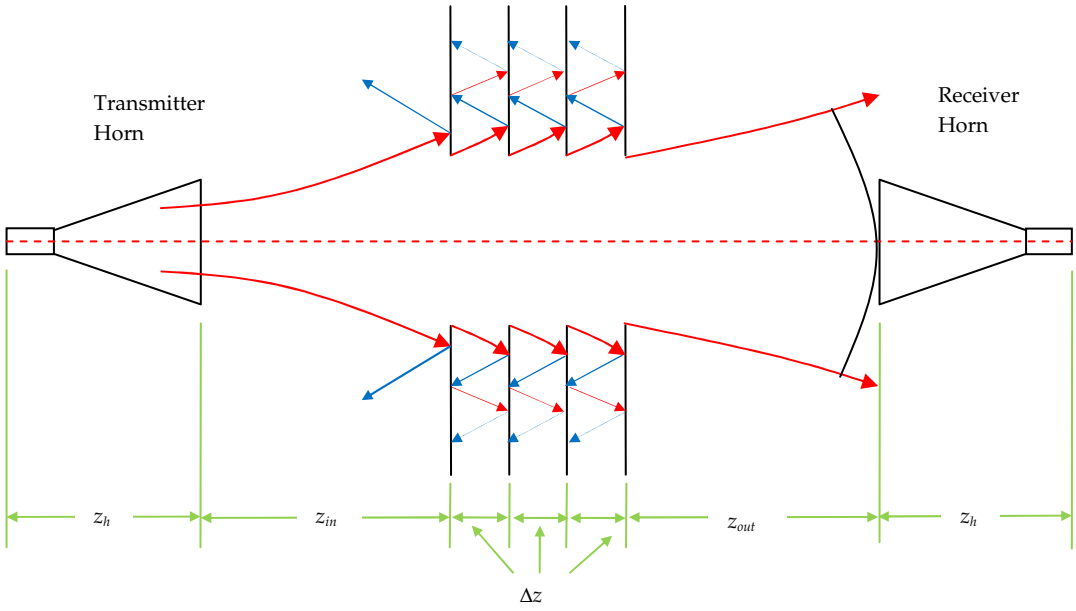

Figure 4-50 - Quasioptical representation of the stray light baffle structure placed between two unmatched corrugated horns.

Two configurations of this baffle cavity system were modelled using the mode-matching technique and measured experimentally. These two systems are defined solely by the input and output distances (which are equal given that the baffle is located midway between the horns):

1. $z_{in\text{-}1} = z_{out\text{-}1}$ = 100.0 mm
2. $z_{in\text{-}2} = z_{out\text{-}2}$ = 60.0 mm

These two configurations were chosen to provide different levels of truncation for the incident beam from the transmitting horn. Using ABCD analysis the Gaussian beam approximation of the propagating beam is calculated for the chosen upper and lower frequency limits of the horns. These beam parameters are listed below in Table 4-8.

Parameter	Unit		Baffle # 1		Baffle # 2	
Frequency	GHz		85	110	85	110
Horn aperture radius: a	mm	7.134				
Waist at horn aperture: w_{ha}	mm	4.59				
Phase radius of curvature at horn aperture: R_{ha}	mm	80.0				
Beam radius at first aperture: w_{01}	mm		25.5	20.23	15.72	12.64
Edge taper at first aperture: Te_{01}	dB		-12.0	-19.11	-31.65	-48.97
Beam radius at second aperture: w_{01}	mm		29.55	23.38	19.68	15.69
Edge taper at second aperture: Te_{01}	dB		-8.95	-14.29	-20.18	-31.73
Beam radius at third aperture: w_{01}	mm		33.61	26.56	23.69	18.81
Edge taper at third aperture: Te_{01}	dB		-6.92	-11.08	-13.92	-22.08
Beam radius at fourth aperture: w_{01}	mm		37.68	29.74	27.73	21.96
Edge taper at fourth aperture: Te_{01}	dB		-5.51	-8.84	-10.16	-16.21
Beam radius at receiver horn: w_{01}	mm		62.71	49.35	42.67	33.65
Phase radius of curvature at receiver horn: R_{ha}	mm		250.27	250.99	170.88	171.93

Table 4-8 - Gaussian beam parameters for transmitted horn beam propagating throughout two baffle cavity configurations. Baffle 1 corresponds to 100 mm distance while baffle 2 corresponds to a 60 mm distance.

The mode matching model for this system was developed in the same manner as for the horn-horn cavities in Section 4.5 with the beam scattering at the truncating apertures determined using the truncating aperture scattering matrix described previously in Section 4.2.4. The approximation made for the truncating aperture scattering matrix in Equation 4.43 is that the outer radius of the aperture is infinite. This approximation is considered valid for these baffle cavity examples where the outer radius of 100.0 mm is more than sufficient to ensure there is practically no radiation scattered beyond the outer rim of the baffle. It is evident from Figure 4-50 that any possible scattered radiation will not be coupled to the receiver horn due to high angular scattering and is thus considered lost. The order of the scattering matrices is thus described below in Figure 4-51. The component scattering matrices are cascaded in the usual manner to provide a complete scattering matrix of the baffle cavity.

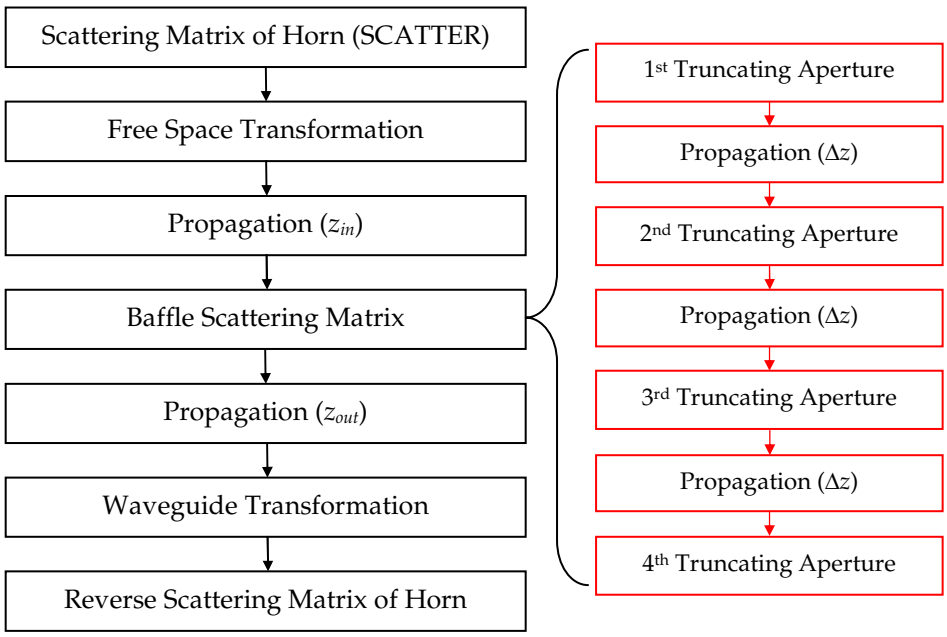

Figure 4-51 - Flow chart illustrating order of component scattering matrices for baffle cavity structure

The reflected and transmitted amplitude response patterns as predicted from theory and measured in the laboratory are compared below in Figure 4-52.

The predicted S_{11} profile for baffle # 1 exhibits some extra resonance structures of higher amplitude at approximately 92 GHz and 101 GHz that are not seen in the measured results. As with the earlier arrangement with just two horns facing each other exact agreement is not observed between the measured and simulated cases. Certainly the extra resonances seen in the simulated data at 92 GHz and 101 GHz are features not reproduced in the experimental measurements. We do observe that the levels of power coupling between the horns are predicted and some features or characteristics of the standing wave pattern are observed.

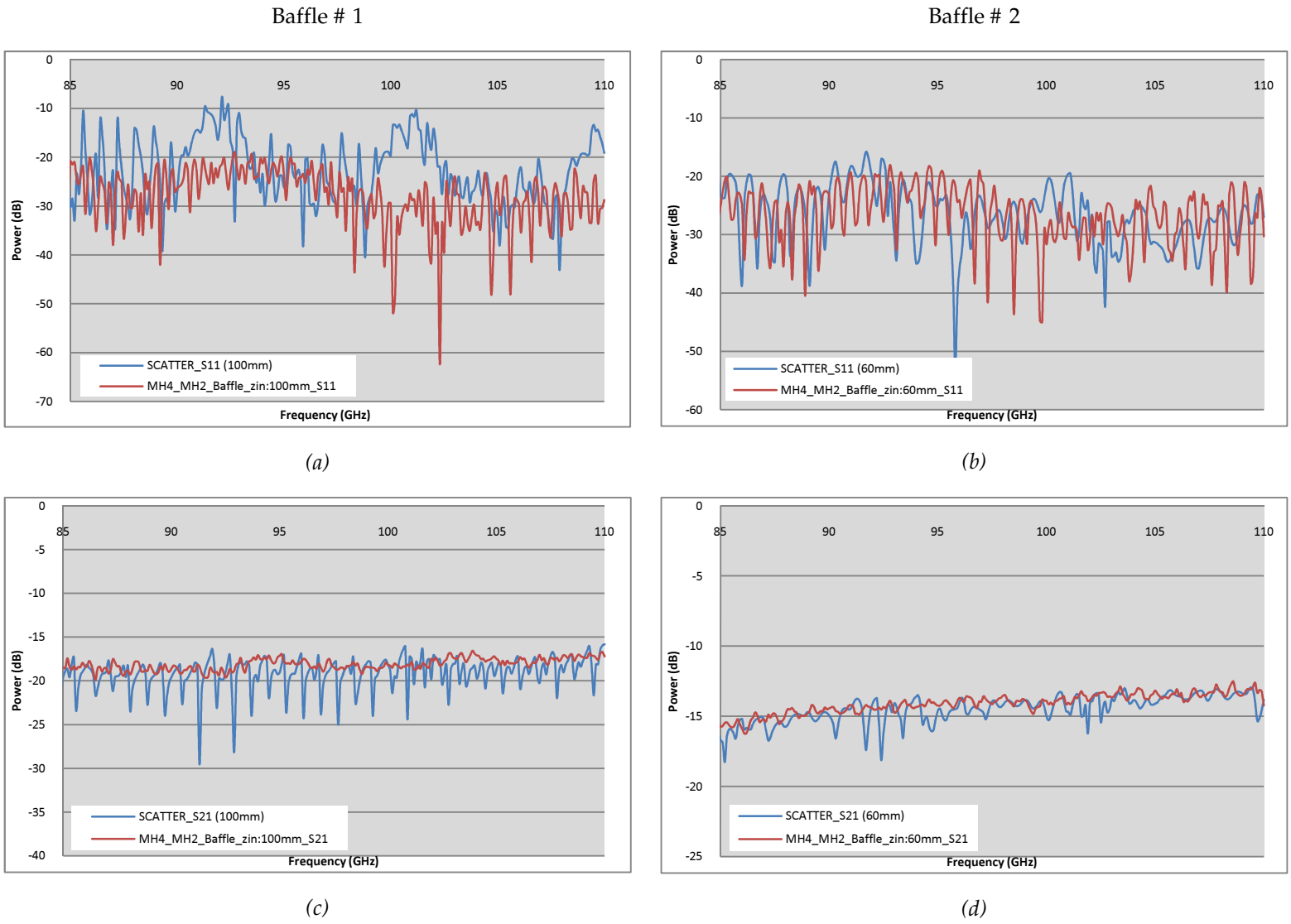

Figure 4-52 - Predicted (in blue) and measured (in red) amplitude response patterns for reflected S11 component (top) and transmitted S21component (bottom)

A number of factors again need to be considered in making the comparison between theory and experiment. Firstly we do not see agreement between the horns in isolation due to the reasons outlined earlier including the extra transition region in the horn not modelled and the high degree of sensitivity of the standing wave pattern to the horn geometry. In addition here alignment of the horns and baffle is difficult and this could alter the features produced in the standing wave pattern. Also in the model the baffle outer radius was infinitely wide and so the radiation reflects outwards in a different way to the experimental arrangement. This could account for the higher resonances seen at 92 and 101 GHz. Further analysis where the correct annular ring using the correct radii needs to be implemented to see if the effect disappears. The transmission levels are well reproduced in the model and closely agree with the measured data over the band. This example illustrates that although the exact resonances are not reproduced the levels and degree of reflection and transmission are well represented. The tolerances of such a system were difficult accurately account for. The placement of the baffle structure within the cavity was achieved manually by hand and thus degrees of freedom were undoubtedly introduced. An extension of this work would require a quantification of these alignment tolerances and an appropriate error analysis performed.

To clarify the effect of the structure of the baffle upon this cavity arrangement the entire baffle was removed and the S-parameters re-calculated using SCATTER and the corresponding measurements taken. This was performed for Baffle #1 arrangement, where the deviances of the S_{11} profile between theory and experiment are most pronounced. Removing the baffle structure essentially creates a simple horn-horn cavity exactly like those analysed in Section 4.5. The comparison plots for this cavity arrangement are illustrated below in Figure 4-53.

The comparison between predictions and measurements in Figure 4-53 reveal some interesting results. With the baffle structure removed the predicted S_{11} profile in Figure

4-53(a) exhibits a greatly altered structure to that seen in Figure 4-52 (a) above. This indicates the effect of the baffle structure on the returned power is dominant. However, the agreement of prediction and measurement here is poor, with the measurement data exhibiting a strong resonance pattern between approximately 88 GHz and 102 GHz. This may still be attributed to improper alignment between the horns, as was indicated earlier. Comparing the measured profiles of Baffle #1 with and without the baffle structure in Figure 4-54 we can see that the effect of the baffle upon power reflected back into the receiver horn is subtle. This makes sense physically as that power reflected by the baffle structures will radiate outward past the aperture of the receiving horn and is essentially lost. It may be that this baffle does not truncate the beam significantly enough to see any of the extra resonant structures predicted by theory. However, as we shall see in the following section the effect of the baffle on the S_{11} profile, although apparently negligible, does exist and can be quantified. The predicted transmission profile in Figure 4-53 (b) closely reproduces the measurement profile over the entire band.

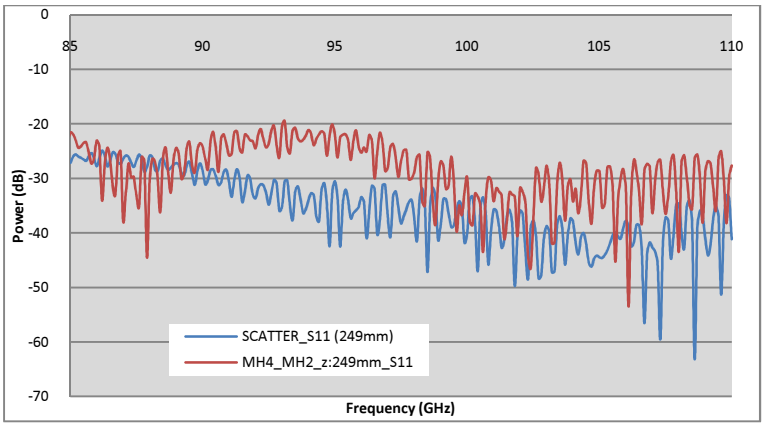

(a)

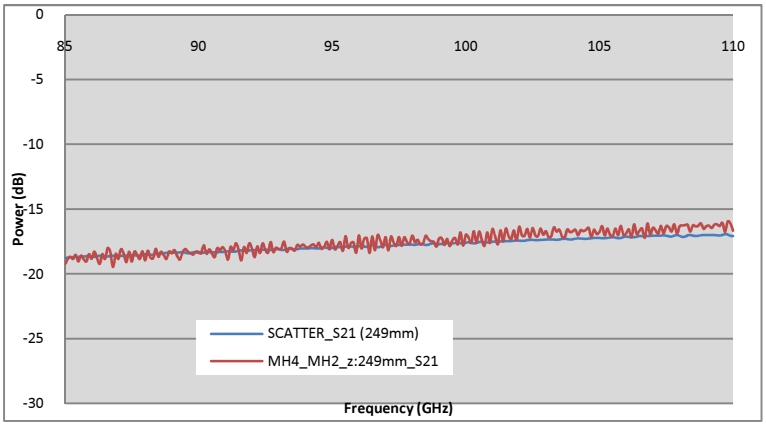

(b)

Figure 4-53 – Comparison of predicted (blue) and measured (red) S_{11} (top) and S_{21} (bottom) patterns for horn-horn cavity with interhorn distance z: 249 mm i.e. Baffle # 1 with baffle structure removed.

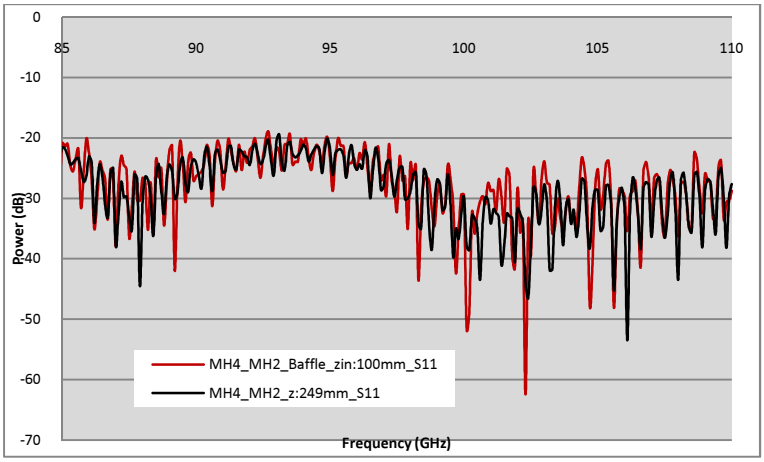

Figure 4-54 - Comparisons of measured S_{11} profiles for Baffle #1 both with (red) and without baffle (black)

4.6.1 Fourier Signal Analysis of Baffle Response Patterns

The stray light baffle structure essentially operates/can be interpreted as a spatial filter, permitting only the desired paraxial/centralised beams through while removing any possible undesired higher order beam structures. With this concept in mind, the amplitude response patterns from this baffle structure represent the reflected and transmitted signals in the spatial frequency domain. The transmission and reflection properties of the system are encoded within this frequency spectrum and they can be analysed using Fourier signal analysis. The Fourier Transform [FT] of a time variant signal will convert it to the frequency domain. Hence the Inverse FT of the frequency response signal will convert it to a time variant signal. This temporal function is then converted into the spatial domain by dividing by the speed of light c. The spatial sampling Δx is dependent on the frequency sampling Δf by the following relation:

$$\Delta x = \frac{1}{N}\frac{c}{\Delta f} \tag{4.98}$$

where N is the total number of sampling points and c is the speed of light. For the measured and predicted amplitude response patterns the frequency step size was 0.1 GHz (10^8Hz) over the bandwidth of the cavity (85 GHz to 110 GHz), giving 351 sampled points. This gave a spatial sampling of 8.57 mm. The transmitted and reflected spatial signals for the two different baffle configurations were calculated from the measured and predicted amplitude response spectra and are plotted below in Figure 4-55. The measured data are plotted as coloured broken lines while the predicted data are plotted as solid black lines. There are a set of four measurement results taken for each baffle arrangement, each of which was obtained after resetting the baffle and horns. This was done to ensure the best possible alignment of all optical elements.

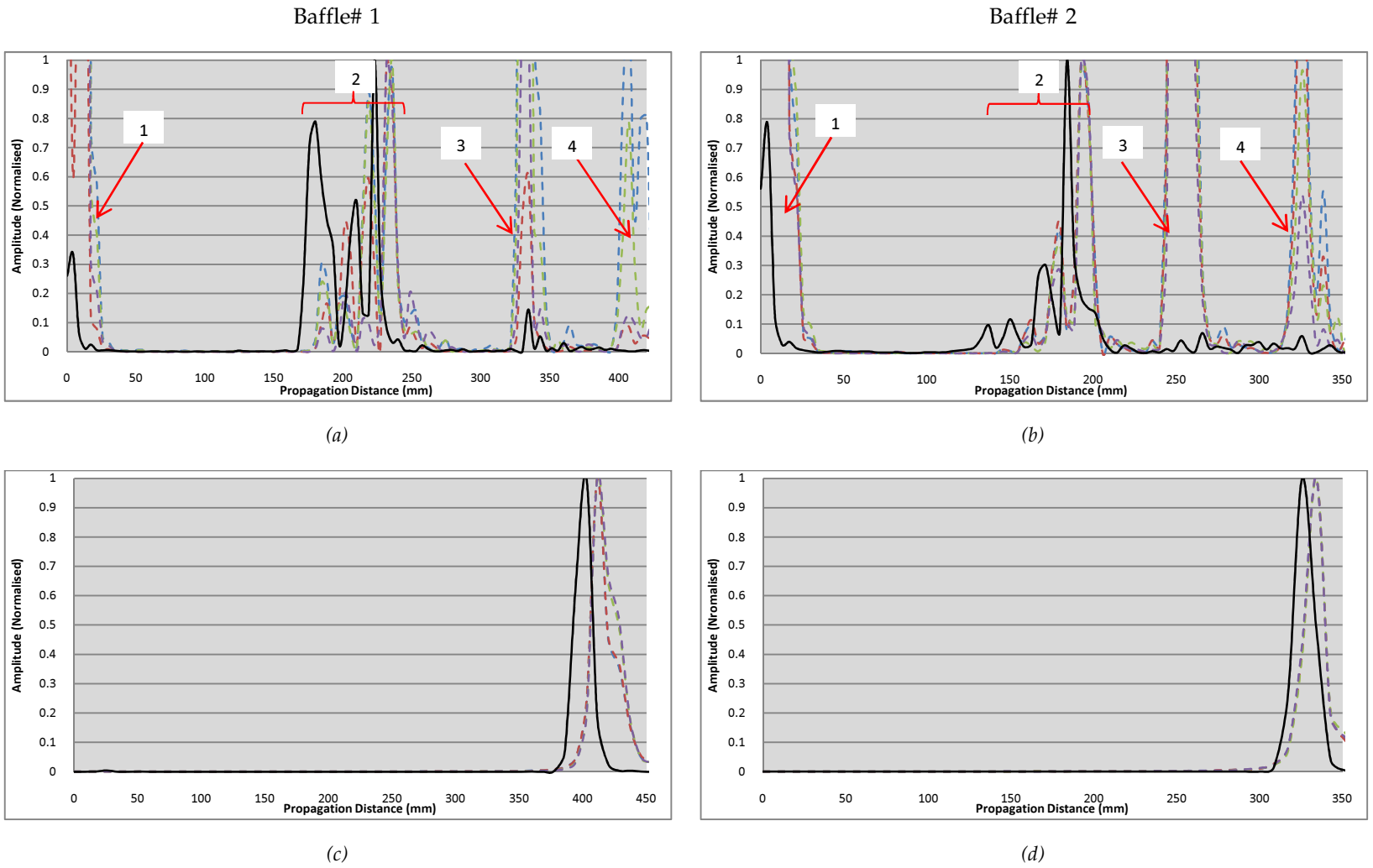

Figure 4-55 - Spatial amplitude response patterns for baffles# 1 and 2 - reflected response patterns: (a) and (b), transmitted response patterns: (c) and (d). Measured results are plotted as broken coloured lines while mode-matching predictions are plotted as a solid black line. Peaks in reflected plots (a) and (b) represent locations of reflecting structures of horns and baffle structure. Peaks in transmitted plots (c) and (d) represent location of throughput coupling to receiver horn.

The reflected spatial amplitude response patterns highlight the structures within the baffle cavity which partially reflect the beam travelling from left to right. The reflecting structures are numbered one to four and refer to the sequential elements within the baffle cavity from which the propagating beam is reflected.

The first reflection structure in Figure 4-55 (a) and (b) represents the partial reflection of the beam by the waveguide transition section of the transmitting horn. This occurs at our reference distance of zero corresponding to the throat of the transmitting horn. The second reflection structure is a group of amplitude peaks representing the partial reflection by each of the four annular rings that comprise the baffle located 100 mm in front of the horn that has an axial length of 80 mm. The axial distance of these structures approximately agrees with the layout of the baffle structure. In Baffle# 1 the first annular ring is located a distance $z_h + z_{in\text{-}1} = 180$ mm from the back of the horn, while for Baffle# 2 the distance is $z_h + z_{in\text{-}2} = 140$ mm. In Figure 4-55 (a) the measured data show four peaks representing each of the four annular structures. The predicted data show only three peaks however given relatively large sampling distance of 8.57 mm we can reasonably conclude the missing structure is grouped with one of the others i.e. they overlap. The correct inter baffle distance is also seen at 16 mm intervals In Figure 4-55 (b) the predictions and measurements both display four amplitude peaks. The third reflection structure represents the reflection of the beam at the aperture of the receiver horn at a distance of $z_h + z_{in\text{-}1} + 3*\Delta z + z_{out\text{-}1} = 329.0$ mm for Baffle# 1 and $z_h + z_{in\text{-}2} + 3*\Delta z + z_{out\text{-}2} = 249.0$ mm for Baffle# 2. The fourth reflection structure represents the reflection of the beam at the back of the receiver horn at a distance of z_h beyond the aperture. The transmitted spatial amplitude structures for Baffles 1 and 2 in Figure 4-55 (c) and (d) display a single peak that represents the complete transmission of the beam from the back of the transmitter horn to the back of the receiver horn which coincides with the final reflection structure in Figure 4-55 (a) and (b). There is a slight spatial disagreement between the predicted and measured data. This is accounted for by the extra propagation distance of approximately 6.5 mm by the rectangular to circular waveguide

transition section in the feed horn that is not taken into account by the SCATTER code. With this correction applied to the results there is good agreement between measurements and predictions from the mode-matching technique.

It should be noted that there exists significant disagreement between the relative amplitudes of the various reflection peaks for prediction and measurement in Figure 4-55 (a) and (b). The data were normalised for the amplitude peaks of the truncating baffle structure so as to convey the exact positions of the various structures. This is evident from the measured data where the first, third and fourth peaks are scaled above unity. The predicted results display reflection peaks of greater amplitude than displayed by the measured data. This is attributed to the approximation made by the truncating aperture scattering matrix (Equation 4.43) which assumes an infinite outer rim for the aperture element. This would confine reflected power within the walls of the individual baffle gaps and thus contribute to the large reflection peaks. A solution to this problem would be to redefine the truncating aperture scattering matrix as a true annular structure by integrating between the inner and outer radii. There likely exists some degree of alignment and/or pointing error for the measurement set up which would inevitably lead to a degree of unpredictable beam scattering which would account for the slight differences between prediction and measurement.

The results from this Fourier signal analysis provide an excellent confirmation of the mode-matching theory against experimental measurement for a complicated optical structure. It is also a powerful tool to investigate where reflections occur in an optical system and to predict the wavelength or frequency of a standing wave baseline. This is particularly important for spectrometers where this baseline can influence the characteristics of the measured spectra. In applying the Fourier signal analysis to the patterns predicted by SCATTER it also verifies all the overlap integrals and use of complex conjugates to take care of inversion of phase fronts upon reflection as if this was carried out incorrectly information would fall in the negative Fourier space and equate to negative distance values. This would mean that the predictions would be

unphysical and this serves as a good check to verify the scattering technique applied throughout this chapter.

4.7 Conclusion

In this chapter a theoretical framework to analyse the standing waves within a quasioptical cavity arrangement is described. The theory of mode-matching as it applies to waveguide structures is described. The complete scattering matrix description of feed horn cascaded with freespace transformation matrices is given, which when combined with the free space scattering matrices of beam guide components allows for the forward and backward propagating power to be tracked. The technique of combining scattering matrices, known as cascading, is verified by accurately describing the reflectance profiles for several multiple thin-film arrangements, which exhibit increased or decreased reflectance over a chosen finite bandwidth.

The method of describing the S-parameters of a corrugated horn including freespace transformation to the appropriate free space mode set is employed to model the standing waves set up between two uncoupled horns at close propagation distances. Such horn-horn cavity arrangements have been previously studied by [30], [36] but were concerned with the standing wave patterns within the spatial domain as the horns were moved relative to one another for a fixed frequency. Arguing for a more physically applicable system, the horn-horn cavities modelled and measured in this chapter maintained fixed inter horn distances while the frequency domain resonances across the bandwidth of the horns were analysed. Multiple reflections were set up between the horns, leading to quasi-systemic standing wave patterns. Disparities between the measured and predicted return loss profile of an individual horn remain unresolved. This has been accounted for by the effect of the waveguide transition region at the back of the horn. Further investigation is warranted here through alternate means (FDTD) to verify this hypothesis. In an attempt to resolve this disparity several variations of the *94 GHz* feed horn structure were modelled using SCATTER. The

purpose of this test was to determine the robustness of the reflection and transmission properties of the horn with the introduction of minor (<0.5%) surface errors to the corrugations. The effect of these errors on the horn profile was shown to have a significant effect on the return loss profile for the horn.

Using several combinations of these altered horns the reflected and transmitted standing wave patterns of various horn-horn cavities were predicted and compared against measurement. The agreement of predictions with the measured data was varied. Predictions of the reflected amplitude profile of the cavities exhibited gross pattern agreement with measurement over a finite bandwidth. The predicted transmission profiles exhibited less structural pattern agreement with measurement, yet accurately predicted the average amplitude level. These results indicate that despite the disparate return loss profiles for the individual altered horns, the standing wave pattern of the cavity dominates. The structure of the 'eigenmode' responsible for a specific amplitude transmission dip was analysed for a horn–horn cavity with z = 10 mm for combinations of four altered horn profiles. The results indicated that the resonant eigenmode maintained similar spatial forms for each of the different horn-horn cavities.

In the final section of this chapter a novel stray light baffle structure is introduced into the horn-horn cavity. While the predictions perform well against experiment in transmission, the reflected amplitude profile is routinely misrepresented by theory. This may be due to the assumptions made by the truncating aperture scattering matrix and thus this issue requires some further investigation. Using Fourier signal analysis the spatial form of the baffle structure was found for both measurement and prediction with very good agreement. This technique has potential as an elegant analysis technique for future cavity models.

5. Quasioptical and Physical Optics Analysis of the ALMA Band 5 Front End Optics

5.1 Introduction

In this chapter, a full quasioptical and physical optics analysis of the Band 5 front end optics channel of the Atacama Large Millimetre Array (ALMA) is presented. This work was performed in conjunction with the Band 5 design and development group who work at the Group for Advanced Receiver Development (GARD) at the Chalmers Technical University in Gothenburg, Sweden. The work presented here was of significant importance to the group at GARD owing to the need for verification and/or improvements to the Band 5 front end optics channel design. The author presented a thorough analysis and verification of the performance of the system, with suggested improvements or amendments to the design reviewed by the ALMA optics review board. An extended scientific visit to GARD was also undertaken in summer 2009 to assist with experimental testing of the optics.

An overall review and description of the ALMA instrument is given in Section 5.2, and the front end optics of the Band 5 channel is described in Section 5.3.

5.2 The ALMA Antenna

The ALMA antenna is a classic Cassegrain design (12m) with the primary reflector a symmetric paraboloidal reflector and symmetric hyperboloidal secondary reflector mounted on 4 support legs. The antenna will operate on an elevation over azimuth mount. The quality of these reflectors is integral to the performance of ALMA, and as such, each antenna will have 2 arcsec absolute pointing over the sky, and 0.6 arcsec tracking, which are extremely accurate specifications for antennas of this type and size. In addition to accurate pointing, a high degree of surface accuracy on the primary and secondary reflector surfaces in essential. The surface accuracy goal is 20 μm rms and the

hard specifications are for 25 µm rms, which will provide surface efficiencies at 300 GHz/900 GHz of 94%/57% and 91%/41% respectively [92].

The ALMA instrument will observe over a frequency range of 30 GHz to 950 GHz, which is divided into 10 separate observing channels or bands. This division allows optimisation of both noise performance and antenna coupling over the entire frequency band. The windows for each observing channel are implemented as self contained cartridges and are arranged concentrically around the centre of a 990 mm diameter Dewar flask cryostat cartridge centred on the telescope axis. The secondary reflector illuminates each channel in the same focal plane, with no switching mirror required for channel selection. Channel selection is achieved by simply adjusting the telescope pointing. The optical design for each channel allows for frequency independent coupling to the antenna. The geometry of the ALMA antenna is illustrated below in Figure 5-1 while the geometric parameters are listed in Table 5-1 [93].

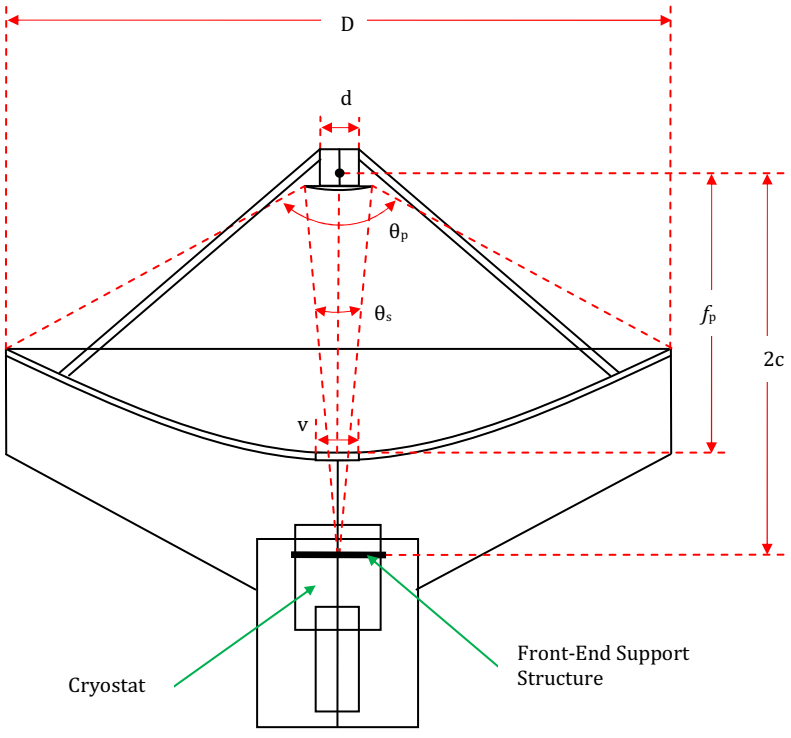

Figure 5-1 – Geometrical configuration of ALMA 12m Cassegrain antenna showing location of front end support structure and cryostat - parameters are listed below in Table 5-1

Parameter	Symbol	Unit	Value
Primary Aperture Diameter	D	m	12.0
Focal Length of Primary	f_p	m	4.8
f/D of Primary	f/D_p	-	0.4
Secondary Aperture Diameter	d	m	0.75
Antenna f/D	f/D	-	8.0
Secondary Eccentricity	e	-	1.10526
Primary Angle of Illumination	θ_p	°	128.02
Secondary Angle of Illumination	θ_s	°	7.16
Primary and Secondary Foci Distance	2c	m	6.177
Primary Vertex Hole	v	m	0.75

Table 5-1 - ALMA Antenna optical parameters

Each receiver band will be contained within a modular cartridge, which allows for individual testing and large-scale production by separate research and development groups. This also allows for easy installation or access for maintenance without disrupting the overall operation of the antenna. The nominal focal plane of the antenna is located a distance of 6.177 m from the prime focus and the top surface of the cryostat is aligned with this plane.

The layout of the receiver windows on the cryostat plane is shown below in Figure 5-2 [94]. The location of the Band 5 cartridge window is highlighted in red. Because of the predefined volume available for each of the 10 channels or bands the optical designs are constrained by the mechanical considerations.

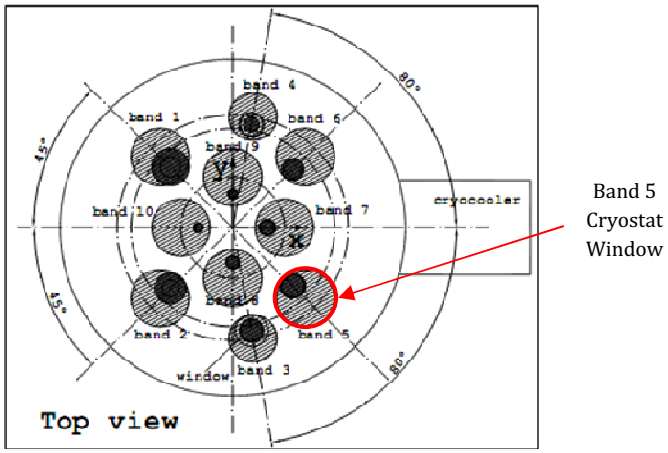

Figure 5-2 - ALMA Cryostat window layout - top down view [94]

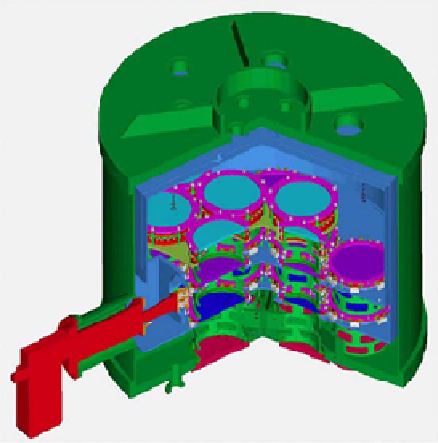

Figure 5-3 - Cut-away of the ALMA cryostat cabin displaying the various cooling shields and IR filter windows for the receiver channels [94].

5.3 The Band 5 Front End Optics

This section details the various design criteria and considerations for the optics of the ALMA receivers. The initial optics scheme of the ALMA front end receivers is reported in [95], from which the following section is developed.

Due to the wide frequency coverage (30 to 950 GHz) each of the ALMA receivers is designed differently, though they do share some similar characteristics and criteria. All channels utilise a feed horn or quasioptical radiator and one or two focusing elements. Each receiver uses a combination of either lenses or off-axis mirrors to focus radiation from the antenna focal plane to the feed horn. Geometrical optics was used to obtain the focal parameters and propagation distances for the optical elements while quasioptical theory was used to determine component sizes. To achieve the highest degree of power coupling a scatterer and aperture clearance of five times the beam radius for the lowest operating frequency is required. Each of the ALMA receivers is designed to receive two orthogonal linear polarisations that are coincident on the sky and maintain a cross polar energy level of at least -24 dB below the copolar power level [96]. Coupling to the antenna is frequency independent with an aperture efficiency of over 80%. Gaussian beam approximations of the optics gives a subreflector edge taper of -12 dB. This gives the highest coupling efficiency to a point source (i.e. aperture efficiency) when the beam

is launched by a conical corrugated horn. When all higher order modes are included the actual edge taper will be closer to *-10.9 dB* [3]. Highest efficiency, rather than maximal antenna gain over system temperature (G/T) is desired for ALMA since the noise contribution due to diffraction is considered to be relatively small [96].

The designs for the receiver channels are split into three categories, representative of the differences of the beam sizes at the different frequencies. The operating frequency ranges for the 10 receiver channels and Category assignments are reported in Table 5-2 below. The span of the receiver channel frequency ranges over the atmospheric transmission windows at the ALMA site at the Chajnantor plain [19] are illustrated below in Figure 5-4.

Receiver Channel	Category	Lower Frequency (GHz)	Higher Frequency (GHz)
1	A	31	45
2	A	69	90
3	B	84	116
4	B	125	164
5	C	165	211
6	C	211	275
7	C	275	370
8	C	385	500
9	C	602	720
10	C	787	950

Table 5-2 - The operating frequency ranges and category assignments for the 10 ALMA receiver channels

The Category A receivers (Bands 1 & 3) are at the longest wavelength ranges and as such are the most restrictive in terms of opto-mechanical size. Optical elements at these frequencies would be too large to place inside the Dewar flask and so only the feed horns are cooled and all accompanying optics remain at ambient temperatures. A single lens located on top of the cryostat is used to couple antenna radiation to the feed horn.

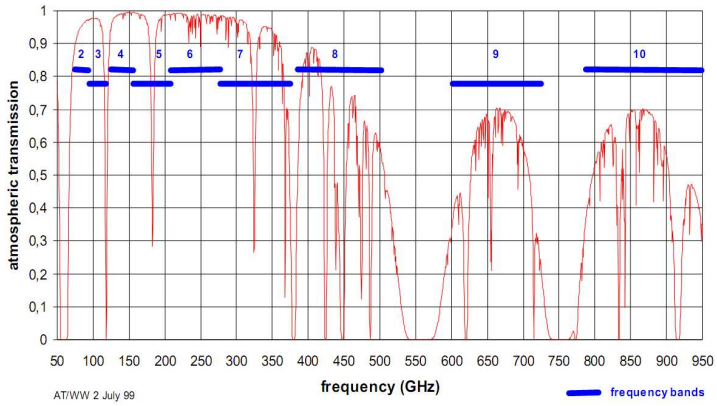

Figure 5-4 - Atmospheric transmission at the Chajnantor plane overlaid with the operating frequency range for each of the 10 ALMA receiver channels (blue line) - [19]

A single feed horn is used for each band and the orthogonal polarisations are distinguished using an orthomode transducer. An example of a Category A receiver (Band 1) is illustrated below in Figure 5-5.

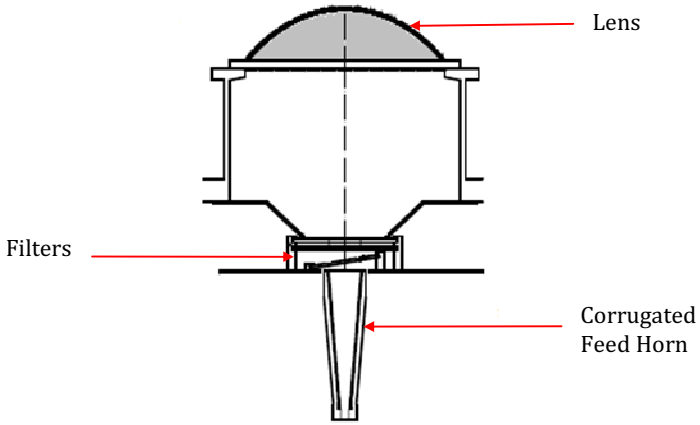

Figure 5-5 - Optical layout for Category A receiver - ALMA Band 1 [95].

The Category B receivers (Bands 3 & 4) contain a combination of cooled and ambient temperature reflective optics. The reflective optics for these receivers consists of a tilted plane mirror that reflects radiation incoming from the antenna subreflector to an off-axis ellipsoidal reflector. This ellipsoidal reflector re-directs the radiation to the feed horn. The ellipsoidal reflector maintains its two focal points within the feed horn and at the antenna focal plane, which is re-oriented via the tilted plane mirror. These bands also use a single corrugated feed horn with orthomode transducers located at the rear

waveguide section. The general design of this class of receiver is displayed below in Figure 5-6.

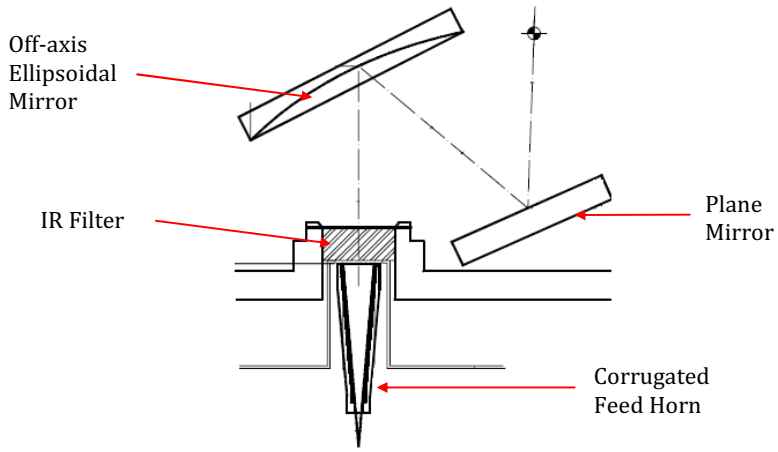

Figure 5-6 – General optical layout for Category B receivers [95]

For Category C receivers (Bands 5 - 10) all optical components are small enough to be placed inside the cryostat. Internally the optics vary between the cartridges according to the specific constraints of the channel but they do share come common features. Imaging for all of these receivers is performed using a pair of cooled off-axis ellipsoidal reflectors. As with the lower frequency categories corrugated feed horns are used. The lower frequency receiver channels (Bands 5 and 6) achieve dual polarisation through the usual approach of an OMT. For the remaining higher frequency channels it was not possible to reliably utilise OMTs and polarisation separation is achieved quasioptically through use of a wire grid polariser to generate two optically equivalent yet orthogonally polarised beam paths. This quasioptical diplexing of the beam path will be covered in more detail in Chapter 6. An example of the optical layouts of these two variations on the Category C receiver channel are illustrated below in Figure 5-7.

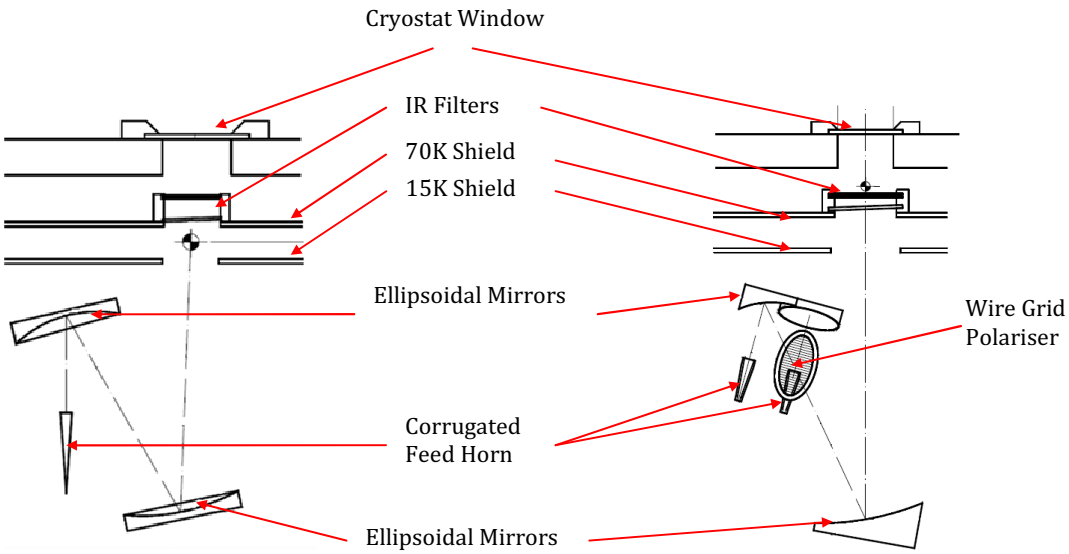

Figure 5-7 - Examples of the optical configuration of the two variations of the Category C receiver channels (Band 7 front end optics on the right) [95]

The Band 5 receiver is the lowest frequency Category C receiver and operates at a central frequency of 187 GHz with upper and lower frequencies of 211 GHz and 163 GHz respectively (c.f. Table 5-2). The entire cartridge, including the optics, is cryogenically cooled in several stages. Waveguide couplers and orthomode transducers are used for Local Oscillator (LO) injection and polarisation separation respectively. The optical design of this system was determined from the initial ALMA receiver optics design **[95]**.

The optics of Band 5 is comprised of two off axis ellipsoidal mirrors, which allow for frequency independent coupling of radiation from the antenna Cassegrain focal plane to the feed horn. The focusing mirror bending angles were determined as a compromise between maintenance of low cross polar power leakage and opto-mechanical limits. Owing to the location of the Band 5 receiver system on the top plate of the cryostat, the incoming beam enters through the receiver cryostat window at an angle of 2.38° to the vertical. The incident beam is reflected through an angle of 32.38° by the next mirror, and then reflected down by an angle of 30° by the subsequent mirror, focusing the beam

into the feed horn. Distances between optical elements were initially determined using geometrical optics i.e. the ray-tracing approximation in the optical layout. The optical layout of the receiver is displayed below in Figure 5-8

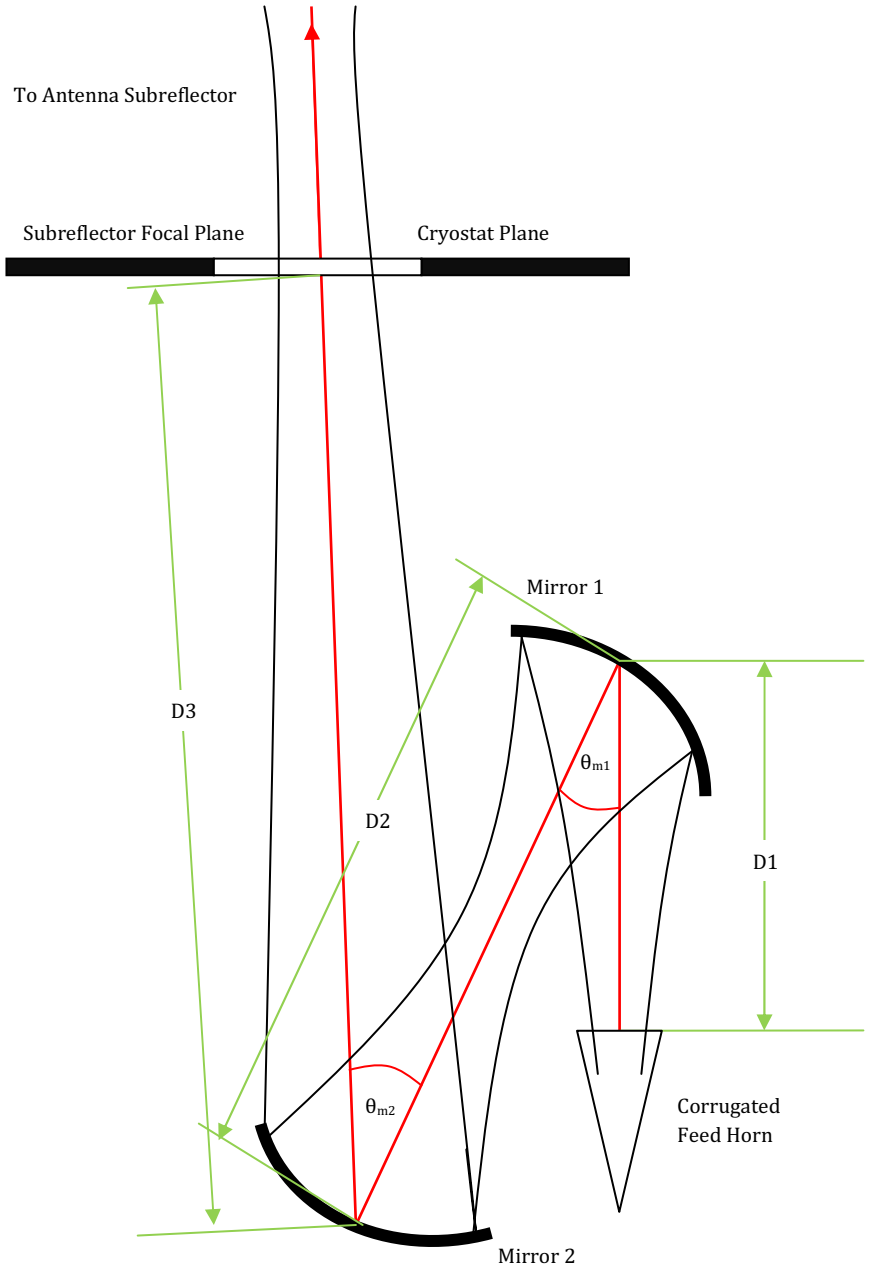

Figure 5-8 - ALMA Band 5 Front End Optics Layout - for analysis purposes using reciprocity, the first reflector after the feed horn is titled Mirror 1, and the subsequent reflector Mirror 2.

Parameter	Units	Value	Description
D1	**mm**	60.05	Feed horn aperture to Mirror 1
D2	**mm**	140.0	Mirror 1 to Mirror 2
D3	**mm**	229.82	Mirror 2 to Cryostat Plane (z=0)
D4	**mm**	5887.94	Mirror 2 to Subreflector Vertex
D5	**mm**	111.3	Subreflector Vertex to Edge
θ_{m1}	°	30.0	Mirror 1 bending angle
f_{m1}	**mm**	32.756	Mirror 1 focal length
θ_{m2}	°	32.38	Mirror 2 bending angle
f_{m2}	**mm**	67.192	Mirror 2 focal length

Table 5-3 - ALMA Band 5 Front End Optics parameters as described in Figure 1.1.

Parameter	Units	Value	Description
R_{axial}	**mm**	60.0	Horn axial length
R_{slant}	**mm**	60.169	Horn slant length
a	**mm**	9.0	Aperture diameter
θ_{horn}	°	4.29	Horn angle

Table 5-4 - ALMA Band 5 Feed Horn Parameters

5.4 Analysis

The first stage of analysis for the Band 5 front end optics involved investigating the effect on performance of several modifications to the currently prescribed system parameters. These modifications were developed to ascertain whether overall system performance in terms of the design goals could be improved upon while the system was still in the design stage. The modifications to the system were restricted in that they could not require any large scale overhaul of the system. Due to mechanical constraints the first of these changes to the system design was to determine to what degree the system performance was affected by smaller scale truncation of the beam at the scatterer surfaces i.e. how well would the system perform with a scatterer clearance of less than 5w in diameter? This information was required by the GARD Institute in light of manufacturing issues. As Band 5 is the lowest frequency category C receiver, achieving maximum power coupling requires large component sizes. This has the potential to lead to opto-mechanical limit problems in the development and

construction stages of the system. If it could be shown that system performance is within acceptable limits for a lower degree of beam truncation then this would be favourable. To this end three degrees of mirror truncation have been analysed using PO, each being multiples of the lower frequency beam waist: $4.0w_{163}$, $4.5w_{163}$ and $5.0w_{163}$.

The second of these design modifications was to the shape of the mirror surfaces. Optimal beam coupling from the antenna focal plane to the feed horn is a major factor in system performance, and design of the off-axis reflectors is crucial to achieving this goal. Initial ALMA design parameters maintain that reflector surfaces for Category C receivers would be designed using traditional geometrical optics, providing uniformity across all channels. While for the higher frequency channels (Bands 8, 9 & 10) this can be deemed sufficient since these frequencies are closer to the geometrical limit ($\lambda \rightarrow 0$), it can be shown that for lower frequency channels a geometrical optics description of the reflecting surfaces will not provide optimum beam coupling due to phase curvature issues. The beam is diffraction dominated and the effects of beam spreading must be accounted for more rigorously. To illustrate the benefits of a more accurately matched reflector surface over the prescribed geometrical method two versions of the Band 5 optics have been analysed: a 'Geometrical' and a 'Quasioptical' optics version. For each of these setups the three degrees of truncation of the beam mentioned above have been applied, producing a total six systems for analysis.

5.4.1 Quasioptical Analysis

The Band 5 front end optical system can be viewed as a first order approximation as a paraxial quasioptical system, where the reflectors can be treated as simple phase transformers and the field from the feed horn is treated as a fundamental Gaussian beam. Choosing the correct Gaussian field description of the corrugated feed will yield an excellent approximation of the field from the feed horn. For a Gaussian beam with a waist $w = 0.6435\ a$, where a is the aperture radius of the feed horn [42] 98% of the beam power from the horn will be contained within the fundamental mode. Using this

Gaussian beam approximation the location of the phase centre of the horn behind the aperture and the size of the horn beam waist are determined.

Treating this system as scalar and on-axis will not allow for examination of optical aberrations or power leakage into the cross polar due to the offset mirrors. However it will allow the parameters of the beam as it propagates through the system to be determined, which are then used to determine the size of the system components. The system is modeled in this manner using ABCD matrices; specifically the propagation and thin lens matrices (c.f. Table 2.3)

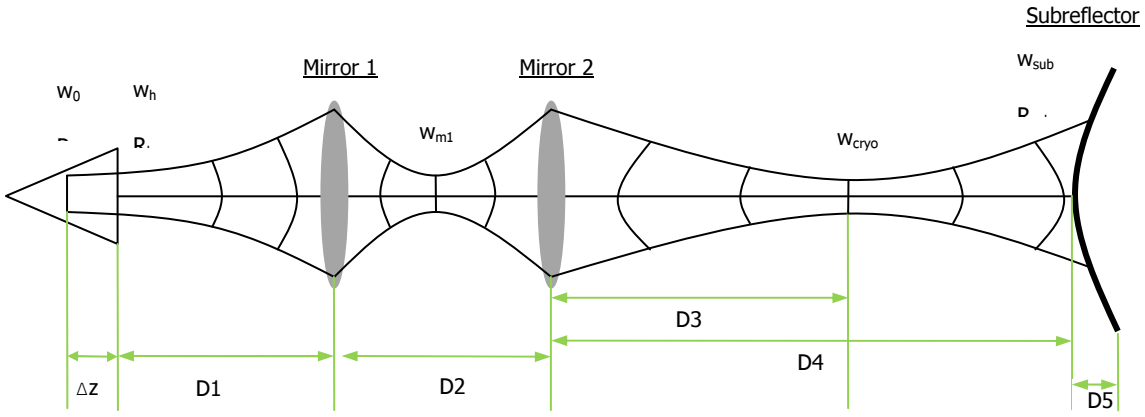

Figure 5-9 - ALMA Band 5 quasioptical analysis layout – paraxial representation of the band 5 front end optics with thin lenses representing the offset ellipsoidal reflectors.

The table below (Table 5-5) lists the Gaussian beam parameters for the optical system for the highest, middle and lowest frequencies (211, 187 and 163 GHz respectively) from the phase centre of the feed horn through to the subreflector of the antenna. It can be seen that the location of the phase centre and the beam waist w_0 are frequency dependent, while the beam waist at the aperture w_{ha} is frequency independent.

Parameter	Symbol	Units		Frequency (GHz)		
Frequency		GHz		163	187	211
Horn Aperture Radius	a_h	mm	4.5			
Horn Axial Length	L_h	mm	60.0			
Horn Slant Length	R_h	mm	60.17			
Horn Waist	w_0	mm		2.82	2.79	2.77
Horn Waist Offset	Δz	mm		-3.23	-4.18	-5.22
Horn Aperture Waist	w_{ha}	mm	2.9			
Waist at Mirror 1	w_{m1}	mm		13.45	12.06	11.02
Waist at Mirror 2	w_{m2}	mm		16.72	15.76	15.06
Waist at Cryostat Plane	w_{cryo}	mm		11.01	9.6	8.51
Waist at Subreflector Vertex	w_{sub}	mm		312.84	312.84	312.84
Waist at Subreflector Edge	w_{sub}	mm		318.79	318.79	318.79
Edge Taper (Vertex)	Te	dB		-12.48	-12.48	-12.48
Edge Taper (Edge)	Te	dB		-12.02	-12.02	-12.02

Table 5-5 - ALMA Band 5 - fundamental Gaussian beam optics parameters

The phase radius of curvature for the Gaussian beam approximation to the horn field is taken to be the slant length of the horn and is thus also frequency independent. The determination of the Gaussian beam parameters throughout the optical train can be calculated by using either the source beam parameters from the phase centre of the horn or at the aperture plane, however the frequency independent beam parameters at the latter location allow for quicker calculation. It is shown that the design goal of a frequency independent edge taper of approximately -12 dB at the edge of the subreflector is achieved.

5.5 Reflective Optics Design

For both the Geometrical and Gaussian optics versions of system the off-axis ellipsoids have similar layouts (due to volume constraints). The ellipsoids of each system will have different conic parameters, reflecting the different radii of curvature. They are equivalent in the sense that they must maintain the same focal length, reflection angle

and are located in the same place. The common layout for each mirror is shown below in Figure 5-10 and Figure 5-11. Note that the figures are not to scale.

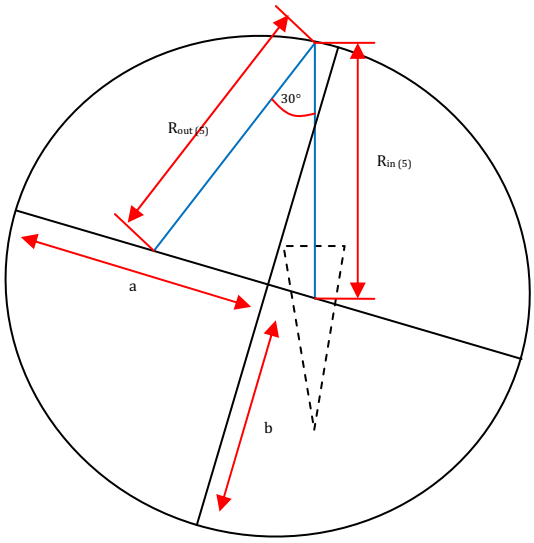

Figure 5-10 – Layout and orientation of ellipsoidal surface for Mirror 1

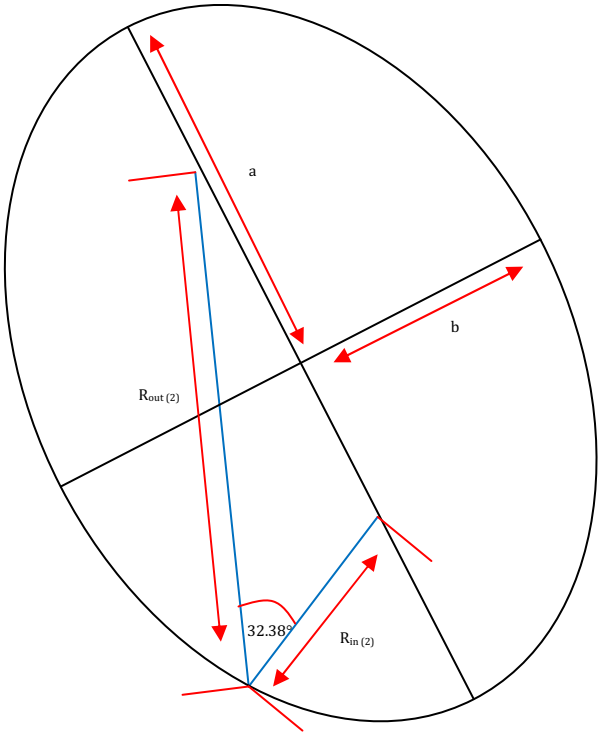

Figure 5-11 - Layout and orientation of ellipsoidal surface for Mirror 2

5.5.1 'Geometrical Optics' Parameters

In the geometrical limit, the input and output radii of curvature R_{in} and R_{out} of the optical beam as it enters and leaves the optical element are simply dependent of the focal length f of the element, as given by the following equation [33]:

$$\frac{1}{f} = \frac{1}{R_{in}} + \frac{1}{R_{out}} \tag{5.1}$$

Using this relation the parameters for the two off-axis ellipsoidal reflectors are calculated. In the geometrical limit, the input and output radii of curvature are set to be the beam object and image distance, as in the geometrical ray tracing method. The object distance in the case of an optical system containing a feed horn source is from the vertex of the horn to the optical element. From this initial input distance and the focal lengths of the two reflectors, the entire system can be described.

5.5.2 'Quasioptical' Parameters

For the 'Quasioptical' layout the input and output radii of curvature of the ellipsoids match the incident and reflected phase radii of curvature of the central frequency beam. Recall from Chapter 2 (Equation 2.12) that the phase radius of curvature for a Gaussian beam is calculated as:

$$\begin{aligned} R_{in} &= d_{in}\left(1+\left(\frac{\pi w_{in}^2}{\lambda d_{in}}\right)^2\right) \\ R_{out} &= d_{out}\left(1+\left(\frac{\pi w_{out}^2}{\lambda d_{out}}\right)^2\right) \end{aligned} \tag{5.2}$$

Beyond the geometrical limit the radius of curvature of the beam no longer matches that of the input distance. From Equations 5.2 it can be seen that the longer the wavelength becomes, and hence the further away from the geometrical limit, the radius of curvature of the beam has become larger than the propagation distance from the beam waist. The relationship between the geometrical and 'Quasioptical' parameters is best illustrated by comparing their ellipsoidal mirror parameters in Table 5-6 below.

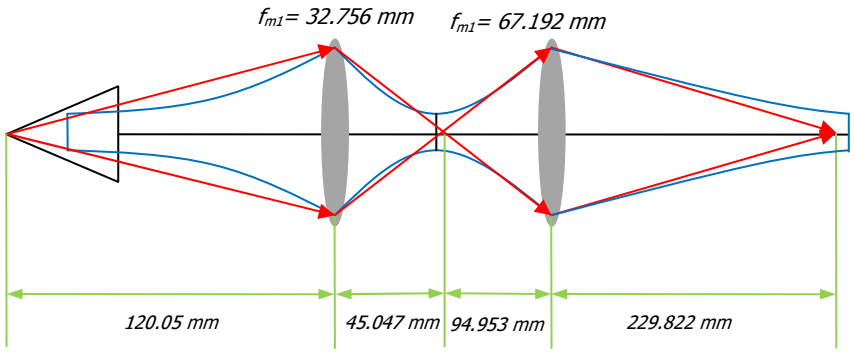

Figure 5-12 – On axis representation of the Band 5 front end optics illustrating the geometrical ray tracing beam paths from the feed horn apex to the antenna focal plane (in red). The more physically relevant representation of the quasioptical beam throughout the optical train is highlighted in blue, illustrating the disparity between the 'Geometrical' and 'Quasioptical' configurations of the optical system.

Parameter	Unit	Geometrical		Quasioptical	
		Mirror 1	Mirror 2	Mirror 1	Mirror 2
Input Radius	**mm**	120.05	94.953	67.87	81.917
Output Radius	**mm**	45.047	229.82	63.32	373.69
Major axis – a	**mm**	82.549	162.388	65.594	227.861
Minor axis – b	**mm**	71.033	141.93	63.32	168.127
Eccentricity – e		0.509458	0.485891	0.26098	0.674968
Conic constant – k		- 0.259547	- 0.23609	- 0.068112	- 0.455581
Radius of Curvature - R	**mm**	61.1232	124.049	61.126	124.052

Table 5-6 - Parameters for ellipsoidal reflectors Mirrors 1 & 2 for Geometrical and Quasioptical configurations

Notice from Table 5-6 the relatively large differences in the reflector characteristics for the two versions of the system. This highlights the disparity between the geometrical approximation and the long wavelength quasioptical description of the beams.

5.5.3 Reflector Rim Truncation

As previously mentioned, one of the stated goals for the ALMA front end optics for all bands was a scatterer diameter clearance of $5.0w$, where w is the Gaussian waist of the

beam at the band's lowest frequency. This is to ensure maximum power conservation of the beam within the cartridge. However, this may present spatial management problems in designing the physical system components. It is easy to model any version of the system using physical optics for an ideally large reflector to conserve power, but putting this into practice is more difficult.

To determine the loss, if any, in performance of the Band 5 cartridge for a decrease in reflector clearance/increase in reflector truncation, three levels of clearance were analysed; diameters of *4.0w*, *4.5w* and *5.0w* for Mirrors 1 & 2, where *w* is the beam radius at the mirror surface for the lowest frequency (163 GHz). The specific radii for the Band 5 reflectors are given below in Table 5-7. The values for the beam waist at the reflectors are taken from the ABCD analysis presented in Table 5-5. The beam waist at Mirror 1 is 13.45 mm and the waist at Mirror 2 is 16.73 mm.

The fractional power of a fundamental Gaussian beam contained within these diameters will give varying degrees of power conservation. In a process similar to that illustrated in Figure 2.28, by normalising incident power to unity the relative conserved power output after a series of reflections is a product of the conserved power at each reflector. The levels of power conservation hof each scatterer radius are given by the edge taper calculation from Equation 2.5 and are listed below in Table 5-8 as a power budget analysis of the Band 5 optical train.

Truncation	**Units**	**Radius of Mirror 1**	**Radius of Mirror 2**
2.0 * w_{163}	**mm**	26.9	33.46
2.25 * w_{163}	**mm**	30.263	37.643
2.5 * w_{163}	**mm**	33.625	41.825

Table 5-7 - Reflector rim radii

Truncation	Mirror 1	Mirror 2	Subreflector Edge Taper	Total Power	Edge Taper(dB)
2.0 * w_{163}	0.99967	0.99967	0.93718	0.93655	11.98
2.25 * w_{163}	0.99996	0.99996	0.93718	0.93709	12.01
2.5 * w_{163}	0.99999	0.99999	0.93718	0.93715	12.02

Table 5-8 - Power budget of ALMA Band 5 for fundamental Gaussian beam

Providing that the power from the horn is normalised to unity, then the net power reaching the subreflector from the horn is given in Table 5-8 as *Total Power*. The net effect of the reduced radii upon the subreflector edge taper is evident. There is a difference of 0.04 dB between edge taper values for the largest and smallest reflector rim radii. Though this reduction in coupling is to be expected it is extremely small and thus unlikely to have any major effect on overall system performance. These figures are for the fundamental Gaussian beam, which is an approximation of the horn aperture field. The maximum coupling between the fundamental Gaussian beam and the horn aperture field is equal to 0.99, meaning that 98% of the power is contained within the fundamental Gaussian beam. Also the optics is represented with equivalent lenses to the off axis mirrors meaning that projection and shadowing are not accounted for at all here. A full PO analysis is presented in Section 5.6 below where these effects are included.

5.6 EM Beam Predictions

PO analysis testing of the various Band 5 configurations was conducted using GRASP9. The source field of the corrugated horn was represented using the Tabulated Planar Source object, as described in Chapter 2, where the complex aperture field of the feed horn was generated using the mode-matching software *SCATTER*. So as to calculate the most accurate beam predictions, both the PO and PTD tools were utilised. The beams were predicted at the three planes – the antenna focal plane, the subreflector vertex plane and the farfield of the main antenna. The various system configurations for the optics were named as *Geometrical 4.0w, Geometrical 4.5w, Geometrical 5.0w, Quasioptical*

4.0w, Quasioptical 4.5w and Quasioptical 5.0w. All results presented here refer to these 6 different system configurations. The 3D OpenGL layout of the Band 5 front end optics as it appears in GRASP9 is illustrated below in Figure 5-13.

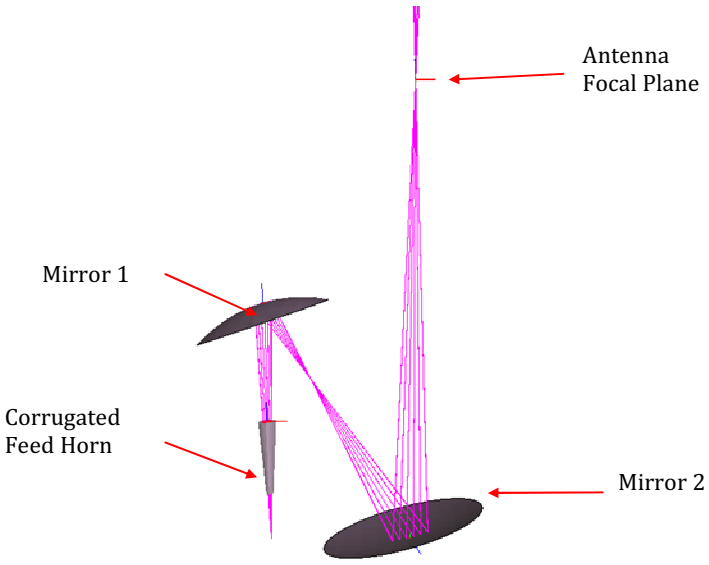

Figure 5-13 - 3D OpenGL illustration of the Band 5 front end optics with ray-tracing analysis showing the imaging of the beam from the antenna focal plane to the corrugated feed horn

5.6.1 Beam Quality Assessment

As a basic determination of output beam quality, a Gaussian beam fitting routine was applied to the predicted beams for the central frequency (187 GHz) at the focal plane. This iterative approach calculates the best fit Gaussian to the two dimensional beam, calculating its location from the nominal position in terms of Cartesian offsets and tilt angles. This allows the beam symmetry, tilt and lateral offsets to be estimated for the beam. The coupling of the output beam to its Gaussian equivalent as calculated from ABCD analysis of the system is known as the Gaussicity of that beam. This Gaussicity is simply calculated as a normalised overlap integral of the equivalent Gaussian field, E_{Gauss} and the output field, E_{out} – c.f. Equation 5.3 below.

$$\eta_{Gaussicity} = \frac{\iint E_{Gauss} E_{out}^{*} dxdy}{\iint E_{Gauss} E_{Gauss}^{*} dxdy \iint E_{out} E_{out}^{*} dxdy} \tag{5.3}$$

Parameter		**Geometrical**			**Quasioptical**		
Rim Radius	mm	4.0w	4.5w	5.0w	4.0w	4.5w	5.0w
Gaussicity	%	99.09	98.93	98.53	98.93	98.77	98.364
waist	mm	9.582	9.577	9.577	9.47	9.46	9.45
x-offset	mm	-0.2437	-0.2477	-0.2503	0.0543	0.0565	0.065
y-offset	mm	-0.0016	0.0009	-0.0001	0.0038	0.001	0.0005
z-offset	mm	-5.814	-3.82	-1.133	-3.099	-0.684	2.673
x-tilt	°	-2.712	-2.715	-2.719	-2.512	-2.515	-2.515
y-tilt	°	-0.00003	-0.0001	-0.00007	-0.00006	$4.4*10^{-6}$	0.00003

Table 5-9 - Results of Gaussian fitting routine applied to the predicted focal plane beams for the 6 configurations of the Band 5 optics

Notice from these results the trend of the Gaussicity calculation. In going from the smallest rim to the largest rim the Gaussicity value decreases. As the collecting area of the reflectors increase they will convey more of the higher order mode structure of the beam as it propagates throughout the system, thereby increasing total power conservation. These higher order mode features will decrease the coupling efficiency of the output beam to a fundamental Gaussian. In going from the 'Geometrical' to the 'Quasioptical versions the Gaussicity calculations are slightly lower. This is counter to the prediction that the Gaussian optics version will improve the beam quality, yet these results are for the best fit Gaussian from an iterative fitting routine and can be interpreted as not accurately representing the predicted Gaussian approximation to the beam at the focal plane. Another assessment of beam quality calculates the Gaussicity of the predicted beam with the waist and complex phase radius of the Gaussian field as predicted by the ABCD analysis from Table 5-5 at the same plane. The table below lists the results of this Gaussicity calculation for the three characteristic frequencies of the channel (163 GHz, 187 GHz and 211 GHz).

Reflector Rim	Unit	Geometrical			Quasioptical		
		163 GHz	187 GHz	211 GHz	163 GHz	187 GHz	211 GHz
4w	%	98.40	98.61	98.30	98.84	98.80	98.47
4.5w	%	98.31	98.44	98.21	98.71	98.64	98.38
5w	%	97.71	98.05	97.99	98.09	98.23	98.13

Table 5-10 - Gaussicity calculations for predicted beams of six configurations of Band 5 optics

The trend of decreasing Gaussicity values for increasing reflector area continues for the results of this Gaussicity calculation. Notice also that the Gaussicity values for the 'Quasioptical' configuration are higher than those of the 'Geometrical', thus confirming the improved phase transforming abilities of this version.

5.6.2 Power Budget Analysis

As a method of determining power conservation within an optical system, the PO calculations in GRASP9 are very useful. As part of calculating the PO currents induced on the surface of a scatterer, the software can calculate the power in the incident field. This process was outlined previously in Section 2.4.1.1. The plots below track the conserved power for Mirrors 1 and 2 in both Geometrical and Quasioptical versions of the optics as predicted by PO calculations.

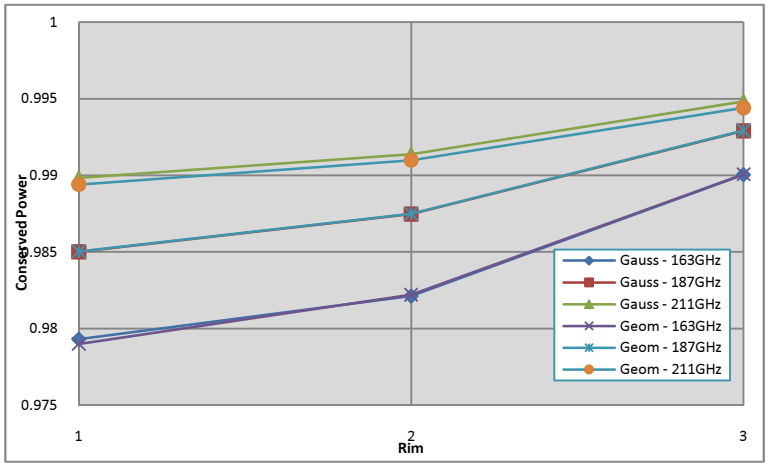

Figure 5-14 - Power conserved by Mirror 1 for Geometrical and Quasioptical versions of the optics. Rims 1, 2 and 3 refer to 4.0w, 4.5w and 5.0w.

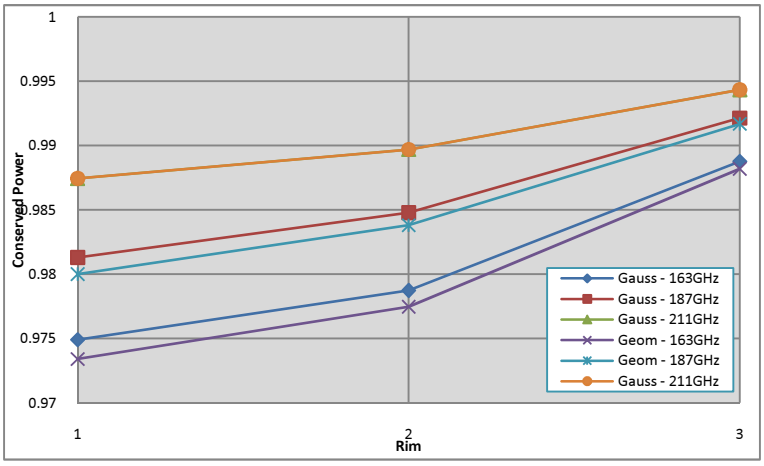

Figure 5-15 - Power conserved by Mirror 2 for Geometrical and Gaussian versions of the optics. Rims 1, 2 and 3 refer to 4.0w, 4.5w and 5.0w.

In comparing the conserved power for the first mirror (Figure 5-14) it is observed that there is relatively no difference between the 'Geometrical' and 'Quasioptical' systems. This is due to the fact that the first mirror intercepts the beam from the corrugated feed horn in the same manner for both versions. The results for the second mirror, plotted in Figure 5-15 exhibit higher conserved power for the 'Quasioptical' system over the 'Geometrical'. This indicates the improved beam conservation by the 'Quasioptical' design over the 'Geometrical'.

In the following table the edge taper levels at the subreflector for all versions of the front end optics are reported.

Rim	**Parameter**	**Units**	Freq	Geom	Quasi	Freq	Geom	Quasi	Freq	Geom	Quasi
4.0w	**T_E**	dB	163	-10.71	-11.18	187	-11.25	-11.40	211	-11.65	-11.45
	Power	%		91.5	92.4		92.5	92.8		93.2	92.8
4.5w	**T_E**	dB		-11.05	-11.29		-11.53	-11.73		-11.73	-11.43
	Power	%		92.1	92.6		93.0	93.2		93.3	92.8
5.0w	**T_E**	dB		-11.17	-11.34		-11.55	-11.80		-11.72	-11.42
	Power	%		92.4	92.7		93.0	93.4		93.3	92.8

Table 5-11 - Edge tapers and conserved power normalised to feed horn power at the ALMA subreflector as calculated by PO calculation in GRASP

The maximum aperture efficiency for an unblocked Gaussian illumination is 0.815, giving an edge taper of -10.9 dB. If the blockage effect of the subreflector is included the maximum aperture efficiency drops to 0.803 with the edge taper dropping to approximately -10.8 dB. The PO predicted values for edge taper for all configurations of the system are very close to this optimum value. Note in the above table the differences in power conservation between the two optical versions of the channel. In going from Geometrical to Gaussian the power conservation has been increased for the middle to lower section of the bandwidth, while being decreased in the upper frequency limit. The differences in power conservation are small, but nonetheless they indicate the influence of the shape of the optics on the beam at the subreflector. As expected, an increase in rim diameter gives an increase in conserved power. This is most evident once again for the middle and lower frequencies, having larger beam sizes. The upper frequency beam, being of smaller size, is at the same level of conservation for all rim diameters.

5.6.3 Cross Polar Power Efficiency

One distinct problem in creating off-axis reflecting optics systems is the leakage or cross-talk between the co and cross polarised fields [97]. The EM GRASP9 calculations keeps track of the cross polar field throughout the system. The cross polar power levels presented below were calculated through integrating the total power in the cross-polar beam over a 2D beam and normalising against the total power in the co-polar beam. The beam was sampled at both the focal plane and the subreflector vertex plane. This is given by the following equation:

$$XsP = 10\log_{10}\left[\varepsilon_{xsp} \Big/ \varepsilon_{cop}\right] \tag{5.4}$$

where ε_{cop} and ε_{xsp} are the total power levels of the co and cross polar distributions respectively and are determined numerically by integrating the complete fields over their selected area.

Freq	Rim	XsP (dB) - Geom		XsP (dB) - Quasi	
		FP	SUB	FP	SUB
163	**4.0*w***	-31.13	-31.46	-31.05	-31.31
	4.5*w*	-30.96	-31.19	-30.97	-31.05
	5.0*w*	-30.83	-31.04	-30.85	-30.89
187	**4.0*w***	-32.28	-32.54	-32.17	-32.47
	4.5*w*	-32.09	-32.43	-32.21	-32.32
	5.0*w*	-32.01	-32.35	-32.13	-32.31
211	**4.0*w***	-29.17	-29.23	-29.19	-29.30
	4.5*w*	-29.07	-29.16	-29.12	-29.19
	5.0*w*	-29.02	-29.10	-29.07	-29.11

Table 5-12 - Cross polar power normalised against co polar power predicted at the focal plane (FP) and subreflector vertex plane (SUB)

The cross polar efficiency of the system can be determined when the values given above in Table 5-12 are compared against the cross polar power levels for the aperture of the feed horn below in Table 5-13.

Freq (GHz)	163	187	211
XsP (dB)	-37.40	-36.43	-29.42

Table 5-13 - Cross polar power levels at the corrugated feed horn aperture

Evidently each configuration of the optics conserves the cross polar power levels relatively equally. The low cross polar levels at the horn aperture are well maintained through the optics to the focal plane position and on to the subreflector. These results are very favourable given that the requirements of the system call for cross-polar levels to be under -23 dB.

5.6.4 Aperture Efficiency

Aperture efficiency refers to the coupling of the predicted beam to the antenna subreflector. To achieve this firstly the phase of the predicted beam at the subreflector vertex plane was unwrapped, giving an approximately paraboloidal complex phase front radius. The field is then coupled with a truncated plane wave field or 'top-hat' field. This top-hat field has a diameter equal to that of the subreflector blockage and a

phase radius of curvature of the beam at the subreflector vertex plane as determined from ABCD matrices. This coupling between the top-hat and predicted fields is performed in the same manner as for the Gaussicity calculation in Equation 5.3. An example of the amplitude patterns for a typical predicted subreflector field and an unblocked top-hat field are displayed below in Figure 5-17.

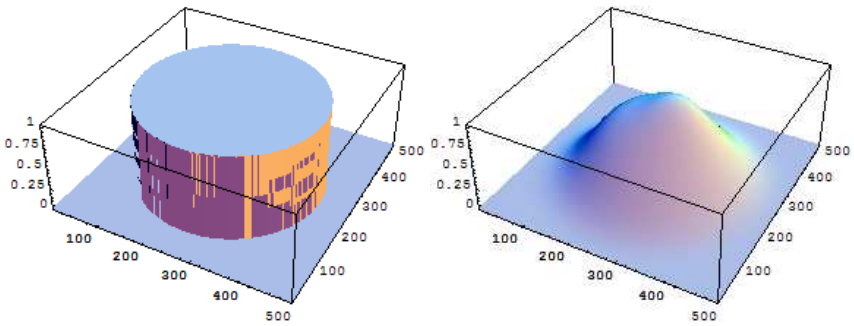

Figure 5-16 – Amplitude patterns of the truncated plane wave or 'top-hat' field (left) and a typical predicted EM field at the subreflector vertex for calculation of aperture efficiency

To include the effects of the subreflector blockage, a scaled shadow representing the blockage is included in the top hat field distribution. The diameter of the blockage is scaled by the same proportion of the diameter of the subreflector over the diameter of the primary. In the case of the ALMA Cassegrain antenna, the subreflector represents a fractional area blockage of approximately 0.4%.

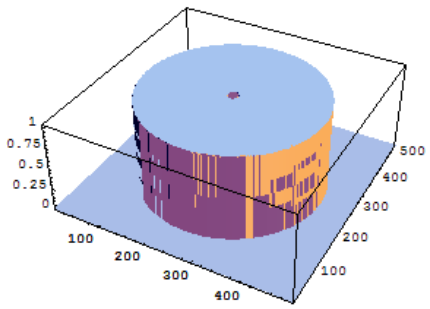

Figure 5-17 - Top-hat field including scaled subreflector blockage

The Ruze factor, as mentioned in Chapter 2 **(**Equation 2.83**)** gives the degradation to the aperture efficiency due to the surface deformations in the primary and secondary reflector surfaces. The Ruze surface error is frequency dependent, with increased error

occurring for increased frequency. The RMS surface deformation for the ALMA antenna's primary and secondary reflectors is 20 μm [96]. This represents an extremely high level of accuracy for such a large reflector antenna, and is thus assumed to be an optimistic figure.

In Table 5-14, η_a is the aperture efficiency including spillover calculated through a coupling integral between the beam at the subreflector and the top hat field. The effects of the blockage are given by $\eta_{a+blockage}$, and the η_e gives the Ruze efficiency. The total efficiency is the product of $\eta_{a+blockage}$ and η_e. This coupling integral performs both the taper efficiency and spillover efficiency calculations as given in Section 2.3.3.

Rim	Parameter	*f* (GHz)	Geom	Quasi	*f* (GHz)	Geom	Quasi	*f* (GHz)	Geom	Quasi
4.0*w*	η_a	163	0.829	0.845	187	0.841	0.855	211	0.851	0.861
	$\eta_{a+blockage}$		0.822	0.838		0.833	0.849		0.844	0.855
	η_e		0.934	0.934		0.924	0.924		0.915	0.915
	η_{total}		**0.768**	**0.783**		**0.770**	**0.784**		**0.772**	**0.782**
4.5*w*	η_a		0.836	0.860		0.845	0.863		0.853	0.865
	$\eta_{a+blockage}$		0.829	0.853		0.838	0.856		0.846	0.859
	η_e		0.934	0.934		0.924	0.924		0.915	0.915
	η_{total}		**0.774**	**0.797**		**0.774**	**0.791**		**0.774**	**0.786**
5.0*w*	η_a		0.836	0.865		0.846	0.866		0.852	0.870
	$\eta_{a+blockage}$		0.829	0.859		0.838	0.859		0.845	0.862
	η_e		0.934	0.934		0.924	0.924		0.915	0.915
	η_{total}		**0.774**	**0.802**		**0.774**	**0.794**		**0.773**	**0.789**

Table 5-14 - Aperture efficiency calculations for the six configurations of the Band 5 front end optics

The ALMA standard for the receiver channel to meet aperture efficiency requirements is a coupling of a simulated field at the subreflector to an ideal truncated plane wave of over 80%. There is no requirement to include the loss of efficiency due to the subreflector blockage or the surface deformations of the antennas reflectors. The values for unblocked aperture efficiency shown in Table 5-14 are all well above this requirement. There is a marked increase in efficiency for the improved 'Quasioptical'

version of the optics over the 'Geometrical' This is to be expected, owing to the more accurate phase transforming performance of the front end optics mirrors. It should also be noted that the best aperture efficiencies, in both versions of the optics, occurs for the largest rim diameters. This is also to be expected, since the lowest beam truncation conserves the most power within the optical path. This is opposite to the results of Gaussicity where the smallest rim diameters gave the largest coupling coefficient to a Gaussian. This can be accounted for by the truncating effect of the rims on the feed beam. A higher degree of truncation will remove the higher order patterns from the overall beam, which will tend to give the beam a more Gaussian shape. However, a high degree of Gaussicity is not required for the ALMA front end optics. A hazard of higher truncation is creating unwanted and unaccountable amount of stray, scattered radiation within the receiver.

The EM beam pattern predictions and analyses for the various configurations of the optics presented in the preceding sections were submitted to the Preliminary Design Review Board for the ALMA Band 5 Front End Optics [51]. Based on these results and recommendations from the Author a final design for assembly and testing was decided upon. The surfaces of the ellipsoidal reflectors were designed using the Gaussian optics method and truncation levels of $2.4w$ and $2.3w$ were deemed sufficient for power conservation. This is the design for the prototype of the front-end optics that is, as of writing, being assembled and tested by GARD. The remainder of this chapter is devoted to the theoretical analysis and experimental measurements from this prototype.

5.7 Antenna Main Beam

It is important to characterise the antenna being modelled in terms of its effectiveness as a directional radiation measuring device. The n the far-field beamwidth the more spatial resolution the telescope will have for detailed observations. What is desirable in a radio antenna is a strong main lobe radiation pattern. However, any finite antenna

aperture will have tertiary power maxima known as minor lobes. These minor lobes have additional power in undesired directions and they should be as minimal as possible. The secondary or sidelobes are usually the largest of the minor lobes. Low sidelobe levels compared against the main beam are necessary, otherwise sources outside the scope of the main beam will add to the total power, giving incorrect observation results. According to [43], sidelobe levels of -20 dB or lower are considered desirable. The far-field radiation patterns of the feed horn coupled through the front end optics to the antenna and on to the sky have been calculated through PO and are displayed below in Table 5-15 below. The primary and secondary reflectors of the ALMA antenna were generated in GRASP9 from the antenna characteristics listed in Table 5-1 above. The diagram below displays a 3D CAD representation of the ALMA antenna as it appears in the GRASP9 environment including ray-tracing of the beam from the Band 5 front-end optics.

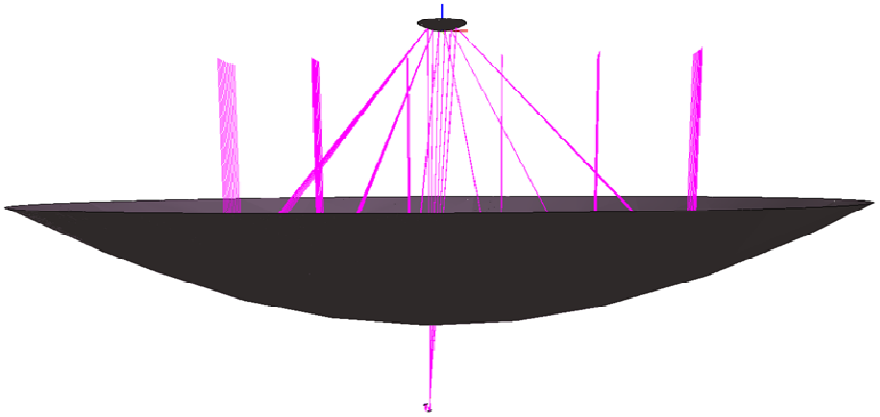

tics

Recall from Section 2.3.4 and the Half Power Beam Width (*HPBW)* is given by Equations 2.84 and 2.85 where λ is the wavelength and D is the diameter of the antenna aperture, which for the ALMA antenna is equal to 12m. The theoretical values of HPBW from Equations 2.84 and 2.85 are listed below in Table 5-15. The predictions from Equation 2.85 are given for an edge taper of -12 dB. The equivalent values from PO predictions are taken from the planar cuts of the antenna main beam – c.f. Figure 5-20.

Parameter	Unit	Theoretical			PO Predictions		
Frequency	GHz	163	187	211	163	187	211
HPBW	arcsec	32.22	28.044	24.876	33.48	29.16	26.064
HPBW (T_e: 12 dB)	arcsec	37.356	32.5617	28.858			

Table 5-15 Half Power Beamwidth (HPBW) values for the ALMA antenna from the theoretical Fraunhofer farfield approximation (left) and from PO calculations (right)

It can be seen from the plots and table that there is very good agreement between the theoretical and calculated PO values for the *HPBW* of the farfield antenna pattern, specifically from the prediction by Equation 2.84 (top most theoretical values in Table 5-15. The disparity between the HPBW values for a 12 dB edge taper and PO predictions are attributed to the inclusion of the central blockage of the subreflector. If the fractional blockage were introduced the side lobe levels would be increased and the main lobe pattern would become narrower [3]. This is reinforced from the comparisons plots between theoretical values for the antenna main beam PO predictions in Figure 5-20 below. PO predictions are given as orthogonal x and y cuts plotted in blue and red respectively, while theoretical predictions are plotted in yellow.

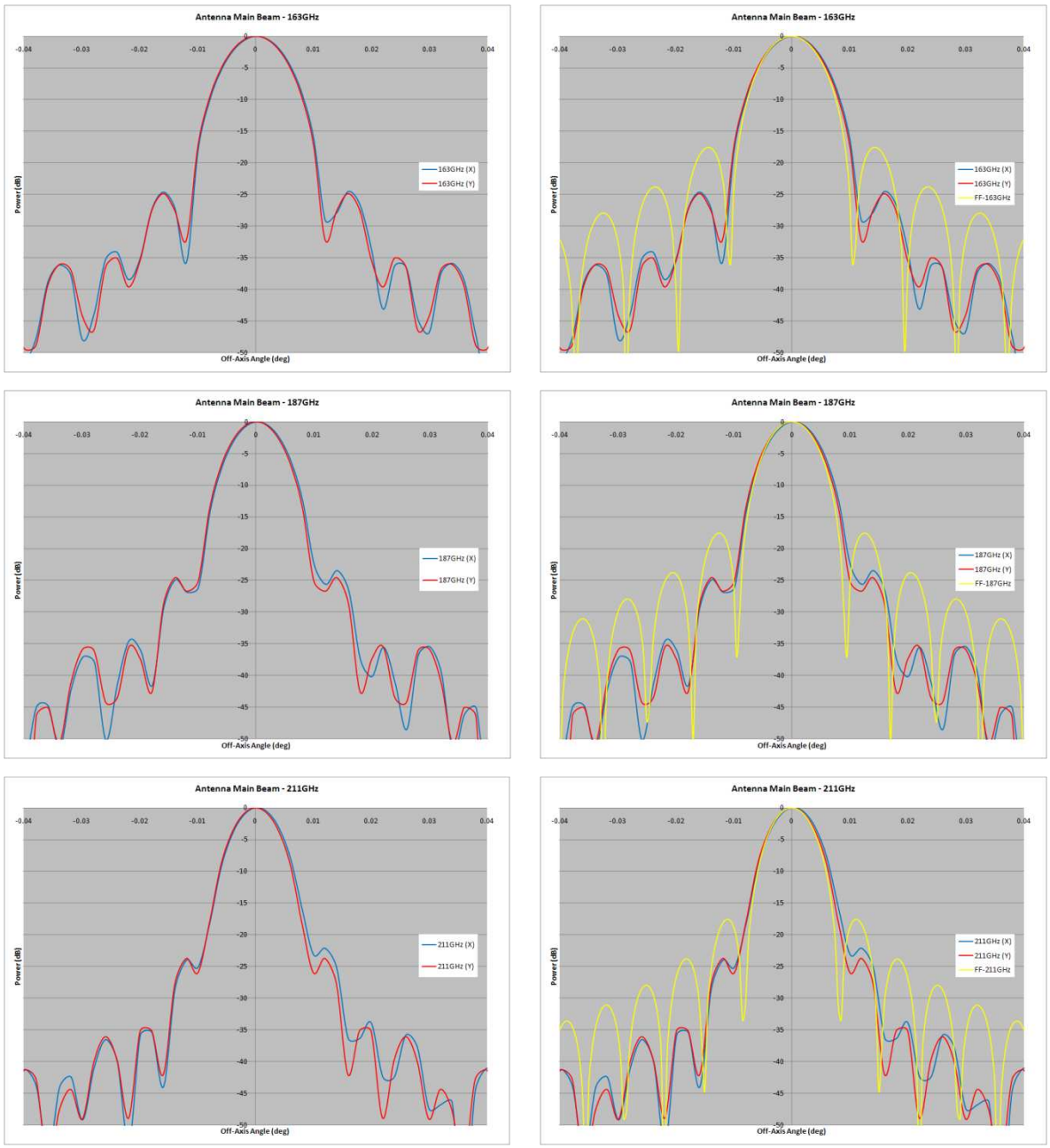

Figure 5-20 - Antenna main beam pattern predictions for the Band 5 front end optics as calculated using PO. Theoretical farfield antenna patterns as calculated from Equations 2.84 yellow) are overlaid on the same plots on the right.

5.8 Experimental Measurements

This section details the results of beam pattern measurements of the electrical field distributions from the prototype Band 5 front end optics. Near field measurements of phase and amplitude were taken at ambient room temperature using a scanning waveguide probe at the desired output planes. These measurements were conducted at the ALMA Band 5 development and testing facility at GARD. The near field measurement system is comprised of an Agilent E836-4B VNA with V05VNA2 Millimetre-Wave Extension Modules with an operating frequency range of 140-220 GHz. The extension modules cover the frequency range of the Band 5 channels. The corrugated feed horn was mounted upon a 2D planar XY scanning frame while the waveguide probe remained fixed in place. In Figure 5-21 the functionality of the near-field measurement system without the front-end optics included is displayed.

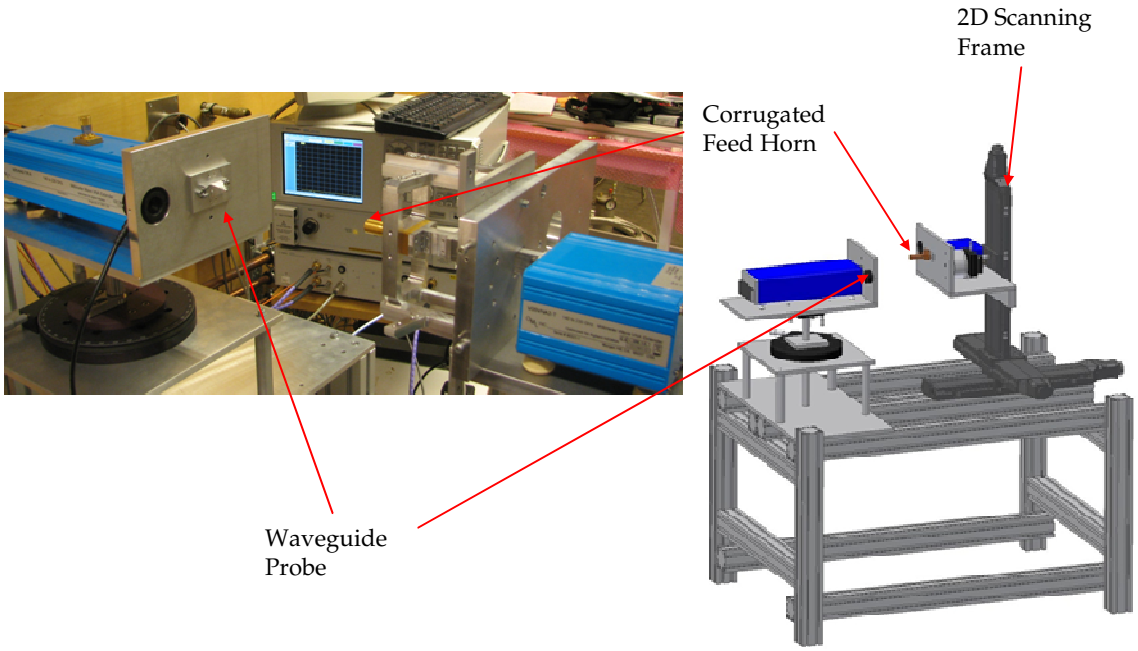

Figure 5-21 – Ambient temperature near field beam pattern scanning measurement system for the Band 5 front end optics

The first measurements taken were of the farfield pattern of the corrugated feed horn with no coupling optics. The orthogonal planar cuts of the farfield for the prototype

corrugated horn exhibited some peculiar asymmetries in the beam patterns. The figures below show these farfield amplitude plots for the prototype horn for a sample of frequencies spanning the operational bandwidth of the system: 163 GHz, 165 GHz, 180 GHz, 183 GHz, 205 GHz and 211 GHz. These planar cuts are compared against PO predictions for the horn calculated by MODAL using the SCATTER calculation for the corrugated horn aperture field.

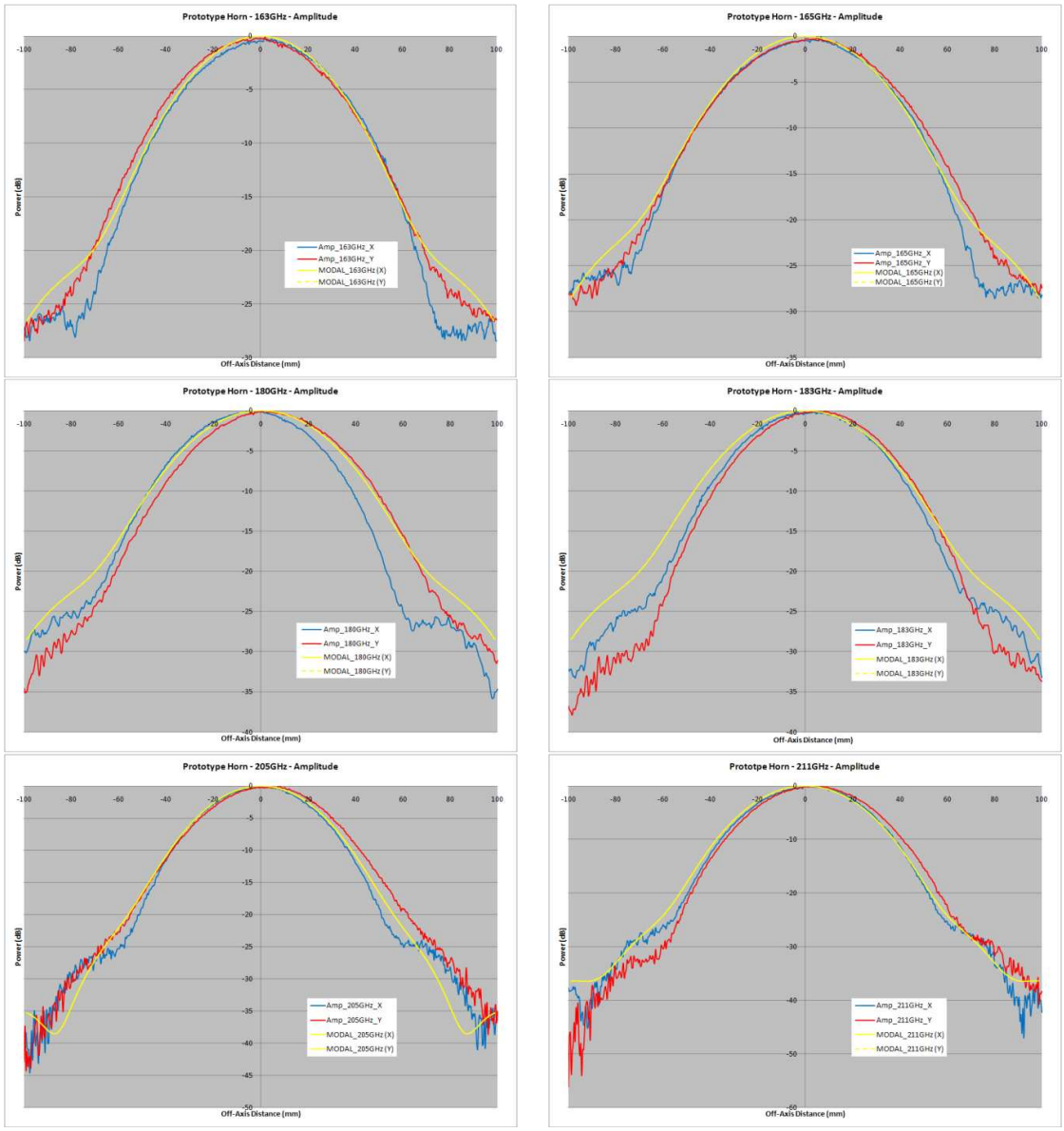

Figure 5-22 - Ambient temperature orthogonal amplitude planar cuts for the prototype corrugated horns. Note the evolution of the beam asymmetry between the x (blue) and y(red) cuts with increasing frequency. PO predictions from MODAL are in yellow

From the above plots it is observed that there is an obvious symmetry disagreement between the x and y amplitude cuts across the horn bandwidth, with the largest distortion occurring for the central frequencies of 180 GHz and 183 GHz. These frequency dependent beam shape distortions implied that there were some errors in the profile of the corrugated horn. All possible alignment errors for the scanning system were minimized using a highly accurate laser tracking tool. The fact that the distortions appear to vary over the bandwidth was evidence that they were inherent in the horn itself and not due to the alignment of the measuring system.

As to where these errors lay within the horn would have been extremely difficult to ascertain. The prototype of the horn was comprised of six individual parts that were designed and constructed in-house: a rectangular WR-5 waveguide, a rectangular to square waveguide extrusion, a square to circular waveguide transition zone of hexagonal cross section and the horn itself was composed of three individual sections that were milled from brass. It was deemed that the likely source of the beam distortions was the result of incorrect alignment of one or more of the individual horn structural components. These hypothesised asymmetries in the geometrical profile of the horn would undoubtedly upset the balanced hybrid condition of the horn and thus lead to unaccountable higher order mode excitation along the length of the horn [98] and manifesting in the output aperture distribution as frequency dependent asymmetries in the beam profile.

To ensure the removal of any alignment errors of the constituent parts, the horn was reconstructed as a single piece by an independent terahertz component contractor (QMC Instruments) so as to remove any possible alignment errors. The plots below display the farfield planar cuts for this new single component horn with PO comparisons against MODAL as before. The agreement between both the x and y amplitude measurements has been greatly improved upon, with only a slight degree of

asymmetry evident for the lowest frequency measurement. Agreement with PO calculations is also excellent, thus validating the performance of the new horn against the prototype.

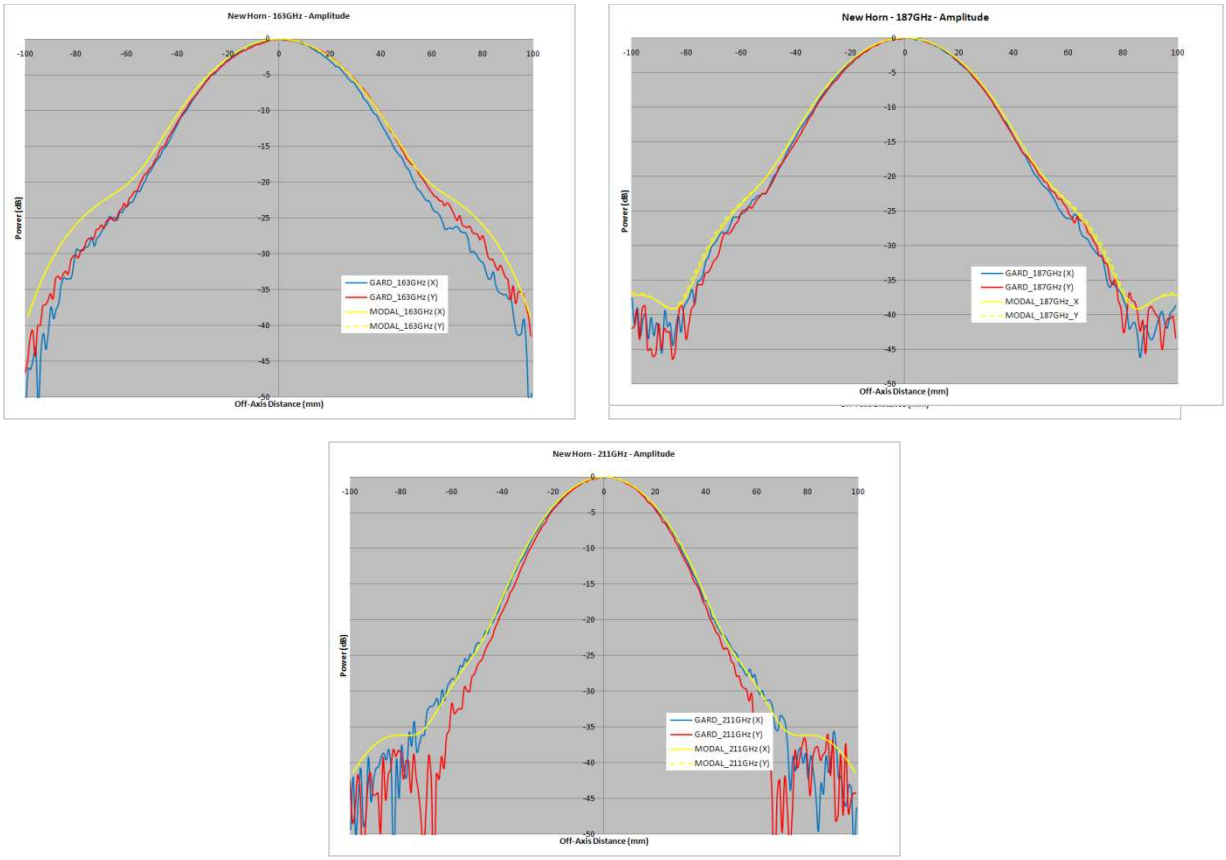

Figure 5-23 - Ambient temperature farfield amplitude plots for the new corrugated horn comprised of a single component. Agreement with SCATTER predictions has increased significantly.

Following the farfield measurements of this new horn, the next measurements taken were ambient temperature amplitude and phase measurements of the horn coupled to the front end optics. Given that the measurements were to be ambient it was possible to locate the measurement plane at the antenna focal plane, at a propagation distance of 229.82 mm from Mirror 2 – c.f. Figure 5-8. The prototype of the Band 5 front-end optics bracket is illustrated below in Figure 5-24.

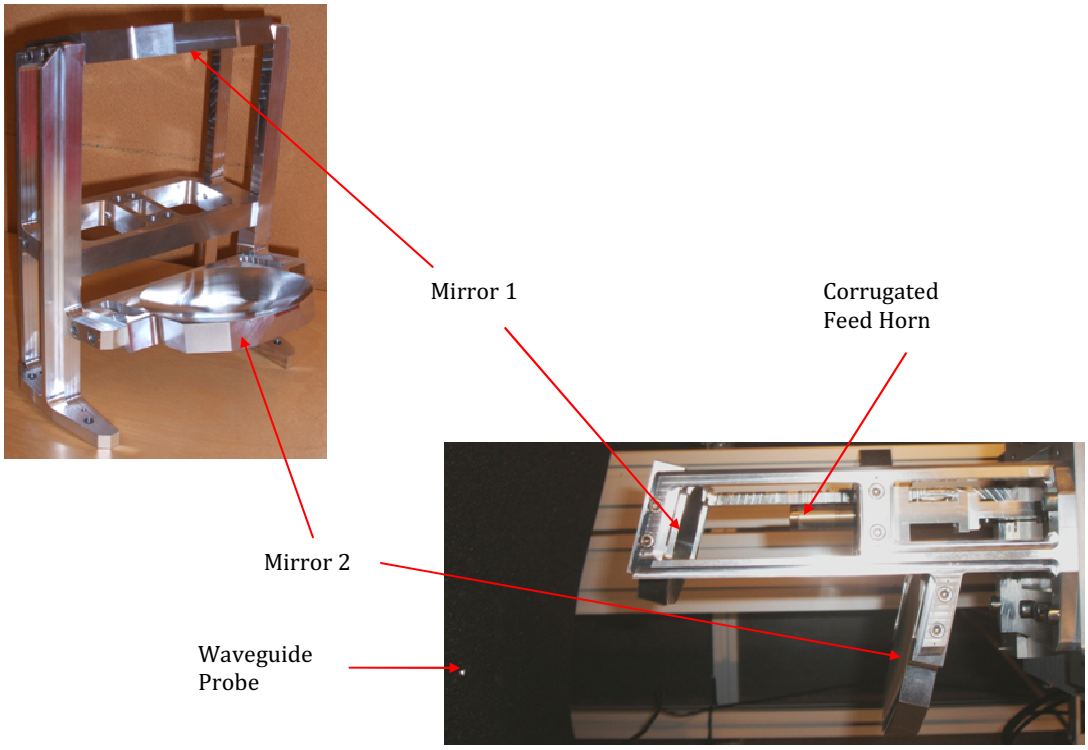

Figure 5-24 -Band 5 front-end optics bracket separate (top) and as mounted within the ambient near-field measurement system (bottom)

The proceeding plots show the recorded amplitude and phase data at the focal plane compared to PO predictions from both GRASP9 and MODAL. The amplitude and phase data are represented as orthogonal planar cuts through the centre of the beam at the focal plane in Figure 5-25 and Figure 5-26 respectively. 2D contour plots of the measured and predicted amplitude and phase data are presented in Figure 5-27 and Figure 5-28 respectively. The measurements and predictions were performed for *163 GHz* (top), *187 GHz* (middle) and *211 GHz* (bottom). Both the amplitude and phase data for measurements and predictions have been normalized to allow for easier visual comparison.

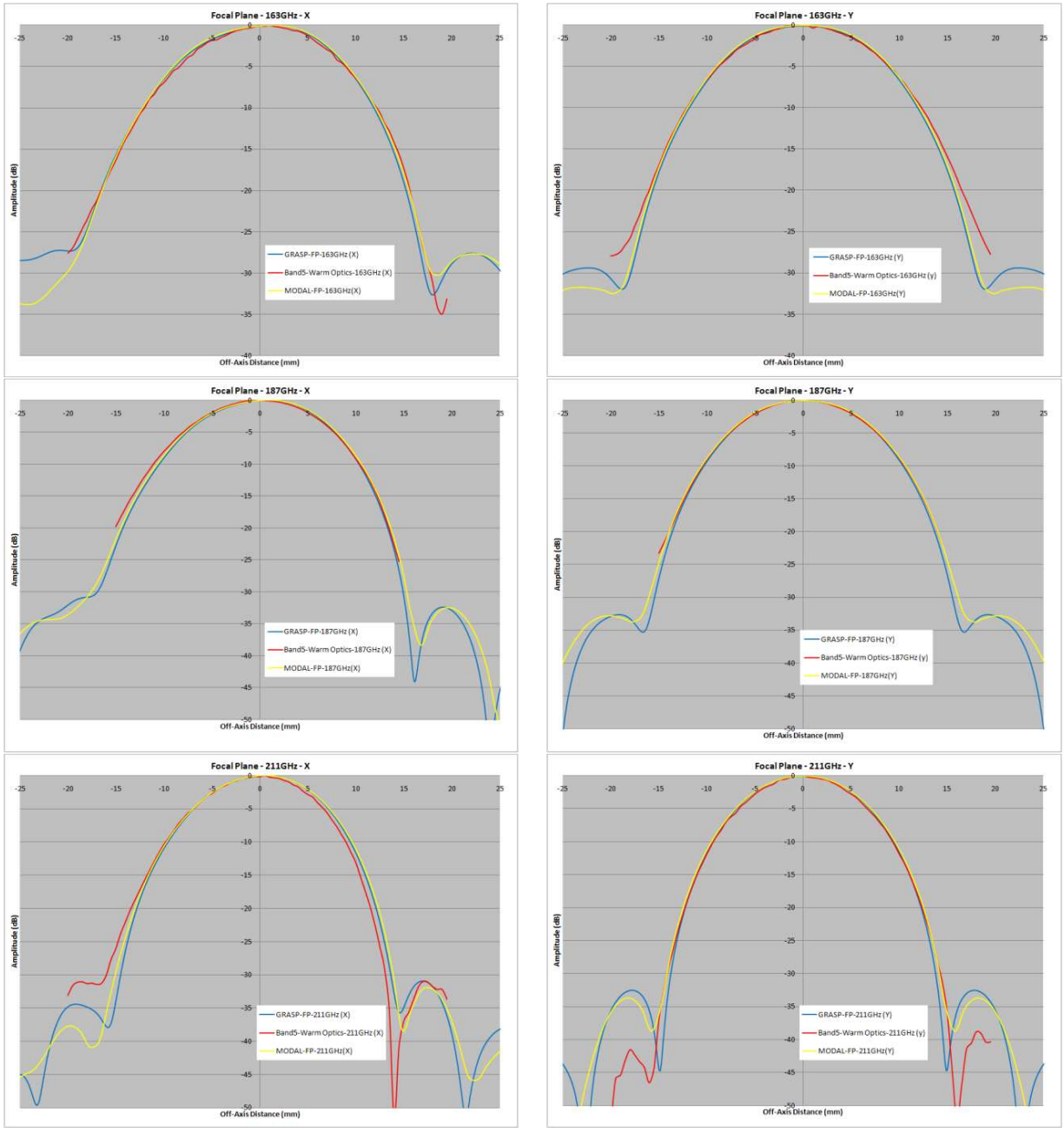

Figure 5-25 - ALMA Band 5 warm optics amplitude measurements(in red) at 163 GHz (top),187 GHz (middle) and 211 GHz (bottom) at focal plane (229.82 mm from M2) compared against predictions from GRASP (in blue) and MODAL (in yellow)

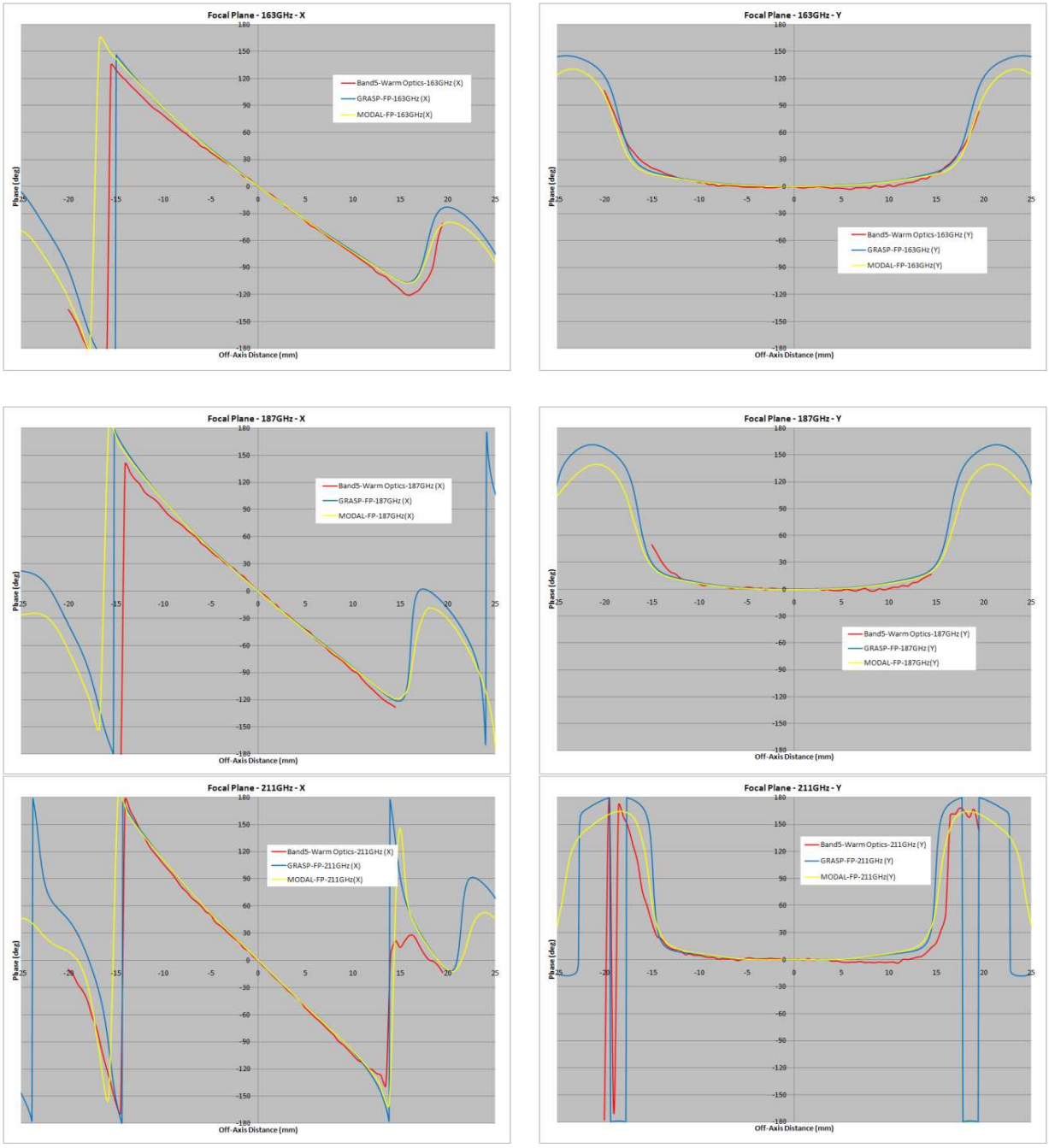

Figure 5-26- ALMA Band 5 warm optics phase measurements (in red) at 163 GHz (top),187 GHz (middle) and 211 GHz (bottom) at focal plane (229.82 mm from M2) compared against predictions from GRASP (in blue) and MODAL (in yellow)

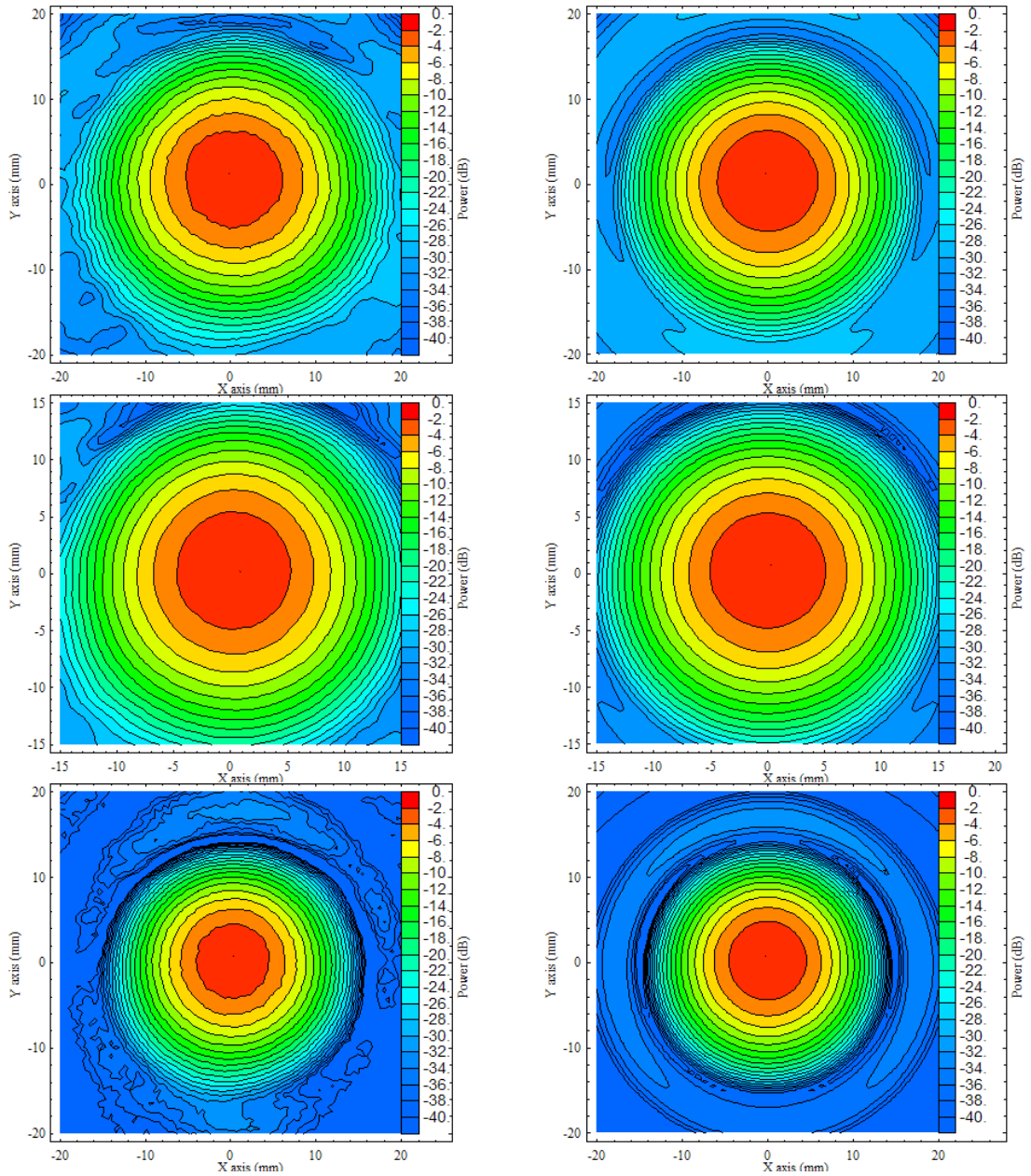

Figure 5-27 - Amplitude contour plots at the antenna focal plane for 163 GHz (top), 187 GHz (middle) and 211 GHz (bottom) - measured (left) and PO predictions (right)

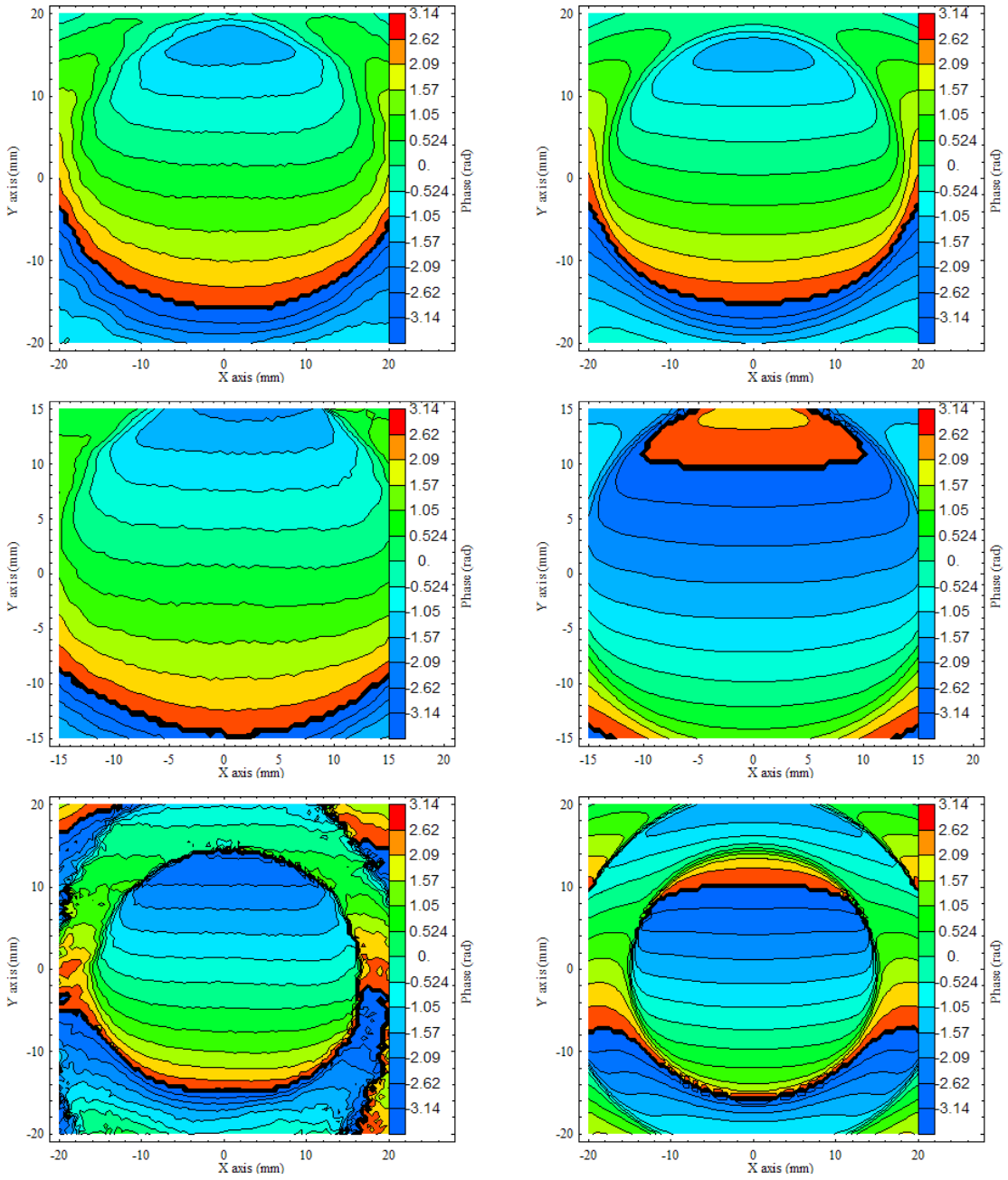

Figure 5-28 - Phase contour plots at the antenna focal plane for 163 GHz (top), 187 GHz (middle) and 211 GHz (bottom) - measured (left) and PO predictions (right)

The comparison plots above reveal a high degree of agreement between the measured and predicted beam data. As a measure of the exact degree of agreement the coupling coefficient between the predicted and measured beams was determined using the standard complex field coupling integral – c.f. Equation 5.3.

Parameter	Unit	163 GHz	187 GHz	211 GHz
Coupling Efficiency	%	99.0	98.5	98.2

Table 5-16 - Coupling coefficients between predicted and measured beam patterns at the focal plane

These results reinforce the conclusion of good agreement between the measured and predicted data.

5.8.1 Cold Beam Pattern Measurements

Near to the time of completion of this thesis the Band 5 receiver channel underwent its first insertion into the cryostat. The first set of cold beam pattern measurements was taken at a measurement plane a distance 67 mm along the optical train from the antenna focal plane (c.f. Figure 5-8). These beam patterns measurements were taken over a range of ± 40 mm with a stepping accuracy of 1 mm. This step size is relatively large yet these initial measurements were taken to determine overall beam shape and pointing. Further measurements will be conducted with significantly increased accuracy.

In Table 5-17 below the measured amplitude and phase data at 187 GHz and 210 GHz are compared against PO predictions from GRASP9. Measured and predicted planar cuts of the cop-polar amplitude are displayed for the three characteristic frequencies (163 GHz, 187 GHz and 211 GHz) in Table 5-18 below.

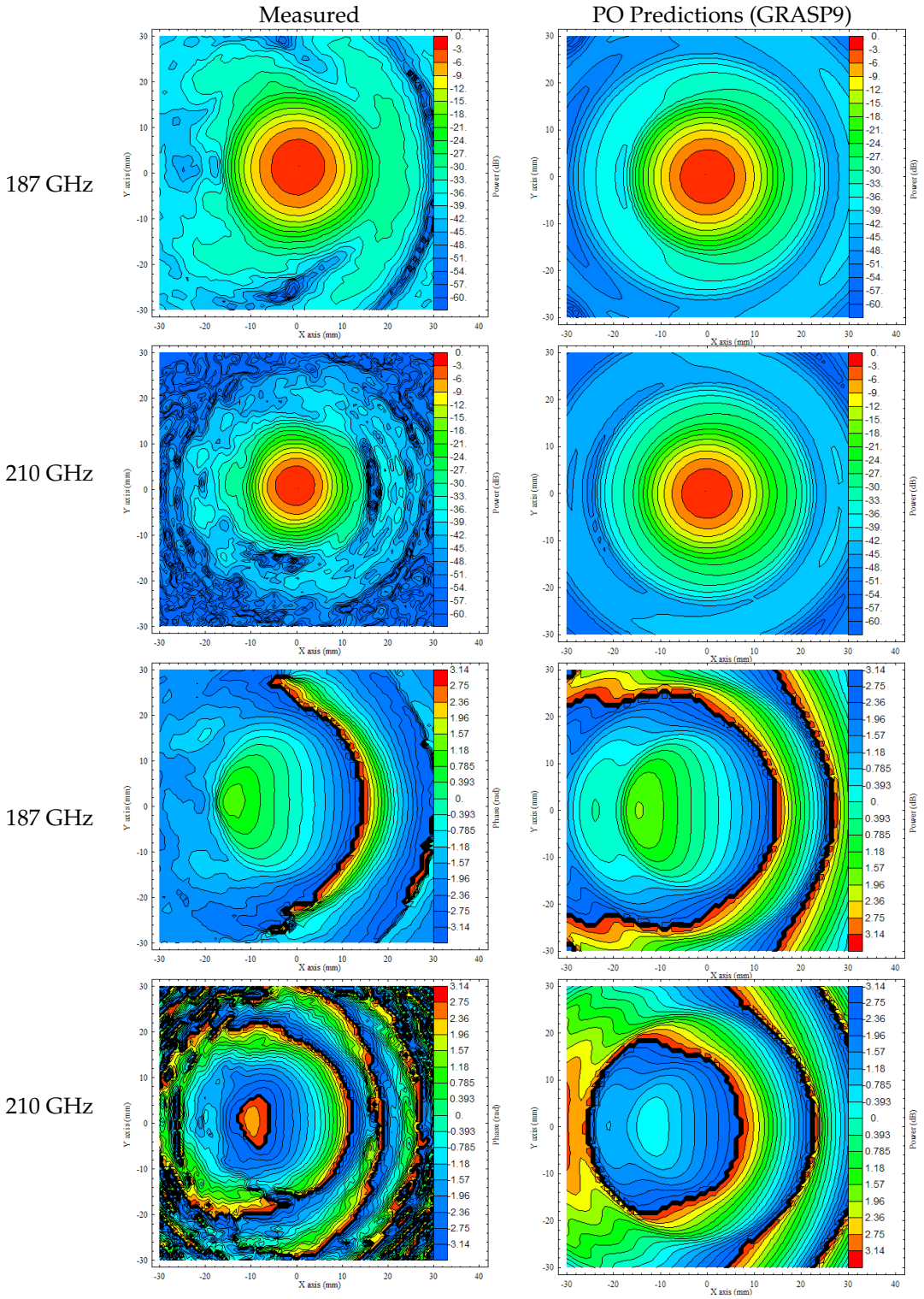

Table 5-17 - Measured (left) and predicted (right) amplitude and phase patterns for Band 5 cartridge after insertion into cryostat.

163 GHz	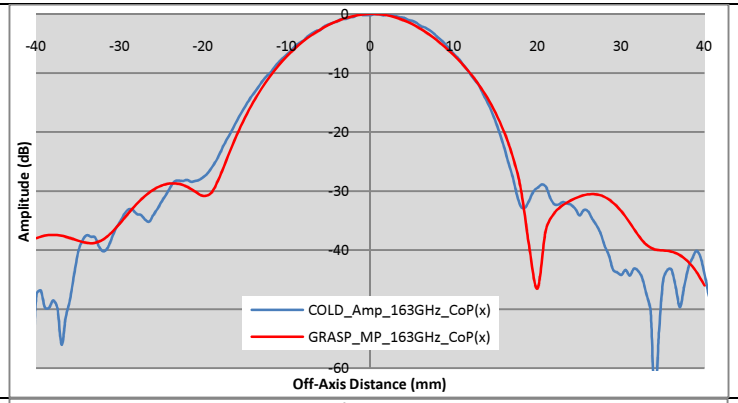	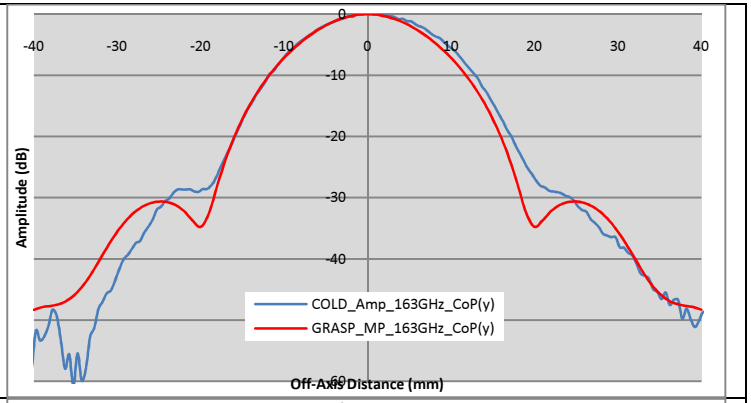
187 GHz	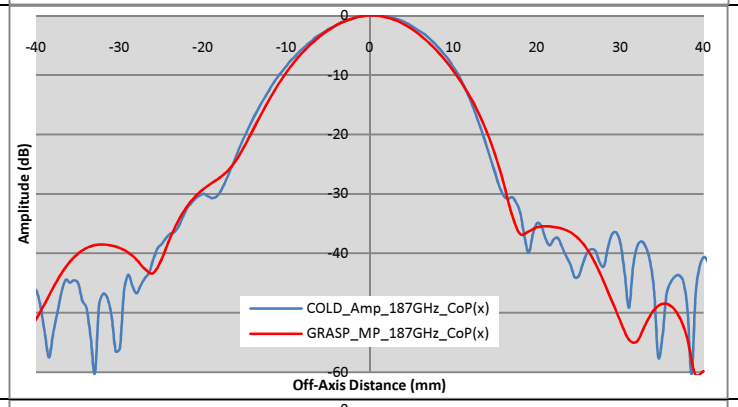	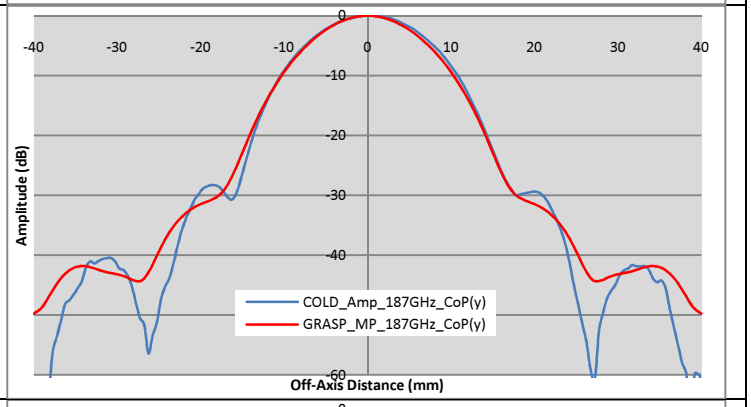
211 GHz	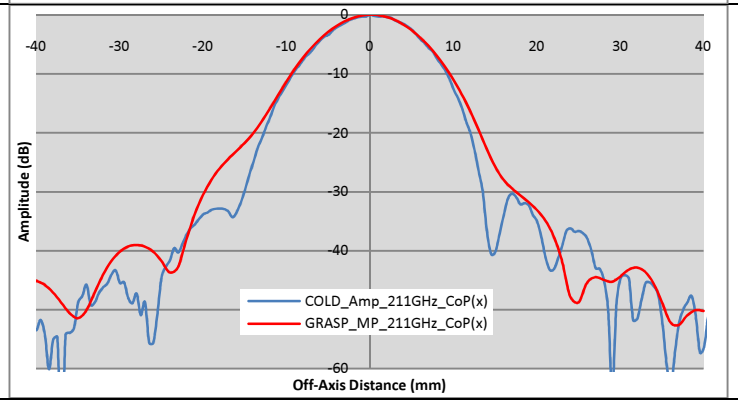	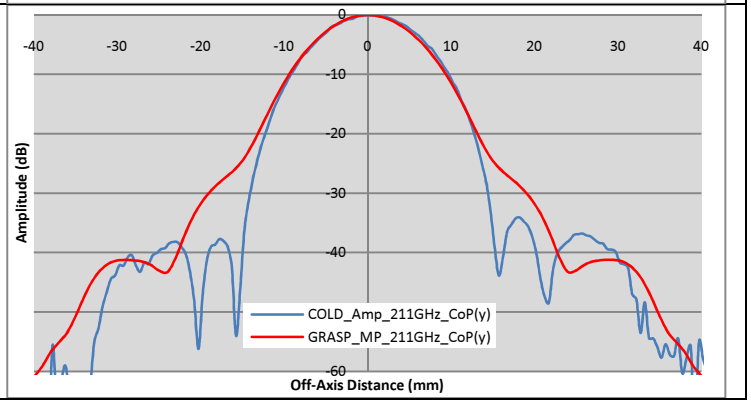

Table 5-18 - Planar amplitude x and y cuts at the new measurement plane - measurement data in blue and predictions (GRASP9) in red

5.9 Conclusions

A full quasioptical and physical optics analysis for various configurations of the Band 5 front end optics system was successfully completed. EM beam pattern predictions were generated at the antenna focal plane and subreflector using PO tools for the full frequency range of the channel. Using these beam pattern predictions the Gaussicity, aperture efficiency and cross polar efficiency values were calculated for all system configurations. These results were presented to both the Band 5 development team at GARD and the ALMA Band 5 Preliminary Design Review 9 (PDR). The recommended 'Quasioptical' definition to the reflector surfaces was implemented and a reflector rim truncation level below the standard ALMA design preference was adopted.

A prototype corrugated horn and optical system were developed in-house at GARD. Preliminary farfield beam pattern measurements of the horn prototype without coupling optics revealed a frequency dependent beam distortion. This was corrected with the construction of the horn as a single piece by an independent microwave components contractor. Beam pattern measurements of this new horn exhibited a much improved beam pattern with excellent agreement to PO predictions. Ambient temperature beam pattern measurements were taken at the antenna focal plane and showed very high coupling to predictions across the system bandwidth. Preliminary cold beam pattern measurements are included and compared to equivalent GRASP PO calculations. Overall good agreement is seen but the experimental measurements are very preliminary at time of writing and further refinements to accurately predict the measurement plane is required. Farfield main beam patterns for the ALMA antenna were predicted again using PO, which exhibited low sidelobes below -20 dB and good main lobe coupling to theoretical Fraunhofer predictions.

6. Further Optical Characterisation of the ALMA Band 9 Front End and Performance Related Modifications to the Cross Polar Power Component

6.1 Introduction

The design and verification of the front end optics of the ALMA Band 9 receiver channel has to date been completed [ref – ALMA Memo 544]. The development of this receiver is the responsibility of ALMA Band 9 team funded through NOVA (Nederlandse Onderzoekschool voor Astronomie) based at the Space Research Organisation of the Netherlands (SRON) Groningen. The initial quasi-optical verification of the optics was also performed at Maynooth by Massimo Candotti who worked with the SRON group as part of his PhD thesis within the Far-Infrared and Submillimetre Research Group [99], [100] in initial physical optics modeling and extensive experimental verification. The ALMA Band 9 cartridge is the most developed of the ALMA cartridges. To date [2009] SRON have completed the construction and testing of 11 cartridges.

The analysis presented in this chapter is chiefly concerned with determining solutions to minimize cross-polar power levels achievable across the bandwidth in this orthogonally polarized heterodyne receiver. One of the specified requirements for all ALMA channels is to have a cross-polar power level of less than -20 dB when normalized against co-polar power. The PO analysis and cold beam pattern measurements conducted as part of the verification of the receiver have revealed that the cross polar power does not achieve this requirement; the predicted cross polar power level of the Band 9 corrugated feed horn itself is approximately -33.4 dB for the central operating frequency (661 GHz) while measured cross polar power levels at the antenna focal plane are approximately between -16.5 dB to -18.5 dB [100]. As part of a series of post-construction tests, the Author was requested to investigate possible improvements to the cartridge design that would reduce the cross polar power level within specification as measured and modeled at the antenna focal plane. The work

presented in this chapter is comprised of the results of the investigation to lower the cross polar power levels through software and experimental analysis and the recommendations presented to the Band 9 group at SRON.

6.2 ALMA Band 9 Front End Optics

The Band 9 cartridge is defined within the ALMA documentation as a Category C receiver [101] which are collectively Bands 5 – 10. Internally, the optical parameters vary between the different bands. For example, Bands 5 and 6 use a single beam path for the two polarisations. For the higher frequency channels a polarising grid is used to split the polarisation into two paths. This is due to the fact that the construction of an effective Orthomode Transducer (OMT) for frequencies above 300 GHz is very difficult. The Band 9 cartridge follows these design criteria. The imaging of the beam from the secondary reflector of the ALMA antenna to the feed horns is achieved using cold reflective optics with two paired off-axis ellipsoidal mirrors. A polarising grid is located at the focal point of the first mirror after the secondary reflector – c.f. Figure 6-1. At this grid the beam is split into orthogonal linearly polarised beams and then follows two equivalent paths to the two orthogonal feed horns. The procedure for the design of all the optics is based on geometrical optics techniques and the bending angles for the mirrors are chosen to minimise the beam distortion at the output of the system [87]. Initial optical designs were proposed by James Lamb [102]. The sky signal is incident on the M3 reflector at an angle of 0.94° relative to the central telescope axis (see Figure 6-1 below). This was due to the off-axis position of the Band 9 cartridge window on the cryostat. The grid works in transmission for the 0P beam and reflection for the 1P beam. The 1P optical train is a duplicate of the 0P optics, but rotated relative to the point of beam incidence on the grid by 125°. The LO beams for each polarisation are coupled to the respective feed horns using a 45° beam splitter placed between the M4 reflectors and the feed horns. The beam splitters and LO optics are not considered in the analysis presented in this thesis and are not shown in Figure 6-1 below.

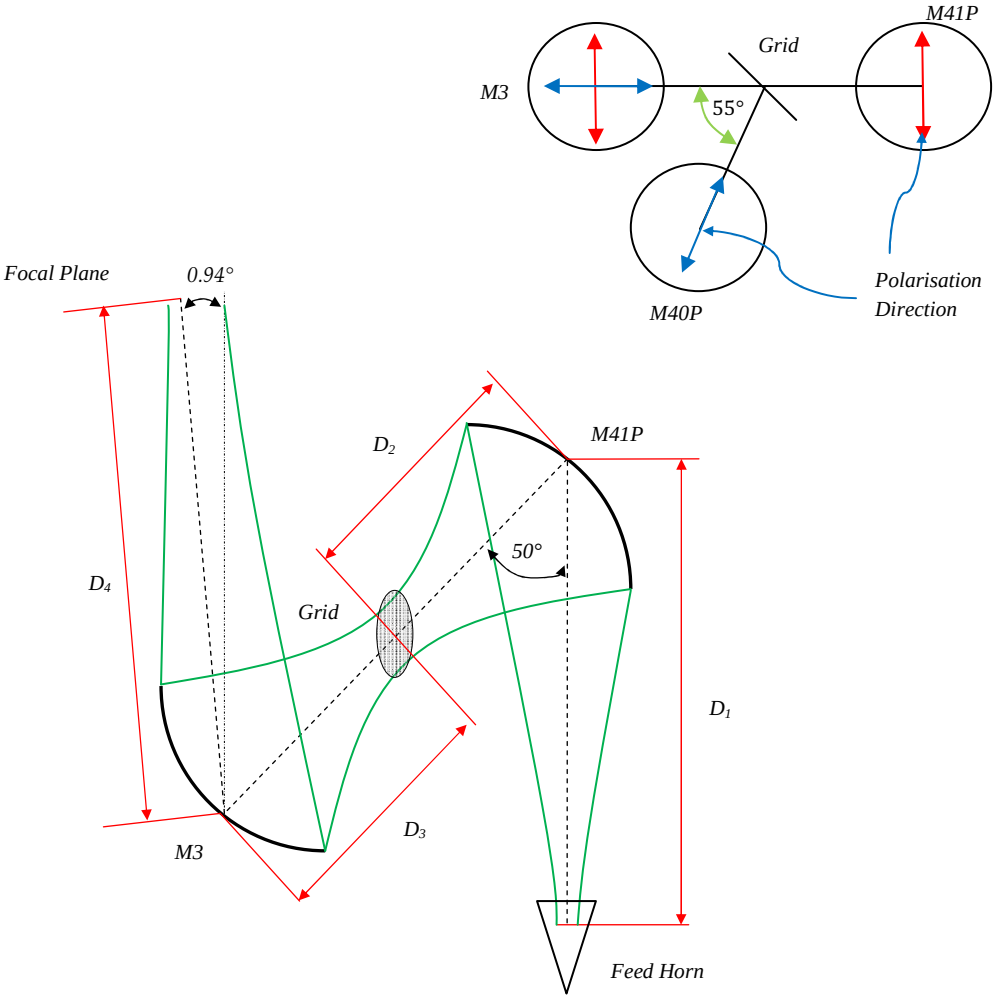

Figure 6-1 - ALMA Band 9 front end optics layout. The two beam polarisations 1P and 0P are orthogonally polarised. The blue arrow indicates the 0P beam, and the red arrow indicates the 1P beam.

The initial quasioptical and signal path analysis of the beam throughout the system has been well reported [99], [100] and the Author will not reproduce previous results other than that which is required for the basis of further work. Initial PO results were duplicated and reproduced for initial validation.

6.2.1 ABCD Analysis

The standard first order ABCD matrix analysis is used to calculate the fundamental Gaussian parameters of the beam as it propagates throughout the system. The source

beam is approximated as a fundamental Gaussian beam with a waist at the aperture of the feed horn of 0.6435*a*, where *a* is the radius of said aperture, and a phase radius of curvature equal to the slant length of the horn. The mirrors are treated paraxially as on-axis thin lens phase transformers and the entire system forms a Gaussian beam telescope that couples the beam waist behind the horn aperture to the antenna focal plane and on to the subreflector.

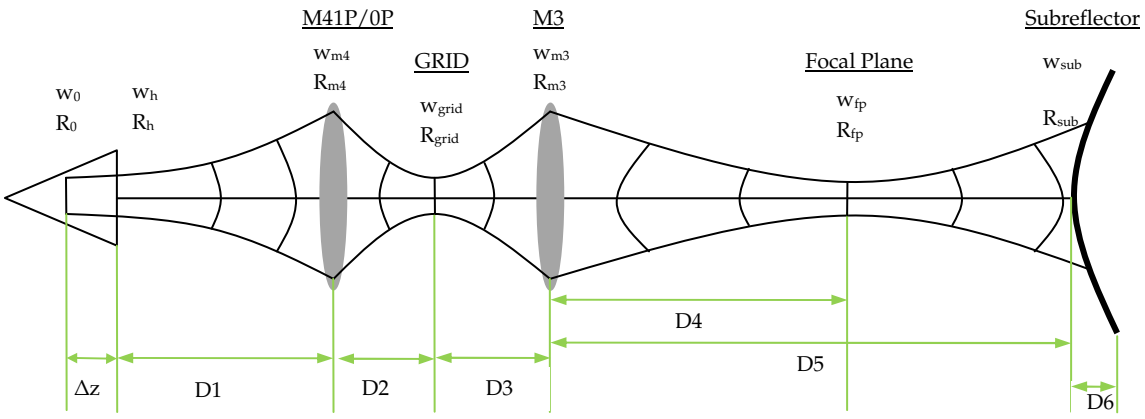

Figure 6-2 - Paraxial layout for Band 5 front end optics from feed horn to subreflector

The ABCD analysis for the signal path from the horn waist through to the subreflector, presented below in Table 6-2 reveals that for a fundamental Gaussian beam approximation of the corrugated horn source field the required frequency independent edge taper at the subreflector of -12 dB is achieved. The beam radii at all important locations are determined, allowing the size of the required 5*w* diameter truncation limit of the optical components to be set.

Parameter	Units	Value	Description
D1	**mm**	44.42	Feed horn aperture to M41P/0P
D2	**mm**	45.9	M41P/0P to Grid
D3	**mm**	50.0	Grid to M3
D4	**mm**	150.0	M3 to Focal Plane (z=0)
D5	**mm**	5883.7	M3 to Subreflector Vertex
D6	**mm**	111.3	Subreflector Vertex to Edge
θ_{m1}	°	50.0	M41P/0P bending angle
f_{m1}	**mm**	24.862	M41P/0P focal length
θ_{m2}	°	50.94	M3 bending angle
f_{m2}	**mm**	39.41	M3 focal length

Table 6-1 - System dimensions for Band 9 Front End Optics - c.f. Figure 5.1

Parameter	Symbol	Units		Frequency (GHz)		
Frequency		**GHz**		602	661	720
Horn Aperture Radius	a_h	**mm**	2.53			
Horn Axial Length	L_h	**mm**	15.44			
Horn Slant Length	R_h	**mm**	15.65			
Horn Waist	w_0	**mm**		1.11	1.06	1.00
Horn Waist Offset	Δz	**mm**		-8.35	-9.07	-9.72
Horn Aperture Waist	w_{ha}	**mm**	1.63			
Beam radius at M41P/0P	w_{m4}	**mm**		7.62	7.41	7.24
Beam radius at Grid	w_{grid}	**mm**		0.95	0.89	0.85
Beam radius at M3	w_{m3}	**mm**		8.34	8.25	8.18
Beam radius at Focal Plane	w_{fp}	**mm**		2.98	2.72	2.49
Beam radius at Subreflector Edge	w_{sub}	**mm**		318.38	318.38	318.38
Edge Taper	T_e	**dB**		-12.0	-12.0	-12.0

Table 6-2 – Fundamental Gaussian beam parameters of Band 9 optics using ABCD analysis

6.2.2 Cross Polar Power Levels

In this section the current cross polar power levels of the Band 9 optics are discussed with attention paid to the corrugated feed horn and the distortion effects of the off-axis optics. The ALMA specifications require that the desired cross polar power levels should be below -20 dB relative to power levels in the main beam, corresponding to a cross polar efficiency of 1.0%. The output cross polar efficiency is determined ultimately by the initial polarisation purity of the source conical corrugated feed horn and to what degree the off-axis ellipsoidal reflectors distort the beam [68].

6.2.2.1 The Conical Corrugated Feed Horn

As previously stated the feed horn of choice for all ALMA channels is the conical corrugated horn. One of the main reasons for this is that they maintain very low cross polar power levels. The geometry of the Band 9 feed horn was specifically designed to maintain low cross polar levels, as well as producing a highly symmetrical beam with low sidelobes.

The complex electromagnetic field patterns at the aperture of the horn were obtained using SCATTER. To provide sufficiently accurate field descriptions the calculations were performed using 20 *TE* and 20 *TM* modes. The SCATTER code generates a scattering matrix description for the entire horn from which the transmitted power levels are obtained. The mode-matched field is dependent on the geometrical cross section of the horn. The mandrel profile for the Band 9 horn is displayed below in Figure 6-3. This planar cut through the horn shows the depths of the corrugations and their position along the optical axis.

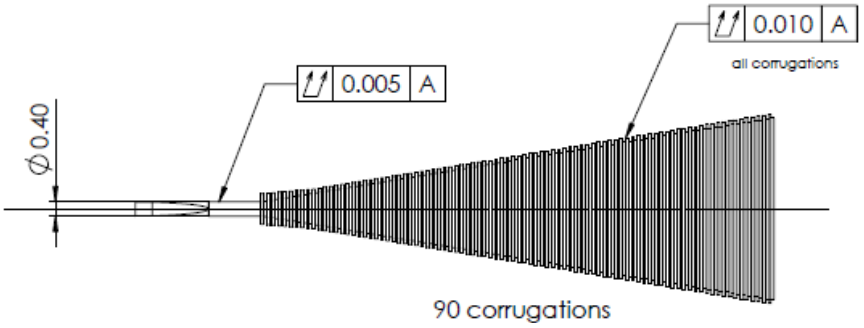

Figure 6-3 - Cross section of the mandrel profile for ALMA Band 9 corrugated horn

Recall from Chapter 4 that the transverse electric field E_{aper} is written as a linear sum of *TE* and *TM* modal fields (Equation 4.84). The co polar field is represented as the cosine dependent from Equation 4.84 and the cross polar field is sine dependent. The contour plots below in Figure 6-4 illustrate the co and cross polar components of the complex aperture field.

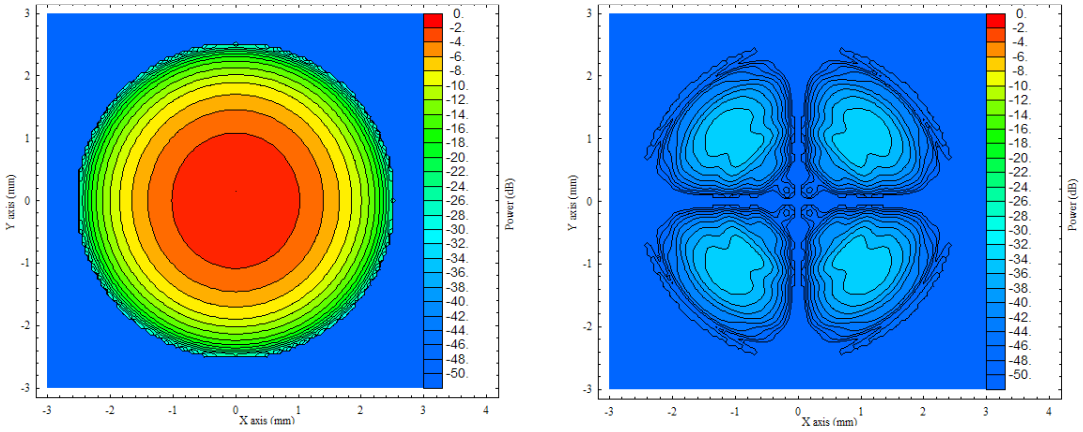

Figure 6-4 - Predicted co polar (left) and cross polar (right) fields of Band 9 feed horn aperture using 40 modes [SCATTER]

The cross polar power level of the feed horn at the aperture was determined from this mode-matched field to be -33.34 dB (0.045%. efficiency)

6.2.2.2 Off-Axis Mirrors

Off axis mirrors will introduce cross talk between the co and cross polarised components [103] as well as spatial aberrations such as coma and astigmatism [97]. These distortions are usually minimised with the inclusion of a paired off-axis reflector with the appropriate bending angle [104]. Obviously, the greater the off-axis bending angle the greater the degree of scattering and spatial aberrations.

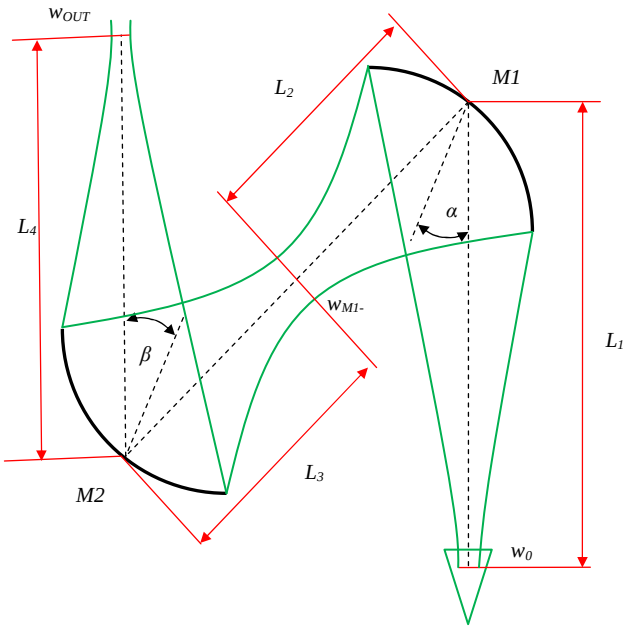

Figure 6-5 - Optical configuration for a typical pair of off-axis ellipsoidal reflectors.

Applying Dragone's Rule for off-axis bending angles of conic reflectors from [104] the optimum bending angle α between paired off-axis reflectors is given as

$$\alpha = \arctan\left(\tan(\beta)\left(\frac{\frac{L_3}{L_4+1}}{\frac{L_2}{L_1+1}}\right)\right) \tag{6.1}$$

where the variables α, β, L_1, L_2, L_3 and L_4 are illustrated above in Figure 6-5 for a typical pair of off-axis ellipsoidal reflectors that couple the waist from a feed horn w_0 to the waist at the output plane $w_{out.}$ Applying this relation to the Band 9 optics the optimal angle of reflection for *M41P/0P* is predicted to be *29.31°*. This is significantly smaller

than the actual bending angle of 50°. This larger bending angle was deemed necessary for opto-mechanical reasons; the 'vertically' aligned beam from *M41P/0P* to the feed horn allowed for a straightforward design of the mixer subassembly and LO coupling optics, as well as creating the necessary space for the solid mounting frame for the polarising grid.

The degree to which this off-axis bending will distort the incident beam is accounted for by [97] where the fractional loss in power that is scattered out of an incident fundamental Hermite-Gaussian mode into higher order modes is given as

$$\Delta P_{Amp} = \frac{1}{8}\left(\frac{w_m}{f}\right)^2 \tan^2(\theta_i) \tag{6.2}$$

where w is the beam radius at the mirror, θ_i is the angle of incidence and f is the focal length. The amount of power scattered into the orthogonal linear polarisation state is twice this amplitude distortion;

$$\Delta P_{XsP} = \frac{1}{4}\left(\frac{w_m}{f}\right)^2 \tan^2(\theta_i) \tag{6.3}$$

The cross polarisation losses for a system of a number of off-axis mirrors is given by

$$\Delta P_{XsP} \approx \left| \sum_{j=0}^{n} \frac{1}{2\sqrt{2}} \left(\frac{w_m}{f}\right)_j \tan(\theta_i)_j \exp\left(-j\Delta\phi_{k\to k+1}\right) \right|^2 \tag{6.4}$$

where $\Delta\phi_{k\to k+1}$ is the fundamental mode phase slippage between mirror k and mirror $k+1$. By using the Gaussian beam parameters obtained from the fundamental mode ABCD analysis of the Band 9 optics the total loss of power from the co polar component to the cross polar component from the feed horn to the output focal plane is predicted to be 4.1 dB. For the Band 9 system this implies an increase in the cross polar power from -33.4 dB at the horn aperture to approximately -29.3 dB at the focal plane. This is still well within the accepted constraints for the channel.

A more accurate quantification of the degree to which the paired off-axis reflectors affect the polarisation purity of the system is achieved through PO calculations. The cross polar power levels at the output focal plane without the effects of the grid were predicted using GRASP9 by removing the polarising grid object completely for the transmitted path and replacing it with a simple plane reflector for the reflected path. At the focal plane the cross polar power levels were predicted as -29.6 dB for the reflected 1P beam and -29.54 dB for the transmitted 0P beam. This shows that the mirrors perform relatively well in maintaining low cross polar power levels, with an approximate increase of only 3.8 dB from the cross polar level of the horn aperture to the focal plane. The previous result as predicted by [97] is therefore a close match to this PO result, with the disparity being accounted for by the more accurate description of the complex field distribution of the propagating beam. The cross polar leakage predicted by Equation 6.4 is for a fundamental Gaussian mode approximation of the beam also rather than an actual corrugated aperture field. The co and cross polar amplitude distributions at the focal plane for the 0P and 1P beams as predicted by GRASP9 without the wire grid polariser are illustrated below in Figure 6-6.

The polarising grid and how the horn beam polarization orientation intercepts the grid lines will influence the cross polar efficiency of the system. As reported in [97] for the case of a system consisting of appropriately paired off-axis ellipsoidal reflectors the cross polarisation introduced by one reflector will be cancelled out at the output by the cross polarisation introduced by the subsequent reflector. This accounts for the low level of cross polar power predicted for the Band 9 front end optics without the wire grid polariser. The inclusion of the polariser will disrupt this arrangement as it will remove the cross polarisation generated by *M41P/0P* that would otherwise be compensated for by the cross polarisation introduced to the beam by M3. In Table 6-3 below the cross polar power levels at the focal plane as calculated from PO predictions with the grid calculations included and as measured by [100] on the warm optics prototype of the Band 9 channel are presented. Also presented in Figure 6-7 below are

the co and cross polar field distributions at the antenna focal plane as predicted by GRASP9 PO with the wire grid polariser included. The increase in cross polar power with the inclusion of the grid is evident when comparing Figure 6-6 and Figure 6-7. The effect of the grid is such that the cross polar power levels no longer meet the expected minimum criterion for the ALMA front end channels of *-20 dB*. The expected cross polar power pattern without the grid included exhibits a similar quadruple-pole pattern to that from the feed horn aperture. With the grid included, at its particular orientation, this cross polar pattern at the focal plane now displays a double lobe shape indicating non ideal interaction with the grid. The net effect of the grid on the co-polar beam is still negligible however, with coupling efficiency between the co polar beam patterns with and without the grid for both beam paths calculated at over *99%*. This ensures that the co polar beam is correctly aligned with the grid wires.

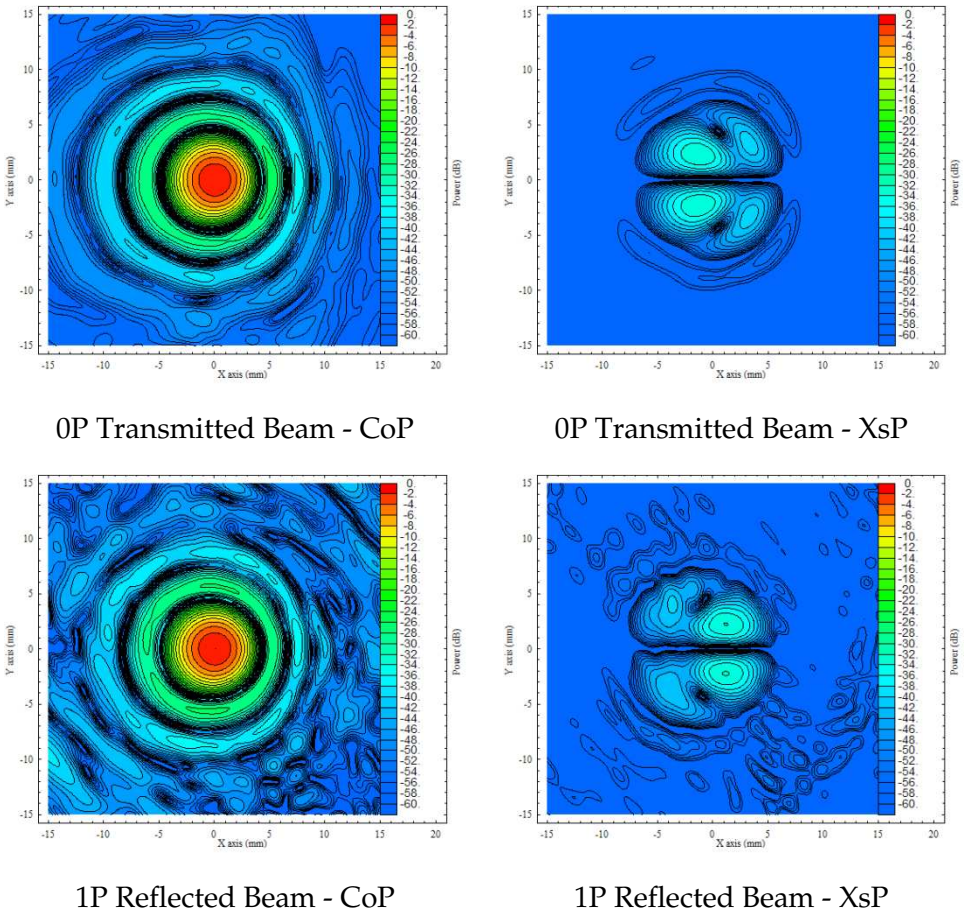

Figure 6-6 - Predicted co and cross polar beam patterns at the focal plane with polarising grid removed from calculations

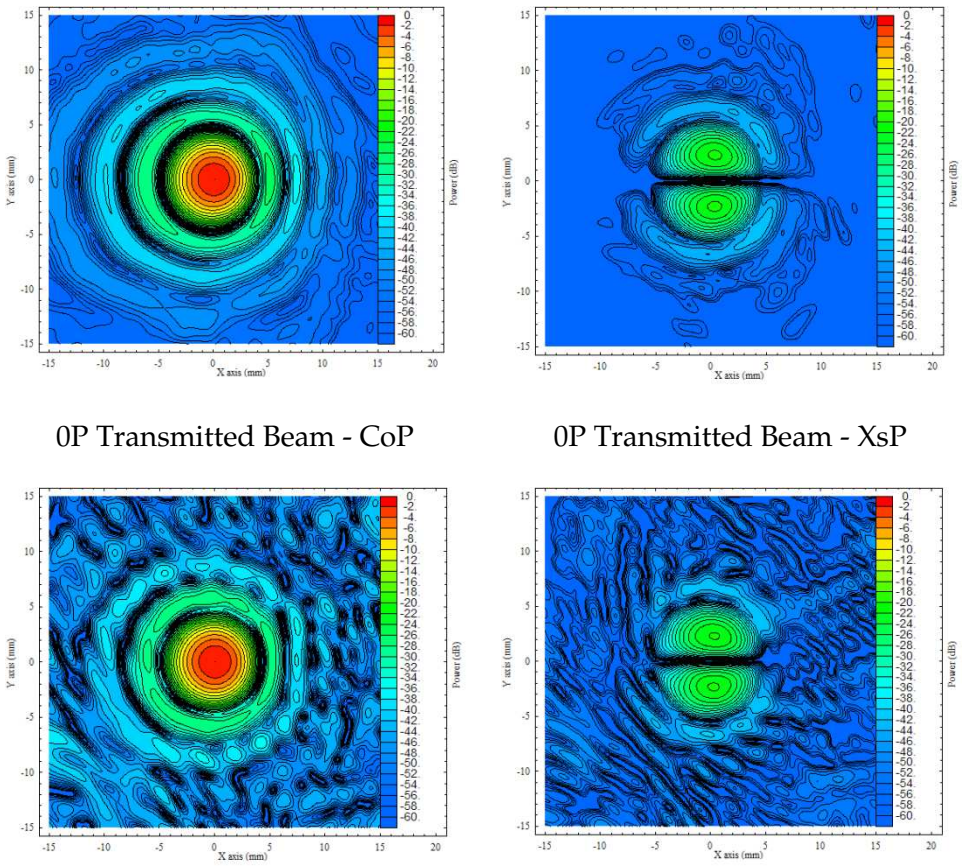

Figure 6-7 - Predicted co and cross polar beam patterns at the focal plane with the polarising grid calculation included

Parameters	Units	Beam	
		0P	1P
Predicted Cross Polar	dB	-18.08	-18.18
Predicted Cross Polar	%	1.56	1.52
Measured Cross Polar	dB	-18.5	-16.5
Measured Cross Polar	%	1.41	2.24

Table 6-3 - Predicted and measured (warm optics - [100]) cross polar power levels at the Band 9 focal plane for the central frequency (661 GHz)

For a beam with two orthogonal polarisations incident upon a grid, the co polar component, which for convention will be taken to be polarised orthogonally to the grid lines, will be transmitted through the grid (transmission axis). The cross polar

component, which is collinearly polarised with the ideal grid lines, will be reflected backwards. This is the basic working premise of the grid for the transmitted 0P beam while the opposite holds for the reflected 1P beam, with the co polar component being reflected by the grid, and thus maintained within the system and the cross polar component being transmitted through the grid and thus out of the system. The optimal working condition for this grid is therefore that the incident beam is comprised of two orthogonally polarised components, or equivalently that the grid intercepts the beam at the appropriate angle to ensure this orthogonality. As shall be proven later throughout this chapter, this is not the case for the Band 9 system. For now it is sufficient to state that the polarising grid in its current configuration and projection effects deteriorates the cross polar efficiency of the Band 9 system. Further analysis of the nature of the projection effect upon the grid surface will be detailed in Section 6.4.

6.3 Geometrical and Quasioptical Design of Reflectors

This section details an investigation into the theoretical improvement to the phase transforming properties of the off-axis reflectors *M3* and *M41P/0P*. The process is similar to that presented for ALMA Band 5 (Chapter 5) where a geometrical and long-wavelength approach to designing the conic surfaces of the reflectors were compared in terms of aperture efficiency and cross polar power.

As stated in the previous section the design of the optics of the Band 9 channel were designed using geometrical optics. The geometrical optics method is considered a reasonable method for the Band 9 channel, owing to the relatively high operating frequency range (611 – 720 GHz). However, it can be concluded that there is room for improvement in the output beam in terms of both cross polar power levels and aperture efficiency/beam coupling to the subreflector through re-designing the ellipsoidal surfaces using Quasioptics. Using this method would ensure that the radius of curvature of the reflectors will be matched accurately to the complex phase radius of curvature of the incident beam at the centre frequency. The parameters required to describe the ellipsoidal surfaces are calculated from ABCD analysis.

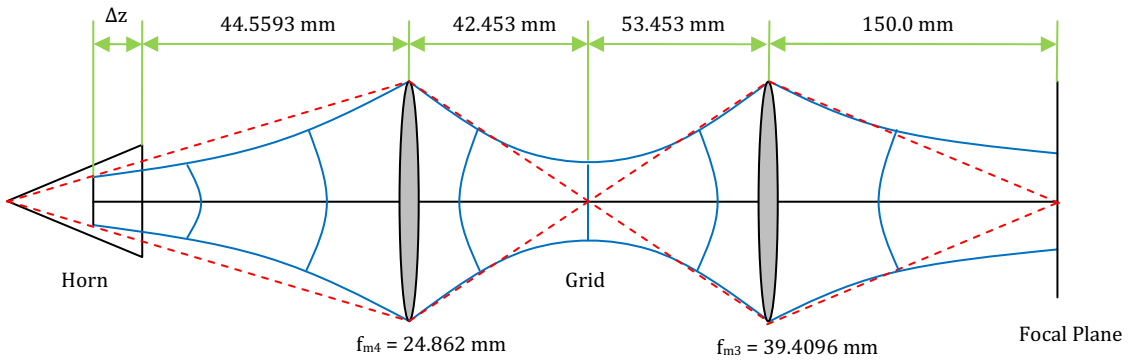

Figure 6-8 – Paraxial layout of Band 9 optics showing Geometrical (red) and Quasioptical (blue)

Figure 6-8 above displays a comparison between the classic ray-tracing representation of the geometrical optics (shown as the broken red line) and the phase front representation of the true quasioptical beam (the blue lines). Using ABCD analysis the beam waists at each of the focal points of the system are calculated – c.f. Table 6-2. Using these values the input and output phase radii of curvature for the beams are determined for the central frequency of the system. From these values, the new parameters of the ellipsoidal reflectors are determined - Table 6-4.

Parameter	**Units**	**Geometrical**		**Quasioptical**	
		M3	**M4**	**M3**	**M4**
Major Axis: a	**mm**	101.729	51.2266	110.838	49.0961
Minor Axis : b	**mm**	80.8415	45.7411	86.0372	44.2005
Eccentricity: e		0.60703	0.45022	0.6304	0.43529
Conic Constant: k		-0.36849	-0.20269	-0.3975	-0.1895
Radius of Curvature: R	**mm**	64.243	40.843	66.7857	39.7932

Table 6-4 - Parameters for ellipsoidal reflectors for Geometrical and Quasioptical versions of Band 9

6.3.1 EM Beam Predictions

To study the effects of changing the parameters of the ellipsoidal reflectors in the Band 9 system, both versions were implemented in GRASP9. The mode-matching software SCATTER was used to generate the vector aperture field of the feed horn. The beam predictions at the focal plane were used to determine both aperture efficiency/coupling to the antenna and cross polar power.

6.3.1.1 Gaussicity

The Gaussicity assessment of beam quality first used in Section 5.6.1 was used as a first order examination of the effect of the altered reflector surfaces on the beam. The PO predictions of the central frequency beam were taken at the antenna focal plane.

Optical Beam	Gaussicity (%)
Geometrical – 1P	96.19
Geometrical – 0P	97.10
Gaussian – 1P	96.81
Gaussian – 0P	97.24

Table 6-5 - Fundamental Gaussicity calculations at the antenna focal plane for the central frequency

A slight increase in coupling to the fundamental Gaussian beam is observed for both beam paths. This is validation of the improved beam transformation by the modified Gaussian design. However, the increased coupling can be considered practically negligible. This is expected given that the high operating frequency of the system is a relatively close match to the geometrical limit coupled with a good off axis reflector receiver design.

6.3.1.2 Cross Polar Power

Cross polar power levels at the antenna focal plane are calculated in the typical manner by normalising the cross polar beam with respect to the co polar beam. The table below compares cross polar power levels for the geometrical and Gaussian optics.

Optic Version	Units	Cross Polar Power	
		0P	1P
Geometrical	dB	-18.08	-18.18
Quasioptical	dB	-18.24	-18.22

Table 6-6 - Predicted cross polar power levels at the focal plane for the Geometrical and Gaussian optics versions of the Band 9 system

There is a slight predicted decrease in cross polar power levels at the focal plane with the modified Quasioptical version of the system. However, this increase in efficiency is extremely minimal, and would be very difficult to record experimentally. This is yet again a further validation of the improvement in system performance found with the Gaussian optics version, but as with predicted the Gaussicity, is negligible at best.

6.3.1.3 Antenna Aperture Efficiency

The antenna aperture efficiency for the two versions of the Band 9 optics was calculated in the same manner as for the Band 5 optics (c.f. Chapter 5). The field distribution at the subreflector vertex plane is coupled to the ideal phase transformed top-hat field. The reduction in coupling due to the shadow of the subreflector on the primary reflector is included in these calculations. This additional calculation is arbitrary however as the effect of the modified reflector surfaces are under scrutiny here.

Optical Version	Units	Cross Polar Power	
		0P	1P
Geometrical	%	85.08	85.08
Quasioptical	%	86.06	85.96

Table 6-7 - Predicted aperture efficiencies for the Geometrical and Quasioptical versions of the Band 9 system

There is an increase in the aperture efficiency of the system with the new Quasioptical modification of the order of 1%. This result is potentially interesting for any future upgrades or redesigns of the ALMA optics.

6.3.2 Conclusions

As the results from Sections 6.3.1.1 to 6.3.1.3 show, the Gaussian optics modification to the off-axis mirror surfaces ensure increased Gaussicity, lower cross polar power levels at the focal plane and an increase in coupling to the antenna. This represents an overall improvement in system performance that validates the quasi-optical modification. Unfortunately due to the advanced stage of the ALMA Band 9 frontend the individual parameters improvements would be difficult to retrofit to the already manufactured cartridges. As stated prior to this analysis this outcome is unsurprising given the relatively high operating frequency range of this channel. A geometrical design of the off-axis optics of the Band 9 channel has been verified to still be very applicable here.

6.4 Modification of the Band 9 Wire Grid Polariser

What follows is an analytical and experimental treatment of the Band 9 wire grid polariser and its effect upon the cross polar power levels for the system. The work presented involves a discussion of the working principles behind polarisers and wire grid polarisers specifically, with attention being primarily paid to their orientation relative to incident radiation over the physical properties of the wires that comprise such grids, such as the dimensions of the wires or the wire spacing and frequency. In reality no alterations to the physical structure of the Band 9 polarising grid were possible as the channel had already been well developed, with 11 cartridges already having been constructed and tested by the NOVA group at the time of writing. The only scope to potentially improve cross polar levels was the possibility to alter the rotation angle of the grid wires, and this formed the foundation of the work presented here. The analysis consists of an analytical treatment of the intersection of planes of variable orientation through Euler angles, PO predictions of suggested alterations to the polarising grid plane and warm optics beam pattern measurements conducted with the Band 9 optics prototype at SRON, Groningen. The topic was also further investigated using a lower frequency (100 GHz) equivalent version with a wire grid polariser tested

at NUI Maynooth. A similar effect in cross polar power was also recently reported by the ALMA Band 7 team where a conference paper [105] by Lazareff heuristically reports a similar phenomenon there in their lower frequency channel.

6.4.1 Polarisers

The polarisation of electromagnetic radiation describes the orientation of wave oscillations perpendicular to the direction of propagation. The purpose of a linear dichroic polariser in an optical system is to isolate a single linear polarisation from an unpolarised source. The polariser transmits radiation with electromagnetic oscillations along a transverse direction orthogonal to the direction of absorption. This preferred direction is referred to as the *transmission axis (TA)* of the polariser [33]. In an ideal polariser the transmitted radiation is linearly polarised in the same direction as the *TA*. The state of polarisation of the transmitted radiation can be determined through a second dichroic polariser, known as an analyser, as shown below in Figure 6-9.

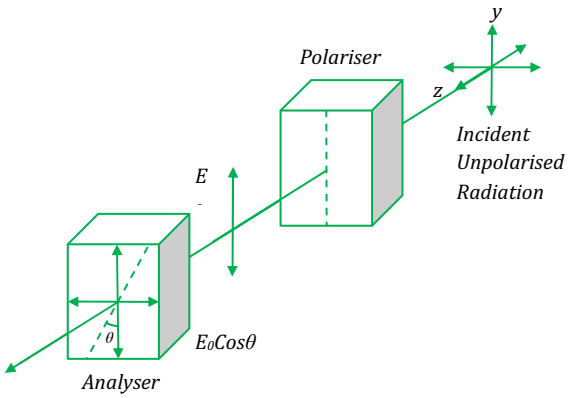

Figure 6-9 - Orthogonal dichroic polarisers acting in a polariser/analyser pair

As the angle of the *TA* of the analyser is rotated about the optical axis, the irradiance of light transmitted from the analyser varies. This variation of transmitted light is governed by Malus' law,

$$I = I_0 \cos^2 \theta \tag{6.5}$$

where I_0 represents the irradiance of the beam incident on the polariser, θ is the angle of the analyser as it is rotated about the optical axis and I is the irradiance of the light transmitted from the analyser [33]. The variation of transmitted irradiance for a polariser according to Equation 6.5 is illustrated below in Figure 6-10.

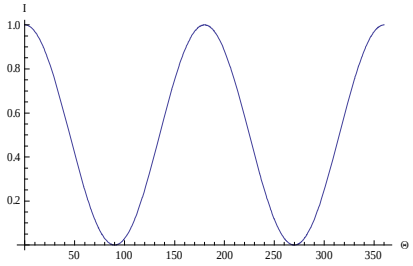

Figure 6-10 - Variation of transmitted irradiance from a polariser/analyser pair as a function of rotation angle θ

A wire grid polariser functions as a reflective polariser, meaning that only permitted polarisations are transmitted while the remainder is reflected. If the incident wave is polarised along the directions of the wires the induced conduction electrons are driven along the length of the wires in unrestricted movement. The physical response of the wire grid is thus essentially the same as that of a thin metallic sheet [77].These excited electrons generate a forward as well as a backward travelling wave, with the forward travelling wave cancelling exactly the incident wave in the forward direction. As a result, the incident wave is completely reflected and nothing is transmitted in the forward direction. If the incident wave is polarised perpendicular to the wire grid the current generated by the excited electrons is insufficient to cancel the incident field in the forward direction. Thus there is considerable transmission of the incoming radiation, and the wire grid is said to operate as a dielectric.

6.4.2 Band 9 Wire Grid Polariser

The Band 9 wire grid polariser located at the geometrical interfocal point between mirrors M3 and M40P/M41P serves as a beam splitter to the incident unpolarised

radiation from the antenna into two orthogonally polarised beams. The transmitted (0P) and reflected (1P) beams are coupled to their respective feed horns by the equivalent off-axis mirrors M40P and M41P. A significant effect of this polarising grid is that not only does it transmit/reflect the co-polar component of the 0P/1P beams respectively; the cross-polar components of both beams are prevented from propagating completely throughout the system, i.e. at the grid the cross-polar component of the 0P beam is reflected and the cross-polar component of the 1P beam is transmitted. For the polarising grid to successfully distinguish between the co-polar and cross-polar components they must be mutually orthogonal. For the transmitted path the beam co-polar polarisation must be perpendicular to the grid lines as it impinges on the grid to achieve the maximum power transmission through the grid. For the reflected path the converse is true, with maximum reflection of the beam achieved for the beam co-polar polarisation impinging on the grid surface parallel to the grid lines.

The grid was modelled in GRASP as an ideal grid object (Section 2.4.5.2). In the ideal grid calculation a set of equivalent currents for the grid surface are calculated on the basis of the reflection and transmission coefficients of the grid. For each PO integration point on the grid it is assumed that the incident radiation behaves locally as if it were a plane wave, whereupon the Poynting's vector can be used to calculate the direction of incidence. This plane wave approximation generally works well for most optical systems. However, it was noted for initial PO predictions there was a suspicious disparity between the 0P and 1P cross polar power levels. After further investigation by TICRA it was determined that the ideal grid PO object does not work correctly in this instance, where it is located close to the beam waist between mirrors M41P/0P and M3. The plane wave approximation technique will break down when placed at or near a beam waist. At this beam position the field will have a significant radial component; i.e. along the direction of propagation and hence perpendicular to the plane of the grid wires, which is not accurately represented by a local single plane wave. This was amended by TICRA with the release of a plane wave expansion tool in a beta version of

the GRASP package, and later in an official release. This tool expands the field incident upon the grid in a series of plane waves, each with their own local direction vector. These individual plane waves are then used to calculate the induced currents on the grid. This method is more accurate as the induced currents are calculated by exact plane waves rather than local approximations. The consequence of this new method was to provide the previously reported cross polar levels at the focal plane; -18.08 dB for the 0P beam and -18.18 dB for the 1P beam.

From Figure 6-1 it is evident that the plane of the grid is not strictly transverse to the optical path and thus there is a projection effect of the incident radiation to the plane of the grid. The question was raised as to whether the Band 9 polarising grid could be manipulated to provide improved transmission/reflection of the desired copolar components, or reduce the degree of cross polar power leakage in the output plane.

6.4.3 Euler Angles

Euler angles are a convenient formulation for describing the orientation of a vector plane in three dimensions. They are regularly encountered as a method of providing a complete description of the motion of rigid bodies within the Lagrangian formulation of mechanics [106]. This rotation is important in context of the Band 9 optics to understand the true orientation of the transmission axis of the grid relative the polarisation rotation of the incident beams and figuring out why cross polar levels of power are affected by this projection effect. Euler angles are best visualised in the Cartesian coordinate frame. A transformation from one Cartesian coordinate frame to another can be described using the appropriate transformation matrices that describe the required rotation about any of the three frame axes. The main convention followed here is that which is widely used in celestial mechanics, applied mechanics and aeronautical orientation.

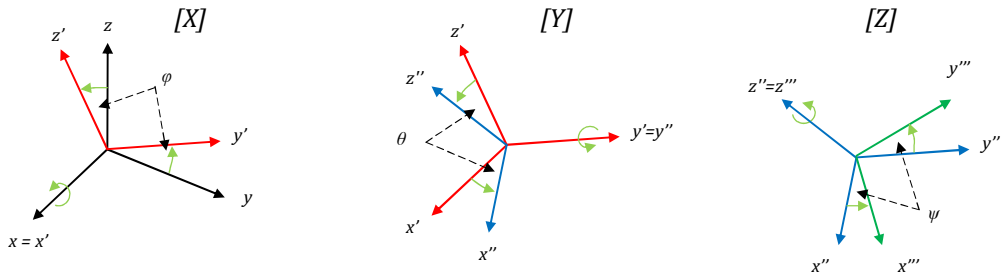

Figure 6-11 - The rotations that define the Euler angles – ref Classical Mech.

The sequence of rotations employed in the above figure is begun by rotating the initial coordinate frame *{x,y,z}* by an angle φ counter clockwise about the *x* axis to form the next *{x′,y′,z′}* coordinate frame. This is performed by the*[X]* transformation matrix. The next transformation, performed by the *[Y]* transformation matrix, is counter clockwise about the *y′* axis, forming the *{x′′,y′′,z′′}* coordinate frame. The final transformation, the *[Z]* transformation, is counter clockwise about *z′′* frame, resulting in the final *{x′′′,y′′′,z′′′}* coordinate frame. The transformation matrices *[X]*, *[Y]* and *[Z]* are given below as [106]:

$$[X]=\begin{bmatrix}1 & 0 & 0\\ 0 & \cos(\varphi) & \sin(\varphi)\\ 0 & -\sin(\varphi) & \cos(\varphi)\end{bmatrix} \tag{6.6}$$

$$[Y]=\begin{bmatrix}\cos(\theta) & 0 & \sin(\theta)\\ 0 & 1 & 0\\ -\sin(\theta) & 0 & \cos(\theta)\end{bmatrix} \tag{6.7}$$

$$[Z]=\begin{bmatrix}\cos(\psi) & \sin(\psi) & 0\\ -\sin(\psi) & \cos(\psi) & 0\\ 0 & 0 & 1\end{bmatrix} \tag{6.8}$$

The transformation from one coordinate system to another can be represented by the transformation matrix equation:

$$\begin{Bmatrix}x'\\ y'\\ z'\end{Bmatrix}=A\begin{Bmatrix}x\\ y\\ z\end{Bmatrix} \tag{6.9}$$

where $\{x,y,z\}$ is the fixed or starting frame of reference, $\{x',y',z'\}$ is the rotated frame and A is the rotation matrix that completely describes the relative orientation of the two systems. The rotation matrix A can describe a single rotation about an axis or a combination of multiple rotations making up the relative orientation of the two systems. The orientation of the rotated coordinate frame relative to the original frame can be described in terms of the projection of the rotated frame axes onto the original coordinate frame. This technique will be described in further detail in the proceeding section for the Band 9 polarising grid.

6.4.4 Orientation of the Band 9 Polarising Grid

The plane of the Band 9 wire grid polariser can be visualised as being rotated about two separate axes relative to the optical axis. In Figure 6-12 below the orientation of the grid plane by fixing the optical axis in the horizontal xz plane is illustrated. This is a useful representation as this is the same layout that is used for the low frequency test facility described later in this section. In the first layout, the grid plane is orthogonal to the optical axis. In the following layout the grid is rotated about the x axis by 40° towards the optical plane – this represents the off-axis bending angle of M4-0P and M4-1P. Lastly the grid is rotated about the new y'' axis by 27.5°, which serves to reflect the 1P beam component.

The issue under investigation is whether there exists an orientation of the grid wires other than the nominal that permits an improved co-polar beam throughput and cross-polar beam reflection for the transmitted path and vice-versa for the reflected beam path. Given that the transmitted and reflected beam paths are equivalent in terms of optics and for the sake of simplicity all considerations to the plane of polarisation of the incident optical beam and subsequent diagrams will refer to the transmitted beam only

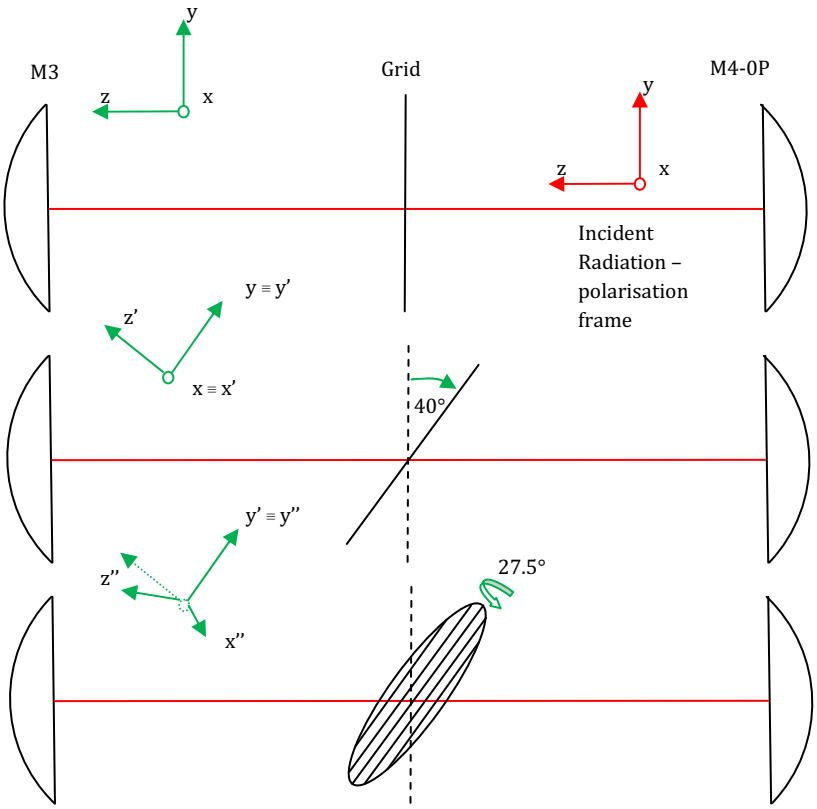

Figure 6-12 - Orientation of Band 9 polarising grid relative to optical axis between mirrors M3 and M4-0P

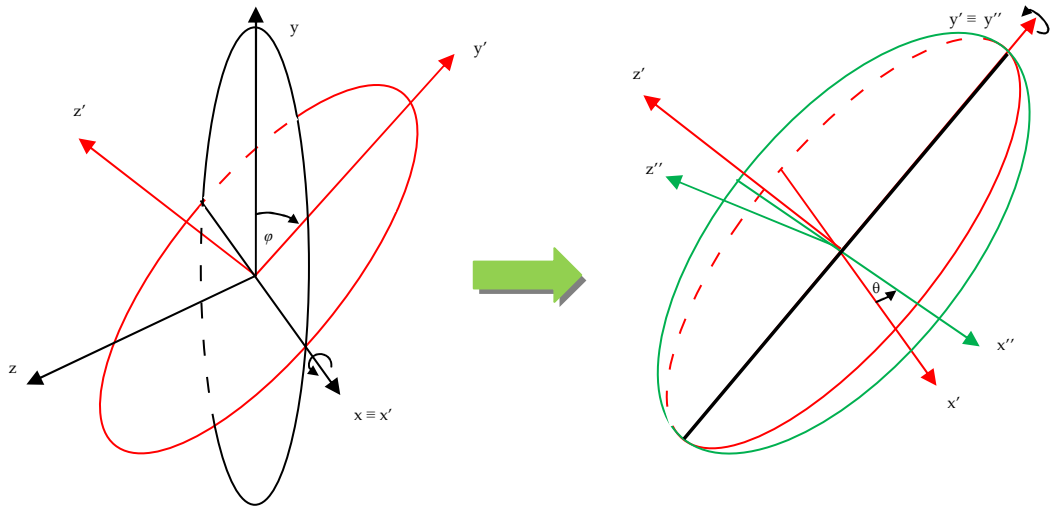

Figure 6-13 - Isometric representation of the orientation of the Band 9 polarising grid in terms of angular rotations about the coordinate axes

The figures above show an isometric representation of the two rotations that make up the orientation of the polarising grid. The orientation of the Band 9 polarising grid lines relative to the incident optical plane of polarisation can be described using the Euler angles described above The radiation incident upon the grid of coordinate frame $\{x'',y'',z''\}$ can be visualised as being aligned with the original $\{x,y,z\}$ coordinate frame – that is to say the co-polar component from *M4* is aligned with the x axis and the cross polar component aligned with the y axis. The orientation of the plane of the polarising grid relative to the plane of polarisation can be described in terms of the projections of the polarisation axes onto the plane of the grid. For example, if the y' axis is traced back to the original $\{x,y,z\}$ frame, there is no net projection angle upon the grid surface, i.e. the y' and y coordinate axes (and indeed by consequence the y'' axis) are all within the same plane – c.f. Figure 6-14 below.

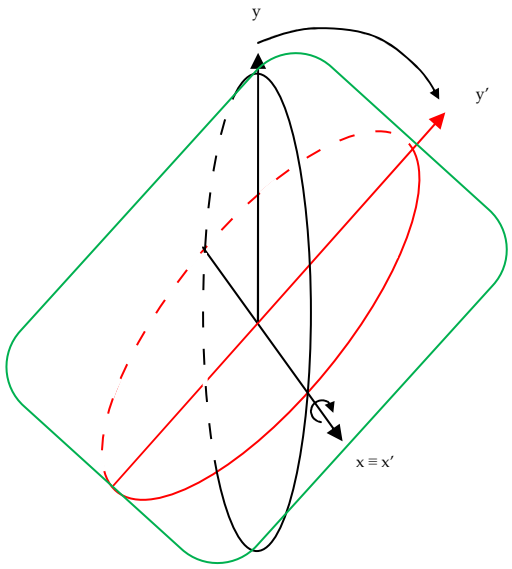

Figure 6-14 - Isometric representation of the first rotation of the grid plane about the x axis, revealing that the y and y' axes are within the same plane (green plane)

This implies that for grid wires that are aligned with the y''axis, they are thus co aligned with the incident y axis. The conclusion of this is that, for the system in its current configuration, the grid lines are aligned at the optimal angle for operation. To check this hypothesis the nominal configuration was implemented with varying grid wire

orientations in GRASP9 and the cross polar power levels of the 1P and 0P beams were recorded at the focal plane. The variation of the angle of the grid wires about the optimal 'vertical' angle is displayed below in Figure 6-15. The results of this test are plotted below in Figure 6-16 as cross polar power levels predicted at the focal plane as a function of grid rotation angle.

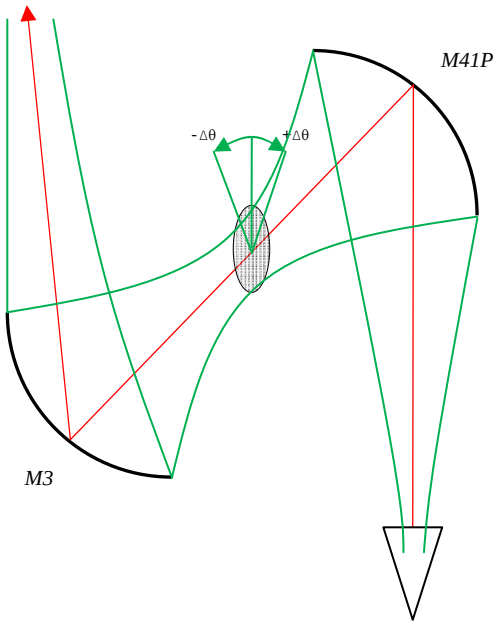

Figure 6-15 - Rotation of the grid wires about the nominal orientation for the Band 9 polarising grid wires

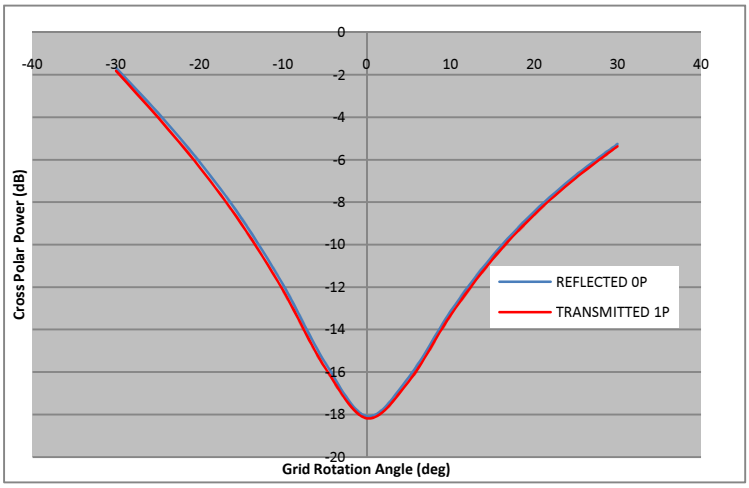

Figure 6-16 – Predicted cross polar power levels (dB) as a function of rotation of the grid wires about the nominal (vertical) angle

The results prove the hypothesis that in the nominal system configuration the orientation of the grid wires is optimal. At angles away from the nominal the cross polar power levels are vastly increased, following a similar pattern to the typical Malus' law pattern and indicating that the transmission axis of the grid needs to be aligned correctly with the polarisation angle of the incident beam.

Returning to the orientation of the grid plane relative to the polarisation of the incident radiation, it is noticed that though the y, y' and y'' axes are all co aligned within the same plane, the same cannot be said of the x, x' and x'' axes. Observing the grid plane rotations in Figure 6-13 the x and x' axes are equivalent through the first rotation. The next rotation, about the y' axis, moves the x'' axis out of plane of the original x axis. This is best represented using a modification of the grid plane orientation from Figure 6-12 in Figure 6-17 below:

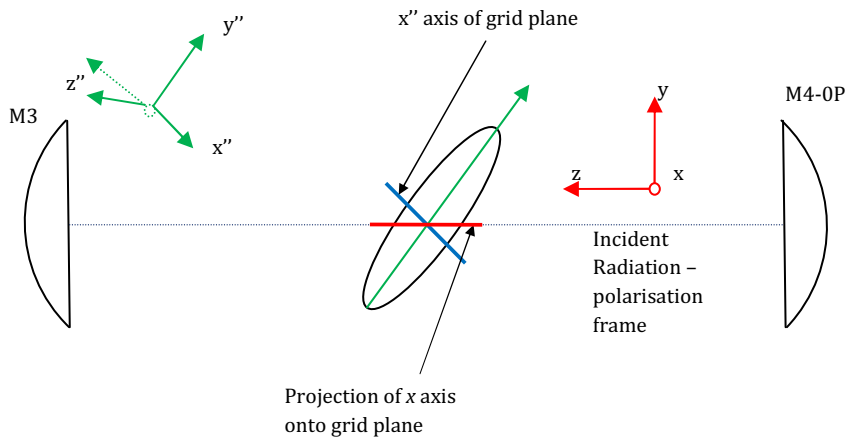

Figure 6-17 - Orientation of the grid plane relative to the incident polarisation showing the projection of the x axis onto the grid plane

From the above figure it is easily shown that the incident angle of polarisation is aligned with the x axis rather than the y axis, it would be projected upon the grid plane in such a way that it is no longer orthogonal to the local y'' axis. Another way of interpreting this is that the projection of the x axis upon the grid plane does not align with the local x'' axis. This projection effect can be exploited with respect to the Band 9 optics. The

above optical configuration, whereby the angle of incident polarisation has been rotated by *90°*, is here on referred to as the 'rotated' version. The next important step for this rotated version of the Band 9 system is to find the optimal angle for the grid wires that are collinear with the projection of the x axis upon the grid surface. This is achieved through the calculation of the appropriate Euler angle rotation matrices.

6.4.4.1 Projection effect upon grid plane

To determine the angle that the projected x axis makes with the x'' axis upon the grid plane the appropriate Euler rotation matrix must first be determined. The complete rotation matrix A that describes the orientation of the grid plane relative to the *{x,y,z}* plane is calculated as a combination of the appropriate transformation matrices given in Section 6.4.3:

$$A = [X][Y] \tag{6.10}$$

where *[X]* and *[Y]* are the x and y axis rotation matrices given by Equations 6.6 and 6.7. This rotation matrix describes firstly rotation about the fixed x axis by an angle φ followed by a rotation about the new y axis, y' by an angle θ. This is achieved in matrix multiplication by firstly inversely rotating about x, then rotating about y and then finally rotating about x. The order of multiplication is in reverse order as per standard Euler transformation matrices [106]

The angle at which the projection of the x'' axis on the grid plane makes with the original x axis, hereafter referred to as ψ_{Grid}, is determined by multiplying the unit x vector by the rotation matrix A. This will give the unit vector of the x'' axis relative to the original x vector. This is now applied to the specific rotation angles of the Band 9 grid. From Figure 6-12 the x rotation angle φ is 40° and the y' rotation angle θ is 27.5°. Applying Equation 6.10 the rotation matrix is given as:

$$A = \begin{bmatrix} 1 & 0 & 0 \\ 0 & \cos(\varphi) & \sin(\varphi) \\ 0 & -\sin(\varphi) & \cos(\varphi) \end{bmatrix} \begin{bmatrix} \cos(\theta) & 0 & \sin(\theta) \\ 0 & 1 & 0 \\ -\sin(\theta) & 0 & \cos(\theta) \end{bmatrix} \tag{6.11}$$

$$A = \begin{bmatrix} 0.766 & 0.297 & 0.570 \\ -0.297 & 0.950 & -0.096 \\ -0.570 & -0.096 & 0.816 \end{bmatrix}$$

The x axis unit vector, given as *[1, 0, 0]* is multiplied by A to give the x'' axis unit vector

$$x'' = A.x$$
$$x'' = [0.766, -0.297, -0.570] \tag{6.12}$$

The projection of the x'' unit vector onto the xy plane is illustrated below in Figure 6-18.

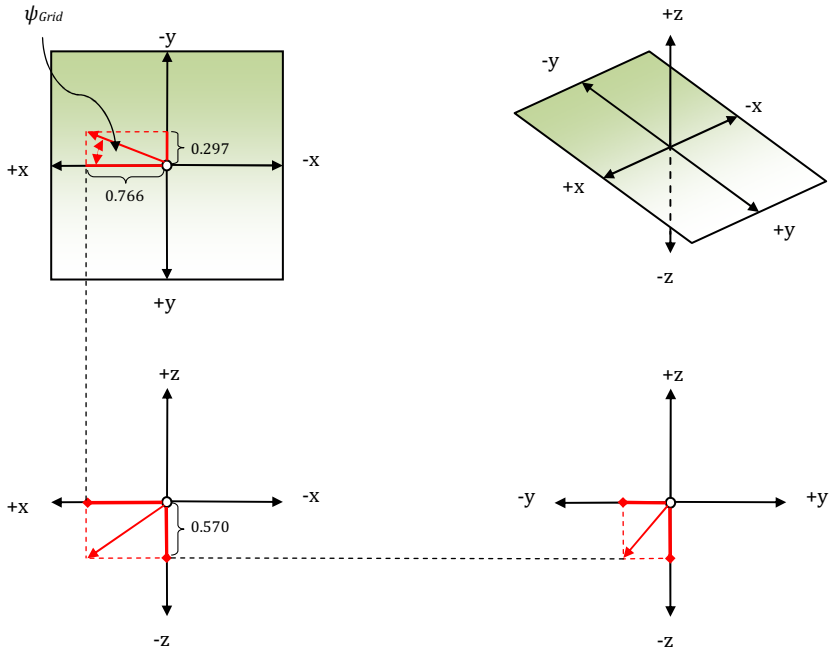

Figure 6-18 - Projection of the x'' unit vector onto the xy plane

The inverse tangent of the y component over the x component of the resultant x'' unit vector gives ψ_{Grid} to be 21.18°, i.e.

$$\psi_{Grid} = \arctan\left[0.297 \diagup 0.766\right] = 21.18° \tag{6.13}$$

This result was verified through both PO calculations and experimental measurements using the Band 9 front end optics at SRON. The source feed horns for the 0P and 1P beams are rotated by 90° and the grid wires are rotated through 111.18° (i.e. 90° + 21.18°). Cross polar power levels are tracked against ψ_{Grid} which is varied about the predicted optimal angle. The results of the PO predictions are presented below in Figure 6-19 below as cross polar power levels as a function of grid wire angle $\psi_{Grid.}$

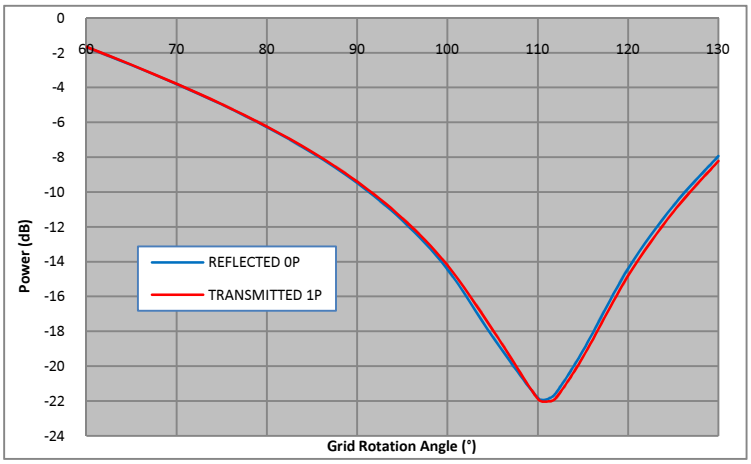

Figure 6-19 - Cross-polar power levels (dB) for the transmitted and reflected beams as a function of grid wire angle ψ_{Grid}

The PO calculations above show a minimum of cross polar power levels at the predicted ψ_{Grid} = 111.18° of -21.96 dB for the 1P beam and -22.02 dB for the 0P beam, thus verifying the predicted optimal angle of rotation of the grid lines. The results in Figure 6-19 above exhibits a Malus' Law style pattern similar to that for the grid rotation testing results from the nominal version (c.f. Figure 6-16). As the grid rotates about the optimum angle of 111.18° there is a noticeable evolution in the profile of the beam pattern. This is illustrated in the predicted cross polar field distributions presented in Figure 6-20 below. Away from the optimum angle of rotation the beam has a single lobe power profile similar to that of the co-polar beam. At these angles away from the optimum value the grid wires are not in the correct alignment relative to the incident co and cross polarisations and thus the observed output beam patterns are a mix of the co and cross polarisations incident upon the grid surface. As the angle of rotation approaches 111.18° the cross polar power profile is reverted to the typical

double lobed structure. There is negligible distortion to the co-polar beam for all of these grid rotation angles; normalised coupling integrals to the co-polar power distribution at the optimum angle reveal a coupling of over 99% for the power distributions at all other angles.

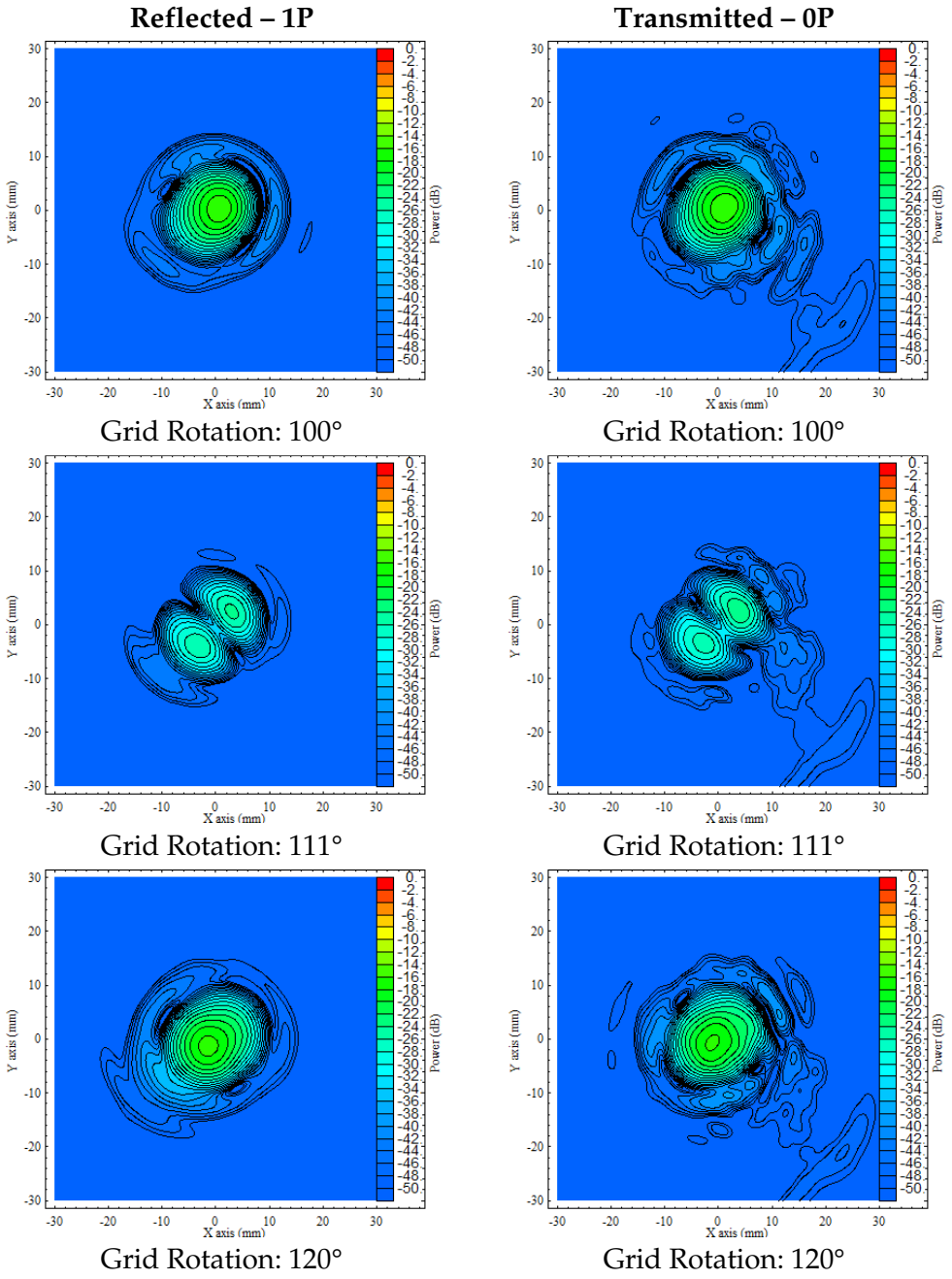

Figure 6-20 - Predicted cross polar power patterns at the focal plane for the reflected and transmitted beams for various grid rotation angles

The valuable conclusion of this analysis is that the new rotated version of the system will produce a decrease in cross polar power levels of approximately $4\ dB$ when compared against the nominal version of the system. These results were verified experimentally using a prototype of the Band 9 front end optics system at SRON described in the next section below.

6.4.5 Experimental Verification

Given that low cross polar power levels (<-20 dB) are a stipulated requirement of all ALMA channels the modification of the horn polarisations and grid rotation angle from the previous section presents a desirable alteration to the existing system. This led to a measurement campaign of the rotated system on the Band 9 front end optics to both verify the PO predictions and determine the feasibility of implementing the required modification to the channel.

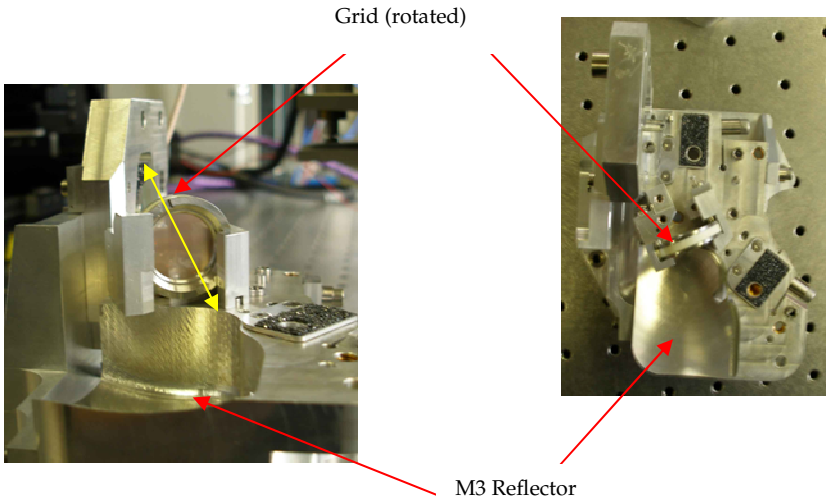

Figure 6-21 -Warm optics assembly of rotated Band 9 channel. Angular alignment of the polarising grid is illustrated (left). The warm optics setup is divided into two sections whereby the M41P/0P reflectors are removed for this photograph

Measurements were conducted on the Band 9 optics channel at SRON. A Phase Locked Loop (PLL) measurement system operating at 670 GHz combined with a warm optics setup was used for beam pattern measurements of the co-polar and cross-polar hbeams. The details of this measurement system are described in further detail in Appendix A.

There were no stringent requirements for accurate beam pointing in such a setup, since cross polar levels are calculated as a normalization against co-polar power. Using the warm optics setup allowed the Author quick access to the wire grid. The warm-optics measurements were achieved using a prototype of the front end optics system, illustrated in Figure 6-21 above. Adjustments to the angular alignment of the grid were performed manually with the aid of a stepped protractor and microscope. The output beam was recorded at the nominal focal plane position and a sample of the results for the same grid rotation angle as presented in Figure 6-20 are displayed below in . The recorded cross-polar levels at the focal plane are normalised against co-polar power and plotted against grid rotation angle in Figure 6-22 below where they are overlaid as dashed lines against the predicted results (solid lines) from Figure 6-19. The exact recorded values of cross polar power are listed in Table 6-8 below.

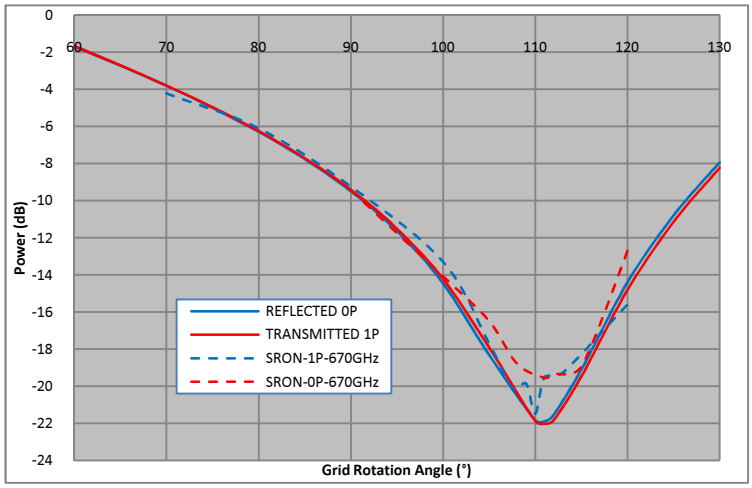

Figure 6-22 - Measured (dashed lines) and predicted (solid lines) cross polar power levels for rotated Band 9 optics channel

The recorded cross-polar power levels at the focal plane are normalised against co-polar power and plotted against grid rotation angle in Figure 6-22 below where they are overlaid as dashed lines against the predicted results (solid lines) from Figure 6-19. The exact recorded values of cross polar power and rotation angle are listed in Table 6-8.

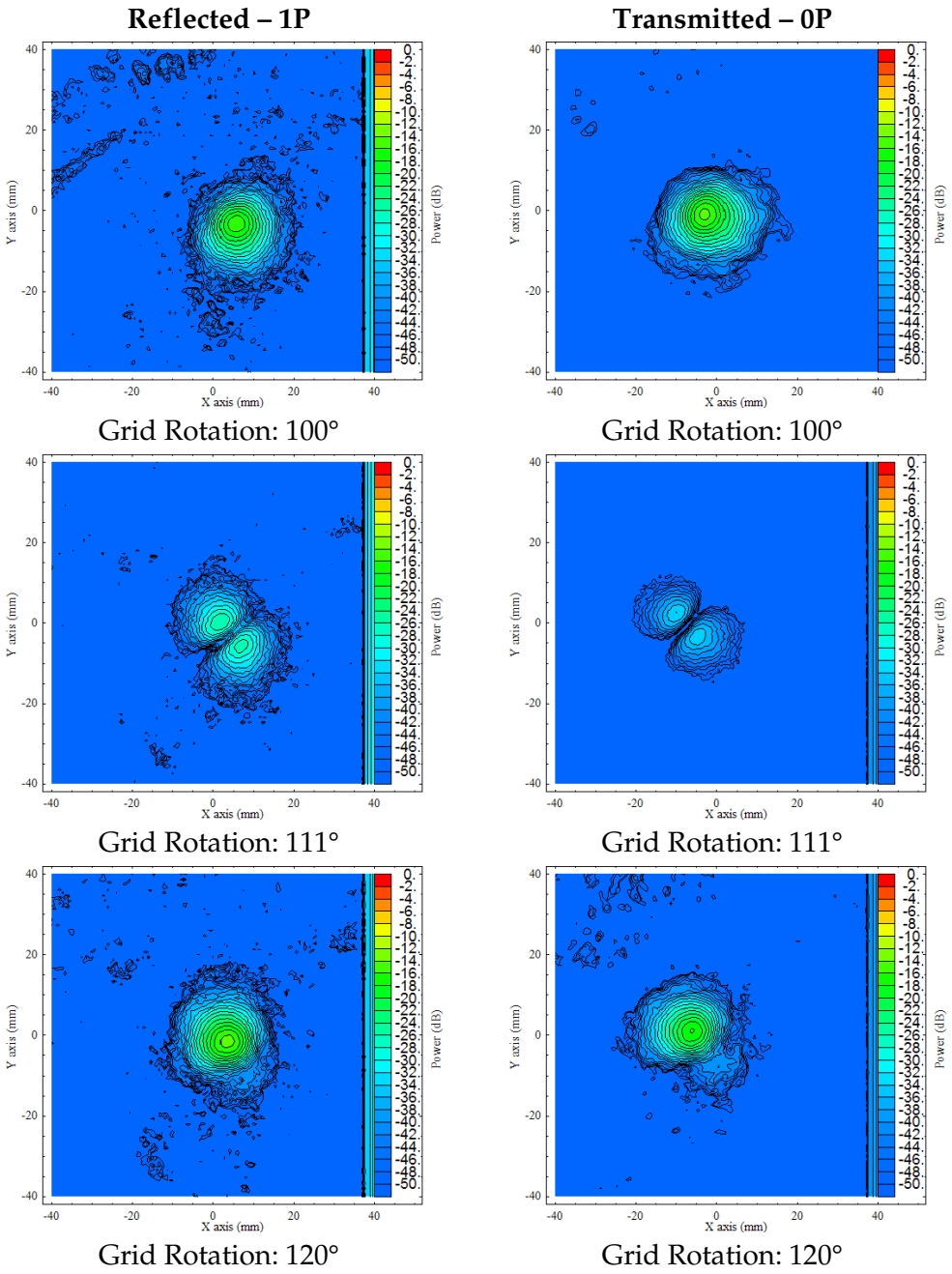

Figure 6-23 - Sample of measured cross polar amplitude patterns at the Band 9 focal plane for the reflected and transmitted beams for various grid wire rotation angles – c.f. Figure 6-20

ψ_{Grid} (°)	Unit	1P	0P
70	dB	-4.21608	----------
80	dB	-6.09915	----------
90	dB	-9.23027	-9.44007
100	dB	-13.2956	-14.0764
105	dB	-17.7016	-16.4928
107	dB	-20.0977	----------
108	dB	----------	-18.774
109	dB	-19.854	----------
110	dB	-21.4772	----------
111	dB	-19.5061	-19.5464
112	dB	----------	-19.3362
113	dB	-19.2645	----------
115	dB	----------	-18.9337
120	dB	-15.5985	-12.7149

Table 6-8 - Measured cross polar power levels for 'rotated' optics as a function of ψ_{Grid}

Comparison between predicted and measured cross-polar power levels against grid rotation show very good agreement – c.f. Figure 6-22. There exists a small degree of discrepancy between predicted and measured power levels and optimal angle of rotation. Minimum cross-polar power is recorded at 110° for the *1P* beam (-21.5 dB*)* and at 111° for the *0P* beam (-19.55 dB*)*. The elevated measured power levels relative to theoretical predictions were also documented for the nominal system and were attributed to the polarization sensitivity of the receiver [100]. The discrepancy observed surrounding the optimum angle of rotation can be accounted for by the relatively crude nature of the experimental setup and rotation accuracy achievable with the manual arrangement used. Rotation of the wire grid polariser was carried out by hand and the angle of rotation was determined through line of sight against a protractor. Achieving higher accuracy would have proved difficult within the allotted time for the measurement campaign and would have required specialized equipment that was not available at the time. The rotation accuracy certainly needs to be accounted for as the largest source of error in this experimental verification.

Though the prototype warm optics setup of the Band 9 front end optics was relatively simple to modify into the rotated system, implementing such an alteration to the existing optical layout would incur a significant redesign of the channel with regards to the LO coupling and signal processing stages of the channel. Of course in a heterodyne receiver the grids play an important role in combining the LO beam with the astronomical signal and rotations effect the orientation of LO feeds also. As a consequence of this the suggested improvement to the system presented here, while of note for future off-axis high-frequency submillimetre optics systems, will not be implemented initially in the ALMA Band 9 channel due to its advanced stage of development. Scope exists to implement this scheme in possible future adaptations of the system.

6.5 Alternative Band 9 'Focusless' Design

As revealed in the analysis presented in Section 6.4, one of the chief causes of the poor cross-polar efficiency of the Band 9 system is the location of the wire grid polariser near the interfocal point between reflectors M3 and M41P/0P. Though this is the obvious location for the grid to achieve the minimum grid diameter (collocated with beam waist), it also ensures that the beam impinging on the grid surface will contain a significant radial component as the complex phase radius of curvature switches direction at the waist.

One hypothesized solution to this problem was to 'remove' the focus of the system and have an alternative optical arrangement to relay the horn aperture field to the ALMA telescope focal plane. This 'focusless' version of the system was hypothesized by the Band 9 project scientist Andrey Baryshev and was investigated by the Author. To remove the interfocal waist from between M3 and M4, the M4 reflector conic is changed from an ellipsoid to a hyperboloid mirror. The M3 reflector will remain an ellipsoidal reflector, but with altered parameters to accommodate the new M4 reflector. The layout of this system is displayed below in Figure 6-24.

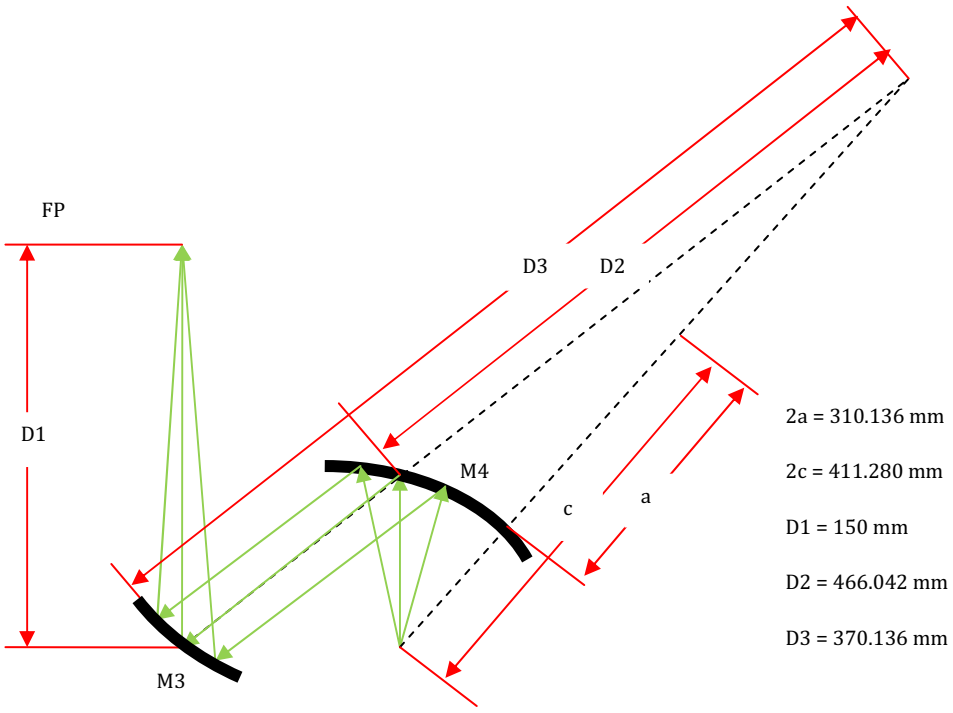

Figure 6-24 - Details of 'focusless' design of Band 9 Optics

The system was analysed using PO in GRASP9, with the standard *5w* rim diameter for the wire grid. Beam pattern predictions at the focal plane for the central frequency are displayed below in Figure 6-25.

Cross polar power levels for this adaptation of the optics are significantly reduced to approximately -28 dB normalised against co-polar power. The suggested adaptation for the rotated version of the optics, with feed horns rotated by *90°* and the grid wires rotated through to the required optimal angle of 111.18° was applied to the focusless design.

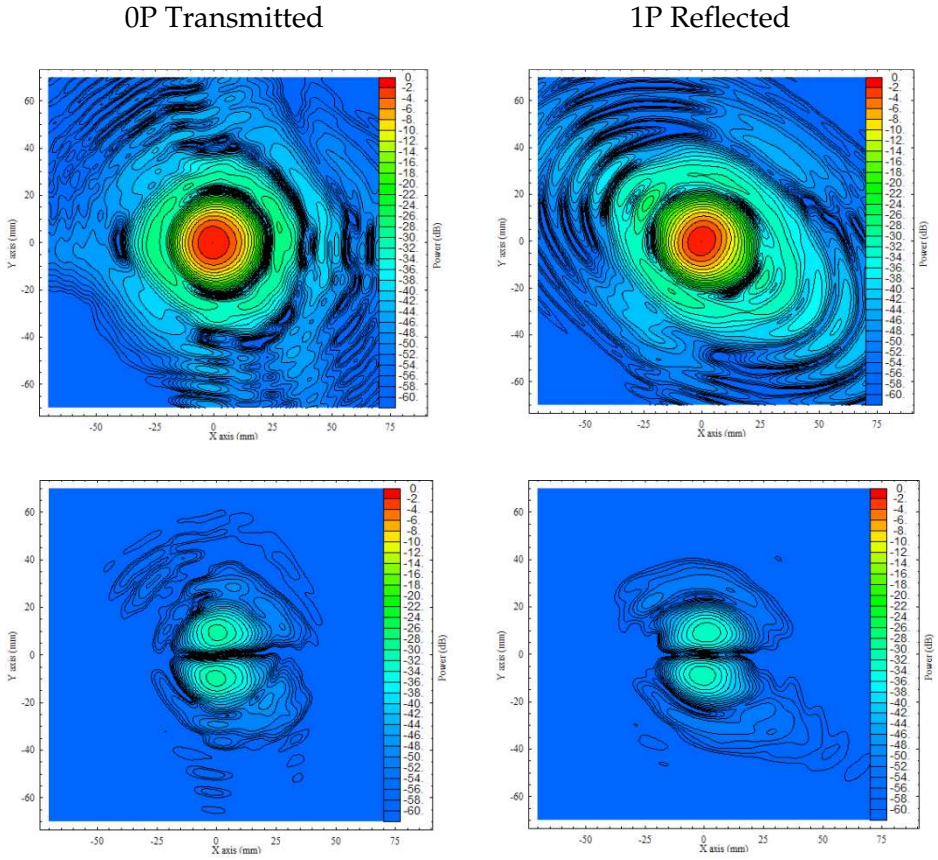

Figure 6-25 - Co-polar and cross-polar beam pattern predictions at the antenna focal plane for the Band 9 'focusless' design - central frequency (661 GHz)

The cross polar power levels are reduced further with this modification to approximately -31 dB for both beam paths at the antenna focal plane. The improvements to the system through the rotation modification as recommended from the analysis of the wire grid polariser in Section 6.4 are thus further justified by this result. The beam pattern predictions at the focal plane for this new 'rotated – focusless' optical layout are presented below.

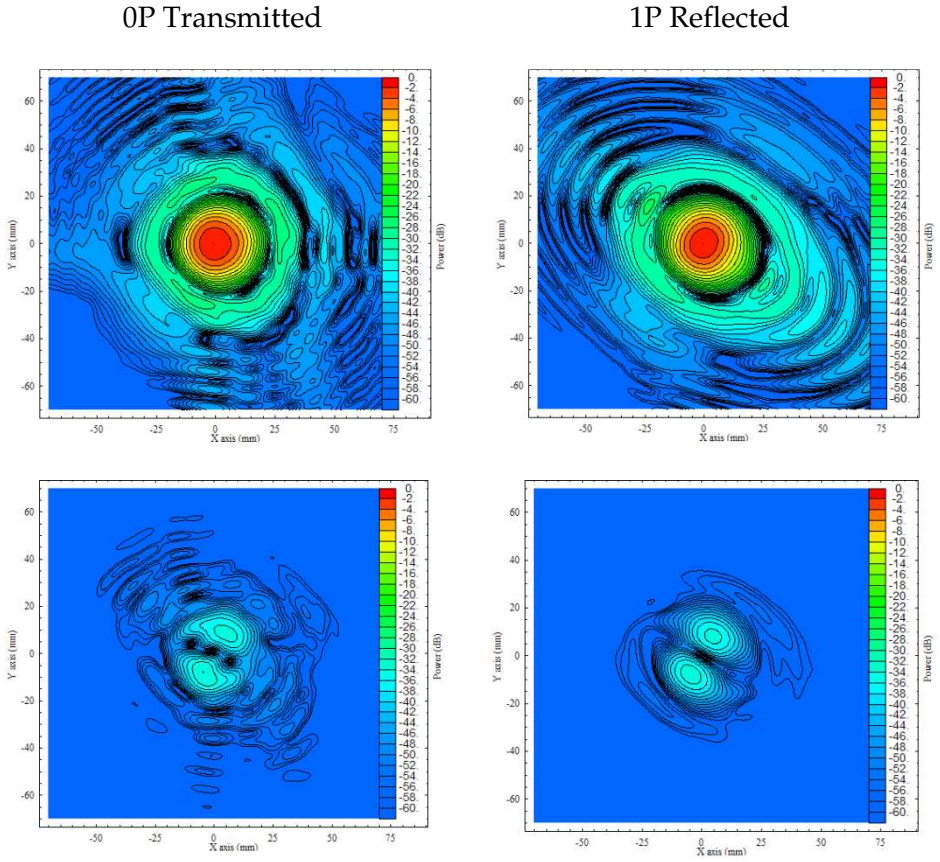

Figure 6-26 - Co-polar and cross-polar beam pattern predictions at the antenna focal plane for the Band 9 'rotated - focusless' design with grid wires rotated to 111.18° - central frequency (661 GHz)

The removal of the beam waist between the mirrors necessitates an increase in the grid diameter from 17 mm for the current nominal configuration to at least 47 mm, which ensures a 5w beam truncation at the lowest frequency. The opto-mechanical constraints of the Band 9 cartridge prohibit such a large grid with current constraints. As such, while this alternative 'focusless' approach to the front-end optics exhibits a more desirable cross polar efficiency, the implementation of such a substantial modification to both the mirror surfaces and the wire grid polariser was deemed to be unrealistic.

6.6 Verification of Grid Projection Effect at Low Frequency

As a complement to the work presented above regarding improvement of the cross-polar efficiency of Band 9 through rotation of the polarising grid lines relative to the incident radiation, a similar polarising grid test facility with a layout to emulate that of Band 9 was developed. This test facility was designed as a low frequency, stripped down version of the Band 9 system, comprised of a of a planar polarising grid, a conical corrugated horn to generate the linearly polarised incident source field and waveguide probe mounted on a 2D planar scanner to record the output field. The corrugated horn used is the same 94 GHz feed horn used for experimental measurements detailed in Chapters 3 and 4.The measurement of this system was achieved using the same near-field scanning arrangement detailed in Section 3.3. A wire grid polariser was purchased from QMC Instruments Ltd. This grid consisted of wires of 10μm diameter spaced by 25μm and assembled on a circular aluminium frame. The frame had an outer diameter of 165 mm with an assembly thickness of 10 mm, leaving an inner diameter of 140 mm. The wire grid polariser was placed at a distance of 70 mm from the horn aperture and was mounted on a gimbal style frame which allowed for rotation about three frame axes: one global axis and two local axes. At this distance the Gaussian beam radius approximating the horn aperture field at 100 GHz is 15.75 mm. The taper ratio (Equation 2.26) of the beam radius to the aperture of the grid is 4.45, ensuring that the entire beam is contained within the grid. The angle of the grid wires was rotatable within this gimbal frame. This layout allowed for multiple orientations of the polarizing grid lines relative to the incident angle of polarization. The angles about which the grid is rotated are equivalent to those referred to in Section 6.4 for the Band 9 grid: the x axis angle φ, the y' axis angle θ and the wire grid angle ψ_{Grid}. A schematic of the layout for this system is illustrated below in Figure 6-26. The wire grid polariser and its mounting within the near field measurement system are displayed in Figure 6-28.

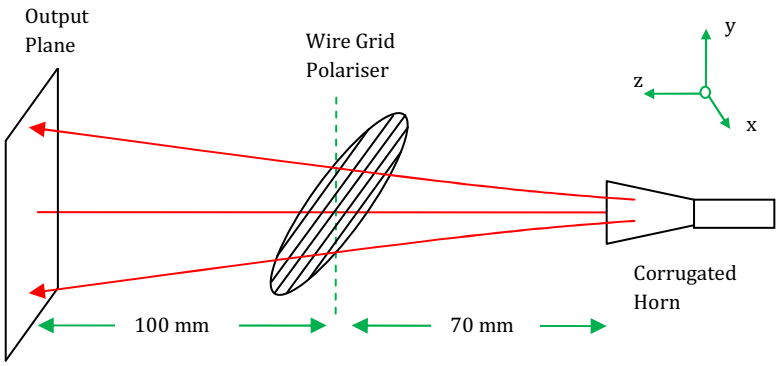

Figure 6-27 - Optical layout for stripped down wire grid polariser test facility

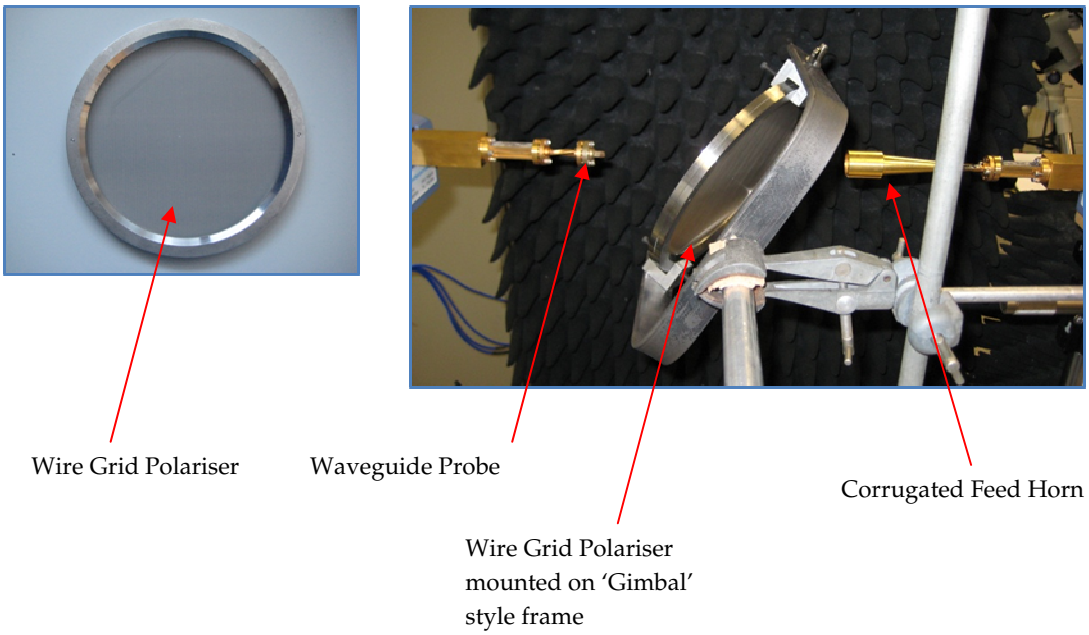

Figure 6-28 - Wire grid polariser (left) and its gimbal-style mounting within the near field scanning system consisting of the corrugated feed horn and waveguide probe.

SCATTER predictions of the complex aperture field of the feed horn reveal a cross polar power level of -35 dB. Co polar and cross polar beam pattern predictions of the mode-matched horn field at the output plane are compared against measurement without the inclusion of the grid below in Figure 6-29.

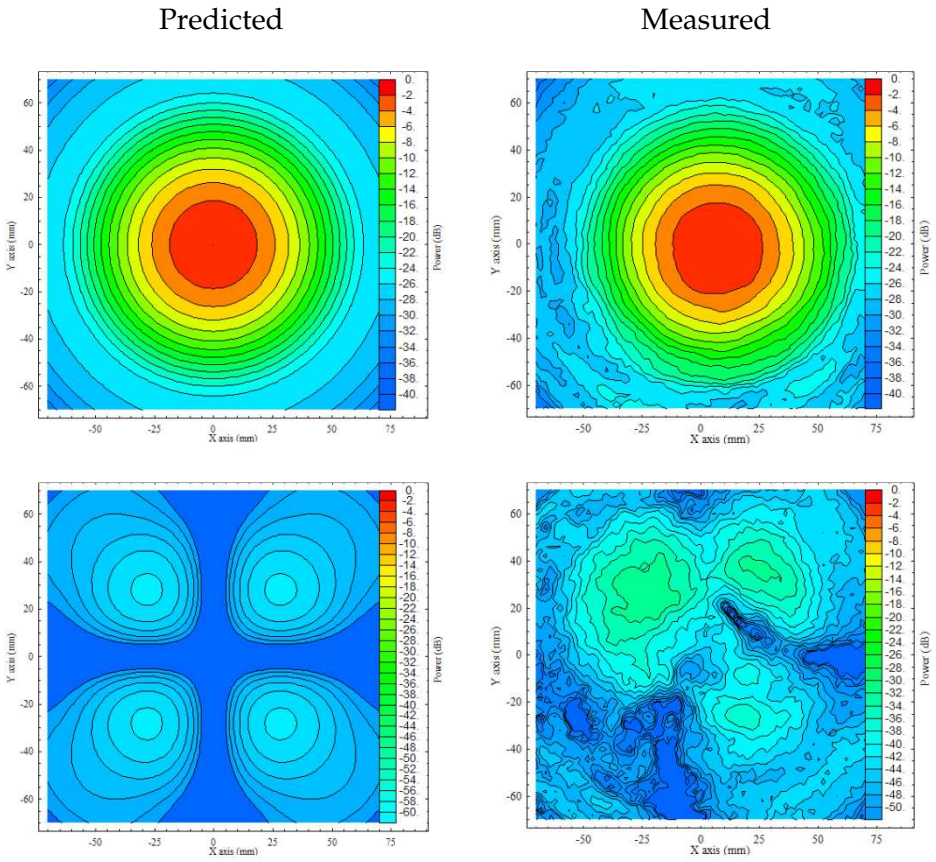

Figure 6-29 - Predicted and measured co and cross polar beam patterns for the 100 GHz corrugated feed horn at the output plane with no grid included

Measured cross polar power levels at the output field are calculated for 100 GHz at approximately -26 dB, while predictions give the cross polar power level to be much lower at -45 dB. These values set the baseline for cross polar power level calculations for the various orientations of the wire grid polariser. The higher levels of measured cross polar power are lightly due to the influence of the waveguide probe (WR10) used to measure the output field. No deconvolution of this aspect of the measurements was incorporated into the simulations using PO. The grid within GRASP9 is also simulated as an ideal grid with ideal characteristics, an assumption which may lead to low levels of disagreement between theory and measurement.

The orientation range for the polarizing grid frame is similar to that as described above in figure (ref diagram above that describes band 9 grid angles). The *xyz* frame is set as

the global coordinate frame with the xy plane orthogonal to and the z axis collinear to the optical axis. The polarization for the feed horn can be aligned along both the xz and yz axes, thus representing the nominal and rotated polarisations for the feed horns from the Band 9 system (c.f. Section 6.4).

The angle of the projection of the x'' axis upon the xy plane (ψ_{Grid}) is calculated using Equations 6.10 to 6.12. The predicted angle of projection is plotted as a function of the the x and y' rotation angles φ and θ in Figure 6-30:

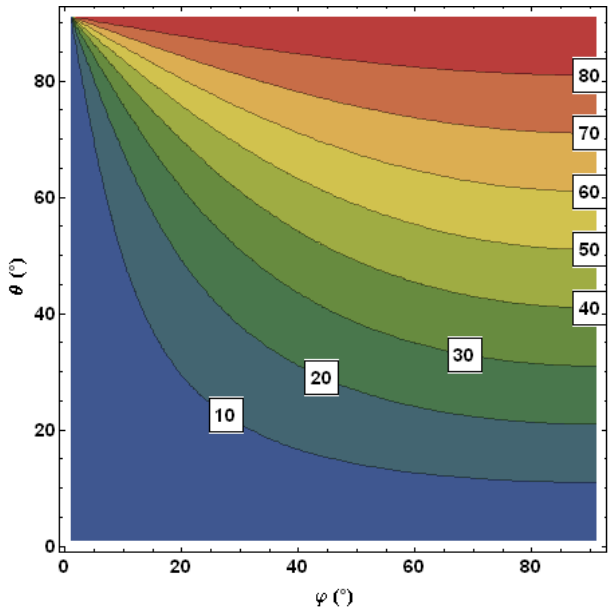

Figure 6-30 - Contour plot of grid rotation angle ψ_{Grid} as a function of φ and θ, both varying from 0 to 90°

The above plot can now be used to find the optimum grid rotation angle ψ_{Grid} for any combination of the rotation angles φ and θ. The transmitted beams for three angular orientations of the wire grid polariser were measured: φ was fixed at 40° and θ varied over 10°, 20° and 22°. From the above contour plot the optimum grid wire alignment angle ψ_{Grid} was determined for the three grid orientations. In Figure 6-31 below ψ_{Grid} is plotted as a function of θ for φ = 40°, and can be visualised as a planar cut through the above contour plot. The resultant optimal grid angles for the three chosen rotation angles of 10°, 20° and 22° are thus predicted as 8.3°, 16.0° and 17.45° respectively.

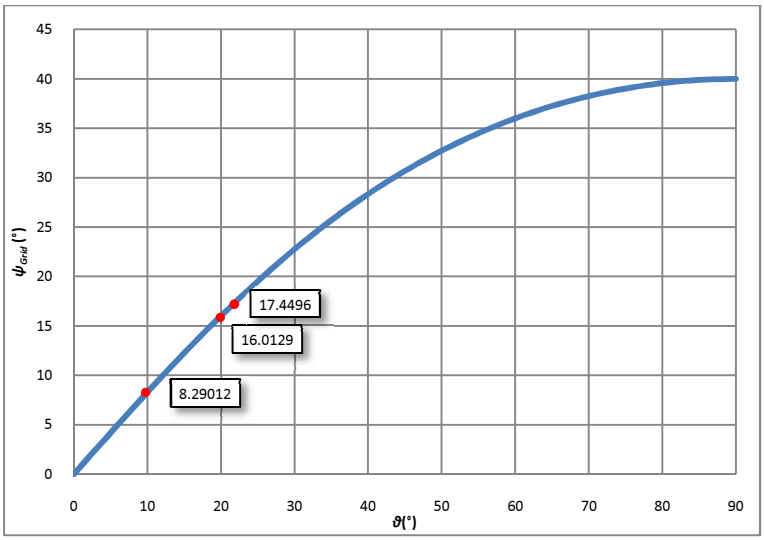

Figure 6-31 - Plot of ψ_{Grid} as a function of θ varied from 0° to 90° with φ fixed at 40°

Transmitted cross-polar power levels were determined in the same manner as for the Band 9 front-end optics by integrating cross polar amplitude over copolar. A 90° waveguide twist facilitated measurement of the cross polar amplitude pattern. As with the Band 9 grid orientation analysis, measurements were compared against PO predictions from GRASP9. Implementation of the system in GRASP9 was typical with the complex field of the aperture of the feed horn generated using SCATTER and the wire grid polariser treated as an ideal grid object.

6.6.1 Results

Predicted and measured beam pattern contour plots of the co and cross-polar beams for the three y' rotation angles (θ = 10°, 20° and 22°) are presented below. For each value of θ there are three distinct sets of co and cross polar contour plots representing three different values of ψ_{Grid}. One at some angle below the optimal angle, one at the optimal angle as predicted from Figure 6-31 and one above the optimal angle.

This first set of contour plots is for the y' rotation angle θ = 10°, with three sets of predicted and measured plots for ψ_{Grid} equal to *0°* (Figure 6-32*)*, *8°* (Figure 6-33*)* and 20° (Figure 6-34*)*. The middle result represents the optimal value of ψ_{Grid}, which is actually equal to 8.29°. It was found that this exact value of grid rotation was difficult to

implement in the experimental setup and it was deemed easier to match to the rounded value *of 8°*. This practice is repeated in subsequent results.

- $\theta = 10°$, $\psi_{Grid} = 0°$

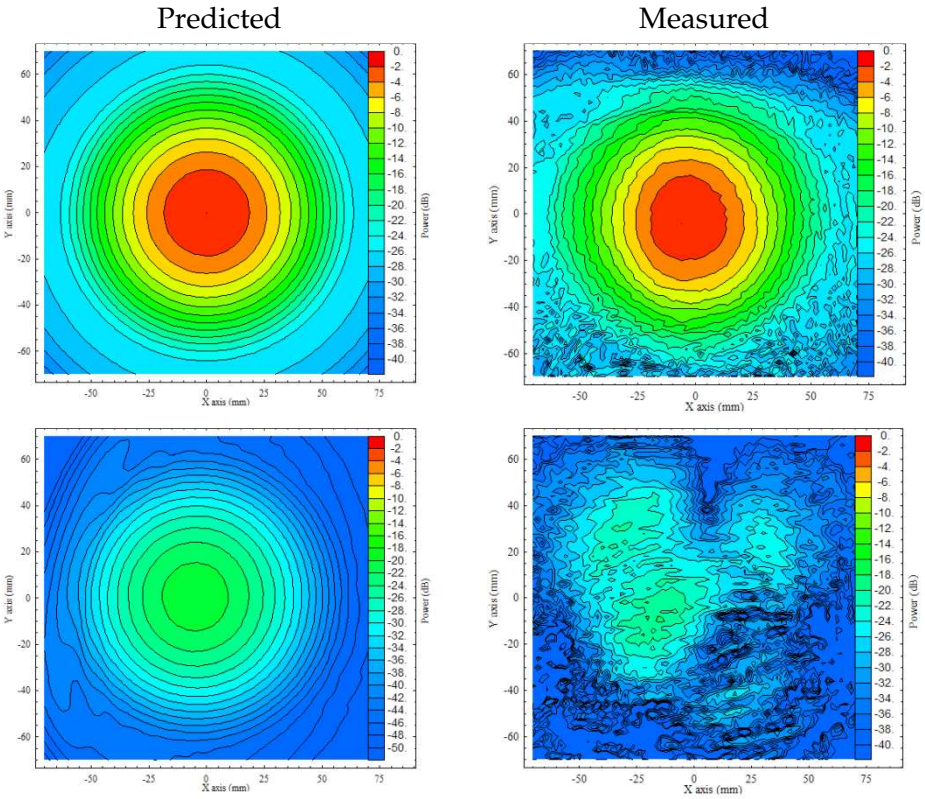

Figure 6-32 - Predicted (left) and measured (right) beam patterns for co-polar (top) and cross-polar (bottom) for $\psi_{Grid} = 0$

- $\theta = 10°$, $\psi_{Grid} = 8°$

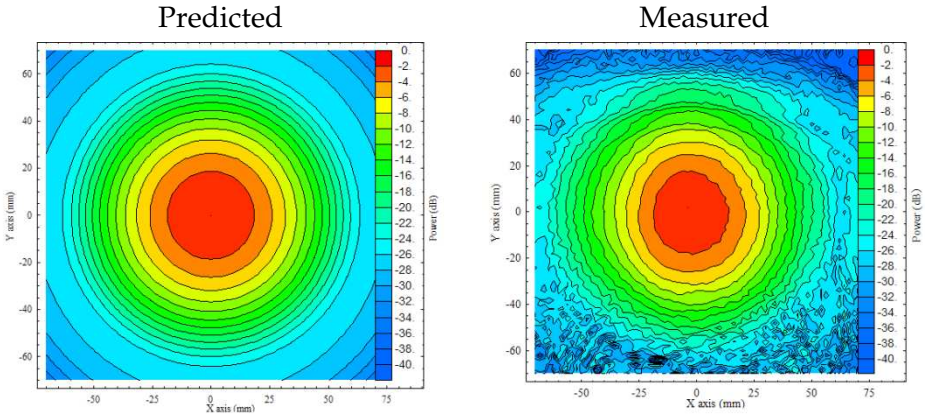

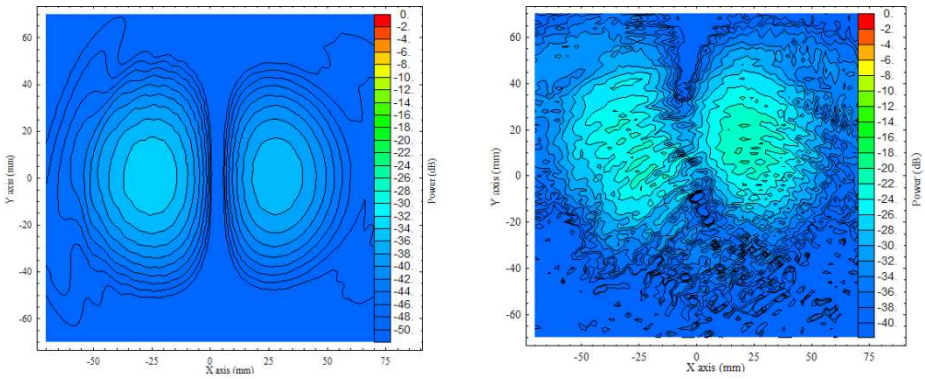

Figure 6-33 - Predicted (left) and measured (right) beam patterns for co-polar (top) and cross-polar (bottom) for ψ_{Grid} = 8°

- $\theta = 10°$, $\psi_{Grid} = 20°$

Predicted Measured

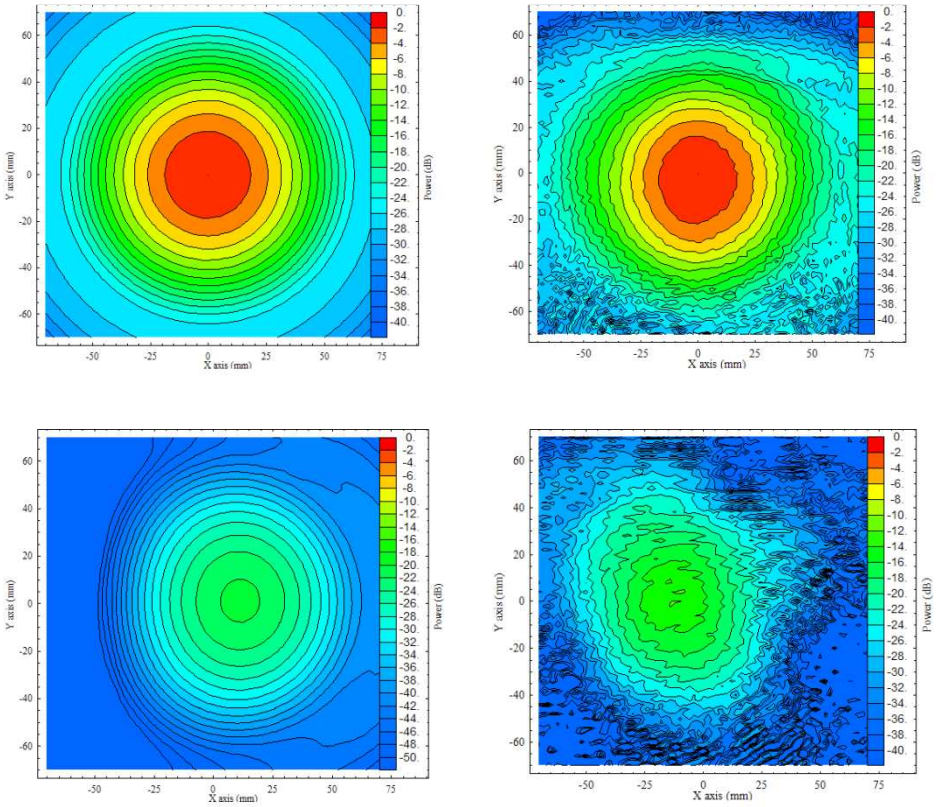

Figure 6-34 Predicted (left) and measured (right) beam patterns for co-polar (top) and cross-polar (bottom) for ψ_{Grid} = 15°

Comparison between experimental and predicted results shows reasonable agreement. The disparity between the predicted and measured beam patterns here is of a similar nature of that previously described for the farfield measurement of the horn field without the grid. For all grid rotations there is negligible alteration to the measured co-polar beam pattern and the evolution of the cross polar is similar to that seen for the Band 9 polarising grid (c.f. Figure 6-20 and Figure 6-22). For grid rotation angles away from the optimal the cross polar beams exhibit the expected pattern of a mixture of the co and cross polar patterns.

At the optimal grid rotation angle the cross polar power pattern has evolved to the typical double lobed pattern, similar to that seen at the focal plane of the Band 9 front end optics. This result is interesting as the grid, even in this optimal configuration, has altered the cross polar power pattern from that seen for the horn transmitting without the inclusion of the grid (i.e. the farfield pattern for the horn). This effect was also noted for the Band 9 front end optics for PO predictions with and without the grid.

As for the Band 9 polarising grid analysis, the cross polar power levels are tracked against grid rotation angle. These values are plotted below in Figure 6-35 in dB. These cross polar power levels have been normalised against the co polar power levels.

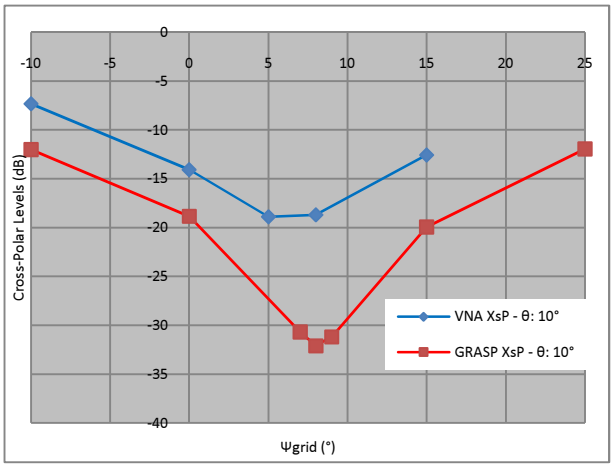

Figure 6-35 - Plot of measured (blue) and predicted (red) cross polar power levels (dB) for varying grid rotation angle

The measured cross polar levels follow a similar trend to that for the predicted results, with a minimum level occurring at the approximate optimal grid rotation angle of *8.29°*. As with the previous comparison of cross polar levels without the grid, the predicted cross polar levels are distinctly lower than the measured levels. The difference might be accounted for in that the model does not include deconvolution or inclusion of rectangular waveguides tapering to circular waveguide in the corrugated feed horn. The relative difference is less important than the trend that the cross polar levels both reach a minimum at the same predicted angle. The plots in Figure 6-36 below are of un-normalised co and cross polar power levels, calculated as a summation integral over the output grid. These plots exhibit the expected overall profile of a maximum of co polar and a minimum of cross polar power for the optimal grid rotation angle.

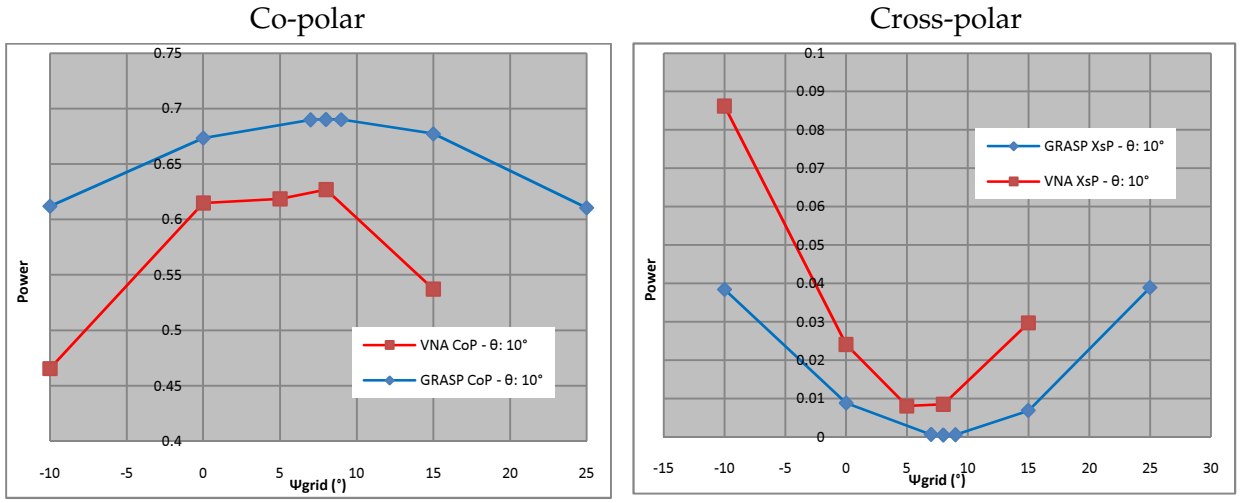

Figure 6-36 - Plots of measured (blue) and predicted (red) co and cross polar power levels as a function of grid rotation angle

Admittedly there are some small discrepancies exhibited in the measured power levels when overlaid with predictions. This is not surprising however, given that there is a considerable margin of error to be expected for the alignment of the grid wires. This was also found to be the case in the analysis of the rotated version of the Band 9 polarising grid. The grid within GRASP9 is also simulated as an ideal grid with ideal

characteristics, an assumption which may lead to low levels of disagreement between theory and measurement.

The following set of contour plots is for the y' rotation angle $\theta = 20°$ and with three sets of predicted and measured plots for ψ_{Grid} equal to *10° (*Figure 6-37*)*, 16° *(*Figure 6-38*)* and 25° *(*Figure 6-39*)*. The middle result (Figure 6-38*)* represents the optimal value of $\psi_{Grid} = 16.02°$.

- $\theta = 20°$, $\psi_{Grid} = 10°$

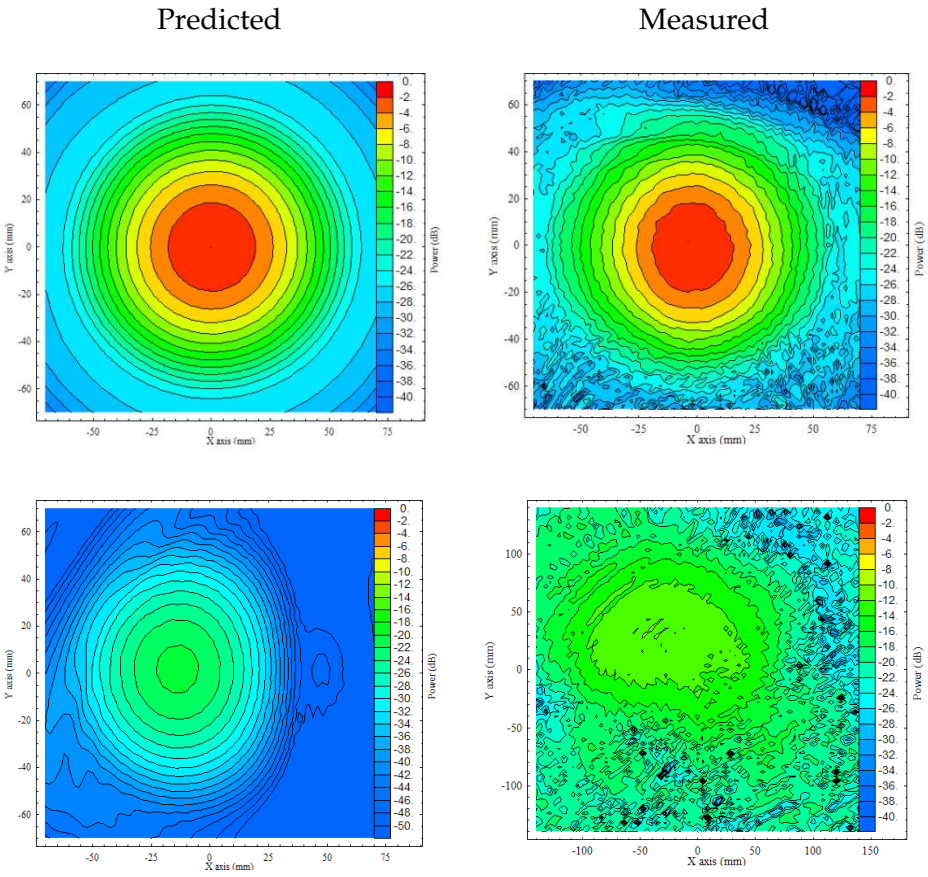

Figure 6-37 Predicted (left) and measured (right) beam patterns for co-polar (top) and cross-polar (bottom) for ψ_{Grid} = 10 °

- $\theta = 20°$, $\psi_{Grid} = 16°$

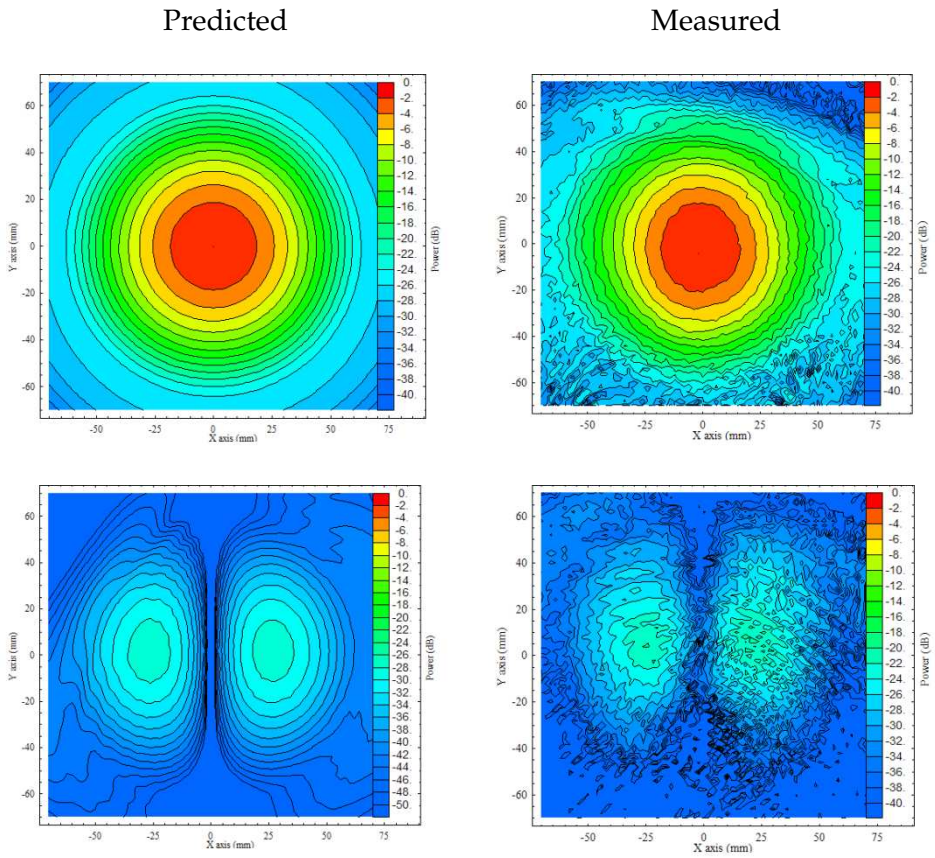

Figure 6-38 Predicted (left) and measured (right) beam patterns for co-polar (top) and cross-polar (bottom) for ψ_{Grid} = 16 °

- $\theta = 20°$, $\psi_{Grid} = 25°$

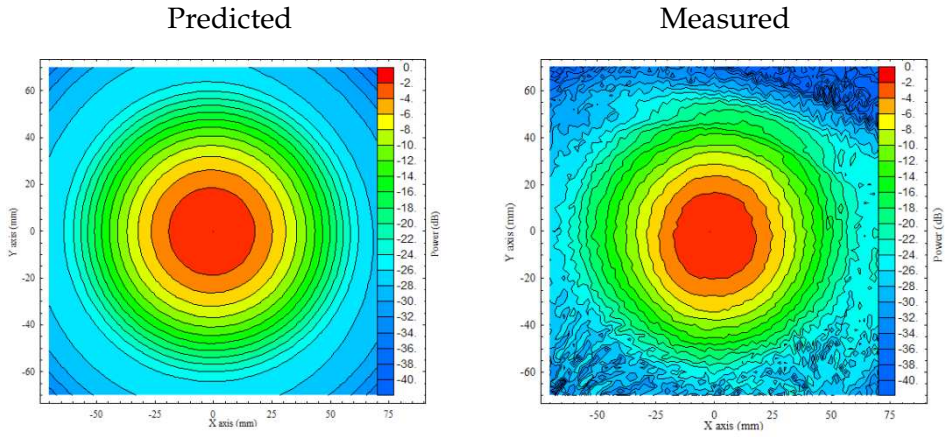

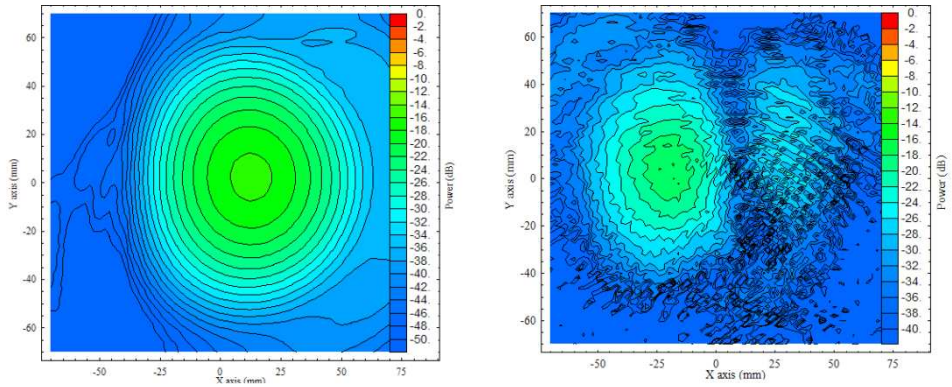

Figure 6-39 Predicted (left) and measured (right) beam patterns for co-polar (top) and cross-polar (bottom) for ψ_{Grid} = 25 °

The comparison between measurement and prediction for θ = 20° is very good. The cross polar power pattern evolves in the same manner as for the previous set of results. The plot below (Figure 6-40) tracks the measured and predicted cross polar power levels in dB against ψ_{Grid}.

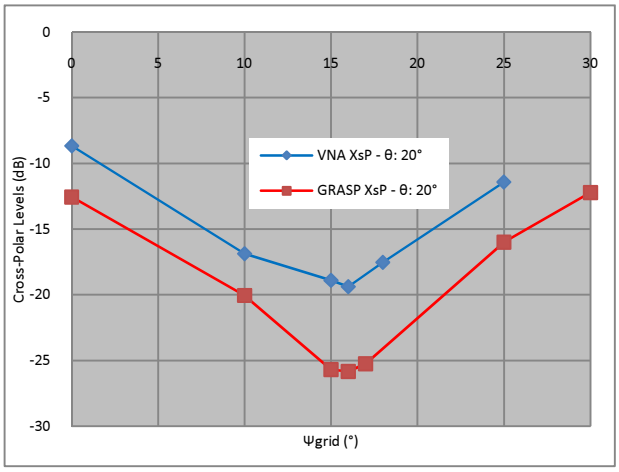

Figure 6-40 - Plot of measured (blue) and predicted (red) cross polar power levels (dB) for varying grid rotation angle ψ_{Grid}

These results follow the same expected pattern as seen in Figure 6-35 with a minimum cross polar power level shown for the approximate optimal grid rotation angle of 16.01°.

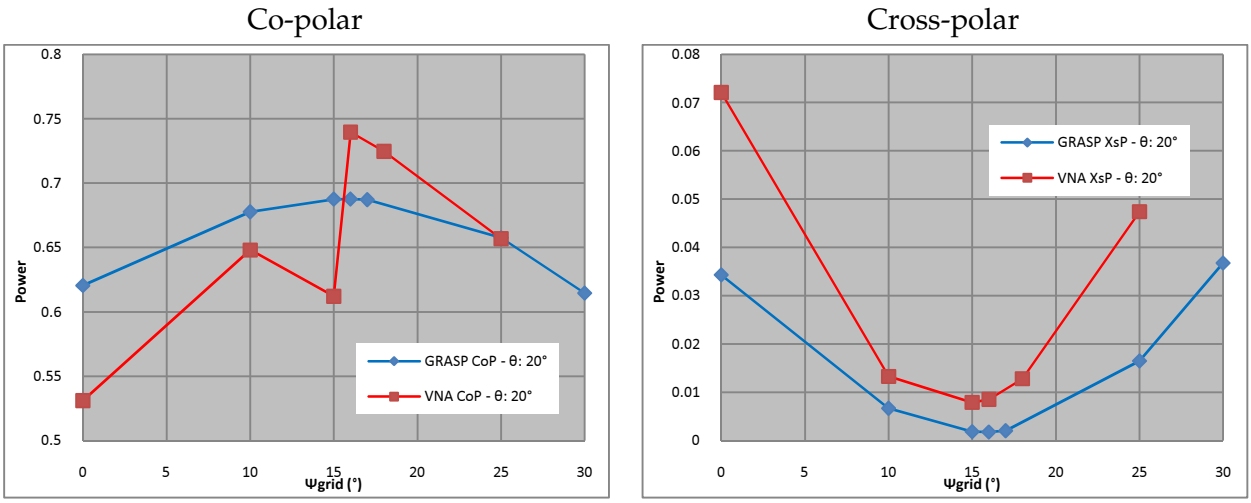

Figure 6-41 - Plots of measured (blue) and predicted (red) co and cross polar power levels as a function of grid rotation angle ψ_{Grid}

Plotting the un-normalised co polar and cross polar power values against grid rotation angle ψ_{Grid} in Figure 6-41 above reveals the expected trend of maximum co polar power and minimum cross polar power occurring for ψ_{Grid} approximately equal to 16.01°. There is however a distinct discrepancy between measurement and predictions for the co polar trend, which is yet again accounted for by human error in aligning the grid wires.

The final set of contour plots below are for the y' rotation angle θ = 22°, with three sets of predicted and measured plots for ψ_{Grid} equal to 10° (Figure 6-42), 17°(Figure 6-43) and 25° (Figure 6-44), with the grid rotation angle of 17° representing the optimal grid rotation angle of 17.45°.

- $\theta = 22°$, $\psi_{Grid} = 10°$

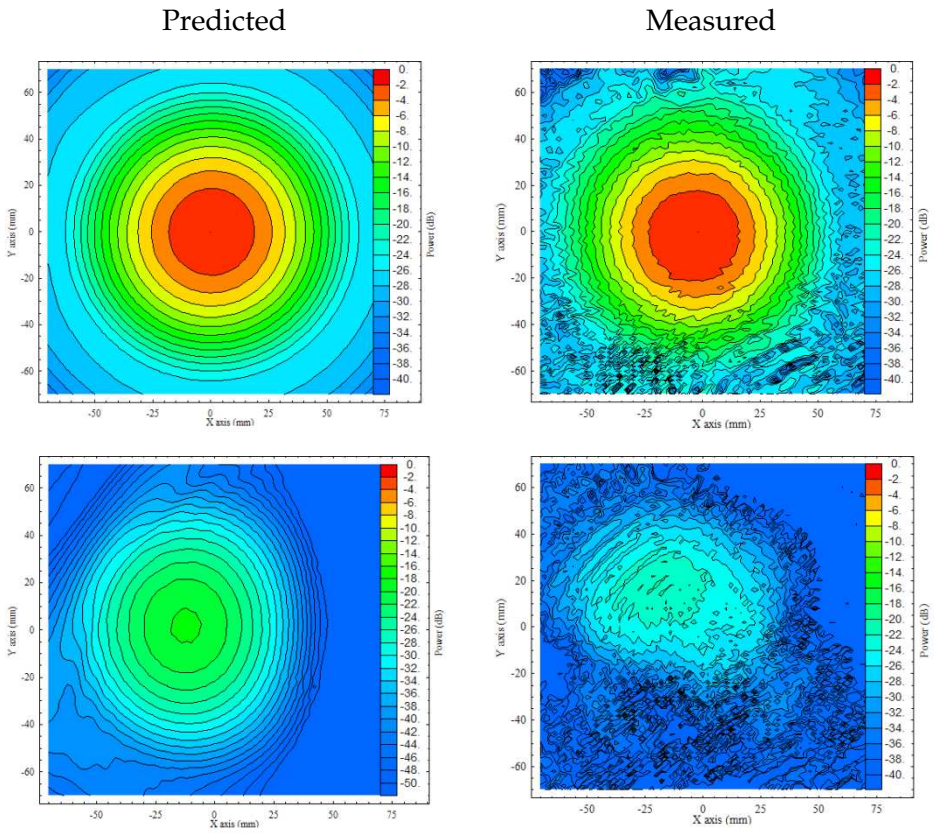

Figure 6-42 - Predicted (left) and measured (right) beam patterns for co-polar (top) and cross-polar (bottom) for ψ_{Grid} = 10 °

- $\theta = 22°$, $\psi_{Grid} = 17°$

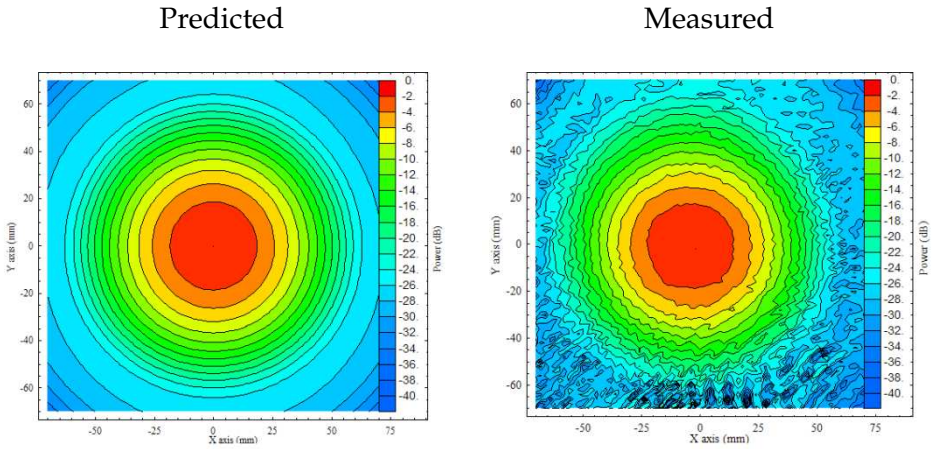

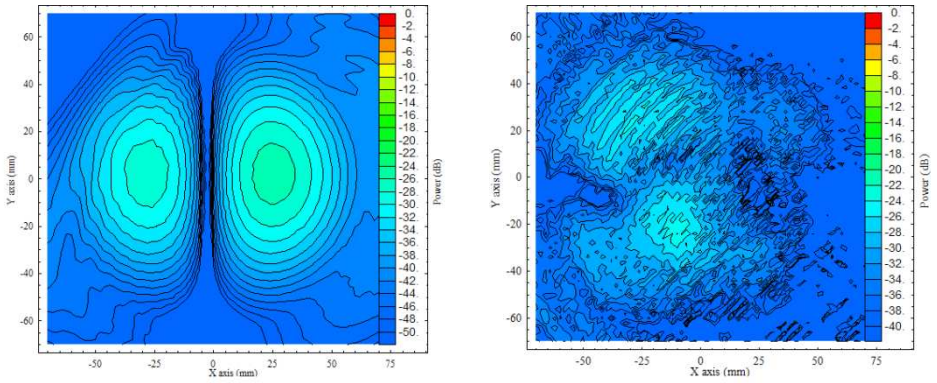

Figure 6-43 - Predicted (left) and measured (right) beam patterns for co-polar (top) and cross-polar (bottom) for ψ_{Grid} = 17 °

- $\theta = 22°$, ψ_{Grid} =25 °

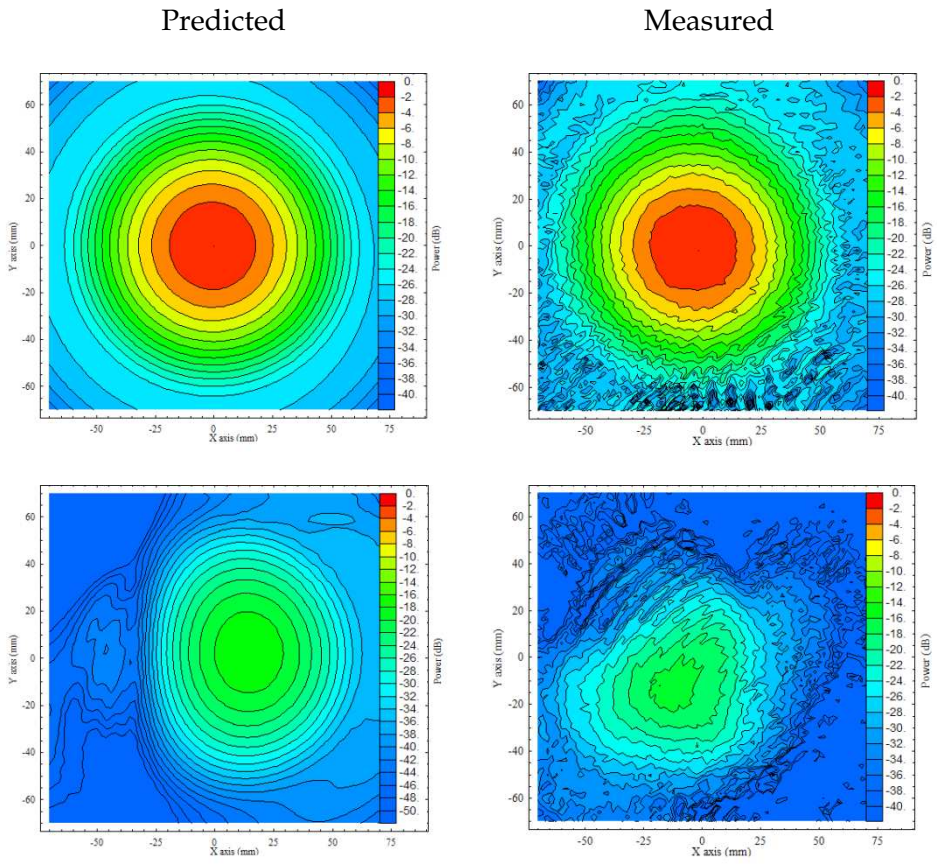

Figure 6-44 - Predicted (left) and measured (right) beam patterns for co-polar (top) and cross-polar (bottom) for ψ_{Grid} = 25 °

Comparisons between measurement and predictions show good agreement for both co and cross polar pattern levels. There are some minor beam distortions evident in the measured beam patterns that can be attributed to the metallic rim housing the polariser. With increasing y' rotation angle θ the plane of the grid begins to intersect the beam with decreased diameter, thereby increasing the truncation effects of the grid. This is most evident in the co polar power patterns – c.f. Figure 6-45 below:

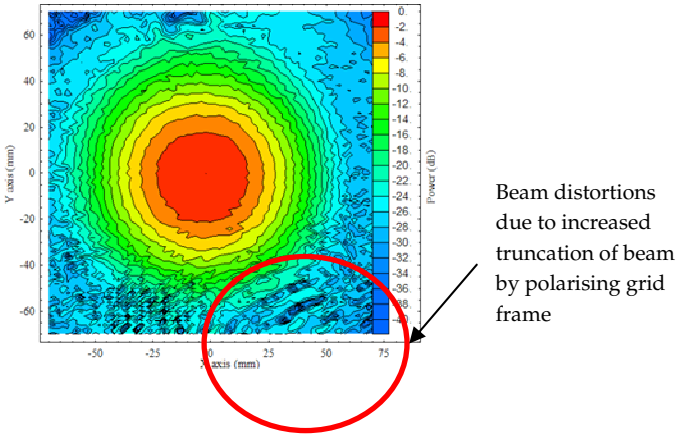

Figure 6-45 - Distortion of co-polar amplitude due to metallic rim of wire grid polariser

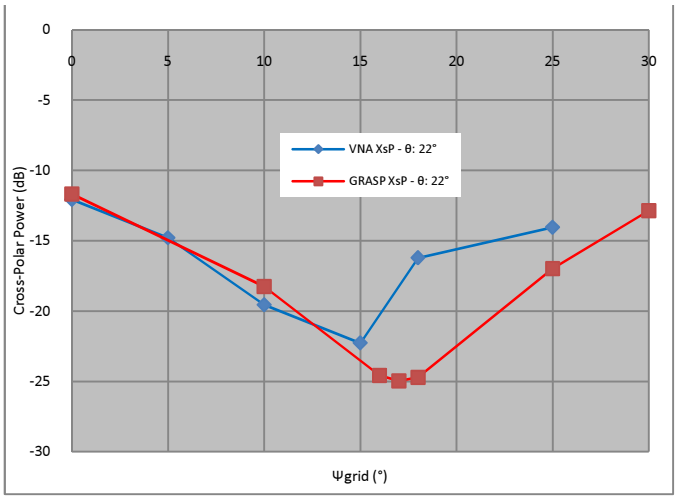

Figure 6-46 - Plot of measured (blue) and predicted (red) cross polar power levels (dB) for varying grid rotation angle ψ_{Grid}

The trend of cross polar power levels against ψ_{Grid} is plotted above in Figure 6-46, which shows relatively good comparisons between measurement and predictions. The measured cross polar power levels show a minimum value at ψ_{Grid} approximately equal to 15°, rather than at the predicted optimum ψ_{Grid} = 17°.

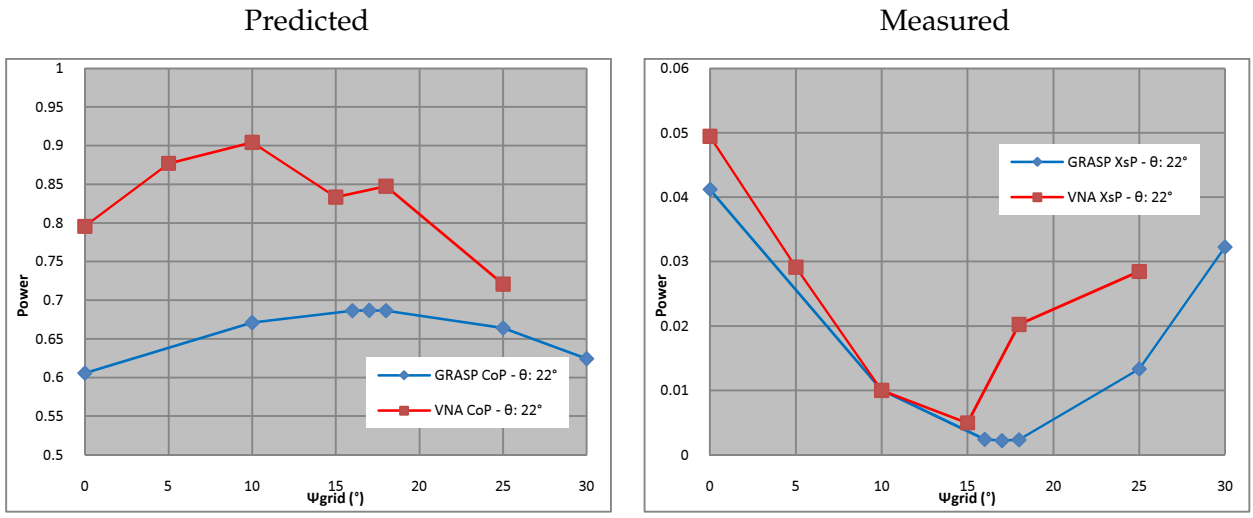

Figure 6-47 - Plots of measured (blue) and predicted (red) co and cross polar power levels as a function of grid rotation angle ψ_{Grid}

The above plots reveal that transmitted co-polar power peaks to a maximum and cross-polar power correspondingly drops to a minimum for the predicted optimum ψ_{grid}. Measured power levels exhibit a degree of disparity compared to predictions. As a consequence the normalised cross polar efficiency (Figure 6-46) also reveals slightly different values for prediction and measurement. This is attributed to the typical human error with aligning the grid wires. The grid object in GRASP9 is treated as an ideal grid object. This assumes perfect transmission and reflection for all perpendicularly and parallel polarised waves respectively, but does not take into account the physical properties of the metallic wires which will likely lead to disagreement between theory and experiment. This was the same electrical object used for the Band 9 PO analysis and the same degree of disparity between prediction and experiment was observed (c.f. Section 6.4) .The influence of waveguide probe is also not accounted for in predictions, however the VNA used in the near field scanning arrangement has excellent dynamic range so this minor effect is considered negligible. The calculation of the optimal grid

wire rotation angle using Euler angle transformation matrices (c.f. Figure 6-30) has been repeatedly verified with each test case.

An interesting conclusion is arrived at when comparing the results from the rotated version of the Band 9 front end optics in Section 6.4 and the 100 GHz polarising grid tests. It is well established that off-axis reflectors, be they ellipsoidal, paraboloidal or some other conic, introduce an element of rotation to the plane of polarisation of an incident linearly polarised EM beam [97], [107] and [108]. In [107] various patterns of polarising grid wires were developed using this geometrical projection effect in an effort to improve transmission and reflection by the polariser. C. Dragone has patented a method for constructing wire grids with optimal transmission/reflection of a linearly polarised beam that has been reflected by an off-axis paraboloidal surface [109]. These 'Dragone' grids are constructed in a similar manner to those from [107] by tracing the geometrical projection introduced by the off-axis reflector onto both plane and curved surfaces. A typical distorted polarisation pattern is shown below.

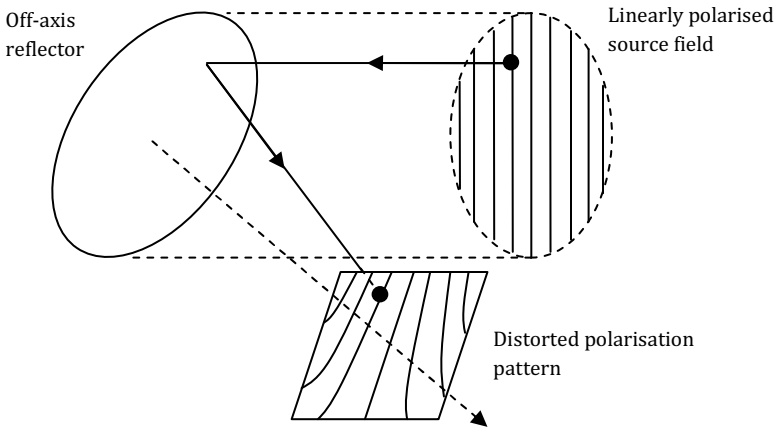

Figure 6-48 - Distortion of polarisation pattern due to geometrical projection effects of off-axis reflector - [107]

The traditional Dragone grid is designed for compensation of the cross polarisation generated by an off-axis paraboloidal mirror. In [109] a planar grid is located between

the focal point and the reflector surface. The grid wires are constructed by tracing the reflected rays onto the grid plane. This is illustrated below in Figure 6-49.

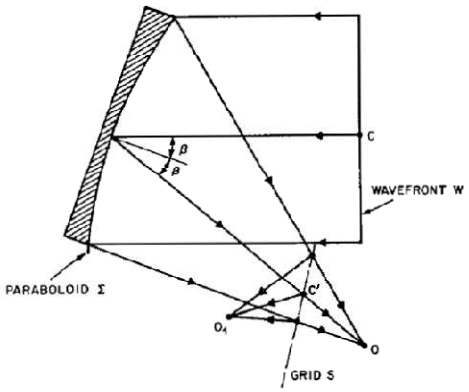

Figure 6-49 - Planar linearly polarised wavefront illuminating off-axis paraboloid with polarising grid located in front of focal point - [109]

The chief difference between the Dragone polarising grid described above and the wire grid polariser in the Band 9 system is that this Dragone grid is designed specifically for reflecting the linearly polarised beam from the input wavefront to the focal plane all within the same plane, whereas the Band 9 grid is rotated about two planes. It is the introduction of this second rotation about y', as seen in Figure 6-12, that introduces the misalignment of the transmission axis of the grid.

It was suggested at design review meetings for the Band 9 front end optics that the implementation of such a Dragone grid should be investigated. After discussion of this concept with TICRA, the developers of GRASP9, it was determined that the modeling and fabrication of such a Dragone grid would prove extremely difficult. For both this reason and the constraints of time and cost the implementation of a Dragone grid for the Band 9 optics was discontinued.

The results of the investigations presented in this chapter show that the determination of the optimal grid wire rotation angle was unaffected by the off-axis reflectors of the Band 9 system. Despite the rotation of the linear polarisation by the off-axis ellipsoidal

reflectors, it has been shown here that the optimal orientation of the grid wires is calculated as if there were no rotation introduced. For the 100 GHz test facility there were no coupling optics between the horn and output plane. This is a valuable conclusion as the fabrication of the modified non-linear polarising grids devised by [107] and [108] requires difficult and precise fabrication methods and they must be tailor made to suit each individual system of off-axis reflectors and they of course have associated bandwidth effects arising out of the varying grid wire spacings along the plane of the grid. Linear wire grid polarisers on the other hand are relatively easier to fabricate.

6.7 Conclusions

This chapter represents the design, analysis and measurement of several modifications to the ALMA Band 9 front end optics. A full PO treatment of an alternate 'Gaussian' optics version for the Band 9 front end optics system was performed. This alternate version of the optics exhibited improved beam Gaussicity, lower cross polar power levels and increased coupling to the ALMA antenna. Overall these improvements were deemed too minor to warrant an overhaul of the optics system, yet the increase in aperture efficiency of ~1% may incur some further investigation based on this analysis.

An in-depth PO analysis of the projection effect of the radiation incident upon the wire grid polariser was conducted. From this analysis an alternate version of the front end optics was generated. In this version of the front end optics the angles of polarisation of the two source feed horns were rotated through 90°. The projection angle of the radiation incident upon the grid was determined through an Euler angle analysis of the local coordinate frame of the polariser. PO predictions of this new system revealed lowered cross polar levels at the antenna focal plane with negligible effect on the co-polar beam. Experimental measurements were performed to test this system and results revealed very good agreement with predictions. As with the 'Quasioptical' modification

to the mirror surfaces, implementation of this improvement to the system would incur significant revision of the mixer and LO assemblies.

In collaboration with Dr. Andrey Baryshev another alternative of the front-end optics was investigated. This 'focusless' adaptation to the system involved replacing the ellipsoid-ellipsoid pair of M3-M41P/0P with an ellipsoid-hyperboloid arrangement. The purpose of this was to remove the formation of a beam waist at the polarising grid and thus improve the cross polar efficiency at the focal plane. Predictions of this focusless system revealed a significant improvement in cross polar efficiency. However, the strict opto-mechanical constraints for the Band 9 cartridge prevented such a design from being considered. However, this modification to the ellipsoid-ellipsoid pair is important for potential optical systems with a similar wire-grid polariser arrangement to that of Band 9 and would warrant further analysis to fully test its performance.

An extension of the analysis of the projection effect on the wire grid polariser was performed. Similar projection effects to that for the Band 9 grid were predicted for a low frequency stripped down version of the Band 9 front end consisting of a single wire grid polariser mounted upon a gimbal frame. Experimental measurements of this system successfully confirmed predictions with excellent agreement.

7. Conclusion

This thesis was concerned with the quasioptical analysis of long wavelength optical systems. Particular emphasis of this technique was to the analysis and verification of the front end optics arrangements for the Band 5 and Band 9 receiver channels of ALMA. In addition to the specific analysis of these systems, a comparative study of commercially available software packages (GRASP9 & ZEMAX) and the Maynooth Optical Design and Analysis Laboratory (MODAL) was performed using novel test cases of interest to the long-wavelength optics regime. The techniques of GBMA and mode-matching were applied to investigating the structure of standing wave patterns in resonant cavities fed by conical corrugated feed horns.

Chapter 1 gives a general overview of the current state of submillimetre astronomy and its unique position within the electromagnetic spectrum. A description of the chief sources of astronomical submillimetre radiation is given. Observations of *the Antennae* (NGC-4038/89) from the Caltech Millimetre Array are highlighted as an example of the purpose and aim of submillimetre observations. A brief overview of current both ground based and space-borne submillimetre telescopes, their characteristics and science goals is outlined. Specific emphasis is placed on ALMA, which upon completion will form the world's largest submillimetre array telescope.

Chapter 2 introduces the theoretical analysis techniques utilised throughout the thesis. A comprehensive review of the theoretical foundations of GBMA was presented. The theory of GBMA was extended to describe the classical optics phenomena of Fresnel diffraction. An added verification of the Fresnel diffraction pattern was achieved through the Fourier Optics technique of the Angular Spectrum of Plane Waves. Comparisons drawn between these two methods revealed that GBMA provided a more accurate and computationally efficient result. The GBMA technique was also developed to accurately model the characteristic Haidinger and Fizeau fringe patterns observed by Michelson interferometers. As the main subject of this thesis is the analysis of the optics that couple feed horns to reflector antennas, a description of the characteristics of

conical corrugated feed horns and Cassegrain antennas is given. A general description of the principles of Physical Optics and the Physical Theory of Diffraction is reported on. Physical Optics analysis, achieved primarily through GRASP9, was used throughout the thesis for the characterisation of several long wavelength optical systems. As such, an introduction to the operation of this software package and that of three others, MODAL, ZEMAX and CST-MWS is detailed.

In Chapter 3 of this thesis a comparison study of GRASP9, MODAL and ZEMAX was performed. This study was an extension of work previously conducted by NUI Maynooth in conjunction with its international research partners as part of a confidence analysis of the various commercial optics software packages available at the time. The purpose of this was to determine the applicability of these packages to the long wavelength regime, with GRASP used as the benchmark for testing. The test case scenarios employed in this report were developed to strenuously test the various software packages and represented highly diffracting systems such as very near field Fresnel diffraction arrangements as well as systems consisting of lenses and off-axis conical reflectors that are common to submillimetre receivers. Two software packages not included in the original study were ZEMAX and MODAL. Since the time of the original report, the primarily geometrical optics software package ZEMAX has developed a degree diffractive optics capability. The MODAL optics tool has been only recently developed in that time. The results from ZEMAX exhibit overall relatively poor agreement with GRASP9 for all but the simplest optical systems. This was a similar result to that of the ray-tracing packages GLAD and CODE-V in the original report. This was unsurprising given that the Physical Optics Propagator tool in ZEMAX utilises a combination of Fourier transforms and Fresnel diffraction integrals to compute the output fields. The results from MODAL exhibited much greater agreement with GRASP9, with only minor deviations observed.

An experimental measurement campaign was embarked upon to model a highly truncating aperture which had a similar arrangement to the first batch of test cases. The

aim of these measurements was to resolve the disparity between GRASP9 and MODAL. While the experimental results compared well with both packages for the gross diffraction pattern, the measurement equipment proved inadequate to accurately account for minor diffraction pattern structure.

Chapter 4 deals with the analysis of standing waves in submillimetre systems fed by corrugated horn antennas. The first part of this chapter introduces the theory of scattering matrices for waveguide structures and their extension to the mode-matching theory as developed by [71]. The scattering matrix description of several beam guide components as outlined by [78] is also detailed. The scattering matrix technique for these freespace beam guides was verified by modeling the reflection profiles for several examples of thin-films. The waveguide and beam guide structures are combined to give a complete analytical description of a feed horn. Previous work by [88] and [76] successfully compared prediction and measurement of several horn-horn cavity arrangements where multiple reflections were tracked with respect to varying interhorn distance. The work presented in this chapter concentrated upon the frequency dependence of standing waves for similar horn-horn cavities for fixed interhorn distances. The amplitude response patterns of these cavities were measured in the laboratory. In an attempt to resolve the disparity between prediction and measurement several theoretical models of these cavities were developed based variations of the corrugated horn geometry profile which were dependent on the machining tolerances for the horn mandrel. The results of this analysis revealed moderate gross structure agreement with measurement data. The minor variations to the horn geometry profile significantly altered the return loss profile of individual horns, but negligible differences were seen for cavity arrangements fed by these horns. A stray light baffle structure was also studied, with similar agreement between predictions and measurement as for the horn-horn cavities. A Fourier signal analysis of the amplitude response patterns of this baffle was performed, revealing very good agreement between predictions and measured data.

Further investigation of these cavity structures is needed, specifically relating to quantifying the effect of the rectangular to circular waveguide transition zone at the back of the feed horns. FDTD techniques were successfully employed using CST-MWS to verify the mode-matching technique. However, the computational intensity of these calculations prevented any further analysis of the horn. One recommendation is to reduce the complexity of the corrugated feed horn structure by employing an equivalent smooth walled horn. The effect of the transition zone may thus be quantified with comparisons made to both mode-matching theory and measurement.

The quasioptical and physical optics analysis of the ALMA Band 5 front end optics is detailed in Chapter 5. The first stage of this analysis was conducted in conjunction with the Band 5 development group at GARD in order to determine the effect of increased beam truncation upon system efficiency. Three levels of truncation were analysed for two versions of the front end optics reflector surfaces using PO calculations. The results of this analysis revealed a sufficient compromise between increased beam truncation and opto-mechanical limits. The prototype front-end optics was consequently developed at GARD based upon these findings. The second stage of this analysis involved a measurement campaign of the corrugated feed horn and front end optics, the results of which revealed excellent agreement with theoretical predictions. An initial set of beam pattern measurements for the receiver inserted into the cryostat also revealed similar levels of agreement with PO predictions.

As of the time of finalizing this thesis there was still extensive testing of the Band 5 prototype optics required. There remains an issue of asymmetry for the higher frequency copolar beam revealed by cold beam patterns measurements. This is possibly due to the presence of the IR filters and their respective housing structures within the cryostat. Further analysis of the optics after cooling can be performed using MODAL, which allows for the PO calculation of dielectrics. When high resolution beam pattern measurements are conducted, they may be used as complex 2D source fields within both GRASP and MODAL to predict the antenna main beam in comparison with the

theoretical results presented in this chapter. Further investigation of the ALMA antenna is also required to include the subreflector support legs.

Chapter 6 is concerned with the extended PO analysis of the ALMA Band 9 front end optics. Although this receiver channel has been previously analysed in [99] there remains an outstanding issue of the levels of cross polar leakage which do not meet ALMA requirements. Several solutions to this problem are discussed here. The first involves a re-working of the reflector surfaces to better match the phase radii of the incident radiation and thus provide better coupling to the antenna. The results revealed an increase in beam Gaussicity, lowered cross polar levels and increased aperture efficiency. However, these improvements were practically negligible and did thus not warrant implementation. The second solution was developed in collaboration with Dr. Andrey Baryshev, and involved removing the inter-mirror focusing of the beam. The formation of a beam waist at the wire grid polariser leads to difficulties in the grid efficiently separating the orthogonal beam components. This was achieved by a novel hyperboloid-ellipsoid reflector arrangement which revealed much lower cross polar power leakage. Although the system was deemed too drastic to implement in the current Band 9 channels, the 'focusless' system warrants further investigation as it would undoubtedly prove useful for possible future developments of the cartridge, as well as for other long wavelength receiver systems.

The final solution to the cross polar power problem was borne out of investigations into the projection effect of the incident beam from the off-axis mirrors onto the polarising grid plane. Through analysis of the geometry of the problem, an alternate system was devised based upon modifying the angle of rotation of the grid wires to ensure improved transmission/reflection. The predictions for this system exhibited lowered cross polar levels at the antenna focal plane. A measurement campaign of this modified system at SRON revealed excellent agreement with predictions. Further investigations of this projection effect were conducted at Maynooth which further verified the previous results.

Appendix A

ALMA Band 9 Measurement System

In this appendix a description of the VNA heterodyne system used for measuring the co and cross polar beams at 670 GHz for the various grid configurations from Section 6.4 is given. The following description makes reference to the accompanying electrical diagram of the PLL system below.

A typical VNA is incapable of direct measurement of signals above 20 GHz. The inclusion of converter waveguide heads will only increase this range up to approximately 350 GHz. To measure signals at higher frequencies than these the heterodyne mixing technique must be employed. The heterodyne mixing arrangement for the Band 9 receiver channel is illustrated below in Figure A-1.

The Gunn oscillator is mechanically tunable for 100-120 GHz whose stability is maintained by the Phase Locked Loop (PLL). The frequency stability of the Gunn oscillator depends on the dimensions of the cavity under scrutiny and the bias voltage applied to the Gunn diode. The PLL provides a variable bias voltage obtained from a closed loop control system which guarantees frequency stability for the Gunn.

The Gunn oscillator maintains a stable signal frequency of $f_G = 670/6 = 111.667$ GHz. Of this Gunn signal, 90% is directed towards the multiplier arrangement and the remaining 10% is directed towards the mixer. Following this 10% signal from the Gunn oscillator, it is mixed with the Local Oscillator (LO) signal of $f_{LO} = 18.62311$ GHz. This mixing results in a multitude of frequencies given by the combinations between the Gunn and LO frequencies. The Intermediate Frequency (IF) of 72 MHz is filtered out from these signal combinations. The PLL compares the 72MHz IF signal with a stable reference 72 MHz signal from a signal generator. The PLL thus serves as an IF monitor which directs 72 MHz signal to a an amplifier and multiplier arrangement which sends

a signal 6 times the IF frequency (432 MHz) to the VNA to be used as the reference signal.

Going back to the *90%* Gunn signal; this portion of the signal is multiplied up to the operating RF of the system (i.e. $6f_{Gunn}$ = 670 GHz). This 670 GHz beam is then transmitted through the optical arrangement and coupled to the receiver horn. This RF output signal is then converted to an electrical signal using a SLED device acting as a sub harmonic mixer. The SLED mixes the RF signal (670 GHz) with the 36th harmonic of the LO signal (equal to 670.432 GHz) which produces a signal 6 times the IF frequency (*432MHz*) which is then coupled to the VNA as the output signal. The following photograph summarises the Gunn oscillator and frequency mixer chain.

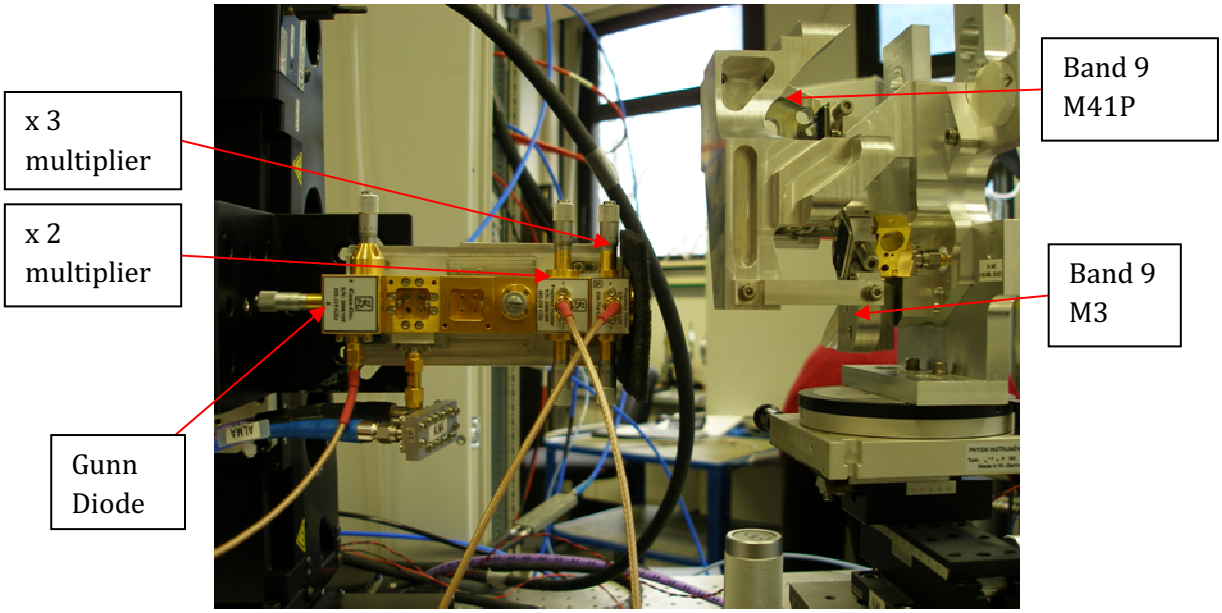

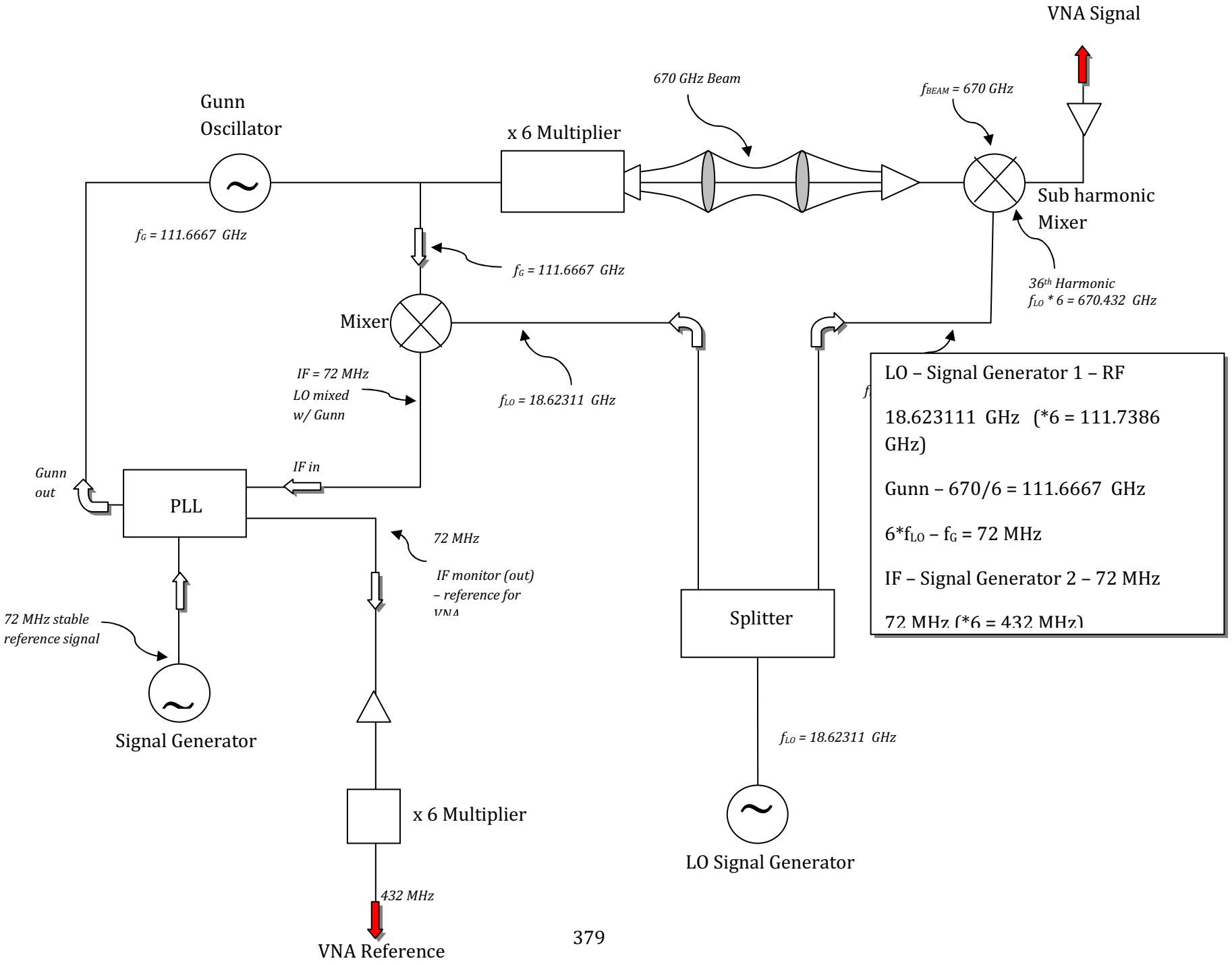
VNA Signal
670 GHz Beam
f_{BEAM} = 670 GHz
Gunn Oscillator
x 6 Multiplier
Sub harmonic Mixer
f_G = 111.6667 GHz
f_G = 111.6667 GHz
36th Harmonic
f_{LO} * 6 = 670.432 GHz
Mixer
IF = 72 MHz
LO mixed w/ Gunn
f_{LO} = 18.62311 GHz
LO – Signal Generator 1 – RF
18.623111 GHz (*6 = 111.7386 GHz)
Gunn – 670/6 = 111.6667 GHz
6*f_{LO} – f_G = 72 MHz
IF – Signal Generator 2 – 72 MHz
72 MHz (*6 = 432 MHz)
Gunn out
IF in
PLL
72 MHz
IF monitor (out) – reference for VNA
72 MHz stable reference signal
Splitter
Signal Generator
f_{LO} = 18.62311 GHz
x 6 Multiplier
LO Signal Generator
432 MHz
VNA Reference

Works Cited

[1] B. F. Burke and F. Graham Smith, *An Introduction to Radio Astronomy*. Cambridge University Press, 1996.

[2] L. Yun-Shik, *Principles of Terahertz Science and Technology*, 1st ed. Springer, 2008.

[3] P. F. Goldsmith, *Quasioptical System: Gaussian Beam Quasioptical Propagation and Applications*. New York: IEEE Press, 1998.

[4] A. E. Siegman, *Lasers*. University Science Books, U.S., 1990.

[5] T. G. Phillips and J. Keene, "Submillimetre Astronomy - Heterodyne Spectroscopy," *Proceedings of the IEEE*, vol. 80, no. 11, pp. 1662-1678, Nov. 1992.

[6] A. G. G. M. Tielens, *The Physics and Chemistry of the Interstellar Medium*. August, U.K.: Cambridge University Press, 2005.

[7] I. F. Mirabel, et al., "The dark side of star formation in the Antennae galaxies," *Astronomy and Astrophysics*, vol. 333, pp. L1-L4, Feb. 1998.

[8] A. R. Gillispie, "CO Observations in Galactic Clouds," *ESO Messenger*, vol. 21, p. 20, 1980.

[9] D. Narayanan, T. J. Cox, C. C. Hayward, J. D. Younger, and L. Hernquist, "The Star-Forming Molecular Gas in High-Redshift Submillimetre Galaxies," *Monthly Notices of the Royal Astronomical Society*, vol. 400, no. 4, pp. 1919-1935, Nov. 2009.

[10] E. Daddi, et al. (2009, Mar.) A CO Emission Line from the Optical and Near-IR Undetected Submillimetre Galaxy GN10. [Online] arXiv:0903.3046v1

[11] T. L. Wilson. (2009, Mar.) Introduction to Millimeter/Sub-Millimeter Astronomy. [Online]. arXiv:0903.0562

[12] P. Cassen, "Protostellar Disks and Planet Formation," in *Extrasolar Planets*. Springer Berlin-Heidelberg, 2006, pp. 369-448.

[13] A. Quirrenbach, "Detection and Characterization of Extrasolar Planets," in *Extrasolar Planets*. Springer Berlin Heidelberg, 2006, pp. 1-242.

[14] R. K. Mann and J. P. Williams, "Massive Protoplanetary Disks in Orion beyond the Trapezium Cluster," *The Astrophysical Journal*, vol. 699, pp. L55-L58, Jul. 2009.

[15] ESA. (2009, Feb.) ESA Science and Technology - Herschel Space Observatory. [Online]. http://sci.esa.int/science-e/www/area/index.cfm?fareaid=16

[16] ESA. (2010, Jan.) ESA Science & Technology - Planck Surveyor. [Online]. http://www.rssd.esa.int/index.php?project=planck

[17] (2009, Nov.) Cornell Caltech Atacama Telescope homepage. [Online]. http://www.submm.org/

[18] http://www.almaobservatory.org/.

[19] NRAO. (2009, Jan.) ALMA NRAO Web site. [Online]. http://www.alma.nrao.edu/

[20] A. Wootten and A. R. Thompson. (2009, Apr.) The Atacama Large Millimeter/submillimeter Array. [Online]. arXiv:0904.3739v1

[21] C. O' Sullivan, et al., "Far-Infrared Optics Design & Verification," *International Journal of Infrared & Millimetre Waves*, vol. 23, no. 7, pp. 1029-1045, Jul. 2002.

[22] D. H. Martin and J. Lesurf, "Submillimetre-wave Optics," *Infrared Physics*, vol. 18, pp. 405-412, Dec. 1978.

[23] P. F. Goldsmith, *Quasioptical Systems: Gaussian Beam Quasioptical Propogation and Applications*. New York: IEEE Press, 1997.

[24] M. Born and E. Wolf, *Principles of Optics: Electromagnetic Theory of Propagation, Interference and Diffraction of Light*. Cambridge University Press, 1997.

[25] G. Goubau and F. Schwering, "On the guided propagation of electromagnetic wave beams," *IRE Transactions on Antennas and Propagation*, vol. 9, no. 3, pp. 248-256, May 1961.

[26] H. A. Haus, *Waves and Fields in Optoelectronics*. Prentice Hall, 1983.

[27] J. A. Murphy, "Aperture Efficiencies of Large Axisymmetric Reflector," *IEEE Trans. on Antennas and Propagation*, vol. 36, no. 4, pp. 571-575, Apr. 1988.

[28] J. A. ,. E. A. Murphy, "Examples of Fresnel diffraction using Gaussian modes," *European Journal of Physics*, vol. 14, no. 3, pp. 121-127, Aug. 1992.

[29] N. Trappe, J. A. Murphy, and S. Withington, "The Gaussian beam mode analysis of classical phase aberrations in diffraction-limited optical systems," *European Journal of Physics*, vol. 24, no. 4, pp. 403-412, 2003.

[30] J. C. Lesurf, *Millimetre Wave Optics, Devices and Systems*. Institute of Physics (IOP) Publishing, 1990.

[31] D. H. Martin and J. W. Bowen, "Long Wave Optics," *IEEE Transaction on Microwave Theory and Techniques*, vol. 41, no. 10, pp. 1676-1690, Oct. 1993.

[32] F. L. Pedrotti, M. L. Pedrotti, and L. S. Pedrotti, *Introduction to Optics*. Benjamin Cummings, 2006.

[33] J. W. Goodman, *Introduction to Fourier Optics*, 2nd ed. McGraw-Hill, 1996.

[34] J. C. Wyant. http://wyant.optics.arizona.edu.

[35] T. Finn, "Quasioptical Verification of HIFI for the Herschel Space Observatory and Standing Waves in Quasioptical Systems," Ph.D. Thesis, National University of Ireland, Maynooth, Maynooth, 2007.

[36] C. A. Bennett, *Principles of Physical Optics*, 1st ed. United States of America: John Wiley & Sons, 2008.

[37] J. Morgan, *Introduction to Geometrical and Physical Optics*. U.S.: McGraw-Hill, 1953.

[38] M. V. Klein and T. E. Furtak, *Optics*, 2nd ed. U.S.A.: J. Wiley & Sons, 1986.

[39] F. A. Jenkins and H. E. White, *Fundamentals of Optics*, 4th ed. U.S.A.: McGraw-Hill, 1965.

[40] J. D. Kraus, *Radio Astronomy*, 2nd ed. Cygnus-Quasar Books, 1986.

[41] R. J. Wylde, "Millimetre-wave Gaussian beam mode optics and corrugated feed horns," *IEEE Proceedings on Microwaves, Optics and Antennas*, vol. 131, no. 4, pp. 258-262, Aug. 1984.

[42] C. A. Balanis, *Antenna Theory: Analysis and Design*, 3rd ed. Wiley-Interscience, 2005.

[43] P. J. B. Clarricoats, *Corrugated Horns for Microwave Antennas*. IEEE Press, 1984.

[44] R. Colgan, *Electromagnetic and Quasi-optical modelling of Horn antennas for Far-IR Space Applications - PhD Thesis*. NUI Maynooth, 2001, PhD Thesis, NUI Maynooth.

[45] J. D. Kraus, *Antennas*, McGraw-Hill, Ed. 1988.

[46] J. Ruze, "Antenna Tolerance Theory - A Review," *Proceedings of the IEEE*, vol. 54, no. 4, pp. 633-640, Apr. 1966.

[47] John Wiley & Sons, *Encyclopedia of RF and Microwave Engineering*. John Wiley & Sons, 1999-2009.

[48] K. Rohlfs and T. L. Wilson, *Tools of Radio Astronomy*, 4th ed. Springer, 2005.

[49] TICRA. GRASP9 Software Description. [Online]. www.ticra.com

[50] M. Whale, N. Trappe, and V. Belitsky, "Physical Optics Analysis of the ALMA Band 5 Front End Optics," in *International Symposium on Space Terahertz Technology (ISSTT)*, Groningen, Netherlands, 2008, pp. 368-372.

[51] M. Whale, et al., "Analysis of two ALMA front end receiver channels using physical optics," in *Proc. of SPIE, Terahertz Technology and Applications*, San Jose, California, U.S.A., 2008.

[52] W. L. ,. T. G. A. Stutzman, *Antenna Theory and Design*. Wiley, 1997.

[53] K. Pontoppidan, *GRASP9 Technical Description*. Copenhagen, Denmark, 2005.

[54] P. Y. Ufimtsev, *Fundamentals of the Physical Theory of Diffraction*. Wiley-IEEE Press, 2007.

[55] E. Gleeson, "Single and multi-moded corrugated horn design for cosmic microwave background experiments," PhD Thesis, NUI Maynooth, 2004.

[56] M. L. Gradziel, D. White, J. A. Murphy, and S. Withington, "Improving the Efficiency of Quasi-optical Analysis and Design of Terahertz Sytstem," in *15th International Symposium on Space Terahertz Technology (ISSTT 05)*, Northampton,

Massachusetts, USA, 2005.

[57] S. Withington, J. A. Murphy, and K. G. ISAAK, "Representation of Mirrors in Beam Waveguides as Inclinde Phase-Transforming Surfaces," *Infrared Physics and Technology*, vol. 36, no. 3, pp. 723-734, 1995.

[58] C. O' Sullivan, et al., "Developments in Quasi-Optical Design for THz," in *Proc. SPIE-04*, Glasgow, U.K., June, 2004, pp. 320-321.

[59] M. L. Gradziel, et al., "Modeling of millimetre-wave and terahertz imaging systems," in *Proceedings of SPIE*, London, United Kingdom, 2004, pp. 154-165.

[60] ZEMAX Development Corporation, *ZEMAX Optical Design Progran - Users Guide*. 2006.

[61] M. N. O. Sadiku, *Numerical Techniques in Electromagnetics*. CRC Press, 2001.

[62] B. Houshmand and T. Itoh, "Introduction to FDTD Method for Planar Microwave Structures," in *Time-Domain Methods for Microwave Structures: Analysis and Design*. Wiley Press, 1998, pp. 1-11.

[63] CST - Computer Simulation Technology, *CST - Microwave Studio User Manual*. 2009.

[64] J. A. Murphy, C. O' Sullivan, D. Henry, and e. al, "Far IR Optics Design and Verification Tools," Final Report of ESA TRP study contract 13043/98/NL/NB (Phase 1), 1999.

[65] C. O' Sullivan, et al., "The Quasi-Optical Design of the QUaD Telescope," in *Millimeter and Submillimeter Detectors for Astronomy II*, Glasgow, Scotland, 2004, p. 396.

[66] G. Cahill, "The Quasioptical Design of the QUaD Telescope," Ph.D. Thesis , Experimental Physics, 2007.

[67] J. A. Murphy, "Distortion of a Simple Off-Axis Gaussian Beam on Reflection from Off-Axis Ellipsoidal Mirrors," *Int. Journal Infrared & Millimetre Waves*, vol. 8, no. 9, pp. 1165-1187, 1987.

[68] T. S. Chu and R. W. England, "An Experimental Broa dBand Imaging Feed," *Bell System Technical Journal*, vol. 62, pp. 1233-1250, May 1983.

[69] N. Hyong-Kim. (2005, Nov.) ZEMAX Knowledge Base. [Online]. http://www.zemax.com/kb/articles/70/1/

[70] A. D. Olver and P. J. B. Clarrioats, *Microwave Horns and Feeds*. IEEE Press, 1994.

[71] K. Zhang and D. Li, *Electromagnetic Theory for Microwaves and Optoelectronics*, 2nd ed. Beijing, China: Springer, 2007.

[72] J. C. Freeman, *Fundamentals of Microwave Transmission Lines*. U.S.A.: John Wiley & Sons, 1996.

[73] M. Hiebel, *Fundamentals of Vector Network Analysis*. Munich, Germany: Rohde & Schwarz GmbH & Co., 2007.

[74] R. J. Wylde, "Millimetre-wave Gaussian beam-mode optics and corrugated feed horns," *IEEE Proc. Microwaves, Optics and Antennas*, vol. 131, no. 4, pp. 258-262, Aug. 1984.

[75] N. Trappe, "Quasi-optical Analysis of the HIFI Instrument for the Herschel Space Observatory," PhD Thesis, NUI Maynoorh, 2002.

[76] E. Hecht, *Optics*, 4th ed. Addison Wesley, 2001.

[77] R. Padman and J. A. Murphy, "A Scattering Matrix Formulation for Gaussian Beam-Mode Analysis," in *Proceedings of ICAP*, vol. 1, York, Apr. 1991, pp. 201-204.

[78] P. J. B. Clarricoats and K. R. Slinn, "Computer Solution of Waveguide-Discontinuity Problems," *IEEE Microwave Symposium Digest*, vol. 67, no. 1, pp. 23-27, May 1967.

[79] A. Wexler, "Solution of Waveguide Discontinuities by Modal Analysis," *IEEE Trans. Microwave Theory Tech.* , vol. 67, no. 1, pp. 11-12, May 1967.

[80] M. Carter, et al., "ALMA Front-end Optics Design Report," ALMA Front End Doc. FEND-40.02.00.00-035-B-REP, 2007.

[81] P. J. B. Clarricoats and A. D. Olver, *Corrugated Horns for Microwave Antennas*.

London: IEEE Press - Peter Peregrinus Ltd, 1984.

[82] ZAX Millimetre Wave Corp. [Online] http://www.millimeterwave.com/

[83] J. A. Murphy, N. Trappe, and S. Withington, "Gaussian beam mode analysis of partial reflections in simple quasi-optical systems fed by feed horns," *Infrared Physics & Technology*, vol. 44, pp. 289-297, 2003.

[84] J. A. Murphy, N. Trappe, and S. Withington, "Gaussian beam mode analysis of partial reflections in simple quasi-optical systems fed by horn antennas," *Infrared Physics & Technology*, vol. 44, no. 4, pp. 289-297, Aug. 2003.

[85] T. Keating, "94 GHz Corrugated Horn," British Patent , 1984.

[86] A. M. Baryshev and W. Wild, "ALMA Band 9 Optical Layout," NOVA/SRON ALMA Memo Series 394, 2001.

[87] N. Trappe, J. A. Murphy, S. Withington, and W. Jellema, "Gaussian Beam Mode Analysis of Standing Waves Between Two Coupled Corrugated Horns," *IEEE Trans. Ant. & Prop.*, vol. 53, no. 5, pp. 1755-1761, May 2005.

[88] S. Withington, M. Hobson, and B. Berry, "Representing the bahaviour of partially coherent optical systems by using overcomplete basis sets," *J. Opt. Soc. Am. A.*, vol. 21, no. 2, pp. 207-217, Feb. 2004.

[89] M. Hobson, B. Berry, and S. Withington, "General approach for representing and propagating partially coherent terahertz fields with application to Gabor basis sets," *J. Opt. Soc. Am. A.*, vol. 21, no. 5, pp. 786-796, May 2004.

[90] N. Trappe, T. Finn, J. A. Murphy, S. Withington, and W. Jellema, "Analysis of standing wave in submillimetre-wave optics," in , San-Jose, California, U.S.A..

[91] J. Kingsley and J. Baars, "Antennas," ALMA Project Book Chapter 4, 2002.

[92] J. Lamb, "Optimized Layout for MMA 12-m Antennas," ALMA Memo Series 246, 1999.

[93] A. Orlowska, B. Ellison, J. Webber, and G. H. Tan, "Cryostat Design Report," ALMA Front End Doc. 40.03.00.00-007-A-REP, 2005.

[94] J. W. Lamb, et al., "ALMA Memo 362 - ALMA Receiver Optics Design," 2001.

[95] M. Carter, et al., "ALMA Front End Optics Design Report (FEND-40.02.00.00-035-B-REP)," 2007.

[96] J. A. Murphy, "Distortion of a Simple Gaussian Beam on Reflection from Off-Axis Ellipsoidal Mirrors," *International Journal of Infrared & Millimetre Waves*, vol. 8, no. 9, pp. 1165-1187, 1987.

[97] P. J. B. Clarricoats and A. D. Olver, *Corrugated Horns for Microwave Antennas*. IEEE Press - Peter Peregrinus Ltd., 1984.

[98] M. Candotti, et al., "Quasi-Optical Verification of the Band 9 ALMA Front End," ALMA Memo Series 544, 2005.

[99] M. Candotti, "Design, Analysis and Optimisation of Quasi-Optical Systems for Sub-mm Astronomy Instrumentation," PhD Thesis, NUI Maynooth, 2007.

[100] J. W. Lamb, et al., "ALMA Receiver Optics Design," ALMA Memo Series 362, 2001.

[101] J. W. Lamb, "Optics Study for ALMA Receivers," ALMA Memo Series 359, 2001.

[102] T. S. Chu and R. H. Turrin, "Depolarization Properties of Offset Reflector Antennas," *IEEE Transactions on Antennas and Propagation*, vol. 21, no. 3, pp. 339-345, May 1973.

[103] C. Dragone, "Offset antennas with perfect pattern symmetry and polarization discrimisation," *Bell System Technology Journal*, vol. 57, no. 7, pp. 2663-2684, Sep. 1978.

[104] B. Lazareff, "Ideal Grid Generates Cross Polarization," in *20th International Symposium on Space Terahertz Technology*, Charlottesville, 2009, pp. P2-D.

[105] D. T. Greenwood, *Principles of Dynamics*, 2nd ed. New Jersey, U.S.A.: Prentice-Hall, Inc..

[106] K. Nakamura and M. Ando, "A Full-Wave Analysis of Offset Reflectot Antennas with Polarisation Grids," *IEEE Trans. Ant. Prop.*, vol. 36, no. 2, pp. 164-170, Feb. 1988.

[107] C. Dragone, "New Grids for Improved Polarization Diplexing of Microwaves in Reflector Antennas," *IEEE Trans. Ant. Prop.*, vol. AP-26, no. 3, pp. 459-463, May 1978.

[108] C. Dragone, "Method and Apparatus for Substantially Reducing Cross Polarized Radiation in Offset Reflector Antennas," N.J., U.S.A. Patent 4 114 535, Mar. 13, 1979.

[109] C. D. Wilson, N. Scoville, S. C. Madden, and V. Charmandaris, "High-Resolution Imaging of Molecular Gas and Dust in the Antennae (NGC 4038/39): Super Giant Molecular Complexes," *The Astrophysical Journal*, vol. 542, pp. 120-127, Oct. 2000.

[110] D. Narayanan, T. J. Cox, C. C. Hayward, J. D. Younger, and L. Hernquist. (2009, May) [Online]. arXiv:0905.2184v2

[111] ESO. (2000, Dec.) Science with ALMA. [Online]. http://www.vt-2004.org/sci/facilities/alma/science/papers/alma-science.pdf

[112] B. A. Wilking, "The Formation of Low Mass Stars," *Publ. Ast. Soc. Pac.* , vol. 101, no. 637, pp. 229-243, Mar. 1989.